Mathematical Modeling of Neuro-Vascular Coupling in Rat Cerebellum

Tina Rasmussen

Center for Mathematical Modeling of Physiological Processes
Department of Control Engineering
Institute of Electronic Systems
Aalborg University
Denmark

ISBN 87-90664-20-5
Doc. no. D-04-4791
November 2004

Copyright 2004 © Tina Rasmussen

This Ph.D. thesis was typeset using LaTeX2$_\varepsilon$ in `report` document class.
Graphs were made in MATLAB® from The MathWorks, Inc.
and in SPIKE2 from Cambridge Electronic Design Limited.
Drawings were made in XFIG.

Contents

Summary . . . xi
Sammenfatning . . . xiii

Nomenclature . . . xv

Preface **1**

Acknowledgments **2**

1 Introduction **3**
1.1 The Technical Field of Study . . . 3
1.2 Background and Motivation . . . 3
1.3 Objectives . . . 5
1.4 The Scientific Methods . . . 5
1.5 The State of the Art and Related Modeling Work . . . 6
1.5.1 Previous Modeling Work and the State of the Art . . . 6
1.5.2 Related Modeling Work . . . 8
1.6 Contributions . . . 10
1.7 Thesis Outline . . . 11

I Phenomenology **13**

2 Overview of the Neuro-Vascular System **14**

3 The Neuronal Subsystem **15**
3.1 General Cell Physiology . . . 15
3.1.1 The Cell Membrane . . . 15
3.1.2 Membrane Potentials . . . 15
3.2 The Physiology of the Nervous System . . . 18
3.2.1 The Nerve Cell . . . 18
3.2.2 Electrical Phenomena inside Nerve Cells . . . 18
3.2.3 Neurotransmission and Synaptic Integration . . . 20
3.3 The Cortex of Cerebellum . . . 22
3.3.1 The Neuronal Organization . . . 22
3.3.2 The Neuronal Function . . . 24

4 The Extracellular Space **26**
4.1 The Structure of the Extracellular Space . . . 26
4.2 The Extracellular and Intracellular Fluids . . . 26
4.2.1 The Extracellular Fluid . . . 26
4.2.2 The Intracellular Fluid . . . 26
4.3 The Role and Function of the Extracellular space . . . 27
4.3.1 The Role of the Extracellular space . . . 27
4.3.2 The Function of the Extracellular space . . . 27

5 The Vascular Subsystem **28**
5.1 The Constituents of the Blood . . . 28
5.2 The Mechanics of the Blood Flow and the Vascular Subsystem . . . 28
5.2.1 The Structure of the Vascular System . . . 28
5.2.2 The Capillary Function . . . 29
5.3 Neural Control . . . 30
5.3.1 The Innervation of the Vessels and the Heart . . . 30
5.3.2 Systemic Regulation Mechanisms . . . 30
5.4 Local Control . . . 30
5.4.1 Auto-Regulation . . . 30
5.4.2 Vasoactive Substances from Endothelium Cells . . . 31

6 Neuro-Vascular Coupling **32**
6.1 System Overview . . . 32
6.2 Do Astrocytes Contribute to Coupling? . . . 33
6.2.1 What are Astrocytes? . . . 33
6.2.2 Morphological Relationship . . . 33
6.2.3 Functional Coupling . . . 34
6.3 Putative Mediators of Neuro-Vascular Coupling . . . 35
6.3.1 NO . . . 35
6.3.2 Adenosine . . . 36
6.3.3 K^+ . . . 36
6.3.4 H^+ . . . 37
6.3.5 CO_2 . . . 37
6.3.6 Multiple Mediators? . . . 38
6.4 Suggested Mechanisms in Case of IO Stimulation . . . 38
6.5 Suggested Mechanisms in Case of PF Stimulation . . . 39
6.6 Comparison of the Two Systems . . . 39
6.7 Discussion of Neuro-Vascular Coupling . . . 39
6.7.1 Properties of the Subsystems and their Interrelations . . . 39
6.7.2 The Validity of the Findings . . . 39
6.7.3 Properties of Putative Mediators . . . 40
6.7.4 Specificity of Mediators . . . 40

7 The Experiments **42**
7.1 Rats as Experimental Objects . . . 42
7.2 Types of Experiments . . . 42
7.3 The Experimental Set-Up and Procedures . . . 43
7.3.1 Animal Preparation . . . 43
7.3.2 Data Acquisition Procedures . . . 43
7.4 Measured Signals . . . 45
7.4.1 Stimulus . . . 45
7.4.2 Field Potential . . . 46
7.4.3 Arterial Blood Pressure . . . 47
7.4.4 Cerebellar Blood Flow . . . 47

8 Summary of Phenomenology **49**

II Methodology **51**

9 Classification of Systems and Models **52**
9.1 Definition of System and Model . . . 52
9.2 Signal Types . . . 52
9.3 Classes of Systems and Models . . . 53
9.3.1 Static versus Dynamic Systems . . . 53
9.3.2 Time-Invariant versus Time-Varying Systems . . . 53

9.3.3 Linear versus Nonlinear Systems . . . 53
9.3.4 Change Oriented versus Discrete Event Driven Systems . . . 54
9.3.5 SISO, SIMO, MISO, and MIMO Models . . . 54
9.3.6 Non-Parametric versus Parametric Models . . . 54
9.3.7 Deterministic versus Stochastic Models . . . 54
9.3.8 Continuous versus Discrete Time Models . . . 54
9.3.9 Distributed versus Lumped Parameter Models . . . 55
9.3.10 Black-, Grey-, and White-Box Models . . . 55
9.4 Discussion of the Classification . . . 55

10 Models of Dynamic Linear Time-Invariant Systems 57
10.1 Discrete Time Model Structures . . . 57
10.1.1 General Discrete Transfer Function Model . . . 57
10.1.2 State-Space Representation of Transfer Functions . . . 58
10.2 Continuous Time Model Structures . . . 58
10.2.1 General Continuous Transfer Function Model . . . 58
10.2.2 State-Space Representations of Transfer Functions . . . 58
10.3 Digitization of Continuous Time Model Structures . . . 59
10.3.1 Numerical Integration . . . 59
10.3.2 Hold Equivalents . . . 59
10.4 The Parameter Vector . . . 60
10.5 Discussion of Models of Dynamic LTI Systems . . . 60

11 System Identification 61
11.1 How to Build Models . . . 61
11.2 What is System Identification? . . . 61
11.3 Structure Determination . . . 61
11.3.1 General Aspects of the Choice of Model Structure . . . 61
11.3.2 Determination of Black-Box Model Structures . . . 62
11.3.3 Determination of Grey-Box Model Structures . . . 62
11.4 Parameter Estimation . . . 62
11.4.1 Choice of Parameter Estimation Method . . . 62
11.4.2 The Prediction Error Method . . . 63
11.5 Iterative Search for the Minimum Point . . . 64
11.5.1 The Newton-Raphson Method . . . 64
11.5.2 The Gauss-Newton Method . . . 65
11.5.3 Computing the Derivative of the Prediction . . . 65
11.5.4 Implementation in MATLAB . . . 65
11.6 Identifiability . . . 66
11.6.1 Definition of Identifiability . . . 66
11.6.2 Identifiability of Black-Box Model Structures . . . 66
11.6.3 Identifiability of Grey-Box Model Structures . . . 66
11.6.4 Remarks concerning Identifiability . . . 67

12 Model Validation 68
12.1 How to Validate Models? . . . 68
12.2 Model Quality . . . 68
12.3 Model Fit . . . 68
12.4 Cross Validation . . . 69
12.5 Sensitivity to Parameters . . . 69
12.5.1 Choice of Model Structure . . . 70
12.5.2 The Parameter Dependent Model Error . . . 70
12.5.3 Relative Parameters and Normed Signals . . . 71
12.5.4 The Sensitivity Ellipsoid . . . 72
12.6 Parameter Accuracy . . . 73
12.6.1 Types of Errors: Variance and Bias . . . 73
12.6.2 Measures of Parameter Accuracy . . . 74

12.7 Discussion of Model Validation . . . 75
12.7.1 The Linear Output-Error Model Structure as a Special Case . . . 75
12.7.2 High Sensitivity is not Equivalent to Good Cross Validation . . . 76
12.7.3 The Origin of Bias Errors . . . 76

13 Summary of Methodology **77**

III Signal and System Analysis **79**

14 Signal Analysis **80**
14.1 Analysis of the Field Potential Signal . . . 80
14.1.1 Analysis of the Full Field Potential Signal . . . 80
14.1.2 Analysis of Field Potential Amplitudes . . . 82
14.1.3 Analysis of the Field Potential Durations . . . 83
14.1.4 Analysis of the Instantaneous Event Frequencies . . . 87
14.2 Analysis of the Cerebellar Blood Flow Signals . . . 89
14.2.1 Comparison of the Signals from the four LDF Probes . . . 89
14.2.2 Characteristic Times in the CBF Signal . . . 91
14.2.3 Influence of the Arterial Pulse on CBF . . . 91

15 System Analysis **95**
15.1 Choice of Input and Output Signals . . . 95
15.2 Transfer Function Estimation . . . 95
15.3 Choice of Resampling Factor . . . 96

16 Discussion of Analysis Results **102**
16.1 Choice of System to be Modeled . . . 102
16.2 Choice of Signals for System Modeling . . . 102
16.2.1 Input Signal . . . 102
16.2.2 Output Signal . . . 102
16.3 Signal Properties . . . 103
16.3.1 Input Signal . . . 103
16.3.2 Output Signal . . . 103
16.4 System Properties . . . 104

17 Conclusion on Analysis **105**
17.1 Conclusion on Signal Properties . . . 105
17.2 Conclusion on System Properties . . . 106
17.3 Conclusions w. r. t. System Modeling . . . 106
17.3.1 Signal Representations . . . 106
17.3.2 System Representations . . . 106

IV Linear Black-Box Models **107**

18 The Input Sampling Transform **108**
18.1 The Input Sampling Transform . . . 108
18.2 Choice of Model Structure . . . 108
18.3 Modeling the Full Time Series . . . 109
18.3.1 The Full Input-Output Data Series . . . 109
18.3.2 Results of Modeling the Full Time Series . . . 109
18.4 Modeling the Short Time Series . . . 114
18.4.1 The Short Input-Output Data Series . . . 114
18.4.2 Results of Modeling the Short Time Series . . . 115
18.5 Discussion of the Input Sampling Transform . . . 120

19 The Input Running Summation Transform **121**
19.1 Review of the Notion of a Running Summation . . . 121
19.2 The Input Running Summation Transform . . . 121
19.3 The Model Structure . . . 122
19.4 Modeling the Full Time Series . . . 122
19.4.1 The Full Input-Output Data Series . . . 122
19.4.2 Results of Modeling the Full Time Series . . . 125
19.5 Modeling the Short Time Series . . . 128
19.5.1 The Short Input-Output Data Series . . . 128
19.5.2 Results of Modeling the Short Time Series . . . 128
19.6 Discussion of the Input Running Summation Transform . . . 133

20 Discussion of Linear Black-Box Models **134**
20.1 The Origin of the Model Deficiencies . . . 134
20.1.1 Properties of the Linear Input Transforms . . . 134
20.1.2 Equivalence of Transfer Functions . . . 135
20.1.3 How to Improve the Model Structure? . . . 135
20.1.4 Can we Exclude that the System is Intrinsically Linear? . . . 136
20.2 Exclusion of System Dynamics . . . 137
20.3 Comparison of Sampling Transform with Running Summation Transform . . . 137
20.4 Comparison with Earlier Modeling Attempts . . . 138
20.5 Comments upon the Applied Methodology . . . 138

21 Conclusion on Linear Black-Box Models **139**
21.1 System Properties . . . 139
21.2 Conclusions with Respect to System Modeling . . . 139

V Grey-Box Models **141**

22 Main Ideas for Grey-Box Models **142**
22.1 Subsystems . . . 142
22.2 Measured and Non-Measured Variables . . . 142
22.3 Time Scales . . . 143
22.3.1 Linear Couplings . . . 144
22.3.2 Nonlinear Couplings . . . 144
22.4 Information Content . . . 144
22.5 Detrending and Scaling of Signals . . . 145
22.6 Discussion of Main Ideas . . . 145
22.7 Conclusion on Main Ideas . . . 147

23 A Linear Grey-Box Model **148**
23.1 The Grey-Box Dynamics Model . . . 148
23.1.1 The Dynamics Model . . . 148
23.1.2 Motivation for the Dynamics Model . . . 148
23.2 Choice of Input Transform . . . 149
23.3 A Linear State-Space Model . . . 149
23.3.1 The Linear State-Space Model Structure . . . 149
23.3.2 The Parameter Vector . . . 150
23.4 Identifiability of the State-Space Model . . . 150
23.5 Choice of Noise Model . . . 151
23.6 Overview of the Linear Grey-Box Model . . . 151
23.7 The System Identification Task . . . 152
23.7.1 Implementation of the Model in MATLAB . . . 152
23.7.2 Information on Experiments and Input-Output Data Sets . . . 152
23.8 The Model Results . . . 153
23.8.1 Model Fit . . . 153

23.8.2 Cross Validation . . . 156
23.9 Conclusion on the Linear Grey-Box Model . . . 156

24 Ideas for Nonlinear Grey-Box Models 157
24.1 Motivation and Physiological Picture . . . 157
24.2 The Input Weight Transform . . . 157
24.3 Discussion of Ideas for Nonlinear Grey-Box Models . . . 158

25 The Input Threshold Transform 159
25.1 The Input Threshold Transform . . . 159
25.2 Implementation of the Model in MATLAB . . . 159
25.3 Model Results . . . 161
25.3.1 Model Fit . . . 161
25.3.2 Cross Validation . . . 164
25.3.3 Sensitivity to the Parameter FPA_0 . . . 164
25.4 Conclusion on the Input Threshold Transform . . . 164

26 The Input Kink Transform 166
26.1 The Input Kink Transform . . . 166
26.2 Implementation of the Model in MATLAB . . . 167
26.3 Model Results . . . 167
26.3.1 Model Fit . . . 167
26.3.2 Cross Validation . . . 171
26.3.3 Sensitivity to the Parameters FPA_0 and α_w . . . 171
26.4 Discussion of the Input Kink Transform . . . 175
26.5 Conclusion on the Input Kink Transform . . . 175

27 Properties of the Grey-Box Model 176
27.1 Time- and Frequency-Domain Model Properties . . . 176
27.1.1 Time-Domain Model Properties . . . 176
27.1.2 Frequency-Domain Model Properties . . . 181
27.2 Sensitivity to Parameters . . . 184
27.3 The Non-Measured Signal $\widetilde{n}(t)$ . . . 186
27.3.1 Interpreting the State Variable $\widetilde{n}(t)$ . . . 186
27.3.2 State Estimator Design — Noise-Free Measurements . . . 186
27.3.3 State Estimator Design — Noise-Corrupted Measurements . . . 188
27.3.4 Estimator Design for the Grey-Box Model . . . 189
27.3.5 Implementation in MATLAB . . . 189
27.3.6 Time Series of $\widetilde{n}(t)$ . . . 189
27.3.7 Comparison to Measurements of $c(NO)$ . . . 191

28 Discussion of Grey-Box Models 192
28.1 Overview of Grey-Box Models . . . 192
28.2 Preconditions for the Grey-box Model . . . 193
28.3 Interpretations of the Grey-Box Model . . . 196
28.3.1 Frequency versus Amplitude . . . 196
28.3.2 Physiological Origin of the Threshold . . . 196

29 Conclusion on Grey-Box Models 197

VI Semi-Physical Models 199

30 Semi-Physical SISO Models 200
30.1 The Idea of Semi-Physical SISO Modeling . . . 200
30.2 The SISO Model Structures . . . 200
30.3 Implementation of the SISO Models in MATLAB . . . 200
30.4 A SISO Model with The Input Sampling Transform . . . 201

30.4.1 The Input Sampling Transform . . . 201
30.4.2 Model Results . . . 201
30.5 A SISO Model with the Input Threshold Transform . . . 203
30.5.1 The Input Threshold Transform . . . 203
30.5.2 Model Results . . . 203
30.6 A SISO Model with the Input Kink Transform . . . 209
30.6.1 The Input Kink Transform . . . 209
30.6.2 Model Results . . . 209
30.7 Discussion of Semi-Physical SISO Models . . . 215
30.8 Conclusion on Semi-Physical SISO Models . . . 215

31 A Semi-Physical MISO Model 216
31.1 Physiological and Mathematical Motivation . . . 216
31.1.1 The Idea of Two Mediators . . . 216
31.1.2 Expected Performance Improvement . . . 216
31.2 The Input Two-Thresholds Transform . . . 217
31.3 Implementation of the MISO Model in MATLAB . . . 217
31.4 Model Results . . . 218
31.4.1 Model Fit . . . 218
31.4.2 Cross Validation . . . 221
31.4.3 Parameter Sensitivity . . . 223
31.5 Properties of the MISO Model . . . 227
31.5.1 Time-Domain Model Properties . . . 227
31.5.2 Frequency-Domain Model Properties . . . 234
31.6 Discussion of the Input Two-Thresholds Transform . . . 238
31.6.1 Mathematical Explanation of the Dips . . . 238
31.6.2 When do the Two Mediators Contribute to Coupling? . . . 238
31.6.3 Performance of the MISO Model . . . 238
31.7 Conclusion on the Input Two-Thresholds Transform . . . 239

32 Discussion of Semi-Physical Models 240
32.1 Selection of Model Structure . . . 240
32.2 The Origin of the Deficiencies of the MISO Model . . . 240

33 Conclusion on Semi-Physical Models 241

VII Concluding Part 243

34 Discussion of Research Results 244
34.1 Which Kind of Neuronal Activity is Coupled to Blood Flow? . . . 244
34.2 How many Mediators are there? . . . 244
34.3 The Origin of Model Deficiencies . . . 245
34.3.1 Variation in Experimental Conditions . . . 245
34.3.2 Technical Limitations . . . 245
34.3.3 The Influence of 50 Hz Noise . . . 245
34.3.4 The Model Structure is not Sufficiently Large . . . 246

35 Suggestions for Further Research 247
35.1 Basic Research: New Questions . . . 247
35.2 Experimental Work . . . 247
35.2.1 Experimental Methods . . . 247
35.2.2 Experiment Design . . . 248
35.3 Modeling and Theoretical Work . . . 248
35.3.1 Modeling Methods . . . 248
35.3.2 A Model for the Case of Parallel Fiber Stimulation . . . 248

36 Applications and Perspectives **250**
36.1 Scanning Tool . . . 250
36.2 Diagnostic Tool . . . 250

37 Conclusion on Research Results **252**
37.1 Conclusion w.r.t. Methodology . . . 252
37.2 Conclusion w.r.t. Signal Properties . . . 252
37.3 Conclusion w.r.t. Model Properties . . . 253
37.4 Conclusion w.r.t. System Properties . . . 254

VIII Bibliography and Appendices **255**

Bibliography **256**

A The Raw Data **262**
A.1 Overview of Experimental Data . . . 262
A.1.1 Inferior Olive Stimulation Experiments . . . 262
A.1.2 Parallel Fiber Stimulation Experiments . . . 262
A.2 Description of the Data Files . . . 265
A.2.1 Stimulus (Channel no. 3) . . . 265
A.2.2 Field Potential (Channel no. 1) . . . 265
A.2.3 Arterial Blood Pressure (Channel no. 6) . . . 265
A.2.4 Cerebellar Blood Flow (Channel no.'s 7–10) . . . 265
A.3 Selected Extracts of Data Files . . . 266
A.3.1 Stimulus . . . 266
A.3.2 Field Potential . . . 266
A.3.3 Arterial Blood Pressure . . . 270
A.3.4 Cerebellar Blood Flow . . . 271

B Post-Treatment of Raw Data **272**
B.1 Stimulation Frequency . . . 272
B.2 Field Potential Amplitude . . . 272
B.3 Field Potential Duration . . . 273
B.4 Relative Cerebellar Blood Flow . . . 274
B.5 Selection of Samples for Plots . . . 277

C Frequency Domain Considerations **279**
C.1 Considerations concerning Functions . . . 279
C.1.1 Continuous-Time Functions . . . 279
C.1.2 Discrete-Time Functions . . . 279
C.1.3 Relationship Between Functions of s and z . . . 279
C.2 Considerations concerning Operators . . . 279
C.2.1 Continuous-Time Operators . . . 279
C.2.2 Discrete-Time Operators . . . 279
C.3 Connections between Functions and Operators . . . 280
C.3.1 Continuous-Time Descriptions . . . 280
C.3.2 Discrete-Time Descriptions . . . 280

Summary

This Ph.D. thesis investigates the mechanisms of neuro-vascular coupling in cortex of cerebellum in healthy male Wistar rats. Specifically, the focus is on the blood flow response to activity in the neurons called climbing fibers. These fibers originate from the inferior olive in the brain stem. In experiments prior to this Ph.D. project rats were anesthetized and given a muscle-relaxing drug. A climbing fiber was activated by stimulating the inferior olive electrically. The extracellularly measured electrical field potential was chosen as indicator of neuronal activity, and the blood flow was measured in nearby capillaries by laser-Doppler flowmetry. The main method in this thesis is system identification, which is a way of constructing parametric mathematical models of a dynamic system by using measurements from the system in order to fit the model's properties to those of the system.

The thesis starts with two introductory parts: **Part I: Phenomenology** presents the research object: The rat cerebellum. Firstly, well-established information about the physiology of the subsystems (the neuronal subsystem, the extracellular space, and the vascular subsystem) of cerebellum is presented. Secondly, research results as well as hypotheses concerning how neuro-vascular coupling is mediated, are presented. Finally, the experiments are described and the measurements obtained during the experiments are presented. **Part II: Methodology** introduces the methods to be applied for mathematical modeling of the neuro-vascular system. This part centers on two subjects: The first is system identification, which is a way of constructing parametric models of a dynamic system by means of measurements of its response (output) to a certain disturbance (input). The prediction error method is applied for parameter estimation. The second subject is model validation, which is the act of assessing the model quality.

The remainder of the thesis presents the outcome of the present Ph.D. study: **Part III: Signal and System Analysis** shows that the field potential signal consists of quiet periods interrupted by fast time-localized excitations (so-called events), which can be well represented by their amplitudes (called field potential amplitudes), whereas the blood flow signal varies on a much slower time scale. The field potential amplitude signal depends dynamically on the stimulation frequency. It also shows that the neuro-vascular system is dynamic. The sampling rate of signals will be reduced by a factor, which is chosen in the end of this part.

The following parts investigate neuro-vascular coupling through application of the methodology to the measurements. Each of the parts investigates an idea of mathematical and/or physiological origin: **Part IV: Linear Black-Box Models** investigates the idea of avoiding *a priori* assumptions. Three features of the vascular response to neuronal activity with various frequencies cannot be explained by these linear models: Frequency saturation and dips during short stimulation sequences, and overgrowth during prolonged stimulation sequences. **Part V: Grey-Box Models** applies the principle of constructing the model structure from information about and hypotheses of how neuro-vascular coupling is mediated. The frequency saturation is explained from a hypothesis that only field potential amplitudes larger than a certain threshold indicate neuronal activity strong enough to cause the release of a vasodilatory chemical substance and thereby to cause blood flow increases. **Part VI: Semi-Physical Models** preserves the feature of the grey-box models which explains the frequency saturation but strips off the rest of the physiological interpretations. That is, the ability of neuronal activity above threshold to elicit vascular responses is included, but the hypothesis of a single vasodilatory substance is exchanged with a general linear dynamic coupling. The first result is that the estimated linear order of the neuro-vascular system is two. Secondly, a third-order linearity is considered, thus leaving room for two substances mediating the coupling. The hypothesis that each of the two vasoactive substances is characterized by its own threshold for release explains the frequency saturation as well as the dips in the vascular response.

Part VII: Concluding Part first provides a discussion of the research results. Afterwards prospective applications and other perspectives are considered. Furthermore, some suggestions for future research objectives and activities are given. Finally, it is concluded that the neuro-vascular system is dynamic,

non-linear, and time-invariant. The final model, which is termed the *3-2-1 model*, possesses the following properties: Its linear order is equal to three. It is based on the hypotheses that neuro-vascular coupling is mediated by two vasoactive chemical substances, and that the action of each of them requires the neuronal activity to overcome a threshold described by one parameter.

Part VIII: Bibliography and Appendices first gives the list of references. The appendices are concerned with the raw data, the post-processing procedures, and frequency-domain considerations, respectively.

Sammenfatning

Denne Ph.D.-afhandling udforsker mekanismerne bag neuro-vaskulær kobling i lillehjernens bark hos raske Wistar rotter af hankøn. Mere specifikt fokuseres der på blodgennemstrømningens reaktion på aktivitet i de neuroner, der kaldes klatrefibre. Disse fibre udgår fra den olivenformede kerne i hjernestammen. I eksperimenter, som er udført før dette Ph.D.-projekt, blev rotter lagt i narkose og givet et muskel-afslappende medikament. En klatrefiber blev aktiveret ved at stimulere den olivenformede kerne elektrisk. Feltpotentialet, målt extracellulært, blev valgt som indikator for nervecelle aktivitet, og blodgennemstrømningen blev målt i nærliggende kapillærer vha. laser-Doppler flowmåling. Den centrale metode i denne afhandling er systemidentifikation, som er en metode til at konstruere parametriske matematiske modeller af et dynamisk system ved at bruge målinger fra systemet til at tilpasse modellens egenskaber til systemets.

Afhandlingen starter med to indledende dele: **Part I: Phenomenology** præsenterer forskningsobjektet: Rottens lillehjerne. Først præsenteres velkendt information om fysiologien af lillehjernens delsystemer (det neuronale delsystem, extracellulærrummet og det vaskulære delsystem). Derefter præsenteres forskningsresultater såvel som hypoteser vedrørende hvordan neuro-vaskulær kobling formidles. Til sidst beskrives eksperimenterne, og de målinger, som blev registreret i løbet af eksperimenterne, præsenteres. **Part II: Methodology** introducerer de metoder, som vil blive anvendt til matematisk modellering af det neuro-vaskulære system. Denne del er centreret om to emner: Det første er systemidentifikation, som er en metode til at konstruere parametriske modeller af et dynamisk system vha. målinger af dets respons (output) på en given forstyrrelse (input). Forudsigelsesfejl-metoden er anvendt til parameter estimering. Det andet emne er model validering, som er det at vurdere model kvaliteten.

Resten af afhandlingen præsenterer udbyttet af dette Ph.D. studie: **Part III: Signal and System Analysis** viser, at feltpotential-signalet består af stille perioder afbrudt af hurtige, tidsligt lokale, anslag (såkaldte begivenheder), som passende kan repræsenteres af deres amplitude (kaldet feltpotential-amplituder), hvorimod blodgennemstrømnings-signalet varierer på en meget langsommere tidsskala. Feltpotential-amplituden afhænger dynamisk af stimulations-frekvensen. Delen viser også at det neuro-vaskulære system er dynamisk. Signalers sampling frekvens vil blive reduceret med en faktor, som bliver valgt i slutningen af denne del.

De følgende dele undersøger neuro-vaskulær kobling ved anvendelse af metodedelen på målingerne. Hver af delene undersøger en ide af matematisk og/eller fysiologisk oprindelse: **Part IV: Linear Black-Box Models** undersøger ideen om at undgå *a priori* antagelser. Tre egenskaber ved det vaskulære respons på nervecelle-aktivitet med forskellige frekvenser kan ikke forklares af disse lineære modeller: Frekvens-mætning og dyk ved kortvarende stimulations-sekvenser, og kraftig vækst ved forlænget varighed af stimulationen. **Part V: Grey-Box Models** anvender princippet om at konstruere model strukturen ud fra information og hypoteser om hvordan neuro-vaskulær kobling formidles. Frekvens-mætningen forklares af en hypotese om at kun feltpotential-amplituder, som er større en en vis tærskel, indikerer nervecelle-aktivitet, som er stærk nok til at forårsage frigørelse af et kar-udvidende kemisk stof og derved forårsage øgning af blodgennemstrømningen. **Part VI: Semi-Physical Models** bevarer de egenskaber ved grå-kasse modellerne, som forklarer frekvens-mætningen, men fjerner resten af de fysiologiske fortolkninger. Det vil sige, at den evne, som feltpotential-amplituder over en vis størrelse har til at forårsage ændringer i blodgennemstrømningen, inkluderes, mens hypotesen om et enkelt kar-udvidende stof udskiftes med en generel lineær dynamisk kobling. Det første resultat er, at den estimerede lineære orden er to. Derefter betragtes en tredie-ordens linearitet, hvilket giver plads til to stoffer, som formidler koblingen. Hypotesen, om at hver af de kar-aktive stoffer er karakteriseret ved sin egen tærskel for frigivelse, forklarer frekvens-mætningen såvel som dykene i det vaskulære respons.

Part VII: Concluding Part diskuterer først forsknings-resultaterne. Derefter betragtes mulige anvendelser samt andre perspektiver. Desuden gives nogle forslag til fremtidige forskningsmål og

-aktiviteter. Til sidst konkluderes det at det neuro-vaskulære system er dynamisk, u-lineært og tids-invariant. Den endelige model, som kaldes for *3-2-1 modellen*, har følgende egenskaber: Dens lineære orden er tre. Den er baseret på hypotesen om, at neuro-vaskulær kobling er formidlet af to kar-aktive kemiske stoffer, og at aktivering af hver af dem kræver at nervecelle-aktiviteten overskrider en tærskel, som er beskrevet ved én parameter.

Part VIII: Bibliography and Appendices indeholder først reference-listen. Tillæggene vedrører rådata, efterbehandlings-procedurer og frekvens-domæne betragtninger.

Nomenclature

Medical Terminology

afferent	carrying impulses towards a center [91]
arachnoid membrane	the thin, delicate, intermediate membranes of the meninges that enclose the brain and spinal cord [91]
astrocyte	comparatively large neuroglial cell type
bolus	a concentrated mass of a substance given rapidly intravenously [91]
caudal	pertaining to any tail-like structure [91]
cerebellum	a large dorsally projecting part of the brain concerned especially with the coordination of muscles and the maintenance of bodily equilibrium, situated between the brain stem and the back of the cerebrum [69]
cerebrospinal fluid	a water cushion protecting the brain and spinal cord from physical impact [91]
cerebrum	an enlarged anterior or upper part of the brain which is considered to be the seat of conscious mental processes [69]
craniotomy	incision through the cranium [91]
distal	farthest from the center [91]
dura, dura mater	a fibrous connective tissue membrane, the outermost of the meninges covering the spinal cord and brain [91]
epilepsy	a recurrent paroxysmal disorder of cerebral function marked by sudden, brief attacks of altered consciousness, motor activity, or sensory phenomena [91]
femoral	pertaining to the thigh bone (femur) [91]
glia	the neuroglia, the non-nervous or supporting tissue of the brain and spinal cord [91]
in vitro	in glass, as in a test tube; refers to a biological process studied outside an intact living organism [73]
in vivo	in the living body or organism; refers to a biological process studied within an intact living organism [73]
inferior olive	inferior olivary nucleus, a large oval body consisting of a convoluted sheet of grey matter enclosing white matter lying in the ventral part of the medulla oblongata and forming part of the reticular system; it gives rise to fibers of the olivocerebellar tract [91]
intraperitoneally	between the layers of the serous membrane lining the abdominal cavity (peritoneum) [91]
leukocyte	a white blood cell [91]
pial surface	the outer side of the pia mater (the innermost of the three meninges) [91]
proximal	nearest the center or point of reference [91]
rectal	pertaining to the rectum (the lower part of the large intestine) [91]

sagittal plane	a vertical plane dividing the body into right and left halves [91]
spreading depression	a rapid and nearly complete depolarization of a sizeable population of brain cells with massive redistribution of ions between intracellular and extracellular compartments, which evolves as a regenerative, "all-or-none" type process and propagates in the manner of a wave through gray matter [89]
trachea	wind-pipe [91]
varicosity	swelling along an axon from which transmitter is liberated [73]

Medical Acronyms

CF	climbing fiber
EPSP	excitatory post-synaptic potential
IO	inferior olive
IPSP	inhibitory post-synaptic potential
PC	Purkinje cell
PF	parallel fiber
PSP	pre-synaptic potential

Chemical Acronyms and Symbols

A	adenosine; a nucleotide containing adenine ($C_5H_5N_5$) and ribose ($C_5H_{10}O_5$) [91]
ADP	adenosine diphosphate
ATP	adenosine triphosphate
Ca^{2+}	calcium ion
$cGMP$	cyclic guanidine monophosphate
CO_2	carbon dioxide
$eNOS$	endothelial isoform of NOS
$GABA$	gamma-aminobutyric acid, an amino acid inhibitory transmitter in the central nervous system [91]
H^+	proton, hydrogen ion
$iNOS$	immunological isoform of NOS
K^+	potassium ion
$nNOS$	neuronal isoform of NOS
NO	nitric oxide, nitric monoxide; a gas; a multifaceted biomolecule: NO is responsible for the basal vasomotor tone, and has been implied in neuronal transduction, synaptic plasticity, neurotoxicity, and coupling of cerebral blood flow to metabolism; nitric oxide is produced not only by the vascular endothelium but also by neurons and by astrocytes [28]
NOS	nitric oxide synthase, an enzyme
sGC	soluble guanylate cyclase

Chemical Terminology

agar	a product which is widely used as a solidifying agent because it is unaffected by bacterial enzymes [91]
hydrolysis	any reaction in which water is one of the reactants, more specifically the combination of water with a salt to produce an acid and a base, one of which is more dissociated than the other [91]
hydrophilic	having a relatively high water solubility; polar [73]

hydrophobic	having a relatively low water solubility; nonpolar [73]
lactic acid	a clear odor-less hygroscopic syrupy carboxylic acid found in sour milk and in many fruits
Ringer solution	a saline solution of recently boiled distilled water containing $NaCl$, KCl, and $CaCl$ [91]

Technical Terminology

bin	the time axis is divided into minor intervals, bins, of a certain duration; events in a signal are collected into these bins
event-sampling	registration of the individual events in a signal
prediction error	error on output predicted from earlier inputs and outputs as well as current input
resample	to change the sampling interval of a signal representation (The MATLAB resample function can change the sampling rate for a sequence to any rate that is a ratio of two integers p and q times the original rate. The length of the resulting sequence is p/q times the length of the original sequence. A low-pass filter is applied to the original signal to prevent aliasing during resampling [55, (p. 1-90)].)
sample	to register a signal at instants being separated by a certain constant time interval (the sampling interval)

Technical Acronyms

LASER	light amplification by stimulated emission of radiation
LDF	laser Doppler flowmetry
MISO	multiple-input-single-output model
SISO	single-input-single-output model

Constants

e	the charge of an electron, $e = 1.603 \cdot 10^{-19}\ C$
F	Faradays constant, $F = N_A \cdot e = 9.65 \cdot 10^4\ \frac{C}{mol}$
k_B	Boltzmann's constant, $k_B = 1.38 \cdot 10^{-23}\ \frac{J}{K}$
R	the gas constant, $R = N_A \cdot k_B = 8.31\ \frac{J}{mol \cdot K}$

Mathematical Symbols

$\arg\min f(x)$	the values of the argument x which minimize the function f
$\mathbb{N}$	the set of natural numbers, $\mathbb{N} = \{1, 2, 3, \ldots\}$, $\mathbb{N}_0 = \{0\} \cup \mathbb{N}$
$\mathbb{R}$	the set of real numbers
$\overline{E}\{\cdot\}$	averaging over samples, i.e. time averaging
$\star$	complex conjugation, $(x + iy)^\star = x - iy$
$cov(\theta_N)$	parameter covariance matrix, $cov(\theta_N) = \overline{E}\left\{(\theta_N - \theta_0)(\theta_N - \theta_0)^T\right\}$
$F(s)$	Laplace transformed function, $F(s) = \mathcal{L}\{f(t)\}$
$F(z)$	z-transformed function, $F(z) = \mathcal{Z}\{f(k \cdot \tau)\}$
$f''(\theta)$	the second derivative / Hessian of the function f, $f''(\theta) = \frac{\partial^2 f}{\partial\theta\partial\theta^T}$
$f'(\theta)$	the gradient of the function f, $f'(\theta) = \frac{\partial f}{\partial\theta}$
i	imaginary unit, $i = \sqrt{-1}$
$\mathbf{I}_n$	n-by-n identity matrix

$\mathbf{v}^T, \mathbf{M}^T$	transposed vector / matrix
$\mathbf{x}^T\mathbf{y}$	scalar product, $\mathbf{x}^T\mathbf{y} = \sum_i x_i y_i$
$\mathbf{x}\mathbf{y}^T$	the matrix with elements $\left\{\mathbf{x}\mathbf{y}^T\right\}_{ij} = x_i y_j$

Other Symbols

$[X]_e$	concentration of the chemical substance X in the extracellular space, $[\,[X]_e\,] = mol/ml$
α_w	kink slope (slope of weight function), $[\alpha_w] = mV^{-1}$
ΔCBF	model error
ΔCBF_{pp}	peak-to-peak value of model error
$\Delta\widetilde{\theta}_{eq,ri}$	maximum value of equivalent error of parameter θ_{ri}, $\Delta\widetilde{\theta}_{eq,ri} = \widetilde{\theta}_{eq,ri\,\max}$
$\Delta\widetilde{\theta}_{N,ri\,\mathrm{tot}}$	total relative parameter uncertainty, $\Delta\widetilde{\theta}_{N,ri\,\mathrm{tot}} = \widehat{\sigma}(\theta_{N,ri}) + \Delta\widetilde{\theta}_{eq,ri}$
ϵ	prediction error, $\epsilon = y - \widehat{y}$
ϵ_{pn}	normed parameter dependent model error, $\epsilon_{pn} = \frac{\epsilon_p}{y_{RMS}}$
ϵ_p	parameter dependent model error
ω	angular frequency, $[\omega] = rad/s$
ω_d	imaginary part of pole, $[\omega_d] = rad/s$
ω_n	undamped natural frequency, $[\omega_n] = rad/s$
$\overline{\epsilon}$	model error, $\overline{\epsilon} = y - y_m$
$\overline{\epsilon}_{RMS}$	root-mean-square model error
ϕ	electric potential, $[\phi] = V$
Ψ	model gradient, $\Psi = \frac{\partial y_m}{\partial \theta}$
ψ	derivative of prediction, $\psi = \frac{\partial \widehat{y}}{\partial \theta}$
σ	real part of pole
τ	sampling interval, $[\tau] = s$
θ	parameter vector, $\dim(\theta) = d$; Heaviside / unit step function: $\theta(x < 0) = 0, \theta(x \geq 0) = 1$
θ_0	limit estimate, $\theta_N \longrightarrow \theta_0$ for $N \longrightarrow \infty$
θ_N	output error estimate of parameter vector based on N samples, $\theta_N = \arg\min C_N(\theta)$
$\theta_{ri\,\max}$	maximum value of the relative parameter vector on the sensitivity ellipsoid, $\theta_{ri\,\max} = L^{-1}\theta_{i\,\max}$
θ_r	relative parameter vector, $\theta_r = L^{-1}\theta$
$\widehat{\sigma}(\theta_{N,i})$	estimate of the spread of the i'th parameter estimate $\theta_{N,i}$
$\widehat{\theta}$	prediction error estimate of parameter vector, $\widehat{\theta} = \arg\min_\theta V_N(\theta)$
$\widehat{\theta}^{(i)}$	the i'th iteration in a numerical search for the prediction error estimate $\widehat{\theta}$
$\widehat{y}$	(one-step ahead) prediction of y
$\widetilde{\theta}_{eq,r}$	equivalent parameter error

$\widetilde{\theta}_{ri\max}$	maximum value of the relative parameter error on the sensitivity ellipsoid, $\widetilde{\theta}_{ri\max} = \theta_{ri\max} - 1$
$\widetilde{\theta}_r$	relative parameter error, $\widetilde{\theta}_r = \theta_r - 1$
$\widetilde{H}$	approximated Hessian of criterion function, $\widetilde{H}(\theta) = \frac{1}{N}\sum_{i=1}^{N} \Psi(t_i,\theta)\Psi(t_i,\theta)^T$
ζ	damping ratio, $\zeta = \sqrt{1 - {\omega_d}^2/{\omega_n}^2}$
BP	arterial blood pressure, $[BP] = mmHg$
$c(X)$	concentration of the chemical substance X, $[c(X)] = mol/ml$
$c_B(X)$	baseline concentration of the chemical substance X, $[c_B(X)] = mol/ml$
C_N	criterion function, $C_N(\theta) = \frac{1}{2N}\sum_{i=1}^{N} \overline{\epsilon}(t_i,\theta)^2$
CBF	relative perfusion, relative cerebellar blood flow
CBF_B	baseline perfusion, baseline cerebellar blood flow; the perfusion level which is reached during periods of no stimulation after transients have died out, $[CBF_B] = PU$
CSD	cross spectral density
CSM	cross spectrum magnitude
d	dimension of the parameter vector, $d = \dim(\theta)$
e	white noise
f	frequency, $[f] = Hz$
f_{Nyq}	Nyquist frequency, $[f_{Nyq}] = Hz$
f_s	stimulation frequency, $[f_s] = Hz$
FP	field potential, $[FP] = mV$
FPA	field potential amplitude, $[FPA] = mV$
FPA_0	threshold position, kink position, $[FPA_0] = mV$
FPA_1, FPA_2	threshold positions, $[FPA_1] = [FPA_2] = mV$
FPA_{pp}	pre-processed field potential amplitude, $[FPA_{pp}] = mV$
FPD	field potential duration, $[FPD] = s$
$G(s)$	transfer function from input u to output y
G, G_τ	continuous / discrete transfer functions
$G_{nu}(s)$	transfer function from input u to state variable n
$G_{yn}(s)$	transfer function from state variable n to output y
H	Hessian of criterion function, $H(\theta) = \frac{\partial^2 C_N(\theta)}{\partial\theta\partial\theta^T}$
H, H_τ	continuous / discrete noise models
H_{rn}	relative normed Hessian, $H_{rn} = \frac{LHL}{{y_{RMS}}^2}$
H_r	relative Hessian, $H_r = LHL$
$L = diag(\theta_N)$	a quadratic d-by-d matrix with the vector θ_N in the diagonal and zeros otherwise
N	number of samples in a time series
n	linear order of state-space model, $n = \dim(\mathbf{x})$; preprocessed NO concentration deviation, $n(t) = \{c(NO)(t) - c_B(NO)\}_{pp}$

n_k	transport delay in units of the sampling interval τ
NSR	noise-to-signal ratio, $NSR = 100 \cdot \frac{\bar{\epsilon}_{RMS}}{y_{RMS}}$, $[NSR] = \%$
P	permeability, $[P] = \frac{m}{s}$
p	time derivative operator, $p = \frac{d}{dt}$
PSD	power spectral density
PSM	power spectrum magnitude
q	forward shift operator, $qx(t) = x(t + \tau)$
R	the ratio of the minor axis of the sensitivity ellipsoid over the major axis, $R = \frac{S_{\max}}{S_{\min}}$
R_i	the ratio of the sensitivity to the i'th parameter over the minimum sensitivity to the i'th parameter, $R_i = \frac{S_i}{S_{i\,\min}}$
$S_{\max}$,$S_{\min}$	maximum / minimum sensitivity of $\epsilon_{p,RMSn}(\theta_r)$
$S_{i\,\max}$, $S_{i\,\min}$	maximum / minimum sensitivity of $\epsilon_{p,RMSn}(\theta_r)$ to the relative parameter θ_{ri}
S_i	sensitivity of $\epsilon_{p,RMSn}(\theta_r)$ to the relative parameter θ_{ri}
T	summation time, $[T] = s$; temperature, $[T] = K$
t	time, $[t] = s$
t_d	transport delay, $[t_d] = s$
t_i	time of occurrence of the i'th sample, $[t_i] = s$
t_j	time of occurrence of the j'th event, $[t_j] = s$
u	input
V	electric potential, $[V] = V$
V_N	loss function, $V_N(\theta) = \sum_{i=1}^{N} \epsilon(t_i, \theta)^2$
w	weight function, $w(FPA) \in [0; 1]$
y	output
y_{mn}	normed model output, $y_{mn} = \frac{y_m}{y_{RMS}}$
y_m	model output (result of a noise-free simulation of the model)
y_{RMS}	root-mean-square output, $y_{RMS} = \sqrt{\frac{1}{N} \sum_{i=1}^{N} y(t_i)^2}$
z	valence
$\mathbf{F}, \mathbf{G}, \mathbf{H}, J, \mathbf{K}$	matrices in a state-space model
$\mathbf{x}$	state vector, $\dim(\mathbf{x}) = n$

Preface

This thesis is submitted to the Faculty of Engineering and Science at Aalborg University, Denmark, in partial fulfillment of the requirements for the degree of Doctor of Philosophy in Biomedical Science and Engineering. The research has been carried out in the period from February 1999 to May 2004 at the Department of Control Engineering, Institute of Electronic Systems, Faculty of Engineering and Science, Aalborg University, Denmark under the supervision of Professor Jakob Stoustrup, Reading Professor Morten Knudsen, and Associate Professor Torben Knudsen from the Department of Control Engineering, and Professor Martin Lauritzen from the Department of Medical Physiology, Faculty of Health Sciences, University of Copenhagen, Denmark.

The research object is neuro-vascular coupling, i.e., the coupling between neuronal activity and the resulting change in blood flow in capillaries nearby, in cortex of cerebellum in healthy male Wistar rats. The motivation for this thesis is a wish to contribute to a deeper understanding of the mechanisms responsible for the coupling through application of mathematical modeling — especially system identification methods — to experimental data from the neuro-vascular system. Therefore, the strategy will be to present not only the final models, but also the steps taken towards them. In other words, to present not only the improvement of the model performance as the work progresses, but most importantly, to present the hypotheses and assumptions — whether of physiological or mathematical origin — and the results of incorporating them into the models. The scope of the thesis is further described in *Chapter 1: Introduction*.

The thesis intents to bridge the rather large gap between physiological descriptions of cerebellum and mathematical modeling of dynamic systems. This is aimed at in two ways: Firstly, by presenting textbook material about the central elements of the two areas. This is done in *Part I: Phenomenology* and *Part II: Methodology*. Secondly, by supplementing the mathematical models with diagrams and text. Nevertheless, readers being familiar with mathematical analysis (functions and ordinary differential equations), linear algebra, and numerical analysis may benefit more from reading the thesis.

Throughout the thesis only the interesting parts of the time series, that is, the parts where the neuro-vascular system behaves dynamically, will be plotted. Therefore, in most plots only selected samples are shown. Appendix B.5 on page 277 describes how samples have been selected for plotting. It will be emphasized whenever all samples are shown.

Symbols like [17] and [17, 34] refer to citations number 17 and 34, respectively, listed in the *Bibliography*. Symbols like [58, (Ch. 3)] and [58, (Sect. 3.2)] refer to a chapter and a section, respectively, in a citation. Cross-references to background material will be denoted by a 'M' in case of the methodology and by a 'P' in case of the phenomenology — for example as in M: Section 9.3.3 (which starts on page 53).

Acknowledgments

I am indebted to my supervisors Professor Jakob Stoustrup, Professor Martin Lauritzen, Reading Professor Morten Knudsen, and Associate Professor Torben Knudsen for their guidance throughout the project and especially for supporting my wish to participate in national as well as international meetings concerning neuro-vascular coupling.

I am also indebted to Claus Mathiesen, Ph.D., NeuroSearch A/S, for supplying the experimental data, which are investigated in this Ph.D. thesis.

Sincere thanks goes to Professor Richard B. Buxton, Center for fMRI, University of California at San Diego, who hosted me in the period January–April 2002. His proposals concerning the development of the grey-box models have been invaluable. Also the discussions with other members of the faculty of the center are acknowledged. Especially, I have benefited from the professional insight as well as the friendship of Elizabeth Yoder, Ph.D. Thanks also go to Eman Ghobrial for computer assistance during my stay.

I am thankful to the staff of the Department of Control Engineering for administrative and technical assistance and support.

Finally, I would like to acknowledge the financial support from the Center for Mathematical Modelling of Physiological Processes, which has been funded by the Faculty of Engineering and Science at Aalborg University, the Danish Ministry of Education, and NeuroSearch A/S.

November 2004, Aalborg, Denmark
Tina Rasmussen

Chapter 1

Introduction

This chapter gives an introduction to the remainder of the present Ph.D. thesis. First, the research field, its background and motivation are described. Secondly, the objectives and the scientific methods are presented. Thirdly, the state of the art is reviewed and the contributions of the present Ph.D. thesis are summarized. Finally, an outline of the thesis is given.

1.1 The Technical Field of Study

This Ph.D. thesis investigates neuro-vascular coupling, that is, the relation between neuronal activity and activity-dependent changes in the blood flow level, in cerebellum of healthy male Wistar rats. The cerebellum is the lower part of the hind-brain. It is responsible for muscle coordination and bodily equilibrium.

More specifically the thesis focuses on the temporal relation between simultaneous measurements of local neuronal activity in cortex, i.e., the tissue forming the outer layer, of cerebellum and the resulting local increases of the blood perfusion in nearby capillaries. The neuronal activity has been evoked by electrical stimulation: Stimulation of the inferior olive in the brain stem activates the neurons termed climbing fibers. In order to suppress normal activity, the rats have been anesthetized and furthermore given a drug which induces muscle relaxation. The extracellularly measured field potential is chosen as indicator of neuronal activity, and the blood flow increase has been measured in nearby capillaries by means of laser-Doppler flowmetry. The thesis does *not* consider the processes, which cause the baseline blood flow level. The baseline blood flow level is reached during periods of no stimulation when transients have died out.

The approach to the research object will be that of developing dynamic parametric mathematical models of the coupling. The mathematical problem may be formulated as a quantitative question:

> *Which properties, i.e., type and size of model structure and values of parameters, must a dynamic mathematical model of the temporal relation between neuronal activity and cerebellar blood flow responses posses in order to be able to reproduce the experimental data?*

1.2 Background and Motivation

First a historical account for the development of experimental techniques is given. This development forms the background for the present Ph.D. thesis. Secondly, the motivation for the thesis is given, that is, it is described which change of approach to the research object this thesis represents and what is expected to be obtained by the change.

Background:

As a result of the development of new experimental techniques, the focus of experimental research has changed:

Assessment of Neuronal Activity and Blood Flow

Over the years lots of information about the structure and function of neurons have been accumulated (Andresen *et al.* [8, 7], Crone *et al.* [24], Euler *et al.* [31], Llinás *et al.* [62], Nicholls *et al.* [73], Sternheim *et al.* [90], Warberg [101, (Ch. 3)]). The same applies to the vascular system (Warberg [101, (Ch. 6)]). Also the extracellular space (Warberg [101, (Ch. 10)], Nicholson *et al.* [75]) and the neuroglia (Nicholls *et al.* [73, (Ch. 6)]) have been investigated.

However, investigation of the temporal *coupling* between local neuronal activity and local changes in blood flow has until the 1990es been hindered by the lack of appropriate measurement techniques for *in vivo* experiments: Measurements of time series of local field potentials have been made since the 1960es (Hubbard *et al.* [42]) and is nowadays a well-established technique (Nicholson [74]). Contrary to this *in vivo* assessment of the blood flow through local brain regions has suffered from the lack of spatial as well as temporal resolution. For instance, the IAP method assesses the flow by means of a bolus injection of the radio-isotope $\left[^{14}C\right]$-iodoantipyrine (IAP) and rely on a simple relation between the tissue and arterial concentrations of the radio-isotope and the blood flow. Thus arterial blood samples must be extracted periodically during the experiment, and a tissue sample at the end of the experiment is required. And the experimental procedure for the assessment of concentrations of the radio-isotope is intricate (Fabricius *et al.* [34]).

The situation changed in the late 1980es with the development of laser-Doppler flowmetry (LDF), which is a non-invasive technique for continuous and real-time measurement of local blood flow (Shephard *et al.* [83], Fabricius *et al.* [34], Barfod *et al.* [9]). We are therefore now in a situation where we have temporal resolution of the neuronal signal as well as of the blood flow signal. Having temporal resolution of both signals, two questions arise:

- How to report this rather large body of measurements?
- Is it possible to extract information on the mechanisms responsible for neuro-vascular coupling from simultaneous measurements of neuronal activity and changes in blood flow?

These challenges call for a new approach to the investigation of the neuro-vascular system: System identification, which is the act of establishing a mathematical model of the system dynamics by means of measurements of input (neuronal activity) and output (blood flow) signals only.

The Mechanisms of Neuro-Vascular Coupling

Even though several suggestions exist, the physiological mechanisms responsible for neuro-vascular coupling are not well understood:

There *is* Coupling It has long been known that there is a morphological relationship between neurons and blood vessels (Nicholls *et al.* [73, (Ch. 6)]). Specifically, it has been established, that neurons and blood vessels in the cerebellum typically are not directly coupled (Iadecola *et al.* [43]), but are interconnected via the extracellular space and, in some cases, neuroglia (for instance the cell type termed astrocytes).

Furthermore, several experimental studies conducted on rats have established that there is also functional coupling in cortex of cerebellum: Local neuronal activity and local changes of cerebellar blood flow are dynamically coupled (Iadecola *et al.* [44], Mathiesen *et al.* [66], Caesar *et al.* [19], Akgören *et al.* [3], Lauritzen [57]).

How is the Coupling Mediated? Currently experimentalists are trying to identify the chemical substances, which mediate the coupling. Some of the chemical substances, for instance K^+, may be measured *in vivo* and deep inside the brain by means of ion- or molecule-selective probes (Caesar [18], Caesar *et al.* [19]). Other mediators, for instance NO, can only be measured *in vitro* (Shibuki *et al.* [85]) or from the surface of the brain (Read *et al.* [79]). Finally, some mediators cannot be directly measured. Instead, their function is investigated indirectly by pharmacological studies. That is, adding a well-known chemical substance and investigating how it changes the neuronal activity and the blood flow makes it possible to set up hypotheses of which substances mediate the coupling (Akgören *et al.* [2, 4]). Independently of the applied experimental technique, it is difficult to establish the mechanisms, because the mediators interact (Dirnagl *et al.* [27], Tian *et al.* [92]).

Furthermore, there exists a number of suggestions to which physiological processes, such as diffusion through the extracellular space and astrocytic siphoning of various chemical substances, are responsible for the coupling (Nicholls *et al.* [73, (Ch. 6)]).

From time to time researchers have tried to summarize all of the experimental results and the associated hypotheses in a single comprehensive picture of the mechanisms responsible for neuro-vascular coupling. Because not only the above-mentioned feedforward mechanisms but also feedback mechanisms are included, these qualitative models are typically quite complex (Berne *et al.* [13], Fillenz *et al.* [35]). None of these qualitative models have been fully confirmed.

Motivation:

The starting point is that we know that there is coupling between local neuronal activity and local blood flow changes. Furthermore, whereas a number of qualitative models of the coupling do exist, the amount of experimental evidence is limited.

The motivation for the present Ph.D. thesis is to contribute to the understanding of the physiological processes, which are responsible for the coupling, by changing the focus from qualitative modeling to quantitative modeling, that is, to mathematical modeling of the neuro-vascular system. The thesis is concerned with basic research in the sense that it seeks the answers to fundamental questions such as:

- How and when is each of the mediators released from the neuron?
- How is each of the mediators transported from the neuron to the blood vessels? Via the extracellular space and/or via neuroglia?
- Which effect does each of the mediators have on the blood vessels? Dilation or constriction?
- How is each of the mediators removed from the blood vessels? By the blood flow? By chemical reactions? In other ways?
- How many mediators are there? (How) do the mediators interact?

During the process of seeking the answers to such questions, it may be necessary to construct *new* qualitative models, that is, new pictures of the physiological processes, which are responsible for the coupling — for instance in the form of hypotheses.

1.3 Objectives

In short the objectives are:

- To construct and validate mathematical models of the neuro-vascular system which are able to mimic major features of the system dynamics.
- To relate properties of the mathematical models and properties of the physiological system.

More specifically: The first objective is mainly quantitative: With the experimental data as starting point to construct mathematical models, which consist of a model structure and a specific set of parameter values, and which are able to reproduce the overall features of the temporal relation between measurements of nerve cell activity and changes in the blood flow level in nearby capillaries. And to quantify the quality of the models. The second objective is mainly qualitative: To interpret elements of the mathematical models in terms of physiology. That is, with the mathematical models as starting point to construct (relatively simple) pictures of the physiological processes responsible for neuro-vascular coupling. And/or oppositely: To construct mathematical models starting from physiological pictures of the processes.

1.4 The Scientific Methods

The thesis focuses on creating mathematical models of the neuro-vascular system by combining mathematical methods (described in Part II) with physiological knowledge (presented in Part I).

The models will be accomplished by repeating two steps until a suitable model is obtained: Model construction and model validation. Performing the steps requires various methods to be applied:

Model Construction:

A parametric model of a dynamic system relates observations of input(s) to the system with output(s) from the system and consists of:

- A model structure containing a dynamics model and a noise model, and
- A set of parameter values.

System identification is a principle for model construction which uses observations from the system in order to fit the model's properties to those of the system. The model structure may be inferred from two sources:

(1) Mathematical arguments:
In this case the results of the signal and system analyses (Part III) will be important background information.

(2) Physiological arguments:
The phenomenology (Part I) in this case constitutes an important basis.

Application of source **(1)** alone leads to black-box models (Part IV). Application of both sources leads to grey-box models (Part V) and semi-physical models (Part VI). In order to fulfill the objectives, the model structures have to be parsimonious, that is, to contain a minimal number of parameters. The parameter values will be estimated by means of the prediction error method. It seeks the parameter vector value which optimizes the fit between the predicted output and the measured output.

Model Validation:

The models will be validated in three ways:

- Model fit:
  The ability of a model to reproduce the behavior of the system is quantified by the noise-to-signal ratio, which is a measure of how well the model output fits the measured output, i.e., the measured cerebellar blood flow.
- Cross validation:
  A model's consistency, that is, how well the model can be reproduced from different sets of measured data, is quantified by the coefficients of variance of the parameters in the model.
- Sensitivity to parameters:
  The sensitivity of the parameter dependent model error to a parameter is a measure of how accurate the estimate of that parameter is.

1.5 The State of the Art and Related Modeling Work

1.5.1 Previous Modeling Work and the State of the Art

A number of parametric mathematical models of the relation between the extracellularly measured potential and the cerebellar blood flow assessed by means of laser-Doppler flowmetry have already been suggested:

I: Static Models

A: Wave-Form Averages
The coupling in rat cerebellum has been investigated during inferior olive stimulation and during parallel fiber stimulation, respectively, for 60 s.

First an average waveform of the field potential excitations resulting from stimulation with a given frequency was found, and then the field potential amplitude was defined as the amplitude of the excitatory post-synaptic potential (EPSP) component of this average waveform. In this way one field potential amplitude was obtained for each stimulation frequency. Next, the summed field

potential amplitudes was defined as this field potential amplitude times the stimulation frequency. Then the amplitude of the blood flow response to stimulation for 60 s (output, ordinate) was plotted versus the summed field potential amplitudes (input, abscissa). For the case of inferior olive stimulation a straight line (a static linear model containing 2 parameters) could be fitted to the data (5 data points). For the case of parallel fiber stimulation a sigmoid function (a static nonlinear model containing 4 parameters) was fitted to the data (7 data points) (1998: Mathiesen *et al.* [66], 2002: reviewed by Lauritzen *et al.* [56]).

These model structures contain a large number of parameters relatively to the number of data points.

B: Running Sums

The coupling in rat cerebellum has been investigated during inferior olive stimulation and during parallel fiber stimulation, respectively, for 60 s.

The field potential amplitudes were extracted from the individual excitations of the field potential. An input signal, termed a running sum, was created by — at each instant — adding all the field potential amplitudes occurring within a time window of a certain duration, termed the summation period, situated right before that instant. Next, for each stimulation frequency, a static linear model was created in the following way: For each summation period, the blood flow values were plotted versus the values of the running sum of field potential amplitudes. A straight line was fitted to the data points (of the order of 600 data points) and the linear correlation coefficient was calculated. The optimal summation period was defined as the period with the highest linear correlation coefficient. Its value depended on the stimulation frequency. For the case of inferior olive stimulation the field potential amplitudes was calculated from the EPSP component. For the case of parallel fiber stimulation, two separate studies were made: One used the amplitude of the presynaptic potential (PSP) component of the field potential; the other used the amplitude of the excitatory post-synaptic potential (EPSP) component (2000: Mathiesen *et al.* [67]).

These models consist of a dynamic linear input transform followed by a static linearity.

II: Dynamic Models

C: Volterra Series

Neuro-vascular coupling in the somato-sensory cortex as a result of forepaw stimulation at 5 Hz has been investigated.

For each choice of stimulus duration ($0-16$ s) and amplitude ($0.5-2$ mA), a single somato-sensory evoked potential (SSEP) waveform was obtained by averaging over the individual SSEP excitations. The amplitude of these average waveforms was used as a measure of neuronal activity. Also the corresponding blood flow responses were averaged over trials. Neural input functions were constructed as specific linear combinations of square wave impulses with durations shorter than the stimulation duration and amplitudes given by the amplitude of the SSEP waveform. Discrete dynamic time-invariant output-error model structures described the blood flow signal as a convolution of either the neural input function with an impulse-response function (first-order Volterra kernel) (a linear model containing 8 parameters) or as a second-order Volterra series (a nonlinear model containing 72 parameters). The Volterra kernels were expanded in terms of windowed functions of sines and cosines. Parameter estimation was done using a least-squares algorithm (2000: Ances *et al.* [6]).

D: Multi-Modeling

The coupling in rat cerebellum has been investigated during inferior olive stimulation for 60 s with frequencies in the range $2-30$ Hz and for 600 s with the frequency 5 Hz.

The input signal was generated by — for each blood flow sample — adding the amplitudes of the field potential events occurring in a window being as long as the sampling interval and placed symmetrically around the sampling instant of the blood flow signal. This is a dynamic linear input transformation. The output signal consisted of the cerebellar blood flow signal. First a simple dynamic model in the form of a standard discrete black-box third-order output-error model structure (6 parameters) was tested. Secondly, a quite complex nonlinear model structure was considered. It consisted of a soft shift (3 parameters) between two Hammerstein model structures. Each of the Hammerstein model structures consisted of a static nonlinearity (2 parameters) followed

by a black-box discrete third-order (6 parameters) or first-order (2 parameter) output-error model structure (2000: Knudsen [53]).

E: Impulse Response Functions
Neuro-vascular coupling in the rat somato-sensory cortex has been investigated during stimulation of the whole whisker pad.

Time series of field potentials were recorded at 16 regularly spaced depths and the recordings were averaged over 60 trials. The resulting signals were transformed by a finite difference formula to the current source distribution. The first principal component was used to collapse the data across the spatial dimension. A neural event was defined as the current sink response to a single electrical stimulus pulse. The hemodynamic response was recorded by laser-Doppler flowmetry and normalized. Finally, interanimal averaging was performed. General linear modeling analysis was then performed. The parameters in the model were adjusted to minimize the residual least-squares errors. The input consisted of delta functions scaled by the amplitudes of the experimentally derived neural events. The output consisted of the hemodynamic response. The hemodynamic response to a very short neural event was modeled as a linear convolution of experimentally obtained measures of neural activity with a suitable hemodynamic impulse response function. The impulse response estimates obtained from individual trials were graphically compared to the group mean (2003: Martindale *et al.* [65]).

These studies may be characterized in various ways:

- Each of the studies **A** through **D** are focused on a specific transformation of the fast varying evoked electrical activity into a slowly varying input signal. The models then relate this input signal to the slowly varying blood flow signal.

- In the study **A** the input signal is averaged over trials (so-called waveform averaged), and in the studies **C** and **E** the input signal is first averaged over trials and afterwards exchanged with a standardized signal. In the study **A** the raw output signal is used, and in the studies **C** and **E** the output signal is averaged over trials. The studies **B** and **D** operates directly on the raw input and output signals.

- Only in study **B** the choice of input transformation is based on a physiological argument.

- The models in studies **C**, **D** and **E** have been constructed by means of system identification techniques.

- The studies **C**, **D** and **E** concern dynamic discrete-time black-box models.

- The model structures investigated in studies **C**, **D** and **E** contain large numbers of parameters and are most likely over-parameterized.

- Even though all of the studies are concerned with parametric models, in none of them the parameter estimates are reported. Furthermore, the model fit is not quantified (study **D** is an exception), cross validation not performed, and the sensitivity to the parameters not assessed.

These characterizations also describe the state of the art in modeling neuro-vascular coupling.

1.5.2 Related Modeling Work

Theoretical Foundation

Application of system identification techniques to biomedical systems has been treated in general (Westwich *et al.* [102]).

Furthermore, control engineering techniques have been applied to physiological systems (Crone *et al.* [26], Ghosh *et al.* [39, 38]) and specifically to the brain (Nemadic *et al.* [72]) and more specifically to the cerebellum (Doya *et al.* [29]).

Partial Models

Chemical Blood Flow Regulation: A comprehensive model of chemical oxygen-dependent cerebral blood flow regulation in the rat has been suggested. It consists of two parts. The first part describes oxygen diffusion from capillary to tissue, the accumulation of vasoactive metabolites in cerebral parenchyma (i.e., the surrounding tissue), and their diffusion towards perivascular space (Ursino *et al.* [98]). The second part describes the reactivity of the cerebral vascular bed to vasoactive metabolites. The main assumption is that the regulation is achieved by the release of two vasodilating substances from hypoxic tissue, i.e., adenosine and H^+ (Ursino *et al.* [99]). An extension of the model includes the reactivity of proximal segments of the cerebrovascular bed and the neurogenic and myogenic feedback regulatory mechanisms besides the action of chemical regulatory factors. The main assumption of this model is that neurogenic reflexes mainly affect the proximal segments of the cerebrovascular bed (i.e., the large intracranial arteries and large and medium pial arteries) whereas small pial arteries and arterioles are basically under the influence of chemical factors released in the surrounding tissue (Ursino [97]). A characteristic of these models is that the values of the parameters in them stem from various experiments performed on subsystems of the investigated system. The cerebral blood flow pattern is thus obtained *a posteriori* by simulation of the final model.

High blood pressure can experimentally be induced by intravenous infusion of a vasoconstricting agent such as angiotensin II, which regulates the contraction of the smooth muscle cells surrounding the blood vessels. As the infusion is continued, a substantial narrowing of the smaller blood vessels is observed, and suddenly the narrowed vessels develop a peculiar patter consisting of alternating regions of constrictions and dilations, giving the vessels the appearance of sausages on a string. This sausage-string pattern has been reproduced by a simple anisotropic elastic model of the vessel wall. According to the model, the cylindrical form of a blood vessel becomes unstable under certain hypertensive conditions (Alstrøm *et al.* [5]).

Cerebrovascular regulation and intracranial pressure dynamics have been studied by means of a model, which assumes that cerebral blood flow regulation is the result of three distinct feedback mechanisms working on pial arteries and arterioles. They represent CO_2 reactivity, tissue hypoxia, and a mechanism (either pressure-dependent or flow-dependent in nature) that does not depend on O_2 or CO_2 directly. The latter is involved in cerebral autoregulation and might represent myogenic or neurogenic regulation, endothelium dependent factors, or a direct effect of blood flow washout on perivascular vasodilatory metabolites. It is assumed that large and medium pial arteries are mainly controlled by a pressure-dependent mechanism, which causes vasodilation during a decrease in cerebral perfusion pressure. Conversely, small pial arteries are controlled by a flow-dependent mechanism, which vasodilates when cerebral blood flow is reduced below normal (Ursino *et al.* [96]). All parameters characterizing intracranial dynamics and cerebral hemodynamics stem from a normal man. The gains of feedback mechanisms have been estimated by fitting the model to experimental data.

Vasomotion: Small arteries and arterioles, as well as muscular venules, often exhibit spontaneous rhythmic changes in caliber, called vasomotion.

The role of the myogenic mechanism in the genesis of microvascular oscillations has been investigated by means of a mathematical model. It was shown that a vascular network formed by a series of several independent effectors, under the action of the myogenic mechanism, may give rise to a positive feedback loop able to induce vascular instability (Ursino *et al.* [95]).

Vasoconstrictors enhance the oscillatory activity, whereas vasodilators depress the oscillations. Blockade of the production of nitric oxide (NO), which is a vasodilator, is therefore expected to abolish vasomotion. But experiments have shown that the opposite is true: Application of a NO synthase inhibitor induces cyclic variations of cortical cerebral blood flow (Dirnagl *et al.* [28]).

Subsystems: The internal dynamics of the subsystems of cerebellum have also been modeled:

The neuronal activity in the rat cerebellar cortex has been investigated by means of a constructed large-scale realistic network model containing the four major cell types of the cortex and the mossy fiber afferents. The model was implemented as a compartmental model in the GENESIS neural simulation system (Dyhrfjeld-Johnsen [30]). The timing of motor responses has been investigated by means of a neural network model based on the synaptic organization of the cerebellum (Buonomano *et al.* [15]). The learning mechanism for the cerebellum has been postulated to be supervised learning (Doya *et al.* [29]).

Monte Carlo simulation of photon migration in tissue has been used to assess the sampling depth, measuring depth and photon pathlength in laser-Doppler flowmetry. The median sampling depth and photon pathlength in skin, liver and brain tissue were calculated for different probe geometries (Jakobsson *et al.* [45]). Inspired by this, experiments have been made to establish the sampling depth in artificial brain tissue as a function of the wavelength of the laser beam and of the separation distance of the transmitting and recording optical fibers in the LDF-probe (Fabricius *et al.* [32]).

The Influence of the Blood Pressure on the CBF

Autoregulation maintains cerebral blood flow almost constant in the face of changes in arterial blood pressure (ABP). A test for impairment of this process has been constructed using only spontaneous fluctuation in ABP. The blood pressure was measured by means of a very rapidly acting servo-system to inflate a finger-cuff with photoplethysmographic feedback control ensuring that the cuff pressure matches finger ABP at all times. The cerebral blood flow velocity (CBFV) was measured in the middle cerebral arteries using transcranial Doppler ultrasound signals. A linear model in the form of a FIR filter of length two samples was fitted to the measurements. The two parameters in the model could be used to distinguish between normal subjects and patients with stenosis of the carotid artery. The latter group was subdivided into a group with reduced cerebrovascular CO_2 reactivity and those showing normal reactivity (Simpson *et al.* [87]).

The coupling between blood pressure and blood flow in the rat kidney has been modeled, assuming autoregulation is active. First a linear non-parametric model in the form of the magnitude of the transfer function was estimated from measurements of arterial blood pressure and renal blood flow. Secondly, a parametric frequency-domain model was fitted to the non-parametric model. The parameters in this model were applied to construct a discriminator between normotensive and hypertensive rats (Knudsen *et al.* [54]).

1.6 Contributions

The main contributions of this Ph.D. thesis concern neuro-vascular coupling in case of stimulation of the inferior olive. They are as follows:

- The characteristics of the input (field potential) and output (relative cerebellar blood flow) signals are emphasized (Part III):
  - The field potential signal varies on a fast time scale of a few milliseconds (10^{-3} s) whereas the relative cerebellar blood flow signal varies on a slow time scale on the order of up to ten seconds (10^{1} s).
  - The information in the field potential signal lies mainly in the amplitude of the time-localized excitations (so-called events). The overall level of the sizes of field potential amplitudes decreases with increasing stimulation frequency. The field potential amplitude depends dynamically on the stimulation frequency: After onset of stimulation of the inferior olive with a constant frequency, the very first field potential amplitudes are very large. The amplitude of the following events decreases very fast towards a minimum size. During the remainder of the stimulation sequence the amplitude slowly increases.
  - The relative cerebellar blood flow response to stimulation with constant frequency is characterized by a fast increase followed by a dip and afterwards an increase which slows down. Oscillations in the arterial blood pressure do not contaminate the relative cerebellar blood flow signal.
- The system analysis shows that most of the system dynamics pertains to frequencies below one Hertz. (Part III)
- The features of the measured output signal which cannot be explained from the measured input signal by a linear dynamic black-box model are emphasized: Frequency saturation and dips during stimulation for short times (60 s), and overgrowth during prolonged stimulation (600 s). (Part IV)
- The phenomenon of frequency saturation is explained by a threshold non-linearity. It describes mathematically the hypothesis that only field potential amplitudes larger than a certain threshold

indicate neuronal activity which causes release of the dominant vasodilatory chemical substance nitric oxide (NO) and thereby evokes blood flow increases. (Part V)

- The phenomena of frequency saturation and dips are explained from the hypothesis that there exists two mediators of neuro-vascular coupling, and that each of the mediators is characterized by its own threshold for release. One of the mediators is clearly vasodilatory, but the effect of the other mediator is unclear (it is most likely vasodilatory, but it could be without effect, or vasoconstrictory). (Part VI)

1.7 Thesis Outline

The thesis is organized as follows: The first two parts (Parts I and II) present background material which may be well-known to some readers. The intermediate parts (Parts III through VI) are devoted to presentations of the research results which form the outcome of the present PhD-project. Afterwards a part (Part VII) summarizes the results and their implications. The final part (Part VIII) contains the list of references and provides auxiliary information of various kinds. The content of each part is now described:

Part I: Phenomenology

This part first provide textbook information about the physiology of cerebellum with an emphasis on the elements of importance to neuro-vascular coupling. Afterwards some of the qualitative theories about how the coupling is mediated are reviewed. The data, which are analyzed and modeled, stem from rat experiments which are also described in this part.

Part II: Methodology

This part contains textbook material on how to construct parametric models of dynamic systems starting from measurements of input and output signals only as well as on how to validate the models.

Part III: Signal and System Analysis

Firstly, the individual signals are analyzed with the purpose of finding characteristics of each signal which may be important during the development of mathematical models of neuro-vascular coupling. Secondly, the frequency content of the neuro-vascular system is analyzed by means of the input and output signals.

Part IV: Linear Black-Box Models

Two linear black-box model structures are investigated with an emphasis on which characteristics of the experimental data they are un-able to reproduce. The essence of each of the models is a combination of a preprocessing procedure with a linear state-space model structure. The preprocessing procedures, which have the form of a linear dynamic transformation of the input from being event-sampled to being sampled, are: The input sampling transform and the input running summation transform, respectively. Three features of the output signal, which cannot be reproduced by these linear models, are emphasized: Frequency saturation and dips during short stimulation sequences, and overgrowth during prolonged stimulation. Finally, it is decided to truncate the time series in order to exclude the data exposing overgrowth and thereby focusing the modeling efforts on the frequency saturation and the dips.

Part V: Grey-Box Models

Information on the physiology of cerebellum (Part I) is now combined with the analysis results (Part III) and the experiences obtained from the linear black-box models (Part IV) in order to create grey-box model structures. They consist of two parts: A preprocessing procedure in the form of a linear or nonlinear dynamic transformation of the input from being event-sampled to being sampled: The input sampling transform (which is linear), the input threshold transform (which is nonlinear and contains one parameter), and the input kink transform (which is nonlinear and contains two parameters). And a second-order linear output-error state-space model structure with coupled and constrained parameters. The couplings and constraints stem from physiological interpretations. The grey-box model with the

input threshold transform explains one of the features, which cannot be reproduced by the linear models: The frequency saturation.

Part VI: Semi-Physical Models

In order to improve the model fit, the grey-box models are stripped for the couplings and constraints on the state-space model parts, which originate from physiological interpretations, whereas the (non)linear input transforms are preserved. The linear order is estimated to be two and the model fit is only slightly improved.

Adapting the interpretation of the state vector, which resulted from the grey-box models, a multiple-input-single-output (MISO) output-error state-space model is created. Each of the two input signals is constructed from the event-sampled signal by means of the input threshold transform. The linear order is given the value three. The MISO model explains the frequency saturation as well as the dips in the output signal.

Part VII: Concluding Part

First a discussion of the research results is provided. Afterwards prospective applications and other perspectives are considered. Furthermore, some suggestions for future research objectives and activities are given. Finally, it is concluded that the field potential is dynamically coupled to the cerebellar blood flow. The final model, which is termed the *3-2-1* (or *countdown*) *model*, possesses the following properties: Its linear order is equal to three, it is based on the hypothesis that neuro-vascular coupling is mediated by two vasoactive chemical substances, and that the action of each of them requires the neuronal activity to overcome a threshold described by one parameter.

Part VIII: Bibliography and Appendices

The bibliography contains the list of references. The appendices provide auxiliary information about the raw data, the post-processing procedures, and finally frequency-domain considerations.

Part I

Phenomenology

The purpose of this part is to provide a basis for understanding the experiments which form the starting point for the work and the results reported in this thesis.

The goal is to create a basis for constructing mathematical models of the relation between neuronal activity and deviations in the blood flow level from its baseline value, which can be interpreted in terms of physiology.

Therefore this part includes the subjects:

- Overview of the Neuro-Vascular System
- The Neuronal Subsystem
- The Extracellular Space
- The Vascular Subsystem
- Neuro-Vascular Coupling
- The Experiments.

The means to fulfill the purpose and to reach the goal will be to present textbook material on the physiology of the neuronal subsystem, the extracellular space, and the vascular subsystem. Furthermore, a number of hypotheses of the nature of neuro-vascular coupling, which have been presented in scientific papers, will be presented and discussed. Finally the experimental procedures as well as the experimental results are presented. This material also stems from scientific journals.

Readers who are familiar with cerebellum may find that most of the material in this part is well-known. For their information a summary of the phenomenology is given in P: Chapter 8.

Chapter 2

Overview of the Neuro-Vascular System

In the following chapters rat cerebellum is described as consisting of three subsystems as illustrated by Figure 2.1:

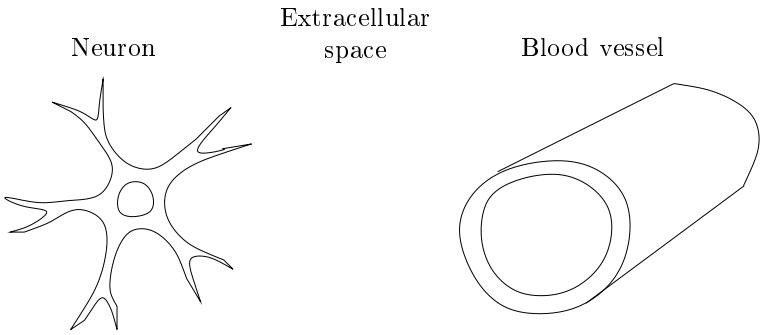

Figure 2.1: A description of the neuro-vascular system as consisting of three subsystems: The neuronal subsystem, the extracellular space, and the vascular subsystem.

The neuronal subsystem (P: Chapter 3), the extracellular space (P: Chapter 4), and the vascular subsystem (P: Chapter 5).

In P: Chapter 6 it is discussed whether these three subsystems are the only ones which contribute to neuro-vascular coupling under the conditions of anesthesia and induced muscle relaxation. Furthermore, some of the hypotheses of how neuro-vascular coupling is mediated, are reviewed.

Chapter 3

The Neuronal Subsystem

This chapter describes the internal structure and function of the neuronal subsystem. The material consists of well-established information about cerebellum and stems from textbooks.

3.1 General Cell Physiology

3.1.1 The Cell Membrane

The cell membrane is around 100 $\AA$ thick and consists of a bimolecular layer of phospholipids, as well as cholesterol, carbon hydrates, and proteins. The phospholipids are amphiphilic molecules, i.e., they contain both a hydrophilic (polar) head and a hydrophobic (nonpolar) tail.

In the bimolecular layer the phospholipids are oriented such that the hydrophilic heads (the phosphate parts) face the aqueous environment, which both surrounds the cells (the extracellular fluid) and is inside them (the intracellular fluid, i.e., the cytoplasm), while their hydrophobic tails (the lipid parts) extend to the middle of the membrane. Due to the lipid properties of the cell membrane, organic apolar substances can rather easily move across it.

The proteins in the cell membrane are divided into integral proteins and peripheral proteins. The *integral proteins* are embedded in the cell membrane and possibly traverse it fully from the outside to its inside. Complexes consisting of $4-6$ of these protein molecules can form water-filled pores, which only allow passage of selected ions (for instance Na^+ or K^+). Such *ion-specific channels* are very important for the ion transport across the cell membrane. Some integral proteins exhibits enzymatic activity (for instance, ATPase-activity), while others can function as receptors. The *peripheral proteins* are found at the inner side of the cell membrane, form the so-called cyto-skeleton, and serve to stabilize the cell membrane.

The cell membrane has three important functions [101, (Ch. 2)]:

- Being a barrier towards the surroundings,
- Binding of molecules in the surroundings (a receptor function), and
- Transport of substances into and out of the cell.

3.1.2 Membrane Potentials

There is normally a voltage difference, a so-called *membrane potential*, across a cell membrane.

We now consider a selectively permeable membrane, i.e., a membrane which is permeable to some, but not to other particles [101, (Ch. 2)].

Equilibrium Potential and Nernst Equation

Specifically, we consider the simple case of a membrane permeable to cations separating two phases – see Figure 3.1. The two phases are solutions of KCl with the concentrations c_1 and c_2. The subscript 1 denotes phase 1, and the subscript 2 phase 2. Thus the membrane is permeable to K^+ but not to Cl^-. If the concentration of KCl is largest in phase 1, $c_1 > c_2$, K^+ will diffuse through the membrane into

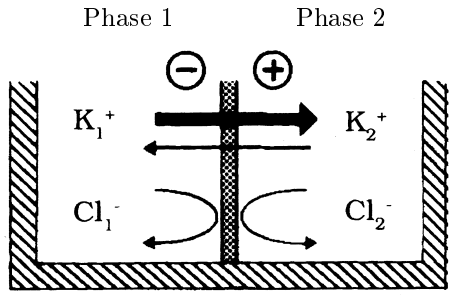

Figure 3.1: Establishment of an equilibrium potential: A selective cation-permeable membrane, which is permeable to K^+-ions, but not to Cl^--ions. The membrane separates two phases with different KCl-concentrations: The KCl-concentration is larger in phase 1 than in phase 2. From Ref. [101, (Ch. 2)].

phase 2 because of the difference in concentrations. Thereby a surplus of positively charged K^+-ions in phase 2 is created and an electrical potential difference arises across the membrane. Thus phase 2 has a higher electrical potential than phase 1. This potential will prevent more diffusion of K^+-ions. And when the potential difference becomes so big that the net diffusion of K^+-ions from phase 1 to phase 2 stops, equilibrium in the system has been reached. In this case as many K^+-ions diffuses from phase 1 to phase 2 as in the opposite direction. The *equilibrium potential* is defined as the potential difference, which has to be applied across the membrane in order that there is equilibrium for the diffusible ion, i.e., in order that there is not net transport.

The equilibrium potential across a selectively permeable membrane can be calculated from the *Nernst equation*:

$$\Delta\phi = \phi_2 - \phi_1 = \frac{R \cdot T}{z \cdot F} \cdot \ln\left(\frac{c_1}{c_2}\right) = \frac{k_B T}{z \cdot e} \cdot \ln\left(\frac{c_1}{c_2}\right), \tag{3.1}$$

where $\Delta\phi$ denotes the potential difference across the membrane for an ion with concentration c_1 on one side of the membrane and c_2 on the other side. R is the gas constant and F is Faradays number. T is the temperature and z the valence of the ion [101, (Ch. 2)].

Diffusion Potential and the Goldman Equation

We again consider a system where a membrane separates two KCl-solutions, and where the concentration of KCl is largest in phase 1. But now the considered membrane is permeable to both K^+ and Cl^-. See Figure 3.2. Let us assume the permeability of Cl^- is larger than that of K^+. K^+-ions as well as Cl^--

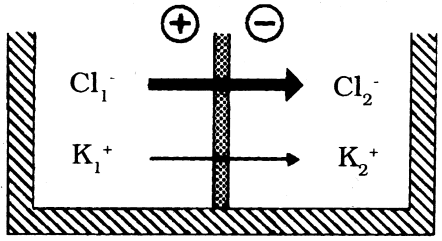

Figure 3.2: Establishment of a diffusion potential: A membrane, which is permeable to both K^+-ions and Cl^--ions but more permeable to Cl^--ions than to K^+-ions. The membrane separates two solutions with the KCl-concentration being higher in phase 1 than in phase 2. From Ref. [101, (Ch. 2)].

ions will now diffuse from phase 1 into phase 2 but due to the higher permeability of Cl^- these ions will diffuse faster and a potential drop through the membrane will arise. The electrical field which is thereby created (phase 2 been negatively charged as compared to phase 1) inhibits the diffusion of Cl^--ions and enhances the diffusion of K^+-ions. As a result a potential difference across the membrane is established of a magnitude which makes the two ions cross the membrane at the same speed. This membrane potential is called a *diffusion potential*.

The membrane potential is determined by the ions, which have the highest concentrations and which have the highest permeabilities. In biological systems, including cell membranes, the most important ions are Na^+, K^+, and Cl^-. The permeabilities are taken into account in the *Goldman equation* which assumes that a constant electrical field across the membrane is established:

$$V_m = \frac{R \cdot T}{F} \cdot \ln \frac{[P(K^+) \cdot c_1(K^+) + P(Na^+) \cdot c_1(Na^+) + P(Cl^-) \cdot c_1(Cl^-)]}{[P(K^+) \cdot c_2(K^+) + P(Na^+) \cdot c_2(Na^+) + P(Cl^-) \cdot c_2(Cl^-)]}, \tag{3.2}$$

where V_m is the membrane potential, and $P(K^+)$, $P(Na^+)$,and $P(Cl^-)$ are the permeabilities of K^+, Na^+, and Cl^-, respectively.

The $Na-K$-Pump and the Resting Potential

As an example consider the conditions in a nerve cell (see Figure 3.3): The intracellular concentrations

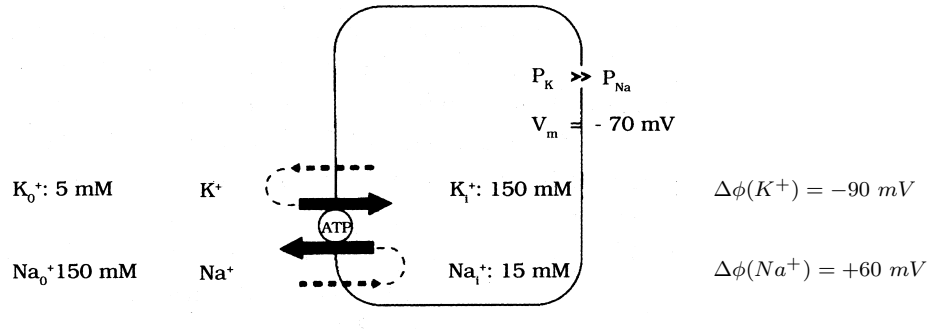

Figure 3.3: The resting potential and the $Na-K$-pump illustrated for a nerve cell for which the membrane permeability for K^+ is much greater than for Na^+: $P(K^+) \gg P(Na^+)$. The equilibrium potentials for K^+ ($\Delta\phi(K^+)$) and Na^+ ($\Delta\phi(Na^+)$) have been calculated by means of the Nernst equation (Equation (3.1)). The measured resting potential, V_m, has been measured in an experiment. Full lines symbolize active transport mediated by the $Na-K$-pump, Dashed lines symbolize passive transport. From Ref. [101, (Ch. 2)].

of K^+ and Na^+ are $c_i(K^+) = 150\ mM$ and $c_i(Na^+) = 15\ mM$, respectively, while the corresponding extracellular concentrations are $c_o(K^+) = 5\ mM$ and $c_o(Na^+) = 150\ mM$. By means of the Nernst equation the equilibrium potentials for Na^+ and K^+, respectively, at a temperature of $T = 37\,^\circ C$ can be calculated. The results are:

$$\Delta\phi(K^+) = \phi_o(K^+) - \phi_i(K^+) = 0.0267 \cdot \ln\left(\frac{5}{150}\right) V \approx -90\ mV \tag{3.3}$$

$$\Delta\phi(Na^+) = \phi_o(Na^+) - \phi_i(Na^+) = 0.0267 \cdot \ln\left(\frac{150}{15}\right) V \approx +60\ mV. \tag{3.4}$$

The measured value of the voltage difference, V_m, across the membrane, i.e., the real membrane potential, is around $-70\ mV$, a value fairly close to the equilibrium potential for K^+. This is explained by the fact that the permeability of K^+, $P(K^+)$, is $40-50$ times greater than the permeability of Na^+, $P(Na^+)$. There is not exact equilibrium since the membrane potential is not exactly equal to the equilibrium potential for the K^+-ion. Therefore there is a small outflow, *efflux*, of K^+-ions from the cell. There is not at all equilibrium in the system for the ion Na^+, and as a result there is an inflow, *influx*, of Na^+-ions.

The concentration difference is not compensated for because of an active transport mechanism which maintains the concentration gradients. This *sodium-potassium pump* consists of an integral membrane protein. At equilibrium the pump constantly pumps K^+-ions into the cell at the same speed as they ooze out, and Na^+-ions out of the cell at the same speed as they ooze in.

Thus across the membrane of the resting cell there exists a potential difference with the inside of the membrane being negative compared to the outside. This potential difference is called the *resting potential*. Notice that the potential is not created by the pumping of Na^+- and K^+-ions — the pumping simply maintains the skew distribution of ions which forms the basis for the diffusion across the membrane that creates the potential.

The energy needed for the $Na-K$-pump to work stems from hydrolysis of ATP. This process is catalyzed by the enzyme $Na^+/K^+ - ATPase$ which is identical to the $Na-K$-pump [101, (Ch. 2)].

Departures from the Resting Potential

A change of the resting potential towards a lower potential difference across the membrane is called a *depolarization*. A change towards a larger potential difference is called a *hyperpolarization*. A return to the normal resting potential is called a *repolarization*. See Figure 3.4.

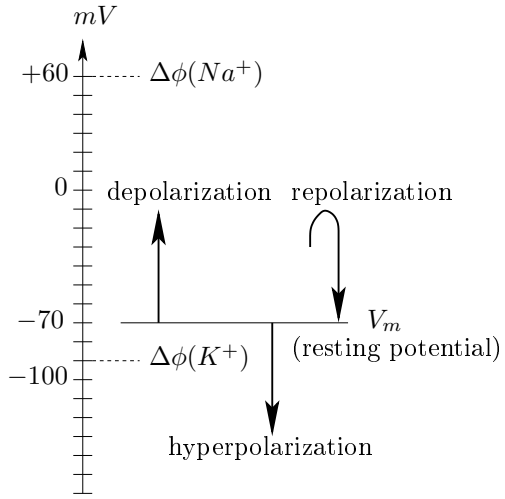

Figure 3.4: Designations for the deviations from the resting potential. The deviations are shown as arrows, and the resting potential is shown as the solid line at -70 mv. The equilibrium potential in nerve cells is denoted by $\Delta\phi(Na^+)$ for Na^+-ions and $\Delta\phi(K^+)$ for K^+-ions. From Ref. [101, (Ch. 2)].

Many factors, called *stimuli*, can provoke changes in the resting potential. If a stimulus is relatively small it causes local, small changes in the resting potential, called *local response*. But if the stimulus is strong enough the resting potential can be broken down so much that an *action potential* is created [101, (Ch. 2)].

3.2 The Physiology of the Nervous System

3.2.1 The Nerve Cell

The nervous system is formed by nerve cells which are called *neurons*. A neuron consists of a cell body, *soma*, and some protuberances which conduct impulses either towards soma, called *dendrites*, or away from soma, called *axons* — see Figure 3.5. The end of an axon is split up into some ramifications called *nerve terminals*. The nerve terminals contain chemical transmitters which are released when an impulse is transmitted to other nerves. This takes place in a *synapse*.

On this ground the nerve cell can be divided into zones:

- a receiving zone (dendrite zone) with a receiving function,
- an impulse creation zone (at the root of the axon) where the electrical impulse is created,
- a conduction zone (the axon) with an impulse conducting function, and
- an output zone (the nerve terminals) where the chemical transmitters ensure that the impulse is passed to another nerve [101, (Ch. 3)].

3.2.2 Electrical Phenomena inside Nerve Cells

Local Response and Electrotonic Potentials

In case a nerve cell is stimulated electrically with impulses below a certain threshold the stimulation results in a small depolarization (a *local response*) of the membrane potential followed by a quick repolarization, and the potential change will not propagate through the nerve cell. Such a local, non-propagating depolarization is called an *electrotonic potential* [101, (Ch. 3)].

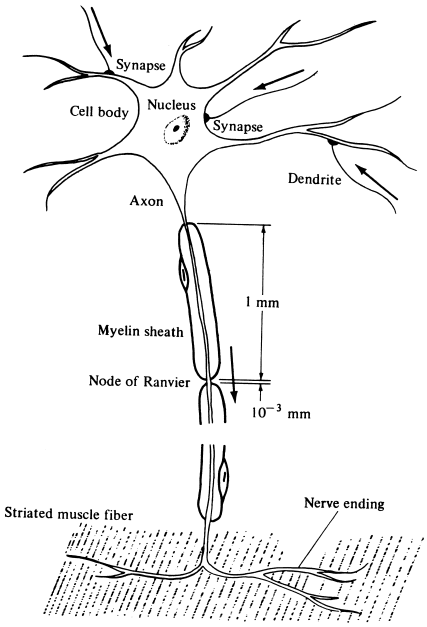

Figure 3.5: Schematic structure of a neuron. Arrows indicate the direction of nerve impulse conduction. From Ref. [90].

The Nerve Impulse: The Action Potential

If the depolarization reaches a value of around 15 mV the membrane potential reaches a value called the *firing level*. At this degree of depolarization the speed of the depolarization is suddenly enhanced and a characteristic potential change called an *action potential* is created — cf. Figure 3.6. An action potential

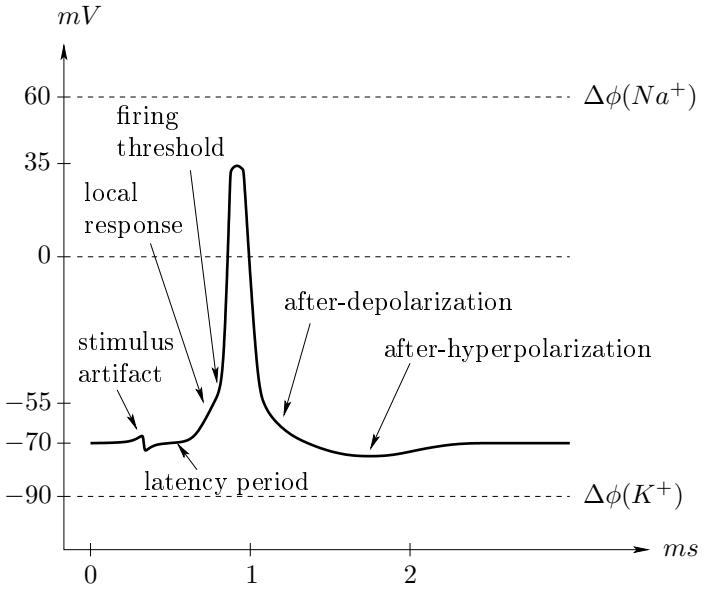

Figure 3.6: The characteristic shape of an action potential. The equilibrium potentials for K^+ ($\Delta\phi(K^+)$) and Na^+ ($\Delta\phi(Na^+)$) are shown as dashed lines. From Ref. [101, (Ch. 3)].

always has the same shape and amplitude — it is independent of the type of stimulation. The shape and amplitude however depends on the state of the nerve fiber [101, (Ch. 3)].

Refractory Period

After an action potential follows a period of changed excitability of the axon: An *absolute refractory period* which lasts throughout the falling phase of the action potential during which no amount of externally applied depolarization can initiate a second regenerative response. Following the action potential there

is a *relative refractory period* during which the threshold for action potential initiation is increased [73, (Ch. 4)].

Nerve Conduction

The propagation of the nerve impulse happens differently in unmyelinated nerves and myelinated nerves:

Unmyelinated Nerves In these nerves impulses are propagated by electrotonic depolarization. The area of the nerve membrane, which is depolarized (that is, where the action potential is 'situated'), attracts positive charges from the outer side of the surrounding membrane areas and shifts negative charges towards these — see Figure 3.7. Therefore the surrounding areas are electrotonic depolarized.

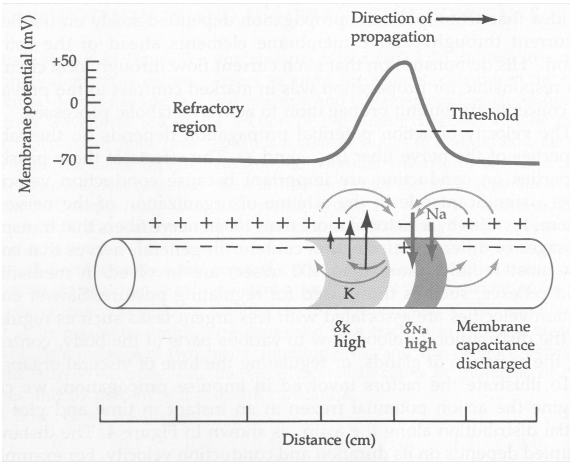

Figure 3.7: Current flow during a nerve impulse at an instant in time. Current flowing into the active region spreads ahead of the impulse to depolarize the membrane toward threshold. Outward potassium current behind the active region causes rapid repolarization. From Ref. [73].

When the depolarization is sufficiently large (the firing threshold is reached), a regular action potential develops, which then causes an electrotonic depolarization of new areas, and thereby the nerve impulse propagates along the nerve membrane. The area behind a propagating action potential is not depolarized, since this area is in the absolute refractory period. Thereby it is secured that the propagation of the nerve impulse continues in the same direction [101, (Ch. 3)].

Myelinated Nerves The propagation of the action potential along myelinated nerves happens by the same principle as in unmyelinated, that is, by electrotonic depolarization. But in the myelinated nerves, the myeline sheaths (the Schwann cells) (cf. Figure 3.5) will isolate, and there cannot run any current in these areas. The electrotonic depolarization therefore only take place at the 'naked' membrane areas (the nodes of Ranvier) between successive Schwann cells, and the impulse propagation happens as jumps from node to node, and is termed *saltatory conduction*. The propagation of nerve impulses in this way is much faster and requires less metabolic energy than in unmyelinated nerves [101, (Ch. 3)].

Rectification of Impulse Propagation Axons can principally lead impulses in both directions. By stimulation at the middle of an axon action potentials will therefore propagate in both directions away form the site of stimulation. In the living organism, impulses normally only propagate in one direction: From the soma along the axon towards the nerve terminals. At the transmission to other nerves — in the synapses — the impulse transmission can only happen in one direction. Synapses thus function as rectifiers [101, (Ch. 3)].

3.2.3 Neurotransmission and Synaptic Integration

The Structure of Synapses

By *neurotransmission* is meant transmission of impulses from one neuron to another. The contact point where this transmission of impulses takes place is called a *synapse*. Synapses are most often created between axon terminals and dendrites [24]. A synapse typically consists of three parts:

- **A pre-synaptic part:**
  The pre-synaptic part consists of a nerve terminal from an afferent neuron. The nerve terminal contains many vesicles. And the vesicles contain neurotransmitter molecules which can be released to the synaptic cleft and mitochondrias which has to do with the energy metabolism of the nerve terminal, since the fast synthesis of transmitter substance requires ATP. There are often thousands of pre-synaptic terminals for each post-synaptic neuron.
- **A post-synaptic part:**
  This is typically made up of the dendrites of the post-synaptic neuron. The cell membrane of the post-synaptic neuron contains receptors for transmitter molecules and possible enzymes to break down the transmitter molecules.
- **A synaptic cleft:**
  The synaptic cleft which is of a size of around $250\,\mathring{A}$ separates the pre-synaptic part from the post-synaptic part.

Neurotransmission is also termed synaptic transmission [101, (Ch. 3)].

The Function of Synapses

Several processes take place in synapses:

- transmission of impulses,
- integration of an impulse with other nerve impulses,
- modification of the nerve impulse, and
- rectification of nerve impulses [101, (Ch. 3)].

There are two main types of synaptic interaction: Electric transmission and chemical transmission.

Electric Synapses An *electric synapse* is a gap junction between two nerve cells — see Figure 3.8. The resistance over a gap junction is less than the resistance between the intracellular fluid and the

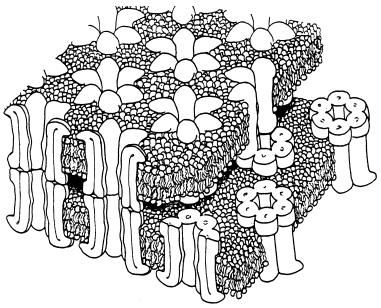

Figure 3.8: An electric synapse: Sketch of gap junction region showing individual connexons (membrane channels) bridging the gap between the lipid membranes of two opposed cells. A connexon connects the cytoplasm of one cell to that of the other. From Ref. [73, (Ch. 5)].

extracellular fluid of a normal cell membrane. In this way a gap junction makes up an electrical coupling between the intracellular potential in two nerve cells in order that a potential change (for instance a nerve impulse) in one nerve cell results in a potential change in the same direction in the other nerve cell. The coupling is usually too weak for an action potential to be transmitted between coupled cells. Instead the coupling seems to mean that if the coupled cells are active the impulse activity will be synchronized. A gap junction can be in two states with high or low resistance, respectively, and shifts between the two states can, for instance, be induced by intracellular changes in pH or Ca^{2+}-concentration. Gap junctions are permeable to substances with molecular weights up to 1000 [24].

Chemical Synapses Chemical synapses are more complex as illustrated by Figure 3.9. The transmission through a chemical synapse is one-way: From the pre-synaptic cell to the post-synaptic cell. The chemical transmitters are contained in cytoplasmatic vesicles inside the pre-synaptic cell. Through a process called *exocytosis* the content of the vesicle is emptied into the extracellular synaptic cleft. In this

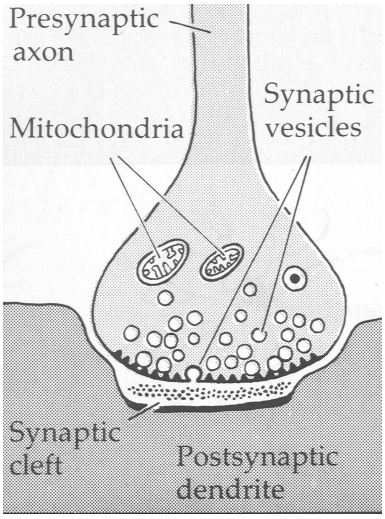

Figure 3.9: At chemical synapses the presynaptic terminal liberates a chemical, the transmitter, in response to a depolarization. Characteristically, at the site of a chemical synapse the two nerve cell membranes are thickened and are farther apart than elsewhere. Vesicles containing transmitter are aggregated close to the presynaptic membrane. Dense material is often present in the synaptic cleft and under the membrane of the post-synaptic cell. The transmitter binds to specialized chemoreceptor molecules that are situated in the post-synaptic membrane. From Ref. [73, (Ch. 1)].

process the membrane of the vesicle fuses with the cell membrane of the axon terminal. The immediate increase of the area of the membrane in the synaptic terminal is compensated by the ligation of new vesicles in areas of the membrane close to the synapse — a process called *endocytosis*. The reaction of the post-synaptic cell to the transmitting substance depends upon which ion permeabilities the receptors of the transmitting substance controls. Transmitting substances which decreases the excitability of the cell are called *inhibitory*, and the resulting potential changes in the post-synaptic cell are called *inhibitory post-synaptic potentials* (IPSP). Similarly, transmitting substances which increases the ion permeability of the post-synaptic cell membrane are called *excitatory*, and the resulting potential changes in the post-synaptic cell are called *excitatory post-synaptic potentials* (EPSP) [24].

Post-Synaptic Integration

Most nerve cells are contacted by thousands of pre-synaptic cells and are continuously bombarded by electrotonic potentials. The impulse-activity of the post-synaptic cell is determined by a translation of some sort, called *post-synaptic integration*, of all of the pre-synaptic potentials into a single impulse pattern in the axon of the cell. This translation is determined by the reaction of the soma-dendrite membrane to potential changes. This response is specific to the cell type, and thus synaptic integration is a property specific to the cell type.

The amplitude of an electrotonic potential decreases as the potential propagates away from the synapse. This is due to the fact that the increase of the conductance induced by the transmitter is limited to the post-synaptic membrane in the region of the synapse. Thus an action potential in a single pre-synaptic axon only results in a minor change of the impulse activity in the post-synaptic cell.

Since electrotonic potentials are not followed by a refractory period the potential changes can be temporally summed. Thus the influence of the individual pre-synaptic axon on the post-synaptic membrane potential is a direct function of the impulse frequency in the axon. The frequency of action potentials in an axon is directly dependent on the membrane potential in the soma region, and is thus controlled by the sum of electrotonic potentials which is transmitted to the membrane of the soma [24].

3.3 The Cortex of Cerebellum

The emphasis of this description of the cortex of cerebellum will first be on the organization of the cells, and afterwards on the function of the cortex during activation.

3.3.1 The Neuronal Organization

The neuronal circuitry of the cerebellar cortex is organized as a repeated pattern of nerve cells. The few types of neurons form layers and directions — see Figures 3.10 and 3.11.

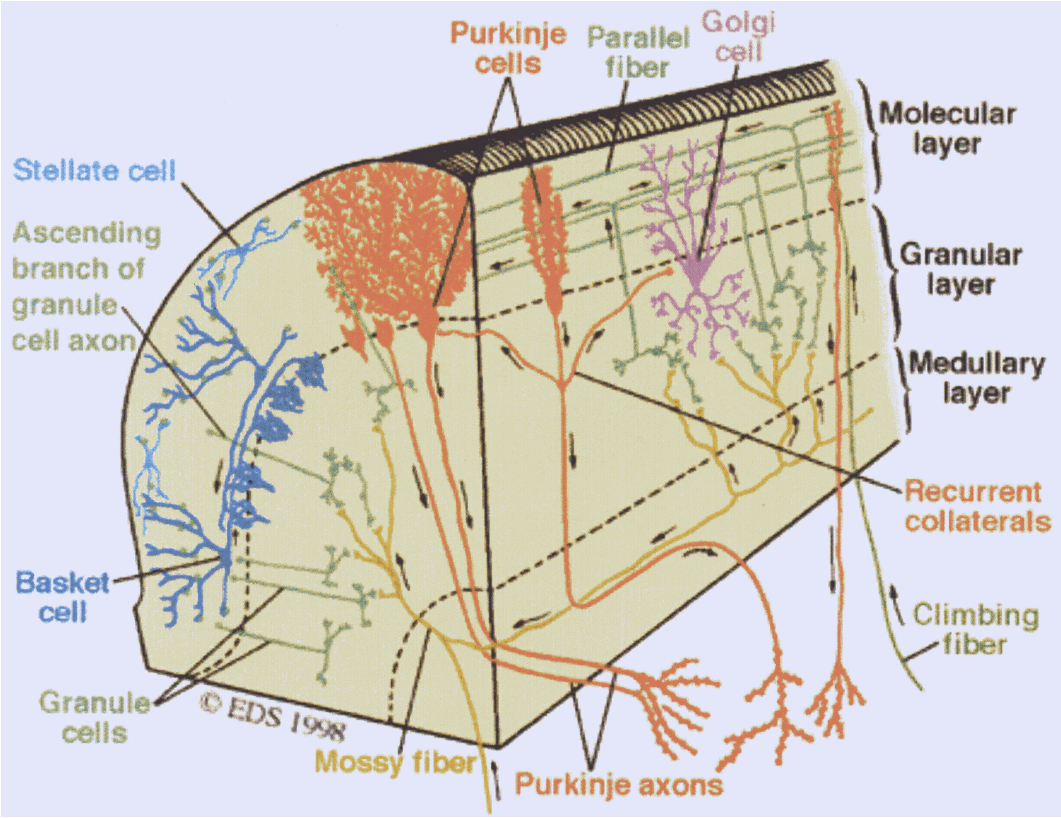

Figure 3.10: The anatomy of the cerebellar cortex: The molecular layer contains the parallel fiber part of granule cell axons, which are running in the transverse plane; dendrites of Purkinje cells, which are flattened so that they lie parallel to the sagittal plane; and interneurons (Basket cells, Stellate cells, and Golgi cells). The granular layer consists primarily of granule cells which receive synaptic input from mossy fibers. In between the molecular and the granular layer is a layer of Purkinje cells. Below the cortex is the medullary layer which consists of white matter. From Ref. [30, (Sect. 2.2)].

Cell Types

The cortex contains five major cell types — see Figure 3.11: *Purkinje cells* (21 μm in diameter), *stellate cells* ($5-12$ μm in diameter), *basket cells* ($5-12$ μm in diameter), *Golgi cells* ($10-24$ μm in diameter), and *granule cells* ($5-8$ μm in diameter) [30, (Sect. 2.2)].

Layers

The cerebellar cortex consists of grey matter, that is, nerve tissue composed mainly of the cell bodies of neurons rather than their processes. The cortex is divided into three layers — see Figure 3.11: The *molecular layer* which is $200-400$ μm deep. The *Purkinje cell layer* which is about 100 μm thick. And the *granule cell layer* which is $400-500$ μm deep [67]. Below is the white matter, which principally consists of (myelinated and unmyelinated) nerve fibers (that is, axonal portions of neurons).

Planes

Two major planes can be found — see Figure 3.10: The *parasaggital plane* in which the dendrites of Purkinje cells and the molecular layer interneurons are aligned, and the *transverse plane* in which the parallel fiber part of the granule cell axons run [30, (Sect. 2.2)] .

Synapses

The basic circuitry of the cerebellar cortex is organized around the *Purkinje cell* — the principal neuron of the cerebellar cortex — from which the final and only output from the cerebellar cortex originates. The activity of Purkinje cells is influenced by two excitatory afferent inputs: Parallel and climbing fibers that excite different parts of the cell — see Figure 3.11 — with important consequences for the evoked activity. The Purkinje cell receive excitatory input from one climbing fiber and thousands of parallel fibers [66].

The *climbing fibers* originate from the inferior olive nucleus in the brain-stem and make strong mono-synaptic excitatory contacts with the proximal dendrites of Purkinje cells [67]. In most adult animals, only one climbing fiber afferent contacts a given Purkinje cell. The contacts are made on groups of post-synaptic spines of primary or secondary dendrites (i.e., close to the cell body). Clusters of several spines are often contacted by *en passant* enlargements of a climbing fiber and as many as 300 spines are contacted by a single afferent climbing fiber [57].

Parallel fibers, the axons of granule cells, provide excitatory synapses to inhibitory interneurons and to the distal dendrites of Purkinje cells thus being in di-synaptic contact with the Purkinje cells. The parallel fibers run transversely in the molecular layer [66].

The two afferent systems differ not only topographically but also with respect to synaptic strength. As a rule, only one climbing fiber contacts a given Purkinje cell. As many as several hundred spines of one target cell are contacted by a single climbing fiber as it winds around the proximal dendritic tree and the cell body giving an extensive interface for synaptic contact to a single Purkinje cell. Each Purkinje cell is contacted by several thousands parallel fibers, each parallel fiber makes only one or a few synapses on the dendritic spines of each Purkinje cell. Climbing fibers form a more powerful mono-synaptic excitatory input onto the Purkinje cells (...) than parallel fibers [4].

Additionally, the cerebellum is under constant inhibitory control by *stellate cells* and *basket cells* in the molecular layer, and *Golgi cells* in the granule cell layer [66]. Parallel fibers form excitatory synapses on stellate and basket cells which in turn inhibit Purkinje cells. Stellate cells have short axons contacting nearby Purkinje cells in the molecular layer while basket cells have axons that run perpendicular to the parallel fibers and contact the cell bodies of more distant Purkinje cells up to 1000 μm perpendicular to the beam of parallel fibers [2].

3.3.2 The Neuronal Function

The function is now described with an emphasis on both electrical phenomenon inside individual neurons and synaptic transmission.

Purkinje cells *in vivo* fire at a rate of 10 to 20 Hz under control conditions, and their activity is modified by two excitatory afferent inputs: Parallel fibers and climbing fibers [57]. For illustration see Figure 3.11.

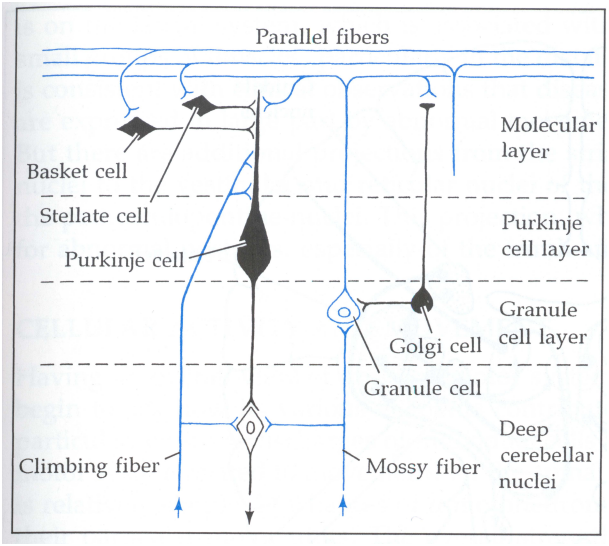

Figure 3.11: Inputs and outputs within the cerebellum. The cerebellar cortex is subdivided into the granule cell layer, Purkinje cell layer, and molecular layer. Open cells make excitatory synaptic connections, filled cells inhibitory connections. The sole output from the cortical layer to cells of the deep cerebellar nuclei is by inhibitory axons from Purkinje cells. Mossy fiber inputs end on granule cells, whose axons ascend to the molecular layer to form a parallel fiber network. Parallel fibers form excitatory synapses on Purkinje cells, stellate cells, basket cells, and dendrites of Golgi cells. Climbing fibers form excitatory synapses on dendrites of Purkinje cells. Both climbing fibers and mossy fibers make excitatory connections with cells in the deep cerebellar nuclei. From Ref. [73, (Ch. 15)].

IO Stimulation

Activation of a climbing fiber, caused by stimulation of the inferior olive (IO), elicits a stereotyped synaptic response, the complex spike (i.e., a large action potential in Purkinje cells followed by high-frequency bursts of smaller action potentials). This action is the result of a strong mono-synaptic input and the intrinsic membrane properties of the proximal part of the dendritic tree of the Purkinje cells: Voltage-dependent conductances and conductances gated by second messenger systems. The transmitter is glutamate and the post-synaptic receptor is an AMPA receptor. In addition, glutamate released from climbing fiber afferents in the cerebellar cortex presynaptically inhibit GABAergic neurotransmission from interneurons converging on the same Purkinje cell via activation of AMPA receptors. This dual AMPA receptor-mediated response of excitation and disinhibition increases the safety factor of cerebellar climbing fiber signals [57].

PF Stimulation

Parallel fiber (PF) stimulation results in the propagation of action potentials in these fibers that trigger the release of the excitatory transmitter glutamate. Glutamate interacts with the so-called AMPA receptor, a glutamate subtype, on the terminal spine branchlets of the Purkinje cells, and as many as 200,000 parallel fibers contact one Purkinje cell. The consequence of parallel fiber stimulation is mono-synaptic excitation of the Purkinje cell by the parallel fibers themselves, and inhibition due to excitation of interneurons. Interneurons release GABA that interacts directly with $GABA_A$ receptors on Purkinje cells, and indirectly by modifying glutamate release from parallel fibers via $GABA_B$ receptors [57].

IO versus PF Stimulation

In summary, IO stimulation produces a short-lasting powerful excitatory input onto Purkinje cells, whereas activity in PFs produce more complex integration in Purkinje cells on a longer time scale [57].

Chapter 4

The Extracellular Space

This chapter describes the internal structure and function of the extracellular space. For the purpose of comparison also the intracellular fluid is considered.

The chapter is based on textbook material as well as scientific journals.

4.1 The Structure of the Extracellular Space

The neurons and glial cells of the brain are mingled together in an opaque mass with the consistency of soft jelly. The cells have complex shapes, yet remain distinct entities bounded by their membranes and separated from each other by an extracellular space [75].

The extracellular microenvironment consists of the narrow gaps between cellular processes, probably not more than $200\mathring{A}$ wide on the average [74]. These spaces form a complex three-dimensional mosaic: The structure of brain extracellular space resembles foam.

The mosaic is so pervasive that the volume fraction (the fraction of volume of the extracellular space to the total volume of tissue) of the molecular layer is 22 %. This feature reflects the need for a significant brain extracellular microenvironment.

The extracellular space is highly connected with generally convex, non-invaginated, cell surfaces. The extracellular space is not uniform in size but has narrow regions that exclude the larger molecules, thus making them take a longer path as they diffuse.

The density of the extracellular matrix is quite sparse [75].

4.2 The Extracellular and Intracellular Fluids

The cells of the organism are bathed in a solution of salt the composition of which remains remarkably constant under changing external conditions.

However, the constitution of the fluid inside the cells is very different from that of the fluid outside the cells. Thus one distinguishes between the *intracellular fluid* and the *extracellular fluid* [101, (Ch. 10)].

4.2.1 The Extracellular Fluid

The extracellular phase is divided into blood plasma and the interstitial phase.

The extracellular fluid is found partly in the vascular bed as plasma (water) and lymph, partly outside the vascular bed in the interstitial space between the cells. Plasma contains around 10 % dry matter (weight/volume) and the solvent is water.

The extracellular phase is characterized by high concentrations of Na^+- and Cl^--ions and a low concentration of K^+-ions [101, (Ch. 10)]. Furthermore it contains hormones [101, (Ch. 8)] and nutrients.

4.2.2 The Intracellular Fluid

Contrary to the extracellular phase the intracellular phase is characterized by low concentrations of Na^+- and Cl^--ions and a high concentration of K^+-ions. The intracellular phase furthermore contains major concentrations of organic phosphates (for instance ATP) and protein-anions [101, (Ch. 10)].

4.3 The Role and Function of the Extracellular space

4.3.1 The Role of the Extracellular space

The extracellular space exists for several reasons. The extracellular space provides an extracellular microenvironment, similar to that of cerebrospinal fluid, but with an additional matrix of proteoglycans and glycosaminoglycans. The matrix composition varies with the cytoarchitectonics, but we know little about its density and we lack reliable evidence that it affects diffusion. The extracellular space allows glucose to reach brain cells from the blood vessels. It provides a low-resistance path that complete the circuit for the transmembrane currents that generate action and synaptic potentials. The extracellular space is also a communication channel between cells. This channel is distinct from classical synaptic transmission, and has been termed extrasynaptic or volume transmission [75].

4.3.2 The Function of the Extracellular space

For many molecules, migration through the extracellular space is governed by diffusion. Diffusion anisotropy was first detected for in the cerebellum. The molecular layer in cerebellum is anisotropic with the apparent diffusion coefficient being smallest across the parallel fibers and in the plane of the pial surface. The apparent diffusion coefficient in the vertical direction is slightly smaller than along the parallel fibers. The anisotropy determined in the cerebellar molecular layer will channel excess excitatory transmitters, that spill over at the synapses, and other neuro-active substances in specific directions. In myelinated tissue, preferential diffusion of neuro-active substances and metabolites, therefore, might occur along the axons. The granular cell layer is isotropic.

Some of the spaces in the brain might restrict the diffusion of macromolecules.

The viscosity of the extracellular space must be close to that in the cerebrospinal fluid.

Stimulation of cells can lead to changes in the volume fraction and in the apparent diffusion coefficient, presumably because cells change their volume, indicating that the extracellular space is a dynamic entity. Nevertheless, the spaces of the brain are never totally occluded [75].

Chapter 5

The Vascular Subsystem

This chapter describes the internal structure and function of the vascular subsystem. This material stems from textbooks on physiology.

5.1 The Constituents of the Blood

Blood consists of cells embedded in plasma.

Plasma is a solution of dry matter in water. The dry matter consists of plasma proteins. Furthermore plasma contains a number of inorganic ions, such as Na^+ and Cl^-, organic molecules (hormones and enzymes, for instance), nutrients, waste products and physically dissolved gases.

Blood cells are divided into red blood cells, called *erythrocytes*, white blood cells, called *leukocytes* and blood platelets, called *thrombocytes*.

The main functions of erythrocytes are to transport oxygen which is bound to the red pigment *hemoglobin* to the tissues and to transport CO_2 (the major waste product of energy production in the tissues) from the tissues to the liver [101, (Ch. 6)].

5.2 The Mechanics of the Blood Flow and the Vascular Subsystem

The purpose of the circulatory system is to provide nutrients to and remove waste products from the cellular interstitium. To do so requires continuous filtration of the interstitium. The filtration is accomplished primarily at the level of capillaries, as fluid moves out of the capillaries at the arteriole end and back into the capillaries at the venous end [47, (Sect. 15.3)].

5.2.1 The Structure of the Vascular System

The circulation can be compared to two pumps connected in series and connected to the vascular system. It can be divided into two main parts: the systemic circulation and the lung circulation.

The blood vessels can be classified as: transport vessels, resistance vessels, exchange vessels, shunt vessels and capacitance vessels — see Figure 5.1.

The transport vessels consist of the larger *arteries*. They have thick walls with lots of elastic elements and smooth musculature. The smooth musculature is innervated by sympathetic nerves with vasoconstrictive effects on the vessels. Transport vessels are rather stiff with a compliance which is much less than that of the thin-walled veins.

The resistance vessels are the *arterioles*. The walls of arterioles contain much fewer elastic elements, but more musculature than the arteries. The diameter of these vessels can thus be reduced significantly.

The exchange vessels consist of the *capillaries* and the smallest veins. Capillaries have thin walls without musculature. The inner side of the vessels are coated with endothelium cells. In most capillaries the endothelium cells do not adjoin each other. Thus there is space between the endothelium cells which allows an appreciable passage of substances out through the capillary wall. The width of the space however varies considerably from region to region. The spaces in the central nervous system, especially

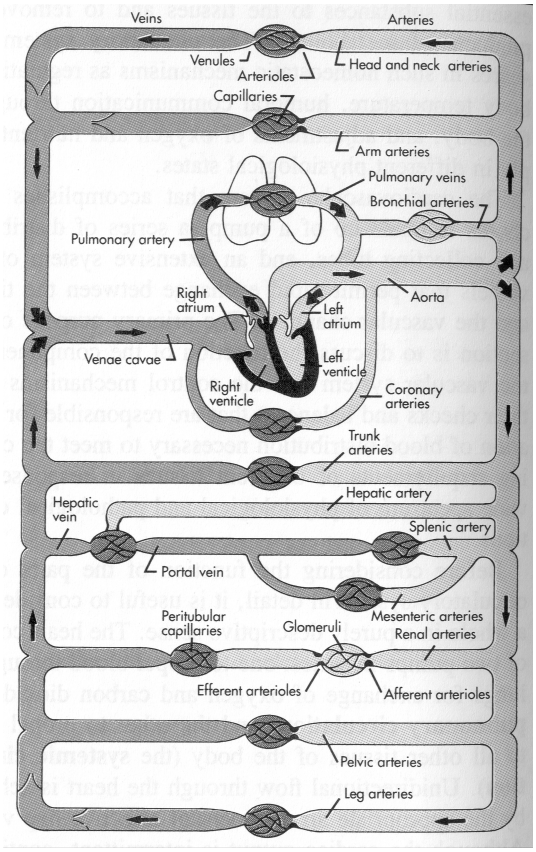

Figure 5.1: Schematic diagram of the parallel and series arrangement of the vessels composing the circulatory system. The capillary beds are represented by thin lines connecting the arteries (on the right) with the veins (on the left). The crescent-shaped thickenings proximal to the capillary beds represent the arterioles (resistance vessels). From Ref. [12, (Ch. 22)].

in the brain, are very narrow and have the character of tight junctions. Therefore the brain capillaries are very tight and do only with difficulty allow passage of selected substances through the wall. This is called the *blood-brain barrier* and denotes the difficult exchange of substances between the blood in the capillaries and the interstitial space in the brain. The blood perfusion in the group of capillaries which get their blood supply from an arteriole — see Figure 5.2 — is controlled by changes in the degree of contraction of the arterioles.

Capacitance vessels consist of the *veins*. These vessels have thin walls but do have a certain content of muscle cells in the walls which allow constriction. The thin, in-elastic walls give the veins a very large compliance (capacity), which makes them suited for undergoing considerable volume changes without significant pressure changes [101, (Ch. 6)].

5.2.2 The Capillary Function

In this area of the vascular bed exchange occurs between the blood and the tissue of oxygen, carbon dioxide, nutrients and waste products.

The passage of substances through the capillary wall can either happen by diffusion through the membrane area or through water-filled membrane pores, or by filtration and osmosis of fluid.

While transport of fluid through the capillary membrane happen by a filtration process, the diffusion process is the dominant transport form of exchange of substances through the capillary membrane. Lipophilic substances like O_2 and CO_2 diffuse directly through the cell membrane of the endothelium cells, while hydrophilic substances like glucose normally pass through the narrow passage through the space between the endothelium cells. There are exceptions. Glucose, for instance, pass through the endothelium cells of the brain capillaries by a facilitated diffusion process. This is why brain tissue — despite the large tightness of the brain capillaries — can get its most important nutritive medium, glucose, supplied in sufficient amounts.

The perfusion through the capillaries is controlled by the degree of constriction of the arterioles, which is regulated partly by nerves, partly by local metabolic products. The nervous control is mainly performed by the sympathetic nervous system. The local metabolites (Ca^{++}, K^{+}, NO, adenosine, lactic

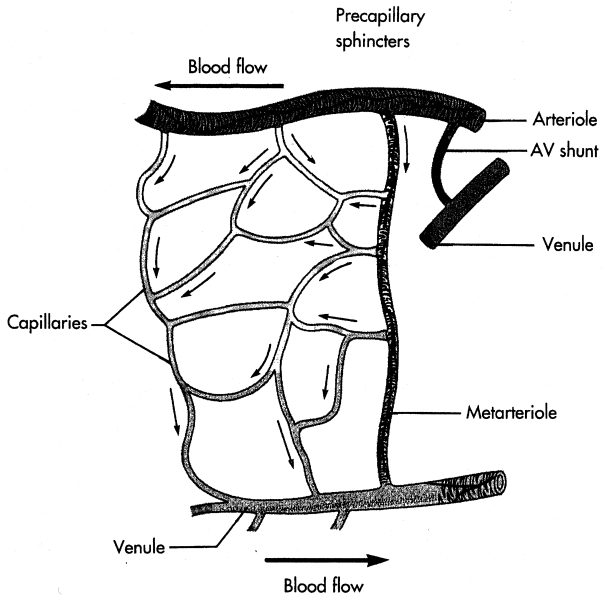

Figure 5.2: Schematic picture of a network of capillaries. On the inside of capillaries there are endothelium cells. From Ref. [47, (Sect. 15.3)].

acid, H^+, CO_2, etc.) act on the smooth musculature of the arterioles and thereby have crucial significance for the distribution of the blood flow through the various capillary areas [101, (Ch. 6)].

5.3 Neural Control

5.3.1 The Innervation of the Vessels and the Heart

All vessels — except the capillaries — in the organism receives nerve signals from the sympathetic nervous system which comprises vasocontrictory as well as vasodilatory nerves.

The heart is innervated by both the sympathetic nervous system and the parasympathetic nervous system [101, (Ch. 6)].

5.3.2 Systemic Regulation Mechanisms

These control mechanisms are executed by the nervous system. From certain pressure sensitive areas (pressure- or baro-receptors) afferent impulses start depending on the size of the blood pressure. These impulses influence centers in medulla oblongata (the prolongation of the spinal cord) which regulate the circulation. Efferent nerve impulses emanate from these centers and reach towards vessels (through sympathetic nerves) and heart (through sympathetic as well as parasympathetic nerves) [101, (Ch. 6)].

5.4 Local Control

5.4.1 Auto-Regulation

Despite variations in the blood pressure some organs and parts of the organism are to a high degree able to maintain a rather constant blood flow as illustrated by Figure 5.3. This phenomenon is called *autoregulation* and is pertaining to the kidneys, the brain, the liver, and the myocardium (the cardiac musculature) [101, (Ch. 6)]. Autoregulation is a local mechanism that makes flow through a tissue responsive to local oxygen demand but relatively insensitive to arterial pressure. In tissues for which the delivery of oxygen is of central importance (for example, the brain and the heart) the local blood flow is controlled to be slightly higher than required, but no higher [47, (Sect. 15.6.1)].

The mechanism behind autoregulation is not fully understood. Especially two hypotheses are dominating: The myogenic and the metabolic hypotheses:

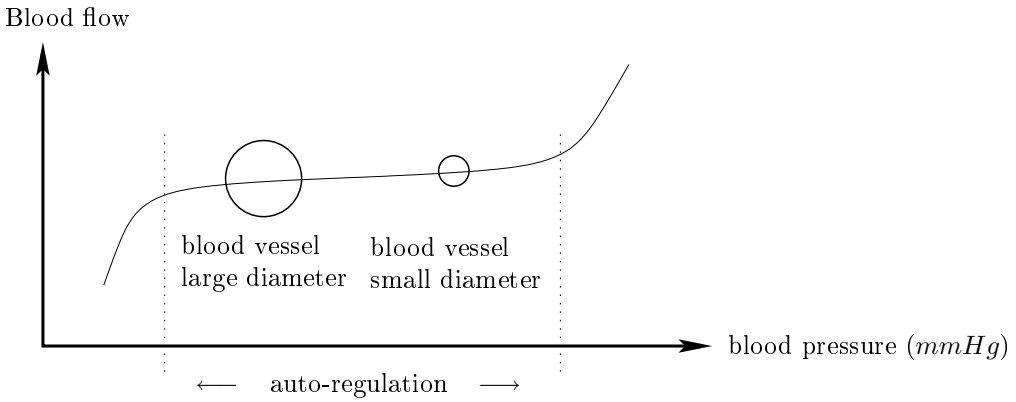

Figure 5.3: Illustration of autoregulation. Within a range of values of the arterial blood pressure the blood flow is almost constant.

- According to the *myogenic hypothesis* a rise in the blood pressure will result in a dilation (distension) of the blood vessels, which reflectorily causes a contraction of the vessel muscles and thereby results in larger resistance followed by decreased blood flow and thus a smaller blood pressure.
- According to the *metabolic hypothesis* vasodilatory substances are created in the tissue which accumulate when the blood flow decreases. In this situation the O_2-tension and the pH in the tissue decrease while the CO_2-tension increases. Furthermore the temperature of the tissue can increase, and K^+-ions and adenosine can accumulate. These factors cause a vasodilatation thus compensating for the primary decrease in blood flow.

The experimental results most strongly support the metabolic theory [101, (Ch. 6)].

5.4.2 Vasoactive Substances from Endothelium Cells

The endothelium cells on the inner side of the vessels produce several vasoactive substances, i.e. substances which influence the dilation or the constriction of the blood vessels. These substances diffuse the short way to the smooth muscle cells of the vessel walls and thereby have a local effect on the constriction degree (vascular tone) of the vessels. The substances include *nitric oxide* (NO) and *prostacyclin* both of which are vasodilatory substances, as well as *endothelins* (three rather alike peptides consisting of 21 amino acids) which are vasoconstrictive [101, (Ch. 6)].

Chapter 6

Neuro-Vascular Coupling

This chapter describes research results concerning as well as theories of the mechanisms responsible for the coupling between local neuronal activity and the resulting local vascular responses.

After a short system overview, the possible function of astrocytes is considered. Then each of the putative mediators are considered separately, and some interactions among them are described. Afterwards the suggested mechanisms involved when stimulating the inferior olive (IO) and the parallel fibers (PF), respectively, are described and compared. Finally, some comments upon the validity of the research results and theories are made.

6.1 System Overview

Neuronal activity produces increases in blood flow that are spatially restricted to the activated region and temporally related to the period of activation, a phenomenon termed *functional hyperemia* [44, 35]. The neuro-vascular system is illustrated by Figure 6.1. The sketch also illustrates that the research object is

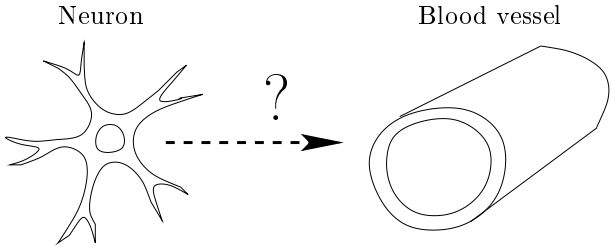

Figure 6.1: An illustration of the neuro-vascular system, and the question of how the coupling is mediated.

the mechanisms responsible for neuro-vascular coupling.

Since Roy and Sherrington [80], it is the prevailing view that during increased neuronal activity, vasodilator products accumulate. These metabolites are thought to diffuse to the blood vessels, which they relax with a subsequent increase in local CBF [100]. This picture clearly attributes an important role to the extracellular space. It is more unclear, when and how neuroglia contributes to coupling. Some of the viewpoints, which have been put forward concerning this issue, are presented in P: Section 6.2.3.

Functional activation dilates arterioles in the activated brain area. Although small arteries and arterioles contain probably < 5 % of the blood volume in the brain parenchyma, they control most of the resistance and therefore blood flow at a local level. If a feeding artery dilates, blood flow in the capillaries and veins of the supplied area increases. This means that flow velocity of cells and plasma as well as cell volume in the region increase [100].

6.2 Do Astrocytes Contribute to Coupling?

6.2.1 What are Astrocytes?

Neuroglia is the tissue that surrounds and supports neurons in the central nervous system [91].

A striking feature of glial cells is the absence of an axon-like process. Action potentials usually cannot be initiated in glial cells. This property makes glial cells fundamentally different from the excitable neurons [73, (Ch. 6)].

In the vertebrate central nervous system neuroglial cells are usually subdivided into two main groups (astrocytes and oligodendrocytes) and several subgroups. Astrocytes are the most predominant type of glial cells in the central nervous system and constitute over 50 % of the cell mass in the brain [35]. Some types of astrocytes make contacts with capillaries and neurons. Oligodendrocytes form myeline around the larger axons [73, (Ch. 6)].

Astrocytes and the extracellular space provide morphological relationships between neurons and blood vessels. Whereas it is generally accepted that the extracellular space plays a role in functional coupling, the role of astrocytes is controversial.

Now follows first a review of information concerning the morphological relationship, and afterwards an account for some of the suggestions concerning the functional coupling provided by astrocytes.

6.2.2 Morphological Relationship

The structural elements of the neuro-vascular system, including neuroglia and extracellular space, are illustrated by Figure 6.2.

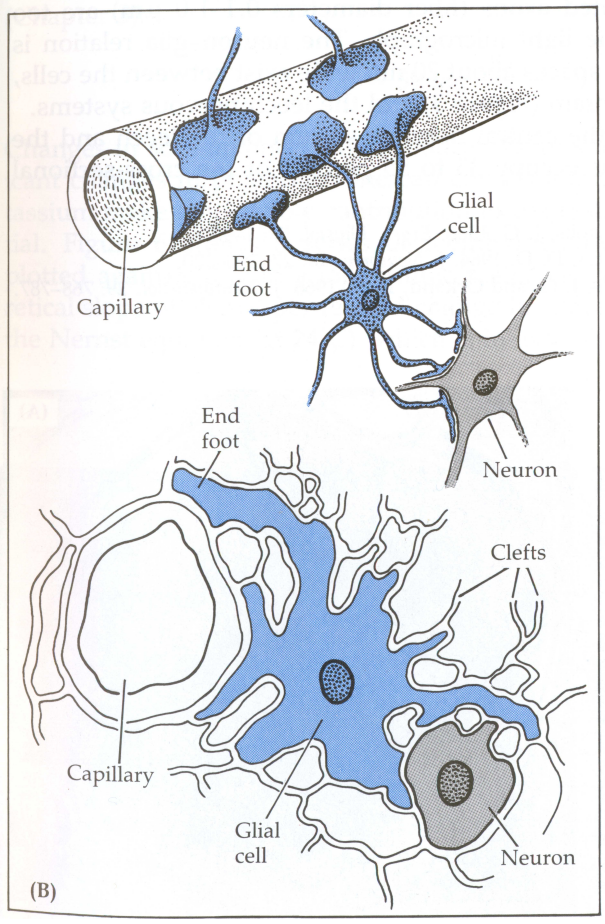

Figure 6.2: Morphology of the neuro-vascular system: Neurons, glia, extracellular space, and blood vessels. The most direct pathway from the capillary to the neuron is through the aqueous intercellular clefts that are open for diffusion. Cell dimensions are not in proportions. From Ref. [73, (Ch. 6)].

Adjacent glial cells are linked to each other by low-resistance connections that permit the direct passage of ions and small molecules between the cells. The connections have the form of gap junctions which link the interiors of the glial cells [73, (Ch. 6)]. The gap junctions between the astrocytic endfeet

allow the passage not only of ions but also metabolic substrates such as glucose and lactate and may act as a diffusion barrier between the blood vascular system and the extracellular compartment [35].

Neurons and glial cells, on the other hand, are always separated from each other by narrow, fluid-filled, extracellular spaces (clefts) that are about 20 nm wide and prevent currents generated by nerve impulses from spreading into neighboring cells.

Astrocytic processes generally surround neurons except where synaptic contacts are made [73, (Ch. 6)], see Figure 6.3.

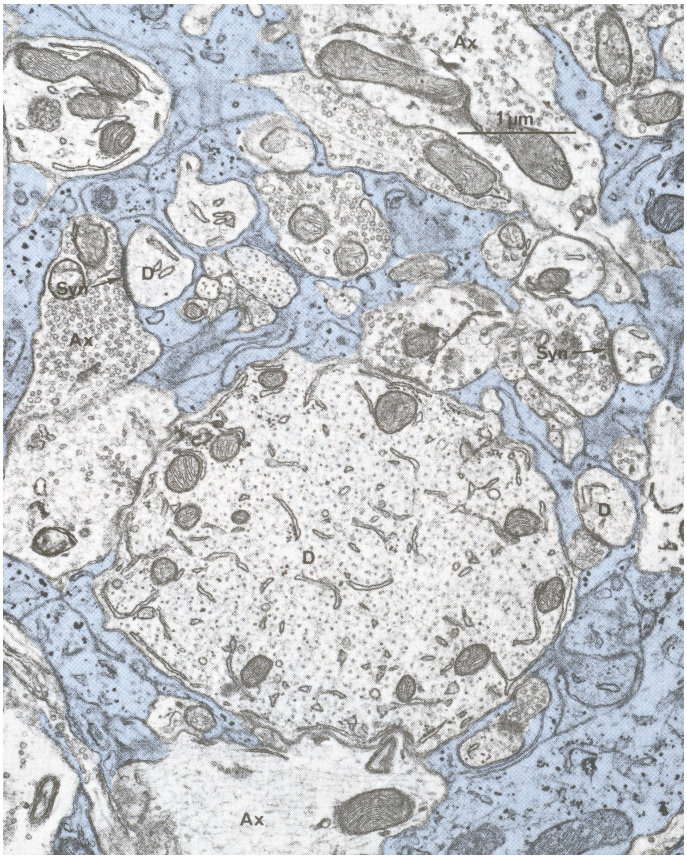

Figure 6.3: Neurons and glial processes in the cerebellum of the rat. The glial contribution is lightly colored. The neurons and glial cells are always separated by clefts about 20 nm wide. The neural elements are dendrites (D) and axons (Ax). Two synapses (Syn) are marked by arrows. From Ref. [73, (Ch. 6)].

6.2.3 Functional Coupling

The interposition of glial cells between capillaries and neurons in the brain, the narrowness of the extracellular spaces, and the intricate anatomical relationship of the two types of cells suggest dynamic interactions [73, (Ch. 6)].

Communication between neurons and astrocytes is rapid [35].

The fluid composition surrounding neurons is influenced by neuroglial cells and by the endothelial cells lining capillaries that constitute the blood-brain barrier.

Neurons influence glial cells by releasing potassium in the intercellular spaces during the conduction of impulses, thereby depolarizing the glial membrane.

An obvious effect of glial cells on fluid environment is to allow the concentration of potassium in the vicinity of neurons of the brain to rise following impulses. Simply by virtue of its presence on the other side of a narrow cleft next to a neuronal membrane, the glial cell allows potassium to build up instead of diffusing into a larger extracellular space. By the same token, had the membranes of another neuron been situated in place of the glial cell, it would have been subjected to a higher potassium concentration. Glial cells, therefore, separate and group neuronal processes, allowing local potassium buildup and preventing cross talk.

An attractive concept is that glial cells might regulate the potassium concentration in intercellular clefts, a process known as *spatial buffering*. According to this hypothesis, glial cells act as conduits for rapid uptake of potassium from the clefts to preserve the constancy of the environment. Clearly,

nonuniform depolarization of glial cells causes current to flow and results in the movement of potassium ions. Since glial cells are coupled to each other, potassium would follow the lines of current flow entering in one region and leaving at another [73, (Ch. 6)].

6.3 Putative Mediators of Neuro-Vascular Coupling

To serve as a mediator of neuro-vascular coupling, a substance should

- be produced and released in response to increased neuronal activity, and
- be a potent vasodilator or vasoconstrictor.

The chemical mediators that have received the most attention are NO, adenosine, K^+, H^+, and CO_2 [100, 18]. They are all vasodilators.

This section considers each of the chemical substances, which have been proposed as mediator of neuro-vascular coupling, separately. The following is described:

- Where and how the substance is released from the neuron.
- How the substance moves from the neuron to the vessels.
- How the substance causes vasoactivity.
- How the substance is removed from the blood flow.

Afterwards it is discussed how the mediators may interrelate.

6.3.1 NO

The gaseous bioradical nitric oxide (NO) has entered the field of putative mediators of coupling. In fact, NO might be regarded as the "ideal" molecule for coupling: It is produced locally by neurons and/or astrocytes upon glutamate receptor activation; it is also diffusible, short-lived, and a potent vasodilator [100]. NO has been assigned a unique role as an intercellular messenger in the nervous system because it can diffuse a long distance and penetrate cell membranes freely [86].

Production of NO

NO is the product of the enzyme nitric oxide synthase (NOS). There exists three isoforms of the enzyme: Neuronal NOS ($nNOS$), endothelial NOS ($eNOS$), and immunological NOS ($iNOS$).

Of the isoforms of nitric oxide synthase, the neuronal type ($nNOS$) is distributed widely in the brain [85]. In cerebellum, $nNOS$ is present at high concentration. Purkinje cells and climbing fibers do not contain $nNOS$-activity. $nNOS$ is expressed by basket cells, granule cells and their processes parallel fibers, and by glial cells [4]. In fact, parallel fibers are the main NO source in the cerebellar molecular layer [85].

In the central nervous system, the production of the diffusible messenger nitric oxide (NO) is typically brought about as a result of influx of Ca^{2+} through N-methyl-D-aspartate ($NMDA$) receptor channels, which stimulates the Ca^{2+}/calmodulin-dependent enzyme $nNOS$ tethered nearby. Although widespread, this is not the only mechanism, as activation of non-$NMDA$ receptors and voltage-sensitive Ca^{2+} channels can also lead to NO formation [14]. L-arginine is a substrate for NOS synthesis [85]: The brain parenchymal enzyme NOS forms NO from L-arginine [27]. Thus the increase in regional CBF during neuronal activation depends on the concurrent occurrence of two signals: One for the activation of the enzyme and the other for the supply of substrate [35].

Release of NO

NO is produced in response to synaptic activity [4]:

Endogenous NO release might be triggered by increases in intracellular calcium in Purkinje cell dendrites following climbing fiber activation and the resultant activation of NO synthase [86].

NO is released from parallel fibers upon Ca^{2+} influx into the nerve terminals, as is glutamate. Although the same Ca^{2+} channels in the presynaptic region of parallel fibers may be involved in the release of NO and glutamate, NO is not released via exocytosis [85].

Transport of NO from Neurons to Vessels

Because membranes provide no greater barrier to nitric oxide than to oxygen or carbon dioxide, diffusion away from a single cell producing nitric oxide is more significant than reactions of nitric oxide within the cell [10].

NO is a Vasodilator

The CBF responses to NO are mainly or exclusively mediated via $cGMP$ synthesis by guanylate cyclase: NO binds to ferrous heme in guanylate cyclase [10] and thereby activates soluble guanylate cyclase in vascular smooth muscle (but not in Purkinje cells). Guanylate cyclase synthesizes $cGMP$. Thereby tissue levels of $cGMP$ are increased [4]. The activation of vascular smooth muscle leads to CBF increases [4].

NO is a mediator, not a modulator, of the cerebellar CBF increase elicited by neuronal activity. Locally synthesized NO is particularly important for the initiation of the vasodilation [2].

In vivo NO is a powerful vasodilator and regulates resting cerebral blood flow [35].

Removal of NO

NO is removed by the blood flow since hemoglobin strongly binds NO [85]. Due to rapid destruction by oxyhemoglobin, nitric oxide cannot be transported through the vasculature [10].

6.3.2 Adenosine

Adenosine is a neuro-modulator, and adenosine receptors are widely distributed in the central nervous system, pointing to a basic role of adenosine in neurotransmission. Adenosine receptors can be found on neurons, astrocytes, and brain microvascular endothelial cells. Therefore it is likely that adenosine has functions beyond being a product of compromised energy metabolism. Although the mechanisms by which adenosine may be released in a transmitter/modulator fashion are not well characterized, it is conceivable that adenosine may be released from neurons or astrocytes not only as a result of energy failure, but also upon stimulation [100].

Production of Adenosine

Two pathways for the production of adenosine have been identified:

In one, adenosine arises from hydrolysis of $5' - AMP$. The $5' - AMP$ is formed from the breakdown of ATP and results from the imbalance between energy-utilizing and energy-generating reactions.

In the other pathway, adenosine arises from the hydrolysis of S-adenosylhomocysteine. It is the product of about 40 different methylation reactions in which the methyl group of S-adenosylmethionine is transferred to the various methyl acceptors yielding S-adenosylhomocystine as a demethylated product [13].

Release of Adenosine

Adenosine is released upon depolarization of climbing fibers [4].

Adenosine is a Vasodilator

The purine nucleotide, adenosine, is a potent vasodilator [32]. In brain, adenosine causes pial vessel dilation, and the smaller pial vessels are more reactive than are the larger pial vessels [13].

Removal of Adenosine

Adenosine is *not* removed by the blood flow, since the blood-brain barrier does not allow reabsorption into the blood flow of either adenosine or H^+ [98]. However, adenosine is rapidly in-activated by cellular uptake and deamination or phosphorylation [32]. The result is a rapid biological turnover of adenosine [100].

6.3.3 K^+

Considerable advances have been made in the understanding of K^+-dependent vasorelaxation. However, direct evidence for the potassium hypothesis of coupling is still lacking [100].

Release of K^+

Several basic processes of excited nerve cells, e.g., action potentials and synaptic transmission, result in increased extracellular potassium concentration ($[K^+]_e$) [19].

Transport of K^+ from Neurons to Vessels

K^+ may be transported from neurons to vessels through the extracellular space or through neuroglia:

A local increase in the extracellular potassium concentration is immediately buffered by extracellular diffusion, ionic currents in glial cells (the spatial buffering mechanism, see P: Section 6.2.3) and active uptake of K^+ by glial cells due to increased activity of the $Na^+ - K^+$ pump [19].

The attractive hypothesis of K^+ *siphoning* suggests that K^+ furthermore is transported from neurons to the arteriole wall through the glial cell type astrocytes: K^+ is released by active neurons, taken up by astroglial cells, and transported to glial endfeet, where the K^+ is released in the proximity of cerebral arterioles [100]. The possible function of astrocytes in neuro-vascular coupling is further discussed in P: Section 6.2.

K^+ is a Vasodilator

Increases of $[K^+]_e$ induce vasodilation in surrounding blood vessels: Elevations of $[K^+]_e$ in the microenvironment of the vascular wall hyperpolarize the cell membrane of vascular smooth muscle through activation of the $Na^+ - K^+$ pump and through inwardly rectifying K^+ channels. The delayed rectifier potassium channel also contributes to relaxation of cerebral vessels in response to modest increases in $[K^+]_e$. As a consequence of smooth muscle hyperpolarization, voltage-dependent Ca^{2+} channels close, the intracellular Ca^{2+} concentration decreases and smooth muscle relaxation and vasodilation occur. Besides its direct action on the blood vessel, elevation of $[K^+]_e$ also increases metabolism by stimulating the $Na^+ - K^+ - ATPase$ which leads to increased production of the potent vasodilators lactate, adenosine, and H^+. In fact, K^+ is in general a potent vasodilator in the cerebral circulation [19].

Removal of K^+

The K^+ is cleared from the brain by the increased blood flow [100].

6.3.4 H^+

Protons probably do not contribute to coupling:

A transient increase in the tissue lactate concentration during neuronal activation has been demonstrated. Direct measurement of extracellular pH under physiological stimulation conditions are lacking. Due to the increase in lactate, decreases in the extracellular pH are expected. Since tissue acidosis during activation is transient whereas CBF remains elevated during sustained activation, it is unlikely that the entire response can be explained by changes in pH [100].

6.3.5 CO_2

CO_2 is a Vasodilator which is Removed by the Blood Flow

One of the first chemical agents found to have a strong effect on CBF was carbon dioxide, which fit nicely with Roy and Sherrington's original proposal [80], because CO_2 is the natural end product of oxidative glucose metabolism. Carbon dioxide is a gas which readily dissolves in water, and combines with water to form bicarbonate ions (HCO_3^-) and H^+. This has two important consequences: The high solubility of CO_2 allows blood to carry it away efficiently from the tissue, and the amount of CO_2 present directly affects the pH. In fact, CO_2 has a potent effect on the intracellular pH of the brain because it passes easily across the blood-brain barrier and cellular membranes. In contrast, charged molecules do not easily cross the blood-brain barrier, so a change in the pH of blood at a constant CO_2 level has little effect on the intracellular pH of brain. But raising the arterial pCO_2 from its normal resting value increases the global blood flow. The brain is evidently very sensitive to pH changes, and the large CBF response may serve to increase the clearance rate of CO_2 and provide some control over pH changes.

The global response to altered arterial CO_2 content is most likely a nervous response initiated by CO_2 receptors in the large vessels, but the evident importance of maintaining a constant pH in the brain

suggests that H^+ may also exert a local control over CBF. Numerous studies have shown that local acidosis causes dilation, and alkalosis constriction, of the brain arterioles [17].

6.3.6 Multiple Mediators?

The question whether NO is a permissive factor for coupling or a true mediator has been raised: NO has been implicated in mediating or modulating the cerebrovasodilation by CO_2, H^+, adenosine, and K^+. In other words, NO is involved in the responses of the cerebral circulation to all the major putative mediators of coupling. The complicated interrelationships between NO and other mediators, which are not yet fully understood, underscore that it is unlikely that there is one major mediator of coupling. Rather, many different molecules that are produced by increased neuronal and glial metabolism interact and produce local vasodilation [100].

In case there are multiple mediators, they may interact. Some examples, for which conclusive evidence exist, are:

- Adenosine is involved in coupling of CBF to neuronal activation. NO is involved in this response as well. There is an interaction between the vasodilator pathways of adenosine and NO [27].
- Both adenosine and NO are involved in coupling of cerebral blood flow to neuronal activation and there is an interaction between the vasodilator pathways of adenosine and NO [35].
- Adenosine and NO interacts: A NO-donor, at a concentration giving synaptic depression, enhances basal and stimulus-induced adenosine release in hippocampal slices [14].
- Besides its direct action on the blood vessel, elevation of $[K^+]_e$ also increases metabolism by stimulating the $Na^+ - K^+ - ATPase$ which leads to increased production of the potent vasodilators lactate, adenosine, and H^+. In fact K^+ is in general a potent vasodilator in the cerebral circulation [19].
- Both K^+ and adenosine may act as vasodilators via the $NO - cGMP$ pathway [19].
- Extracellular pH increases CBF via NO in the brain [92]. The sensitivity of blood vessels to vasodilators depends on extracellular pH ($[H^+]_e$) and $\left[Ca^{2+}\right]_e$ [19].
- NO play a role in the hypercapnic (i.e., following CO_2 exposure) rise of CBF [33].

In other cases, there are only indications that multiple mediators contribute to coupling: The CBF response typically peaked twice with intervals of $10 - 20\ s$ during activation of both climbing fibers and parallel fibers. This might relate to different vasoactive compounds being active during the period of stimulation. For example, the first CBF peak might relate to the early, non-exhausted phase of neuronal activity, which is delayed and reduced by nitric oxide synthase inhibitors. The second peak might relate to accumulation of vasoactive metabolites, e.g., adenosine, as the electrophysiological response adopts during continuous activation [67].

6.4 Suggested Mechanisms in Case of IO Stimulation

Stimulation of the inferior olive in the brain stem activates climbing fibers.

One result is an increase in intracellular calcium in Purkinje cell dendrites (which are post-synaptic). This activates NOS and the result is endogenous NO release into the extracellular space [86]. NO reaches the arterioles via diffusion through the extracellular space [10]. NO causes elevation of the $cGMP$ level in vascular smooth muscle cells [86]. Therefore the arterioles dilates and the flow increases. The NO is destroyed in the blood flow [85].

Another result is depolarization of climbing fibers (which are pre-synaptic). This leads to release of adenosine from the climbing fibers. As adenosine causes pial vessel dilation, the result is blood flow increase. Adenosine is rapidly in-activated by cellular uptake and deamination and phosphorylation [32].

Extracellular K^+ is of limited importance to CBF regulation [18].

Thus, CBF increases evoked by climbing fiber stimulation depend on both the $NO - cGMP$ pathway and adenosine [4]. But K^+ does not contribute.

6.5 Suggested Mechanisms in Case of PF Stimulation

Stimulation of parallel fibers activates these fibers (which are pre-synaptic).

One result is that the parallel fibers release glutamate, which activates glutamate receptors on Purkinje cells (which are post-synaptic) and interneurons (which are both post-synaptic and pre-synaptic), resulting in their depolarization [44]. Both pre- and post-synaptic sources contribute to the increases in the extracellular potassium concentration ($[K^+]_e$) [19]. Potassium traverses the extracellular space by diffusion and the astrocytes by siphoning [19, 100]. Potassium hyperpolarizes vascular smooth muscle cell membranes. Therefore voltage-dependent Ca^{2+}-channels close, the intracellular Ca^{2+} concentration decreases causing smooth muscle relaxation [19]. The K^+ is cleared by the increased blood flow [100].

Another result is that NO is released into the extracellular space: The main source of NO in the molecular layer is parallel fibers (which are presynaptic), not climbing fibers (which are pre-synaptic) or Purkinje cells (which are post-synaptic) [85]. As in the case of IO stimulation, NO reaches the arterioles via diffusion through the extracellular space. NO causes elevation of the $cGMP$ level in vascular smooth muscle cells [86]. Therefore the arterioles dilates and the flow increases. The NO is destroyed by oxyhemoglobin [10].

Adenosine does not contribute to the CBF increase in response to stimulation of the parallel fibers [19].

Thus, CBF increases evoked by parallel fiber stimulation depend on an intact $NOS-cGMP$ pathway but is independent of adenosine [4]. Also K^+ contribute to coupling.

6.6 Comparison of the Two Systems

The neuro-vascular system, which is involved, when the inferior olive is stimulated, possess the following properties: The neuronal circuitry is mono-synaptic and involves two cell types: The climbing fiber and the Purkinje cell. The evoked field potential consists of one element: The EPSP component. The extracellular space contributes to coupling, but astrocytes do not play a role. The coupling is mediated by two vasodilators: Nitric oxide and adenosine, whereas potassium ions does not contribute.

Similarly, the system, which is involved during parallel fiber stimulation, may be characterized as follows: The neuronal circuitry is di-synaptic and involves three cell types: The parallel fibers, inhibitory interneurons, and the Purkinje cell. The evoked field potential consists of two elements: A PSP and an EPSP component. Both the extracellular space and astrocytes contributes to coupling. The coupling is mediated by two vasodilators: Nitric oxide and potassium ions, whereas adenosine does not contribute.

6.7 Discussion of Neuro-Vascular Coupling

6.7.1 Properties of the Subsystems and their Interrelations

The three subsystems are of three different types: The function of neurons is governed by electrical phenomena (embedded in soft condensed matter: The nerve cell membrane) which take two forms: Nerve conduction (inside neurons) and neurotransmission (across synapses). The extracellular space is governed by chemical phenomena (embedded in a matrix in the form of an anisotropic fluid). The blood flow may be described by fluid mechanics (embedded in an elastic material: The blood vessels).

In contrast to many technical systems, which are governed by electronic properties, the function of cerebellum is governed by ionic and molecular properties. In other word, information is carried through the neuro-vascular system by ions and molecules. This is a general property of the brain [74].

Because K^+-ions, which are transported through astrocytes, seem to be important for coupling in case of parallel fiber stimulation, we suggest that astrocytes have to be taken into account when trying to explain the underlying mechanisms. On the other hand, astrocytes may not have any function for or influence on coupling during inferior olive stimulation.

6.7.2 The Validity of the Findings

A large part of the reviewed information stems from pharmacological studies, which are rather indirect. Only a few direct measurements of the mediators and the processes by which they mediate the coupling have been reported. Therefore some contradictions exist.

Furthermore, it is difficult on the basis of measurements of the concentration changes of a single vasodilator to conclude whether or not that substance regulates the local cerebral circulation. Further studies are needed with simultaneous measurements of the putative mediators to elucidate possible interactions among the vasoactive substances and their relative importance for the cerebellar circulation in response to increased neuronal activity [19].

6.7.3 Properties of Putative Mediators

According to Caesar [18], to serve as a mediator of neuro-vascular coupling, a substance should

(1) be a potent vasodilator,

(2) be produced and released in response to increased neuronal activity,

(3) show a temporal change in tissue concentration that closely follows the changes of blood flow, and

(4) reach concentrations in the vicinity of the vessels that will increase blood flow to the same degree as observed with identical concentrations of exogenously administered substance.

Similarly, Berne *et al.* [13] suggest, that to serve as a mediator of metabolically induced vasodilation, a substance must meet certain criteria. It must

(1) be a potent vasodilator that originates from an endogenous source;

(2) be released in response to an imbalance between parenchymal oxygen supply and need and have ready access to the arterioles;

(3) show a temporal change in tissue concentration that closely follows the changes in blood flow;

(4) reach concentrations in the vicinity of the resistance vessels that will increase blood flow to the same degree as observed with identical concentrations of exogenously administered substance, and

(5) respond in the same manner to potentiators and inhibitors whether the vasodilator material is administered exogenously or is released endogenously.

We suggest, that in case of multiple mediators it is possible that some of the mediators are vasoconstrictors. Furthermore, we emphasize, that the third property does not necessitate, that the relation between tissue concentration and blood flow changes is static. It can just as well be dynamic. The fourth (and fifth) property is mainly of interest to experimentalists investigating the mechanisms through pharmacological studies.

Note the distinction between neuronal activity and metabolic activity.

6.7.4 Specificity of Mediators

Experimental Conditions

How neuro-vascular coupling is mediated may depend strongly upon the experimental conditions. We emphasize that this thesis investigates neuro-vascular coupling in the cerebellar cortex of male Wistar rats, which are anesthetized and exposed to a specific muscle-relaxing drug.

The mechanisms mediating the coupling may be quite different under other conditions, such as *in vitro* brain slices, awake animals, or the application of other anesthetics or drugs. Also, in other animals the mechanisms may be differnet. The dominating physiological processes may depend on whether individual neurons (local activity) or brain regions (involving metabolism) is considered.

A variety of experimental conditions have been used. For example, Shibuki and Kimura [85] have made *in vitro* studies of brain slices. The brain slices stem from rats, which were not given any anesthetics or muscle-relaxing drug. Note, that there is no blood flow to remove NO. They concluded, that NO is important for parallel fiber experiments but not for inferior olive stimulation experiments. The conclusion reached by Akgören *et al.* [4] from *in vivo* experiment was that NO contribute to coupling in both types of experiments.

Do different Brain Regions use different Mediators?

Which chemical substances mediate the coupling may depend upon which brain region is considered and on which part of the neuronal circuit is being stimulated:

- The role of a given metabolite depends on the vascular bed and the metabolic challenge [71].
- The difference in the role of NO in the response to activation in cerebral cortex and cerebellum suggests that the role of NO in the mechanisms of functional hyperemia is regionally specific [44].
- $nNOS$ is not found either in Purkinje cells or in climbing fibers. Parallel fibers and basket cells in the molecular layer contain $nNOS$. The released NO was derived from parallel fibers, or from basket cells driven synaptically by PF inputs [85].

We emphasize that this thesis investigates neuro-vascular coupling during stimulation of the inferior oive and the parallel fibers, respectively.

Chapter 7

The Experiments

This chapter contains a description of the acquisition of the experimental data which form the basis for the research presented in this thesis. The experiments were conducted by the research group headed by Prof. Dr. Martin Lauritzen at the Panum Institute, University of Copenhagen.

Most of the material in this chapter stems from scientific journals on neurophysiology which describe the experimental procedures as well as the experimental results.

7.1 Rats as Experimental Objects

The rat brain is feasible as a model of the human brain as the rat shares a number of properties with humans: The rat is a mammalian vertebrate, i.e., it has breasts, from which milk is available for the nourishment of the newborn, and it has a vertebral column (i.e., a spinal column) [91]. And the rat brain has the same basic structures as the human brain: cerebrum, cerebellum, brain-stem, spinal cord, etc. [11, (Sect. 1.2.1)].

Furthermore, the rat cerebellar cortex was used as a model since this brain region does not easily generate waves of spreading depression [44], and cannot generate the epilepsy that is common after stimulation of the cerebral cortex [67]. Also, the neuronal circuitry of the rat cerebellar cortex is well-defined [4].

7.2 Types of Experiments

Two types of experiments have been conducted:

- **Inferior Olive Stimulation:**
  Stimulation of the inferior olive in the brain-stem activates climbing fibers. Activation of a climbing fiber (which makes strong mono-synaptic contact to a Purkinje cell — see Figure 3.11 on page 25) evokes large excitatory post-synaptic potentials (EPSP), which trigger large action potentials in Purkinje cells. Each of these action potentials is followed by a high-frequency burst of action potentials, a so-called complex spike [66]. In comparison with the EPSP, the pre-synaptic component (PSP) is negligible [67]. Thus, the field potentials evoked by climbing fiber stimulation only contain one component.

- **Parallel Fiber Stimulation:**
  Stimulation of a bunch of parallel fibers (which make di-synaptic contacts to Purkinje cells — see Figure 3.11 on page 25) results in large action potentials in these fibers as well as in small mono-synaptic excitatory post-synaptic potentials (EPSP) and di-synaptic inhibitory post-synaptic potentials (IPSP) which modulate the spontaneous firing of action potentials, in the form of simple spikes, from Purkinje cells [66]. Thus, the field potentials evoked by parallel fiber stimulation can be separated into a pre-synaptic potential (PSP) (associated with the action potentials of the parallel fibers) and a post-synaptic potential [67].

Separate stimulation of these two afferent fiber systems therefore makes it possible to examine the coupling of neuronal activity and cerebellar blood flow secondary to activity in an excitatory, mono-synaptic and

in a mixed excitatory-inhibitory, di-synaptic pathway, respectively. The neuronal activity is related to the spike activity of the Purkinje cells, and the extracellular field potentials elicited by stimulation of the two fiber systems [66].

7.3 The Experimental Set-Up and Procedures

7.3.1 Animal Preparation

Male Wistar rats, weight of $320 - 350\ g$, were anesthetized with halothane and maintained on halothane in 30% O_2, 70% N_2O. Catheters were inserted in the femoral artery for recording of arterial blood pressure and sampling of blood for measurement of blood gases and pH, and in the femoral vein for the slow infusion of saline. Rats were placed in a stereo-tactic head-holder, and the cranial bone and the dura were removed over the cerebellar cortex. A pool was build around the craniotomy site with 5 % agar in Ringer solution for superfusion of the cerebellar surface with artificial cerebrospinal fluid at 37 $^{\circ}C$. Muscle relaxation was induced after the end of the surgical procedure by a bolus injection of succinyl methyl-chloride intraperitoneally followed by continuous infusion through an intraperitoneal catheter. The trachea was cannulated and the animals were ventilated with a volume respirator throughout the experiments to maintain arterial pH as well as values of blood gases at constant values. The temperature was monitored with a rectal probe and maintained at 37 $^{\circ}C$ with a heating pad. The experiments were started at the earliest one hour after the surgery was finished in order to obtain stable anesthesia, heart rate, blood gas values, pH, arterial blood pressure, and CBF responses [67]. The experimental set-up is shown in Figure 7.1.

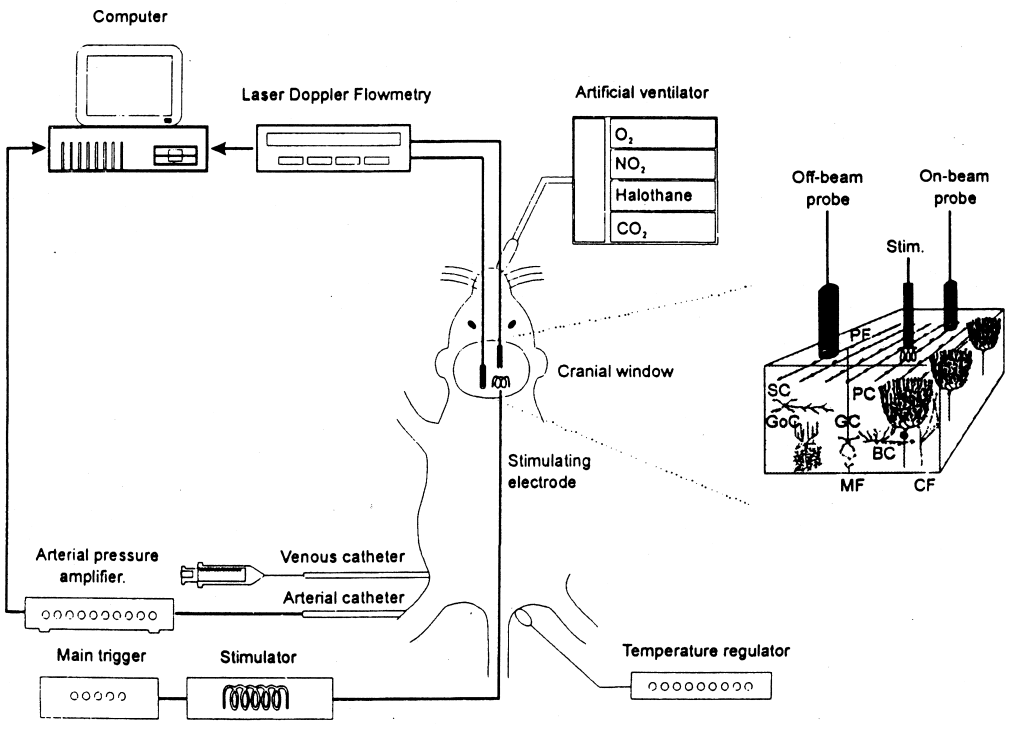

Figure 7.1: Schematic drawing of the experimental set-up. And a view of rat cerebellar cortex with two laser-Doppler probes and a bipolar stimulating electrode positioned on the cerebellar surface. Positions of the probes on-beam and off-beam are indicated. From Ref. [2].

7.3.2 Data Acquisition Procedures

The positions of the electrodes and probes in the rat cerebellar cortex are shown on Figure 7.2. Care was

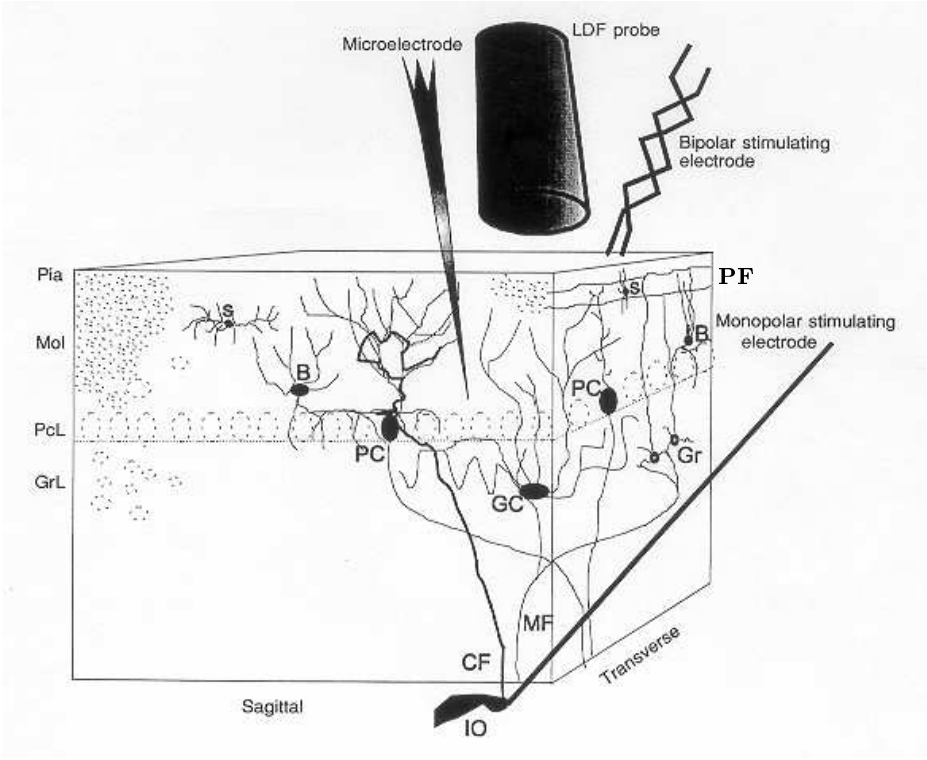

Figure 7.2: Three-dimensional drawing showing the functional anatomy of the rat cerebellar cortex as well as the laser-Doppler probe (LDF), stimulating and recording electrodes. The functional anatomy includes the pial surface (Pia), the molecular layer (Mol) (thickness $200-400\ \mu m$), the Purkinje cell layer (PcL) (thickness of about $100\ \mu m$), and the granule cell layer (GrL) (thickness $400-500\ \mu m$), and the white matter below. The cell types are: Purkinje cells (PC), the inferior olive (IO), basket cells (B), stellate cells (S), Golgi cells (GC), granule cells (Gr), parallel fibers (PF), climbing fibers (CF), and mossy fibers (MF). Climbing fibers were stimulated by a mono-polar electrode lowered into the caudal part of the inferior olive, which projects to the lobule V and VI of the vermis region. The superficial parallel fibers were stimulated by a bi-polar stimulating electrode. Field potentials were recorded by a glass microelectrode. CBF was recorded by a LDF probe located $0.3-0.5\ mm$ above the pial surface. From Ref. [67].

taken to avoid surface vessels when positioning the electrodes as well as the probes [67].

Stimulation Procedures

Climbing fibers were excited using constant current stimulation with $200\ \mu s$ long pulses with amplitudes between $100\ \mu A$ and $400\ \mu A$ via a mono-polar electrode lowered stereotaxically into the caudal part of the inferior olive.

Parallel fibers were stimulated using $200\ \mu s$ long biphasic square current pulses with amplitudes of $0.5-2.0\ mA$ via two Teflon insulated and twisted platinum-iridium wires, making up a bi-polar electrode, placed on the cerebellar surface. The electrode for PF stimulation was placed $300-600\ \mu m$ lateral to the recording electrode and the LDF probe.

In both cases stimulation frequencies in the range $2-30\ Hz$ were applied [67].

Recording Procedures

Recording was performed using the SPIKE2 programme with an interface. The digital sampling rate was $7\ kHz$ for the field potential signal, $100\ Hz$ for the blood pressure trace, and $10\ Hz$ for the CBF traces [67].

Microelectrodes Recordings of electrical signals from the cerebellar cortex were obtained using single-barrel glass electrodes filled with 2 M $NaCl$. The tip diameter was approximately 2 μm, and the electrode impedance varied between 2 and 5 $M\Omega$ [67]. The reference electrode consisted of low-impedance $Ag - AgCl$ wire resting in the agar pool [66].

Electrical recordings were filtered and amplified: Evoked field potentials[1] were amplified 1000 times in the frequency range between 0.1 Hz and 3 kHz. Field potentials evoked by climbing fibers were recorded at a depth of $300 - 400$ μm, corresponding to the proximal dendrites and the Purkinje cell body layers. Field potentials evoked by parallel fibers were recorded at a depth of 200 μm, corresponding to the distal part of the dendrites of the Purkinje cells [67]. Compare with Figure 7.2.

Catheter The arterial blood pressure was measured by cannulating the trachea and inserting a catheter in the femoral artery [67].

Laser-Doppler Flowmetry The cerebellar blood flow was continuously monitored by laser-Doppler flowmetry, a non-invasive technique for real-time recording of CBF. Green laser light (543 nm) and near-infrared laser light (780 nm) were used. The maximal laser intensities were 0.9 mW for the green laser and 1.25 mW for the near-infrared laser.

The laser-Doppler probe was used at a fixed position $0.3 - 0.5$ mm above the pial surface. The positions of the LDF probe and the microelectrodes were adjusted to monitor the area most activated during stimulation of both climbing and parallel fibers [67].

7.4 Measured Signals

All data was collected by means of the data acquisition programme SPIKE2 [20].

Information characterizing the individual experiment as well as examples of the raw data series are given in Appendix A. In each experiment the following signals were monitored:

7.4.1 Stimulus

As mentioned: In case of inferior olive stimulation, the stimulus was mono-polar with amplitudes of around 200 μA. And in case of stimulation of parallel fibers, the stimulus was bi-polar with amplitudes of around 1 mA. In both cases the stimulation frequencies lie in the range $2 - 30$ Hz — see Figure 7.3.

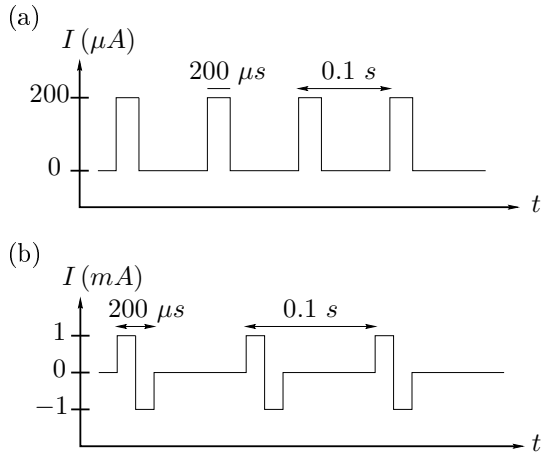

Figure 7.3: Illustration of the stimulation currents supplied by the (a) mono- and (b) bi-polar electrode, respectively. In these examples the stimulation frequency is 10 Hz.

Only the time of occurrence of each stimulus event was registered. Examples are shown in Appendices A.2.1 and A.3.1.

[1] Single unit spike activity could similarly be recorded by applying a bandpass filter covering the range $300-3000$ Hz [66].

7.4.2 Field Potential

The field potential is generated by the extracellular current flow, secondary to ionic fluxes across the nerve cell membrane. The field potential represents the summation of extracellular current flow produced by activity of ensembles of cells close to the recording electrode. This signal gives information about the synchronized neuronal activity in the stimulated region. Thus the field potential is only an indicator of nerve cell activity. However, the field potential is the strongest available indicator.

In the climbing fiber system, passive and active post-synaptic activity, including Purkinje cell spiking, determine the waveform and amplitude of the field potential. However, it is unlikely that pre-synaptic action potentials in the climbing fibers contribute significantly to the extracellular potentials, because of the slenderness and low density of these structures.

In the parallel fiber system, pre-synaptic action potentials, post-synaptic slow potentials and dendritic calcium spikes all contribute to the field potential [66].

Figure 7.4 shows field potentials evoked by climbing fiber and parallel fiber stimulation, respectively. Field potentials evoked by climbing fiber stimulation — see *A* in Figure 7.4 — are the result of post-

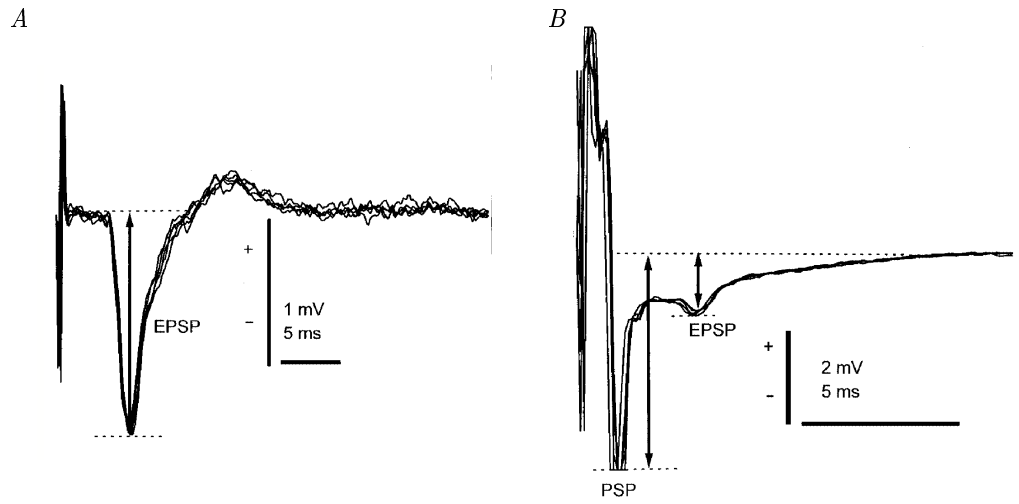

Figure 7.4: Field potentials recorded in the cerebellar cortex. *A:* Climbing fiber evoked field potentials (five single sweeps) recorded at a depth of 300 μm. The arrow indicate the amplitude of the excitatory post-synaptic potential (EPSP). *B:* Parallel fiber evoked field potentials (five single sweeps), recorded at a depth of 200 μm, consisting of a pre-synaptic potential marked PSP and an excitatory post-synaptic potential marked EPSP. The amplitudes of the PSP and EPSP are marked by the double-headed arrows. From Ref. [67]. Note that the evoked field potential excitation is a time-localized excitation with a shape characteristic for the type of stimulation experiment.

synaptic excitation (EPSP) with a characteristically large negative phase. Field potentials evoked by parallel fiber stimulation — see *B* in Figure 7.4 — consist of a large pre-synaptic potential (PSP) and a smaller excitatory post-synaptic potential (EPSP) [67].

The amplitudes of the PSP and EPSP components of the field potentials are calculated by an algorithm supplementing the SPIKE2 programme. Figure 7.4 shows the field potentials used for these calculations with the relevant amplitudes indicated by arrows [67]. Further information on the EPSP algorithm is given in Appendix B.2.

Examples of the registered signals are shown in Appendices A.2.2 and A.3.2.

7.4.3 Arterial Blood Pressure

As mentioned the arterial blood pressure was measured by cannulating the trachea and inserting a catheter in the femoral artery [67]. The pressure was measured in units of $mmHg$.

Examples of the arterial blood pressure traces are described and shown in Appendices A.2.3 and A.3.3.

7.4.4 Cerebellar Blood Flow

General Considerations

The laser Doppler technique is a method for monitoring micro-vascular perfusion [78, (Ch. 1)].

The Physical Principle The assessment of cerebellar blood perfusion was done by means of a laser Doppler technique: A beam of laser-generated monochromatic light being scattered by moving blood cells will undergo a slight change in wavelength (a Doppler shift). Static objects do not cause such change. The magnitude and frequency distribution of the shifted light is related to the number and velocity of moving blood cells, no matter the direction of movement [78, (Ch. 1)]. The Doppler shift is proportional to the velocity of the red blood cells whereas the amplitude of the Doppler-shifted signal is proportional to the concentration of moving blood cells in the tissue [32].

The Measured Objects The moving objects measured are mainly red blood cells but leukocytes and platelets also contribute. The LDF probe does not react to the flow of fluids with a uniform refractive index such as blood plasma. Due to the diffuse scattering of the light within the tissue, the signal is almost independent of the direction of cell movement. Thus a blood cell moving away from the probe tip will contribute to the signal as much as a cell passing sideways in front of the probe tip [78, (Sect. 10.1)].

The Output The blood cell perfusion (flux) is defined as [78, (Sect. 10.6)]

$$\begin{aligned}\text{Blood cell perfusion} &= \text{number of blood cells moving in the measuring volume (CMBC)} \\ &\quad \cdot \text{mean velocity of the cells } (v_m).\end{aligned} \tag{7.1}$$

The concentration of moving blood cells (CMBC) is proportional to the number of blood cells moving through the tissue at normal velocities. This means all cells which cause Doppler shifts within the measuring range of the LDF probe ($20\,Hz - 24\,kHz$). The CMBC value increases linearly with the number of cells [78, (Sect. 10.7)]. The mean velocity of the cells (v_m) is related to the frequency distribution of the Doppler shifted light.

Specific Practical Considerations

The measurements were done by means of an instrument called PeriFlux, which is a flow-meter consisting of a LDF probe and an analyzing unit. The PeriFlux allows evaluation of micro-vascular blood perfusion in real-time [78, (Sect. 10.11)].

The Operating Principle of The Flowmeter Monochromatic light from a laser is guided through an optical fiber (the transmitting fiber) to the tissue, where diffuse scattering, partial absorption, and spectral broadening due to the Doppler effect take place. A portion of the scattered light is captured by two separate optical fibers (the receiving fibers) that conduct it to two photodetectors [77, (p. 58)]. At the surface of the photodetector, demodulation takes place and results in a photocurrent proportional to the instantaneous light intensity. The fluctuations in the preamplifier output voltage corresponds to the Doppler signal produced by the moving scatterers. The magnitude and frequency of the fluctuations produced by the Doppler effect are related to the concentration and velocity of the moving blood cells, respectively [77, (p. 63)] — which thus can be found by electronically processing the preamplifier output voltage.

The Output from the Flowmeter The PERIFLUX is a laser-Doppler flow-meter with an output signal linearly related to the blood cell average velocity multiplied by the cell volume fraction [77, (p. 67)].

The basic unit of measurement used in the PERIFLUX is the Perfusion Unit (*PU*). One *PU* equals 1/250 of the flux value in a so-called Motility standard. Since the *PU* is arbitrary, it cannot be given any physiological definition such as the actual number of cells flowing through a given volume of tissue during a given time period. Thus, PERIFLUX perfusion values must be compared relative to one another and are not absolute [78, (Sect. 10.2)]. This is a weakness of the method.

The measurements were made by means of a four-channel probe containing four LDF probes — see Figure 7.5. Each of the LDF probes is named by its color and the distance between the transmitting and

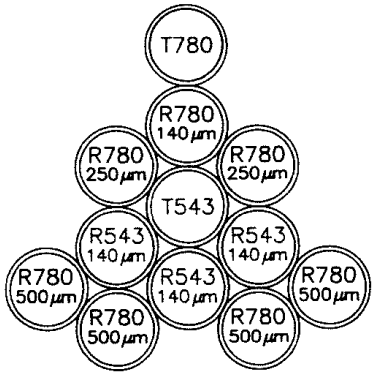

Figure 7.5: Organization of optical fibers in the tip of the four-channel laser-Doppler probe. The fibers are denoted according to whether they are transmitting (T) or receiving (R), and by the wavelength of the laser light (543 *nm* (green) or 780 *nm* (near-infrared)). Also the distance (140 μm, 250 μm, and 500 μm) of the receiving fiber from the transmitting fiber is shown. The outer diameter of an optical fiber is 0.15 *mm*. From Ref. [32].

the receiving optical fibers of the probe:

Gr140 Green laser light of a wavelength of 543 *nm* and a fiber separation of 140 μm.
The maximal sampling depth is roughly estimated to be 0.25 *mm*. In rat cerebellar cortex this depth corresponds to the upper part of the molecular layer [67].

Re140 Near-infrared laser light of a wavelength of 780 *nm* and a fiber separation of 140 μm.
The maximal sampling depth is roughly estimated to be 0.5 *mm*, which in rat cerebellar cortex corresponds to the molecular layer including the Purkinje cell layer [67].

Re250 Near-infrared laser light of a wavelength of 780 *nm* and a fiber separation of 250 μm.
The maximal sampling depth is roughly estimated to be 1 *mm*, which in rat cerebellar cortex corresponds to the granule cell layer.

Re500 Near-infrared laser light of a wavelength of 780 *nm* and a fiber separation of 500 μm.
The maximal sampling depth is roughly estimated to be 2 *mm*, which in rat cerebellar cortex corresponds to the deep cerebellar nuclei.

The light received by the green probe is filtered to remove the near-infrared light and vice versa [32]. The sampling depths of the LDF probes — in rat cerebellar cortex — have been estimated in an experiment performed on artificial brain tissues by Fabricius *et al.* [32], and theoretically investigated by Jakobsson *et al.* [45].

Examples of the LDF signals are described and shown in Appendices A.2.4 and A.3.4.

Chapter 8

Summary of Phenomenology

Overview of the Neuro-Vascular System

The neuro-vascular system pertaining to rat cerebellum is described as consisting of three subsystems: The neuronal subsystem, the extracellular space and the vascular subsystem.

The Neuronal Subsystem

First the cell membrane and membrane potentials are described. Secondly, electrical phenomana pertaining to nerve cells are described: Electrotonic potentials and action potentials, nerve conduction, synapses and neurotransmission. Finally, the cortex of cerebellum is described, firstly with an emphasis on the neuronal organization (cell types, layers, planes and synapses), secondly with an emphasis on the neuronal function during inferior olive stimulation and during parallel fiber stimulation, respectively. The major difference between the two types of experiments is, that the neuronal circuitry, which is activated by inferior olive stimulation, is mono-synaptic, whereas the neuronal circuitry, which is activated by parallel fiber stimulation, is di-synaptic and includes an inhibitory interneuron.

The Extracellular Space

First the structure of the extracellular space is described. Secondly, the extracellular and the intracellular fluids are described. Finally, the role and function of the extracellular space is described.

The Vascular Subsystem

The constituents of the blood are described. The structure of the vascular subsystem (arteries, arterioles, capillaries, veins) and the capillary function are described. Control of blood flow takes two forms: Neural control and local control. Local control is subdivided into autoregulation and regulation by vasoactive (i.e., vasodilatory or vasoconstrictory) substances. An important feature is that the smooth muscle cells around arteries and arterioles react to vasoactive substances whereas capillaries do not react.

Neuro-Vascular Coupling

After a simple system overview, the putative mediators of neuro-vascular coupling are presented. They are: Nitric oxide, adenosine, potassium ions, hydrogen ions, and carbon dioxide, which are all vasodilators. The possibility of there being multiple mediators is presented. The neuroglial cell type astrocytes is presented and the morphological relationship as well as the functional coupling they make between neurons and blood vessels are described. Then the suggested coupling mechanisms involved in case of inferior olive and parallel fiber stimulation, respectively, are presented, and the two types of systems are compared. Finally a discussion of neuro-vascular coupling is given.

The Experiments

The experiments have been performed on healthy male Wistar rats, weight $320-350\,g$, which were aerated with a mixture of O_2 and NO_2. The rats were anesthetized with halothane and given an injection of the muscle-relaxing drug succinyl methyl-chloride.

The arguments for using rats are presented, and the differences in field potential measurements obtained in the two types of experiments (inferior olive versus parallel fiber stimulation) are described. Afterwards, the experimental set-up and procedures (animal preparation, stimulation procedures, and recording procedures) are described. Finally, the measured signals (stimulus, field potential, arterial blood pressure, and four traces of cerebellar blood flow) are presented.

Part II

Methodology

The purpose of this part is to present some of the concepts and methods of mathematical modeling of dynamic systems, which will be applied throughout this thesis. The part comprises four subjects:

- Classification of Systems and Models
- Models of Dynamic Linear Time-Invariant Systems
- System Identification
- Model Validation.

The goal of this part is to provide some insight into the field of mathematical modeling of dynamic systems.

The means will be reviews of central concepts and methods supplemented with discussions of how they relate to the present problem of modeling neuro-vascular coupling in rat cerebellum. Accordingly, most of the material in this part consists of textbook material.

Readers who are familiar with system modeling will find that most or all of the material in this part is well-known. For their information, a summary is provided in M: Chapter 13 which describes the specific choices of methods made for the work which led to the results presented in this thesis. All readers are encouraged to read the discussions at the end of the chapters (M: Sections 9.4, 10.5, and 12.7) as these sections concern how the concepts relate to the present problem of modeling neuro-vascular coupling in rat cerebellum.

Chapter 9

Classification of Systems and Models

This chapter introduces a number of system and model classes which will turn out to be useful throughout this thesis. In the end of the chapter (M: Section 9.4) a preliminary discussion of the relevance of these concepts to the task of modeling neuro-vascular coupling is given.

9.1 Definition of System and Model

The concept of *system* will denote an object or a collection of objects whose properties we want to study.

We will seek answers to questions about various system properties. Many — but not all — questions can be answered by experimentation [61, (Sect. 1.1)].

The models — "the hypotheses", "the laws of nature", "the paradigms" — can be of a more or less formal character, but they all have the fundamental property that they try to link observations to some pattern [61, (p. 11)]. Loosely put, a model of a system is a tool we use to answer questions about the system without having to do an experiment [61, (Sect. 1.2)]. Throughout this thesis the term *model* will denote a description of a system.

This thesis focuses on *mathematical models*. By this we mean that the relationships between quantities that can be observed in the system are described as mathematical relations in the model.

9.2 Signal Types

In systems/models there are usually signals and variables that influence other variables in the system, but are not themselves influenced by the behavior of the system. Such a signal will be termed an *external signal*. An external signal can be one of two types: If we have the external signal at our disposal, to influence the system's behavior, we talk of an *input* or control signal. An external signal that we, in the application in question, cannot influence or choose, we will call a *disturbance signal*.

A model and a dynamic system always contain a number of variables, or signals, whose behavior is our primary interest. We will call such signals *outputs*.

Other model variables will be called *internal variables* [61, (Sect. 3.2)].

Accordingly, a system may be illustrated by a so-called *block diagram* as shown in Figure 9.1.

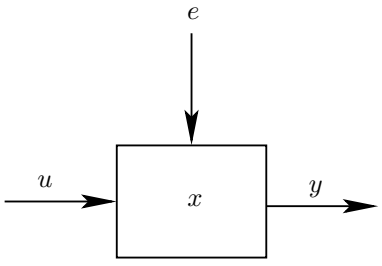

Figure 9.1: A block diagram illustrating a system with input u, output y, internal variable x, and disturbance e.

9.3 Classes of Systems and Models

This section presents a number of adjectives used to describe various classes of systems and models.

9.3.1 Static versus Dynamic Systems

A system is usually characterized by a number of variables that change with time. If there are direct, instantaneous links between these variables, the system is termed *static*.

For other systems the variables can change also without direct outside influence, and their values will thereby also depend on earlier applied signals. Such systems are called *dynamic* [61, (Sect. 1.6)]. For illustration see Figure 9.2.

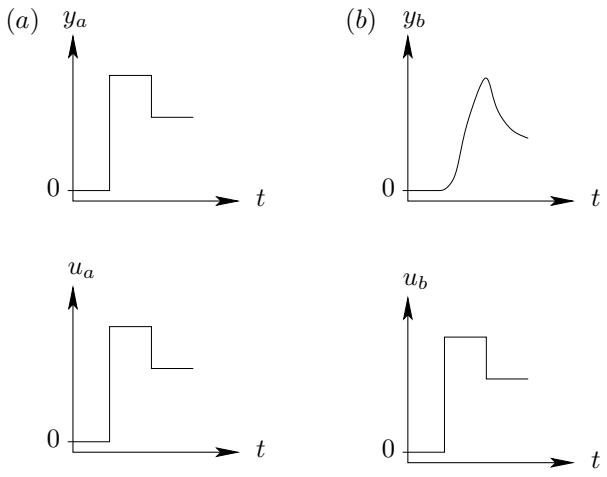

Figure 9.2: Example of input-output relationship for (a) a static and (b) a dynamic system. The u's denote input signals, and the y's output signals. Note that the step response of a static system is a step, whereas that of a dynamic one is not.

A mathematical model of a dynamic system typically consists of a collection of differential and/or difference equations [61, (Sect. 3.1)].

9.3.2 Time-Invariant versus Time-Varying Systems

A system is said to be *time-invariant* if its response to a certain input signal does not depend on absolute time [58, (p. 18)]. Otherwise it is termed a *time-varying* system.

If the system is time-invariant then the parameters in a model of it are constant in time and can be determined once and for all. However, if the parameters vary with time, recursive methods are needed [52, (p. 9)].

9.3.3 Linear versus Nonlinear Systems

A system is said to be *linear* if its output response to a linear combination of inputs is the same linear combination of the output responses to the individual inputs [58, (p. 18)]; i.e., if it obeys the *law of superposition*. If a system does not obey the law of superposition it is termed *non-linear*. For illustration see Figure 9.3.

Nearly all systems are inherently nonlinear if no restrictions are placed on the allowable values of the inputs. If the values of the inputs are confined to a sufficiently small range, the originally nonlinear model of a system may often be replaced by a linear model whose response closely approximates that of the nonlinear model. This type of approximation is desirable because analytical solutions to linear models are more easily obtained. In other applications, the nonlinear nature of an element may be an essential feature of the system and should not be avoided in the model [23, (Sect. 1.4)].

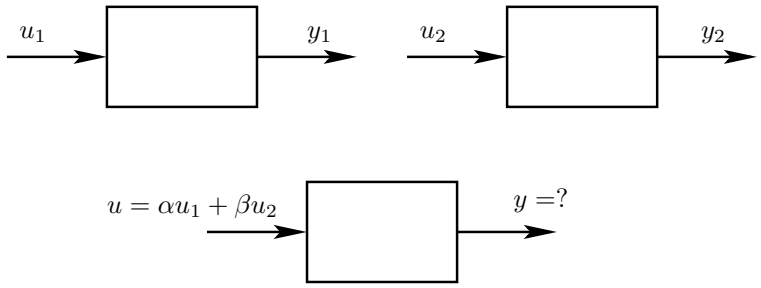

Figure 9.3: The concepts of linear and nonlinear systems. The system's response to the input signal u_1 is the output signal y_1, and similarly the response to u_2 is y_2. If the response y to the linear combination $u = \alpha u_1 + \beta u_2$ is $y = \alpha y_1 + \beta y_2$ the system is termed linear. Otherwise it is termed nonlinear.

9.3.4 Change Oriented versus Discrete Event Driven Systems

The physical world is usually described in terms of continuous changes in the signals and variables we are interested in. We call such systems *change oriented*.

For systems constructed by humans the course of events is different in many cases. The underlying changes take place in terms of discrete events, which occur more or less randomly. Such systems are called *discrete event driven* systems [61, (Sect. 1.6)].

9.3.5 SISO, SIMO, MISO, and MIMO Models

The mathematical features of models depend on whether the input and the output, respectively, is a single variable (a scalar) or a vector of variables. Thus models may be classified as being single-input-single-output (SISO), single-input-multiple-output (SIMO), multiple-input-single-output (MISO), or multiple-input-multiple-output (MIMO).

9.3.6 Non-Parametric versus Parametric Models

A linear time-invariant model can be described by its transfer functions or by the corresponding impulse responses. Methods which aim at determining these functions by direct techniques without first selecting a confined set of possible models result in models called *non-parametric models* since they do not (explicitly) employ a finite-dimensional parameter vector in the search for a best description [58, (p. 168)].

On the other hand, methods which do explicitly employ a finite-dimensional parameter vector in the search for a best description result in *parametric models*. A parametric model consists of

- A model structure, and
- An estimate of the parameter vector.

9.3.7 Deterministic versus Stochastic Models

A model is termed *deterministic* if it works with an exact relationship between measurable and derived variables and expresses itself without uncertainty.

A model is *stochastic* if it also works with uncertainty or probability concepts. A stochastic, mathematical model contains quantities that are described using stochastic variables or stochastic processes [61, (Sect. 1.6)].

9.3.8 Continuous versus Discrete Time Models

A mathematical model that describes the relationship between time continuous signals is called *time continuous*. Differential equations are often used to describe such a relationship.

In practice, the signals of interest are most often obtained in sampled form, that is, as a result of discrete time measurements. A model that directly expresses the relationships between the values of the

signals at the sampling instants is called a *discrete time* model. Such a model is typically described by difference equations [61, (Sect. 1.6)].

9.3.9 Distributed versus Lumped Parameter Models

Many physical phenomena are described mathematically by partial differential equations. The events in the system are so to speak dispersed over the space variables. This description is called a *distributed parameter model* [61, (Sect. 1.6)]. The variables in a distributed parameter model thus depend both on time and the position in space.

If the events are described by a finite number of changing variables, we talk of *lumped parameter models*. Such models are usually expressed by ordinary differential equations [61, (Sect. 1.6)]. The variables in a lumped parameter model only depend on time. They have no spatial dependence.

9.3.10 Black-, Grey-, and White-Box Models

Sometimes the model structure is obtained after careful modeling. Then a model with some unknown physical parameters is constructed from basic physical laws and other well-established relationships. Such a model is called a *white-box model*.

In other cases, standard model structures may be employed without reference to the physical background. Such a model, whose parameters are basically viewed as vehicles for adjusting the fit to the data and do not reflect physical considerations in the system, is called a *black-box model*.

Model structures containing both adjustable parameters without physical interpretation *and* parameters with physical interpretation may, accordingly, be termed *grey-box models* [58, (Sect. 1.4)].

9.4 Discussion of the Classification

In this section comments upon the relevance of some of the classes to the modeling of neuro-vascular coupling will be given.

Static versus Dynamic Systems

Static relations are mostly used for describing equilibrium properties and steady-state conditions. The data treated in this thesis shows no sign of approach to steady-state conditions — see Appendix A on page 262. Thus we expect it to be appropriate to describe the neuro-vascular system as a dynamic system. This feature will be further investigated in Chapter 15 on page 95.

Linear versus Nonlinear Systems

Let it be emphasized that there is no such thing as a real biological/physiological system which *is* linear — the notion of a linear system is basically a mathematical abstraction! Nevertheless, both in the literature as well as in this thesis there is much focus on linear systems and models. As mentioned the reason is two-fold:

- Due to the laws of superposition, the properties of linear systems and models are relatively easy to investigate.
- In many cases, a system which is intrinsically nonlinear may be well approximated by a linear model in a neighborhood of (i.e., a domain around) a chosen operating point. The requirements are that the system variables vary smoothly, that is, they do not expose cusps or discontinuities (such as phase transitions) within the domain.

Since we do not know the true system equations we will start out by assuming that the system is linear and study the deficiencies of the chosen linear model. Afterwards we have to consider which nonlinearities we can incorporate in the model structure in order to improve the performance of the model.

Note that it is only possible to identify the nonlinearities if the chosen input sequences trigger the nonlinearity, i.e., if the input sequences force the system outside the range of validity of a linear approximation. This problem is connected to the concept of identifiability which is presented in M: Section 11.6 on page 66.

SISO, SIMO, MISO, and MIMO Models

A priori, the models describing neuro-vascular coupling in case of climbing fiber activation will be SISO models, as the cerebellar blood flow will be explained only from the amplitude of the excitatory post-synaptic potential. Similarly, the models concerning parallel fiber stimulation will be MISO models as the field potential has two components: The pre-synaptic action potential and the excitatory post-synaptic potential. See P: Figure 7.4 on page 46.

Non-Parametric versus Parametric Models

This thesis focuses on parametric models. One reason is that parametric models may give insight into the physiological mechanisms involved in neuro-vascular coupling. Another reason is that maybe certain parameters could become useful for various medical applications. For instance, if the value of a parameter can be used to distinguish between healthy subjects and subjects suffering from a disease, then such a parameter could be a useful tool in diagnostics. Therefore, a number of general linear parametric model structures are presented in M: Chapter 10.

Deterministic versus Stochastic Models

As will be clarified in M: Chapter 10 the model structures to be considered in this thesis consist of two parts: A system dynamics model described by a deterministic part. And a noise model which — as the noise sources are unknown (and therefore unpredictable) — will be described by stochastic variables.

Distributed versus Lumped Parameter Models

As described in P: Section 7.3.2 on page 43 the measurements, which will be the starting point for the model construction, consist of time series of samples of signals. Each signal is measured in a single point in space (i.e., in zero-dimensional space). Therefore, the dynamic equations will contain no spatial terms, only temporal. Accordingly, the resulting models will be lumped parameter models consisting of ordinary differential equations.

Black-, Grey-, and White-Box Models

As mentioned in M: Section 9.4 a focus in this thesis is on models containing parameters which can be interpreted in terms of physiology. Robert E. Kearney [102, (Sect. IB)] has, however, argued that: *"For a model to provide insight, it should*

- *Depend only on the properties of the system and not on the input properties. If it does, then the nature of the dependence must be understood.*
- *Minimize a priori assumptions. In particular, assumptions about the structure of the system should be avoided to ensure that the model reflects the system, and not the experimenter's preconceived notion of what the system should be.*
- *Be possible to relate the model parameters or structure to the underlying system."*

In this thesis we will sometimes follow the idea of minimizing a priori assumptions and let the modeling work take its beginning from purely mathematical considerations. At other times the opposite argument will be invoked: By taking physiological insight into account we will be able to pick out adequate choices for (especially) nonlinearities from the enormously large pool of possible choices. Therefore, in this thesis we will start by constructing black-box models and afterwards physiological insight will be taken into account in order to improve the performance of the models. The resulting models will thus be grey-box models.

Chapter 10

Models of Dynamic Linear Time-Invariant Systems

This chapter presents a number of general model structures which will be applied throughout the modeling parts of this thesis. The model structures can be divided into two subclasses [23, (Sect. 3.1 and 3.2)]:

- **Input-Output Equations**
  Input-output equations are a result of elimination of all variables except the inputs, noise signals, and outputs, and their derivatives [58, (Sect. 3.2)]. In the linear case such equations are also termed transfer function models.
- **State-Space Equations**
  In the state-space form the relationship between input, noise, and output signals is written as a system of first-order differential or difference equations using an auxiliary state vector [58, (Sect. 4.3)]. In addition to their computational advantages, state-space equations can be used to obtain considerable insight into the system behavior [58, (Sect. 3.2)].

First discrete time model structures are presented and afterwards continuous time model structures. With the purpose of using the continuous time model structures together with sampled input and output signals it is finally considered how to digitize continuous time model structures.

In the following u will denote the input, y the output, and $\{e(t)\}$ is *white noise*, i.e., a sequence of independent (identically distributed) random variables. The notation will be for SISO systems. The extra work involved in dealing with models of multi-variable systems (i.e., SIMO, MISO, and MIMO systems) has been described by Ljung [58, (Sect. 2.5)].

10.1 Discrete Time Model Structures

10.1.1 General Discrete Transfer Function Model

Assume that the variables are observed at the *sampling instants* $t = k \cdot \tau, k = 1, 2, 3, \ldots$ where τ is the *sampling interval*. We introduce the *forward shift operator* q by:

$$qx(t) = x(t + \tau). \tag{10.1}$$

General linear models can in the time domain be described symbolically by

$$y(t) = G_\tau(q)u(t) + H_\tau(q)e(t), \tag{10.2}$$

which says that the measured output $y(t)$ is a sum of one contribution that comes from the measured input $u(t)$ and another contribution that comes from the noise $H_\tau(q)e(t)$. The symbol G_τ then denotes the dynamic properties of the system, that is, how the output is formed from the input. For linear systems $G_\tau(q) = \sum_{k=1}^{\infty} g(k)q^{-k}$ is an operator called the *transfer function* from input to output. The symbol H_τ refers to the noise properties, and is called the *noise model*. It describes how the disturbances at the output are formed from some standardized noise source $e(t)$. For linear systems $H_\tau(q) = \sum_{k=0}^{\infty} h(k)q^{-k}$ [59, (p. 1-5)]. We will only consider noise models for which the zeroth coefficient is equal to one, $h(0) = 1$. Such a filter is termed *monic* [58, (p. 27)].

10.1.2 State-Space Representation of Transfer Functions

The *innovations form* of the state-space model reads [59, (p. 3-10)]:

$$\begin{aligned} \mathbf{x}(t+\tau) &= \mathbf{F}\mathbf{x}(t) + \mathbf{G}u(t) + \mathbf{K}e(t), && (10.3)\\ y(t) &= \mathbf{H}\mathbf{x}(t) + Ju(t) + e(t). && (10.4) \end{aligned}$$

The linear *order* of this model structure is $n = \dim(\mathbf{x})$. This equation is equivalent to Equation (10.2) with

$$\begin{aligned} G_\tau(q) &= \mathbf{H}(q\mathbf{I}_n - \mathbf{F})^{-1}\mathbf{G} + J, && (10.5)\\ H_\tau(q) &= \mathbf{H}(q\mathbf{I}_n - \mathbf{F})^{-1}\mathbf{K} + 1, && (10.6) \end{aligned}$$

where $\mathbf{I}_n$ denotes the n-by-n identity matrix.

10.2 Continuous Time Model Structures

10.2.1 General Continuous Transfer Function Model

We introduce the *time derivative operator* by

$$p = \frac{d}{dt}. \tag{10.7}$$

In continuous time, a basic time domain description of a linear system subject to additive random disturbances reads [58, (Sect. 2.1)]

$$y(t) = G(p)u(t) + H(p)e(t). \tag{10.8}$$

The equivalent s-domain description is found by applying the Laplace transform[1]:

$$Y(s) = G(s)U(s) + H(s)E(s). \tag{10.9}$$

10.2.2 State-Space Representations of Transfer Functions

The directly parameterized innovations form of the state-space model reads [58, (Sect. 4.3)]:

$$\begin{aligned} \dot{\mathbf{x}}(t) &= \mathbf{F}\mathbf{x}(t) + \mathbf{G}u(t) + \mathbf{K}e(t), && (10.10)\\ y(t) &= \mathbf{H}\mathbf{x}(t) + Ju(t) + e(t). && (10.11) \end{aligned}$$

Equation (10.10) is termed the *state-variable equation* and Equation (10.11) the *output equation* [23, (Sect. 3.1)]. The linear *order* n is defined as $n = \dim(\mathbf{x})$. Note that this model structure contains additive noise. The total noise contribution is split into two terms: *Measurement noise*, $e(t)$, acting on the output, and *process noise*, $\mathbf{K}e(t)$, acting on the states. The linear filter $\mathbf{K}$ is called the *Kalman gain matrix* [58, (Sect. 4.3)].

The state-space model is equivalent to an input-output model in the s-domain [52, (Sect. 2.1)]:

$$\begin{aligned} Y(s) &= G(s)U(s) + H(s)E(s), && (10.12)\\ G(s) &= \mathbf{H}(s\mathbf{I}_n - \mathbf{F})^{-1}\mathbf{G} + J, && (10.13)\\ H(s) &= \mathbf{H}(s\mathbf{I}_n - \mathbf{F})^{-1}\mathbf{K} + 1. && (10.14) \end{aligned}$$

Note that for a state-space model of *output-error* type $y(t) = G(p)u(t)+e(t)$ we have $\mathbf{K} \equiv \mathbf{0}$ and $H \equiv 1$.

[1] The Laplace transform and other frequency domain considerations are shortly treated in Appendix C on page 279.

10.3 Digitization of Continuous Time Model Structures

Now the question is: Given a continuous transfer function $G(p)$, which discrete transfer function $G_\tau(q)$ will have approximately the same characteristics? We will present two approaches to this task [36, (Ch. 4)]:

- Numerical Integration, and
- Hold Equivalents.

There are a number of specific digitization rules within each of these approaches. Only a few will be presented here. The default choice of Matlab is to use the zero-order hold (ZOH) equivalent [60, (p. 4-39)].

10.3.1 Numerical Integration

These methods result in approximate formulas that correspond to replacing the differentiation operator p by a difference approximation [58, (p. 26)].

Forward Rectangular Rule

The forward Rectangular Rule is also called Euler's rule. This method does *not* guarantee a stable, discrete system from a stable, continuous prototype [36, (Sect. 4.5)].

The discrete transfer function $G_\tau(q)$ is obtained from a given continuous transfer function $G(p)$ by the substitution [36, (Sect. 4.2)]

$$p \longleftarrow \frac{q-1}{\tau}, \tag{10.15}$$

that is,

$$G_\tau(q) \approx G\left(\frac{q-1}{\tau}\right). \tag{10.16}$$

This approximation corresponds to assume that $\dot{x}(t)$ is constant during the period $k\tau < t < (k+1)\tau$ [51, (Sect. 4.6)].

Trapezoid Rule

The trapezoid Rule is also known as Tustin's Method as well as the bilinear transformation.

The discrete transfer function is obtained from a given continuous transfer function by the substitution [36, (Sect. 4.2)]

$$p \longleftarrow \frac{2}{\tau} \cdot \frac{q-1}{q+1}, \tag{10.17}$$

that is,

$$G_\tau(q) \approx G\left(\frac{2}{\tau} \cdot \frac{q-1}{q+1}\right). \tag{10.18}$$

This approximation assumes that $\dot{x}(t)$ varies linearly over the period $k\tau < t < (k+1)\tau$ [51, (Sect. 4.6)].

10.3.2 Hold Equivalents

These are techniques for taking a sequence of samples and extrapolating or holding them to produce a continuous signal [36, (Sect. 4.4)].

Zero-Order Hold Equivalent

The zero-order hold (ZOH) equivalent to $G(p)$ is given by [36, (Sect. 4.4.1)]

$$G_{h0}(q) \approx (1-q^{-1})\mathcal{Z}\left\{\frac{G(s)}{s}\right\} = \frac{(q-1)}{q}\mathcal{Z}\left\{\frac{G(s)}{s}\right\}, \tag{10.19}$$

where $\mathcal{Z}\{Y(s)\}$ means $\mathcal{Z}\left\{\mathcal{L}^{-1}[Y(s)]\right\}$. $\mathcal{Z}$ denotes the z-transform, and $\mathcal{L}^{-1}$ the inverse Laplace transform. The ZOH equivalent is also known as the step invariant equivalent and corresponds to assume that the input $u(t)$ is constant during the period $k\tau < t < (k+1)\tau$ [51, (Sect. 4.6)].

Triangle Hold Equivalent

The triangle hold equivalent to $G(p)$ is given by [36, (Sect. 4.4.2)]

$$G_{tri}(q) \approx \frac{(q-1)^2}{\tau q} \mathcal{Z}\left\{\frac{G(s)}{s^2}\right\}. \tag{10.20}$$

The triangle hold equivalent is also termed the ramp invariant and corresponds to assume that the input u varies linearly over the period $k\tau < t < (k+1)\tau$ [51, (Sect. 4.6)].

10.4 The Parameter Vector

In most cases it is impractical to make the specification of G_τ and H_τ by enumerating the infinite sequences $\{g(k)\}$ and $\{h(k)\}$ introduced in M: Section 10.1.1 on page 57. Instead one chooses to work with structures that permit the specification of G_τ and H_τ in terms of a finite number of values. Rational transfer functions and finite-dimensional state-space descriptions are typical examples of this. Quite often it is not possible to determine these coefficients a priori from knowledge of the physical mechanisms that govern the system's behavior. Instead the determination of all or some of them must be left to estimation procedures. This means that the coefficients in question enter the model as parameters to be determined. We shall generally denote such parameters by the vector θ, and thus have a model description

$$y(t) = G_\tau(q,\theta)u(t) + H_\tau(q,\theta)e(t). \tag{10.21}$$

The *parameter vector* θ then ranges over a subset of $\mathbb{R}^d$ where d is the dimension of θ: $d = \dim(\theta)$ [58, (Sect. 4.1)].

10.5 Discussion of Models of Dynamic LTI Systems

The model structures presented in this chapter contain a model of the noise in the output signals. Sometimes the measurements of the inputs to the system may also be noise corrupted (errors-in-the-variables). For the model structures presented in this chapter to make sense requires the assumption that all noise effects can be lumped into an additive term $H(p,\theta)e(t)$ at the output. According to Ljung [58, (Sect. 4.3)] this corresponds to regarding the measured input values as the actual inputs to the process, and assuming that their deviations from the true stimuli will be propagated through the system and lumped into the deviations from the true output signals.

As mentioned in the beginning of this chapter state-space equations can be used to obtain considerable insight into the behavior of the system. For this reason the modeling work will be centered around the development of state-space models. Ljung has suggested to create grey-box models in the form of the state-space model structure by combining a physical parameterization of the dynamics part with a black-box parameterization of the noise properties [58, (Sect. 4.3)]. Since in this thesis we focus on modeling the physiological properties of the neuro-vascular system, we have only little interest in the noise model. For this reason we will mainly apply linear as well as non-linear model structures of the output-error type.

The model structures presented in this chapter have full flexibility in the sense that for a given linear order they contain the maximal possible number of parameters. In this way they are typical black-box model structures. These general model structures can easily be changed into representations of grey-box models. For instance, fixing a specific parameter in the **H** matrix in a state-space representation like Equations (10.10)–(10.11) to the value zero corresponds to assume that the output does *not* depend on a certain state variable. Thus representations of grey-box models may be obtained by imposing constraints on a general black-box model structure. Thus a grey-box model contains fewer parameters than the equivalent black-box model. This may be an advantage since, according to Ljung [58, (Sect. 4.3)], *"Using fewer parameters has some positive effect on the estimation procedure: The variance of the parameter estimates will decrease."* However, as will be noted in M: Section 11.6.4 on page 67, it may also be a nuisance.

Chapter 11

System Identification

This chapter describes a number of aspects of the task of constructing parametric models of dynamic systems by means of system identification methods.

11.1 How to Build Models

There are two basic and quite different principles for model construction [61, (Sect. 1.4)]:

- **Physical modeling**
  One is to break down the properties of the system to subsystems whose behaviors are known. Or alternatively: To subsystems for which hypotheses can be made, or for which generally recognized relationships exist. This principle has also been termed theoretical modeling [49, (Sect. 2.1)] and deductive modeling [52, (p. 5)].
- **Identification**
  The other is to use observations from the system in order to fit the model's properties to those of the system. This principle has also been termed experimental modeling [49, (Sect. 2.1)] and inductive modeling [52, (p. 5)].

Employing a combination of physical modeling and identification is denoted *grey-box modeling* [49, (Sect. 2.1)].

Sometimes it is necessary first to do some nonlinear transformations of the original measured data. A combination of such a transformation based on physical insight and simple model structures is termed *semi-physical modeling* [61, (Sect. 10.4)].

11.2 What is System Identification?

System identification is parametric modeling of a dynamic system by means of experimental data [52, (p. 6)]. System identification can be subdivided into

- Structure determination, and
- Parameter estimation.

The structure can be determined from experiments as well as physical laws [49, (p. 17)]. Parameter estimation is the act of determining the values of the parameters in a dynamic system with a given structure, by means of experimental data [52, (p. 6)]. Thus the estimation problem is to deduce an estimate of the unknown parameter vector from the observations of input u and output y [103, (Sect. 2)].

11.3 Structure Determination

11.3.1 General Aspects of the Choice of Model Structure

The route to a particular model structure involves, at least, three steps [58, (Sect. 16.1)]:

(1) To choose the *type* of the model structure.
This involves, for example, the selection between nonlinear and linear models, between input-output, black-box and physically parameterized state-space models, and so on.

(2) To choose the *size* of the model structure.
This involves issues like selecting the order of a state-space model or the degrees of the polynomials in a polynomial representation of transfer functions. It also contains the issue of which variables to include in the model description.

(3) To choose the model *parameterization*.

A most natural approach to search for a suitable model structure is simply to test a number of different ones and to compare the performance of the resulting models [58, (Sect. 16.2)]. This subject is strongly connected to the problem of model validation which is elaborated upon in M: Chapter 12.

Young [103, (Sect. 7)] has noted that *"The problem of model structure identification is very important in practice: It is clearly of little use having a sophisticated parameter estimation algorithm if the model structure (e.g. canonical form and order) is not firmly established."*

11.3.2 Determination of Black-Box Model Structures

A larger model will always give a lower value of the loss function V_N, since it has been obtained by minimizing over more parameters. If the values of the loss function are plotted as a function of the model order, a strictly decreasing function is obtained. To start with, the value of V_N decreases since the model includes more and more of the system's relevant properties. But even after a 'correct' model order has been passed, the loss function continues to decrease. The reason is that the extra — and unnecessary — parameters are used to fit the model to the specific disturbance signals in the present data set. This is called *over-parameterization* and does not serve any purpose since the model will be used when other disturbances affect the system. On the contrary, the model will be worse because of the over-parameterization. The goal is to find the transition from relevant model parameterization to over-parameterization [61, (Sect. 10.4)].

For the case of the state-space model structure MATLAB provides an automatic model order selection: The choice of linear order takes its starting point from the relative importance of the dimensions of the state vector $\mathbf{x}$. The singular values of the Hankel matrices of the impulse response are calculated. The order is chosen such that the singular values for higher orders are comparatively small [60, (p. 4-120)].

11.3.3 Determination of Grey-Box Model Structures

M. Knudsen [49, (Sect. 2.1)] has noted that *"Estimating physical parameters the model structure must clearly be determined by theoretical modeling. The structure determination is particularly crucial in this case, as the accuracy of the estimated parameter values depends entirely on the correctness of the structure."*

11.4 Parameter Estimation

11.4.1 Choice of Parameter Estimation Method

Choice of Method of Data Processing

As the data to be used for estimation is sampled, we will employ a discrete-time estimation procedure. However, as models taking physical insight into account typically appear in the form of continuous-time models, digitization of the resulting grey-box model structures will be necessary[1].

Choice of Parameter Estimation Method

Parameter estimation methods can be divided into two main groups: Minimization methods (which seek the parameter values that minimize the sum of squared prediction errors) and correlation methods (which

[1] The various combinations of continuous/discrete-time models with continuous/discrete-time estimation procedures have been considered by Young [103, (Sect. 4)].

seek the parameter values that make the prediction error independent of earlier inputs and outputs and functions of those) [52, (p. 9 and 24)].

Throughout this thesis the prediction error method (PEM), as described by Ljung [58] and implemented in the MATLAB system identification tool-box [59], will be employed. The PEM[2] is a minimization method.

11.4.2 The Prediction Error Method

Definition of the Prediction Error

Given a description

$$y(t) = G_\tau(q)u(t) + H_\tau(q)e(t), \tag{11.1}$$

we will discuss how to predict $y(t)$, i.e., how to find the estimate $\widehat{y}(t \mid t-\tau)$ given measurements of input $u(s), s \le t$ and output $y(s), s \le t-\tau$.

First we study the noise model

$$v(t) = H_\tau(q)e(t) = (H_\tau(q)-1)e(t) + e(t). \tag{11.2}$$

Note that — because $H_\tau(q)$ is assumed to be monic (cf. M: Section 10.1.1 on page 57) — the part $(H_\tau(q)-1)e(t)$ only depends on the values of e at times earlier than t, $e(s), s < t$. If $\{e(t)\}$ is white noise, i.e., a sequence of independent (identically distributed) random variables with zero mean value, we thus have that the two parts $(H_\tau(q)-1)e(t)$ and $e(t)$ are statistically independent, and that the conditional expectation of $v(t|t-\tau)$ is[3]

$$\widehat{v}(t|t-\tau) = (H_\tau(q)-1)e(t). \tag{11.3}$$

Now we manipulate the equations:

$$\begin{aligned} e(t) &= H_\tau(q)^{-1}v(t), & (11.4)\\ \widehat{v}(t|t-\tau) &= (H_\tau(q)-1)H_\tau(q)^{-1}v(t) = \left(1 - H_\tau(q)^{-1}\right)v(t), & (11.5)\\ v(t) &= H_\tau(q)e(t) = y(t) - G_\tau(q)u(t). & (11.6) \end{aligned}$$

Second, the conditional expectation of $y(t)$, given the information in question, is

$$\begin{aligned} \widehat{y}(t|t-\tau) &= G_\tau(q)u(t) + \widehat{v}(t|t-\tau)\\ &= G_\tau(q)u(t) + \left(1 - H_\tau(q)^{-1}\right)v(t)\\ &= G_\tau(q)u(t) + \left(1 - H_\tau(q)^{-1}\right)\left(y(t) - G_\tau(q)u(t)\right). \end{aligned} \tag{11.7}$$

Collecting the terms results in the following expression for the (one-step-ahead) *prediction* $\widehat{y}(t|t-\tau)$

$$\widehat{y}(t|t-\tau) = H_\tau(q)^{-1}G_\tau(q)u(t) + \left[1 - H_\tau(q)^{-1}\right]y(t). \tag{11.8}$$

Now, having observed the input-output data u, y, the *prediction errors* $\epsilon(t)$ can be computed as [58, (Sect. 3.2)]:

$$\epsilon(t) = y(t) - \widehat{y}(t|t-\tau) = H_\tau(q)^{-1}\left[y(t) - G_\tau(q)u(t)\right]. \tag{11.9}$$

These errors are, for given data y and u, functions of G_τ and H_τ. These in turn are parameterized by entries in the state-space matrices defined in (10.3)–(10.4). Whenever needed we will emphasize the dependence of ϵ, $\widehat{y}$, G_τ, and H_τ on the parameter vector θ by writing $\epsilon(t,\theta)$, $\widehat{y}(t|\theta)$, $G_\tau(q,\theta)$, and $H_\tau(q,\theta)$.

The Loss Function

The most common parametric identification method is to determine estimates of G_τ and H_τ by minimizing the *loss function*[4]

$$V_N(\theta) = \sum_{i=1}^{N} \epsilon^2(t_i), \tag{11.10}$$

[2] Young discusses a number of classes of minimization methods, which are not based on the prediction error, in his survey [103, (Sect. 5)].

[3] The details of this argument are given in Ref. [58, (Sect. 3.2)].

[4] This is just one of several possible choices of loss function [58, (Sect. 7.2)].

that is, (as G_τ and H_τ are parameterized by θ) to determine the estimate $\widehat{\theta}$ of the parameter vector by

$$\widehat{\theta} = \arg\min V_N(\theta) = \arg\min \sum_{i=1}^{N} \epsilon^2(t_i), \tag{11.11}$$

where i runs over all N samples. This is called a *prediction error method* (PEM) [59, (p. 3-14)].

11.5 Iterative Search for the Minimum Point

This section presents one of many[5] methods of moving around in the parameter space in the search for the parameter value $\widehat{\theta}$ which minimizes[6] the loss function $V_N(\theta)$. At the end of this section information about how the methods have been implemented in MATLAB, is provided.

11.5.1 The Newton-Raphson Method

For many model structures the function $V_N(\theta)$ is a rather complicated function of θ, and the minimizing value $\widehat{\theta}$ must then be computed by numerical search for the minimum. The most common methods for this are based on the *Newton-Raphson method*. This is a method to solve the equation

$$g(x) = 0 \tag{11.12}$$

numerically for x by iteratively selecting[7]

$$x^{(i+1)} = x^{(i)} - \left[g'(x^{(i)})\right]^{-1} \cdot g(x^{(i)}). \tag{11.13}$$

Here $g'(x)$ is the derivative of $g(x)$ with respect to x. A *step length parameter* $\mu^{(i)}$ is often used to adjust the update so that $x^{(i+1)}$ is guaranteed to be better than $x^{(i)}$:

$$x^{(i+1)} = x^{(i)} - \mu^{(i)} \cdot \left[g'(x^{(i)})\right]^{-1} \cdot g(x^{(i)}). \tag{11.14}$$

This method can be used to minimize the loss function $V_N(\theta)$. We search for a minimum by solving the — usually nonlinear — equation

$$V_N{}'(\widehat{\theta}) \equiv \frac{\partial}{\partial\theta} V_N(\theta)_{|_{\theta=\widehat{\theta}}} = 0. \tag{11.15}$$

Since $V_N(\theta)$ is a real-valued function of θ and θ is a d-dimensional vector, the gradient of $V_N(\theta)$ is a d-dimensional column vector. Applying (11.14) gives

$$\widehat{\theta}^{(i+1)} = \widehat{\theta}^{(i)} - \mu^{(i)} \cdot \left[V_N{}''(\widehat{\theta}^{(i)})\right]^{-1} \cdot V_N{}'(\widehat{\theta}^{(i)}). \tag{11.16}$$

Here $V_N{}''(\theta)$ is the second derivative (the *Hessian*) of $V_N(\theta)$ with respect to θ (a $d \times d$ matrix) and $V_N{}'(\theta)$ is the gradient (a $d \times 1$ vector). The step length $\mu^{(i)}$ is determined so that $V_N(\widehat{\theta}^{(i+1)}) < V_N(\widehat{\theta}^{(i)})$ [61, (Sect. 9.3)].

---

[5] Methods for solving nonlinear equations are treated in many textbooks on numerical analysis, for instance Refs. [48, (Ch. 3)] and [82, (Ch. 5 and 7)].

[6] The computation of the estimate by means of the PEM approach as well as other methods is thoroughly treated by Ljung [58, (Ch. 10)].

[7] Let $y = g(x)$. Taylor expansion to first order around the i'th iteration gives $y = g(x) \approx g(x^{(i)}) + g'(x^{(i)}) \cdot (x - x^{(i)})$. Since $g(x) = 0$ the $(i+1)$'th iteration can be chosen as $x^{(i+1)} = x = x^{(i)} - \left[g'(x^{(i)})\right]^{-1} g(x^{(i)})$. Note that, for this procedure to converge to a zero of g, it is required that the initial value $x^{(0)}$ is sufficiently close to that zero, or that the graph of g has a prescribed shape [48, (Sect. 3.2)].

11.5.2 The Gauss-Newton Method

In order to use Equation (11.16), derivatives and second derivatives of the loss function $V_N(\theta)$ are needed. Consider the quadratic loss function

$$V_N(\theta) = \sum_{i=1}^{N} \epsilon(t_i)^2 = \sum_{i=1}^{N} \left(y(t_i) - \widehat{y}(t_i\,|\,\theta)\right)^2 . \tag{11.17}$$

Direct, term-wise differentiation of this expression gives

$$V_N{}'(\theta) = \sum_{i=1}^{N} -2 \cdot \frac{\partial}{\partial\theta}\widehat{y}(t_i\,|\,\theta) \cdot \left(y(t_i) - \widehat{y}(t_i\,|\,\theta)\right), \tag{11.18}$$

$$\begin{aligned} V_N{}''(\theta) &= 2 \cdot \sum_{i=1}^{N} \left(\frac{\partial}{\partial\theta}\widehat{y}(t_i\,|\,\theta)\right) \cdot \left(\frac{\partial}{\partial\theta}\widehat{y}(t_i\,|\,\theta)\right)^T \\ &\quad -2 \cdot \sum_{i=1}^{N} \left(\frac{\partial^2}{\partial\theta^2}\widehat{y}(t_i\,|\,\theta)\right) \cdot \left(y(t_i) - \widehat{y}(t_i\,|\,\theta)\right). \end{aligned} \tag{11.19}$$

In general we approximate the second derivative $V_N{}''(\theta)$ by neglecting the second sum in Equation (11.19). Close to the minimum point it is small, and it is then unnecessary to compute the second derivative of $\widehat{y}(t_i\,|\,\theta)$. With this term canceled in the expression for $V_N{}''(\theta)$, Equation (11.16) is usually called the *Gauss-Newton method* [61, (Sect. 9.6)]. If we denote the derivative of the prediction by

$$\psi(t_i, \theta) = \frac{\partial}{\partial\theta}\widehat{y}(t_i\,|\,\theta), \tag{11.20}$$

we can rewrite the derivative and the approximated second derivative of V_N as

$$V_N{}'(\theta) = -2\sum_{i=1}^{N} \psi(t_i, \theta)\epsilon(t_i, \theta), \tag{11.21}$$

$$V_N{}''(\theta) \approx \widetilde{V}_N''(\theta) = 2\sum_{i=1}^{N} \psi(t_i, \theta)\psi(t_i, \theta)^T. \tag{11.22}$$

Note that the expression for $\widetilde{V}_N''$ should be interpreted with care: The (j,k)'th matrix element is

$$\left\{\widetilde{V}_N''(\theta)\right\}_{jk} = 2\sum_{i=1}^{N} \psi_j(t_i, \theta) \cdot \psi_k(t_i, \theta). \tag{11.23}$$

11.5.3 Computing the Derivative of the Prediction

Now it only remains to describe how the derivatives

$$\psi(t_i, \theta) = \frac{\partial}{\partial\theta}\widehat{y}(t_i\,|\,\theta) \tag{11.24}$$

are computed. The computation of these depends on the model structure used [61, (Sect. 9.6)]. We will not investigate this further. However, examples are treated in Ref. [61, (Sect. 9.6)].

11.5.4 Implementation in MATLAB

As mentioned in Footnote 7 on page 64, for the Newton-Raphson method to converge towards a minimum the iterative search must be initiated close to that minimum. Thus only convergence towards a *local* minimum is guaranteed [58, (Sect. 10.5)]. This property is inherited by the Gauss-Newton method. Thus also the Gauss-Newton method does not necessarily find the global minimum. Depending on the choice of model structure there are different ways to minimize or get around this problem:

In case of a state-space model the subspace method in the form of the MATLAB function `n4sid` is first used to find an initial value of the parameter vector $\theta^{(0)}$. The Gauss-Newton algorithm is then initiated

at that value [60, (p. 3-42)]. As part of the subspace method the state-space model is recast as a linear regression model.

In case of grey-box models we may apply the direct but time-consuming method of testing many initial values $\theta^{(0)}$.

11.6 Identifiability

11.6.1 Definition of Identifiability

We use the term identifiability to describe that a certain parameter can be uniquely identified from the input-output signal data. If two different parameter vectors θ_1 and θ_2 give rise to identical predictions they cannot be separated by identification methods. We shall say that a certain parameterization is *identifiable* at $\theta_\star$, if

$$\widehat{y}(t\,|\,\theta) \equiv \widehat{y}(t\,|\,\theta_\star) \Longrightarrow \theta \equiv \theta_\star. \tag{11.25}$$

There are two different reasons why this condition may not hold. One is that two different values of θ simply give identical input-output properties in the model. The other reason is that we do get different models with different values of θ, but because of deficiencies in the input the predictions are still the same.

Note that it can be very difficult to decide whether a parameter in a model is identifiable [61, (Sect. 9.4)].

11.6.2 Identifiability of Black-Box Model Structures

SISO State-Space Model Structures

The matrices $\mathbf{F}(\theta)$, $\mathbf{G}(\theta)$, $\mathbf{H}(\theta)$, and $\mathbf{K}(\theta)$ in the discrete-time state-space model structure (with $J \equiv 0$)

$$\mathbf{x}(t+\tau) = \mathbf{F}(\theta)\mathbf{x}(t) + \mathbf{G}(\theta)u(t) + \mathbf{K}(\theta)e(t), \tag{11.26}$$

$$y(t) = \mathbf{H}(\theta)\mathbf{x}(t) + e(t) \tag{11.27}$$

contain a total of $n^2 + 3 \cdot n$ parameters (n is the dimension of the state vector $\mathbf{x}$, $n = \dim \mathbf{x}$) and thus cannot be 'filled' with parameters, since the corresponding input-output description

$$y(t) = G_\tau(q,\theta)u(t) + H_\tau(q,\theta)e(t), \tag{11.28}$$

$$G_\tau(q,\theta) = \mathbf{H}(\theta)\left[q\mathbf{I} - \mathbf{F}(\theta)\right]^{-1}\mathbf{G}(\theta), \tag{11.29}$$

$$H_\tau(q,\theta) = \mathbf{H}(\theta)\left[q\mathbf{I} - \mathbf{F}(\theta)\right]^{-1}\mathbf{K}(\theta) + 1 \tag{11.30}$$

is defined by $3 \cdot n$ parameters only. Thus the SISO state-space model structure is not a priori identifiable as it is over-parameterized.

It is, however, possible to obtain identifiable structures by seeking parameterizations of the matrices that involve $3 \cdot n$ parameters. One such parameterization is the *observer canonical form*. It is described in Ref. [58, (Sect. 4.6)].

11.6.3 Identifiability of Grey-Box Model Structures

Modeling physical processes typically leads to a continuous-time state-space model summarized as

$$y(t) = G(p,\theta)u(t) + v(t). \tag{11.31}$$

For proper handling we should sample G, and include a noise model H before testing for identifiability.

A simpler test to apply is the continuous-time test

$$G(s,\theta) = G(s,\theta_\star) \text{ for almost all } s \Longrightarrow \theta = \theta_\star \,? \tag{11.32}$$

This is, however, not a 'secure' test! When sampling $G(p)$, ambiguities may occur: Two different $G(p)$ can give the same $G_\tau(q)$. However, with a carefully selected sampling interval, this ambiguity should not cause any problems. Thus Equation (11.32) is a reasonable test for identifiability of the corresponding model structure at $\theta_\star$. This is a difficult problem. Except for special structures there are no general techniques available other than brute-force solution of the equations underlying Equation (11.32) [58, (Sect. 4.6)].

11.6.4 Remarks concerning Identifiability

Un-identifiability is a situation where (infinitely) many minima $\widehat{\theta}$ give rise to exactly the same low value of the loss function $V_N(\widehat{\theta})$.

A grey-box model structure can be obtained from a black-box state-space model structure by imposing constraints on its parameters, i.e., either by fixing some parameters to certain values or by coupling them to each other. Therefore, the grey-box model structure contains fewer parameters than the corresponding black-box state-space model structure. But the prediction error and therefore the loss function may be far more complicated functions of their fewer parameters than those of the corresponding black-box model [58, (Sect. 4.3)]. Furthermore, if the black-box state-space model structure is un-identifiable (cf. M: Section 11.6.2), this property may very well be inherited by the resulting grey-box model structure.

Chapter 12

Model Validation

12.1 How to Validate Models?

It is not difficult to build models of systems — the difficulty lies in making them good and reliable. For the model to be useful, we have to have confidence in the results and predictions that are inferred from it. Such confidence can be obtained by verifying or validating the model. In principle, model validation is done by comparing the model's behavior with the system's and evaluating the difference.

All models have a certain domain of validity. This may determine how exactly they are able to describe the system's behavior. It is important to understand that *all models have a limited domain of validity.*

Note that there is a fundamental limitation in models and simulation: It is hazardous to use a model outside the area it has been validated for [61, (Sect. 1.5)].

12.2 Model Quality

What do we mean by a good model? This should mean that it is close to the true description. In practice, no "true" descriptions are available, and the model quality must thus be judged on different grounds. We note two basic facts [61, (Sect. 9.4)]:

- Model quality is typically related to the ability of the model to reproduce the behavior of the system. This usually means that the model's simulated or predicted output is in good agreement with the outputs produced by the system.
- Model quality is also related to the model's consistency, that is, how well the model can be reproduced from different measured data sets. Regardless of the statistical formalism that can be developed around these facts, it is obvious that it is necessary to question the resulting model if it varies much with the segment of data it was computed from. Conversely, confidence is gained in a model obtained with small variations from different measurement data under varied conditions and maybe with different identification methods.

In the following the measures of model quality are divided into three groups, which are treated separately: Model fit (Section 12.3), cross validation (Section 12.4), and parameter accuracy (Section 12.6).

12.3 Model Fit

In the following y_m will denote the *model output.* y_m can be calculated as a noise-free simulation of the model. For a linear model structure $y(t) = G(p)u(t) + H(p)e(t)$, the model output is $y_m(t) = G(p)u(t)$.

Ljung has noted that the loss function V_N is not always an appropriate measure for comparing models [59, (p. 3-71)]: *"Be careful when comparing loss function values between different structures that use very different noise models. An OE model may have a better input-output fit, even though it displays a higher value of the loss function than, say, an ARX model."* Thus when comparing model structures we need measures of the degree of explanation, i.e., the model fit, which do not depend on the noise models.

With the purpose of comparing model structure performances several quality measures will be applied throughout this thesis. In order to investigate the nature of the model deficiencies we will also apply graphical methods:

First of all we will compare the model output y_m, i.e., the output obtained by a noise-free simulation of the model, with the measured output y, and show the *model error* which is defined as the difference between the measured output and the model output. The model error will be denoted by two symbols Δy and $\overline{\epsilon}$ depending on the context.

$$\Delta y(t_i, \theta) = y(t_i) - y_m(t_i, \theta) = \overline{\epsilon}(t_i, \theta). \tag{12.1}$$

Secondly, we will calculate the *noise-to-signal ratio* NSR which is defined as the root-mean-square model error normalized to the root-mean-square output signal:

$$NSR(\theta) = 100 \cdot \frac{\overline{\epsilon}_{RMS}(\theta)}{y_{RMS}} = 100 \cdot \frac{\sqrt{\sum_{i=1}^{N} \overline{\epsilon}(t_i, \theta)^2}}{\sqrt{\sum_{i=1}^{N} y(t_i)^2}} = 100 \cdot \frac{\sqrt{\sum_{i=1}^{N} \left(y(t_i) - y_m(t_i, \theta)\right)^2}}{\sqrt{\sum_{i=1}^{N} y(t_i)^2}} \quad [\%]. \tag{12.2}$$

As an auxiliary measure we will furthermore list the *peak-to-peak value of the model error* Δy_{pp} which is defined as

$$\begin{aligned} \Delta y_{pp}(\theta) &= \max_{i \in [1,N]} \Delta y(t_i, \theta) - \min_{i \in [1,N]} \Delta y(t_i, \theta) \\ &= \max_{i \in [1,N]} \{y(t_i) - y_m(t_i, \theta)\} - \min_{i \in [1,N]} \{y(t_i) - y_m(t_i, \theta)\}. \end{aligned} \tag{12.3}$$

If a model reflects the dynamics of the system well its resulting noise-to-signal ratio and peak-to-peak value of model error will be low. For a very perfect model the model error tends to zero and thus the noise-to-signal ratio also tends towards zero, whereas for a very poor model the noise is close to the signal and thus the noise-to-signal ratio approaches 100 %.

Note, however, that [50, (Sect. 1.1)] *"a good fit (...) only indicates that the model structure is adequate for expressing the system behavior for a particular input signal."* Whether a good fit also implies accurate parameter estimates is the subject of M: Section 12.6.

12.4 Cross Validation

In order for a model to be considered 'good', it is not enough that the model can track the dynamics in the data. Also consistency is necessary, i.e., that the estimated parameter values $\widehat{\theta}$ do no vary 'too much' from time series to time series. Therefore the estimated parameter values obtained from several time series should be compared.

The purpose of cross validation is to reveal over-parameterization. If the dimension of the parameter vector θ is too large the model performance will not be sensitive to the unnecessary parameters, and their estimates may vary much from time series to time series — cf. M: Section 11.3.2 on page 62.

Three measures are used for the comparison: The mean value, the standard deviation, and the *coefficient of variance* which is defined as the standard deviation divided by the mean value [52, (p. 21)].

If a model reflects the system's dynamics, the standard deviation and therefore also the coefficient of variance will be small. More specifically, for a parameter to be considered physical or physiological its coefficient of variance should be very low, for instance below one.

12.5 Sensitivity to Parameters

M. Knudsen [49, (p. 45)] has noted that *"Most system identification methods can provide an estimate of the covariance of the estimate of unknown parameter values, in addition to the parameter estimates. Obviously this information is very valuable for assessing reliability, e.g. in form of confidence intervals, of the estimated parameter values.*

The reliability of the covariance information depends, however, on assumptions and idealizations, necessary for modeling the noise as a stationary stochastic process. In practical applications it is often difficult to evaluate these approximations and their impact on the results. Generally it is much simpler — based on physical insight — to evaluate approximations in deterministic than in stochastic models."

In this section the notion of parameter sensitivity is introduced. In the next section, the sensitivity will be related to the parameter accuracy, i.e., the quality of an obtained parameter estimate.

12.5.1 Choice of Model Structure

The model is a continuous-time, possibly nonlinear, output-error model

$$y(t) = y_m(t) + e(t), \tag{12.4}$$

and the procedure for minimizing the performance function is operating directly on the physical/continuous-time parameters [50, (p. 3)]. The simulation model may be in state-space form or a combination of linear dynamic transfer functions and static nonlinearities. In both cases the *model output* can be expressed as [50, (Sect. 1.1)]

$$y_m(t, \theta) = F(u_N, \theta), \tag{12.5}$$

where θ is a vector containing the physical parameters, and u_N is the input vector with N samples. F denotes a, normally nonlinear, function of u_N and θ. The quadratic *criterion function* $C_N(\theta)$ to be minimized is

$$C_N(\theta) = \frac{1}{2N} \sum_{i=1}^{N} \overline{\epsilon}(t_i, \theta)^2, \tag{12.6}$$

where the *model error* is

$$\overline{\epsilon}(t, \theta) = y(t) - y_m(t, \theta), \tag{12.7}$$

and the parameter estimate of θ based on N input-output data points u_N and y_N is then the value θ_N minimizing $C_N(u_N,\ y_N,\ \theta)$:

$$\theta_N = \arg\min_{\theta} C_N(u_N,\ y_N,\ \theta). \tag{12.8}$$

12.5.2 The Parameter Dependent Model Error

It is intuitively comprehensible that an accurate estimate of a parameter θ_i requires $V_N(\theta)$ to be sensitive to θ_i, and that — roughly — the most sensitive parameters will be estimated most accurately. Because of the quadratic nature of $V_N(\theta)$, it is unfit for sensitivity calculations. Instead the root-mean-square of a so-called parameter dependent error is introduced.

The model error, $\overline{\epsilon}(t)$ may be split into two parts: The minimum value $\epsilon_0(t, \theta_N)$ caused by noise and imperfect model structure, and a part $\epsilon_p(t, \theta)$ caused by θ being different from the estimate $\theta_N = \arg\min C_N(\theta)$. The latter part,

$$\epsilon_p(t, \theta) = y_m(t, \theta_N) - y_m(t, \theta), \tag{12.9}$$

we shall denote the *parameter dependent model error* [50, (Sect. 1.2)].

By a first order Taylor expansion around θ_N we obtain

$$\epsilon_p(t, \theta) = y_m(t, \theta_N) - y_m(t, \theta) \approx \Psi(t, \theta_N)^T (\theta_N - \theta), \tag{12.10}$$

where Ψ is the *model gradient* at $\theta = \theta_N$

$$\Psi(t, \theta_N) = \frac{\partial y_m(t, \theta)}{\partial \theta}_{|_{\theta=\theta_N}} = \frac{\partial F(u_N, \theta)}{\partial \theta}_{|_{\theta=\theta_N}}. \tag{12.11}$$

The model gradient can be determined by numerical differentiation. The j'th element is estimated by giving the j'th parameter θ_j a very small deviation $\Delta\theta_j$ while the remaining parameters are kept fixed and calculating the corresponding output of the simulation model $y_m(t, \theta_j + \Delta\theta_j)$ [51, (Sect. 3.4)]:

$$\Psi_j(t) \approx \frac{\Delta y_m(t, \theta_j)}{\Delta\theta_j} = \frac{y_m(t, \theta_j + \Delta\theta_j) - y_m(t, \theta_j)}{\Delta\theta_j}. \tag{12.12}$$

The root-mean-square parameter dependent error $\epsilon_{p,RMS}(\theta)$ is

$$\epsilon_{p,RMS}(\theta) = \sqrt{\frac{1}{N} \sum_{i=1}^{N} \epsilon_p(t_i, \theta)^2}. \tag{12.13}$$

The *Hessian* H at $\theta = \theta_N$ is

$$H(\theta_N) = \frac{\partial^2 C_N(\theta)}{\partial\theta\partial\theta^T}_{|_{\theta=\theta_N}} = \frac{1}{N}\sum_{i=1}^{N}\left\{\Psi(t_i,\theta)\Psi(t_i,\theta)^T - \frac{\partial\Psi(t_i,\theta)}{\partial\theta}\cdot\overline{\epsilon}(t_i,\theta)\right\}_{|_{\theta=\theta_N}}. \tag{12.14}$$

If we neglect the second term of H we obtain an *approximate Hessian* $\widetilde{H}$ at $\theta = \theta_N$

$$\widetilde{H}(\theta_N) \approx \frac{1}{N}\sum_{i=1}^{N}\Psi(t_i,\theta)\Psi(t_i,\theta)^T_{|_{\theta=\theta_N}}. \tag{12.15}$$

This expression means that the (j,k)'th matrix element is

$$\left\{\widetilde{H}(\theta_N)\right\}_{jk} = \frac{1}{N}\sum_{i=1}^{N}\Psi_j(t_i,\theta)\cdot\Psi_k(t_i,\theta)_{|_{\theta=\theta_N}}. \tag{12.16}$$

Using these expressions we find the following approximation[1] to the root-mean-square parameter dependent error [50, (Sect. 1.2)]

$$\epsilon_{p,RMS}(\theta) \approx \sqrt{(\theta-\theta_N)^T\widetilde{H}(\theta_N)(\theta-\theta_N)}. \tag{12.18}$$

12.5.3 Relative Parameters and Normed Signals

As the estimated values of the individual parameters may be very different, a comparison of absolute sensitivities has little implication. Relative parameter sensitivities are more meaningful, and they can be obtained by introducing the *relative parameter vector* θ_r and the corresponding *relative Hessian* H_r by

$$\theta_r = L^{-1}\theta, \tag{12.19}$$
$$H_r = L^T H L = LHL. \tag{12.20}$$

where $L = diag(\theta_N)$ is a quadratic matrix with the vector θ_N in the diagonal and zeros elsewhere. For brevity, some of the equations will be expressed in terms of the *relative parameter error* $\widetilde{\theta}_r$ which is defined as

$$\widetilde{\theta}_r = \theta_r - \theta_{N,r} = \theta_r - 1, \tag{12.21}$$

where $\theta_{N,r} = L^{-1}\theta_N = 1$ and 1 denotes a d-dimensional column vector with all elements equal to one.

To make the values of the individual sensitivities meaningful, the *normed signals* are introduced by

$$y_{mn} = \frac{y_m}{y_{RMS}}, \tag{12.22}$$
$$\epsilon_{p,RMSn} = \frac{\epsilon_{p,RMS}}{y_{RMS}}. \tag{12.23}$$

where

$$y_{RMS} = \sqrt{\frac{1}{N}\sum_{i=1}^{N}y(t_i)^2}. \tag{12.24}$$

The *relative normed model gradient* is then (since $L\Psi = \frac{\partial y_m}{\partial\theta_r}$)

$$\Psi_{rn} = \frac{L\Psi}{y_{RMS}}, \tag{12.25}$$

---

[1]

$$\frac{1}{N}\sum_{i=1}^{N}\epsilon_p(t_i,\theta)^2 \approx \frac{1}{N}\sum_{i=1}^{N}(\theta-\theta_N)^T\Psi(t_i,\theta_N)\Psi(t_i,\theta_N)^T(\theta-\theta_N)$$
$$= (\theta-\theta_N)^T\left[\frac{1}{N}\sum_{i=1}^{N}\Psi(t_i,\theta_N)\Psi(t_i,\theta_N)^T\right](\theta-\theta_N) = (\theta-\theta_N)^T\widetilde{H}(\theta_N)(\theta-\theta_N). \tag{12.17}$$

and the *relative normed Hessian* consequently

$$H_{rn} = \frac{H_r}{{y_{RMS}}^2} = \frac{LHL}{{y_{RMS}}^2}. \tag{12.26}$$

Inserting these in the expression for $\epsilon_{p,RMSn}$ gives[2] [50, (Sect. 1.2)]

$$\epsilon_{p,RMSn}(\theta_r) = \sqrt{\frac{1}{N}\sum_{i=1}^{N} \epsilon_{pn}(t_i,\theta_r)^2} \approx \sqrt{(\theta_r - 1)^T \widetilde{H}_{rn}(1)(\theta_r - 1)}. \tag{12.28}$$

Note that $H_{rn}(1)$ means $H_{rn}(\theta_r)_{|_{\theta_r=1}}$.

12.5.4 The Sensitivity Ellipsoid

The *sensitivity* of $\epsilon_{p,RMSn}(\theta_r)$ to one relative parameter θ_{ri} — while the remaining relative parameters are fixed to the value one — is then

$$S_i = S_{ni} = \frac{\partial \epsilon_{p,RMSn}}{\partial \theta_{ri}} = \sqrt{h_{rnii}}, \tag{12.29}$$

$$h_{rnii} = \left\{ \widetilde{H}_{rn}(\theta_{N,r}) \right\}_{ii} = \left\{ \widetilde{H}_{rn}(1) \right\}_{ii}. \tag{12.30}$$

To obtain accurate parameter estimates, large sensitivities to the individual parameters is a necessary requirement. It is not sufficient, however, as the sensitivity to a combination of two or more parameters may be much smaller than the individual sensitivities, indicating a high correlation between the parameters. This problem can be illustrated in the two-dimensional parameter space, where iso-curves given by $\epsilon_{p,RMSn} = constant$ are ellipses as illustrated in Figure 12.1. We will use the name *sensitivity ellipsoid*

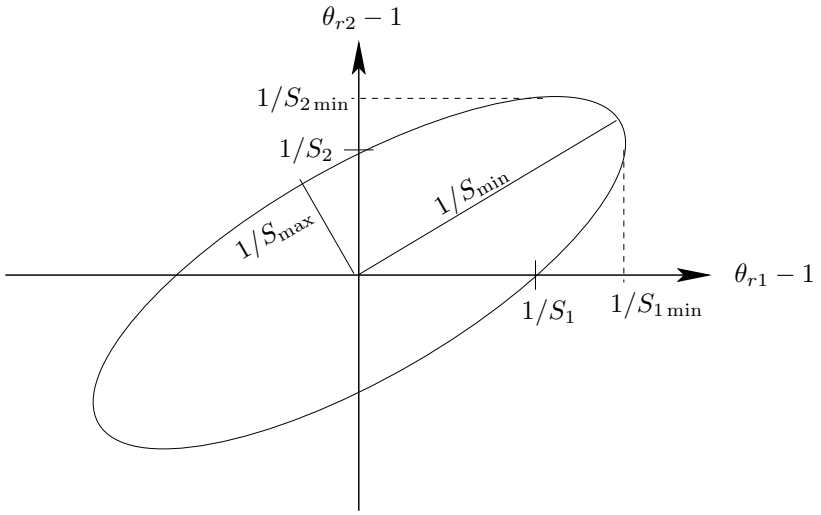

Figure 12.1: The sensitivity ellipse $\epsilon_{p,RMSn}(\theta_r) = 1$ with some characteristic sensitivities. S_i: sensitivity to θ_i alone; $S_{i\,\min}$: minimum sensitivity to θ_i; $S_{\min}$: minimum sensitivity; $S_{\max}$: maximum sensitivity. Reproduced from Ref. [50, (Sect. 1.2)].

as the distance from the center to any point on the ellipsoid represents the reciprocal sensitivity in that direction.

[2]

$$\begin{aligned} \epsilon_{p,RMSn}(\theta_r) &= \frac{\epsilon_{p,RMS}}{y_{RMS}} \approx \frac{\sqrt{(\theta-\theta_N)^T \widetilde{H}(\theta_N)(\theta-\theta_N)}}{y_{RMS}} \\ &= \sqrt{(\theta-\theta_N)^T L^{-1} \cdot \frac{L\widetilde{H}(\theta_N)L}{{y_{RMS}}^2} \cdot L^{-1}(\theta-\theta_N)} = \sqrt{(\theta_r-1)^T \widetilde{H}_{rn}(1)(\theta_r-1)}. \end{aligned} \tag{12.27}$$

Various characteristic sensitivities are indicated in Figure 12.1. A very elongated ellipsoid, where the ratio R of the minor axis over the major,

$$R = \frac{S_{\max}}{S_{\min}}, \tag{12.31}$$

is much larger than one, indicates large differences in sensitivities in various directions in the parameter space. If, furthermore, the directions of the ellipsoid axes differ from the parameter axes, the sensitivity is minimal for a linear combination of the parameters, $\theta_{r2} - \alpha\theta_{r1} = 0$, where α is the slope of the major axis. This indicates that the parameters are correlated. As it appears from Figure 12.1, the correlation is high when the ratio

$$R_i = \frac{S_i}{S_{i\min}} \tag{12.32}$$

is much larger than one. The ratios R and R_i are, accordingly, characteristic for the shape and direction of the ellipsoid and hence for the sensitivities.

These sensitivities and ratios can be calculated from $\widetilde{H}_{rn}$ as

$$S_{\max} = \sqrt{\lambda_{\max}}, \tag{12.33}$$

$$S_{\min} = \sqrt{\lambda_{\min}}, \tag{12.34}$$

where λ is an eigenvalue of $\widetilde{H}_{rn}$. Also the minimum sensitivity of θ_i, $S_{i\min}$, is easily determined from $\widetilde{H}_{rn}$. As shown in [49, (App. 3)], the maximum value of θ_i on the ellipsoid is

$$\widetilde{\theta}_{ri\max} = \theta_{ri\max} - 1 = \sqrt{\widetilde{H}_{rn}^{-1}(1)_{ii}}, \tag{12.35}$$

and the minimum sensitivity to θ_i is

$$S_{i\min} = \frac{1}{\widetilde{\theta}_{ri\max}} = \frac{1}{(\theta_{ri\max} - 1)} = \frac{1}{\sqrt{\{\widetilde{H}_{rn}^{-1}(1)\}_{ii}}}. \tag{12.36}$$

The four most characteristic sensitivity measures are summarized in Table 12.1 together with an indication of their best values, i.e., the values which signify most accurate parameter estimates. It may be emphasized

$S_{\min}$	Minimum sensitivity. Inverse of major half axis.	As large as possible
$S_{i\min}$	Minimum sensitivity to θ_i.	As large as possible
$R = \frac{S_{\max}}{S_{\min}}$	Ratio of maximum and minimum sensitivity in any direction. Ratio of half axes.	As close to one as possible
$R_i = \frac{S_i}{S_{i\min}}$	Ratio of sensitivity to θ_i alone and minimum sensitivity to θ_i. $R_i \gg 1$ indicates correlation between parameters.	As close to one as possible

Table 12.1: Characteristic parameter sensitivity measures.

that as the shape of the ellipsoid is determined by $\widetilde{H}(\theta_N)$, the values of the sensitivity measures are determined by the input signal u_N (cf. Equations (12.5)–(12.14)) [50, (Sect. 1.2)].

12.6 Parameter Accuracy

12.6.1 Types of Errors: Variance and Bias

Model inadequacy can take two, principally different, shapes:

One is the model error that arises because noise influences on the measurements and system. If an experiment is repeated with exactly the same input, the output will not be exactly the same because the noise is not reproduced. Because of this the resulting model will be different. Such model variations are called *variance errors*. Variance errors can typically be reduced by using longer measurement sequences.

The other model inadequacies originate from under-modeling, i.e., from deficiencies in the model structure. The model is simply not capable of describing the system, even if it should be fitted to noise-free data. Such errors will be called systematic errors, or *bias errors*. Bias errors are noticed as variations in the model when it is fitted to data that have been collected during different conditions (even if the measurement intervals are long enough to make the variance errors insignificant). The reason is that different conditions (operating point, input characteristics and so on) bring out different aspects of the system's properties and the model is fitted to the dominating system properties.

A good model is thus one that has both small variance and bias errors [61, (Sect. 9.4)].

12.6.2 Measures of Parameter Accuracy

The model fit expressed by the minimum value of the criterion function $C_N(\theta_N)$ or the noise-to-signal ratio $NSR(\theta_N)$ can be related to the parameter estimation accuracy by means of a sensitivity measure.

The model error can be split into three components

$$\overline{\epsilon}(t,\theta) = y(t) - y_m(t,\theta) = \epsilon_x(t) + \epsilon_m(t) + \epsilon_p(t,\theta), \tag{12.37}$$

where ϵ_x is caused by noise, ϵ_m by under-modeling, and the parameter dependent error ϵ_p by θ being different from the optimal value $\theta_N = \arg\min C_N(\theta)$. As the first two error components are independent, the minimum value of the criterion function is [51, (Sect. 6.3)]

$$C_N(\theta_N) = \min_\theta C_N(\theta) = \frac{1}{2}\cdot\overline{\epsilon}_{RMS}{}^2(\theta_N) = \frac{1}{2N}\sum_{i=1}^{N}\overline{\epsilon}(t_i,\theta_N)^2 = \frac{1}{2}\left(\epsilon_{x,RMS}{}^2 + \epsilon_{m,RMS}{}^2\right). \tag{12.38}$$

We now consider the effect of each of the two error components on the parameter estimation accuracy.

Noise

First the variance in the parameter estimates caused by noise is investigated.

We assume that the model structure is correct, i.e., $\epsilon_m \equiv 0$, and that the error $\epsilon_x(t)$ is white and Gaussian distributed. The parameter covariance matrix is

$$cov(\theta_N) = \overline{E}\left\{(\theta_N - \theta_0)(\theta_N - \theta_0)^T\right\}, \tag{12.39}$$

where θ_0 denotes the limit estimate ($\theta_N \longrightarrow \theta_0$ for $N \longrightarrow \infty$) and $\overline{E}$ denotes averaging over samples, i.e., time-averaging. Since the error is white and Gaussian distributed an estimate of the parameter covariance matrix of the asymptotic ($N \longrightarrow \infty$) distribution reads [58, (Sect. 9.3)]

$$\widehat{cov(\theta_N)} = \frac{2}{N}C_N(\theta_N)H^{-1}(\theta_N). \tag{12.40}$$

Consequently an estimate of the spread of the i'th parameter estimate $\theta_{N,i}$ reads

$$\widehat{\sigma}(\theta_{N,i}) = \sqrt{\frac{2}{N}C_N(\theta_N)\left\{H^{-1}(\theta_N)\right\}_{ii}}. \tag{12.41}$$

By inserting Equations (12.36) and (12.38) into Equation (12.41), the spread of the relative parameter estimate[3] can be expressed as:

$$\sigma(\theta_{N,ri}) = \frac{1}{\sqrt{N}}\frac{\epsilon_{x,RMSn}}{S_{i\,\min}}. \tag{12.43}$$

Since the model structure is correct $NSR(\theta_N) = 100\cdot\overline{\epsilon}_{RMSn}(\theta_N) = 100\cdot\overline{\epsilon}_{x,RMSn}$. Thus, under the assumption that the model deficiencies are only caused by noise, the maximal estimated relative parameter spread can be expressed by physical significant quantities:

$$\sigma(\theta_{N,ri}) = \frac{1}{\sqrt{N}}\frac{NSR(\theta_N)}{S_{i\,\min}} \quad [\%]. \tag{12.44}$$

[3] Let $\widehat{P}_N(\theta_N) = \widehat{cov(\theta_N)}$. Then

$$\widehat{P}_{N,r}(\theta_N) = L^{-1}\widehat{P}_N(\theta_N)(L^{-1})^T = \frac{2}{N}C_N(\theta_N)\left(L^T H(\theta_N)L\right)^{-1} = \frac{2}{N}C_N(\theta_N){H_r}^{-1}(\theta_N). \tag{12.42}$$

Therefore $\widehat{P}_{N,rn}(\theta_r)_{|_{\theta_r=1}} = {y_{RMS}}^2\cdot\widehat{P}_{N,r}(\theta_N) = \frac{2}{N}C_N(\theta_N){H_{rn}}^{-1}(1)$.

This important result says that [51, (Sect. 6.3)] *"The relative spread, caused by noise, of the estimate of θ_i is proportional to the noise-to-signal ratio, inverse proportional to the parameter sensitivity, and inverse proportional to the square root of the number of data points."*

Under-Modeling

Next the bias in the parameter estimates caused by under-modeling is addressed.

Assume that there is no noise effect, i.e., $\epsilon_x \equiv 0$, and that the model structure is in-correct $\epsilon_m \neq 0$. We introduce the concept of *equivalent parameter error* $\widetilde{\theta}_{eq,r}$ defined as the relative parameter errors in the set

$$S_{eq,r} = \left\{ \widetilde{\theta}_{eq,r} \in \mathbb{R}^d \mid \epsilon_{p,RMSn}(\widetilde{\theta}_{eq,r}) = \epsilon_{m,RMSn} \right\}, \tag{12.45}$$

that is, the relative parameter errors that would cause an output error $\epsilon_{p,RMSn}$ equal to the error actually caused by under-modeling $\epsilon_{m,RMSn}$. Equation (12.45) describes an ellipsoid equal to the sensitivity ellipsoid (12.18) multiplied by $\epsilon_{m,RMSn}$

$$\widetilde{\theta}_{eq,r}^T H_{rn} \widetilde{\theta}_{eq,r} = {\epsilon_{m,RMSn}}^2. \tag{12.46}$$

According to Equation (12.35) the maximum value of the equivalent error of parameter θ_i is

$$\Delta\theta_{eq,ri} = \widetilde{\theta}_{eq,ri\max} = \theta_{eq,ri\max} - 1 = \frac{\epsilon_{m,RMSn}}{S_{i\min}}. \tag{12.47}$$

Now $NSR(\theta_N) = 100 \cdot \epsilon_{m,RMSn}$. Under the assumption that the model deficiencies are solely caused by under-modeling the maximal relative parameter error can therefore be expressed as

$$\Delta\theta_{eq,ri} = \frac{NSR(\theta_N)}{S_{i\min}} \quad [\%]. \tag{12.48}$$

This means that [51, (Sect. 6.3)]: *"The error on the estimate of θ_i caused by under-modeling is simply the noise-to-signal ratio divided by the parameter sensitivity."*

Noise and Under-Modeling

In most practical applications there is both noise and under-modeling. We then define the *total relative parameter uncertainty* $\Delta\theta_{N,ri\,\mathrm{tot}}$ as the sum of the relative parameter spread and the relative equivalent parameter error

$$\Delta\theta_{N,ri\,\mathrm{tot}} = \sigma(\theta_{N,ri}) + \Delta\theta_{eq,ri} = \frac{1}{S_{i\min}} \left(\frac{\epsilon_{x,RMSn}}{\sqrt{N}} + \epsilon_{m,RMSn} \right). \tag{12.49}$$

A fundamental problem when using Equation (12.49) is how to split the output error up into the two parts caused by noise and under-modeling, respectively. If $\epsilon_{x,RMSn}$ and $\epsilon_{m,RMSn}$ are of the same order of magnitude, the effect of under-modeling is dominating, since typically $N > 100$, i.e. $\sqrt{N} > 10$. A worst case parameter error can be calculated by assuming the total output error is caused by under-modeling, and a best case by assuming the total output error is caused by noise. A feasible way to split the output error up into the two parts is to measure an output sequence with zero input and calculate $\epsilon_{x,RMSn}$ from this [51, (Sect. 6.3)].

12.7 Discussion of Model Validation

12.7.1 The Linear Output-Error Model Structure as a Special Case

For the special case of a linear continuous-time output-error model structure (cf. M: Section 10.2 on page 58) we have:

$$y(t) = y_m(t) + e(t), \tag{12.50}$$

$$y_m(t) = G(p)u(t) = \widehat{y}(t), \tag{12.51}$$

$$\overline{\epsilon} = \epsilon, \tag{12.52}$$

i.e., the model output is identical to the prediction, and the model error is identical to the prediction error (since the noise filter $H \equiv 1$). Furthermore

$$C_N(\theta) = \frac{1}{2N} \cdot V_N(\theta), \tag{12.53}$$

$$H(\theta) = C_N{}''(\theta) = \frac{1}{2N} \cdot V_N{}''(\theta), \tag{12.54}$$

$$NSR(\theta) = 100 \cdot \frac{\sqrt{2 \cdot C_N(\theta)}}{y_{RMS}} = 100 \cdot \frac{\sqrt{V_N(\theta)}}{\sqrt{N} \cdot y_{RMS}} \propto \sqrt{V_N(\theta)}, \tag{12.55}$$

$$\theta_N = \widehat{\theta}. \tag{12.56}$$

Thus in this special case the prediction error method of letting the parameter estimate $\widehat{\theta}$ be the parameter value which minimizes the loss function $V_N(\theta)$ is fully equivalent to seeking the parameter value which minimizes the noise-to-signal ratio $NSR(\theta)$.

The other linear model structures contain a noise model $H \neq 1$. Therefore also the prediction depends on the noise model H — not only the system model G. Thus the noise-to-signal ratio (cf. M: Section 12.3) can be used for comparing different model structures but it is not a valid criterion function.

For non-linear output-error model structures minimization of the criterion function C_N is also equivalent to minimization of the noise-to-signal ratio NSR.

For non-linear model structures containing a noise model $H \neq 1$ neither the prediction error method nor the sensitivity approach apply.

12.7.2 High Sensitivity is not Equivalent to Good Cross Validation

Note that a deep global minimum in the loss function V_N means that the equivalent parameter gives a high degree of explanation of the system's behavior. However, the model performance can be strongly sensitive to a parameter even though the parameter estimate varies from time series to time series, i.e., even though the cross validation (cf. M: Section 12.4) is bad. This will for instance be the case if the corresponding variable ought to be scaled.

12.7.3 The Origin of Bias Errors

In M: Chapter 10 we introduced a number of standard model structures. From these we conclude that bias errors may be a result of three different types of model structure deficiencies:

- Non-linearities are wrong or missing,
- The linear order is wrong, and/or
- The transport delay is wrong.

Chapter 13

Summary of Methodology

The methodology is parted into four chapters, each of which treats a certain aspect of the task of creating dynamic models of systems from measurements of input and output signals.

System and Model Classifications

The notions of system and model are introduced as well as a number of signal types: Input u, disturbance e, and output y signals, internal variables x.

A number of classifications of systems and models are introduced: Static vs. dynamic; time-independent vs. time-varying; linear vs. non-linear; change oriented vs. discrete event driven; SISO, SIMO, MISO, and MIMO; non-parametric vs. parametric; deterministic vs. stochastic, continuous-time vs. discrete-time; distributed vs. lumped parameter; black-, grey-, and white-box.

Models of Dynamic Linear Time-Invariant Systems

A mathematical model of a system on the form $y(t) = G(\theta)u(t) + H(\theta)e(t)$ contains both a dynamics model in the form of a transfer function $G(\theta)$ and a noise filter $H(\theta)$, which are specified in terms of the parameter vector θ. Model structures are divided into two subclasses: Input-output vs. state-space model structures. For each of the cases discrete-time models and continuous-time models the following parameterizations are described: General transfer function model, and state-space representation of transfer functions.

Two approaches to digitization of continuous-time model structures are: Numerical integration (methods: forward rectangular rule, trapezoid rule), and hold equivalents (methods: zero-order hold equivalent, triangle hold equivalent).

System Identification

System identification is the task of constructing mathematical models of a dynamic system by fitting the model properties to those of the system. The system properties are represented by observations of input to and output from the system. System identification can be subdivided into structure determination and parameter estimation.

Structure determination consists in choosing the type and the size of the model structure as well as the model parameterization.

One method of performing parameter estimation, the prediction error method, is described. Two ways of performing the iterative search for the point in the parameter space, which results in the minimal value of the loss function, are described: The Newton-Raphson method and the Gauss-Newton method.

The term identifiable is used to characterize a parameter whose value can be uniquely found from the input-output measurements. The conditions, under which black-box and grey-box state-space model structures are identifiable, are considered.

Model Validation

The measures of model quality are subdivided into three groups concerned with model fit, cross validation, and parameter accuracy, respectively.

Two measures are used for validation of the model fit: Primarily the noise-to-signal ratio and subsidiary the peak-to-peak value of the model error.

Three measures are used for cross validation: The mean values, the standard deviations and the coefficients of variance of the parameter estimates.

Validation of the parameter accuracy is based on a sensitivity approach which applies to linear and non-linear output-error model structures. The sensitivity ellipsoid concept is developed from a linear approximation to the parameter dependent model error. Characteristic measures of the sensitivity of the model performance to parameters are: The minimum sensitivity, the minimum sensitivity to the i'th parameter θ_i, the ratio R of the minor axis to the major axis of the sensitivity ellipsoid, and the ratio R_i of the sensitivity to the i'th parameter θ_i alone and the minimum sensitivity to the i'th parameter. Measures of parameter quality are related to the sensitivity measures by assuming that the model deficiencies are caused solely by noise (causing variance errors) or under-modeling (causing bias errors), respectively.

Part III

Signal and System Analysis

The purpose of this part is to analyze the experimental data series in order to extract information about the signals themselves as well as about the system.

The goal is two-fold:

- To choose a subset of the experimental data to be used for system modeling.
- To provide a solid background for developing mathematical models being able to reproduce the measured changes in cerebellar blood flow from measured neuronal activity.

The means to achieve these goals will be various methods from basic signal and system analysis as described in, for instance, the tutorial of Ref. [55].

Chapter 14

Signal Analysis

The purpose of this chapter is to analyze the measured input and output signals separately.

The goal is two-fold:

- Since a vast amount of data has been made available by the research group headed by Prof. Dr. Martin Lauritzen there is a need to pick out a subset to work with.
- To find some characteristics of each of the input and output signals. We will especially investigate properties of the signals which might be of importance to the task of modeling the neuro-vascular system.

14.1 Analysis of the Field Potential Signal

The evoked field potential signal is now analyzed in order to create a better understanding of the input signal. Only the inferior olive stimulation experiments are considered.

As a data file containing a 7 kHz sampled field potential signal is quite big, it is a goal to identify which information the field potential signal contains, and from this choose a simpler signal representation.

14.1.1 Analysis of the Full Field Potential Signal

The *power spectrum magnitude* (PSM) of a signal g is mathematically defined [55, (p. 1-63 and 1-68)] as

$$PSM(f) = 10 \cdot \log |P_{gg}(f)|, \tag{14.1}$$

with $P_{gg}(f)$ being the *power spectral density*[1] (PSD) of the signal g

$$\begin{aligned} P_{gg}(f) &= \int_{-\infty}^{\infty} R_{gg}(t') \cdot e^{-2\pi \cdot f \cdot t'} dt', \\ R_{gg}(t') &= E\{g(t) \cdot g(t+t')\}. \end{aligned}$$

$R_{gg}(t')$ is the auto-correlation function and $E\{\cdot\}$ denotes the expectation value operator [55, (p. 1-61)]. The function $P_{gg}(f)$ has the property that $P_{gg}(f)df$ is equal to the power of the signal g in the frequency band $[f, f+df]$ [55, (p. 1-64)].

A crude estimate of the PSD is the *periodogram* which is a real-valued function defined as [55, (p. 1-64 and 2-91)]

$$\hat{P}_{gg}(f) = |g(f)|^2 = g(f) \cdot g^*(f), \qquad 0 \leq f < f_{Nyq}, \tag{14.2}$$

where

$$g(f) = \int_{-\infty}^{\infty} g(t') \cdot e^{-2\pi \cdot f \cdot t'} dt' \tag{14.3}$$

is the Fourier transform of $g(t)$, $*$ denotes complex conjugation and f_{Nyq} is the Nyquist frequency.

The PSD function in MATLAB averages and scales modified periodograms of detrended sections of the signal according to Welch's method [55, (p. 1-67)]. The optional FFT length has been set to 4096.

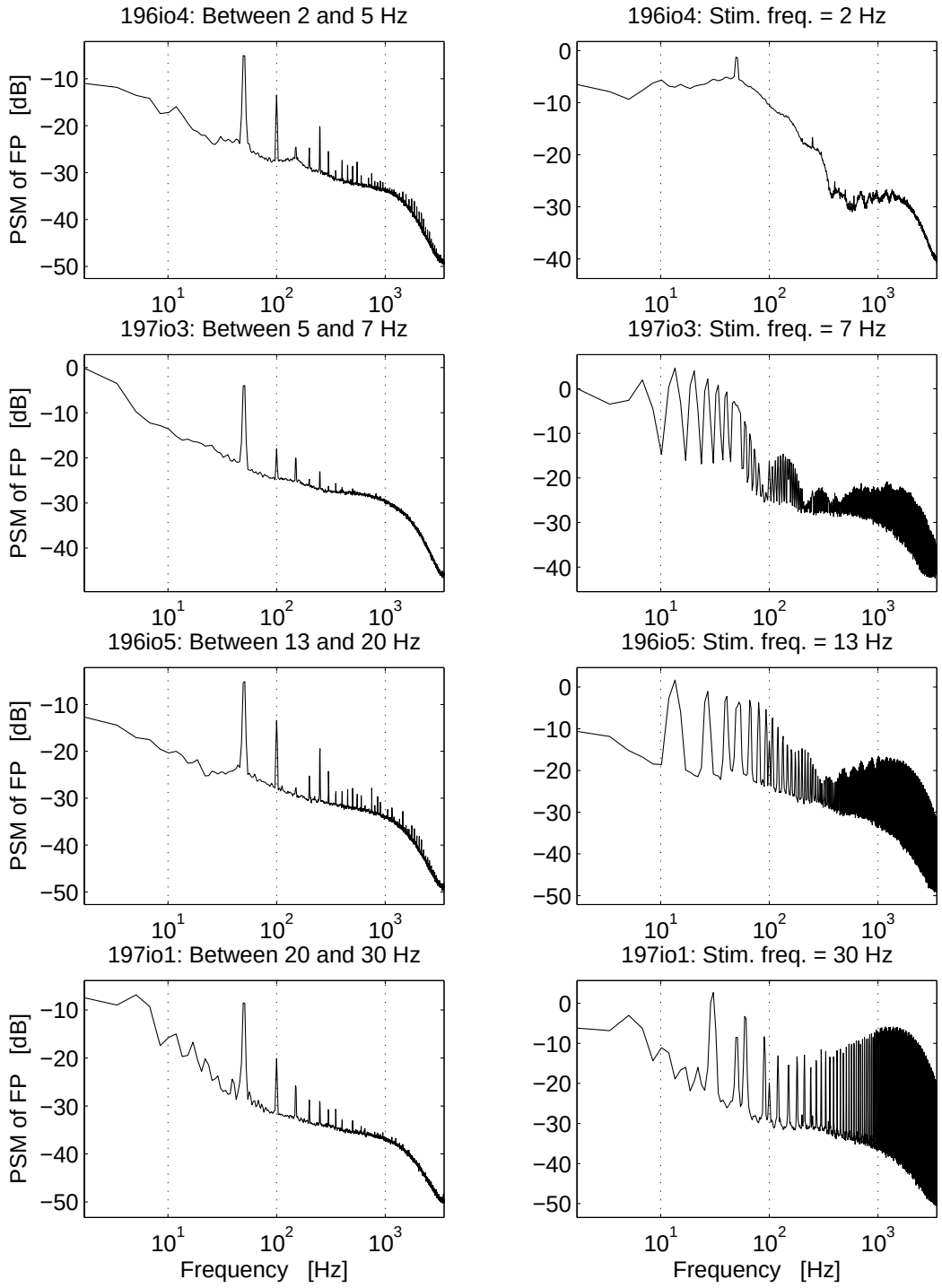

Figure 14.1: Power spectrum magnitude (PSM) for chosen intervals of the field potential signal (FP). The panels in the left column show the PSM for time intervals where the inferior olive is *not* stimulated. These intervals are typically 240 s long. The panels in the right column show the PSM for time intervals where the inferior olive has been stimulated with various frequencies. These intervals are 60 s long. Note the strong 50 Hz components originating from the network voltage. Note also the quite broad ranges of high frequencies occurring during stimulation (panels in the right column).

The results of this analysis are shown in Figure 14.1 for various portions of the FP signal. It is seen that the FP signal contains a very strong 50 Hz artifact originating from the network voltage. Note also that during stimulation not only the particular stimulation frequency occurs in the spectrum but also a rather broad range of higher frequencies. This feature may be due to the fact that (contrary to the 50 Hz artifact) the time-localized excitations of the FP signal are not well represented by sinusoids or other periodic signals — cf. Ref. [58, (Sect. 2.3)].

14.1.2 Analysis of Field Potential Amplitudes

There is tradition for letting the local excitations of the FP signal be represented by their amplitudes, FPA, alone. Examples are in case of the cerebellar cortex Refs. [66, 67] and in case of the somato-sensory cortex Refs. [6, 76]. Therefore the variation in time of the FPA signal is now investigated.

The calculation of the stimulation frequency is described in Appendix B.1 on page 272. The amplitudes of the EPSP components (see P: Figure 7.4 on page 46) are found by means of a SPIKE2 script which is described in Appendix B.2.

The time development of the stimulation frequency and the evoked field potential amplitude, respectively, are shown in Figure 14.2 for the four cases of inferior olive stimulation. Notice that, in the

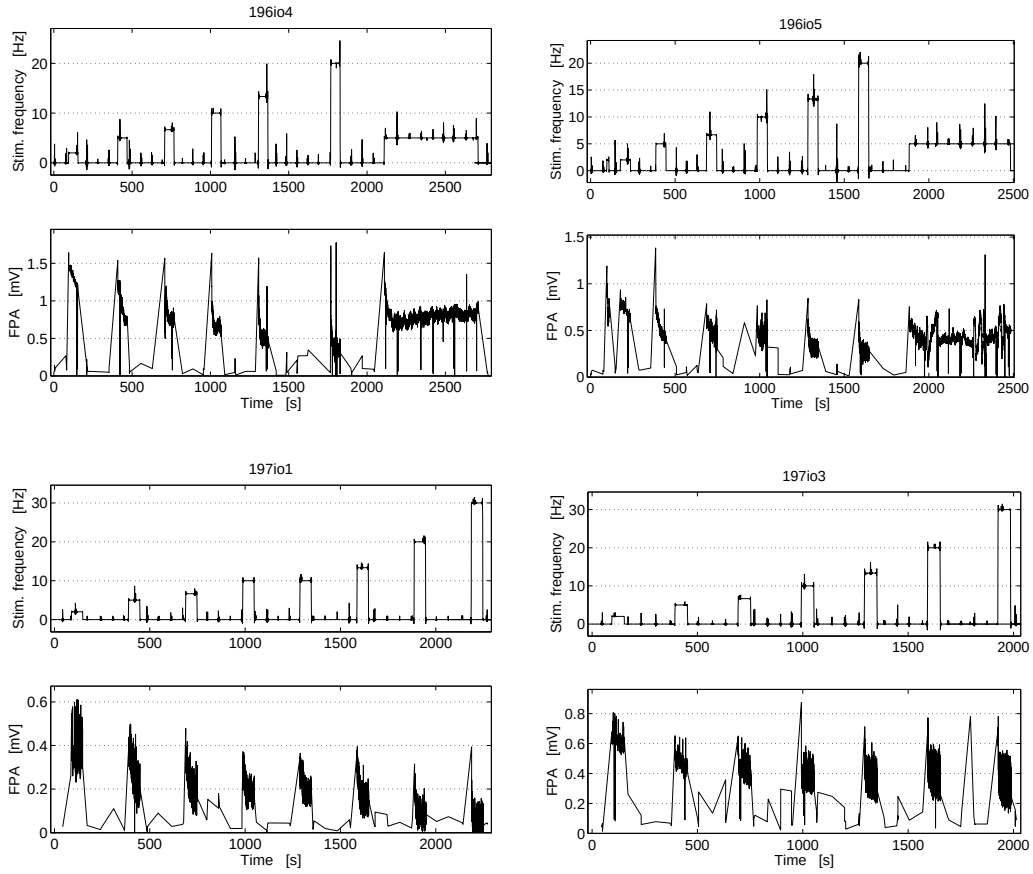

Figure 14.2: The time development of the frequency of the applied stimulation and the evoked field potential amplitudes (FPA) for the four cases of inferior olive stimulation. All samples are shown. The stimulation frequency signals have been resampled by a factor 10 to create a 1 Hz sampled signal.

cerebellar cortex, a single stimulus event evokes a single field potential event with a certain amplitude. Thus also the frequency of evoked field potential amplitudes varies in time.

To make the features of the FPA signals more clear, the signals were averaged by dividing the time axis into bins ten times longer than the sampling time of the CBF signal, i.e., 1 s long, and averaging the

[1] Frequencies, f, are measured in units of periods per seconds; angular frequencies, $\omega = 2\pi f$, in radians per second.

field potential amplitudes within each bin. Also the standard deviation within each bin was calculated. The results are shown in Figure 14.3.

From this analysis it can be concluded that, in case of inferior olive stimulation, the average field potential amplitude decreases significantly as the stimulation frequency increases. Note that the variation in the FPA size may be due to a combination of several distinct contributions — cf. Figure 14.1:

- The 'true' field potential, i.e., the 'background' (low- and intermediate-frequency) parts of the power spectrum (up to around 500 Hz) originating from the time-localized excitations.
- Frequency-localized noise at 50 Hz originating from the network voltage.
- High-frequency noise pertaining to frequencies above 500 Hz.

Furthermore, during stimulation with a particular frequency, the field potential amplitude decreases with time — at least within the first 30 s after onset of stimulation. There is some indication that the field potential amplitude increases slowly when the stimulation continues beyond 60 s. A sketch illustrating this behavior is shown in Figure 14.4. The standard deviation, however, seems unaffected by the stimulation frequency as well as the stimulation duration.

Thus, the information content of the FPA signal is not well described by the frequency, f, and the field potential amplitude averaged over 60 s, $\langle FPA \rangle_{60\,s}$, as suggested in Ref. [66]. Instead we will claim that the averaged FPA signal $\langle FPA \rangle_{1\,s}(t)$ depends dynamically on the stimulation frequency. But this property is inherited from the FPA signal, and we will therefore also claim that the FPA signal depends dynamically on the stimulation frequency.

Finally, for a particular stimulation frequency — for instance 10 Hz — the overall FPA level is *not* identical for the four time series. This variation might be a result of variation in the position of the measurement probe relative to the charge distribution which is the origin of the field potential.

14.1.3 Analysis of the Field Potential Durations

It is now investigated whether there is any information in the duration (FPD) of the time-localized excitations of the field potential. The duration of an EPSP component is here defined as twice the area between the field potential and the reference level divided by the field potential amplitude, and is found by means of a SPIKE2 script which is described in Appendix B.3 on page 273. Note, that *a priori* the variation in FPD will be much higher than the variation in FPA since an amplitude is more well-defined than a duration.

The time developments of the stimulation frequency and the durations of the field potential excitations, respectively, are shown in Figure 14.5 for the four cases of inferior olive stimulation.

To make the features of the FPD signals more clear, the signals were averaged by dividing the time axis into bins ten times longer than the sampling time of the CBF signal, i.e., 1 s long, and averaging the field potential durations within each bin. Also the standard deviation within each bin was calculated. The results are shown in Figure 14.6.

From this analysis it is concluded that, in case of inferior olive stimulation, the average field potential duration is independent of the stimulation frequency — for frequencies above 5 Hz. Below 5 Hz the field potential duration decreases with decreasing stimulation frequency. Thus it has been confirmed that — for stimulation frequencies above 5 Hz — the majority of the information content in the field potential signal resides in the amplitudes of the time-localized excitations. The level of the estimated durations, however, seems to vary from rat to rat: For rat no. 196 it is around 8 ms, for rat no. 197 $15 - 20$ ms.

The standard deviation, however, seems to increase with the stimulation frequency. The variation in the standard deviation of the duration is quite natural since the area is much more sensitive to variation in the reference level (caused by low-frequency noise in the field potential) than the amplitude. (The majority of the area between the field potential and the reference level is situated right below the reference level.)

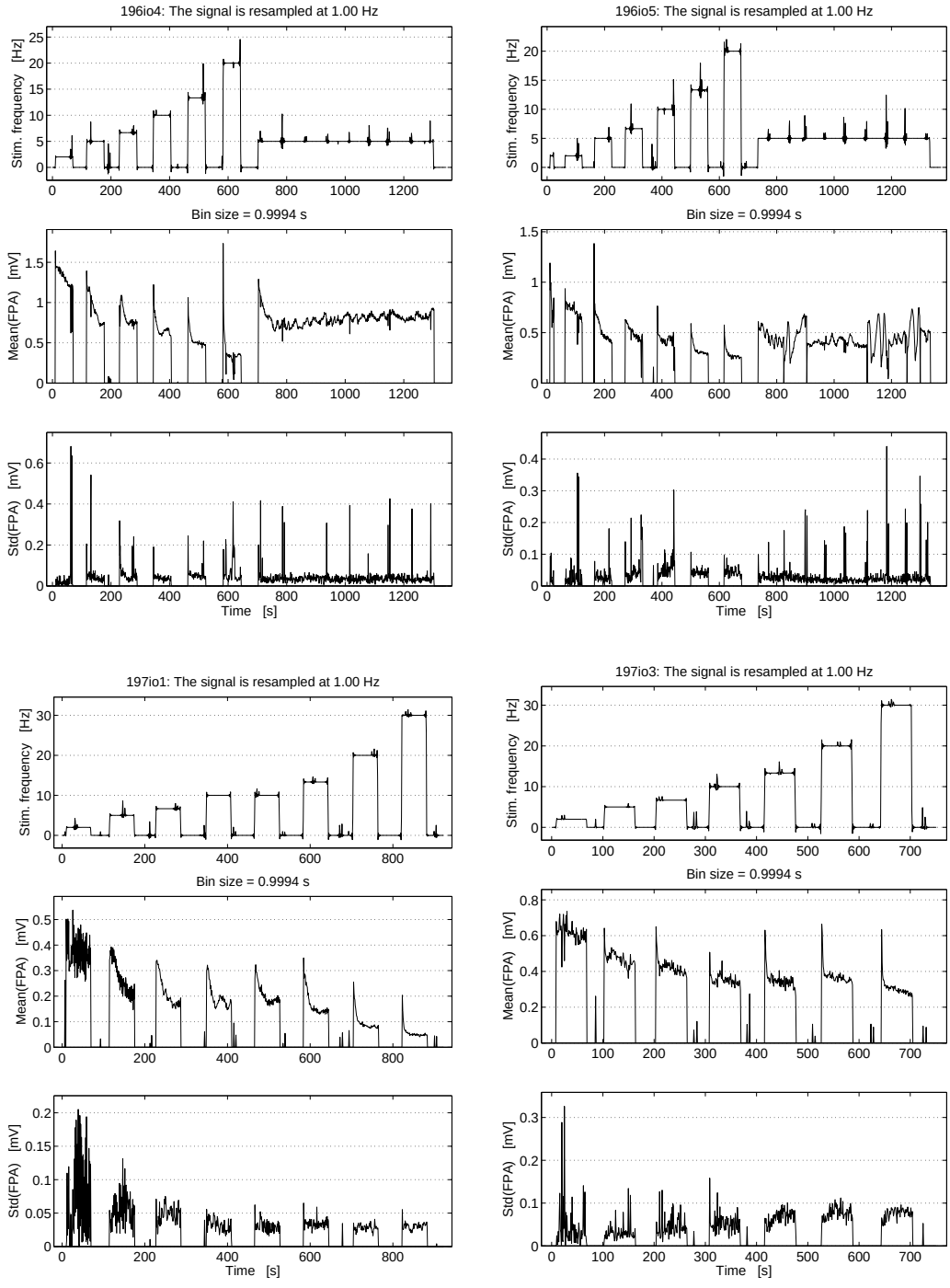

Figure 14.3: The frequency of the applied stimulation and the arithmetic mean value (*mean*) as well as the standard deviation (*std*) of the evoked field potential amplitudes (FPA) within each bin for the four cases of inferior olive stimulation. Note the strong decrease in the average FPA as the frequency is increased. Note also the strong time-dependence of the mean during stimulation with a particular frequency. The standard deviation, however, is almost independent of the frequency as well as the duration. Furthermore, for a particular stimulation frequency the overall FPA level vary somewhat among time series.

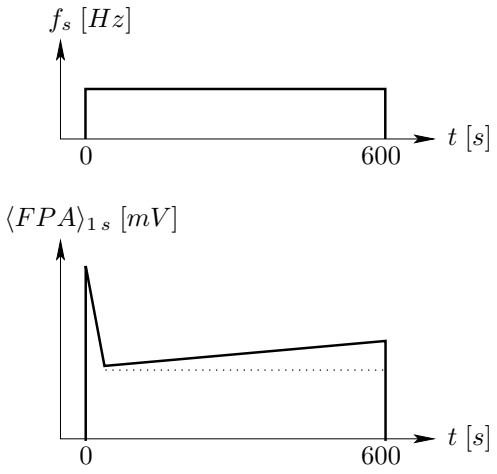

Figure 14.4: Sketch illustrating the dynamic dependence of the average field potential amplitude signal, $\langle FPA \rangle_{1\,s}$, on time during stimulation of the inferior olive with a single frequency f_s.

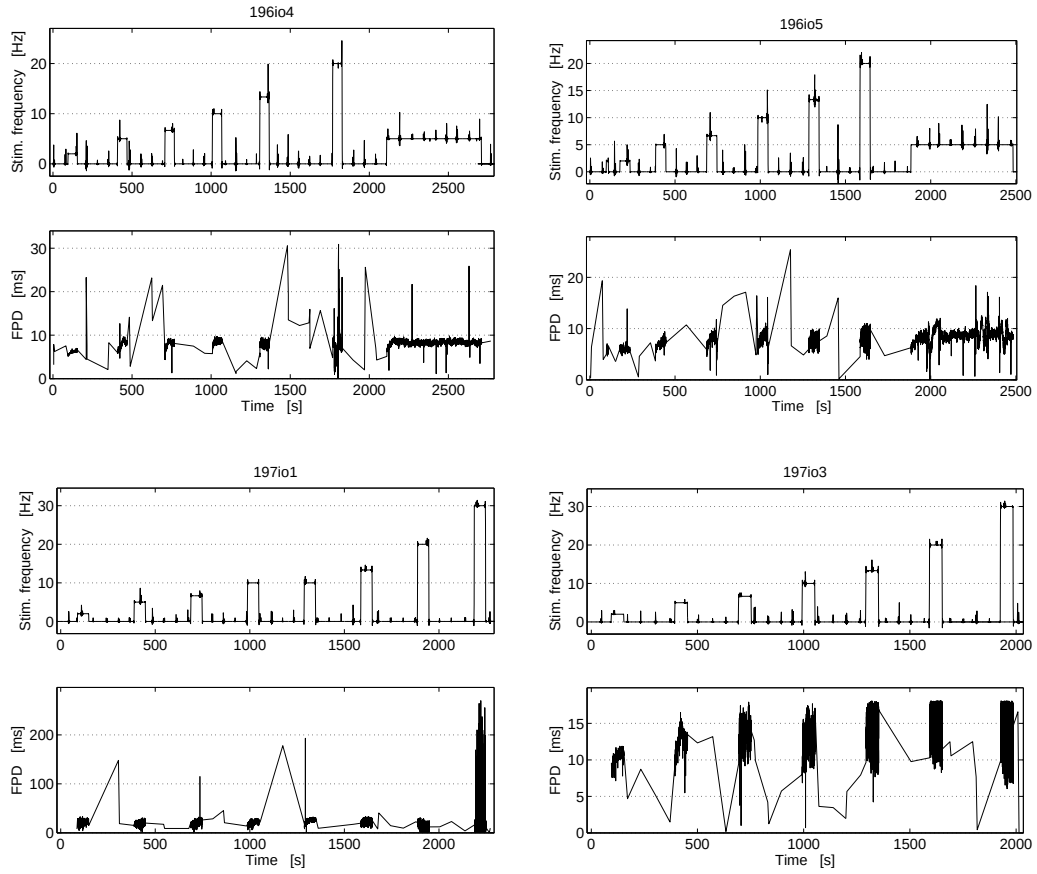

Figure 14.5: The time development of the frequency of the applied stimulation and the duration of the evoked field potential excitations (FPD) for the four cases of inferior olive stimulation. All samples are shown. Note that — except for a number of outliers during the quiet periods of no stimulation — in each case there seems to be a quite constant level of duration.

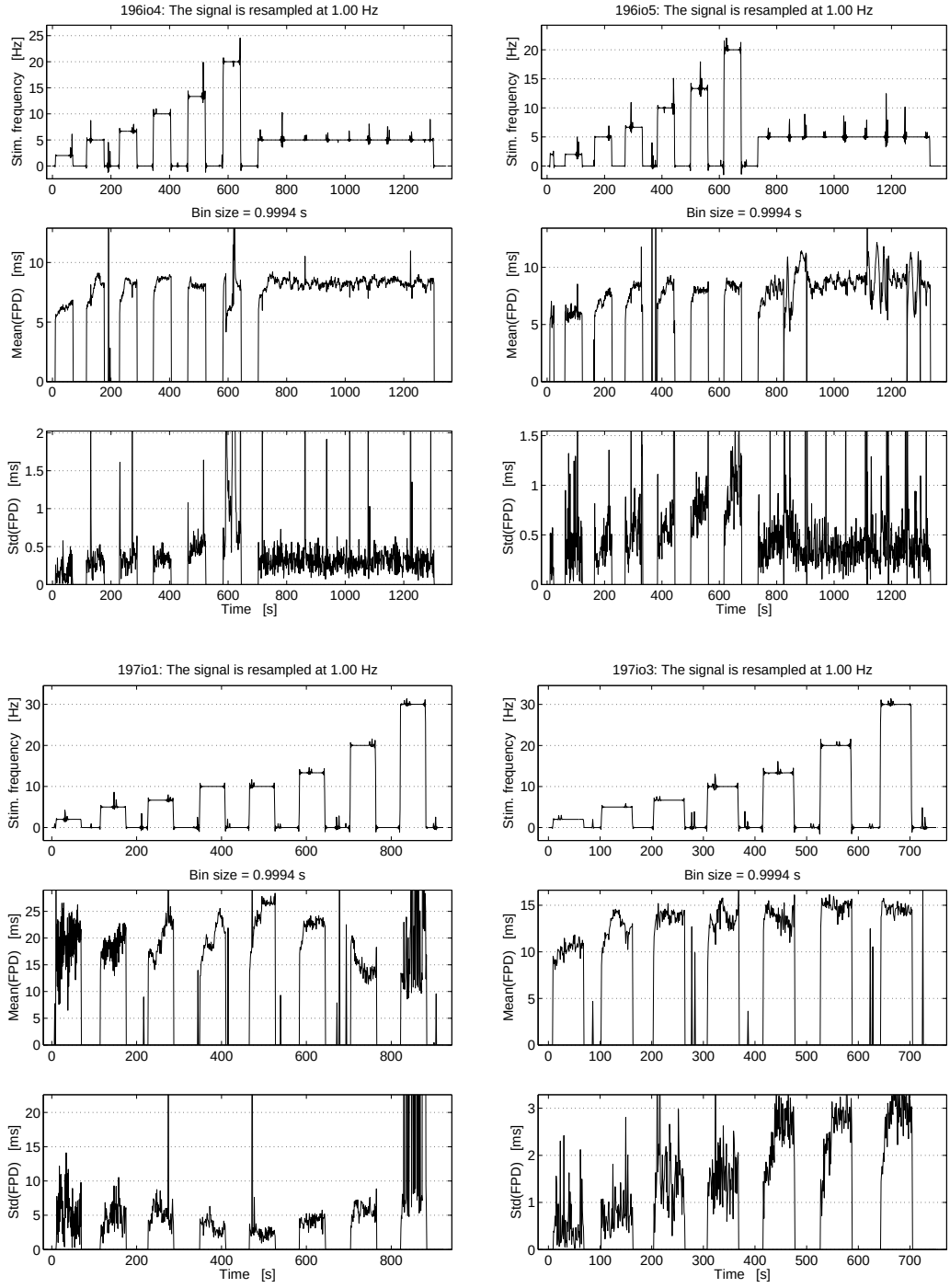

Figure 14.6: The frequency of the applied stimulation and the arithmetic mean value (*mean*) as well as the standard deviation (*std*) of the evoked field potential durations (FPD) within each bin for the four cases of inferior olive stimulation. Note that the average field potential duration does not depend on time and only very weakly on frequency — as long as the stimulation frequency is kept above 5 Hz. Below 5 Hz the field potential duration decreases with decreasing stimulation frequency. There is some indication that the standard deviation increases with the frequency. Note also, that the overall level of FPD's is larger for rat no. 197 (around 8 ms) than for no. 196 ($15 - 20$ ms).

14.1.4 Analysis of the Instantaneous Event Frequencies

In order to investigate the coupling between the stimulation (being an externally determined signal) and the internal response, the instantaneous event frequencies[2] of the stimulation and the FPA signal, respectively, are studied. The *event frequency* of an event-sampled signal is defined as

$$f_e(t_i) = \frac{1}{t_i - t_{i-1}}, \tag{14.4}$$

where t_i is the time of occurrence of event number i.

As seen from Figure 14.7 there are numerous 'extra' stimulation events not being determined by the experimentalists. However, most of these events are inherited by the FPA signal. (A few of the FPA events have deliberately been excluded — cf. Appendix B.2.) Thus we need not change the statement that *"one stimulation event evokes one FPA event"*.

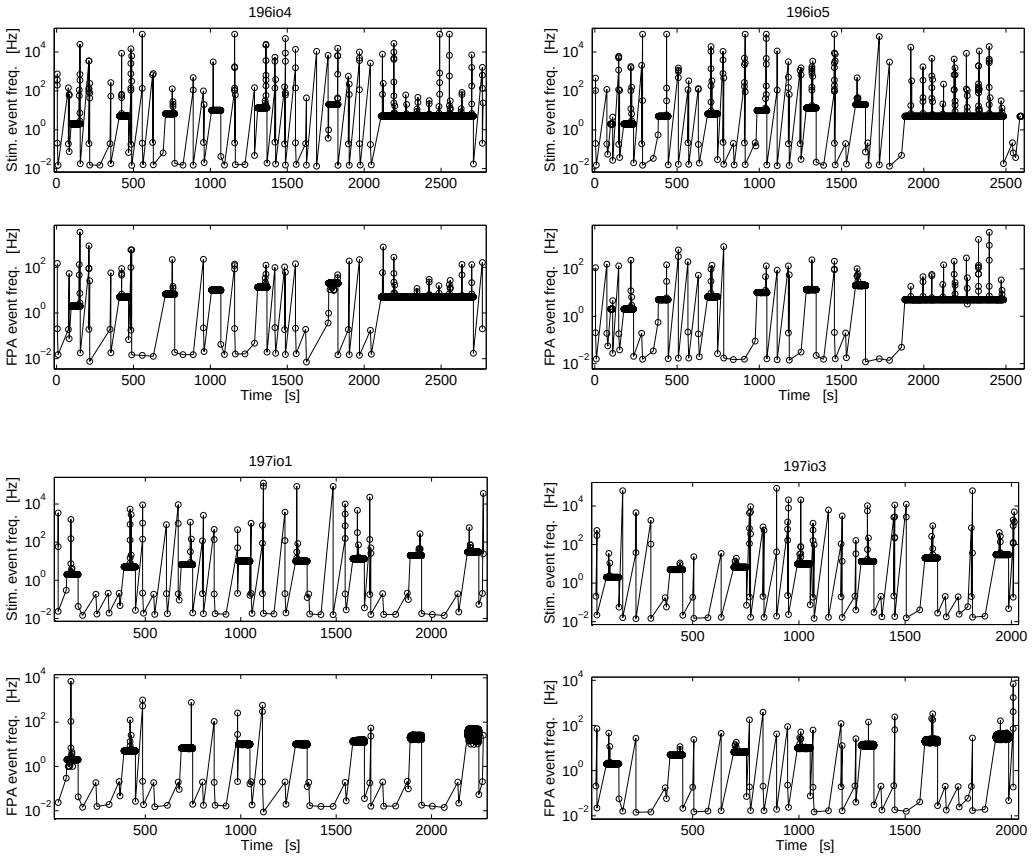

Figure 14.7: The instantaneous stimulation and FPA event frequencies are shown on logarithmic scales. In this way all data can be shown. Note that besides the expected events — determined by the experimentalist — there are numerous extra (noisy) events.

In order to emphasize the deviations from the designed stimulation sequences the same data is shown with a normal frequency scale in Figure 14.8. The instantaneous frequencies have some distinct features:

- The extra stimulation events appear almost periodically with a period of around 60 s. This feature is further emphasized by Figure A.3 on page 266.
- During stimulation the stimulation frequency is very well defined — for all frequencies.

[2] Usually when analyzing events in neuronal signals the distribution of the inter-spike-intervals (ISI) is considered. Examples are found in Refs. [30] and [70]. Since in case of the field potential in cerebellum the event frequency is determined by the stimulation the *distribution* of ISI's is not relevant.

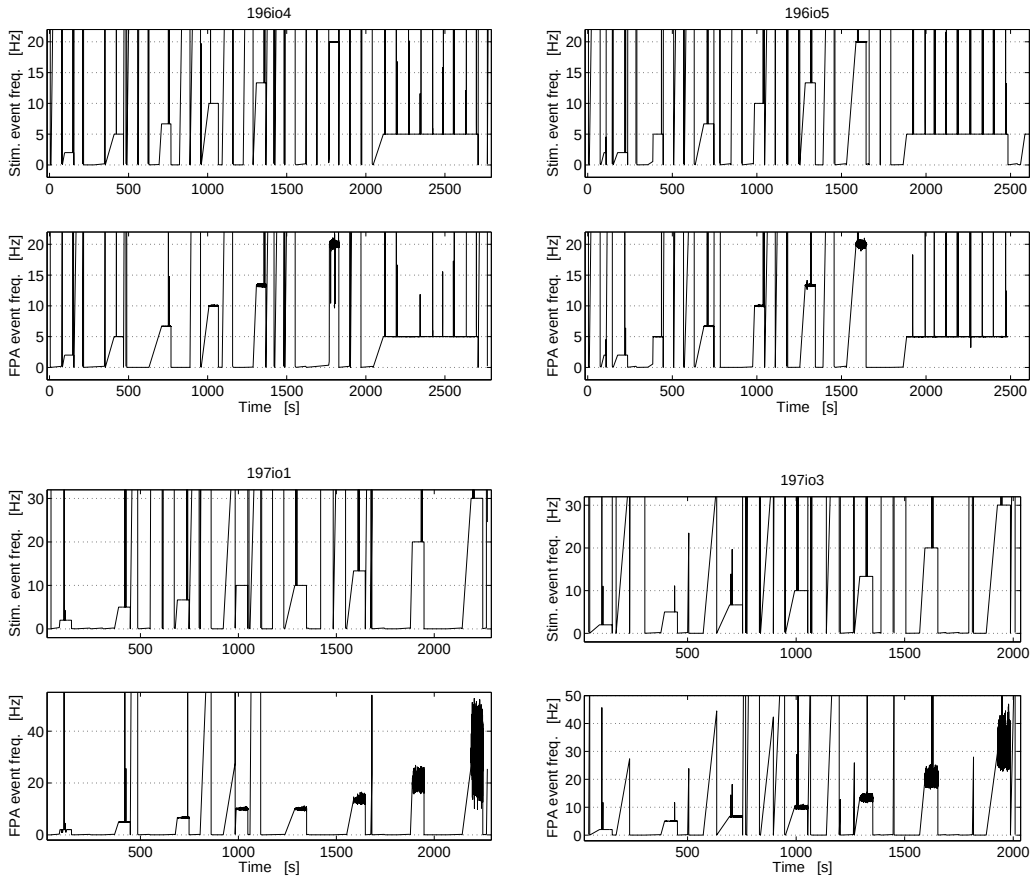

Figure 14.8: The instantaneous stimulation and FPA event frequencies are shown on normal scales. In this way it is emphasized how well-defined the frequencies are. Note that the stimulation event frequency is very well defined during stimulation — except from some almost periodically occurring noisy events. Note also that when the stimulation frequency exceeds 10 Hz the estimated frequency of FPA events fluctuates considerably around the value of the stimulation frequency.

- For low frequencies the frequency of FPA events is also very well defined, and it is identical to the stimulation frequency.
- For high frequencies the FPA event frequency deviates considerably from the stimulation frequency. The reason is that at high stimulation frequencies the evoked FPA's are small. Therefore the influence of the 50 Hz artifact as well as other noise components may alter the time of occurrence of the FPA event calculated by the SPIKE2 script — cf. Appendix A.3.2 on page 266. Stimulation frequencies higher than 30 Hz may cause the evoked FPA's to drown totally in noise — cf. Figure 14.3 on page 84.

14.2 Analysis of the Cerebellar Blood Flow Signals

In this section the relative cerebellar blood flow is analyzed with the purpose of creating a better understanding of the output signals. Both the inferior olive stimulation experiments and the parallel fiber stimulation experiments are considered.

As there are four CBF signals — one from each of the four LDF probes (cf. P: Section 7.4.4 on page 47) — it is a goal to choose which of them to use when modeling the neuro-vascular system.

The generation of the relative CBF signals is described in Appendix B.4.

14.2.1 Comparison of the Signals from the four LDF Probes

With the purpose of choosing which output signal to use for system modeling, the time-development of the relative CBF signals from the four LDF probes — in response to the stimulation sequences shown in the upper panels — are compared in Figures 14.9 (climbing fiber activation experiments) and 14.10 (parallel fiber stimulation experiments).

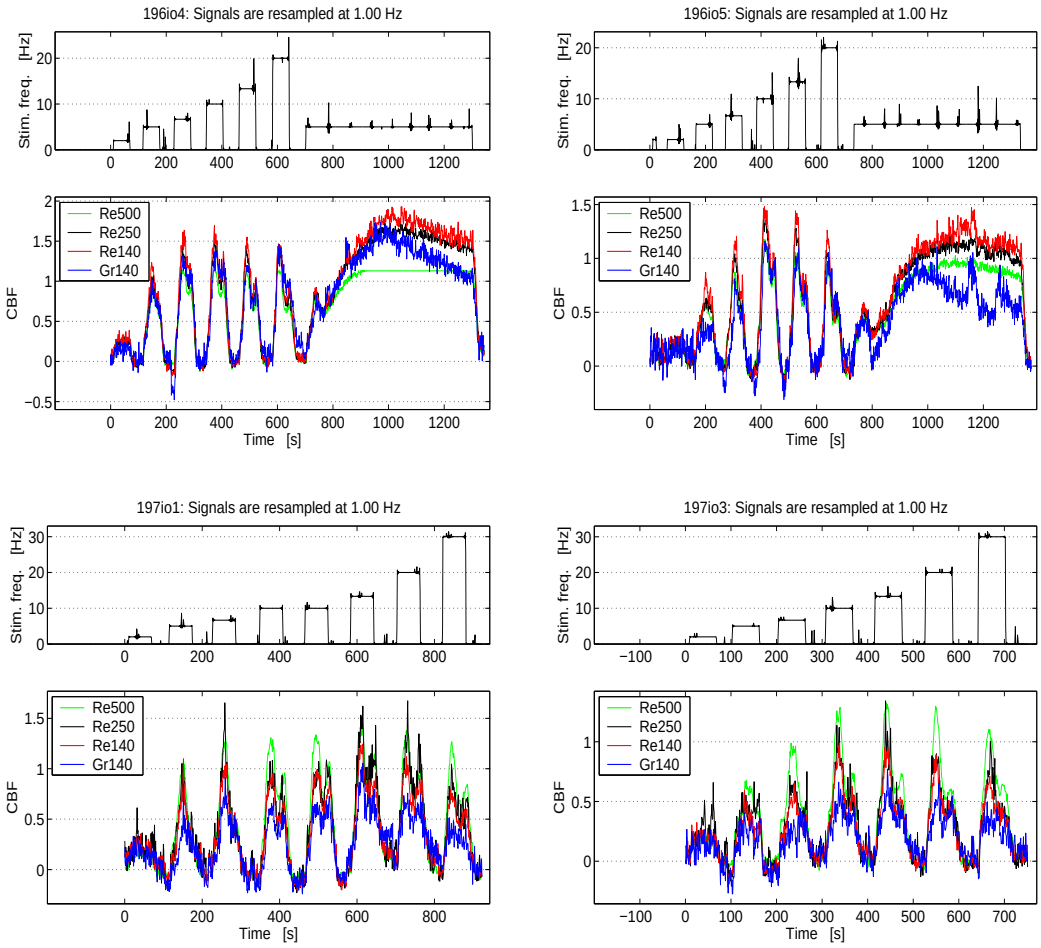

Figure 14.9: The development in time of the signals from the four LDF probes in the four cases of stimulation of the inferior olive resulting in climbing fiber activation. The time series have been resampled by a factor 10. Note that for rat no. 196 the probe `Re140` gives the largest response whereas for rat no. 197 the responses of the three red probes are quite similar.

It is seen that there are significant differences in the amplitudes of the signals from the four probes. To ensure that the developed models capture as little noise as possible, the signals with the largest responses are chosen for further analysis, i.e.

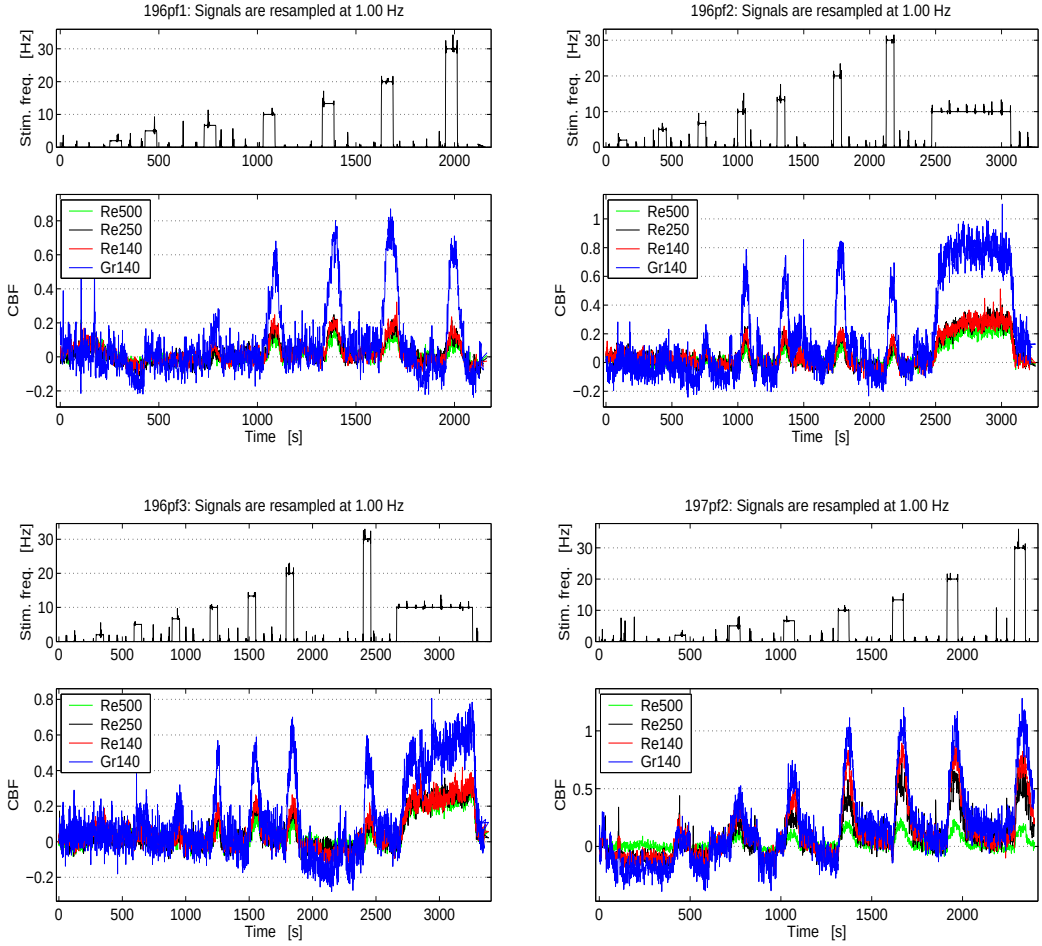

Figure 14.10: The development in time of the relative CBF signals from the four LDF probes in the four cases of stimulation of parallel fibers. All samples are shown. The time series have been resampled by a factor 10. Note that in all experiments the response of the probe `Gr140` is larger than the responses of the three red probes.

- In case of inferior olive stimulation the signal from the LDF probe `Re140` will be chosen for analysis and modeling.
- In case of parallel fiber stimulation the signal from the LDF probe `Gr140` will be considered.

In both cases the time evolution of the green laser light signal differs significantly from those of the red laser light signals, whereas the responses of the three red probes are quite similar. The reason may be that the blood flow response to stimulation varies with depth. Note that the estimated maximal measurement depths of the four probes are different (cf. P: Section 7.4.4 on page 47). From the estimated maximal probing depths of the four probes it is concluded that

- IO stimulation results in CBF increases both in the molecular layer and the Purkinje cell layer.
- PF stimulation results in CBF increases mainly in the upper part of the molecular layer.

Notice also, that when the stimulation sequence extends beyond a certain limit, a new kind of dynamics seems to take over. For inferior olive stimulation the cross-over occurs at around 25 s, for parallel fiber stimulation at around 95 s after the onset of stimulation.

Furthermore, it is characteristic for both inferior olive and parallel fiber stimulation that the maximal blood flow response increases with the stimulation frequency up to 10 Hz and decreases for higher frequencies. This phenomenon may be termed *frequency saturation*.

14.2.2 Characteristic Times in the CBF Signal

By zooming into the Figures 14.9 and 14.10 the following characteristics are found for the stimulation sequences being 60 s long[3]:

In case of IO stimulation the blood flow response starts by a fast increase towards a local maximum, followed by a fast decrease towards a dip bottom. Then the response slowly increases until the end of stimulation. Finally the response decreases fast towards its baseline value. An example of this behavior is shown in Figure A.12 on page 271.

In case of PF stimulation the blood flow response increases almost linearly with time until the end of stimulation. Afterwards the response decreases quite slowly towards its baseline value. Thus there is no dip. An example of this behavior is shown in Figure A.13 on page 271.

In both cases the characteristic increase and decrease times are of the order of a few tens of seconds. And the times are in general shorter for low and high frequencies than for intermediate frequencies. These features are emphasized by the statistical values listed in Tables 14.1 and 14.2.

Frequency	Onset to local max	Onset to dip	Stim. off to baseline	
2 Hz	20.75	33.75	20.75	Mean $[s]$
	3.30	5.44	14.38	Std $[s]$
	0.16	0.16	0.69	Cv
5 Hz	32.25	50.50	23.50	Mean $[s]$
	4.86	5.07	11.09	Std $[s]$
	0.15	0.10	0.47	Cv
7 Hz	34.50	49.50	25.00	Mean $[s]$
	2.89	4.36	6.88	Std $[s]$
	0.08	0.09	0.28	Cv
10 Hz	30.20	49.80	26.00	Mean $[s]$
	3.49	0.84	7.18	Std $[s]$
	0.12	0.02	0.28	Cv
13 Hz	24.75	46.75	26.25	Mean $[s]$
	2.22	2.22	0.96	Std $[s]$
	0.09	0.05	0.04	Cv
20 Hz	23.00	44.00	25.25	Mean $[s]$
	1.83	4.24	5.44	Std $[s]$
	0.08	0.10	0.22	Cv
30 Hz	22.50	44.00	21.00	Mean $[s]$
	3.54	2.83	5.66	Std $[s]$
	0.16	0.06	0.27	Cv

Table 14.1: The mean values ($mean$), standard deviations (std) and coefficients of variance (cv) of the characteristic times in the blood flow response to inferior olive stimulation. The reported times are: The time from on-set of stimulation to the local maximum, the time from on-set to the dip bottom, and the time from the stimulation is turned off to the baseline value is reached. Note that the mean values in general are higher for intermediate frequencies than for low and high frequencies.

14.2.3 Influence of the Arterial Pulse on CBF

It has been noticed by Nielsson [77, (p. 67)] that *"besides dynamic light scattering in the tissue there may be other sources of Doppler signals such as the possible contribution from vessel walls moving synchronously with the arterial pulse"*.

In the following it is investigated whether the CBF signals are contaminated by changes caused by oscillations in the arterial pulse. This is done by estimating the following characteristics of the two signals:

[3] The 600 s long sequences will not be considered since they do not occur in all the time series.

Frequency	Mean $[s]$	Std $[s]$	Cv
2 Hz	25.25	13.20	0.52
5 Hz	44.50	47.51	1.07
7 Hz	35.75	4.27	0.12
10 Hz	51.25	12.69	0.25
13 Hz	53.50	10.02	0.19
20 Hz	55.50	9.54	0.17
30 Hz	44.50	5.00	0.11

Table 14.2: The mean values (*mean*), standard deviation (*std*) and coefficient of variance (*cv*) of the time it takes the CBF signal to decreases from its value when the stimulation is turned off to the baseline value has been reached in case of parallel fiber stimulation. Note that the mean value in general is higher for intermediate frequencies than for low and high frequencies.

- The power spectrum magnitude of a signal g which has been defined in Section 14.1.1 on page 80.
- Similarly, the *cross spectrum magnitude* of two signals g and h is mathematically defined as [55, (p. 1-68)]

$$CSM(f) = 10 \cdot \log |P_{gh}(f)|, \tag{14.5}$$

with $P_{gh}(f)$ being the *cross spectral density function* (CSD) between the signals g and h [55, (p. 1-64)]

$$\begin{aligned} P_{gh}(f) &= \int_{-\infty}^{\infty} R_{gh}(t') \cdot e^{-2\pi \cdot f \cdot t'} dt', \\ R_{gh}(t') &= E\{g(t) \cdot h(t+t')\}. \end{aligned}$$

$R_{gh}(t')$ is the cross-correlation function.

A crude estimate of the CSD is the *periodogram* which is a complex-valued function defined as [55, (p. 1-64 and 1-71)]

$$\hat{P}_{gh}(f) = g(f) \cdot h^*(f), \quad 0 \le f < f_{Nyq}. \tag{14.6}$$

The CSD function in Matlab averages and scales modified periodograms of detrended sections of the signals according to Welch's method [55, (p. 1-67)]. The optional FFT length has been set to 4096.

The power spectrum magnitude of the arterial blood pressure, BP, the power spectrum magnitude of the CBF signal as well as the cross spectrum magnitude between BP and CBF are shown in Figure 14.11 for the four cases of inferior olive stimulation, and in Figure 14.12 for the four cases of parallel fiber stimulation.

It is clear that the main blood pressure wave — the arterial pulse — fluctuating with a frequency of 6 Hz is beyond the Nyquist frequency (5 Hz) of the CBF signal and thus cannot influence it. Furthermore, the minor 3 Hz fluctuation in the arterial blood pressure of rat no. 196 does not at all occur in the CBF signal. Note that Figure A.10 on page 270 shows that the minor 3 Hz component is due to a slight amplitude-modulation of the arterial pulse. The cross spectrum magnitudes further emphasize that the arterial pulse does not influence the CBF signal. Thus no pre-filtering seems necessary before using the CBF signal for system identification purposes.

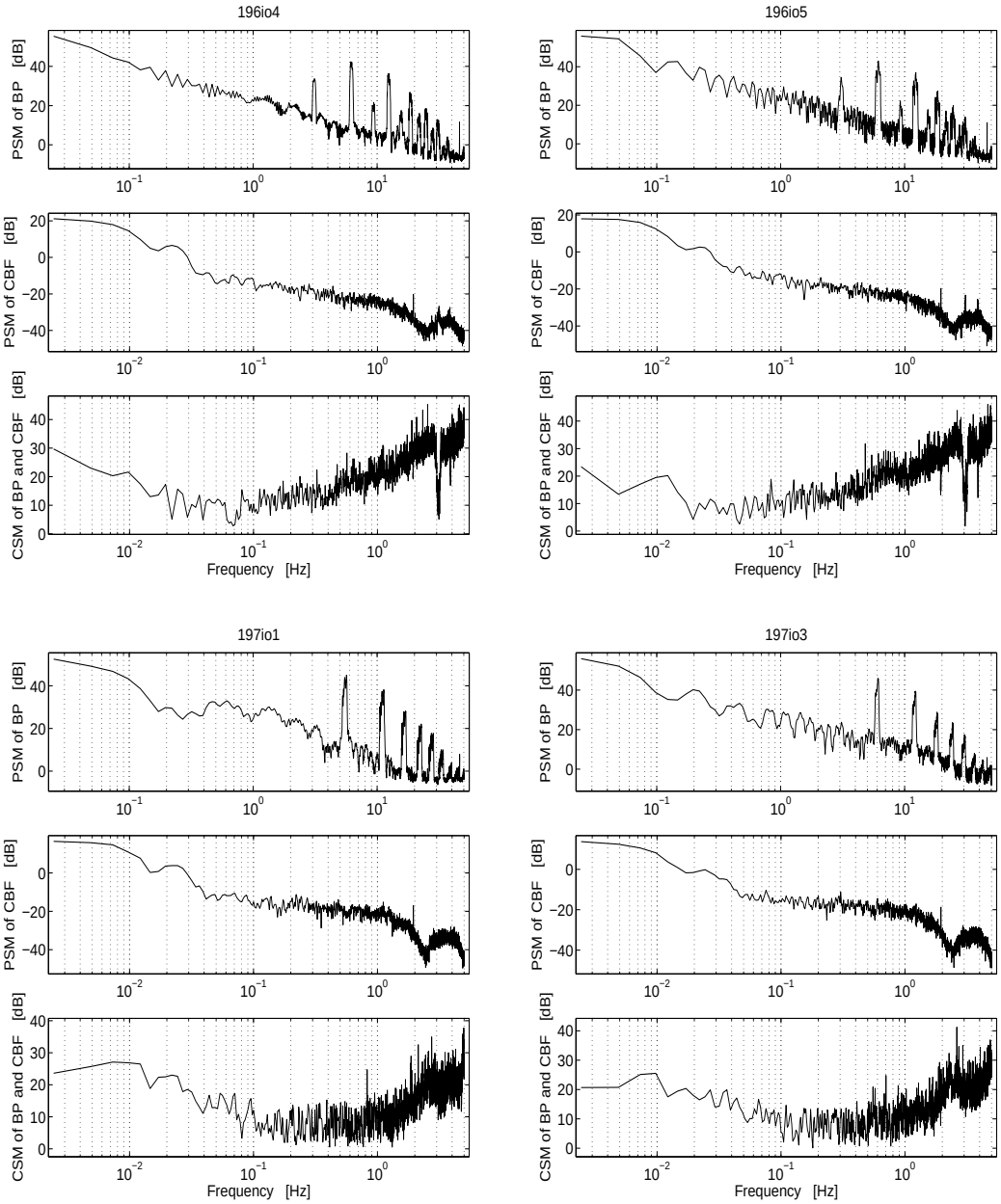

Figure 14.11: The power spectrum density magnitude (PSM) of the arterial blood pressure (BP), the PSM of the CBF, and the cross spectrum magnitude (CSM) between BP and CBF — for the cases of climbing fiber activation. Note that the blood pressure of rat no. 196 has two strong components: A 3 Hz and a 6 Hz oscillation. Rat no. 197 only has a 6 Hz component — the arterial pulse — in the blood pressure. The CBF signals do not contain these frequency components. The lack of strong frequency components in the CSM emphasizes that the CBF traces are *not* influenced by the arterial pulse. (The very narrow 2 Hz fluctuation in the CBF signal may be an apparatus artifact.)

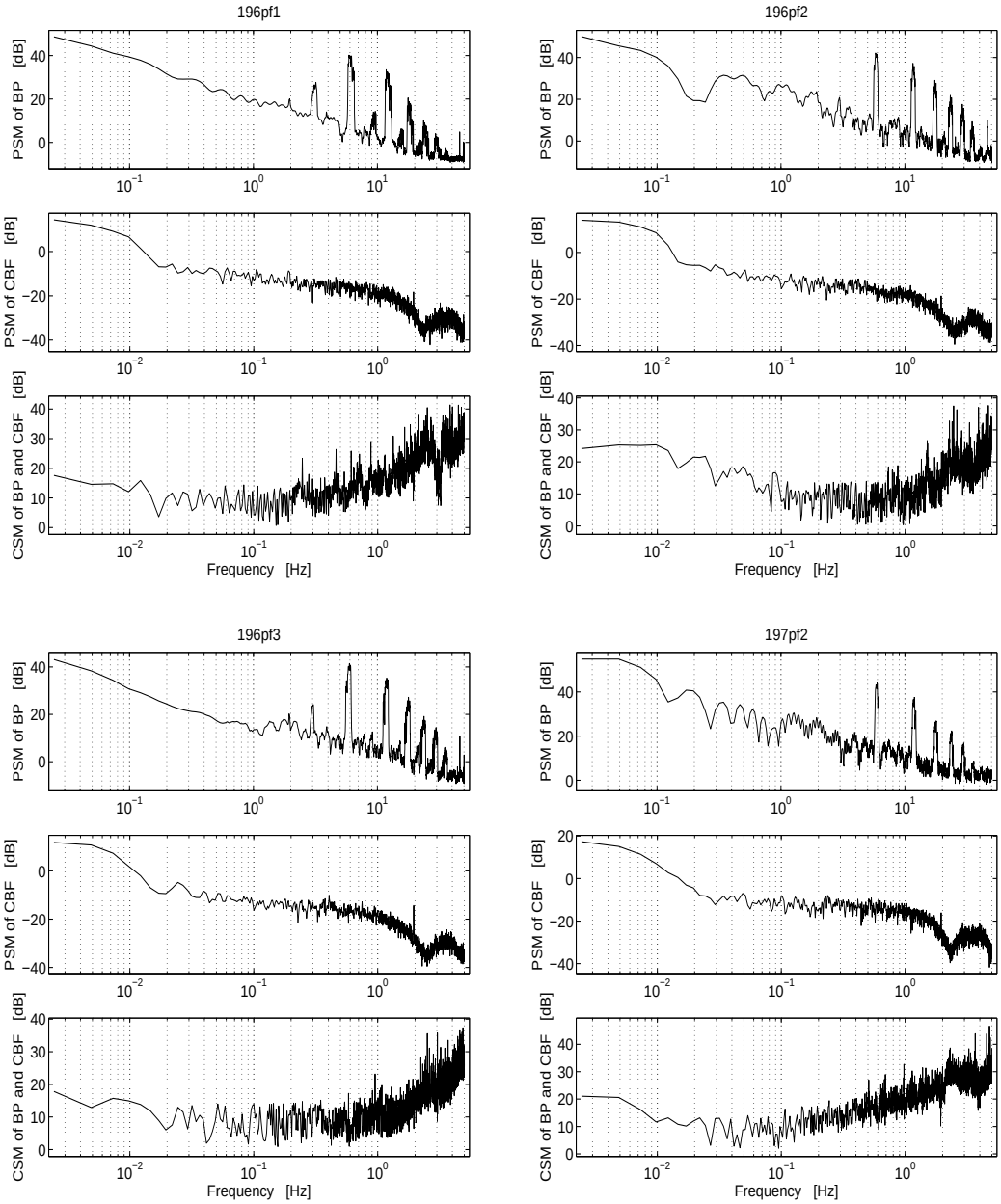

Figure 14.12: The power spectrum density magnitude (PSM) of the arterial blood pressure (BP), the PSM of the CBF, and the cross spectrum magnitude (CSM) between BP and CBF — for the cases of parallel fiber activation. As in the IO cases the blood pressure of rat no. 196 contains both a 3 Hz and a 6 Hz oscillation whereas BP of rat no. 197 only has a 6 Hz component. Also in these cases of PF stimulation the CBF traces have *not* been influenced by the arterial pulse. (The very narrow 2 Hz fluctuation in the CBF signal may be an apparatus artifact.)

Chapter 15

System Analysis

The purpose of this chapter is to analyze the system by means of the measured input and output signals. There are two goals: To provide information about the system. And to choose a resampling factor common to the input and output signals to be used throughout the modeling phase.

Only the inferior olive stimulation experiments will be considered.

15.1 Choice of Input and Output Signals

In order to describe the system from measured input-output time series we first need to choose which input and output to consider.

For the output we will choose the CBF signal as measured by the LDF probe `Re140` (cf. Section 14.2.1). The sampling frequency of this signal is 10 Hz.

The choice of input is more subtle. We would like to use the field potential amplitude signal because it is a less spacious representation of the electrical activity than the full field potential signal. However, this signal is event-sampled with the frequency of events varying between 2 Hz and 30 Hz. Thus we need to convert the FPA signal into a 10 Hz sampled signal.

The simplest way to convert the FPA signal into a 10 Hz sampled signal might be the following: Sum the sizes of the FPA's within bins being 0.1 s long and symmetrically positioned around the sampling instants of the CBF signal, i.e., create the pre-processed FPA signal

$$FPA_{pp}(t) = \sum_{t-\frac{\tau}{2}<t_i\leq t+\frac{\tau}{2}} FPA(t_i). \tag{15.1}$$

The sampling instant of the CBF signal is denoted by t, and the event instant of the FPA signal is denoted by t_i. τ denotes the sampling interval of the CBF signal.

Thus we will use the following input and output signals for the analysis:

$$u(t) = FPA_{pp}(t) = \sum_{t-\frac{\tau}{2}<t_i\leq t+\frac{\tau}{2}} FPA(t_i), \tag{15.2}$$

$$y(t) = CBF(t). \tag{15.3}$$

These signals are shown in Figure 15.1.

15.2 Transfer Function Estimation

Consider a system for which input u, output y, and disturbance v are related by

$$y(t) = G(p)u(t) + v(t), \tag{15.4}$$

where G is the transfer function (cf. Sect. 10.1.1). If $u(t)$ and $v(t)$ are uncorrelated the spectral densities are related by [61, (Sect. 8.6)]

$$P_{yu}(f) = G(f)P_{uu}(f). \tag{15.5}$$

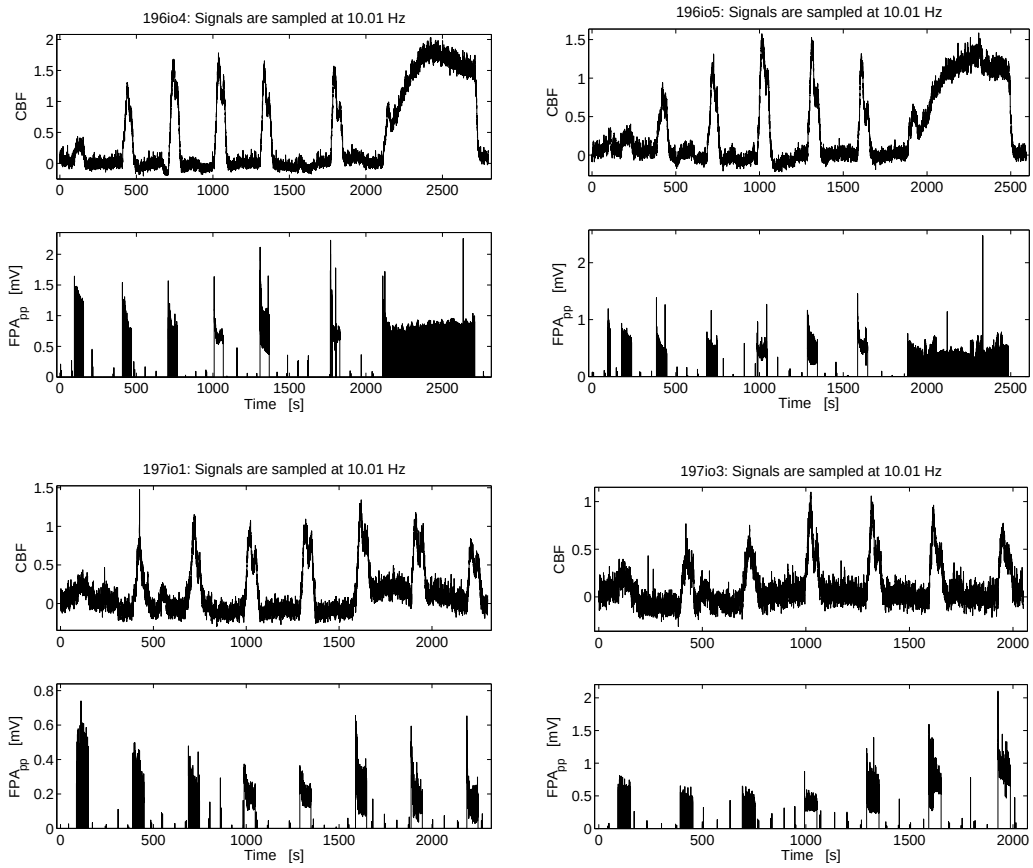

Figure 15.1: The 10 Hz sampled input (FPA_{pp}) and output (CBF) signals for the four climbing fiber time series. All samples are shown.

Thus a natural estimate of the transfer function $G(f)$ may be calculated from estimates of the spectral densities as

$$\widehat{G}(f) = \frac{\widehat{P}_{yu}(f)}{\widehat{P}_{uu}(f)}. \tag{15.6}$$

The MATLAB function `tfe` estimates the transfer function using the same way (Welch's method) of averaging periodograms as earlier was used for estimation of spectral densities [55, (p. 1-72)].

As $\widehat{G}(f)$ is a complex function, the *amplitude spectrum* $|\widehat{G}(f)|$ and the *phase spectrum* $\widehat{\phi}(f)$ are shown in a so-called *Bode plot*. These functions are connected to the transfer function by the relation [58, (Sect. 2.3)]

$$\widehat{G}(f) = |\widehat{G}(f)| \cdot e^{i\widehat{\phi}(f)}. \tag{15.7}$$

15.3 Choice of Resampling Factor

First we study the frequency contents of the input and output signals: The power spectrum magnitudes of u and y, respectively, are shown in Figure 15.2. The power spectrum magnitude of the preprocessed field potential amplitude signal is characterized by a few very narrow and strong components at 2 Hz, ~ 3.3 Hz, and 4 Hz — besides dynamics in a very broad band of low frequencies. Also the cerebellar blood flow signal contains a very broad band of low frequencies — besides a narrow artifact at 2 Hz.

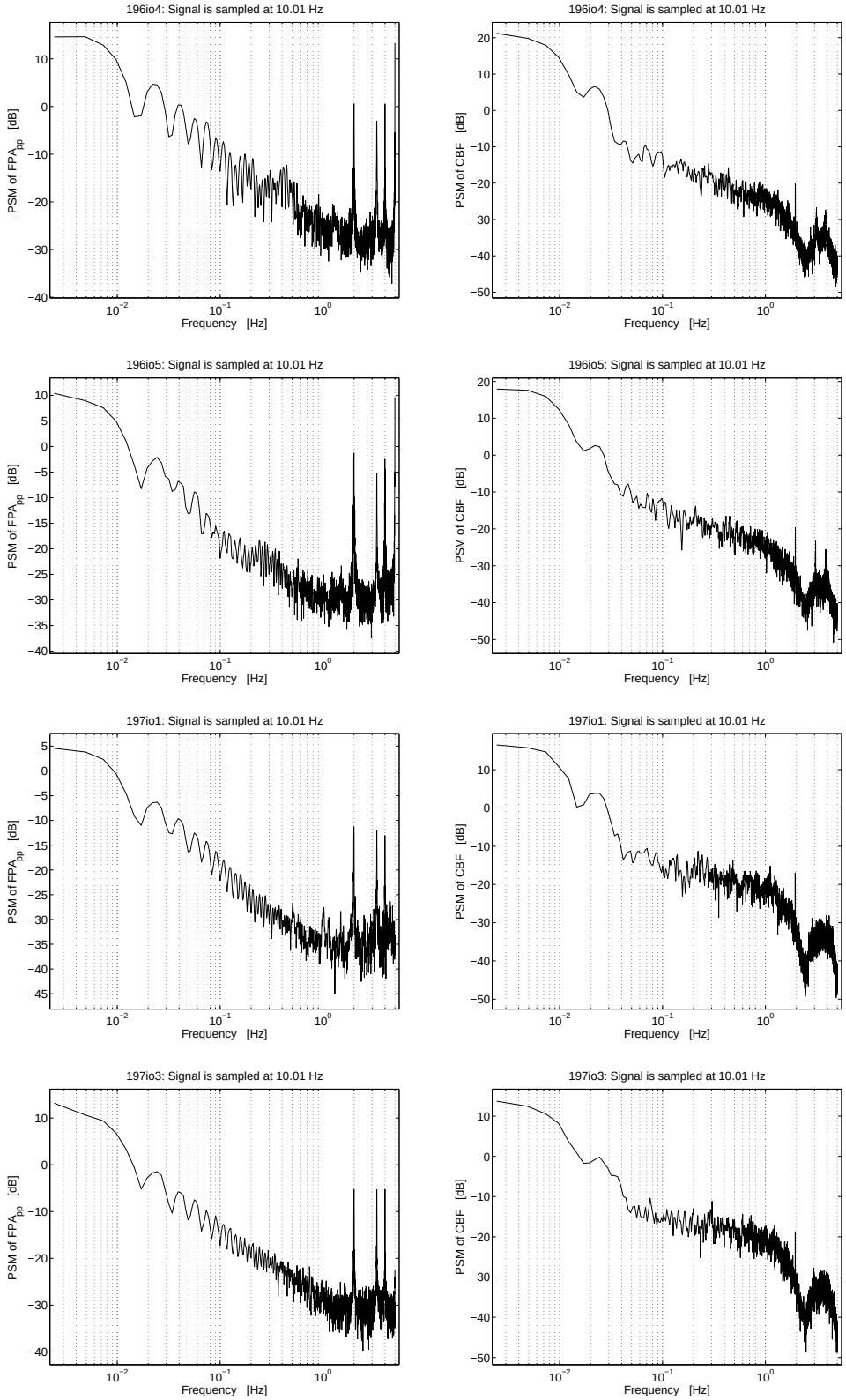

Figure 15.2: Left panels: The power spectrum magnitude of the preprocessed field potential amplitude signal FPA_{pp} for the four climbing fiber time series. Note the narrow components at 2 Hz, ~ 3.3 Hz, and 4 Hz. Right panels: The power spectrum magnitude of the relative cerebellar blood flow signal CBF for the four climbing fiber time series. Note that there is very little power pertaining to frequencies above the narrow 2 Hz artifact.

Now the procedure for system analysis presented in Section 15.2 is applied to the data shown in Figure 15.1. The resulting transfer function estimates are shown in Figure 15.3. It is seen that most of

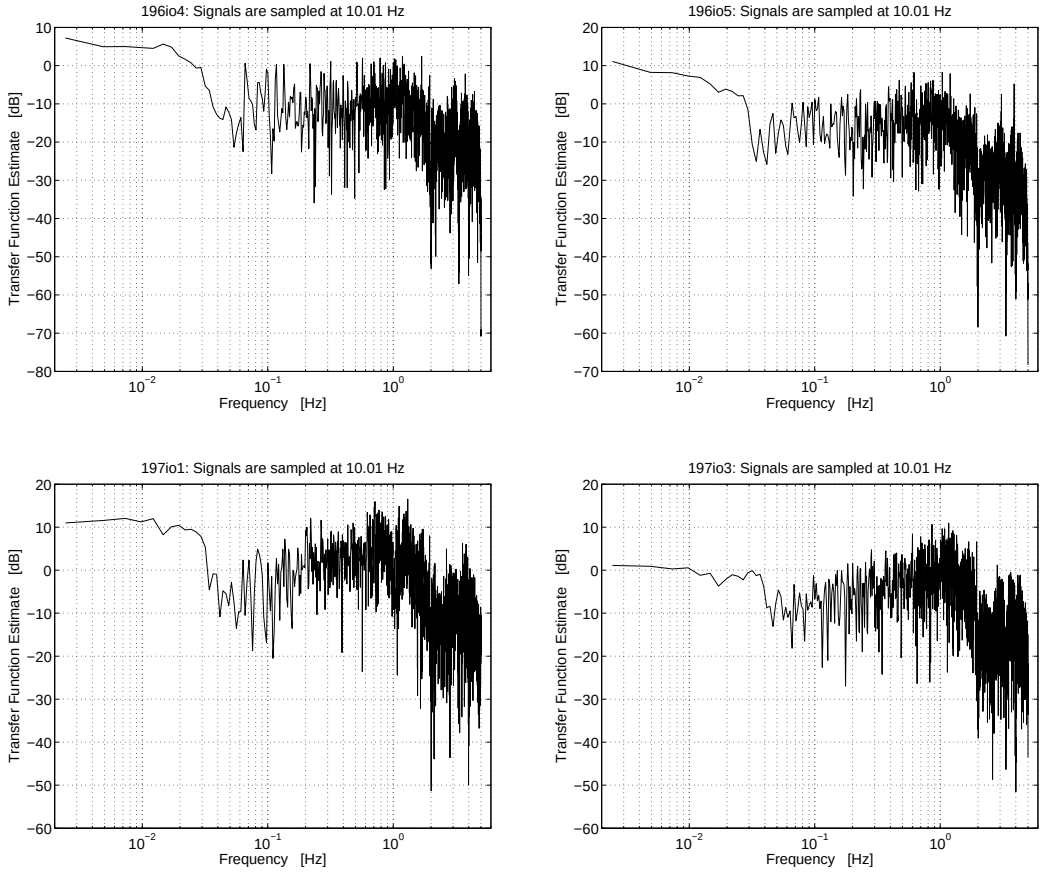

Figure 15.3: The magnitude of the transfer function estimates for the four climbing fiber time series — calculated from the 10 Hz sampled signals. Note that most of the system dynamics is characterized by frequencies below 1 Hz.

the system dynamics takes place at frequencies below 1 Hz.

The high-frequency part of the system dynamics may be attributed to noise. In order to get rid of the high-frequency part of the dynamics, the input and output signals are resampled by a factor 10 to obtain 1 Hz sampled signals. This procedure has the advantage that the MATLAB resampling function applies a low-pass FIR filter to the sequences to prevent aliasing during resampling [55, (p. 1-91)]. In this way the 2 Hz, 3.3 Hz and the 4 Hz artifacts are also eliminated. Furthermore the file sizes are thereby reduced by a factor 10. The resulting input-output time series are shown in Figure 15.4. It is seen that the signals have been somewhat smoothed. But they still seem to contain some high-frequency dynamics.

That the signals have been somewhat smoothed is further emphasized by the power spectra of the resampled signals shown in Figure 15.5 which clearly do not contain any strong high-frequency components.

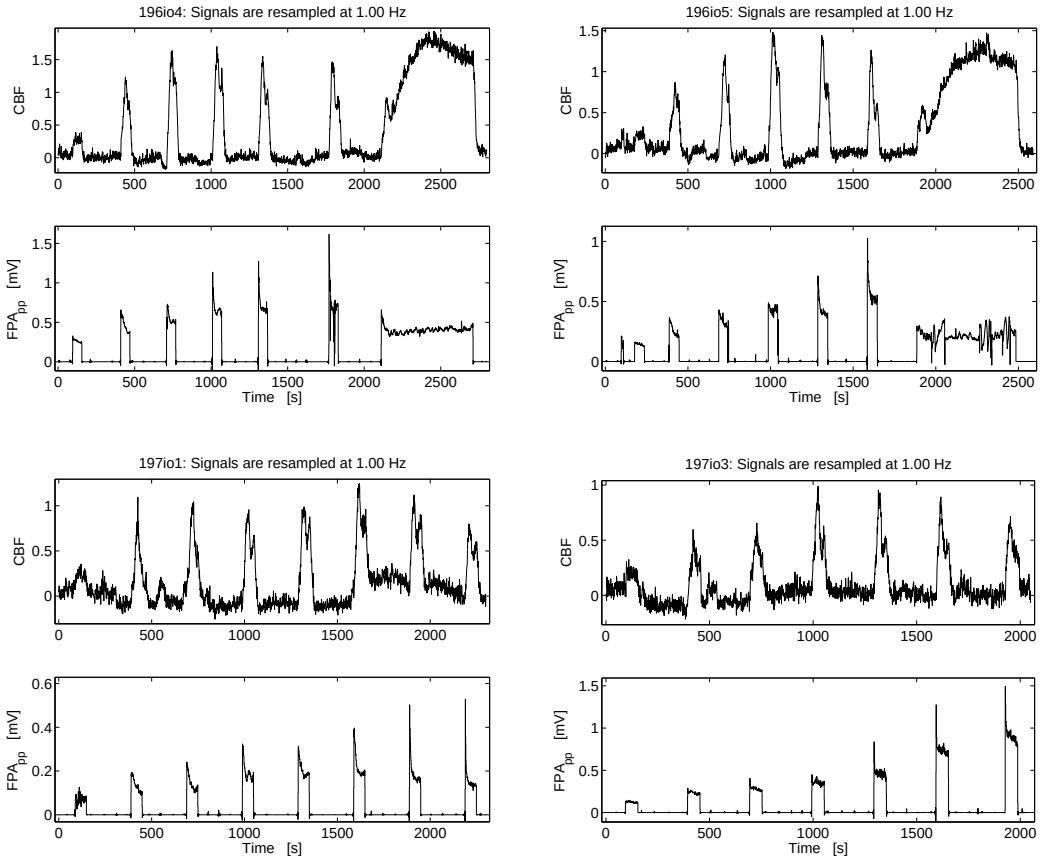

Figure 15.4: The input (FPA_{pp}) and output (CBF) signals resampled at 1 Hz for the four climbing fiber time series. All samples are shown. Note that compared to the original signals shown in Figure 15.1 the resampled signals appear somewhat smoothed.

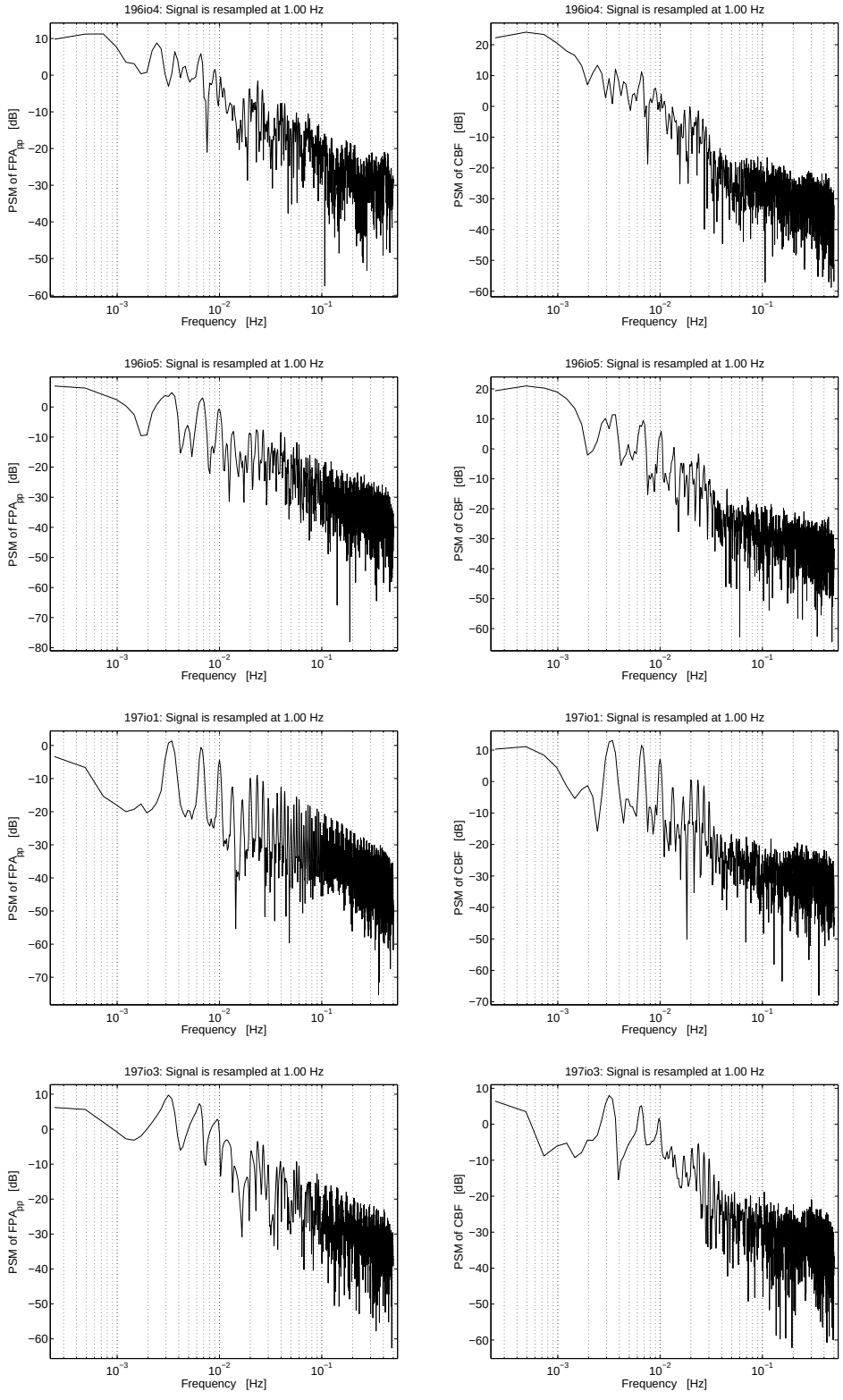

Figure 15.5: Left panels: The power spectrum magnitude of the preprocessed field potential amplitude signal FPA_{pp} for the four climbing fiber time series — after resampling by a factor 10. Note that the resampling eliminates the 2 Hz, ~ 3.3 Hz, and 4 Hz components — cf. Figure 15.2. Right panels: The power spectrum magnitude of the relative cerebellar blood flow signal CBF for the four climbing fiber time series — after resampling by a factor 10. Note that the resampling eliminates the 2 Hz artifact appearing in Figure 15.2.

From the resampled input-output data series new transfer function estimates can be calculated. The results are shown in Figure 15.6. These transfer function estimates contain dynamics on all frequency

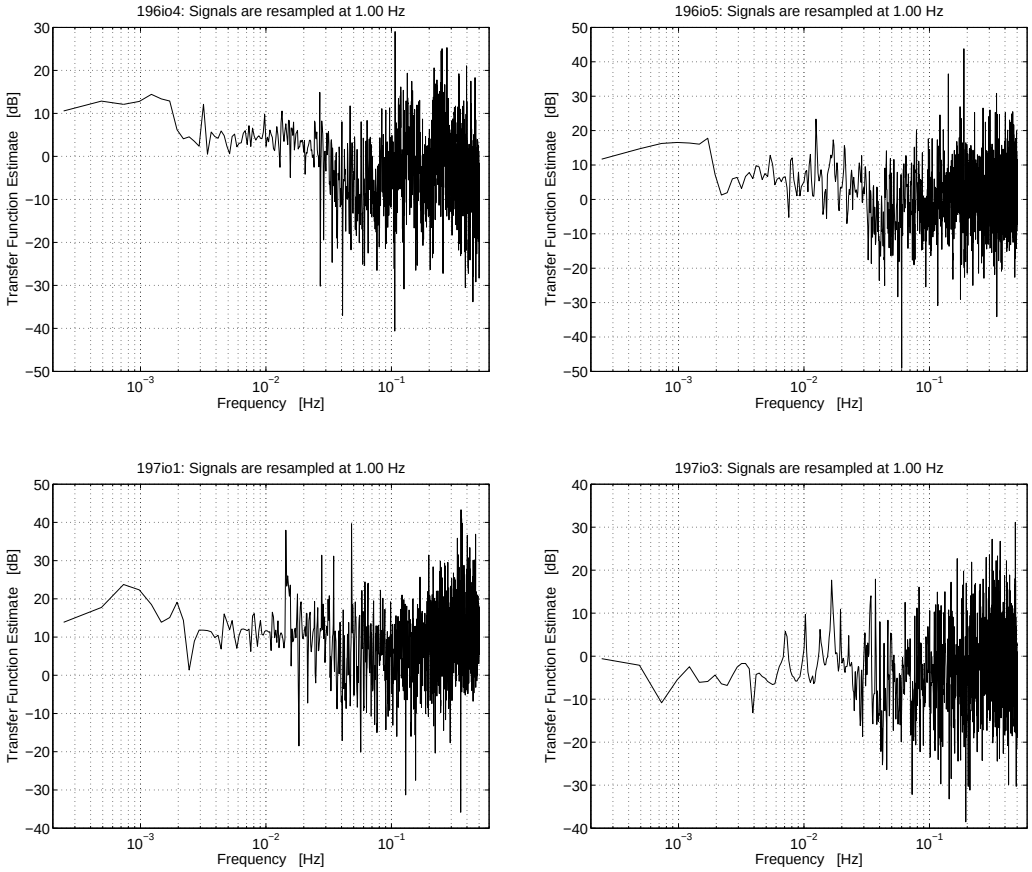

Figure 15.6: The magnitude of the transfer function estimates for the four climbing fiber time series — calculated from the signals resampled to 1 Hz. Note that the estimates indicate that the system contains dynamics on all frequency scales.

scales. We will take the standpoint that this is an important feature of the particular biological system.

Chapter 16

Discussion of Analysis Results

16.1 Choice of System to be Modeled

The following parts only consider models of the climbing fiber system. The main reason is the limited project time. Another reason is that the neuronal circuitry of the climbing fiber system (being a mono-synaptic system) is simpler than that of the parallel fiber system (a di-synaptic system). As it is possible that this difference should be reflected by the models, we will start the modeling work by focusing on the climbing fiber system.

16.2 Choice of Signals for System Modeling

16.2.1 Input Signal

The input to the models could be chosen among several possibilities: The stimulation sequence could be chosen but was not, because this signal is external to the neuronal circuitry and modeling its relation to neuronal signals would impose an extra element in the models. The full field potential signal, at a first glance, seems a natural choice. The field potential signal, however, consists of rather quiet periods interrupted by time-localized excitations. As shown in P: Figure 7.4 on page 46 these excitations are rather alike, and — as shown in Sections 14.1.2 and 14.1.3 — the main characteristics of the field potential signal are the times of occurrence and amplitudes of the excitations. This information is exactly the one of the field potential amplitude signal and therefore this event-sampled signal will be chosen as input signal. This feature also means that we can characterize the neuro-vascular system as being discrete event driven — cf. M: Section 9.3.4 on page 54.

The stability of the shape of the time-localized excitations of the field potential might be a property useful for noise-reduction. We have also seen that the size of the field potential amplitudes depend dynamically on their frequency. These properties are suited for treatment by the wavelet transform — see Ref. [46]. For instance, one could expand the field potential signal on a basis consisting of a typical wave-form times the transverse subspace.

Section 14.1.1 showed that the field potential signal is influenced by frequency-localized noise. It would of course be preferable to eliminate this 50 Hz artifact prior to system modeling. The SPIKE2 programme does neither allow the construction of a notch filter nor stop-band filtering with a sufficiently narrow stop-band. And MATLAB has difficulties with handling such a big file as the 7 kHz sampled field potential signal. Therefore we will refrain from eliminating the 50 Hz artifact.

16.2.2 Output Signal

Iadecola *et al.* [44, (p. 946)], who also use laser-Doppler flowmetry to monitor cerebellar blood flow, make the qualitative statement that *"the increase in cerebellar blood flow evoked by PF stimulation is not secondary to changes in arterial pressure or blood gases, because these parameters were closely monitored and controlled and did not differ between unstimulated and stimulated groups."* It is our impression that they are referring to *global*, i.e., systemic, changes of blood flow — which would also change the baseline level. A similar conclusion may be reached for the IO and PF experiments treated in this thesis by visual

inspection of Figures A.1 and A.2 on pages 263–264. In Section 14.2.3 a similar conclusion regarding the *local* influence of the arterial pulse on the response of the LDF probes has been reached by quantitative analysis.

16.3 Signal Properties

16.3.1 Input Signal

There seems to be a tradition for investigating and describing the CBF signal as being nonlinear in the stimulation *frequency*. For the case of cerebellum an example is the paper by Mathiesen *et al.* [66] where the *average* field potential amplitude times the frequency is used as input function. However, the analysis in Section 14.1 showed that the frequency alone does not describe the input well. For the case of somato-sensory cortex an example is the paper by Nielsen *et al.* [76]. In that case the FPA size does only very weakly depend dynamically on the stimulation frequency. However, above a certain stimulation frequency the FPA level splits into two levels. Therefore it is not enough to consider the frequency as the only input. The origin of the tradition for focusing on the stimulation frequency alone may be the use of blood flow assessment techniques which make it difficult or impossible to measure electrical potentials simultaneously. For instance, applying the BOLD fMRI technique (blood oxygen level dependent functional magnetic resonance imaging) involves using high magnetic fields (several Tesla) which complicate measurement of electric potentials. Only recently simultaneous recordings of electrical signals (currents) and fMRI responses have been made [63].

Section 14.1.3 shows that in cerebellum the duration of the EPSP component does not change with time or frequency (when the frequency is kept above 5 Hz). A similar conclusion has been reached for the somato-sensory cortex by Ances *et al.* [6, (Table 1)] who show that the positions of the maximum and minimum points relatively to the stimulus event time do not vary with the duration of the stimulation sequence. On the other hand, the analysis in Section 14.1.2 shows that in cortex of cerebellum the field potential amplitudes first decrease very fast and then slowly increase — cf. the panel '196io4' in Figure 14.3 on page 84. Contrary to this behavior the average somato-sensory evoked potentials decrease as the duration of the stimulation sequence is increased according to Ances *et al.* [6, (Table 1)]. According to Nielsen *et al.* [76, (Figure 3)], the time-dependence of the evoked potentials in somato-sensory cortex depends strongly on frequency. Thus we may conclude that also for the somato-sensory evoked potentials all information resides in their amplitudes.

The variation in the overall level of field potential duration as well as field potential amplitude from rat to rat may originate from the fact that the magnitude of the measured potential depends strongly upon the distance from the probe to the distribution of current sources and sinks, which causes the field potential. In other words, the magnitude of the field potential depends strongly upon the position of the probe relatively to the source-sink configuration. The degree of variation in the shape of the time-localized excitations of the field potential is exemplified by Appendix A.3.2 on page 266.

16.3.2 Output Signal

Even though there are no dips in the CBF signals for the cases of parallel fiber stimulation, it should still be noted that the rate of increase is significantly slowed down (the slope of the CBF curve is decreased) when the stimulation lasts for more than around 95 s.

According to Table 14.1 on page 91 the dips in the CBF signals can be avoided by limiting the duration of the stimulation sequences so that they do not exceed 20 s.

Note from Figure 14.3 on page 84 that sometimes there are also dips, i.e., local minima, in the average field potential signal $\langle FPA \rangle_{1s}$. However, as the dips are not always clear we will refrain from analyzing whether their positions are correlated to the positions of the dips in the CBF signal.

The CBF response to stimulation with a given frequency does not seem to vary significantly among time series. Contrary to this — as mentioned in Section 16.3.1 — the average FPA level vary significantly among time series.

16.4 System Properties

Now we have plenty of evidence that the neuro-vascular system, which is involved during inferior olive stimulation, is dynamic (cf. M: Section 9.3.1 on page 53):

- When FPA_{pp} makes a step (Figure 14.3) the resulting CBF response slowly increases (Figure 14.9). Thus the step response is *not* a step.
- The transfer function estimates (Figure 15.6) contain lots of dynamics at non-zero frequencies: $\hat{G}(f) \neq A_0 \cdot \delta(f)$.

Thus, when choosing model structures, we will only consider models of dynamic systems — cf. M: Chapter 10.

The system may furthermore be characterized as discrete event driven (cf. M: Section 9.3.4 on page 54), since the only information content of the input signal resides in the amplitudes of the time-localized excitations ('events') of the field potential signal.

Let us shortly consider another system: Let the input be the 50 Hz network voltage (a source being external to cerebellum) and the output be the field potential (which is internal to cerebellum). The presence of the harmonics of the 50 Hz oscillation in the output (cf. Figure 14.1) then shows that this system is strongly[1] nonlinear.

[1] The output from a linear system, which is driven by a harmonic (sinusoidal) input with a given frequency, is a harmonic signal with the same frequency. The response of a nonlinear system to a harmonic input will, on the other hand, typically be periodic but not harmonic.

Chapter 17

Conclusion on Analysis

17.1 Conclusion on Signal Properties

The field potential signal (input) evoked by stimulation of the inferior olive is characterized by the following properties:

- The size of the field potential amplitude depends dynamically on the stimulation frequency. The standard deviations of the field potential amplitudes within bins of a duration of one second are independent of the stimulation frequency and of the time elapsed since onset of stimulation.
- For a particular stimulation frequency the order of magnitude of the field potential amplitudes varies from time series to time series. It is hypothesized that this variation is due to variation in the probe position relative to the source-sink configuration.
- The duration of the time-localized excitations of the field potential does not vary much throughout a time series. Thus the field potential duration is independent of the stimulation frequency and the time elapsed since onset of stimulation.
- The level of field potential durations varies from rat to rat.
- The instant stimulation event frequency is very well defined — except from a number of periodically occurring noisy events.
- The field potential signal contains a strong 50 Hz component originating from the network voltage.
- The instantaneous frequency of field potential amplitude events is identical to the instantaneous stimulation event frequency for low stimulation frequencies. For higher stimulation frequencies, the instantaneous frequency of field potential amplitude events fluctuates significantly around the value of the instantaneous stimulation event frequency. It is hypothesized that the fluctuations are caused mainly by high-frequency noise but also the 50 Hz artifact might contribute.

The cerebellar blood flow responses (output) are characterized by the following properties:

- For IO stimulation the responses of the three red LDF probes are very similar, and they are larger than the response of the green LDF probe. For PF stimulation the response of the green LDF probe is superior to the responses of the three red probes.
- The maximum blood flow response to stimulation with a particular frequency increases with frequency from low to medium frequencies, then saturates and decreases from medium to high frequencies.
- The blood flow response to IO stimulation for tens of seconds with a particular frequency is characterized by a fast increase towards a local maximum followed by a fast decrease towards a dip bottom. Then the response slowly increases until the end of stimulation and finally approaches the baseline level fast. The blood flow response to PF stimulation for tens of seconds characteristically increases almost linearly for the duration of the stimulation and then decreases quite fast towards the baseline value when the stimulation is turned off.

- The arterial blood pressure contains one strong frequency component: The arterial pulse.
- The measured CBF signals are *not* contaminated by oscillations caused by vessel walls moving synchronously with the arterial pulse.

17.2 Conclusion on System Properties

In case of inferior olive stimulation, the coupling between evoked neuronal activity and blood flow responses in rat cerebellum has been characterized as follows: The neuro-vascular system is

- discrete event driven, and
- dynamic.

17.3 Conclusions w. r. t. System Modeling

17.3.1 Signal Representations

- As the majority of the information content in the 7 kHz sampled field potential signal resides in the amplitudes of the time-localized excitations, the signal will be represented by pairs of the time of occurrence and the amplitude of the j'th excitation: $(t_j, FPA(t_j))$. The frequency of events of this event-sampled signal lies in the range $2 - 30$ Hz.

  In order to be able to do system identification with the 10 Hz sampled cerebellar blood flow signal CBF as output, we need to provide preprocessing procedures in order to convert the event-sampled FPA signal into a 10 Hz sampled input signal. The resulting signal will be termed a *preprocessed field potential amplitude signal* and denoted by FPA_{pp}. A major task in the system modeling process will be to choose appropriate preprocessing procedures.

- To ensure that the developed models capture as little noise as possible, the output signals with the largest amplitudes should be chosen for modeling purposes, i.e.,

  - In case of inferior olive stimulation experiments the signal from the LDF probe `Re140` will be used as output signal in the models.
  - In case of parallel fiber stimulation experiments the signal from the LDF probe `Gr140` should be chosen as output signal in models.

  Remember that the major contributions to the signals from these two LDF probes stem from the outermost layers of the cerebellar cortex.

- In order to get rid of some high-frequency components of the signals of the order of a few Hertz, the input (preprocessed field potential amplitude signal) and output (relative cerebellar blood flow signal) will be resampled by a factor of ten. In this way also aliasing effects are avoided.

17.3.2 System Representations

- As mentioned earlier (cf. P: Section 7.2 on page 42) the neuronal structure involved when stimulating the inferior olive is simpler than that of the parallel fiber system. This is expected to be reflected by mathematical models of the system. Therefore we will only consider models of neuro-vascular coupling in case of inferior olive stimulation.
- Since the system analysis showed that the neuro-vascular system is intrinsically dynamic we will only consider dynamic models of the coupling between neuronal activity and blood flow changes in rat cerebellum.
- The characteristic duration of time-localized excitations of the field potential signal has been shown to be of the order of a few tens of milliseconds. The characteristic times of the cerebellar blood flow signal has been shown to be of the order of a few tens of seconds. Therefore the system models need to include ways of coupling fast dynamics to slow.

Part IV

Linear Black-Box Models

This part is concerned with general linear dynamic models connecting input and output without reference to the physiological mechanisms which mediate the coupling between neuronal activity and blood flow changes in cerebellum. The purpose is to investigate to which degree the neuro-vascular system can be approximated by a linear dynamic model.

Since the data acquisition rate of the event-sampled input (the field potential amplitude signal) varies throughout an experiment, the mean to develop the models will be to examine various linear preprocessing procedures converting the input into a sampled signal. More specifically, we will consider two examples of linear dynamic input transforms:

- The Input Sampling Transform
- The Input Running Summation Transform.

The goal is to characterize the deficiencies of the linear models. Such characterizations may be useful when making suggestions for nonlinearities to be incorporated into the model structure.

Chapter 18

The Input Sampling Transform

18.1 The Input Sampling Transform

The event-sampled field potential amplitude signal is transformed into the sampled input signal in the following way: The FPA events, which occur at frequencies in the range $2 - 30\ Hz$, are collected into bins of a length determined by the sampling rate of the CBF signal, i.e., bins of a size of approximately $0.1\ s$. Now the FPA's within each bin are summed:

$$FPA_{pp}(t) = \sum_{t-\frac{\tau}{2}<t_j\leq t+\frac{\tau}{2}} FPA(t_j). \tag{18.1}$$

In this expression t denotes the sampling instants of the CBF signal, t_j the time of occurrence of the j'th FPA event, and τ the sampling interval of the CBF signal. This *preprocessed FPA signal*, FPA_{pp}, is thus the result of a linear dynamic transformation of the original input FPA. We will call it the *input sampling transform* because its only effect is to convert from event-sampling to sampling — it has no filtering effect (neither low-pass nor high-pass).

18.2 Choice of Model Structure

The purpose of this first modeling work will be to investigate which characteristics cannot be covered by a linear model structure. Furthermore we will focus on whether a transport delay should be included in the model structure.

For these purposes we choose a linear model structure with maximum flexibility: A black-box SISO state-space model structure (cf. M: Section 10.2.2 on page 58)

$$\dot{\mathbf{x}}(t) = \mathbf{F}\mathbf{x}(t) + \mathbf{G}u(t-t_d) + \mathbf{K}e(t), \tag{18.2}$$
$$y(t) = \mathbf{H}\mathbf{x}(t) + Ju(t-t_d) + e(t), \tag{18.3}$$

which contains a transport delay t_d from input to output, and with the input and output being

$$u(t) = FPA_{pp}(t), \tag{18.4}$$
$$y(t) = CBF(t). \tag{18.5}$$

We will investigate the performance of this model structure as a function of the transport delay t_d. This is accomplished in the following way: A number of transport delays are investigated separately. For each value of the transport delay t_d, the linear order $n = \dim \mathbf{x}$ is estimated. Finally the value of the loss function V_N is calculated. Since the relationship between neuronal activity and perfusion is causal, only non-negative transport delays, $t_d \geq 0$, are investigated.

18.3 Modeling the Full Time Series

18.3.1 The Full Input-Output Data Series

First we consider only the inferior olive experiments which contain the results of both types of stimulation:

- Short stimulation sequences: Stimulation for 60 s with various frequencies in the range $2 - 30$ Hz,
- Long stimulation sequence: Stimulation for 600 s with the frequency 5 Hz.

Two data series, no. 196io4 and 196io5, are thus investigated. We will term these series the *full time series*.

The results of the preprocessing procedure are input-output data sets with a sampling frequency of 10 Hz as shown in Figure 18.1. As mentioned in Section 15.3 on page 96 the signals will be resampled

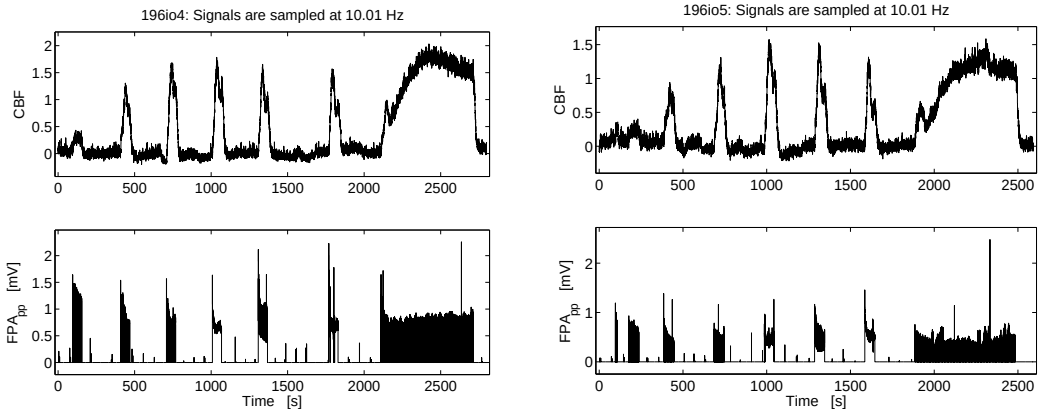

Figure 18.1: The input sampling transform applied to the full time series: All samples are shown. The preprocessed field potential amplitude signal (input FPA_{pp}) (bottom panels), and the measured signal from the LDF probe `Re140` (output CBF) (top panels). Both signals are sampled at 10 Hz. For the two cases of IO stimulation which contain both types of stimulation sequences: Short (60 s long) ones with various frequencies, and a long one (600 s) at frequency 5 Hz. Note that both the input and output signals contain a lot of high-frequency dynamics.

to 1 Hz in order to prevent aliasing as well as to reduce the noise in the signals. The results are shown in Figure 18.2.

18.3.2 Results of Modeling the Full Time Series

Model Fit

With the purpose of comparing the performance (cf. M: Section 12.3 on page 68) of this model structure with that of others, the peak-to-peak value of the model error ΔCBF_{pp} as well as the noise-to-signal ratio NSR are listed in Table 18.1. Their quite high values reflect a very bad fit between the model output and the measurements (see also Figure 18.3).

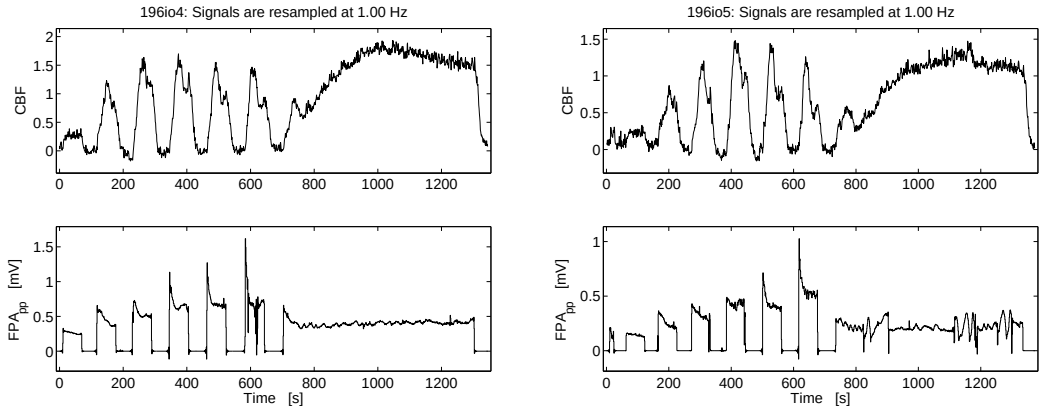

Figure 18.2: The input sampling transform applied to the full time series: The input (FPA_{pp}) and output (CBF) signals resampled at 1 Hz for the two experiments (196io4 and 196io5) which contain both short (60 s) and long (600 s) stimulation sequences. Note by comparison to Figure 18.1 that the high-frequency dynamics has been eliminated.

Series	ΔCBF_{pp}	NSR [%]
196io4	1.58266	43.4
196io5	1.73692	50.1
Mean	1.65979	46.8

Table 18.1: The linear black-box model with the input sampling transform applied to the full time series: The peak-to-peak value of the model error ΔCBF_{pp} and the noise-to-signal ratio NSR obtained for each of the two full inferior olive time series. The bottom line lists their arithmetic mean values. Note that the peak-to-peak values (which are around 1.7 times the baseline value of the CBF response) and the noise-to-signal ratio values (which are around 40 %) are very high.

For each of the two time series the model with the value of the parameter vector which gives the lowest value of the loss function V_N is simulated, and the model output is compared to the measured output in Figure 18.3. To emphasize the deficiencies of the model also the model error ΔCBF (cf. M: Section 12.3 on page 68) is depicted. We conclude from this figure that three features of the experimental data have

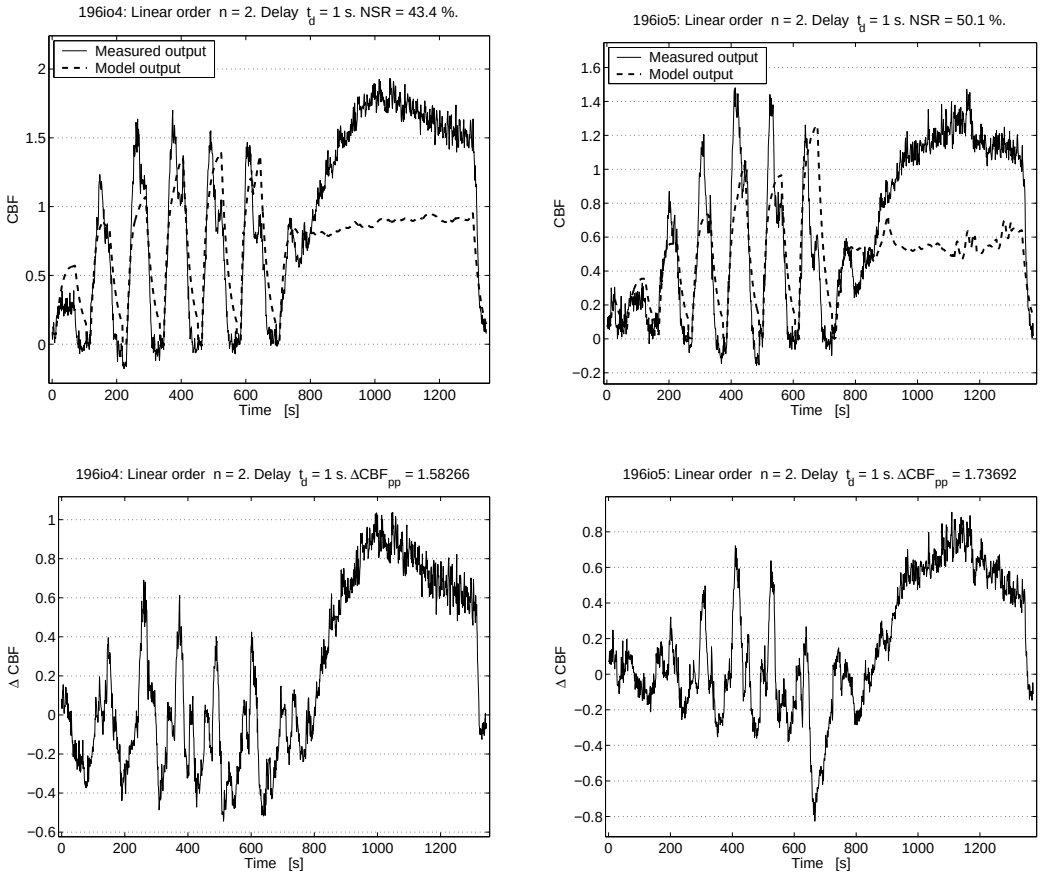

Figure 18.3: The linear black-box model with the input sampling transform applied to the full time series: Top panels: Comparison of the measured output with a noise-free simulation of the model estimated from each of the full time series 196io4 and 196io5. Bottom panels: The model error ΔCBF, i.e., the difference between the measured output and a noise-free simulation of the linear black-box state-space model, estimated from each of the full time series 196io4 and 196io5. Note the systematic errors due to deficiencies in the linear model structure. Three features of the experimental data have not been explained by the linear model: Frequency saturation, dips, and overgrowth during long stimulation sequences. The largest discrepancies occur during the 600 s long stimulation sequences.

not been covered by the model consisting of the linear dynamic input sampling transform in combination with a linear black-box state-space model:

- **Frequency saturation:**
  The maximum of the measured blood flow response to stimulation for 60 s is larger for intermediate stimulation frequencies than for low and high frequencies (cf. Section 14.2.1 on page 89). The linear model over-estimates the blood flow response to low and high frequencies, but under-estimates the blood flow response to intermediate frequencies.

- **Dips:**
  The measured blood flow response to stimulation with a particular frequency makes a dip. The bottom of the dip is reached after stimulation for around 45 s (cf. Table 14.1 on page 91). The simulated response only decreases but does not increase again afterwards.

- **Overgrowth during prolonged stimulation:**
  When the stimulation sequence continues beyond the dip (at around 45 s after the onset of stimulation) the measured blood flow response increases drastically. The linear model significantly under-estimates the response after 60 s.

On the other hand, the experimental data exposes the same dynamics, and the deviations of the model dynamics from the system dynamics are of the same kind for the two time series. Therefore we expect the two time series to be the results of the same system dynamics. Thus a single model — which includes the three features mentioned above — should be able to explain the two experiments.

Estimates

The estimates of the linear order n as well as the transport delay t_d, which have been obtained from the two experiments, are listed in Table 18.2. Note the consistency: The sets of estimates obtained from the two full time series are almost identical: $n = 2, t_d = 1\ s$.

Series	n	t_d $[s]$
196io4	2	1
196io5	2	1
Mean	2	1

Table 18.2: The linear black-box model with the input sampling transform applied to the full time series: The estimated linear order n and the transport delay t_d obtained for each of the two full inferior olive time series. The bottom line lists their arithmetic mean values. The linear order has been estimated to be $n = 2$, and the transport delay to be of the order of a single sample: $t_d = 1\ s$.

Sensitivity to Transport Delay t_d

The dependence of the estimated linear order n and the resulting loss function V_N on the transport delay t_d are shown in Figure 18.4. The loss function is sensitive to the transport delay. Nevertheless, for

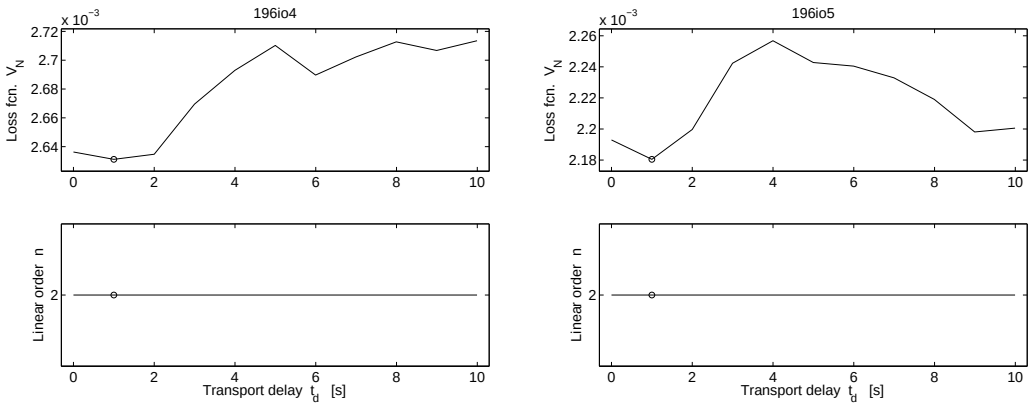

Figure 18.4: The linear black-box model with the input sampling transform applied to the full time series: The loss function V_N (top panels) and the linear order n (bottom panels) of a linear black-box state-space model estimated from each of the full time series 196io4 (left panels) and 196io5 (right panels). Note that for 196io4 the minimum of V_N is unambiguous whereas for 196io5 the value of V_N at $t_d = 9\ s$ is close to the global minimum value at $t_d = 1\ s$. Note also that the estimate of the linear order is $n = 2$ independently of the value of the chosen transport delay t_d. The transport delay has been estimated to $t_d = 1\ s$ for both time series.

the experiment 196io5 the estimate of the transport delay t_d is close to be ambiguous since the value of V_N at $t_d = 9\ s$ is close to the global minimum value. The estimate of the linear order $n = 2$ is independent of the transport delay t_d for both experiments.

18.4 Modeling the Short Time Series

18.4.1 The Short Input-Output Data Series

The largest discrepancies between the measured output and the output obtained by a noise-free simulation of the black-box state-space model occur during the 600 s long stimulation sequence. We suggest that the discrepancies are caused by a nonlinearity which is linearizable if the stimulation duration is limited to short times. (How short the sequences should be to fully eliminate the effects of the nonlinearity will be discussed in Section 20.2 on page 137.)

Therefore we will now investigate the performance of the same linear model when applied to time series with all the stimulation sequences being 60 s long. By truncating each of the two time series 196io4 and 196io5 at the instant being 60 s into the 600 s long stimulation sequence these two time series can also be used for this purpose. Thus we can use all four time series. We will term these series the *short time series*. They are shown in Figure 18.5.

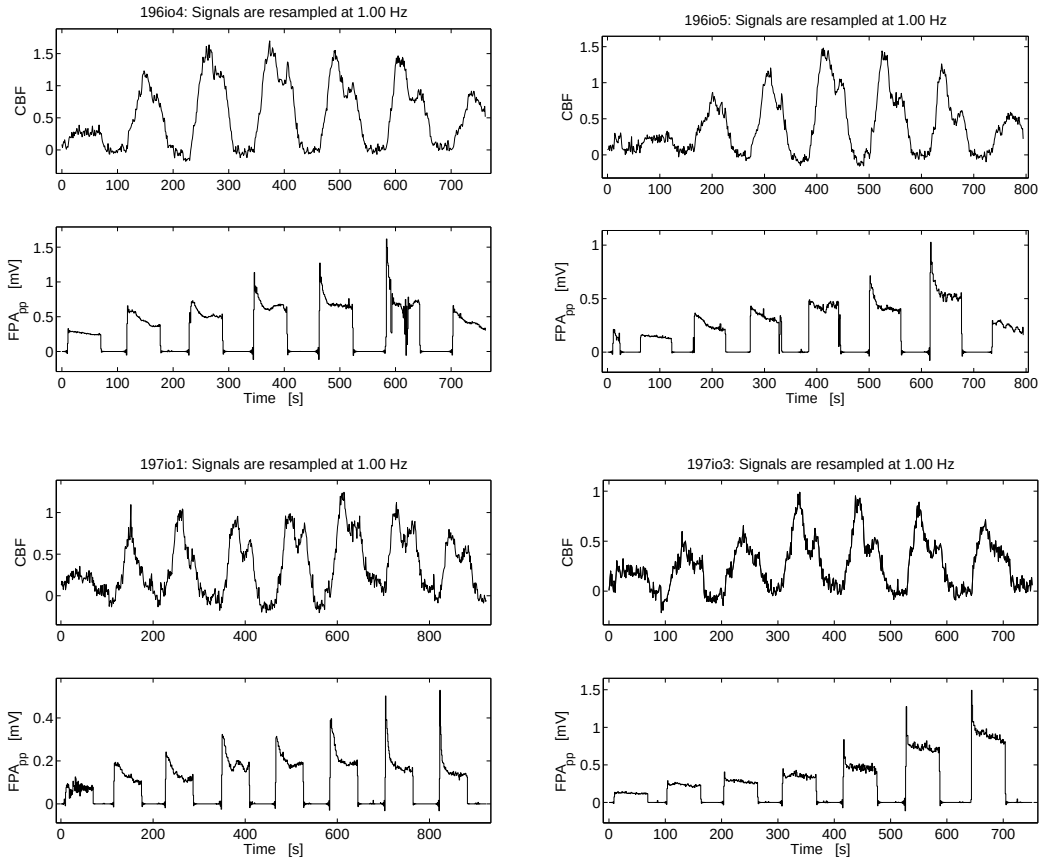

Figure 18.5: The input sampling transform applied to the short time series: The parts of the input-output data sets for inferior olive stimulation where all of the stimulation sequences are 60 s long. The time series have been resampled to 1 Hz.

18.4.2 Results of Modeling the Short Time Series

Model Fit

The peak-to-peak value of the model error ΔCBF_{pp} as well as the noise-to-signal ratio NSR are listed in Table 18.3. By comparison to Table 18.1 on page 110 we note that for the experiments performed on

Series	ΔCBF_{pp}	NSR [%]
196io4	1.04554	25.4
196io5	1.32848	35.8
197io1	0.87437	38.7
197io3	1.09028	54.3
Mean	1.08467	38.5

Table 18.3: The linear black-box model with the input sampling transform applied to the short time series: The peak-to-peak value of the model error ΔCBF_{pp} and the noise-to-signal ratio NSR obtained for each of the four inferior olive time series. The bottom line lists their arithmetic mean values. Note that for the two series 196io4 and 196io5 both ΔCBF_{pp} and NSR have been significantly reduced by the truncation of the long stimulation sequences — cf. Table 18.1 on page 110.

rat no. 196 the model fit has been significantly improved by the exclusion of the parts of the data which extends beyond stimulation durations of 60 s.

The dynamics models which give the best fit to the experimental data are simulated and the resulting model outputs are compared to the measured outputs in Figure 18.6. The equivalent model error signals ΔCBF are shown in Figure 18.7. We conclude from these figures that — as expected — two features of the short stimulation sequences have not been covered by the model consisting of the linear dynamic input sampling transform in combination with a linear black-box state-space model:

- **Frequency saturation:**
  The maximum of the measured blood flow response to stimulation for 60 s is larger for intermediate stimulation frequencies than for low and high frequencies (cf. Section 14.2.1 on page 89). The maximum of the equivalent model output increases with increasing stimulation frequency.

- **Dips:**
  The measured blood flow response to stimulation with a particular frequency makes a dip. The bottom of the dip is reached after stimulation for around 45 s (cf. Table 14.1 on page 91). The simulated response only decreases but does not increase again afterwards.

As these features are systematic they are due to deficiencies of the linear model structure. Furthermore, the experimental data exposes the same dynamics, and the deviations of the model dynamics from the system dynamics are of the same kind for the four short time series. Therefore we expect these four time series to be the results of the same system dynamics. Thus a single model — which includes the two features mentioned above — should be able to explain the four experiments.

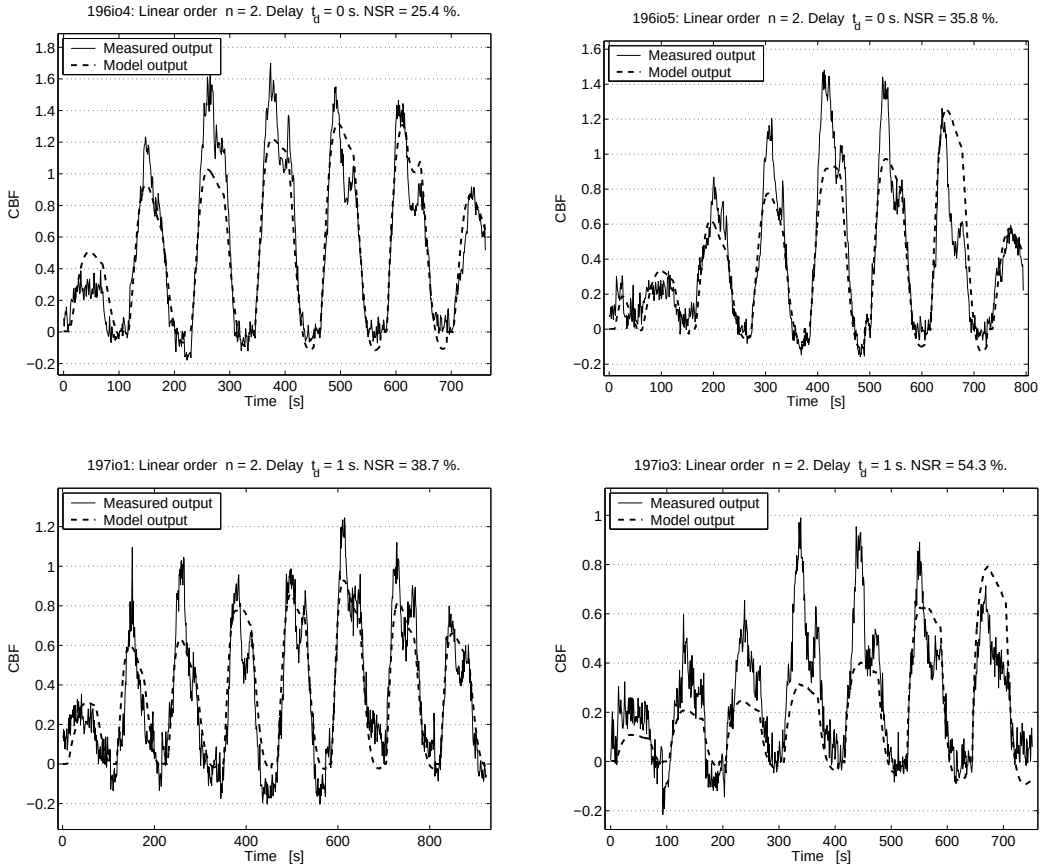

Figure 18.6: The linear black-box model with the input sampling transform applied to the short time series: Comparison of the measured output with a noise-free simulation of the linear black-box state-space model with the preprocessed field potential signal FPA_{pp} as input. Note that two features of the measurements have not been covered by the linear model: The frequency saturation and the dips.

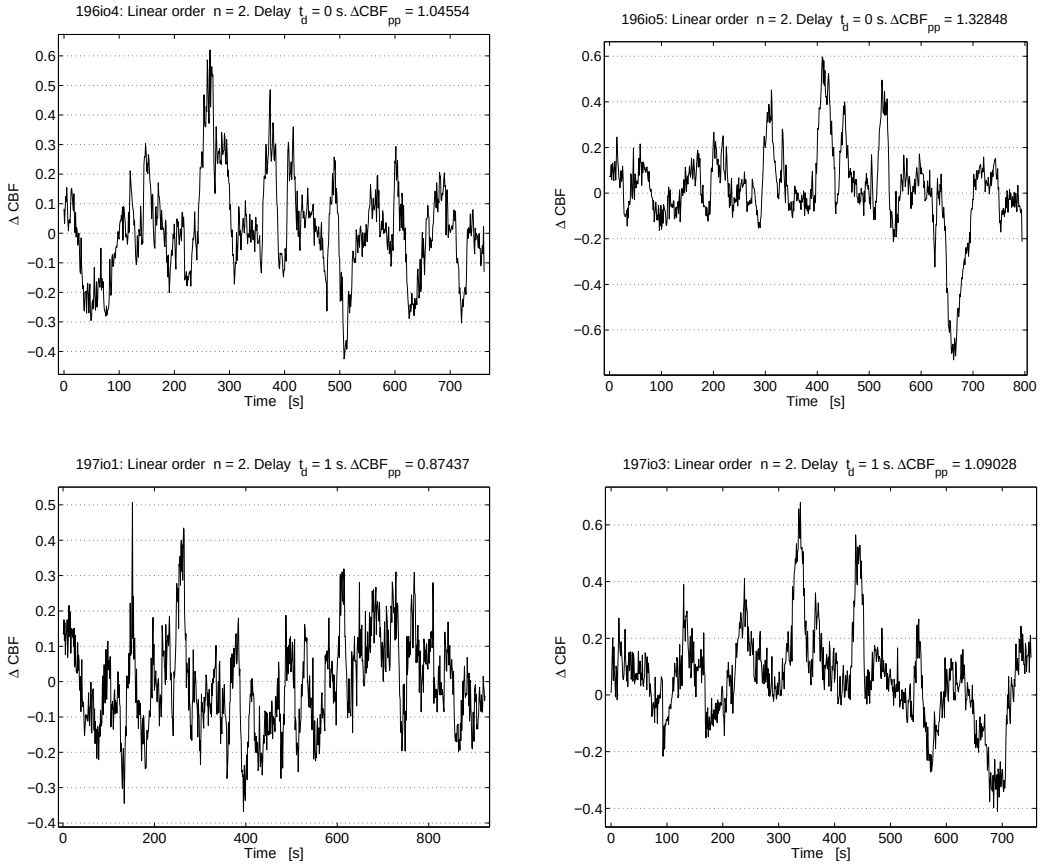

Figure 18.7: The linear black-box model with the input sampling transform applied to the short time series: The model error ΔCBF, i.e., the difference between the measured output and a noise-free simulation of the linear black-box state-space model. Note that the systematics in the time development of the model error indicates that these errors are caused by the fact that the model structure is too simple. For rat no. 196 the discrepancies are only large during stimulation. Especially for the experiment 197io1 the model fit is also quite bad during the quiet periods without stimulation — this deficiency is caused by the time development of the baseline CBF level.

Estimates

The estimates of the linear order n as well as the transport delay t_d obtained from the four experiments are listed in Table 18.4. The linear order is estimated to be $n = 2$. The transport delay is estimated to

Series	n	t_d $[s]$
196io4	2	0
196io5	2	0
197io1	2	1
197io3	2	1
Mean	2	1

Table 18.4: The linear black-box model with the input sampling transform applied to the short time series: The estimated linear order n and the transport delay t_d obtained for each of the four inferior olive time series. The bottom line lists their arithmetic mean values. Note that the linear order n is estimated to be $n = 2$. The transport delay has been estimated to be close to $t_d = 1$ s. The same value as has been obtained for the full time series — compare with Table 18.2 on page 112.

be very small: $t_d \leq 1$ s.

Sensitivity to Transport Delay t_d

The dependences of the estimated linear order n as well as the resulting loss function V_N on the transport delay t_d are depicted in Figure 18.8. Note that for each time series the estimate of the linear order n is independent of the choice of transport delay t_d. In all four cases the estimate is $n = 2$. Furthermore, the estimates of the transport delay t_d are not well-defined since the loss function V_N is very flat around the global minimum. However, the order of magnitude of the transport delay is clear: A few seconds corresponding to a few samples.

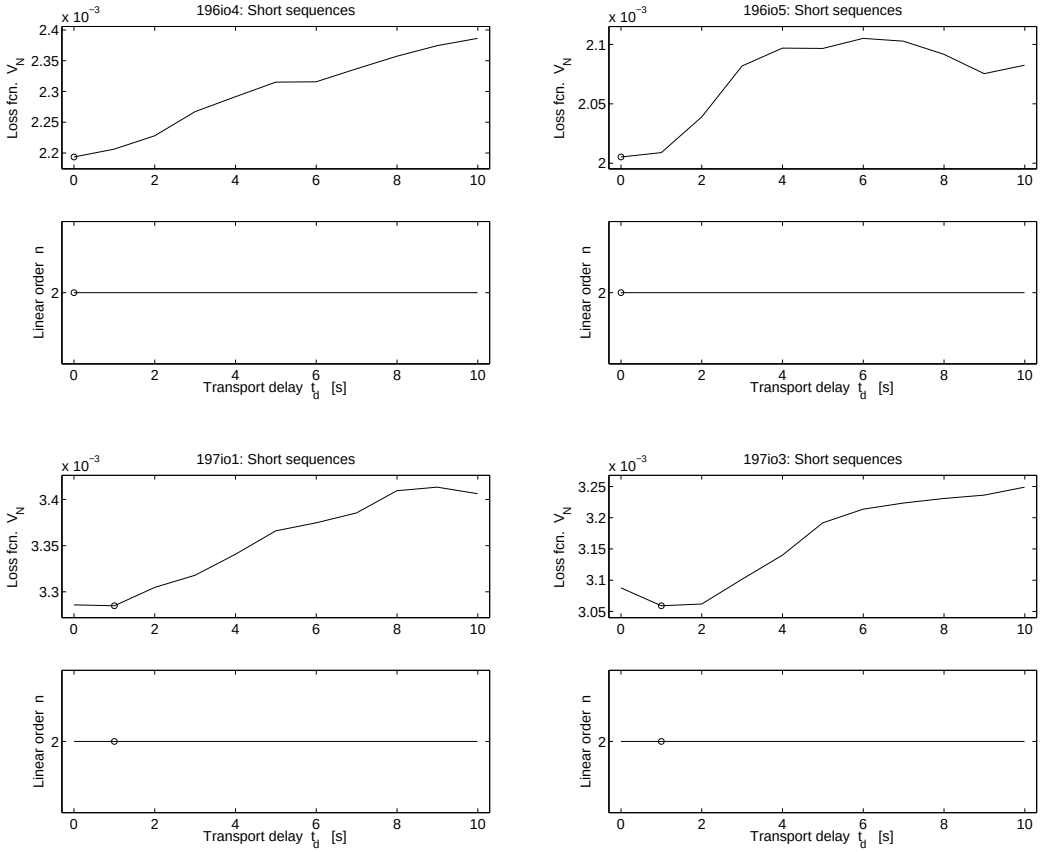

Figure 18.8: The linear black-box state-space model with the input sampling transform applied to the short time series: The dependence of the loss function V_N and the estimate of the linear order n on the transport delay t_d. Only the parts of the input-output data sets for inferior olive stimulation where all of the stimulation sequences are $60\,s$ long have been used for system identification. Note that for these short stimulation sequences the estimate of the linear order is $n = 2$ independently of the choice of transport delay t_d. The transport delay is estimated to be very small $t_d = 0 - 1\ s$. However, as there are values of V_N which are close to the minimum values the estimates of the transport delay t_d are not particularly well-defined. However, their order of magnitude is clear: A few samples, that is, a few seconds.

18.5 Discussion of the Input Sampling Transform

Properties of the Input Sampling Transform

Since the pre-processing procedure sums up the field potential amplitudes occurring in time intervals of equal size, the information content residing in the frequency of FPA events is moved to the amplitude of the pre-processed signal FPA_{pp}.

The model does not preserve causality, as the input sampling transform operates on FPA events occurring up to 0.05 s later than the associated CBF sample. As the resampled signals vary on a much slower time scale (~ 1 s), we will claim that moving the bins these 0.05 s back in time, thus creating the input

$$FPA_{pp}(t) = \sum_{t-\tau<t_j\leq t} FPA(t_j), \tag{18.6}$$

will not change any of the results.

Comparison of Full with Short Sequences

We cannot avoid the dips without cutting the time series into pieces. However, we have shown that we can minimize the effect of the overgrowth (second increase) on the model properties without eliminating the effect of frequency saturation by truncating the long stimulation sequence when it has lasted for 60 s — compare Tables 18.1 (page 110) and 18.3 (page 115). Doing this makes it possible to focus on incorporating the other two effects (frequency saturation and dips) into the model.

The transport delay t_d has been estimated to be of the order of a few samples, i.e., a few seconds. This is a quite small value compared to the characteristic times of the CBF signal (cf. Table 14.1 on page 91). Therefore it is acceptable to exclude the transport delay from the model structure. Doing this will significantly decrease the total run time of a program performing the estimation, since the run time is proportional to the number of transport delay values which are tested.

Chapter 19

The Input Running Summation Transform

19.1 Review of the Notion of a Running Summation

The inspiration to the model which is developed in this chapter stems from the hypothesis stated by Mathiesen *et al.* [67] saying that *"if the increases in CBF were temporally coupled, albeit indirectly to neuronal activity, then it would be possible to model the time course of the vascular response by integrating the neuronal activity over time during all phases of the vascular response"*. This hypothesis was converted into a mathematical model by summing the evoked field potential amplitudes occurring within a time interval, T, around the time of a measurement of the CBF response. They called this pre-processed input a *running summation*, $\text{run}\sum_T FPA$. It is a dynamic linear input transform.

In Ref. [67] it was shown that the idea of such a running summation to some extend could account for the connection between evoked field potential amplitudes and the cerebellar blood flow response. The preconditions for this model were the following:

- The CBF signal was assumed to be proportional to the running summation of field potential amplitudes:
$$CBF \propto \text{run}\sum_{T(f)} FPA. \tag{19.1}$$
This is a static linear model of the coupling between the transformed input and the output.
- The time interval, $T(f)$, over which the sum ran differed from one stimulation frequency, f, to another.

The result thus was a set of local models: One model for each stimulation frequency f.

19.2 The Input Running Summation Transform

We will look for a global model accounting for the connection between input and output during the full experiment — covering all of the various stimulation frequencies. The same pre-processing strategy of a running summation will be used, i.e., the input will be

$$FPA_{pp}(t) = \text{run}\sum_{T} FPA(t) = \sum_{t-T<t_j\leq t} FPA(t_j), \tag{19.2}$$

where the time t is the sampling instant of the CBF signal, and t_j is the time of occurrence of the j'th FPA event. This expression will be called the *input running summation transform*. The idea is to search for that (global!) value of T which optimizes the fit between model output and measured cerebellar blood flow.

But the model will be looked for in a much larger model class than just a simple proportionality. The model class will again be dynamic models in the form of linear higher order differential equations (cf. M: Chapter 10).

Note that this linear dynamic transformation is an example of a *filtering transform*, since — for summation times T longer than the sampling interval τ of the CBF signal, $T = k \cdot \tau, k \in \mathbb{N}$ — it has low-pass filtering effect. We will investigate this feature in Section 20.1.1 on page 134. For $T = \tau$ the running summation transform is equivalent to the sampling transform introduced in Chapter 18 which has no filtering effect.

19.3 The Model Structure

As in Chapter 18 the purpose of this modeling work will be to investigate which characteristics cannot be covered by a linear model structure. Furthermore we will focus on whether a transport delay should be included in the model structure.

For these purposes we consider a linear model structure with maximum flexibility: A black-box SISO state-space model structure

$$\dot{\mathbf{x}}(t) = \mathbf{F}\mathbf{x}(t) + \mathbf{G}u(t - t_d) + \mathbf{K}e(t), \tag{19.3}$$
$$y(t) = \mathbf{H}\mathbf{x}(t) + Ju(t - t_d) + e(t) \tag{19.4}$$

including a transport delay t_d from input to output, and with the input and output being

$$u(t) = FPA_{pp}(t), \tag{19.5}$$
$$y(t) = CBF(t). \tag{19.6}$$

We will investigate the performance of this model structure as a function of the transport delay: t_d. This is accomplished in the following way: A number of transport delays are investigated separately. For each value of the transport delay t_d the linear order $n = \dim \mathbf{x}$ is estimated. Finally the value of the loss function V_N is calculated. Again the system is expected to be causal and only non-negative transport delays, $t_d \geq 0$, are investigated.

19.4 Modeling the Full Time Series

19.4.1 The Full Input-Output Data Series

Again we first consider only the inferior olive stimulation experiments which contain the results of both types of stimulation:

- Short stimulation sequences: Stimulation for 60 s with various frequencies in the range $2 - 30$ Hz,
- Long stimulation sequence: Stimulation for 600 s with the frequency 5 Hz.

Two data series, no. 196io4 and 196io5, are thus investigated.

The results of the preprocessing procedure are input-output data sets with a sampling frequency of 10 Hz as shown in Figure 19.1. Furthermore the signals will be resampled to 1 Hz in order to prevent aliasing as well as to reduce the noise in the signals. The results are shown in Figure 19.2.

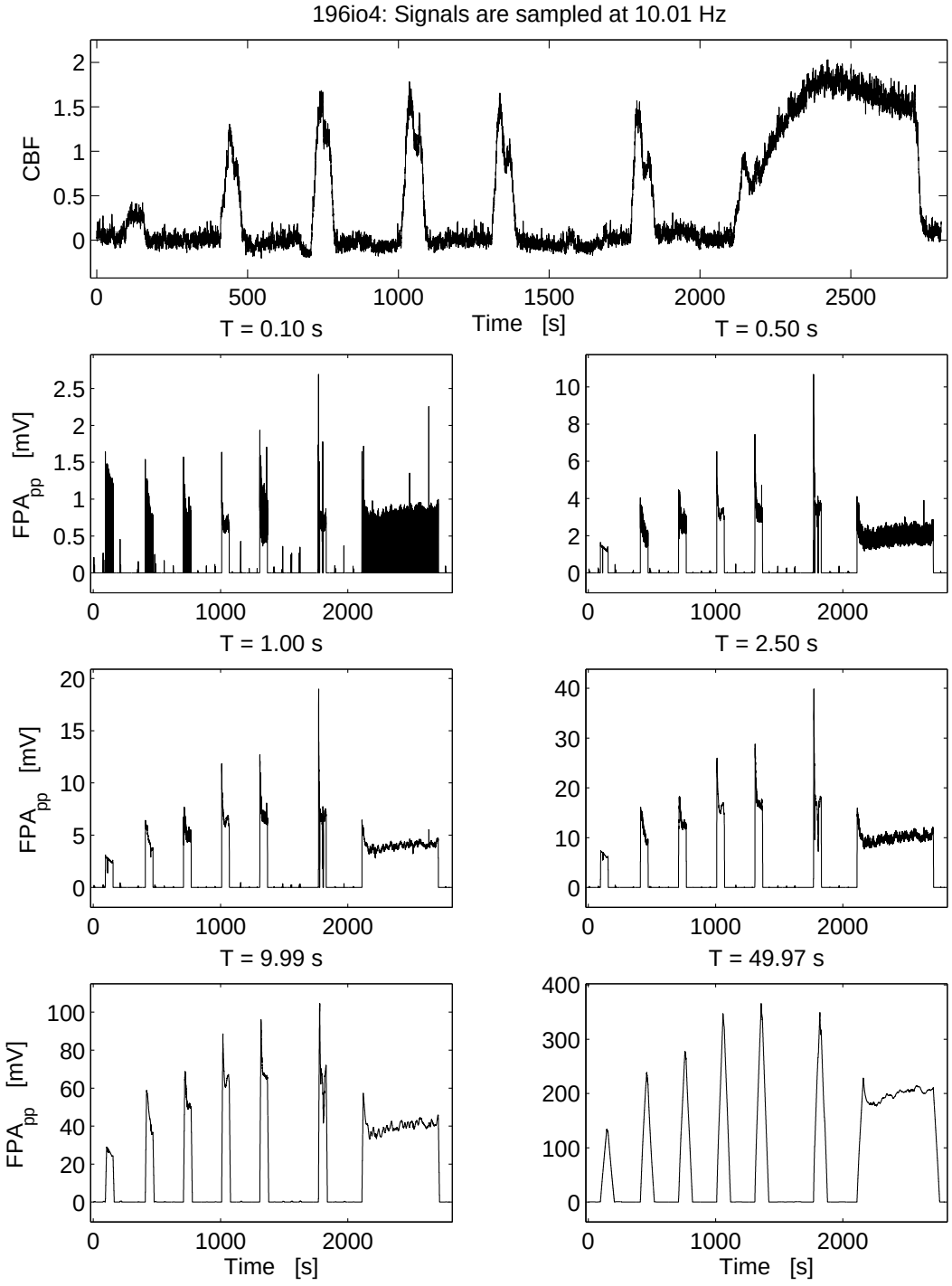

Figure 19.1: The input-output time series obtained by the input running summation transform applied to the full time series 196io4: All samples are shown. Top panel: The measured CBF signal. Other panels: Six examples of the running summation of field potential amplitudes FPA_{pp}. For the full time series which contain both types of stimulation sequences: Short (60 s long) ones with various frequencies, and a long one (600 s) at frequency 5 Hz. Note that for $T > \tau$ the transform has low-pass filtering effect. For $T \gg \tau$ the dips in FPA_{pp} have been eliminated for all of the short stimulation sequences.

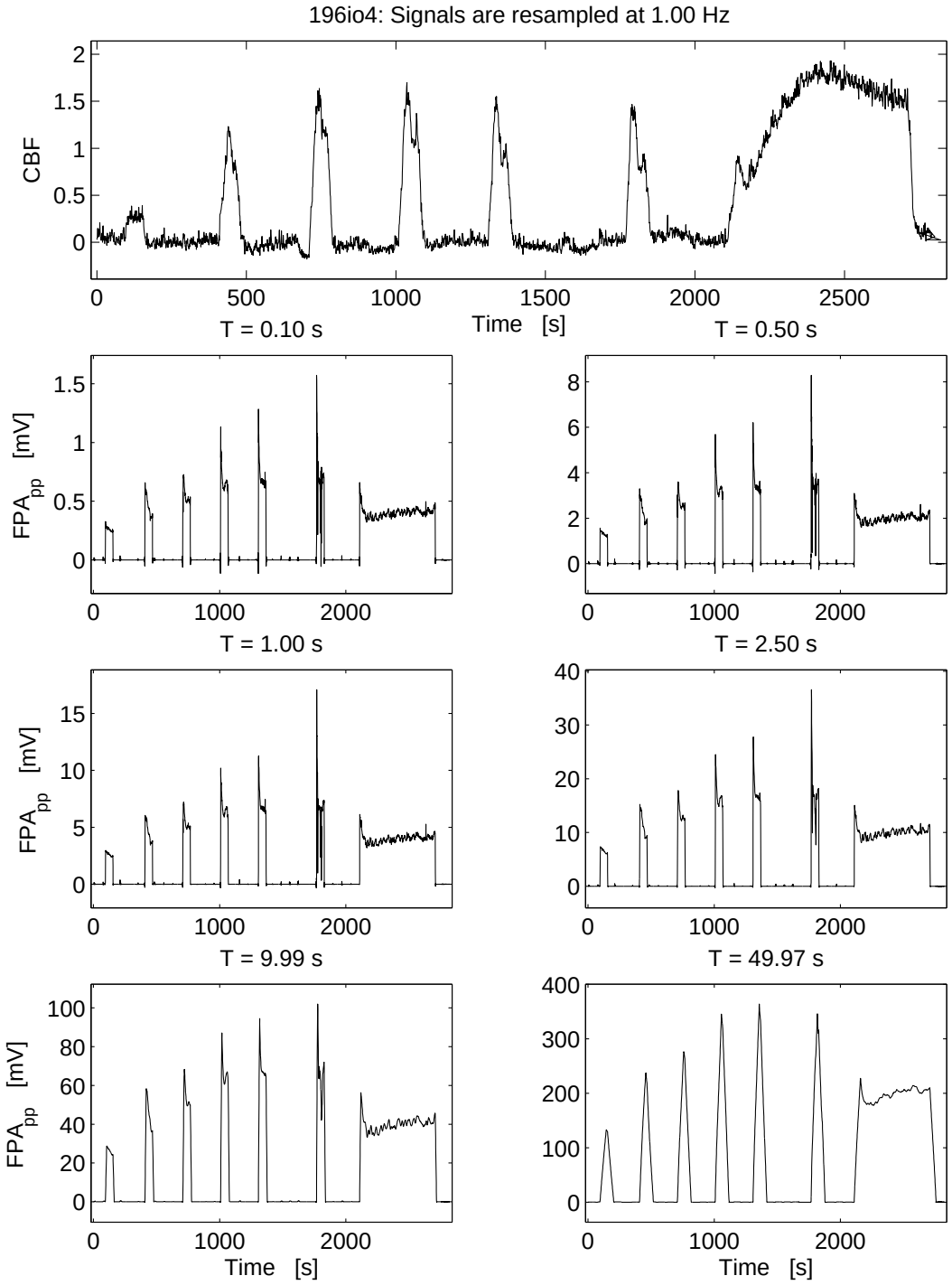

Figure 19.2: The input-output time series obtained by the input running summation transform applied to the full time series 196io4: All samples are shown. Top panel: The measured CBF signal. Other panels: Six examples of the running summation of field potential amplitudes FPA_{pp}. For the full time series 196io4 which contains both types of stimulation sequences: Short (60 s long) ones with various frequencies, and a long one (600 s) at frequency 5 Hz. The signals have been resampled at 1 Hz. Note that for $T \geq q_{rs} \cdot \tau \approx 1\ s$, where q_{rs} is the resampling factor ($q_{rs} = 10$) the resampling has no effect — compare with Figure 19.1.

19.4.2 Results of Modeling the Full Time Series

Model Fit

The obtained peak-to-peak value of the model error ΔCBF_{pp} as well as the noise-to-signal ratio NSR are listed in Table 19.1. As for the input sampling transform presented in Chapter 18 the obtained values

Series	ΔCBF_{pp}	NSR [%]
196io4	1.59182	46.0
196io5	1.72671	51.8
Mean	1.65926	48.9

Table 19.1: The linear black-box model with the input running summation transform applied to the full time series: The peak-to-peak value of the model error ΔCBF_{pp} and the noise-to-signal ratio NSR obtained for each of the two inferior olive time series which contain a 600 s long stimulation sequence. The bottom line lists their arithmetic mean values. Note that the quite high values are of the same order of magnitude as (actually slightly higher than) those obtained for the input sampling transform — compare with Table 18.1 on page 110. Thus inclusion of the parameter T has not improved the model performance.

are quite high.

For each of the two time series the model with the value of the parameter vector which gives the lowest value of the loss function V_N is simulated, and the model output is compared to the measured output in Figure 19.3. We conclude from this figure that three features of the experimental data have not been covered by the model consisting of the linear dynamic input running summation transform in combination with a linear black-box state-space model:

- **Frequency saturation:**
  The maximum of the measured blood flow response to stimulation for 60 s is larger for intermediate stimulation frequencies than for low and high frequencies (cf. Section 14.2.1 on page 89). The linear model over-estimates the blood flow response to low and high frequencies, but under-estimates the blood flow response to intermediate frequencies.

- **Dips:**
  The measured blood flow response to stimulation with a particular frequency makes a dip. The bottom of the dip is reached after stimulation for around 45 s (cf. Table 14.1 on page 91). The simulated response only decreases but does not increase again afterwards.

- **Overgrowth during prolonged stimulation:**
  When the stimulation sequence continues beyond the dip (at around 45 s after the onset of stimulation) the measured blood flow response increases drastically. The linear model significantly under-estimates the response after 60 s.

These un-explained features are the same which could not be covered by the input sampling transform investigated in Chapter 18. This means that the summation time T — and the idea of a running summation — does not improve the model performance.

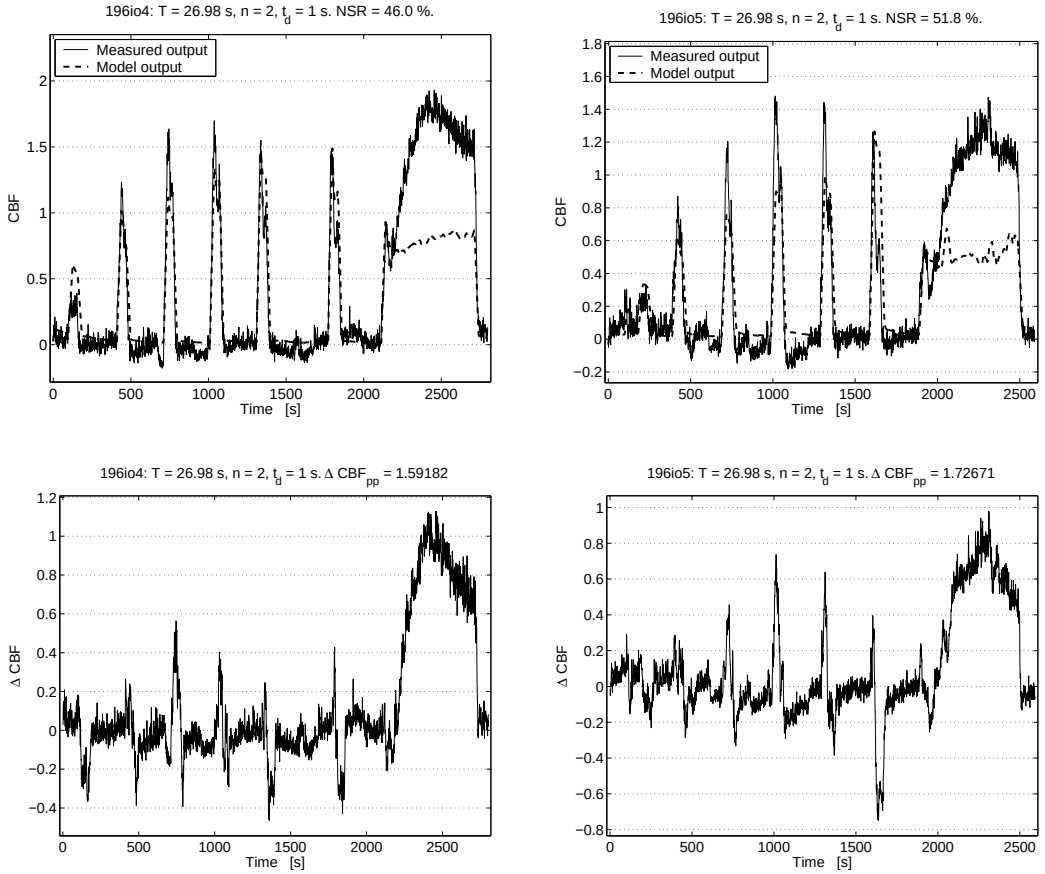

Figure 19.3: The linear black-box with the input running summation transform applied to the full time series: All samples are shown. Top panels: Comparison of the measured output with the model output, i.e., a noise-free simulation of a linear black-box state-space model, estimated from each of the full time series 196io4 and 196io5. Bottom panels: The model error ΔCBF, i.e., the difference between the measured output and the noise-free simulation, for each of the time series 196io4 and 196io5. Note that three features of the experimental data have not been covered by the linear model: Frequency saturation, dips, and overgrowth during extended stimulation. Furthermore, the model outputs are almost identical to the traces which are obtained for the input sampling transform in Figure 18.3 on page 111.

Estimates

The estimates of the summation time T, the linear order n, and the transport delay t_d are shown in Table 19.2. Note that the sets of values of the estimates obtained from the two series are identical. The

Series	T $[s]$	n	t_d $[s]$
196io4	26.98	2	1
196io5	26.98	2	1
Mean	26.98	2	1

Table 19.2: The linear black-box model with the input running summation transform applied to the full time series: The summation time T, the linear order n, and the transport delay t_d obtained for each of the two inferior olive time series which contain a 600 s long stimulation sequence. Below their arithmetic mean values are listed. Note that the values of n and t_d are identical to the values obtained for the input sampling transform — cf. Table 18.2 on page 112. The estimates of T deviate by two orders of magnitude from the value $T = \tau$ for the input sampling transform.

values of T deviates by two orders of magnitude from the value $T = \tau \approx 0.1$ s used for the input sampling transform.

Sensitivity to Summation Time T

The dependence of the loss function V_N as well as the estimates of the linear order n and the transport delay t_d on the summation time T are shown in Figure 19.4. For both time series the loss function V_N is

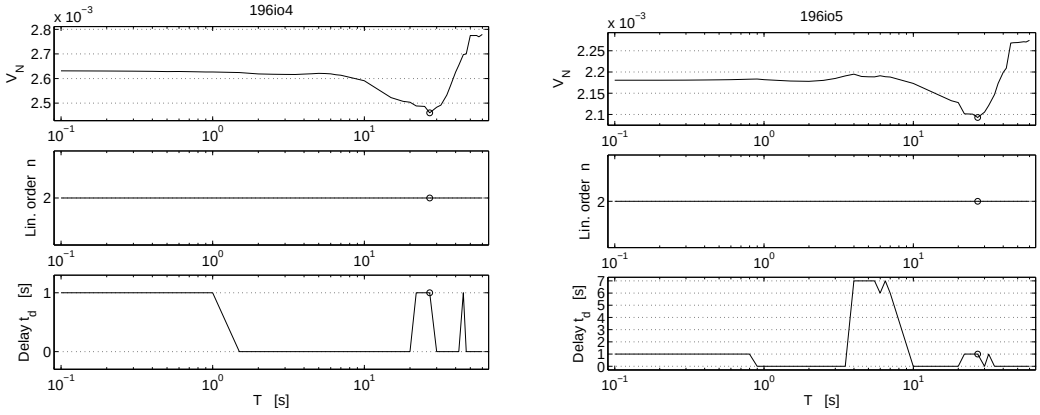

Figure 19.4: The linear black-box model with the input running summation transform applied to the full time series: The dependence of the loss function V_N (top panels), the estimates of the linear order n (middle panels) and the transport delay t_d (bottom panels) on the summation time T for each of the time series 196io4 and 196io5, respectively. Note that, in both cases, there is only a single — thus global — well-defined minimum point. Note also that the linear order n for all values of the summation time T is estimated to $n = 2$. Similarly, the estimates of the transport delay t_d are practically in-sensitive to the summation time T.

though weakly — sensitive to the summation time T: As T is varied, V_N only varies with a few percent. The global minimum of V_N is found at $T = 26.98$ s. The estimates of the linear order n are independent of the summation time T. In general the estimates of the transport delay t_d are of the order of a single samples — with some variation.

19.5 Modeling the Short Time Series

19.5.1 The Short Input-Output Data Series

As for the input sampling transform presented in Chapter 18 the largest discrepancies between the measured output and the output obtained by a noise-free simulation of the black-box state-space model occur during the 600 s long stimulation sequence. We suggest that the discrepancy is caused by a nonlinearity which is linearizable if the stimulation duration is limited to short times.

Therefore we will now investigate the performance of the input running summation transform when applied to time series with all the stimulation sequences being 60 s long. By truncating each of the two time series 196io4 and 196io5 at the instant being 60 s into the 600 s long stimulation sequence these two time series can also be used. Thus we can use all four time series.

19.5.2 Results of Modeling the Short Time Series

Model Fit

The obtained peak-to-peak values of the model error ΔCBF_{pp} as well as the noise-to-signal ratios NSR are listed Table 19.3. By comparison to Table 19.1 on page 125 we conclude that for the experiments

Series	ΔCBF_{pp}	NSR [%]
196io4	1.01738	25.0
196io5	1.29080	36.1
197io1	0.80044	38.1
197io3	0.97705	57.9
Mean	1.02142	39.3

Table 19.3: The linear black-box model with the input running summation transform applied to the short time series: The peak-to-peak value of the model error ΔCBF_{pp} and the noise-to-signal ratio NSR obtained for each of the four inferior olive time series with only 60 s long stimulation sequences. Below their arithmetic mean values are listed. Note that for the two experiments performed on rat no. 196 the model fit has been significantly improved by the truncation of the long stimulation sequences — cf. Table 19.1 on page 125. However, the model fit has not been improved (on the contrary it becomes worse) by the inclusion of the parameter T — cf. Table 18.3 on page 115.

performed on rat no. 196 the model fit has been significantly improved by the exclusion of the parts of the data which extend beyond stimulation durations of 60 s. Contrary to this the inclusion of the parameter T has not improved the model fit — cf. Table 18.3 on page 115. Actually the fit is slightly worse.

The dynamics models which give the best fit to the experimental data are simulated and the model outputs are compared to the measured outputs in Figure 19.5. The equivalent model error traces are shown in Figure 19.6. We conclude from these figures that two features of the short stimulation sequences have not been covered by the model consisting of the input running summation transform in combination with a linear black-box state-space model:

- **Frequency saturation:**
  The maximum of the measured blood flow response to stimulation for 60 s is larger for intermediate stimulation frequencies than for low and high frequencies (cf. Section 14.2.1 on page 89). The maximum of the equivalent model output increases as the stimulation frequency is increased.

- **Dips:**
  The measured blood flow response to stimulation with a particular frequency makes a dip. The bottom of the dip is reached after stimulation for around 45 s (cf. Table 14.1 on page 91). The simulated response only decreases but does not increase again afterwards.

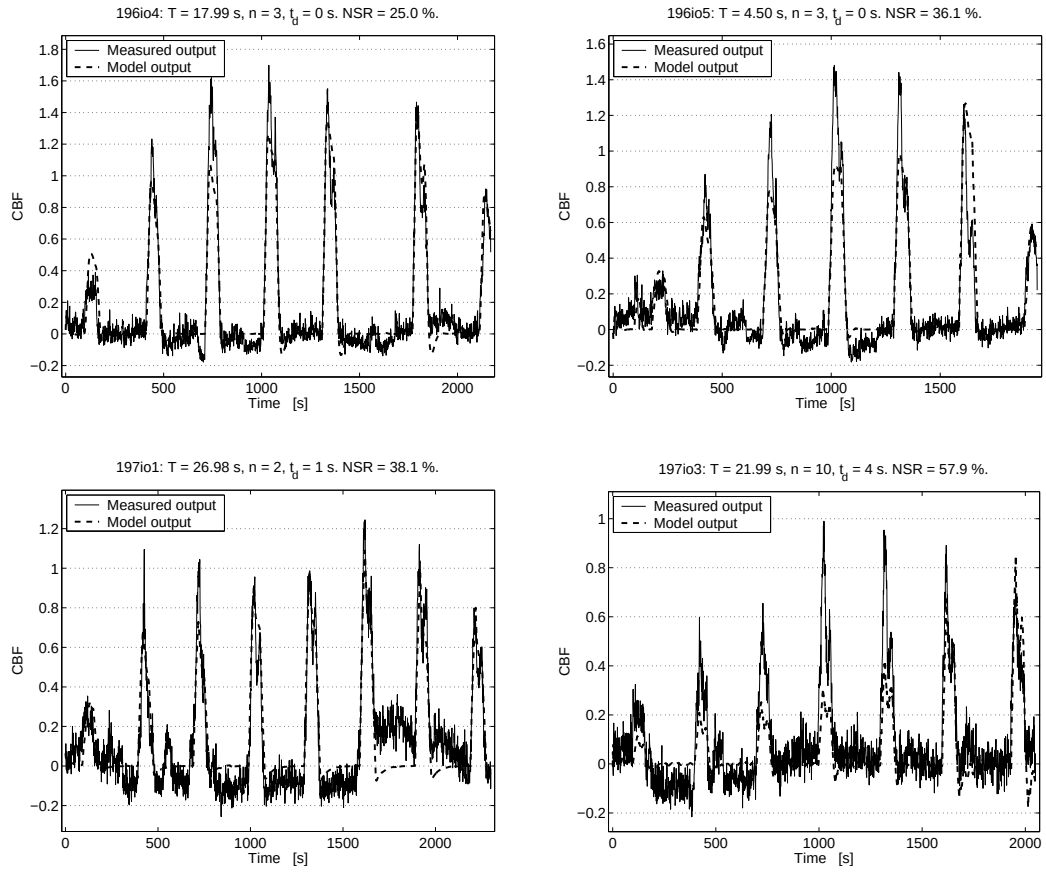

Figure 19.5: The linear black-box model with the input running summation transform applied to the short time series: All samples are shown. Comparison of the outputs obtained by noise-free simulations of the linear state-space models to the measured outputs. Note that the same two features (frequency saturation and dips), which cannot be explained by the input sampling transform, cannot be explained by the input running summation transform either — compare with Figure 18.6 on page 116.

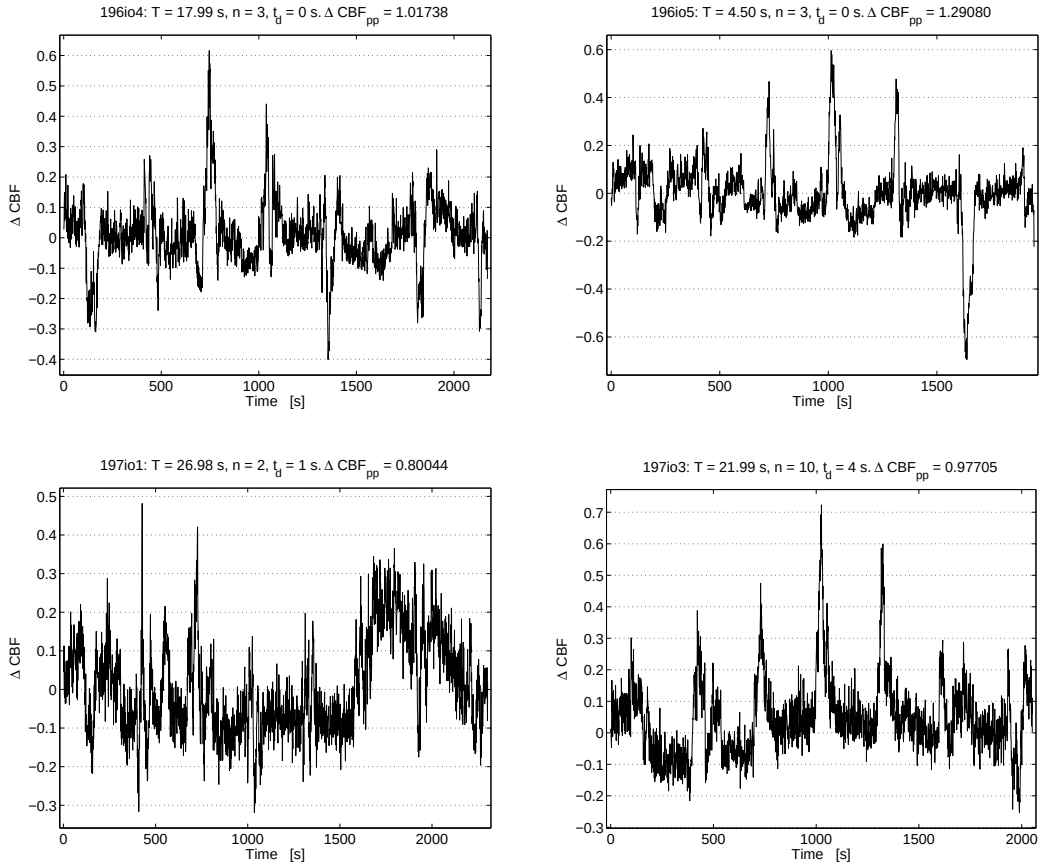

Figure 19.6: The linear black-box model with the input running summation transform applied to the short time series: All samples are shown. The model error traces ΔCBF obtained from the parts of the input-output data sets for inferior olive stimulation where all of the stimulation sequences are 60 s long. Note that the systematics in the time development of the model error traces indicates that these errors are caused by the fact that the model structure is too simple.

Estimates

The estimates of the summation time T, the linear order n, and the transport delay t_d are listed in Table 19.4. Note the variations in the estimates of T. Note also that these summation times are around

Series	T $[s]$	n	t_d $[s]$
196io4	17.99	3	0
196io5	4.50	3	0
197io1	26.98	2	1
197io3	21.99	10	4
Mean	17.86	5	1

Table 19.4: The linear black-box model with the input running summation transform applied to the short time series: The estimated summation time T, the linear order n, and the transport delay t_d obtained for each of the four inferior olive time series. Below their arithmetic mean values are listed. Note that the estimates of T for rat no. 196 differ by an order of magnitude. Note the quite large deviation of the estimate of the linear order n for the time series 197io3 from the other three time series. The transport delays are consistently estimated to be very small, $t_d \approx 1\ s$. Compared to the results for the full time series — cf. Table 19.2 on page 127 — the estimates of T for 196io4 have been changed significantly by the truncation of the long stimulation sequence.

180 times as large as the summation time used for the sampling transform in Chapter 18: $T \sim 180 \cdot \tau$. The estimate of T for the time series 196io5 is one order of magnitude smaller. There are also quite large variations in the estimates of the linear order n. Contrary to this the transport delay is in three out of four cases estimated to very small: $t_d \approx 1\ s$.

Sensitivity to Summation Time T

The dependences of the loss function V_N as well as the estimates of the linear order n and the transport delay t_d on the summation time T are depicted in Figure 19.7. Note that, in each experiment, the loss

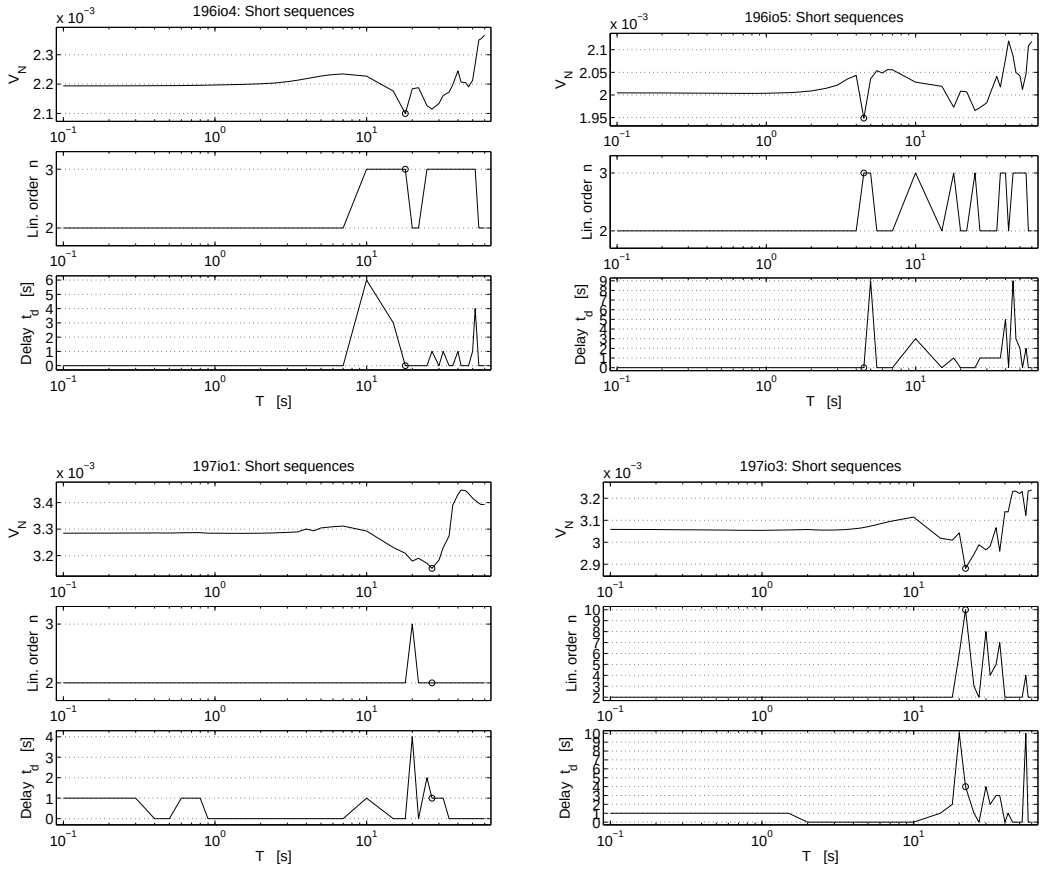

Figure 19.7: The linear black-box model with the input running summation transform applied to the short time series: The dependence of the loss function V_N as well as the estimates of the linear order n and the transport delay t_d on the summation time T. Only the parts of the input-output data sets for inferior olive stimulation where all of the stimulation sequences are 60 s long have been used for system identification. Note, that the value of the loss function only varies a few percent when the summation time is varied. Furthermore, the specific value of the minimum point of the loss function V_N is not always well-defined: Some of the local minima have values very close to that of the global minimum. However, the order of magnitude is well defined in three out of four cases: Around 20 seconds. Note also, that — in contrast to the case of the full time series — the estimate of the linear order n vary with the summation time T — compare with Figure 19.4 on page 127. The estimates of the transport delay t_d vary slightly with the summation time T. For many values of the summation time T the transport delay t_d is estimated to be zero or a single sample, i.e., one second.

function V_N is only slightly sensitive to variations in the summation time T — V_N only varies a few percent. Furthermore, in three out of four cases the value of the estimate of T is not well-defined as there are local minima of V_N with values close to the global minimum. But the order of magnitude is clear: Around 20 seconds. The fact that the linear order is estimated to be higher than two in three out of four cases seems to be a coincidence, since, in each case, the linear order for many other values of the summation time T is estimated to be $n = 2$. Even though the estimates of the transport delay t_d vary somewhat with the choice of summation time T they are usually very small: Zero or a single sample, i.e., a single second.

19.6 Discussion of the Input Running Summation Transform

Properties of the Input Running Summation Transform

When $T > \tau$ we can conceive the input running summation transform as a kind of memory: A FPA event is remembered for a time T and then abruptly forgotten by the system. We will claim that it would be more natural if an event was 'slowly forgotten'. Or, in other words, that the effect of a FPA event on the system decreases with the time elapsed since the occurrence of the event. Mathematically, this could be expressed as

$$u(t) = \sum_{t-T<t_j\leq t} w(t-t_j)\cdot FPA(t_j) \tag{19.7}$$

with the weights fulfilling

$$w(t-t_j) < w(t-t_k) \quad \text{for} \quad t_j < t_k. \tag{19.8}$$

Comparison of Full with Short Sequences

The performance of this linear model is improved when the long stimulation sequence is truncated after a duration of 60 s — compare Tables 19.1 and 19.3 — just as in case of the input sampling transform. Thus we again suggest that this is done in order to minimize the effect of the overgrowth (second increase) on the model properties, and thereby focus the modeling work on the frequency saturation and the dips.

The summation time T seems not to be a good parameter: Even though the loss function V_N is somewhat sensitive to it, its inclusion in the model structure has not improved the model performance at all. The estimate of the linear order depends strongly on whether the long stimulation sequence is to be covered by the model or not: It is estimated to be $n = 2$ for the short time series, but in the range $n = 2 - 10$ in case of the short time series. The transport delay $t_d \approx 1$ s independently of whether the long stimulation sequence is truncated or not.

Chapter 20

Discussion of Linear Black-Box Models

20.1 The Origin of the Model Deficiencies

20.1.1 Properties of the Linear Input Transforms

We have studied two linear input transforms — the sampling transform and the running summation transform:

$$u_s(t) = \sum_{t-\frac{\tau}{2}<t_j\leq t+\frac{\tau}{2}} FPA(t_j), \tag{20.1}$$

$$u_T(t) = \sum_{t-T<t_j\leq t} FPA(t_j). \tag{20.2}$$

In case $T = k\cdot\tau, k\in\mathbb{N}$ the running summation transform can be rewritten in terms of the sampling transform[1]:

$$u_T\left(t+\frac{\tau}{2}\right) = \sum_{t+\frac{\tau}{2}-k\cdot\tau<t_j\leq t+\frac{\tau}{2}} FPA(t_j) = \sum_{t-\frac{\tau}{2}-(k-1)\cdot\tau<t_j\leq t-\frac{\tau}{2}-(-1)\cdot\tau} FPA(t_j) \tag{20.3}$$

$$= \left(\sum_{t-\frac{\tau}{2}-(k-1)\cdot\tau<t_j\leq t-\frac{\tau}{2}-(k-2)\cdot\tau} + \sum_{t-\frac{\tau}{2}-(k-2)\cdot\tau<t_j\leq t-\frac{\tau}{2}-(k-3)\cdot\tau}\right.$$

$$\left. + \cdots + \sum_{t-\frac{\tau}{2}-1\cdot\tau<t_j\leq t-\frac{\tau}{2}-0\cdot\tau} + \sum_{t-\frac{\tau}{2}-0\cdot\tau<t_j\leq t-\frac{\tau}{2}-(-1)\cdot\tau}\right) FPA(t_j) \tag{20.4}$$

$$= \sum_{i=0}^{k-1}\left(\sum_{t-\frac{\tau}{2}-i\cdot\tau<t_j\leq t-\frac{\tau}{2}-(i-1)\cdot\tau} FPA(t_j)\right) = \sum_{i=0}^{k-1}\left(\sum_{t-\frac{\tau}{2}-i\cdot\tau<t_j\leq t+\frac{\tau}{2}-i\cdot\tau} FPA(t_j)\right) \tag{20.5}$$

$$= \sum_{i=0}^{k-1} u_s(t-i\cdot\tau) = \sum_{i=0}^{k-1} q^{-i}u_s(t). \tag{20.6}$$

This is a special case of the finite impulse response (FIR) filter (cf. [55, (p. 2-105)])

$$u_w\left(t+\frac{\tau}{2}\right) = \sum_{i=0}^{k-1} w(i)\cdot u_s(t-i\cdot\tau) = \sum_{i=0}^{k-1} w(i)\cdot q^{-i}u_s(t), \tag{20.7}$$

corresponding to the following choice of filter coefficients: $\{w(i)\}_{i\in[0;k-1]}$ with $w(i) = 1$.

This means that the running summation transform can be obtained by applying this specific finite impulse response filter to the sampling transform. Or with other notation:

$$u_T\left(t+\frac{\tau}{2}\right) = G_k(q)u_s(t), \tag{20.8}$$

[1] The forward shift operator q has been introduced in M: Section 10.1.1 on page 57.

$$G_k(q) \quad = \quad \sum_{i=0}^{k-1} q^{-i}. \tag{20.9}$$

From a frequency-domain perspective the linear filter G_k is a quite peculiar filter to apply, since — as shown in Figure 20.1 — its frequency response is oscillatory. To emphasize the low-pass behavior of the

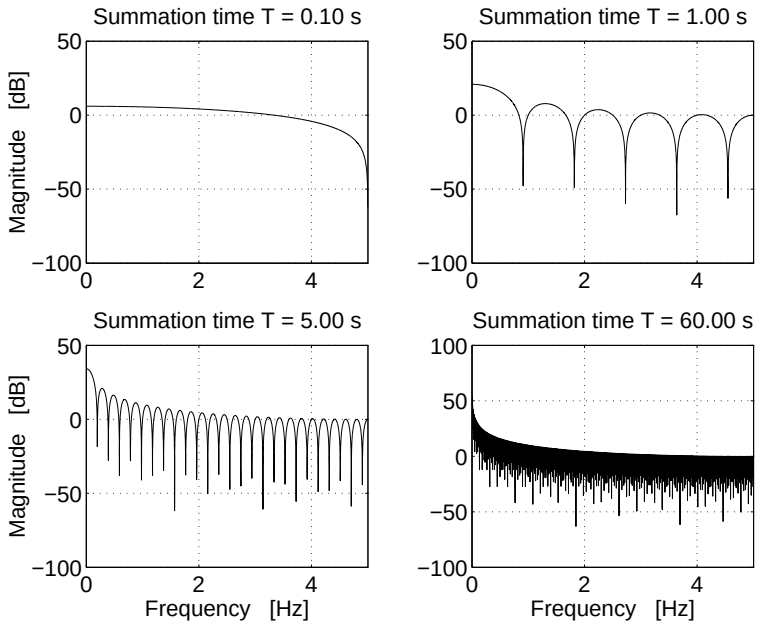

Figure 20.1: The magnitude of the frequency response of the discrete linear FIR filter $G_k(q) = \sum_{i=0}^{k-1} q^{-i}$ for four values of the summation time $T = k \cdot \tau$, where τ is the sampling interval of the CBF signal. Note the low-pass, but oscillatory behavior. The magnitude in decibel $[dB]$ is calculated as $M_{dB}(f) = 20 \cdot \log |G_k(f)|$.

filter, the frequency response is shown with a logarithmic frequency scale in Figure 20.2.

Note that the estimated summation times T correspond to very high order FIR filters: For instance $T = 4.50\ s$ (Table 19.4 on page 131) is equivalent to a 45th order FIR filter ($k = T/\tau = 45$), whereas $T = 26.98\ s$ (Table 19.2 on page 127) corresponds to a 270th order FIR filter ($k = T/\tau = 270$).

20.1.2 Equivalence of Transfer Functions

We note that the model error traces ΔCBF obtained from the two linear input transforms are very similar (compare Figures 18.3 (page 111) and 19.3 (page 126)): They have the same features and are of the same order of magnitude. The model outputs can be written[2]

$$y_{m1}(t) \quad = \quad G_1(q)u_s(t), \tag{20.10}$$

$$y_{m2}(t) \quad = \quad G_2(q)u_T(t) = G_2(q)G_k(q)u_s(t). \tag{20.11}$$

Since $y_{m1}(t) \sim y_{m2}(t)$ we have $G_1(q)u_s(t) \sim G_2(q)G_k(q)u_s(t)$ and thus $G_1(q) \sim G_2(q)G_k(q)$. Thus the poles of G_1 and G_2 must be the same. This is natural since due to the nature of G_k the time constants of the system are reflected only by the poles of G_1 and G_2, respectively.

20.1.3 How to Improve the Model Structure?

We can conclude that the two linear model structures already presented are in-sufficient to describe the system dynamics. There are three obvious[3] ways to improve the model performance: We can test

[2] We have suppressed the time shift $\frac{\tau}{2}$ since it is small compared to the characteristic times in the CBF signal (cf. Section 14.2.2 on page 91).

[3] We could also choose to transform the output signal instead. (If a static transform was applied, the resulting model would be a Wiener model [58, (Sect. 5.2)].) We would, however, still have to transform the event-sampled input signal into

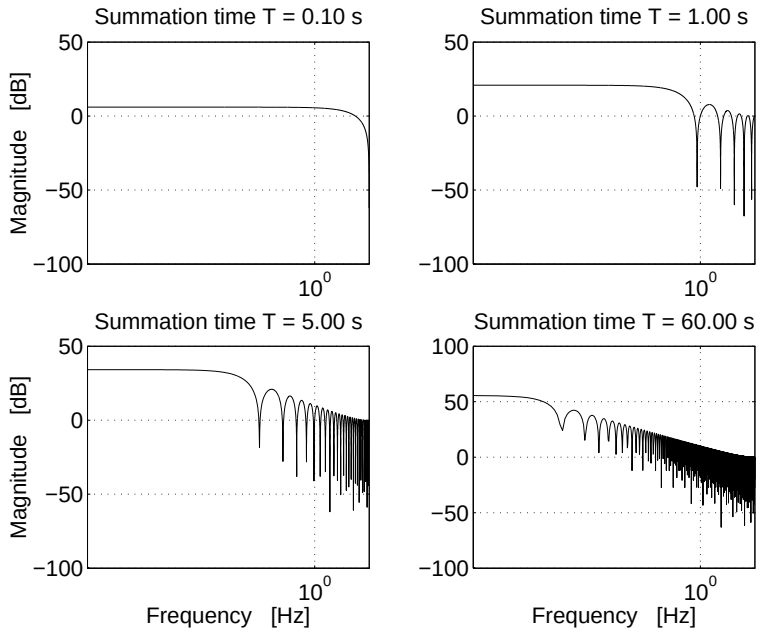

Figure 20.2: The magnitude of the frequency response of the discrete linear FIR filter $G_k(q) = \sum_{i=0}^{k-1} q^{-i}$ for four values of the summation time $T = k \cdot \tau$, where τ is the sampling interval of the CBF signal. The frequency scale is logarithmic. Note that the breakpoint frequency moves towards lower frequencies as the summation time T is increased. When the summation time is decreased towards the sampling time ($T \longrightarrow \tau_+$) the effect of the filter is decreased. The magnitude in decibel $[dB]$ is calculated as $M_{dB}(f) = 20 \cdot \log(|G_k(f)|)$.

- Other linear input transforms,
- Nonlinear input transforms, and
- Nonlinear black-box state-space models.

With respect to other linear filters we have considered a filter composed of the sampling transform followed by a specific choice of a FIR filter $\{w(i)\}_{i\in[0;k-1]}$. Other choices of FIR filters could be considered. Also infinite impulse response (IIR) filters (cf. Ref. [55, (p. 1-35)]), corresponding to $\{w(i)\}_{i\in[0;\infty[}$, could be tested.

20.1.4 Can we Exclude that the System is Intrinsically Linear?

Now take a closer look on Figure 20.3 which shows an example of the input-output data set obtained by the input sampling transform.

Note that during stimulation for 60 s the overall level of the FPA_{pp} signal increases with increasing stimulation frequency whereas the corresponding CBF response first increases and then (after $t \sim 400$ s) decreases. We termed this phenomenon frequency saturation. This phenomenon clearly violates the principle of superposition (cf. M: Section 9.3.3 on page 53): The principle of superposition states that the response to a larger input is a larger output. Thus the frequency saturation cannot be a linear effect.

With respect to the dips and the overgrowth for long stimulation durations the picture is obscured in several ways: First, (for a given stimulation frequency, for instance 5 Hz) these effects are mixed: We cannot study the overgrowth during prolonged stimulation and at the same time avoid the dips. Second, it is possible to study the dips while not having the long stimulation duration. But because the duration of the dips is rather short they are obscured by noise. In total we cannot in this simple way exclude that the dips and the overgrowth for long stimulation durations are due to un-realized linear system dynamics.

a sampled signal.

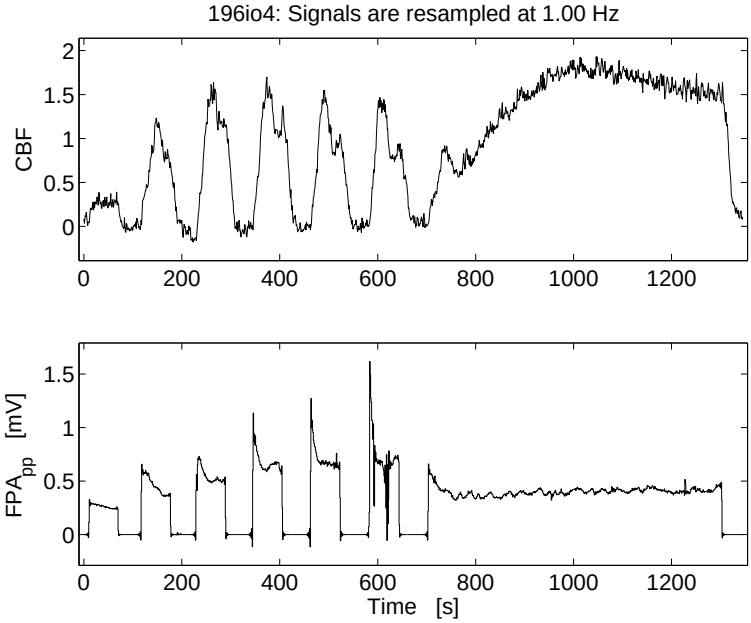

Figure 20.3: The input sampling transform applied to the full time series 196io4 which contain both short (60 s) and long (600 s) stimulation sequences. The input (FPA_{pp}) and output (CBF) signals have been resampled at 1 Hz. These data have also been shown in Figure 18.2 on page 110.

20.2 Exclusion of System Dynamics

We have seen that, both in case of the linear input transform without memory and in the case with memory, the model performance is significantly improved when the 600 s long stimulation sequence is truncated after 60 s. The analysis in Section 14.2.2 on page 91 furthermore showed that for all stimulation frequencies the local maximum before the dip in the CBF signal is reached *later* than 20 s after the onset of stimulation. Therefore we pose the hypothesis that all effects of the overgrowth during prolonged stimulation are excluded if the stimulation duration is kept below 20 s, i.e., the system equations are linearizable in the stimulation duration.

20.3 Comparison of Sampling Transform with Running Summation Transform

Model Performances

By comparing the performance measures listed in Table 19.3 (page 128) with the values shown in Table 18.3 (page 115) we reach the conclusion that the running summation preprocessing procedure is not better than the sampling preprocessing procedure. This means that the performance of the linear black-box model does not depend on the chosen linear preprocessing procedure. Since the estimate of the summation time T is not well defined we will exclude the parameter T from the model structure.

Linear Order of State-Space Model

As the estimates are in the rather large range $n \in [2;\ 10]$ we cannot make a strict conclusion about the linear order. The most frequent occurring value is $n = 2$. Assume that $n = 2$ is a good estimate. Now, the presence of nonlinearities in the neuro-vascular system, which have not been included in the model structure, will have a tendency to result in over-estimation of the linear order n. Thus we expect the true linear order to be two or lower.

Parameter Values

Comparing the Tables 18.2 (page 112), 18.4 (page 118), 19.2 (page 127), and 19.4 (page 131) we reach the conclusion that in most cases the estimate of the transport delay t_d is of the order of zero or a single sample, i.e., less than one second. This means that the transport delay is significantly lower than the characteristic times in the output signal (cf. Table 14.1 on page 91). Therefore we will exclude the transport delay t_d from the model structure.

20.4 Comparison with Earlier Modeling Attempts

As mentioned the running summation was first suggested by Mathiesen *et al.* in Ref. [67]. The suggested static models of the relation between run $\sum_{T(f)} FPA$ and CBF are local in the sense that one model covers one stimulation frequency. The maximum fits were obtained by using summation times $T(f)$ with the values $T(f) = 20\ s$ for $f = 2 - 15\ Hz$ and $T(f) = 30\ s$ for $f = 30\ Hz$. These values are of the same order of magnitude as the values obtained by the global dynamic model investigated in Chapter 19.

Knudsen [53] also investigated the running summation transform. Using a global static linear relation a summation time of $T = 26\ s$ was obtained. Knudsen also considered a dynamic linear model in the form of the input sampling transform in combination with a discrete third-order linear output-error model and found the same deficiencies as have been found in this part: Frequency saturation and dips during short stimulation experiments, and overgrowth during prolonged stimulation sequences.

20.5 Comments upon the Applied Methodology

Estimation of Linear Model Order

MATLAB's automatized choice of linear order of a black-box state-space model takes its starting point from the relative importance of the dimensions of the state vector. The singular values of the Hankel matrices of the impulse response are calculated. The order is chosen such that the singular values for higher orders are comparatively small [60, (p. 4-120)].

Identifiability of Black-Box State-Space Model

As mentioned in M: Section 11.6.2 on page 66 the linear black-box state-space model structure is not identifiable. MATLAB provides two ways of ensuring identifiability: As mentioned one way is to choose the observer canonical form of the model structure. The other way is to let the parameterization of the matrices be completely free and let MATLAB automatically select a basis for the state-space realization which gives well-conditioned calculations [60, (p. 3-42)]. Since in this part we have not focused on the values of the parameter vector, a completely free parameterization has been used.

Sensitivity

Since the used linear black-box state-space model contains a noise model different from the identity matrix $H \neq 1$ (since $\mathbf{K} \neq \mathbf{0}$ — cf. M: Section 10.2.2 on page 58) we cannot apply the sensitivity approach presented in M: Section 12.5 on page 69. Therefore we have used the less rigorous method of studying the dependence of the loss function V_N on a number of parameters.

Other Model Properties

Considerations of bias and variance errors as well as other model properties will be postponed until better performance has been reached — by including appropriate nonlinearities in the model structure.

Chapter 21

Conclusion on Linear Black-Box Models

21.1 System Properties

We have tried out two linear dynamic input pre-processing procedures:

- The input sampling transform, and
- The input running summation transform.

Three features of the experimental data could not be covered by a model consisting of one of the two linear dynamic input pre-processing procedures in combination with a linear black-box state-space model:

- **Frequency saturation:**
  The maximum of the measured blood flow response to stimulation for 60 s is larger for intermediate stimulation frequencies than for low and high frequencies. The maximum of the model output (which is obtained by simulation of the linear models) increases as the stimulation frequency is increased.
- **Dips:**
  The measured blood flow response to stimulation with a particular frequency makes a dip. The bottom of the dip is reached after stimulation for around 45 s. The simulated response only decreases but does not increase again afterwards.
- **Overgrowth during prolonged stimulation:**
  When the stimulation sequence continues beyond the dip at 45 s after the onset of stimulation the measured blood flow response increases drastically. The linear model significantly underestimates the response after 60 s.

We have shown that the frequency saturation violates the principle of superposition and therefore must be a non-linear effect.

Furthermore, the linear order of the neuro-vascular system is around two. The transport delay from input to output is close to zero.

21.2 Conclusions with Respect to System Modeling

The input-output data from the four experiments exposes the same system dynamics. Furthermore, the deviations of the linear dynamics models from the system dynamics are of the same kind for the four experiments. Therefore we expect the four time series to be the results of the same — nonlinear — system dynamics. Thus a single model — which includes the three features mentioned above — should be able to explain the four inferior olive stimulation experiments.

The negative effects of the overgrowth for long stimulation durations on the performance of the linear models are significantly reduced if the stimulation sequences are truncated when they have lasted for 60 s. It has been hypothesized that the effects of the dips as well as the overgrowth for long stimulation durations can be avoided if the stimulation duration is kept below 20 s.

In the following parts we will focus on two features which we will attempt to incorporate into the model: Frequency saturation and dips. Therefore we will consider the truncated time series.

In all cases the estimate of the transport delay is zero or only a few seconds, that is, considerably smaller than the characteristic times in the perfusion signal. Since we do not have a clear indication that the model structure should include a transport delay, in the following parts we will *not* include a transport delay.

Part V

Grey-Box Models

The idea of physical modeling is to break down the properties of the system to subsystems whose behaviors are known — cf. M: Section 11.1 on page 61. Since the present physiological system is not fully described, but currently is exposed to intense research, such a task cannot be carried through. Therefore the goal of this part will be limited to develop models by combining three types of information:

- Physiological insight obtained from literature studies (scientific books and journals). Elements of this insight have been presented in Part I.
- The analysis results presented in Part III.
- The experiences obtained during the experimental modeling which led to the linear black-box models presented in Part IV.

According to M: Section 9.3.10 on page 55 the resulting models will be grey-box models.

Only data from inferior olive stimulation experiments will be considered. However, occasionally comments upon how an idea would have to be treated in case of parallel fiber stimulation experiments will be given. As described in Section 21.2 on page 139 stimulation sequences exceeding 60 s will be truncated.

Chapter 22

Main Ideas for Grey-Box Models

The mathematical models which are developed in this part originates from a set of main ideas which are presented in this chapter. These ideas will be common to models of the two neuro-vascular systems which are involved during inferior olive stimulation experiments and parallel fiber stimulation experiments, respectively.

22.1 Subsystems

The physiological experiment involves evoking electrical activity in the neurons and measuring the resulting excitations of the field potential as well as the change in blood flow in capillaries nearby. However, these subsystems, the one being an electric system, the other a fluid dynamic system, do not interact directly (cf. P: Chapter 6 on page 32), but both interact with an intermediate subsystem: The extracellular space characterized by the concentrations of various chemical substances. This is illustrated by Figure 22.1.

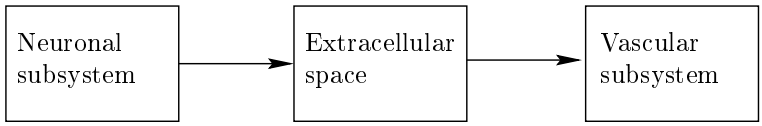

Figure 22.1: A division of the neuro-vascular system in rat cerebellum into three subsystems — inspired by the morphology of cerebellum.

The fact that the neuronal circuitry involved when stimulating the inferior olive (a mono-synaptic system) is different from the one involved when stimulating parallel fibers (a di-synaptic system) — cf. P: Section 3.3.1 on page 22 — probably should be reflected by the equations connecting variables of the neuronal system with those of the extracellular space.

22.2 Measured and Non-Measured Variables

The physiology itself indicates at least two levels of equations as shown in Figure 22.2. The idea is the

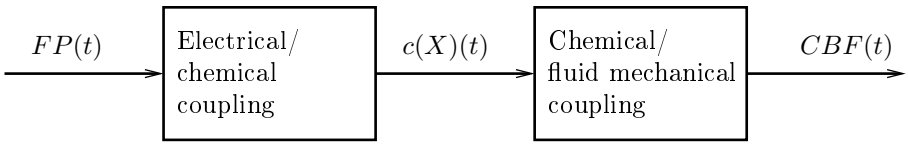

Figure 22.2: A block diagram indicating the need for at least two levels of equations. FP is the field potential, $c(X)$ the concentration of the chemical substance X, and CBF the cerebellar blood flow.

following: Evoked field potentials (FP) indicate neuronal activity (cf. P: Section 7.4.2 on page 46). Neuronal activity causes the release of a chemical substance, X, into the extracellular space (cf. P: Chapter 6 on page 32). The evoked field potential signal being an external input thus acts as a control signal (cf. M: Section 9.2 on page 52). The chemical substance might, however, also be a vasodilator causing the smooth muscles of the arterioles to dilate (cf. P: Chapter 6 on page 32), thereby causing an increase in the capillary blood flow (CBF).

However, since in the present experiments (cf. P: Chapter 7 on page 42) the concentration of the vasodilator $c(X)$ is not measured, it should make up a hidden level in the model structure, thus indicating a state-space model structure of the kind

$$\frac{dc(X)(t)}{dt} = f(c(X)(t), FP(t)), \tag{22.1}$$

$$CBF(t) = g(c(X)(t), FP(t)). \tag{22.2}$$

This is illustrated by Figure 22.3.

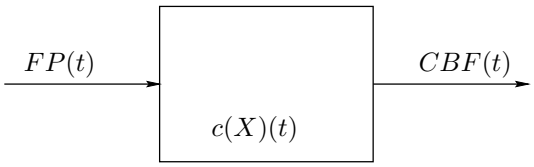

Figure 22.3: Block diagram of a grey-box state-space model of the neuro-vascular system.

22.3 Time Scales

The model connecting input with output has to reach across several orders of magnitude on the time scale: From the field potential varying on a time scale, T_{fast}, of the order of milliseconds (cf. Section 14.1.3 on page 83), to the relative cerebellar blood flow with characteristic times, T_{slow}, of the order of up to tens of seconds (cf. Section 14.2.2 on page 91). Thus the model has to reach across four orders of magnitude — as illustrated by Figure 22.4. This fact indicates the need for creating lumped variables. And thereby the

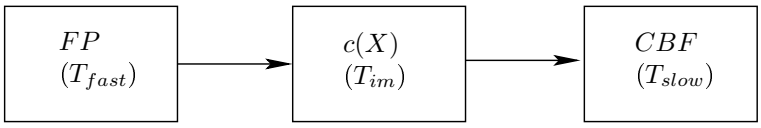

Figure 22.4: Time scales in the subsystems of the neuro-vascular system. T_{fast} is of the order of milliseconds, T_{slow} of the order of up to tens of seconds.

need for pre-processing procedures to bring all variables on the same[1] slow time scale. This is illustrated by Figure 22.5.

The physiology indicates at least one time scale between the input (FP) and the output (CBF): A chemical time scale characteristic of variations in the concentration of the chemical substance X, $c(X)$, in the extracellular space.

Whether the preprocessing procedures should consist of linear and/or nonlinear transformations of the original data depend upon whether the physiological couplings between the three time scales are linear and/or nonlinear. The two types of couplings are now shortly investigated.

[1] In case the input and output signals vary on very different time scales both time scales would be inherited by models of the system. Differential equations that have a great spread of time scales are called *stiff* [61, (p. 99-100, p. 326-327)] and need special treatment.

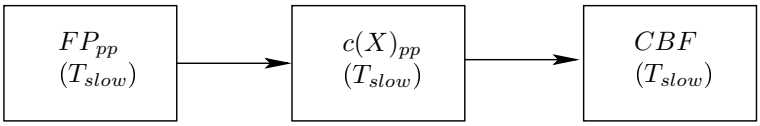

Figure 22.5: The fast and intermediate variables in the neuro-vascular system have been transformed to the slow time scale by means of pre-processing procedures. The resulting variables are given the index *pp*.

22.3.1 Linear Couplings

In case the system is expected to be linear it seems natural to assume that the variable on one time scale do not immediately react to variations on the smaller time scale but rather on the mean value of that variable, thus indicating a model structure of the kind

$$\frac{dc(X)(t)}{dt} = f\left(c(X)(t), \langle FP\rangle_{T_{im}}(t)\right), \tag{22.3}$$

$$CBF(t) = g\left(\langle c(X)\rangle_{T_{slow}}(t), \langle FP\rangle_{T_{slow}}(t)\right), \tag{22.4}$$

where $\langle\cdots\rangle_T$ denotes the time average $\langle h\rangle_T(t) = \frac{1}{T}\cdot\int_{t-\frac{T}{2}}^{t+\frac{T}{2}} h(t')dt'$. T_{im} is the intermediate time scale, $T_{fast} < T_{im} < T_{slow}$, being characteristic for variations in the concentration of the chemical substance. Notice, that time averaging is a linear transformation which also can be viewed as low-pass filtering.

Now to reach a final model having only variations on the scale T_{slow} the variable $c(X)$ is replaced with its time-averaged counterpart[2]:

$$\frac{d\langle c(X)\rangle_{T_{slow}}(t)}{dt} = f\left(\langle c(X)\rangle_{T_{slow}}(t), \langle FP\rangle_{T_{slow}}(t)\right), \tag{22.5}$$

$$CBF(t) = g\left(\langle c(X)\rangle_{T_{slow}}(t), \langle FP\rangle_{T_{slow}}(t)\right). \tag{22.6}$$

Besides averaging, other linear transformations, like integration and convolution, should be considered.

22.3.2 Nonlinear Couplings

In most cases the physiological system is expected to be intrinsically nonlinear. Low-pass filtering of the input and output signals is not an appropriate way of capturing the interesting dynamics of a nonlinear system. Instead other ways of de-modulating the signals must be considered.

22.4 Information Content

Since the data files containing the field potential signals are very large it is now considered how to extract the information content[3] of the FP signal.

As shown in P: Figure 7.4 on page 46 the variation in the waveform of the time-localized excitations of the FP signal is very little between *nearby* events. Furthermore, the analysis in Section 14.1 on page 80 showed that the variation in the shape over longer time intervals mainly pertains to the height, i.e., the amplitude FPA, and *not* to the duration FPD.

Therefore it is feasible to use the time of occurrence and the amplitude of each FPA event instead of the full FP signal. For the case of climbing fiber activation the FPA signal consists of pairs of the event time and the corresponding amplitude of the excitatory post-synaptic potential $(t_j,\ EPSP(t_j))$. For the case of parallel fiber activation the FPA signal would similarly consist of the pairs of the event time and the amplitude of the presynaptic potential $(t_j,\ PSP(t_j))$, and the event time and the amplitude of the excitatory post-synaptic potential $(t_j,\ EPSP(t_j))$ — cf. P: Figure 7.4.

This change in signal representation has the advantage that it reduces the sizes of the data files to be handled significantly.

[2]Since the function $f(x,\cdot)$ is linear Equations (22.3) and (22.5) are equivalent.

[3]The notion of *information content* is here used to denote features of a signal which varies significantly during the time course of an experiment. This is a somewhat weaker sense than the notion of information amount defined within information theory — see Ref. [94].

22.5 Detrending and Scaling of Signals

If a physical level of a signal do not play a role in the model it can be removed from the signal. This is called *detrending*. A standard way of performing detrending is to subtract the mean value [59, (p. 2-8)].

Scaling can be used to get the same order of magnitude of the variables and thereby avoid numerical problems [61, (Sect. 11.2)].

For the case of the CBF signals we have already applied the non-standard way of performing detrending by subtracting the baseline level CBF_B. The CBF signals have furthermore been scaled to the baseline level — cf. Appendix B.4 on page 274. The resulting signals

$$CBF_{rel}(t) = \frac{CBF(t) - CBF_B}{CBF_B} \tag{22.7}$$

have been termed the relative CBF signals.

For the case of the concentration of the chemical substance X, $c(X)$, the situation is more complicated: We can always perform detrending by subtracting the baseline level, and thus create the *concentration deviation signal*

$$n(t) = c(X)(t) - c_B(X). \tag{22.8}$$

However, we can only scale the concentration to the baseline level $c_B(X)$ if it is non-zero, that is, strictly positive, $c_B(X) > 0$. Since this may not be true in general we will not scale concentration variables.

The case of the field potential signal is even more subtle, since we know that the baseline level is zero, $FPA_B = 0$, and thus scaling is impossible. (Detrending would be trivial.) But the size of a measured field potential depends strongly (cf. the point current source [64, (Sect. 8.2.1)]) upon the distance between each source or sink of current in the source-sink distribution and the measurement probe [74, (Sect. 2.3)]. Thus the size of the measured field potential signal is sensitive to the probe position. We will return to this issue in Section 28.2 on page 193.

Note that the ranges of values of the variables are

$$\begin{aligned} FP(t) &\in \mathbb{R}, && (22.9)\\ FPA(t_j) &\geq 0, && (22.10)\\ c(X)(t), c_B(X) &\geq 0, && (22.11)\\ n(t) &\geq -c_B(X), && (22.12)\\ CBF(t) &\geq 0 \quad \text{almost always.} && (22.13) \end{aligned}$$

22.6 Discussion of Main Ideas

Subsystems

The use of such a simple model as the presented division into a few subsystems rises some fundamental questions: Are all of the involved subsystems and all the interconnections between the subsystems identified? Are all of the involved variables for each subsystem, and all couplings between variables identified?

For parallel fiber stimulation experiments, we expect, that it is necessary to include one more subsystem: The glial cell type astrocytes (cf. P: Section 6.2 on page 33). The reason is, that K^+-ions are released during parallel fiber stimulation (cf. P: Section 6.5 on page 39) and are then transported along two pathways from neurons to vessels: Through the extracellular space and through astrocytes. Thus these two subsystems operate in parallel. Furthermore, they are interacting (cf. P: Section 6.3.3 on page 36). In total, we expect that a model of neuro-vascular coupling in case of parallel fiber stimulation need to be more complex than a model of the coupling in case of climbing fiber stimulation.

Note that the vascular subsystem has been described by capillary properties (the perfusion CBF is measured in the capillaries) as well as arteriolar properties (the arterioles, but not the capillaries, react to vaso-active substances).

Measured and Non-Measured Variables

Input and Output Signals

Let us first note that we are not in a position where we can model the 'true' neuro-vascular system. This would require that we were able to fully describe what we mean by terms like 'neuronal activity' and 'cerebellar blood flow', both of which are very complex physiological concepts. Instead we have to deal with certain *indicators* as illustrated by Figure 22.6. We have already stated that the field potential

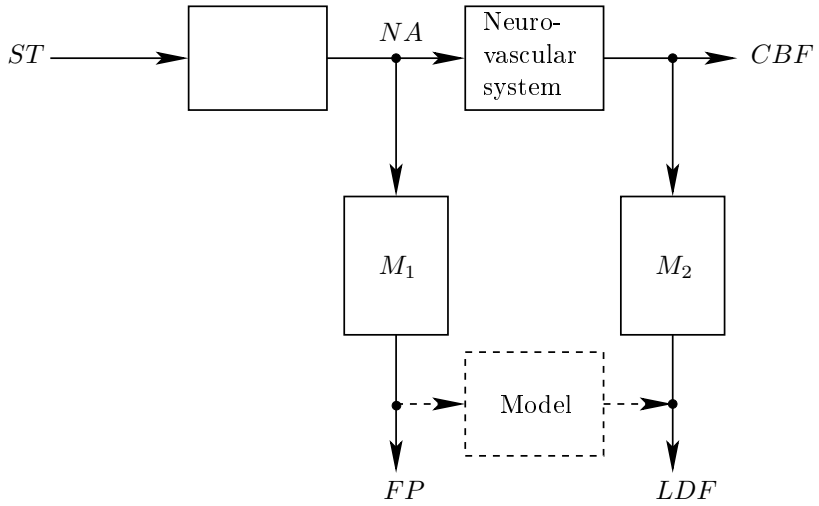

Figure 22.6: Illustration of the relationships between the physiological signals in the neuro-vascular system and the corresponding indicators, i.e. the measured signals. Whereas the neuro-vascular system relates the physiological signals, the model relates the measured indicators. ST: stimulus (external); NA: neuronal activity (internal); CBF: true blood flow; M_1: measurement of neuronal activity; M_2: measurement of blood flow; FP: measured field potential; LDF: blood flow signal measured by LDF.

signal (FP) is only an indicator of the neuronal activity (NA) caused by a stimulation signal (ST). And the LDF signal (LDF) is a signal which is constructed by multiplying a measure of the red blood cell concentration with an average red blood cell speed. Thus this signal is derived from the true perfusion of the capillaries (CBF). The mathematical models, which are developed in this thesis, relates these measured signals, not the physiological signals.

Internal Variables

For the case of IO stimulation, nitric oxide (NO) plays a crucial role as mediator of neuro-vascular coupling (cf. P: Section 6.4 on page 38). Since measurements of the concentration of nitric oxide in the extracellular space are not available, the variable $c(NO)(t)$ has to be an internal variable. Actually, it is quite difficult to measure the local NO concentration. Shibuki *et al.* [85, 86] have fabricated NO probes with a tip diameter of about 300 μm. These probes are thus very large compared to the diameter of, for instance, Purkinje cells, which is around 21 μm (cf. P: Section 3.3.1 on page 22), and they have only been applied for *in vitro* studies of slice preparations.

The situation is different for the case of PF stimulation. The main mediator is K^+-ions (cf. P: Section 6.5 on page 39), it is simple to produce K^+-sensitive microelectrodes with a tip diameter of around $2 - 4$ μm, and measurements have been performed [19, 18]. It seems attractive to start the development of a model of neuro-vascular coupling by modeling the coupling between neuronal activity and the extracellular potassium concentration for two reasons: The relative blood flow response to PF stimulation is smaller and the measurements are more noisy than those obtained during IO stimulation experiments (cf. Appendix A.3.4 on page 271). And the model structure would be smaller due to the lower number of subsystems.

Time Scales

By comparing the $c(K^+)$-signals and the concomitant CBF signals reported in Ref. [19], we conclude that the extracellular potassium concentration varies on a time scale of the order of or slightly faster than the blood flow signal, $T_{im} \leq T_{slow}$. Caesar [18] has also noticed that *"The ion-selective microelectrode and laser-Doppler flowmetry share temporal resolution."* Also the NO measurements in Ref. [85, 86] seem to vary on a time scale of around one second, that is, only slightly faster than the blood flow signal.

Information Content

The idea of using the field potential amplitudes instead of the full field potential signal originates from previous work by Mathiesen *et al.* [66]. Note that — according to the analysis in Section 14.1.3 on page 83 — at low stimulation frequencies it is not true that there is no information in the duration of an excitation of the field potential. This should be considered when evaluating the performance of a model at low frequencies.

Detrending and Scaling of Signals

Caesar *et al.* [19] have measured the baseline level of the extracellular potassium concentration to be $c_B(K^+) \approx 3.5\ mM > 0$, and therefore scaling of this signal could be performed.

Since NO regulates the basal vasomotor tone [28], we expect the baseline concentration level to be strictly positive, $c_B(NO) > 0$, but values seem not to have been reported.

22.7 Conclusion on Main Ideas

Models, which are developed from the ideas presented in this chapter, will be grey-box models because the dynamics model will be inferred from physiology while the noise model will be a black-box model and the parameter values will be estimated by means of the experimental data (cf. M: Section 9.3.10 on page 55).

The presented model principles have potential since for a system which is broken down into subsystems it is possible to experiment with ideas for the nonlinearities in the system: Are they pertaining to the internal dynamics in one or more of the subsystems, or to some of the couplings between the subsystems?

Chapter 23

A Linear Grey-Box Model

23.1 The Grey-Box Dynamics Model

23.1.1 The Dynamics Model

Climbing fiber activity (which has been evoked by stimulation of the inferior olive) causes release of the chemical substance nitric oxide, NO (cf. P: Section 6.4 on page 38). NO is a powerful vasodilator (cf. P: Section 6.3.1 on page 35). In the following it is assumed that (during climbing fiber activity) nitric oxide is the *dominant* mediator of neuro-vascular coupling across the extracellular space. That is, it is assumed that we do not need to take into account other putative mediators.

We suggest the following 2nd order model structure:

$$\frac{dCBF(t)}{dt} = h \cdot n(t) - k \cdot CBF(t), \tag{23.1}$$

$$\frac{dn(t)}{dt} = M(t) - f \cdot n(t) - l \cdot CBF(t). \tag{23.2}$$

In these formulas $n(t)$ is the *preprocessed concentration deviation*, that is, the preprocessed deviation of the concentration of nitric oxide $c(NO)(t)$ in the extracellular space from its baseline value $c_B(NO)$:

$$n(t) = \{c(NO)(t) - c_B(NO)\}_{pp}\,. \tag{23.3}$$

The baseline level $c_B(NO)$ occurs when the climbing fiber is not activated and transients have died out. The function of the unknown preprocessing is to transform the concentration variable $c(NO)(t)$ from the intermediate time scale T_{im} to the slow time scale T_{slow} of the CBF signal (cf. Section 22.3). The term $M(t)$ depends upon the neuronal activity which also causes the field potential $FP(t)$. We assume that the term $M(t)$ is proportional to, and thus linear in, the preprocessed field potential amplitude, i.e.,

$$M(t) = g \cdot FPA_{pp}(t). \tag{23.4}$$

The (so far unknown) preprocessing has the function of transforming the FPA events in the FP signal (which varies on the fast time scale T_{fast}) to the slow time scale T_{slow} of the CBF signal. The model (23.1)–(23.4) is (non-)linear if the term $FPA_{pp}(t)$ is.

23.1.2 Motivation for the Dynamics Model

The parameters in the Equations (23.1)–(23.4) represent various interconnections:

The term containing the parameter h mimics that excess nitric oxide in the extracellular space causes vasodilation (cf. P: Section 6.3.1 on page 35).

The k term represents the tendency of the smooth muscles cells in the vascular wall of the arterioles to relax to their unstrained state (cf. P: Section 5.2.1 on page 28). It prevents CBF from increasing without limits.

The term containing f mimics flux scavenging due to diffusion in the extracellular space (cf. P: Section 4.3.2 on page 27).

The l term represents the fact that the most important sink for nitric oxide and other vasodilators is the blood flow, that is, the perfusion prevents nitric oxide from accumulating in the vessel walls (cf. P: Section 6.3.1 on page 35).

The term containing the parameter g means that neuronal activity (which is indicated by the field potential) causes the release of nitric oxide into the extracellular space (cf. P: Section 6.3.1 on page 35 and P: Section 6.4 on page 38). In case the concentration of nitric oxide in the extracellular space does not react instantly to this indicator of neuronal activity but reacts with a certain transport delay time, $t_d > 0$, the relation should be:

$$M(t) = g \cdot FPA_{pp}(t - t_d). \tag{23.5}$$

However, the experience from the linear black-box models investigated in Part IV is that $t_d \approx 0$ s.

23.2 Choice of Input Transform

It remains to be specified how the continuous and slowly varying preprocessed concentration deviation $n(t)$ reacts to the discrete FPA events.

As a first attempt we choose the preprocessed field potential amplitude signal to be given by the linear dynamic input sampling transform first presented in Section 18.1 on page 108:

$$FPA_{pp}(t) = \sum_{t-\frac{\tau}{2}<t_j\leq t+\frac{\tau}{2}} FPA(t_j). \tag{23.6}$$

According to Equations (23.2)–(23.4) it corresponds to assume that each FPA event contributes to the rate of change of the concentration deviation in proportion to its size, and that the effects of the individual FPA events are accumulated.

23.3 A Linear State-Space Model

23.3.1 The Linear State-Space Model Structure

The model structure (23.1)–(23.4) can be rewritten as a linear state-space model connecting the input

$$u(t) = FPA_{pp}(t) \tag{23.7}$$

(which is a linear dynamic transformation of the original input) with the output

$$y(t) = CBF(t) \tag{23.8}$$

through an internal 2-dimensional state vector

$$\mathbf{x}(t) = \begin{pmatrix} CBF(t) \\ n(t) \end{pmatrix}. \tag{23.9}$$

The linear state-space model reads:

$$\dot{\mathbf{x}}(t) = \mathbf{F}\mathbf{x}(t) + \mathbf{G}u(t), \tag{23.10}$$

$$y(t) = \mathbf{H}\mathbf{x}(t) + Ju(t) \tag{23.11}$$

with the matrices being

$$\mathbf{F} = \begin{pmatrix} -k & h \\ -l & -f \end{pmatrix}, \quad \mathbf{G} = \begin{pmatrix} 0 \\ g \end{pmatrix}, \quad \mathbf{H} = \begin{pmatrix} 1 & 0 \end{pmatrix}, \quad J = 0. \tag{23.12}$$

The purpose of this rewriting is two-fold: To ease the mathematical analysis of the model and to ease the implementation of the model in MATLAB.

At this stage we can conclude that in the process of constructing the dynamics model, we have tacitly made some assumptions: The fact, that element (1,2) in the matrix $\mathbf{H}$ has been fixed to the value zero, $h_{12} = 0$, corresponds to the assumption that the CBF response does *not* depend statically on the concentration deviation n. Similarly, it has been assumed that CBF does *not* depend directly ($J = 0$

and $g_{11} = 0$) on FPA_{pp}, i.e., the coupling of neuronal activity to blood flow always acts through the extracellular space. This assumption may be justified by comparison to the parallel fiber system for which Iadecola [44] has claimed that *"The increases in flow are unlikely to be secondary to direct effects of electrical currents on vascular smooth muscles."*, and that *"It is also unlikely that the changes in CBF are due to activation of vasodilator nerves on cerebellar arteries."*

23.3.2 The Parameter Vector

The parameter vector reads $\theta = (f, g, h, k, l)^T$ and is 5-dimensional. The dynamics model has been constructed such that we expect the parameters in it to be non-negative: $f, g, h, k, l \geq 0$.

From the Equations (23.1)–(23.4) the units of the parameters can be identified. They are:

$$[f] = \frac{1}{s}, \tag{23.13}$$

$$[g] = \frac{mol}{ml \cdot s \cdot mV}, \tag{23.14}$$

$$[h] = \frac{ml}{mol \cdot s}, \tag{23.15}$$

$$[k] = \frac{1}{s}, \tag{23.16}$$

$$[l] = \frac{mol}{ml \cdot s}. \tag{23.17}$$

Note furthermore the units of the following products

$$[g \cdot h] = \frac{1}{s^2 \cdot mV}, \tag{23.18}$$

$$[f \cdot k] = [h \cdot l] = \frac{1}{s^2}. \tag{23.19}$$

The sampling interval has the unit

$$[\tau] = s. \tag{23.20}$$

The sampling interval, τ, of the 1 Hz signals is not exactly equal to one second, but $\tau = 0.99936$ s.

23.4 Identifiability of the State-Space Model

The identifiability properties of the state-space model (23.10)–(23.12) will be addressed by studying the equivalent transfer function description (cf. M: Section 11.6.3 on page 66).

Following M: Section 10.2.2 on page 58 we calculate the transfer function from input u to output y

$$G(s) = \frac{Y(s)}{U(s)} = \frac{CBF(s)}{FPA_{pp}(s)} = \mathbf{H}\left(s\mathbf{I}_2 - \mathbf{F}\right)^{-1}\mathbf{G} + J \tag{23.21}$$

$$= \frac{g \cdot h}{(s+f)(s+k) + h \cdot l} = \frac{g \cdot h}{s^2 + (f+k)s + (f \cdot k + h \cdot l)}. \tag{23.22}$$

From this expression several conclusions arise: Firstly, the grey-box dynamics $G(s)$ is constrained in the sense that it has the form $G(s) = \frac{b_2}{s^2 + a_1 s + a_2}$ which contains 3 parameters, whereas the equivalent 2nd order black-box dynamics reads $G_{bb}(s) = \frac{b_1 s + b_2}{s^2 + a_1 s + a_2}$ and contains 4 parameters (cf. M: Section 10.2 on page 58). Secondly, the parameters g and h are not separately identifiable. Only their product $g \cdot h$ is uniquely identifiable since it appears in the expression as a single parameter. Similar conclusions can be made for $f + k$ and $f \cdot k + h \cdot l$. Thus the model contains 5 parameters, $\theta = (f, g, h, k, l)^T$, but only 3 parameters are identifiable: $g \cdot h$, $f + k$, and $f \cdot k + h \cdot l$.

In order to be able to extract the three identifiable parameters, we perform a so-called similarity[1] transformation. For reasons which will be made clear later on (cf. Section 27.3) we choose to transform

[1] A *similarity transformation* changes the state (and thus the couplings between the input and the state as well as between the state and the output) but preserves the input-output properties (that is, the transfer function $G(s) = \frac{Y(s)}{U(s)}$) [37, (Sect. 7.2.1)].

the model to observer canonical form (cf. M: Section 11.6.2 on page 66, and Ref. [58, (Sect. 4.3)]). The following non-singular matrix T performs this task:

$$\mathbf{x} = \mathbf{T}\widetilde{\mathbf{x}}, \quad \widetilde{\mathbf{x}} = \mathbf{T}^{-1}\mathbf{x}, \tag{23.23}$$

$$\mathbf{T} = \begin{pmatrix} 1 & 0 \\ -\frac{f}{h} & \frac{1}{h} \end{pmatrix}, \quad \mathbf{T}^{-1} = \begin{pmatrix} 1 & 0 \\ f & h \end{pmatrix}, \quad \det \mathbf{T} = \frac{1}{h} \neq 0. \tag{23.24}$$

It results in the following transformations of signals and matrices

$$\widetilde{CBF}(t) = CBF(t), \tag{23.25}$$

$$\widetilde{n}(t) = f \cdot CBF(t) + h \cdot n(t), \tag{23.26}$$

$$\widetilde{\mathbf{x}}(t) = \mathbf{T}^{-1}\mathbf{x} = \begin{pmatrix} \widetilde{CBF}(t) \\ \widetilde{n}(t) \end{pmatrix}, \tag{23.27}$$

$$\widetilde{\mathbf{F}} = \mathbf{T}^{-1}\mathbf{F}\mathbf{T} = \begin{pmatrix} -a_1 & 1 \\ -a_2 & 0 \end{pmatrix} = \begin{pmatrix} -(f+k) & 1 \\ -(f \cdot k + h \cdot l) & 0 \end{pmatrix}, \tag{23.28}$$

$$\widetilde{\mathbf{G}} = \mathbf{T}^{-1}\mathbf{G} = \begin{pmatrix} b_1 \\ b_2 \end{pmatrix} = \begin{pmatrix} 0 \\ g \cdot h \end{pmatrix}, \tag{23.29}$$

$$\widetilde{\mathbf{H}} = \mathbf{H}\mathbf{T} = \mathbf{H} = \begin{pmatrix} 1 & 0 \end{pmatrix}, \tag{23.30}$$

$$\widetilde{J} = J = 0. \tag{23.31}$$

We note, that the new state variable $\widetilde{n}$ has no direct physical interpretation. The unit of $\widetilde{n}$ is

$$[\widetilde{n}] = \frac{1}{s}. \tag{23.32}$$

Furthermore, this form contains the three identifiable parameters $g \cdot h$, $f + k$, and $f \cdot k + h \cdot l$. The model now reads

$$\dot{\widetilde{\mathbf{x}}}(t) = \widetilde{\mathbf{F}}\widetilde{\mathbf{x}}(t) + \widetilde{\mathbf{G}}u(t), \tag{23.33}$$

$$y(t) = \widetilde{\mathbf{H}}\widetilde{\mathbf{x}}(t) + \widetilde{J}u(t). \tag{23.34}$$

23.5 Choice of Noise Model

As we have no interest in the process noise acting on the states $\widetilde{\mathbf{x}}$ we choose to consider the continuous time output-error state-space model structure (cf. M: Section 10.2.2 on page 58)

$$\dot{\widetilde{\mathbf{x}}}(t) = \widetilde{\mathbf{F}}(\theta)\widetilde{\mathbf{x}}(t) + \widetilde{\mathbf{G}}(\theta)u(t), \tag{23.35}$$

$$y(t) = \widetilde{\mathbf{H}}(\theta)\widetilde{\mathbf{x}}(t) + \widetilde{J}(\theta)u(t) + e(t). \tag{23.36}$$

This model structure only contains measurement noise acting on the output.

23.6 Overview of the Linear Grey-Box Model

The Initial Condition

The initial value of the state vector

$$\widetilde{\mathbf{x}}_0 = \widetilde{\mathbf{x}}(t)_{|t=t_0} = \begin{pmatrix} CBF_0 \\ \widetilde{n}_0 \end{pmatrix} = \begin{pmatrix} CBF(t)_{|t=t_0} \\ \widetilde{n}(t)_{|t=t_0} \end{pmatrix} \tag{23.37}$$

at the beginning of the experiment (time t_0) consists of two numbers: The constant CBF_0 which is fixed to the value of the first measurement of CBF; and the parameter $\widetilde{n}_0$ which is estimated, but not reported, since its value is expected to vary from experiment to experiment.

The Model Structure

Continuous time as well as the sampling instant of the CBF signal are denoted t. The sampling interval is denoted τ. The event time of the event-sampled FPA signal is denoted t_j.

$$u(t) = FPA_{pp}(t) = \sum_{t-\frac{\tau}{2}<t_j\leq t+\frac{\tau}{2}} FPA(t_j), \tag{23.38}$$

$$y(t) = CBF(t), \tag{23.39}$$

$$\widetilde{n}(t) = f \cdot CBF(t) + h \cdot n(t) = f \cdot CBF(t) + h \cdot \{c(NO)(t) - c_B(NO)\}_{pp}, \tag{23.40}$$

$$\widetilde{\mathbf{x}}(t) = \begin{pmatrix} CBF(t) \\ \widetilde{n}(t) \end{pmatrix}, \tag{23.41}$$

$$\dot{\widetilde{\mathbf{x}}}(t) = \widetilde{\mathbf{F}}\widetilde{\mathbf{x}}(t) + \widetilde{\mathbf{G}}u(t), \tag{23.42}$$

$$y(t) = \widetilde{\mathbf{H}}\widetilde{\mathbf{x}}(t) + \widetilde{J}u(t) + e(t), \tag{23.43}$$

$$\widetilde{\mathbf{F}} = \begin{pmatrix} -(f+k) & 1 \\ -(f\cdot k + h\cdot l) & 0 \end{pmatrix}, \quad \widetilde{\mathbf{G}} = \begin{pmatrix} 0 \\ g\cdot h \end{pmatrix}, \quad \widetilde{\mathbf{H}} = \begin{pmatrix} 1 & 0 \end{pmatrix}, \quad \widetilde{J} = 0. \tag{23.44}$$

The Parameter Vector

The parameter vector to be estimated contains all of the parameters in the linear grey-box model:

$$\theta_e = (g \cdot h, f + k, f \cdot k + h \cdot l, \widetilde{n}_0)^T, \tag{23.45}$$

which is 4-dimensional. Only the values of the three parameters $g \cdot h$, $f + k$, and $f \cdot k + h \cdot l$ will be reported.

23.7 The System Identification Task

23.7.1 Implementation of the Model in MATLAB

A standard MATLAB function (`idgrey` [60, (p. 4-69)]) is used to implement the grey-box model in the form of a state-space model. The function uses zero-order hold (cf. M: Section 10.3.2 on page 59) to digitize the equations, but returns the continuous-time model parameter values.

The 4-dimensional parameter space is searched through in order to find a (hopefully the global) minimum of the loss function $V_N(\theta)$. For many initial value sets $\theta^{(0)}$ the search routine gets stuck in local, non-optimal, minima of $V_N(\theta)$ (cf. M: Section 11.5 on page 64). Therefore, before the actual identification procedure, a preliminary search is made to find good initial value sets. This is done by testing 100 sets of initial values, which have been found by means of random number generators (`rand`, [68, (p. 400)]), and for each time series choosing the set of initial values which results in the lowest noise-to-signal ratio NSR as the initial value set to start the iterative search from.

The maximum number of iterations used in the search for the minimum of the loss function is changed from the default value 20 to 1000 to ensure enough available iterations to reach the minimum and thereby obtain smoother noise-to-signal ratio surfaces.

23.7.2 Information on Experiments and Input-Output Data Sets

As in the previous part the model is tested on data from experiments performed on two male Wistar rats: No. 196 and no. 197. The conditions specific to each experiment are listed in Table A.1 on page 262.

The FPA signal is preprocessed according to the linear input sampling transform stated in Section 23.2 on page 149, and both the input and output signals are resampled at 1 Hz. The resulting input-output data sets will be used for system identification and are shown in Figure 18.5 on page 114.

23.8 The Model Results

23.8.1 Model Fit

The obtained noise-to-signal ratios NSR are listed in Table 23.1. Also the peak-to-peak values of the model errors ΔCBF_{pp} are listed. Note that the noise level is quite high, and that the peak-to-peak value

Series	ΔCBF_{pp}	NSR [%]
196io4	0.99623	24.5
196io5	1.24162	35.4
197io1	0.87976	37.9
197io3	1.10024	53.4
Mean	1.05446	37.8

Table 23.1: The grey-box model with the input sampling transform: The peak-to-peak values of the model error ΔCBF_{pp} and the noise-to-signal ratios NSR obtained from each of the four inferior olive stimulation experiments. Below their arithmetic mean values (*mean*) are listed. Note that these numbers are very close to those obtained by the equivalent linear black-box model — see Table 18.3 on page 115.

of the model error is of the same size as the signal response itself. This means that the model is *not* able to track *all* of the dynamical properties of the system. The numbers are very close to those obtained by the equivalent linear black-box model (Table 18.3 on page 115). That is a result of two differences: As mentioned in Section 23.4 the state-space part of the grey-box model contains one parameter less than the equivalent black-box model. And the noise model is fixed to the value one in the grey-box model but estimated in the linear black-box model[2].

For each of the four time series the model output is compared to the measured output in Figure 23.1. The corresponding model errors ΔCBF are depicted in Figure 23.2. From these figures it is concluded that there is a high degree of structure in the model errors. Two features of the measured CBF signal cannot be explained by the suggested linear grey-box model:

- **Frequency saturation**:
  The maximum of the measured CBF signal response to stimulation for 60 s is larger for intermediate stimulation frequencies than for low and high frequencies. The maximum model output increases with increasing stimulation frequency.

- **Dips**:
  The measured blood flow response to stimulation with a particular frequency makes a dip around 45 s after the onset of stimulation. The model output only decreases but does not increase again afterwards.

This implies that the model structure is not complete. This conclusion has been expected since already the linear black-box models in Part IV revealed these features. Since there is a high degree of systematics in the model error, it might be rather easy to incorporate these features in the model.

[2] For the linear black-box model, the sum of squared prediction errors is minimized; for the grey-box model, the sum of squared output errors is minimized.

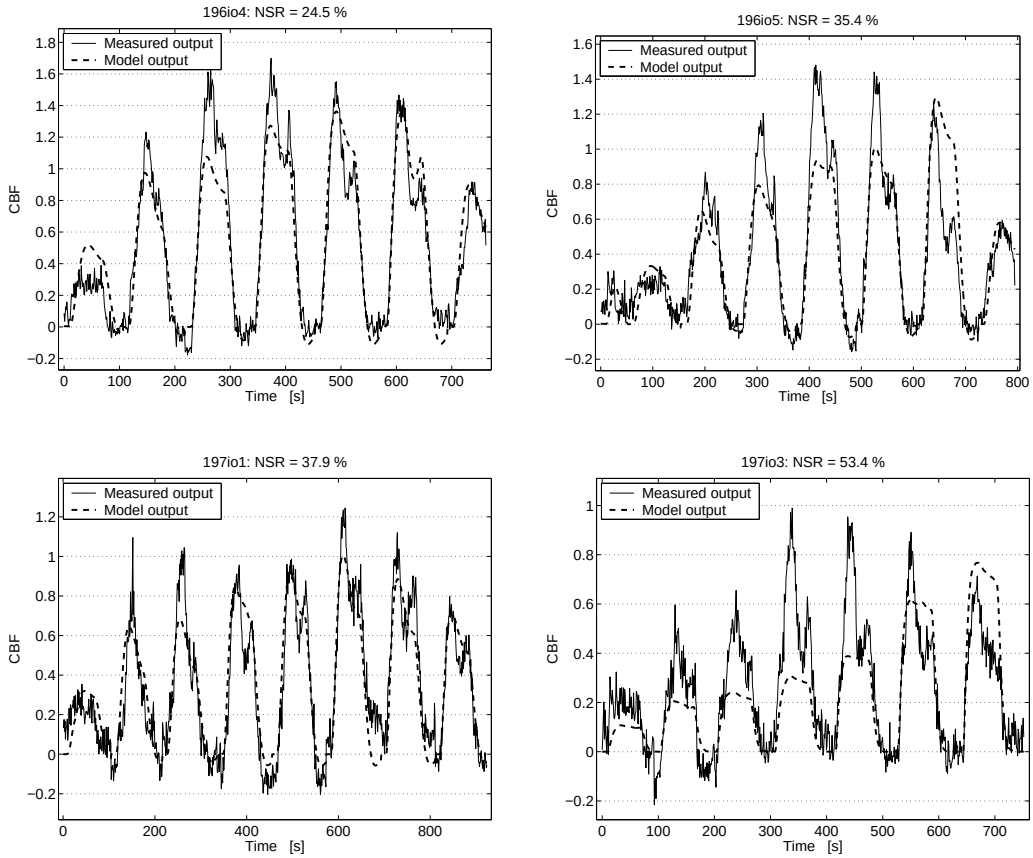

Figure 23.1: The grey-box model with the input sampling transform: Comparison of the model output (dashed line) with the output measured by the LDF probe `Re140` (full line) for each of the four time series. Note that, whereas the measured CBF signal is largest at intermediate stimulation frequencies, the maximum model output increases with increasing stimulation frequency. Note also that the linear grey-box model cannot reproduce the dips in the CBF signal, which occur around 45 s after onset of stimulation.

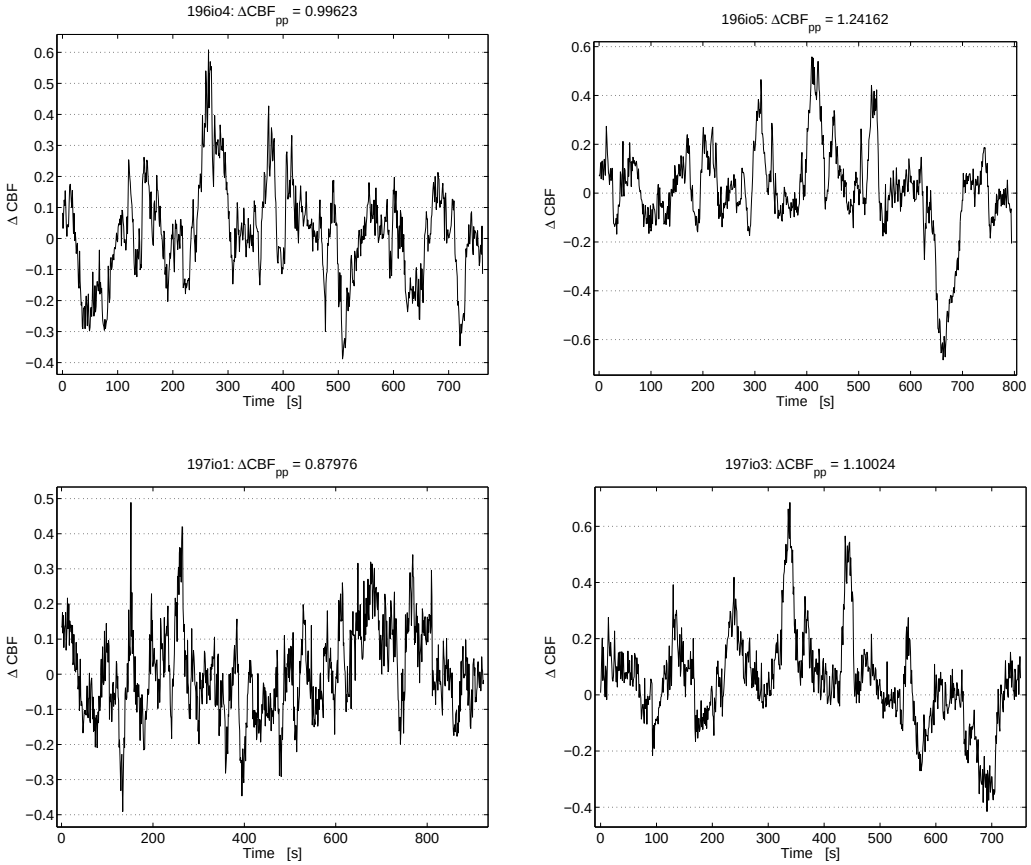

Figure 23.2: The grey-box model with the input sampling transform: The model error ΔCBF, i.e., the difference between the measured output and the model output for each of the four time series. Note the systematics in the time series: The model error is typically positive during stimulation with low frequencies (early in the time series), but negative during stimulation with high frequencies (late in the time series). This is due to the frequency saturation. For a given frequency the model error typically peaks twice. The reason is that the dips cannot be reproduced by the linear model structure.

23.8.2 Cross Validation

The parameter values identified for each of the four time series are listed in Table 23.2. For all parameters

Series	$g \cdot h$ $\left[\frac{1}{s^2 \cdot mV}\right]$	$f + k$ $\left[\frac{1}{s}\right]$	$f \cdot k + h \cdot l$ $\left[\frac{1}{s^2}\right]$
196io4	0.02080	0.13014	0.01210
196io5	0.02721	0.14230	0.01329
197io1	0.04474	0.13202	0.01144
197io3	0.04031	0.40214	0.04905
Mean	0.03327	0.20165	0.02147
Std	0.01116	0.13377	0.01840
Cv	0.33536	0.66336	0.85713

Table 23.2: The grey-box model with the input sampling transform: The parameter values estimated from the four time series. Also listed are their mean values (*mean*), standard deviations (*std*), and their coefficients of variance (*cv*). Note that the coefficient of variance of $g \cdot h$ is smaller than the coefficients of variance of $f + k$ and $f \cdot k + h \cdot l$.

the coefficient of variance is below one, and the coefficients of variance of $f+k$ and $f \cdot k+h \cdot l$ are somewhat higher than that of $g \cdot h$. Even though the values of the coefficients of variance are below one, we may still claim that they are quite high. This has been expected because of the variation in the experimental conditions listed in Table A.1 on page 262. Note that there seems to be a systematic differences between the two rats: The estimates of $g \cdot h$ differs significantly from one rat to the other. This feature may be a result of the lack of scaling of the FPA signal — cf. Section 22.5 on page 145.

23.9 Conclusion on the Linear Grey-Box Model

The grey-box model with the input sampling transform consists of two parts: A linear dynamic transformation without memory of the amplitudes of the discrete events in the field potential signal to a slowly varying signal which forms the input to a linear state-space model with coupled and constrained parameters. The input sampling transform gives equal weight to the amplitude of each field potential event. The relative cerebellar blood flow signal forms the output from the state-space model.

The results of the linear grey-box model with the input sampling transform have revealed severe systematic deficiencies of the linear model structure. The result of the deficiencies is that two features of the measured output signal cannot been covered by the model: Frequency saturation and dips. These deficiencies are of the same kinds as those of the linear black-box models investigated in Part IV.

Chapter 24

Ideas for Nonlinear Grey-Box Models

This chapter is concerned with an attempt to account for the frequency saturation displayed by the cerebellar blood flow signal in case of stimulation of the inferior olive. This is done by changing the linear preprocessing of the field potential amplitude signal into a dynamic nonlinearity. The resulting model can be described by the block diagram shown in Figure 24.1.

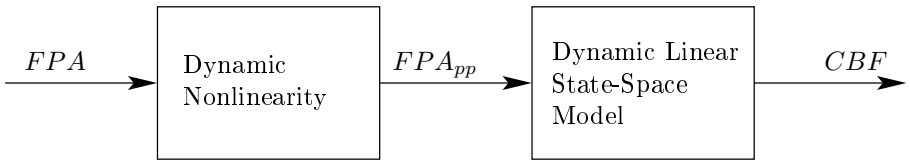

Figure 24.1: A block diagram showing a dynamic model: A dynamic nonlinearity followed by a dynamic linearity. The linear model is taken to be the previously developed grey-box state-space model.

24.1 Motivation and Physiological Picture

For the case of stimulation of the inferior olive, the FPA signal, which consists of the excitatory post-synaptic potential ($EPSP$) amplitudes, has been recorded at the depth of $300 - 400\ \mu m$ below the pial surface (cf. Table A.1 on page 262) corresponding to the proximal dendrites and the Purkinje cell body layers (cf. P: Section 7.3.2 on page 43).

In the soma-dendrite region of a post-synaptic cell the electrical and chemical influences from pre-synaptic axon terminals evoke synaptic potentials. These are initiated in the contact area (the synapse) and propagate across the remainder of the soma-dendrite membrane with decreasing amplitude (cf. P: Section 3.2.3 on page 20).

Inspired by these facts we suggest that larger field potential amplitudes cause *relatively* larger contributions to the change in NO concentration in the extracellular space than do smaller ones. By this is meant that large FPA's result in contributions to the change proportional to their size, whereas smaller FPA's result in contributions significantly smaller than their sizes indicate.

24.2 The Input Weight Transform

The physiological picture described above can be comprised by the previously developed grey-box model by changing the preprocessing of the FPA signal in the following way:

In the transformation of the event-sampled FPA signal into a $10\ Hz$ sampled signal a weight function is used to give higher weight to larger FPA's than to smaller ones:

$$FPA_{pp}(t) = \sum_{t-\frac{\tau}{2}<t_j\leq t+\frac{\tau}{2}} \{FPA(t_j)\cdot w(FPA(t_j))\}\,. \tag{24.1}$$

The registration times of the sampled cerebellar blood flow signal are denoted by t, and the sampling interval by τ. Similarly t_j is the registration time of the j'th event in the event-sampled FPA signal. The function w is the *weight function*. This expression, which will be termed the *input weight transform*, is a nonlinear transformation. This preprocessed FPA signal is taken to be representative of the neuronal activity upon which the concentration of NO in the extracellular space reacts.

The weight function w must posses certain properties:

- The effect of a FPA event cannot be larger than its size suggests. Therefore the values of the weight function must be in the range[1]

$$w(FPA) \in [0, 1]. \tag{24.2}$$

- Since large potentials contribute *relatively* more to the concentration change than smaller ones the weight function must be increasing:

$$\frac{dw}{dFPA} \geq 0. \tag{24.3}$$

This is illustrated by Figure 24.2.

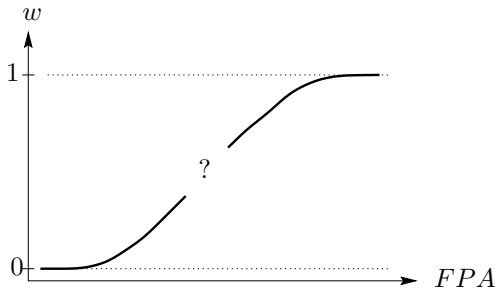

Figure 24.2: A schematic drawing showing the fundamental properties of the weight function w.

The following chapters investigate specific choices of the weight function w.

24.3 Discussion of Ideas for Nonlinear Grey-Box Models

Relation to Other Models

Supervised learning as a strategy to train artificial neural networks has been suggested as a model of cerebellum [29]. The presented type of nonlinearity shares some properties with a type often used when constructing artificial neural networks. Both types involves giving weights to the inputs [88]. But in artificial neural networks the weights represent couplings across synapses, i.e., between pre- and post-synaptic activity. In the model presented here the weights represent couplings between (post-synaptic activity in) a neuron (the Purkinje cell) and its surrounding medium (the extracellular space). On the other hand, the weight function presented here shares some properties with the activation function in artificial neural networks: The activation function is usually monotonically increasing and maps the input domain (the post-synaptic potentials) onto a finite domain [104, 88].

Expected Performance Improvement

From a purely mathematical point of view it is expected that the inclusion of an increasing weight function in the model structure will improve the model performance: The analysis in Section 14.1.2 on page 82 showed that the overall level of FPA values decreases with increasing frequency. On the other hand, according to Section 18.4.1 on page 114 the sampling transformed input increases with increasing frequency. Thus, the weight function will primarily suppress high-frequency FPA events, and thereby decrease the weight transformed input signal at higher frequencies. That is, an increasing weight function will cause frequency saturation (of the input signal).

[1] Choosing the range to be different, $[0,\ a], a \neq 1$, simply corresponds to a scaling of the parameter g in the linear grey-box state-space model (cf. Section 23.3.1 on page 149).

Chapter 25

The Input Threshold Transform

25.1 The Input Threshold Transform

As a first attempt the weight function w of Equation (24.1) is modeled as a Heaviside function:

$$w(FPA) = \theta(FPA - FPA_0) = \begin{cases} 1 & \text{for} \quad FPA \geq FPA_0 \\ 0 & \text{for} \quad FPA < FPA_0 \end{cases} \tag{25.1}$$

with FPA_0 being the *threshold position*. The Heaviside function is illustrated in Figure 25.1.

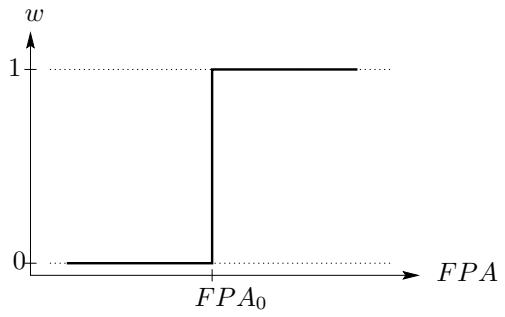

Figure 25.1: The weight function w modeled as a Heaviside function. The threshold position is denoted FPA_0.

The preprocessed FPA signal thus reads

$$FPA_{pp}(t) = \sum_{t-\frac{\tau}{2} < t_j \leq t+\frac{\tau}{2}} \{FPA(t_j) \cdot \theta(FPA(t_j) - FPA_0)\} . \tag{25.2}$$

This nonlinear dynamic transform contains one parameter and will be called the *input threshold transform*. The resulting preprocessed field potential amplitude signal for four values of the threshold position as well as the cerebellar blood flow to be reproduced (resampled to 1 Hz) are shown in Figure 25.2 for the time series 196io5.

25.2 Implementation of the Model in MATLAB

The parameter FPA_0 is estimated by considering how the noise-to-signal ratio NSR varies with the parameter FPA_0. The value of FPA_0 which results in the lowest noise-to-signal ratio is chosen as the estimate of FPA_0.

For each value of the parameter FPA_0 the estimation of the parameters $g \cdot h$, $f+k$, $f \cdot k+h \cdot l$, and $\widetilde{n}_0$ in the linear state-space model is initiated at the values determined from the linear input sampling transform — cf. Table 23.2 on page 156.

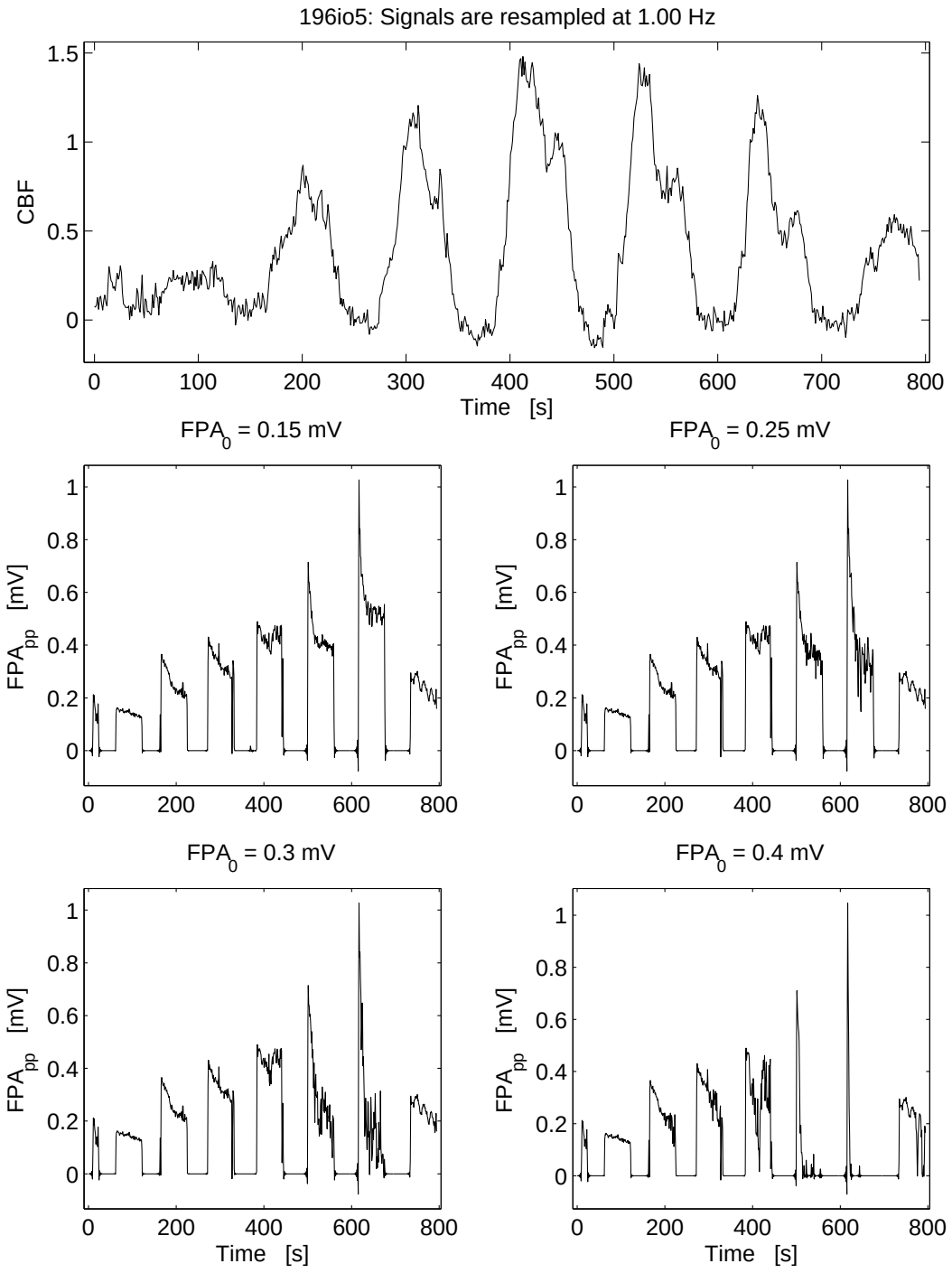

Figure 25.2: Top panel: The cerebellar blood flow signal to be reproduced. Other panels: The FPA signal preprocessed according to the input threshold transform for four values of the threshold position FPA_0. The size of each FPA event is weighted by the value of a Heaviside function. The signals, which are from the time series 196io5, have been resampled by a factor 10. Note that, as FPA_0 is increased, the FPA_{pp} signal content moves from larger frequencies (later in the time series) towards smaller frequencies (earlier in the time series).

25.3 Model Results

25.3.1 Model Fit

In Table 25.1 the obtained peak-to-peak values of the model error ΔCBF_{pp} as well as the noise-to-signal ratios NSR are shown. This table should be compared to Table 23.1 on page 153 which shows the result

Series	ΔCBF_{pp}	NSR [%]
196io4	1.00935	23.9
196io5	0.74357	26.2
197io1	0.88018	37.9
197io3	0.89406	44.1
Mean	0.88179	33.0

Table 25.1: The grey-box model with the input threshold transform: The peak-to-peak values of the model error ΔCBF_{pp} and the noise-to-signal ratios NSR obtained from each of the four time series. Below their arithmetic mean values (*mean*) are listed. The good performance of the model is realized by comparing these values with those obtained by the input sampling transform — cf. Table 23.1 on page 153.

of the input sampling transform. The good performance of the input threshold transform is emphasized by the fact that for two time series (196io5 and 197io3) the noise-to-signal ratio as well as the peak-to-peak value of the model error are significant lower than for the linear models in Chapter 23. For one time series (196io4) only a slight improvement is obtained, and for one series (197io1) no improvement is obtained.

The model outputs are compared to the measured outputs in Figure 25.3. The corresponding model errors ΔCBF are depicted in Figure 25.4. From these figures it is concluded that inclusion of the nonlinearity (characterized by the threshold position FPA_0) in the model structure has satisfactorily taken into account the phenomenon of frequency saturation displayed by the experimental data. However, the dips are still unaccounted for.

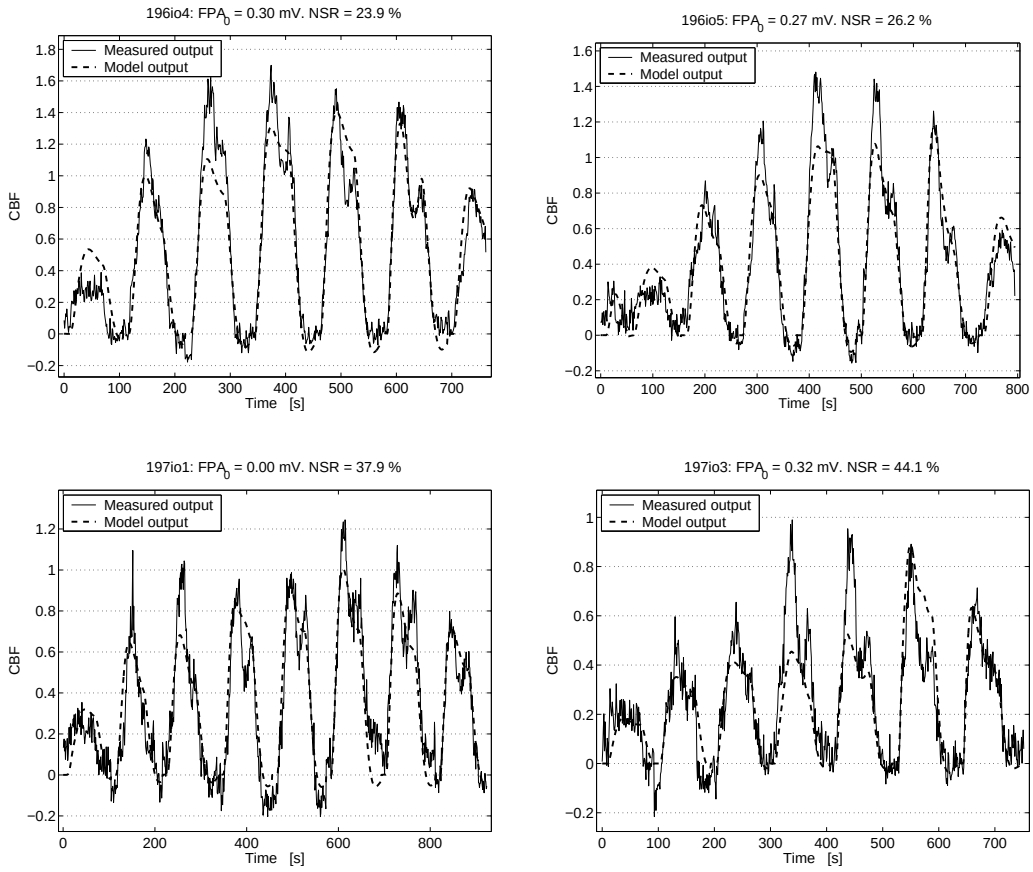

Figure 25.3: The grey-box model with the input threshold transform: Comparison of the output measured by the LDF probe `Re140` with the output obtained by a noise-free simulation of the grey-box model with the input threshold transform. Note that the model is able to track the frequency saturation in the CBF signal but not the dips.

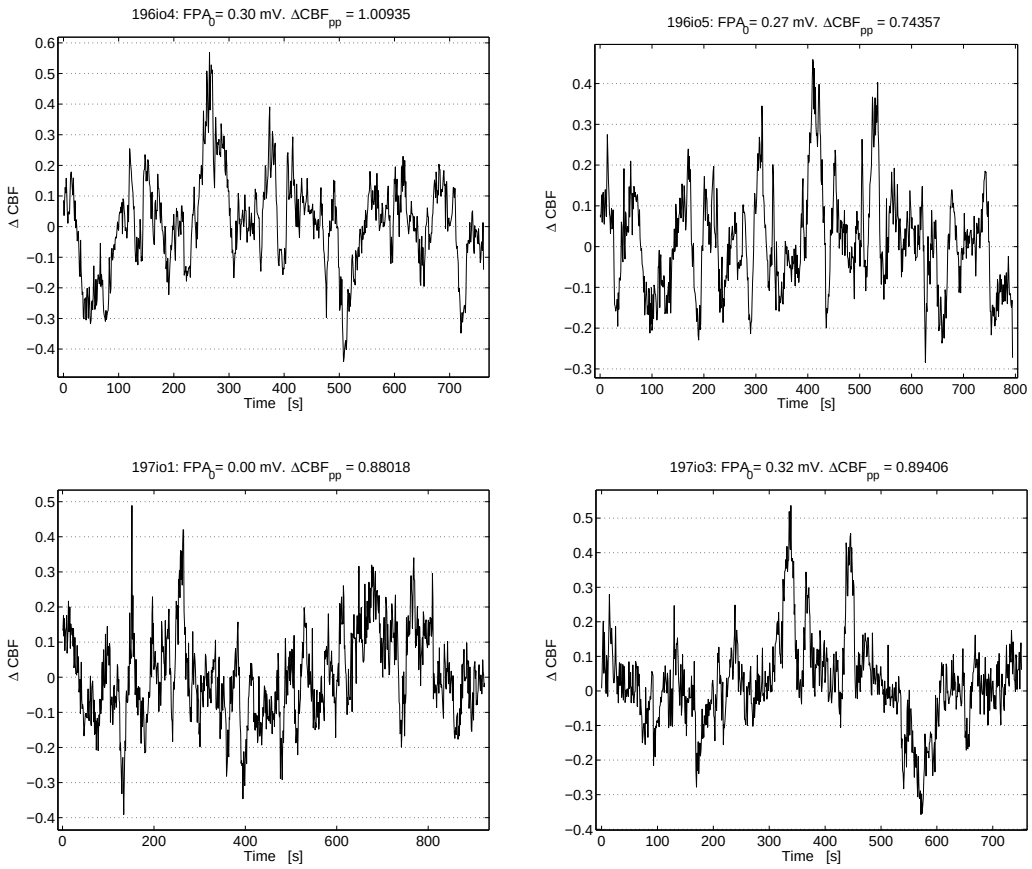

Figure 25.4: The grey-box model with the input threshold transform: The model error ΔCBF obtained from the grey-box model with the input preprocessed by means of the nonlinear input threshold transform. Note that the largest model error values do not occur at onset or end of stimulation but during the dips.

25.3.2 Cross Validation

The parameter values estimated from each of the four time series are listed in Table 25.2. Note that

Series	FPA_0 $[mV]$	$g \cdot h$ $\left[\frac{1}{s^2 \cdot mV}\right]$	$f + k$ $\left[\frac{1}{s}\right]$	$f \cdot k + h \cdot l$ $\left[\frac{1}{s^2}\right]$
196io4	0.30	0.02025	0.12601	0.01141
196io5	0.27	0.02669	0.12912	0.01147
197io1	0.00	0.04481	0.13218	0.01145
197io3	0.32	0.02614	0.18833	0.01947
Mean	0.22	0.02947	0.14391	0.01345
Std	0.15	0.01063	0.02972	0.00401
Cv	0.67	0.36076	0.20652	0.29839

Table 25.2: The grey-box model with the input threshold transform: The parameter values in the nonlinear model estimated from the four time series. Also listed are their mean values (*mean*), standard deviations (*std*), and their coefficients of variance (*cv*). Note that inclusion of the input threshold transform in the model structure has made the coefficients of variance of the parameters $f + k$ and $f \cdot k + h \cdot l$ decrease so much that they are now smaller than the coefficient of variance of the parameter $g \cdot h$ — contrary to the case of the grey-box model with the input sampling transform (cf. Table 23.2 on page 156).

the coefficient of variance of the parameter FPA_0 is below one indicating that FPA_0 has physiological significance. Compared to the linear grey-box model (cf. Table 23.2 on page 156) the coefficient of variance of $g \cdot h$ is practically unchanged. On the other hand, the coefficients of variance of the parameters $f + k$ and $f \cdot k + h \cdot l$ has decreased so much that they are now smaller than the coefficient of variance of the parameter $g \cdot h$. Knowing that the values of the field potential measurements depend on the experimental conditions — especially the position of the probe, which measure the field potential (cf. Section 22.5 on page 145) — this result is expected. Finally, there are not systematic differences between the estimates obtained from the two rats. This result is in contrast to the result of the grey-box model with the input sampling transform, for which the estimates of $g \cdot h$ obtained from the two rats differ.

25.3.3 Sensitivity to the Parameter FPA_0

Figure 25.5 shows the variation in the noise-to-signal ratio NSR with the variation in the threshold position FPA_0. Notice, that for some time series (196io5 and 197io3) the minimum point is very well defined indicating that the noise-to-signal ratio NSR and thus the performance of the model is highly sensitive to the parameter FPA_0. This result further strengthens the conclusion that FPA_0 is a physical parameter.

25.4 Conclusion on the Input Threshold Transform

The grey-box model with the input threshold transform consists of two parts: A nonlinear dynamic transformation without memory of the amplitudes of the discrete events in the field potential signal to a slowly varying signal which forms the input to a linear state-space model with coupled and constrained parameters. The input threshold transform gives equal weight to the amplitudes of the field potential events which are larger than a certain threshold but neglects events with amplitudes below the threshold. The relative cerebellar blood flow signal forms the output from the state-space model.

The phenomenon earlier characterized as frequency saturation (Section 23.9 on page 156) of the CBF response has been explained from the decrease in overall FPA size with increasing frequency.

Inclusion of the nonlinear input threshold transform in the grey-box model significantly improve the model fit. The nonlinearity has taken into account the frequency saturation of the CBF signal but does not explain the dips.

The model fit is highly sensitive to the single parameter (the threshold position) in the nonlinearity. This result indicates that the parameter has physical/physiological significance.

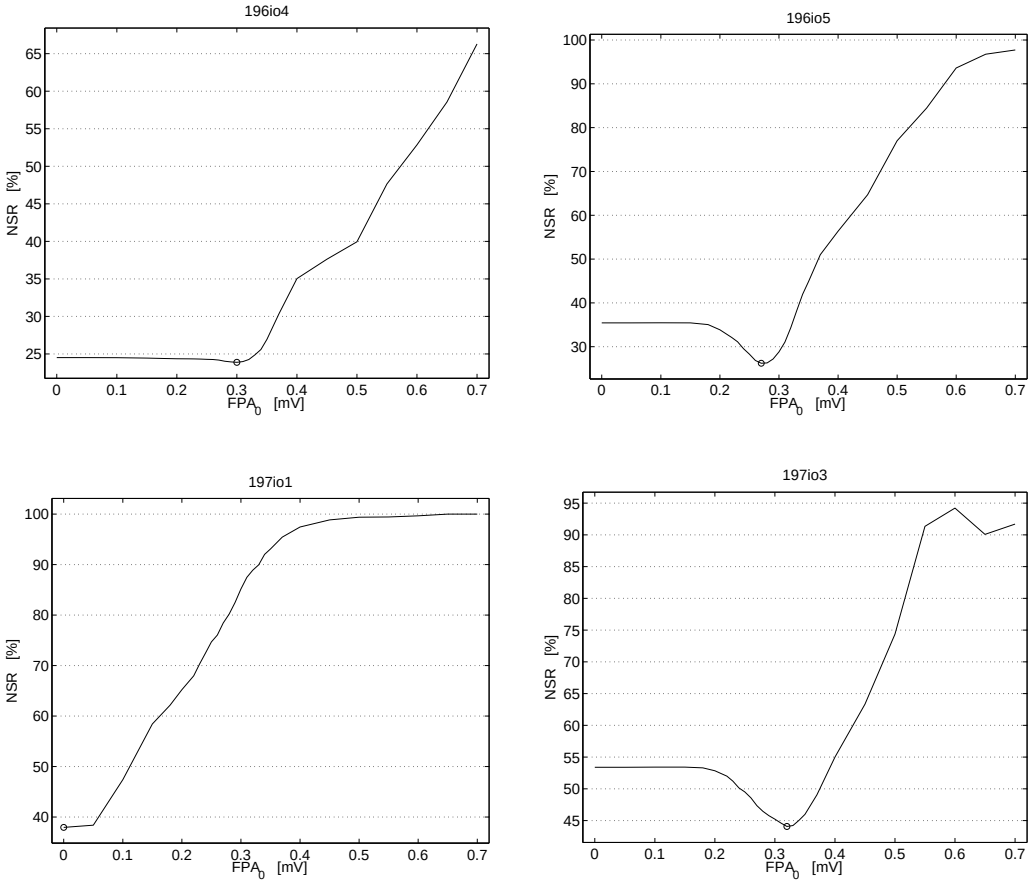

Figure 25.5: The grey-box model with the input threshold transform: The variation in the noise-to-signal ratio NSR with variation in the value of the parameter FPA_0 for each of the four time series. The data points at $FPA_0 = 0\,mV$ correspond to the linear grey-box model investigated in Chapter 23. Note that for two time series (196io5 and 197io3) there is a distinct nonzero minimum point for the noise-to-signal ratio, and in one time series (196io4) there is a weaker nonzero minimum point. For one time series (197io1) the nonlinearity does not improve the model fit.

Chapter 26

The Input Kink Transform

26.1 The Input Kink Transform

Within the paradigm of artificial neural networks a hyperbolic tangent is often used for the processing unit [104]. Furthermore, artificial neural networks have successfully been used to model the internal circuitry of cerebellum [29]. Inspired by these facts the weight function w is now modeled as a hyperbolic tangent with *kink position* FPA_0 and *kink slope* α_w:

$$w(FPA) = \frac{1}{2} \cdot \{1 + \tanh[2 \cdot \alpha_w \cdot (FPA - FPA_0)]\} . \tag{26.1}$$

This weight function is illustrated by Figure 26.1.

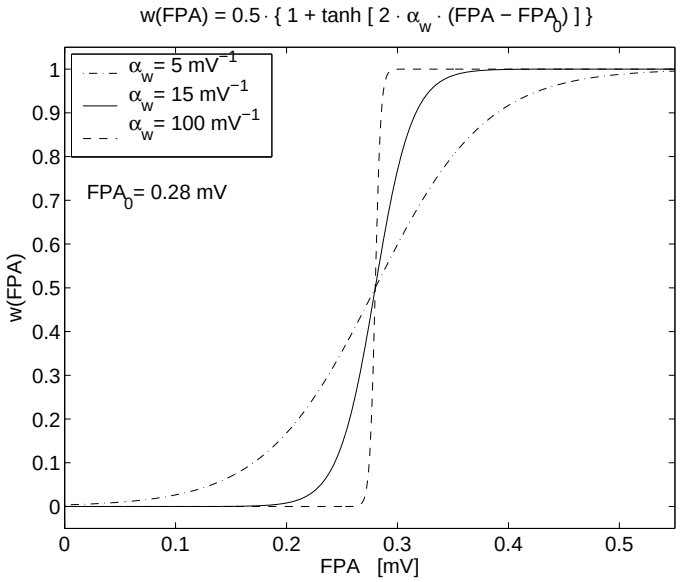

Figure 26.1: The variation in the weight function w with the field potential amplitude (FPA) shown for one value of the kink position FPA_0 and three values of the kink slope α_w.

The field potential amplitude signal is preprocessed according to the formula

$$FPA_{pp}(t) = \sum_{t-\frac{\tau}{2} < t_j \leq t+\frac{\tau}{2}} \{FPA(t_j) \cdot w(FPA(t_j))\} , \tag{26.2}$$

which will be termed the *input kink transform*. It is a dynamic nonlinear transform with the nonlinearity being defined by two parameters: FPA_0 and α_w. The resulting preprocessed field potential amplitude signal for various values of the parameter set consisting of the kink position FPA_0 and the kink slope α_w

as well as the cerebellar blood flow to be reproduced are shown (after resampling to 1 Hz) in Figure 26.2. Note that for $\alpha_w \longrightarrow \infty$ the input kink transform becomes equivalent to the input threshold transform investigated in Chapter 25.

26.2 Implementation of the Model in MATLAB

The parameters FPA_0 and α_w are estimated by considering how the noise-to-signal ratio NSR varies with these parameters. The value of the parameter set which results in the lowest noise-to-signal ratio is chosen as the estimate of the parameter set. For each set of values of these two parameters the estimation of the parameters $g \cdot h, f + k, f \cdot k + h \cdot l$, and $\widetilde{n}_0$ in the linear state-space model is initiated at the values determined from the grey-box model with the input threshold transform — see Table 25.2 on page 164.

26.3 Model Results

26.3.1 Model Fit

In Table 26.1 the obtained peak-to-peak value of the model errors ΔCBF_{pp} as well as noise-to-signal ratios NSR are shown. This table should be compared to Table 25.1 on page 161, which shows the

Series	ΔCBF_{pp}	NSR [%]
196io4	0.91788	23.4
196io5	0.74245	26.2
197io1	0.87765	37.9
197io3	0.89412	44.1
Mean	0.85803	32.9

Table 26.1: The grey-box model with the input kink transform: The peak-to-peak values of the model error ΔCBF_{pp} and the noise-to-signal ratios NSR obtained for the input kink preprocessing procedure for each of the four time series. Also their arithmetic mean values (*mean*) are shown. These values are almost identical to those obtained from the grey-box model with the input threshold transform (cf. Table 25.1 on page 161).

results of the grey-box model with the input threshold transform, as well as Table 23.1 on page 153, which shows the results of the grey-box model with the input sampling transform. Notice that the noise-to-signal ratios as well as the peak-to-peak values of the model errors obtained by the input kink transform are almost identical to the values obtained by the input threshold transform. Inclusion of the extra parameter α_w does not improve the model fit further.

The model outputs for the values of the parameter set (FPA_0, α_w) which give the best fits are compared to the measured output in Figure 26.3. The corresponding model error traces ΔCBF are shown in Figure 26.4. Note that these two figures are almost identical to those obtained from the input threshold transform (Figures 25.3 and 25.4 on pages 162–163).

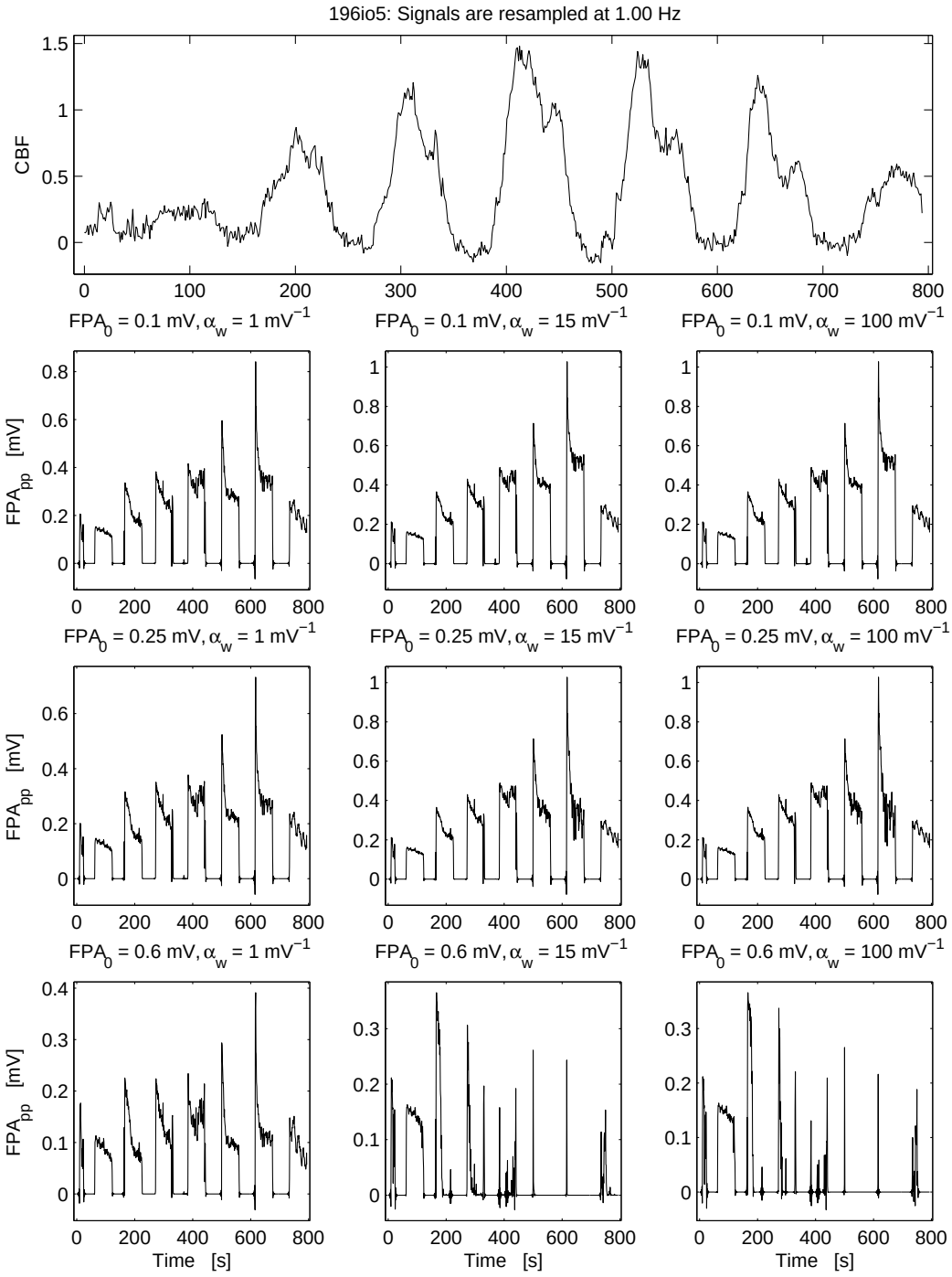

Figure 26.2: Top panel: The cerebellar blood flow to be reproduced. Other panels: The FPA signal preprocessed according to the input kink transform for various values of the parameter set $(FPA_0,\ \alpha_w)$. The size of each FPA event is weighted by the value of a hyperbolic tangent function defined by the parameter set $(FPA_0,\ \alpha_w)$. The signals, which are from the time series 196io5, have been resampled by a factor 10. Note that the effect of changing FPA_0 (from top to bottom) is much more pronounced than the effect of changing α_w (from left to right).

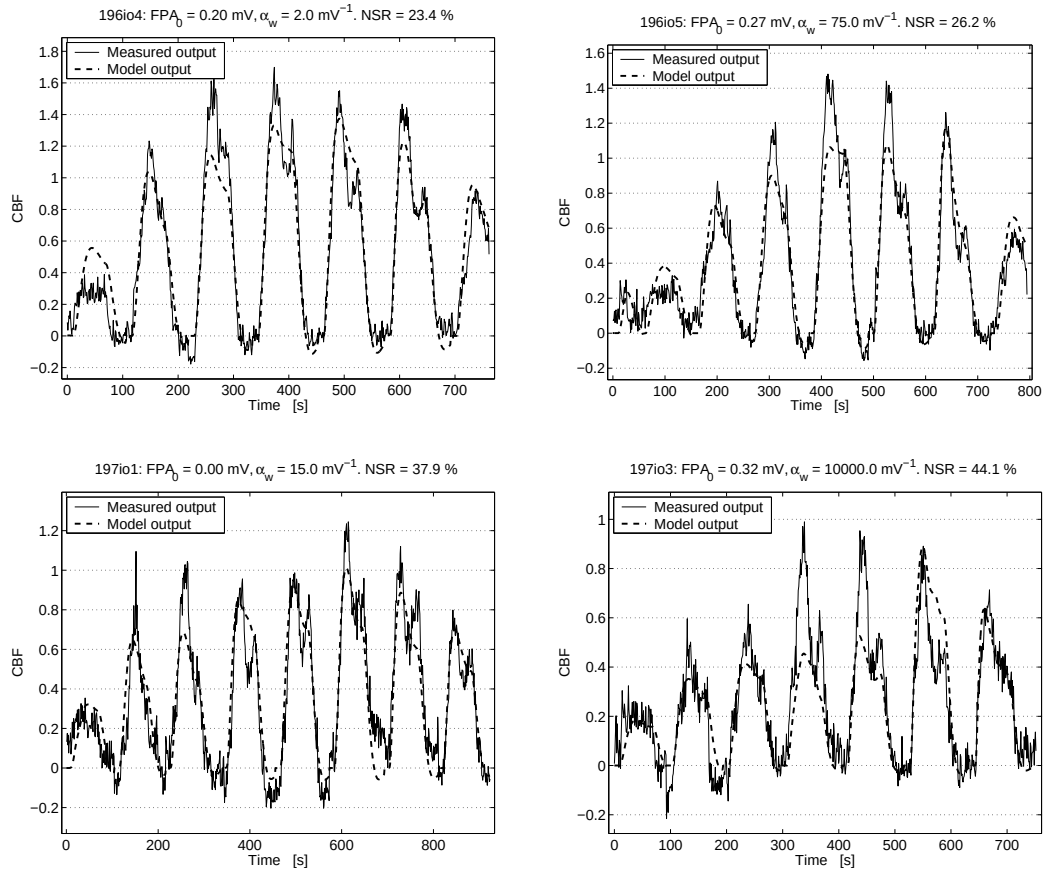

Figure 26.3: The grey-box model with the input kink transform: The output measured by the LDF probe `Re140` (solid line) as well as the output calculated from the grey-box model (dashed line) for each of the four time series. Note that the model output traces are almost identical to those obtained by the grey-box model with the input threshold transform — cf. Figure 25.3 on page 162.

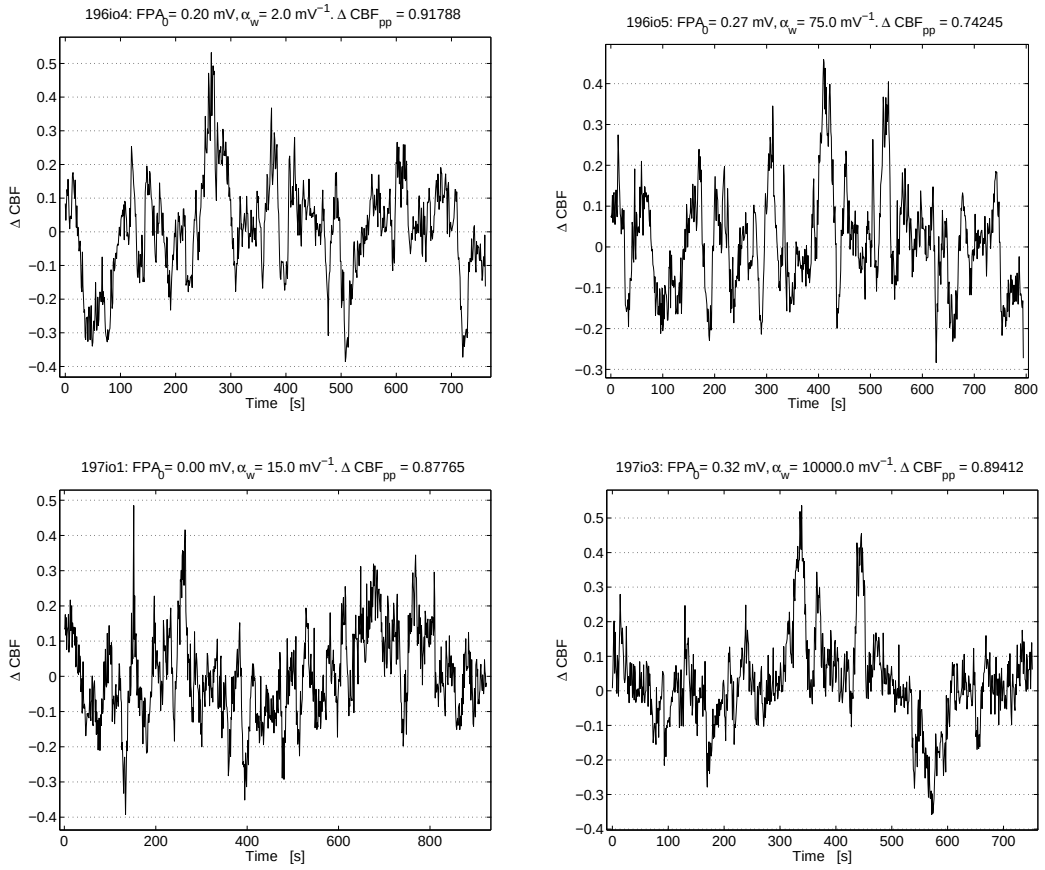

Figure 26.4: The grey-box model with the input kink transform: The model error ΔCBF, i.e., the difference between the output measured by the LDF probe `Re140` and the output calculated from the grey-box model with the input kink transform for each of the four time series. These error traces are almost identical to those in Figure 25.4 on page 163 which are obtained from the grey-box model with the input threshold transform.

26.3.2 Cross Validation

The parameter values estimated from the four time series are listed in Table 26.2. Note that the coeffi-

Series	FPA_0 $[mV]$	α_w $[mV^{-1}]$	$g \cdot h$ $\left[\frac{1}{s^2 \cdot mV}\right]$	$f + k$ $\left[\frac{1}{s}\right]$	$f \cdot k + h \cdot l$ $\left[\frac{1}{s^2}\right]$
196io4	0.20	2.0	0.02090	0.12612	0.01128
196io5	0.27	75.0	0.02669	0.12912	0.01147
197io1	0.00	15.0	0.04478	0.13182	0.01138
197io3	0.32	10000.0	0.02593	0.18695	0.01932
Mean	0.20	2523.0	0.02957	0.14350	0.01336
Std	0.14	4984.8	0.01046	0.02906	0.00397
Cv	0.71	2.0	0.35358	0.20249	0.29728

Table 26.2: The grey-box model with the input kink transform: The values of the parameters in the nonlinear model estimated from the four time series. Also listed are their mean values (*mean*), standard deviations (*std*), and their coefficients of variance (*cv*). Note that the coefficient of variance of the kink slope α_w is larger than one and furthermore much larger than the coefficients of variance of the other parameters. Furthermore, the estimates of $FPA_0, g \cdot h, f + k$, and $f \cdot k + h \cdot l$ are unaffected by the inclusion of the parameter α_w in the model structure — compare with Table 25.2 on page 164.

cient of variance of the parameter FPA_0 is still small indicating that FPA_0 has physiological significance. Contrary to this the coefficient of variance of the kink slope α_w is large indicating that α_w is *not* a physiological parameter and therefore should be excluded from the model. The estimates of the parameters $g \cdot h, f + k$, and $f \cdot k + h \cdot l$ seem to be unaffected by the inclusion of the extra parameter α_w — compare with Table 25.2 on page 164.

26.3.3 Sensitivity to the Parameters FPA_0 and α_w

The variation in the noise-to-signal ratio NSR with variation in the values of the parameters FPA_0 and α_w is depicted in Figure 26.5 for each of the four time series. Notice, that whereas the noise-to-signal ratio NSR and thus the model fit (as expected from Chapter 25) is sensitive to variations in the kink position FPA_0, it is not sensitive to variations in the kink slope α_w — as long as the kink slope is kept above $10\,mV^{-1}$. For lower values of the kink slope the model fit is significantly worse. These facts are emphasized by the plane sections through the noise-to-signal ratio surfaces shown in Figures 26.6 and 26.7.

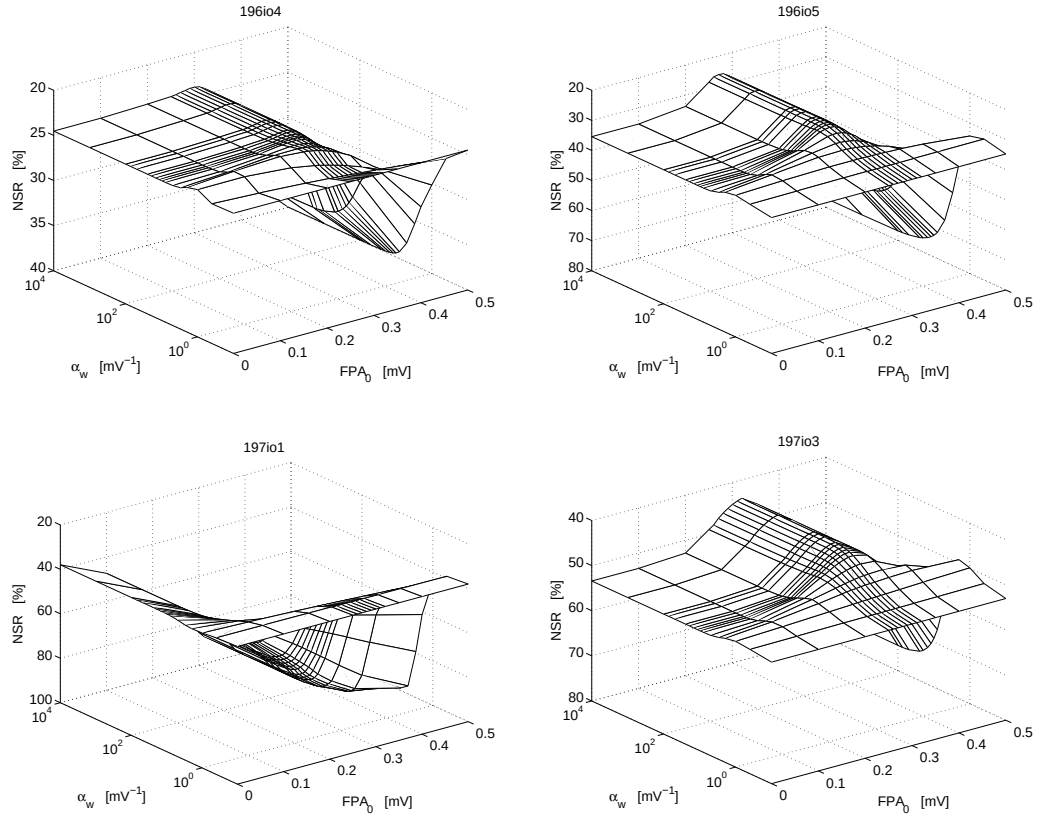

Figure 26.5: The grey-box model with the input kink transform: The variation in the noise-to-signal ratio NSR with variations in the kink position FPA_0 and the kink slope α_w for each of the four time series. Note that the scales on the α_w-axes are logarithmic and that the NSR axes are reversed. The points $(FPA_0,\ \alpha_w) = (0\,mV,\ \infty\,mV^{-1})$ correspond to the linear models in Chapter 23. Note that in general (that is, for $\alpha_w > 10\ mV^{-1}$) the model fit depends on the kink position FPA_0 but not on the kink slope α_w.

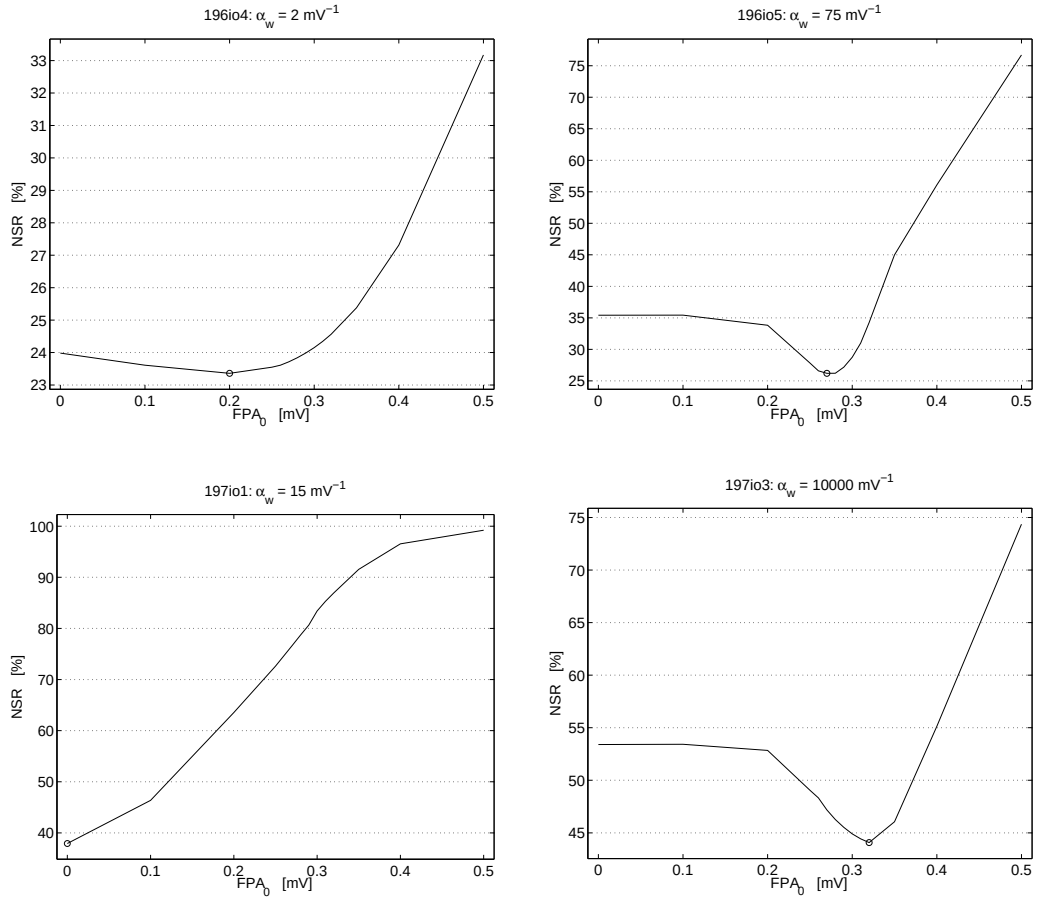

Figure 26.6: The grey-box model with the input kink transform: Plane Sections through the minimum point of the NSR surfaces show the variation in the noise-to-signal ratio with variation in the kink position FPA_0. Note that for two time series (196io5 and 197io3) there is a distinct nonzero minimum point of the noise-to-signal ratio, and for one time series (196io4) there is a weaker nonzero minimum point. For one time series (197io1) the nonlinearity does not improve the model fit. Note also the similarity of these curves with those obtained by the input threshold transform — cf. Figure 25.5 on page 165.

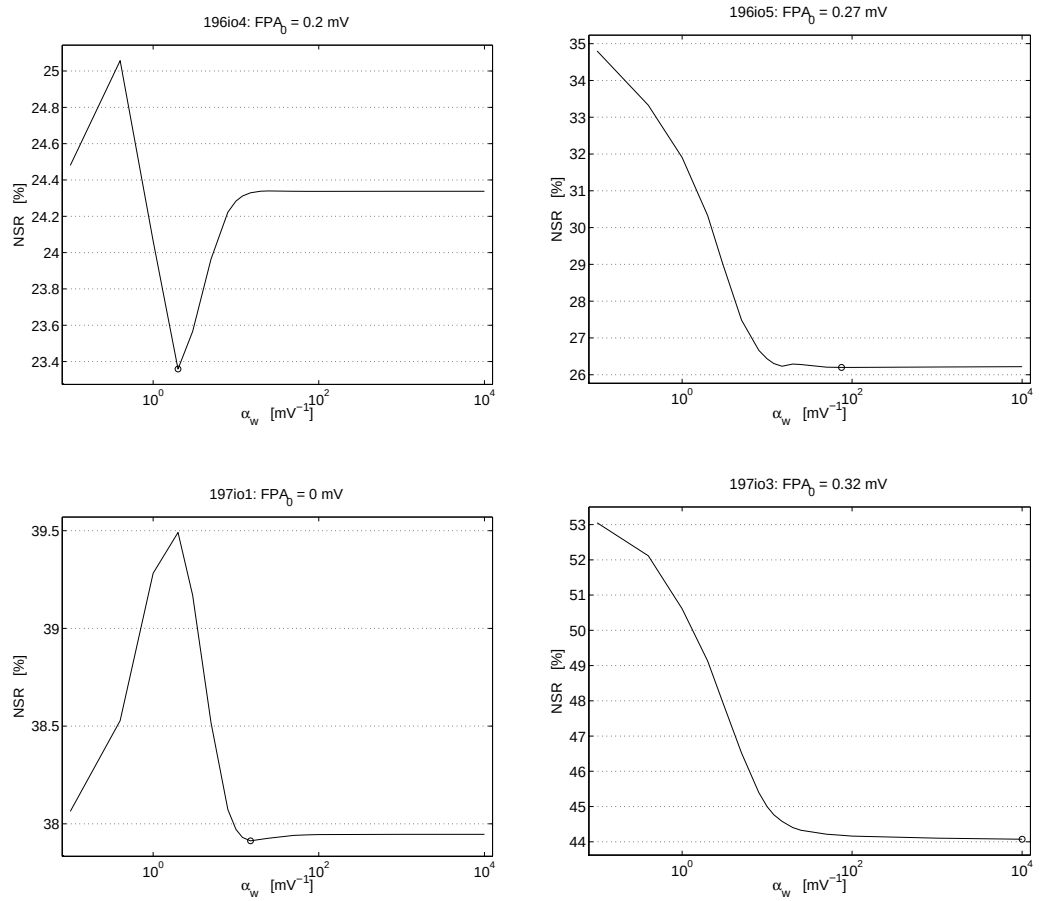

Figure 26.7: The grey-box model with the input kink transform: Plane Sections through the minimum point of the NSR surface show the variation in the noise-to-signal ratio with variation in the kink slope α_w. Note that the scale on the α_w-axes is logarithmic. For sufficiently large α_w (above $\sim$ 10 mV^{-1}) the noise-to-signal ratio is independent of the value of α_w. Below $\sim 10\ mV^{-1}$ it significantly increases.

26.4 Discussion of the Input Kink Transform

The Origin of the Low Sensitivity to α_w

The low sensitivity to the parameter α_w may be due to one of two reasons:

- The parameter α_w is unphysiological, i.e., it does not correspond to any physiological process. Therefore it is not supposed to be in the model structure.
- The data sets are too small to be able to represent all of the systems dynamics.

Since we have not tested all values of α_w, it is possible that a deep global minimum point of NSR is hidden somewhere in the range $\alpha_w > 10\ mV^{-1}$. We will claim that this is unlikely, because no reminiscence of such a minimum can be seen.

Properties of the Input Kink Transform

The hyperbolic tangent function is a smooth function in contrast to the Heaviside function, which is discontinuous. This difference seems not to affect the properties of the model.

We note, that the weight function w is anti-symmetric around the point $(FPA_0,\ \frac{1}{2})$. We do not expect that the use of a weight function with a degree of skewness would change the model results.

26.5 Conclusion on the Input Kink Transform

The grey-box model with the input kink transform consists of two parts: A nonlinear dynamic transformation without memory of the amplitudes of the discrete events in the field potential signal to a slowly varying signal which forms the input to a linear state-space model with coupled and constrained parameters. The input kink transform gives higher weight to events in the field potential with larger amplitudes than to events with smaller amplitudes. The nonlinearity is described by two parameters, and corresponds to smoothing out the input threshold transform. The relative cerebellar blood flow signal forms the output from the state-space model.

Extending the nonlinearity in the grey-box model structure with the extra parameter does not improve the model fit further and the sensitivity to this extra parameter is very low. Therefore, in future investigations it will be excluded from the model structure. The estimates of the parameters in the state-space part of the model have not been changed by the inclusion of the extra parameter in the input kink transform.

Chapter 27

Properties of the Grey-Box Model

In order to learn more about the properties of the neuro-vascular system, this chapter is devoted to further investigations of the grey-box model with the input threshold transform.

27.1 Time- and Frequency-Domain Model Properties

27.1.1 Time-Domain Model Properties

When do the Single Mediator Contribute to Coupling?

Figure 27.1 for each experiment compares a smoothed version of the FPA signal with the threshold position FPA_0. The smoothed signal, $mean(FPA)$, is obtained by dividing the time axis into bins being around 1 s long and calculating the arithmetic mean value of the FPA's occurring within each bin. The standard deviation within each bin, $std(FPA)$, is calculated by a similar procedure. The two signals $mean(FPA) \pm 3 \cdot std(FPA)$ are also shown in the figure. Note, that at low frequencies most of the field potential amplitudes are larger than the threshold position FPA_0, whereas, as the frequency is increased, more and more FPA's are below the threshold. It follows that in experiments, where the stimulation frequency is kept below $\sim 10\ Hz$, the input threshold transform reduces to the input sampling transform. That is, the model is linearizable.

For each of the four experiments the resulting input and output signals, that is, the preprocessed field potential amplitude signal for the value of FPA_0, which gives the lowest noise-to-signal ratio, as well as the cerebellar blood flow signal are shown in Figure 27.2 — after resampling by a factor 10. Since the rate of release of NO into the extracellular space — according to the model — is proportional to the preprocessed field potential amplitude signal, we conclude that: In general NO is released faster at intermediate stimulation frequencies than at low and high frequencies. At low stimulation frequencies NO is released as long as the inferior olive is stimulated; at high frequencies NO is mainly released right after the onset of stimulation.

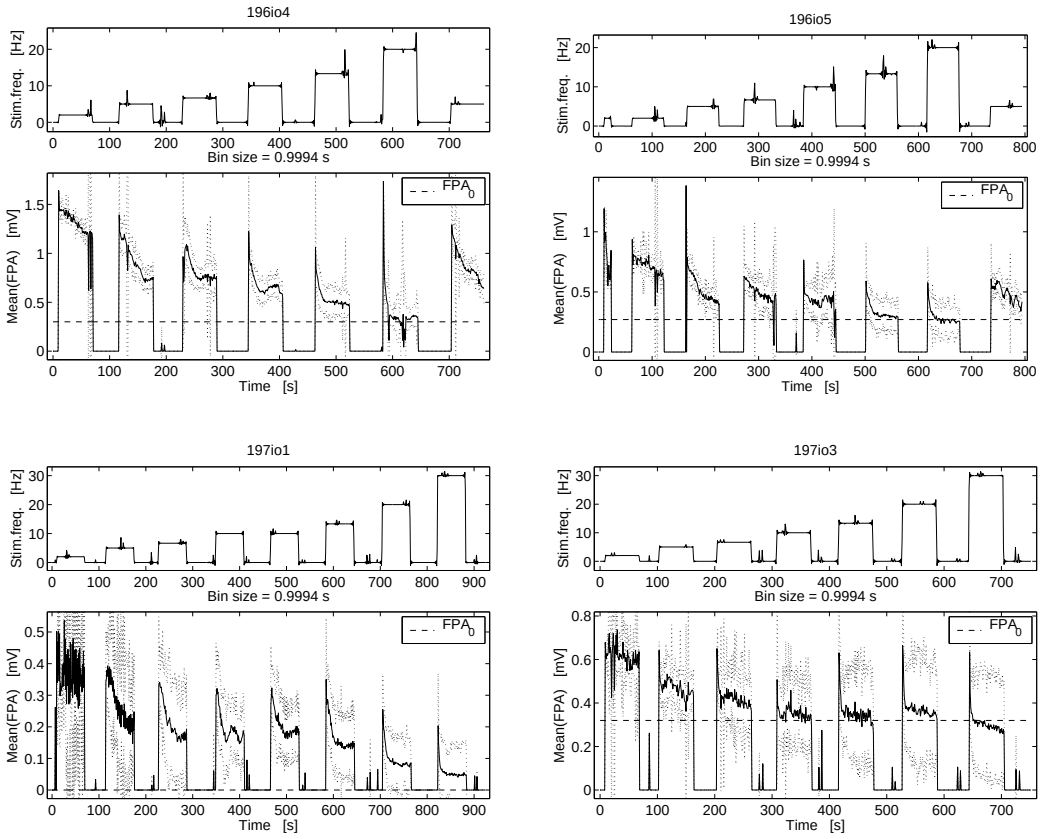

Figure 27.1: The grey-box model with the input threshold transform: Comparison of the estimated threshold position FPA_0 (dashed line) and the smoothed FPA signal ($mean(FPA)$) (solid line). The dotted lines show the two signals $mean(FPA) \pm 3 \cdot std(FPA)$. $Mean(FPA)$ is the arithmetic mean value of the FPA's occurring within each bin of a duration of around 1 s, and $std(FPA)$ is similarly the standard deviation of those FPA's. Note that, as the stimulation frequency is increased, more FPA's fall below the threshold position FPA_0. Furthermore, at stimulation frequencies lower than $\sim$ 10 Hz, the averaged signal usually exceeds FPA_0.

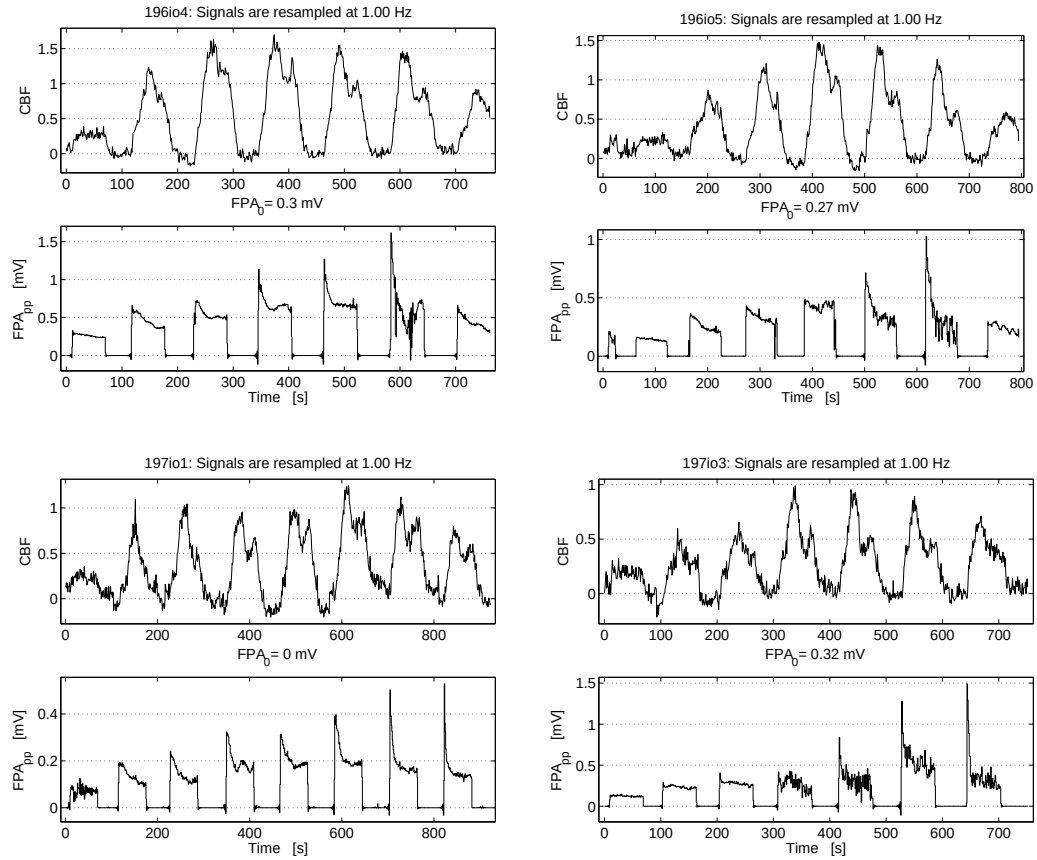

Figure 27.2: The grey-box model with the input threshold transform: The cerebellar blood flow (CBF) signal as well as the preprocessed field potential amplitude (FPA_{pp}) signal for the value of the threshold position FPA_0 which gives the best fit for each of the four time series — after resampling by a factor 10. Remember that, according to the model (23.1)–(23.4), the rate of release of nitric oxide into the extracellular space is proportional to FPA_{pp}.

Time Responses

Now the model's transient behavior is investigated. Specifically, we investigate the output signal $y(t)$, i.e., the CBF signal, which results from exciting the linear part of the model with an input $u(t)$, i.e., a preprocessed field potential amplitude signal $FPA_{pp}(t)$, having a prescribed shape. We perform this investigation without considering how to design a stimulation sequence, which would produce this shape of the u signal.

The *impulse response*, that is, the output signal $y(t) = CBF(t)$, which results from $u(t) = FPA_{pp}(t)$ being an impulse at time zero, $t = 0\ s$, i.e., $u(t) = FPA_{pp}(t) = \delta(t)$, is shown in Figure 27.3. We

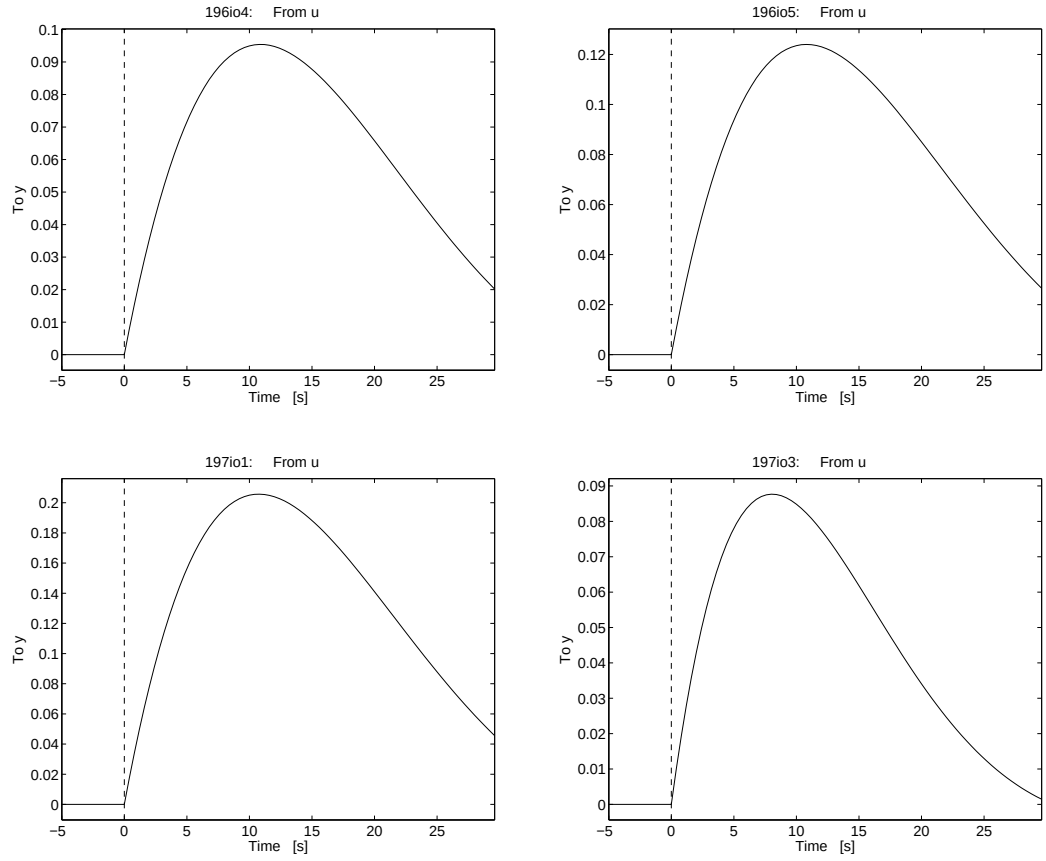

Figure 27.3: The grey-box model with the input threshold transform: The impulse response, that is, the CBF signal ($y(t) = CBF(t)$) resulting from simulation of the linear state-space part of the grey-box model with the preprocessed field potential amplitude signal being an impulse at $t = 0\ s$ ($u(t) = FPA_{pp}(t) = \delta(t)$). Note, that the impulse responses of the models identified from the four different experiments are very alike. The main difference between them is the amplitudes of the CBF signals.

note, that the impulse responses obtained from the four experiments are very alike in shape — only the amplitudes of the CBF responses differ.

Similarly, the *step response* is the output signal $y(t)$, which results from the input being a step of amplitude one at time zero, $u(t) = \theta(t)$. For the linear part of the grey-box model, that is, the model which has the threshold transformed input as input ($u(t) = FPA_{pp}(t)$ with FPA_0) and the cerebellar blood flow signal as output ($y(t) = CBF(t)$), the obtained step responses are shown in Figure 27.4. Also the step responses are very similar in shape, but differ somewhat in amplitude.

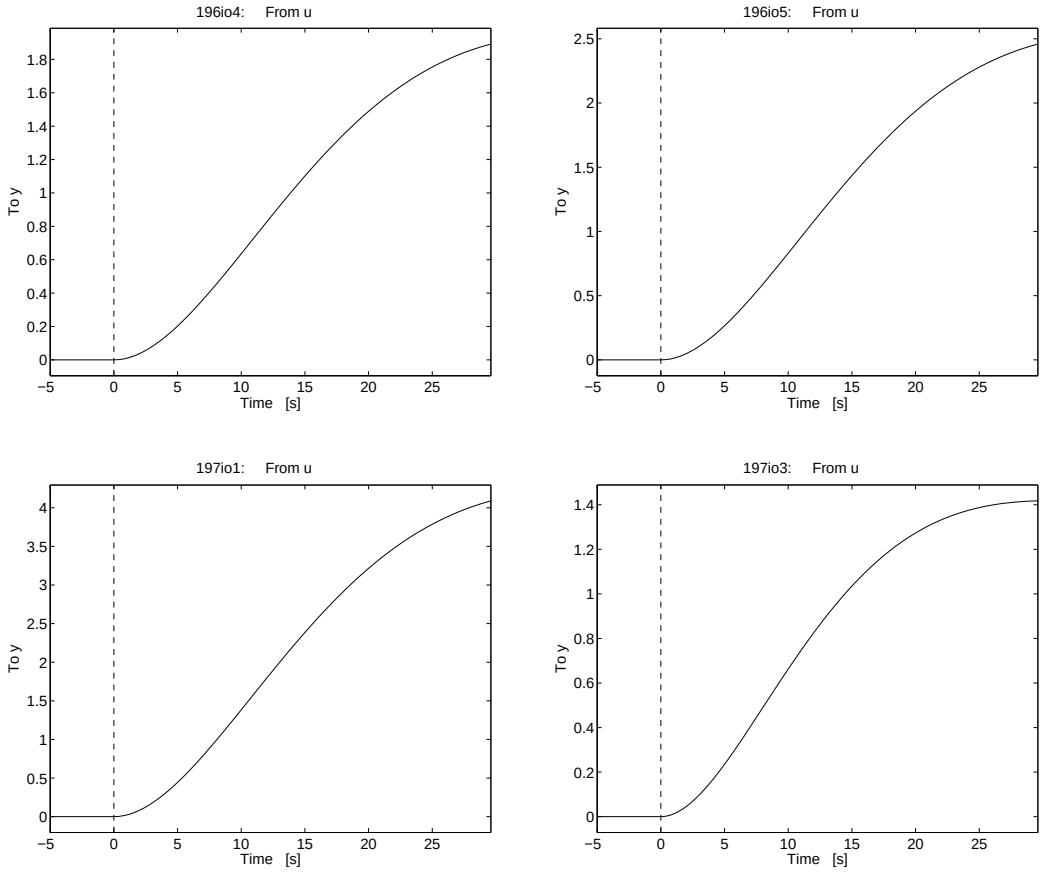

Figure 27.4: The grey-box model with the input threshold transform: The step responses have been calculated from the linear part of the grey-box models, which have been identified from the four inferior olive stimulation experiments. The input u is the threshold transformed input, $u(t) = FPA_{pp}(t)$ with FPA_0, and the output is the CBF signal, $y(t) = CBF(t)$. Note, that the shapes of the step responses are very alike, whereas the amplitudes of the step responses differ somewhat.

27.1.2 Frequency-Domain Model Properties

Poles and Gain

The transfer function in Equation (23.22) can be rewritten in terms of the gain (k_{11}) and the two poles (p_1 and p_2) (as there are no zeros):

$$G(s) = \frac{Y(s)}{U(s)} = \frac{CBF(s)}{FPA_{pp}(s)} = k_{11} \cdot \frac{1}{(s-p_1)\cdot(s-p_2)}. \tag{27.1}$$

Therefore, the cross validation task is now revisited. Note, that $k_{11} = g \cdot h$. The estimates of the gain and the two poles are listed in Table 27.1. The poles are illustrated by pole-zero maps in Figure 27.5.

Series	k_{11}	p_1	p_2
196io4	0.02025	$-0.06301 + 0.08626i$	$-0.06301 - 0.08626i$
196io5	0.02669	$-0.06456 + 0.08545i$	$-0.06456 - 0.08545i$
197io1	0.04481	$-0.06609 + 0.08416i$	$-0.06609 - 0.08416i$
197io3	0.02614	$-0.09416 + 0.10297i$	$-0.09416 - 0.10297i$
Mean	0.02947	$-0.07195 + 0.08971i$	$-0.07195 - 0.08971i$
Std(Re) + std(Im)i	0.01063	$0.01486 + 0.00888i$	$0.01486 + 0.00888i$
Cv(Re) + cv(Im)i	0.36076	$-0.20647 + 0.09901i$	$-0.20647 - 0.09901i$

Table 27.1: The grey-box model with the input threshold transform: The gain (k_{11}) and the two poles (p_1 and p_2) as estimated from each of the four time series. Also shown are their mean values (*mean*), standard deviations of real and imaginary parts ($std(Re) + std(Im) \cdot i$), and coefficients of variance of real and imaginary parts ($cv(Re) + cv(Im) \cdot i$). Note, that the poles have a negative real part corresponding to stable linear system dynamics and an imaginary part corresponding to oscillatory linear system dynamics. Note also that $\mid cv(Im(p_i)) \mid \ll \mid cv(Re(p_i)) \mid \approx cv(f+k)$ — compare with Table 25.2 on page 164. This means that the oscillatory behavior is more well-defined than the stable dynamics.

Note, that the poles have a negative real part corresponding to stable linear system dynamics and an imaginary part corresponding to oscillatory linear system dynamics. The coefficient of variance of the imaginary part of the poles is much smaller than the coefficient of variance of the real part of the poles, and this is comparable to the coefficient of variance of $f + k$ — compare with Table 25.2 on page 164.

In order to describe the stable and oscillatory features, we rewrite the transfer function $G(s)$. First, we note that $G(s)$ is proportional to a transfer function $G_n(s)$, which has a static gain equal to one, $G_n(s)_{|s=0} = 1$:

$$G(s) = \frac{k_{11}}{p_1 \cdot p_2} \cdot G_n(s), \qquad G_n(s) = \frac{p_1 \cdot p_2}{(s-p_1)\cdot(s-p_2)}. \tag{27.2}$$

According to Ref. [37, (Sect. 3.3)] a transfer function $G_n(s)$ with two complex conjugate poles $p_i = -\sigma \pm i\omega_d$ can be rewritten in terms of the *undamped natural frequency* ω_n and the *damping ratio* ζ:

$$G_n(s) = \frac{{\omega_n}^2}{s^2 + 2\cdot\zeta\cdot\omega_n\cdot s + {\omega_n}^2}. \tag{27.3}$$

The real (σ) and imaginary (ω_d) parts of the poles are related to ζ and ω_n as follows:

$$\sigma = \omega_n \cdot \zeta, \qquad \omega_d = \omega_n \cdot \sqrt{1-\zeta^2}. \tag{27.4}$$

We have already stated that $k_{11} = g \cdot h$. Direct calculation shows that $p_1 + p_2 = -(f+k)$ and $p_1 \cdot p_2 = f \cdot k + h \cdot l$. Therefore

$$G(0) = G(s)_{|s=0} = \frac{k_{11}}{p_1 \cdot p_2} = \frac{g \cdot h}{f \cdot k + h \cdot l} = \frac{0.02947}{0.01345} \approx 2.19108, \tag{27.5}$$

$$\omega_n = \sqrt{p_1 \cdot p_2} = \sqrt{f \cdot k + h \cdot l} = \sqrt{0.01345}\ \frac{rad}{s} \approx 0.11597\ \frac{rad}{s}, \tag{27.6}$$

$$\zeta = \frac{\sigma}{\omega_n} = -\frac{1}{2} \cdot \frac{(p_1 + p_2)}{\sqrt{p_1 \cdot p_2}} = \frac{(f+k)}{2\sqrt{f \cdot k + h \cdot l}} = \frac{0.14391}{2 \cdot \sqrt{0.01345}} \approx 0.62044. \tag{27.7}$$

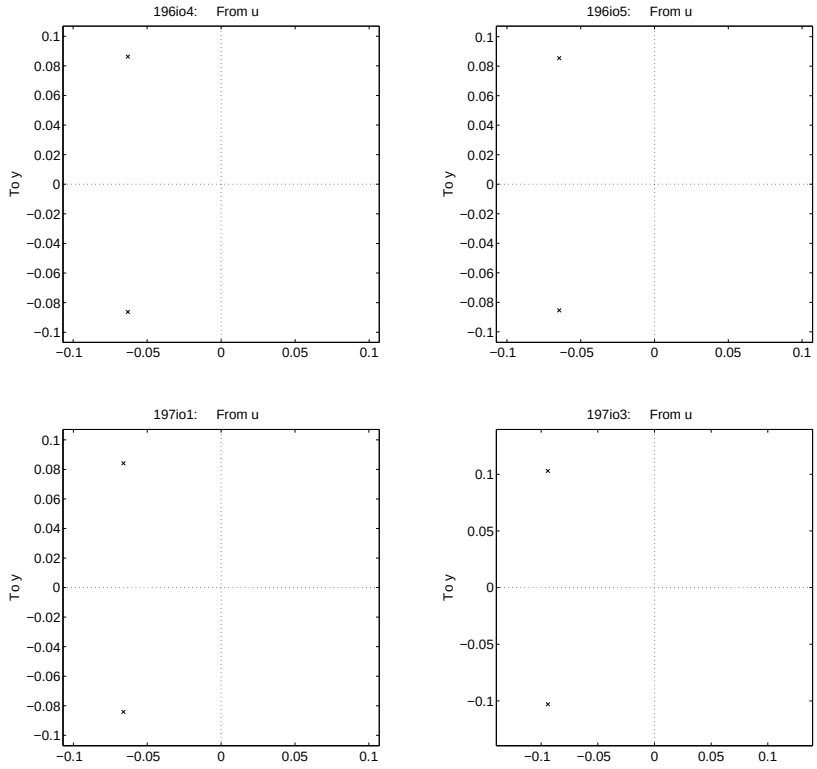

Figure 27.5: The grey-box model with the input threshold transform: Map of poles. Note, that the real and imaginary parts of the poles are almost equal in size. Note also that the values of the poles estimated from the experiment 197io3 differ slightly from the values obtained from the other three experiments.

The undamped natural frequency in units of Hertz is

$$f_n = \frac{\omega_n}{2\pi} \approx 0.01846\ Hz \tag{27.8}$$

and corresponds to a period of

$$T_n = \frac{1}{f_n} \approx 54.17747\ s, \tag{27.9}$$

i.e., a very slow oscillation.

Bode Plots

The Bode plots are shown in Figure 27.6. They display the magnitude $|G(f)|$ and phase $\phi(f)$ of the transfer function $G(f) = |G(f)| \cdot e^{i \cdot \phi(f)}$. The magnitude is shown on a logarithmic scale $M_{dB}(f) = 20 \cdot \log |G(f)|$. Since the estimated model is a continuous-time model, the frequency range in the Bode plots reach far beyond the Nyquist frequency $f_{Nyq} = 0.5\ Hz$ of the resampled input and output signals. Due to the

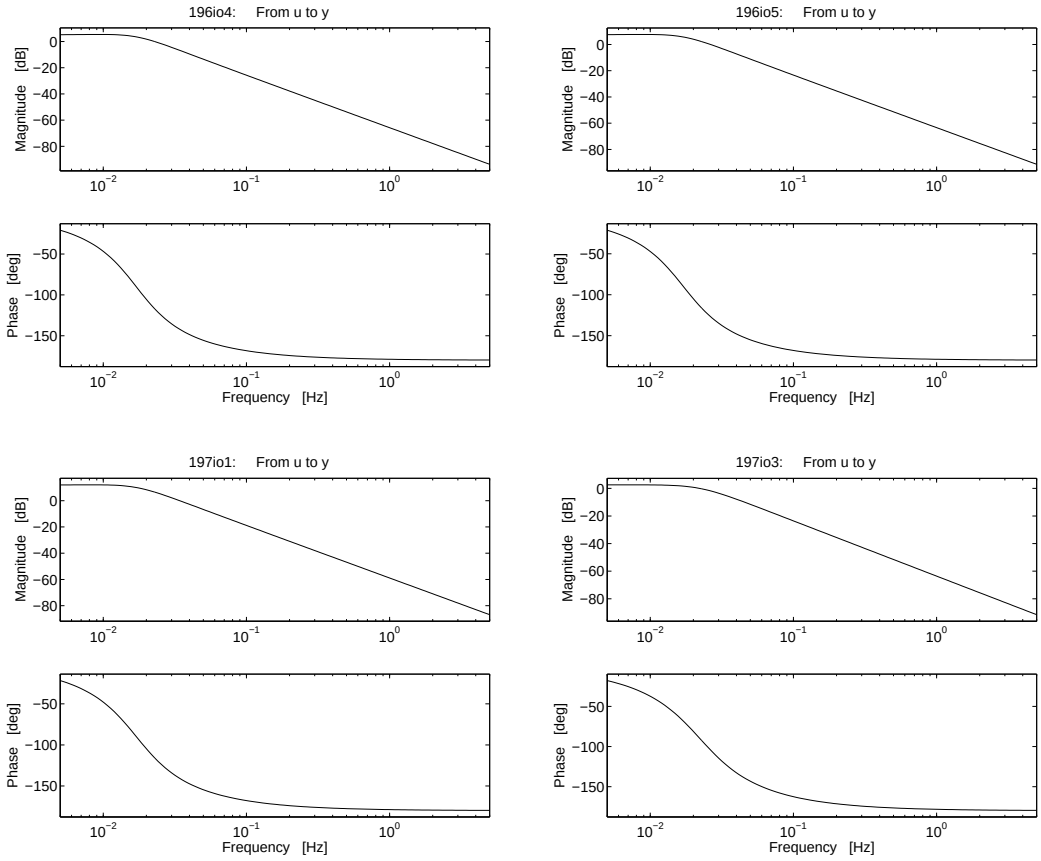

Figure 27.6: The grey-box model with the input threshold transform: Bode plots showing the magnitude $M_{dB}(f) = 20 \cdot \log |G(f)|$ and phase $\phi(f)$ calculated from the estimated transfer function $G(f) = |G(f)| \cdot e^{i \cdot \phi(f)}$. Note that the only feature is a single breakpoint frequency at $f_n \approx 1.8 \cdot 10^{-2}\ Hz = 18\ mHz$.

simple structure of the transfer function — no zeros and a single pair of complex conjugate poles — the only feature of the Bode plots is a breakpoint frequency at $f_n \approx 1.8 \cdot 10^{-2}\ Hz = 18\ mHz$.

27.2 Sensitivity to Parameters

In Section 25.3.3 on page 164 we investigated the sensitivity of the model fit to the parameter FPA_0 in the nonlinear input threshold transform.

In this section we proceed by investigating the sensitivity to the parameters in the linear state-space part of the grey-box model, that is, $\theta_1 = g \cdot h$, $\theta_2 = f + k$, and $\theta_3 = f \cdot k + h \cdot l$. The SENSTOOLS TOOLBOX [50] is applied for this task, and the resulting sensitivity measures have been presented in M: Sections 12.5–12.6.

Sensitivity to Parameters in the Transfer Function

First, the measures, which are related to the half axes of the sensitivity ellipsoid (cf. M: Section 12.5.4), are calculated: The minimum sensitivity $S_{\min}$ and the ratio R of maximum and minimum sensitivities in any direction are listed in Table 27.2. Note, that the values of $S_{\min}$ are high, and the values of R — though different from one — rather low.

Half axes	$S_{\min}$	R
196io4	0.1257	10.6820
196io5	0.1250	10.6627
197io1	0.1084	11.7442
197io3	0.1239	10.1340

Table 27.2: The grey-box model with the input threshold transform: The minimum sensitivity $S_{\min}$ and the ratio of maximum and minimum sensitivities in any direction R. Note, that the values of $S_{\min}$ and R, respectively, do not differ much for the four experiments. The values of $S_{\min}$ are rather high indicating high sensitivity to all parameters. The values of R are rather low, but larger than one, indicating that the sensitivities in various directions in the parameter space are somewhat, but not very, different.

Secondly, the sensitivity to individual parameters is specified by the measures listed in the following two tables (cf. M: Section 12.5.4). The values of the minimum sensitivity $S_{i\,\min}$ to each of the parameters θ_i are shown in Table 27.3. Note that, for each experiment, $S_{3\,\min} > S_{1\,\min} > S_{2\,\min}$.

$S_{i\,\min}$	$g \cdot h$	$f + k$	$f \cdot k + h \cdot l$
196io4	0.2136	0.1869	0.2398
196io5	0.2114	0.1871	0.2398
197io1	0.1833	0.1666	0.2039
197io3	0.2123	0.1797	0.2347

Table 27.3: The grey-box model with the input threshold transform: The minimum sensitivity $S_{i\,\min}$ to the parameter θ_i. Note, that the sensitivity to $f \cdot k + h \cdot l$ is larger than to $g \cdot h$, and the sensitivity to $g \cdot h$ is larger than to $f + k$. But the differences are not large.

The values of the ratio R_i of the sensitivity to the parameter θ_i alone and the minimum sensitivity to the parameter are compared in Table 27.4. Note that, for each experiment, $1.8 < R_2 < R_3 < R_1 < 5.1$.

R_i	$g \cdot h$	$f + k$	$f \cdot k + h \cdot l$
196io4	4.5466	2.1399	4.0883
196io5	4.5681	2.2254	4.0679
197io1	5.0456	2.4019	4.5478
197io3	4.2367	1.8787	3.9268

Table 27.4: The grey-box model with the input threshold transform: The ratio R_i of the sensitivity to the parameter θ_i alone and the minimum sensitivity to the parameter. Note, that the ratio R_i is closest to one for the parameter $f + k$, less close for $f \cdot k + h \cdot l$ and farthest away from one for $g \cdot h$.

Finally, the values of $S_{\min}$ and $S_{i\,\min}$ are smaller for the time series 197io1 than for the three other experiments. Similarly, the values of R and R_i are larger for the time series 197io1 than for the other experiments.

Parameter Accuracy

As explained in M: Section 12.6.2 measures of the parameter accuracy can be related to the sensitivity measures under various assumptions.

Under the assumption that the model deficiencies are only caused by noise, the spread $\sigma(\theta_{N,ri})$ of the estimate of the relative parameter θ_{ri} can be calculated. The results are listed in Table 27.5. Note, that

$\sigma(\theta_{N,ri})$ [%]	$g \cdot h$	$f + k$	$f \cdot k + h \cdot l$
196io4	2.3918	2.7335	2.1307
196io5	2.7768	3.1375	2.4482
197io1	4.3272	4.7598	3.8891
197io3	4.5425	5.3667	4.1085

Table 27.5: The grey-box model model with the input threshold transform: The relative spread $\sigma(\theta_{N,ri})$ of the estimate of θ_i calculated under the assumption that the model deficiencies are only caused by noise. Note, that the values are rather small: $\sigma(\theta_{N,ri}) < 6$ %.

the values are rather small.

Similarly, under the assumption that the model deficiencies are solely caused by under-modeling, the equivalent relative error $\Delta\theta_{eq,ri}$ on the estimate of θ_i can be calculated. The results are listed in Table 27.6. Note, that the values of $\Delta\theta_{eq,ri}$ are large.

$\Delta\theta_{eq,ri}$ [%]	$g \cdot h$	$f + k$	$f \cdot k + h \cdot l$
196io4	111.4695	127.3923	99.2993
196io5	122.5274	138.4420	108.0243
197io1	207.6164	228.3688	186.5945
197io3	205.7711	243.1063	186.1092

Table 27.6: The grey-box model with the input threshold transform: The equivalent relative error $\Delta\theta_{eq,ri}$ on the estimate of θ_i calculated under the assumption that the model deficiencies are solely caused by under-modeling. Note, that the values of $\Delta\theta_{eq,ri}$ are much larger than the values of $\sigma(\theta_{N,ri})$: $\Delta\theta_{eq,ri} > 99\% \gg \sigma(\theta_{N,ri})$.

Note, that the values of $\Delta\theta_{eq,ri}$ are much larger than the values of $\sigma(\theta_{N,ri})$.

27.3 The Non-Measured Signal $\widetilde{n}(t)$

We will now consider how to design an estimator $\widehat{\mathbf{x}}(t)$ of the state vector $\mathbf{x}(t)$. The available knowledge is

- The threshold transformed measurements of the input signal $u(t) = FPA_{pp}(t)$ and the measurements of the output signal $y(t) = CBF(t)$, and
- The estimates of the matrices $\widetilde{\mathbf{F}}, \widetilde{\mathbf{G}}, \widetilde{\mathbf{H}}$, and $\widetilde{J}$ in the state-space part of the grey-box model with the input threshold transform.

The purpose will be to extract information about a non-measured, physiological signal from the state vector.

27.3.1 Interpreting the State Variable $\widetilde{n}(t)$

An Assumption

In Section 23.4 on page 150 we noted, that the transformed state variable $\widetilde{n}(t) = f \cdot CBF(t) + h \cdot n(t)$ has no direct physiological interpretation. However, if the parameters f and h were identifiable, we could calculate the preprocessed concentration deviation signal $n(t)$ from the state variable $\widetilde{n}(t)$.

Therefore, in order to be able to interpret the variable $\widetilde{n}(t)$, we choose to make the assumption, that the time constant of the flux scavenging is much larger than the time constants of the other processes in the system, i.e., that NO diffuses relatively slowly through the extracellular space. This assumption is expressed mathematically as $f \equiv 0\ s^{-1}$. As a result

$$\widetilde{n}(t) = h \cdot n(t) = h \cdot \{c(NO)(t) - c_B(NO)\}_{pp}\,, \tag{27.10}$$

that is, $\widetilde{n}(t)$ is proportional to the (preprocessed) concentration deviation. We will term $\widetilde{n}(t)$ the *scaled concentration deviation*.

If we furthermore assumed that $h \equiv 1\ ml/(mol \cdot s)$, the signal $\widetilde{n}(t)$ would be equal to the concentration deviation. We will not make this assumption, because it is more unlikely. Diffusion through the extracellular space may actually be very slow, but the value of h depends on how powerful a vasodilator nitric oxide is.

How to Estimate $\widetilde{n}(t)$

Since the scaled concentration deviation is a variable in the state vector, we will first apply a so-called Kalman filter $\mathbf{L}$ to determine the *optimal* relative contribution from the noise-corrupted measurements of the input $u(t) = FPA_{pp}(t)$ and output $y(t) = CBF(t)$ signals to the estimate $\widehat{\widetilde{\mathbf{x}}}(t)$ of the state vector $\widetilde{\mathbf{x}}(t)$. Secondly, the estimate $\widehat{\widetilde{n}}(t)$ of the scaled concentration deviation $\widetilde{n}(t)$ is extracted from the state estimate $\widehat{\widetilde{\mathbf{x}}}(t)$.

The following two sections review textbook material on how to design state estimators in case the input and output measurements are noise-free and noise-corrupted, respectively.

Afterwards we will apply the mathematical results to the specific case of the grey-box model with the input threshold transform.

27.3.2 State Estimator Design — Noise-Free Measurements

We consider the noise-free, i.e., deterministic, time-domain model

$$\dot{\mathbf{x}}(t) = \mathbf{A}\mathbf{x}(t) + \mathbf{B}u(t), \tag{27.11}$$
$$y(t) = \mathbf{C}\mathbf{x}(t) \tag{27.12}$$

with $D \equiv 0$.

Open-Loop Estimator

One method of estimating the state is to construct a full-order model of the system dynamics,

$$\dot{\widehat{\mathbf{x}}}(t) = \mathbf{A}\widehat{\mathbf{x}}(t) + \mathbf{B}u(t), \tag{27.13}$$

where $\widehat{\mathbf{x}}(t)$ is the estimate of the actual state $\mathbf{x}$. We know $\mathbf{A}, \mathbf{B}$, and $u(t)$. Hence this estimator will be satisfactory if we can obtain the correct initial condition $\mathbf{x}(0)$ and set $\widehat{\mathbf{x}}(0)$ equal to it. However, it is precisely the lack of information about $\mathbf{x}(0)$ that requires the construction of an estimator. Otherwise, the estimated state would track the true state correctly. Thus, if we made a poor estimate for the initial condition, the estimated state would have a continually growing error or an error that goes to zero too slowly to be of use. Furthermore, small errors in our knowledge of the system ($\mathbf{A}$, $\mathbf{B}$) would also cause the estimate to diverge from the true state.

To study the dynamics of this estimator, we define the error in the estimate to be

$$\mathbf{e}(t) = \mathbf{x}(t) - \widehat{\mathbf{x}}(t). \tag{27.14}$$

Then the dynamics of this error system is given by the autonomous differential equation

$$\dot{\mathbf{e}}(t) = \mathbf{A}\mathbf{e}(t) \tag{27.15}$$

with the initial condition

$$\mathbf{e}(0) = \mathbf{x}(0) - \widehat{\mathbf{x}}(0). \tag{27.16}$$

The error converges to zero for a stable system ($\mathbf{A}$ stable), but we have no ability to influence the rate at which the state estimate converges to the true state. Furthermore, the error is converging to zero at the same rate as the natural dynamics of $\mathbf{A}$. If this convergence rate were satisfactory, no estimation would be required [37, (Sect. 7.5.1)].

Closed-Loop Estimator

Consider feeding back the difference between the measured and estimated outputs and correcting the model continuously with this error signal — as illustrated by the block diagram in Figure 27.7. The

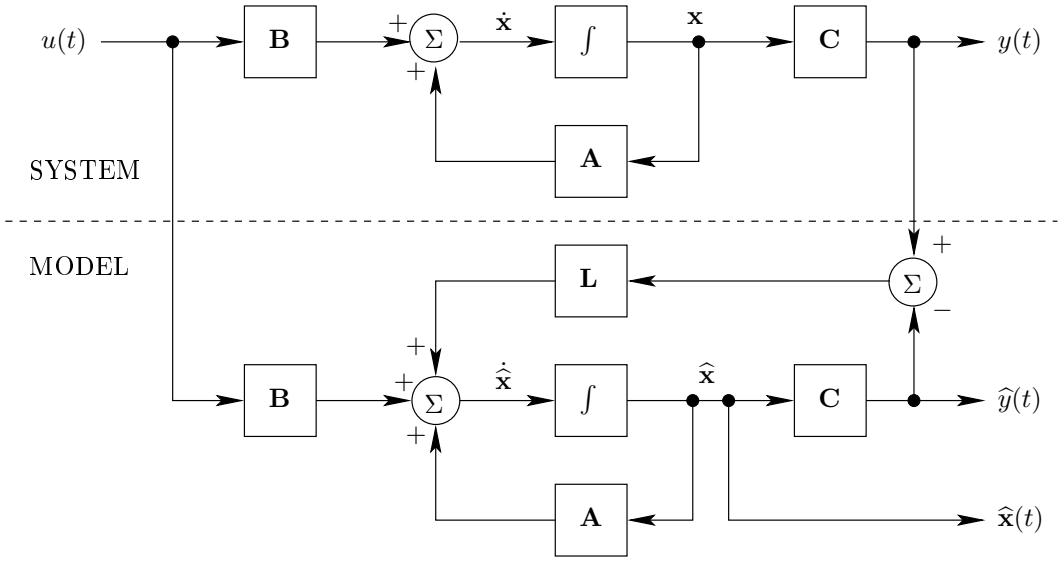

Figure 27.7: Block diagram showing how to extract the closed-loop estimator $\widehat{\mathbf{x}}(t)$ from the noise-free measurements of the input $u(t)$ and the output $y(t)$ signals.

equation for this scheme is

$$\dot{\widehat{\mathbf{x}}}(t) = \mathbf{A}\widehat{\mathbf{x}}(t) + \mathbf{B}u(t) + \mathbf{L}\Big(y(t) - \mathbf{C}\widehat{\mathbf{x}}(t)\Big). \tag{27.17}$$

Here $\mathbf{L}$ is a proportional gain defined as $\mathbf{L} = (\ l_1 \quad l_2 \quad \dots \quad l_n\ )^T$ and is chosen to achieve satisfactory error characteristics. The error is the solution to the following autonomous differential equation:

$$\begin{aligned}\dot{\mathbf{e}}(t) &= \dot{\mathbf{x}}(t) - \dot{\widehat{\mathbf{x}}}(t) = \mathbf{A}\mathbf{x}(t) + \mathbf{B}u(t) - \mathbf{A}\widehat{\mathbf{x}}(t) - \mathbf{B}u(t) - \mathbf{L}\Big(y(t) - \mathbf{C}\widehat{\mathbf{x}}(t)\Big) \\ &= \mathbf{A}\Big(\mathbf{x}(t) - \widehat{\mathbf{x}}(t)\Big) - \mathbf{L}\Big(y(t) - \mathbf{C}\widehat{\mathbf{x}}(t)\Big) = \mathbf{A}\Big(\mathbf{x}(t) - \widehat{\mathbf{x}}(t)\Big) - \mathbf{LC}\Big(\mathbf{x}(t) - \widehat{\mathbf{x}}(t)\Big). \quad (27.18)\end{aligned}$$

That is, the dynamics of the error can be obtained from the error equation

$$\dot{\mathbf{e}}(t) = \Big(\mathbf{A} - \mathbf{LC}\Big)\mathbf{e}(t). \quad (27.19)$$

The eigenvalues of the matrix $\mathbf{A} - \mathbf{LC}$ are the poles of the equivalent transfer function equation in the s-domain

$$s \cdot \mathbf{E}(s) = \Big(\mathbf{A} - \mathbf{LC}\Big)\mathbf{E}(s) \quad (27.20)$$

and thus determines whether the solutions to Equation (27.19) are stable.

If we can choose $\mathbf{L}$ so that $\mathbf{A} - \mathbf{LC}$ has stable and reasonable fast eigenvalues, then $\mathbf{e}$ will decay to zero and remain there — independent of the known forcing function $u(t)$ and its effect on the state $\mathbf{x}(t)$ and irrespective of the initial condition $\mathbf{x}(0)$. This means that $\dot{\widehat{\mathbf{x}}}(t)$ will converge to $\mathbf{x}(t)$, regardless of the value of $\widehat{\mathbf{x}}(t)$. Furthermore, we can choose the dynamics of the error to be stable as well as much faster than the open-loop dynamics determined by $\mathbf{A}$.

Note, that in obtaining Equation (27.19) we have assumed that $\mathbf{A}, \mathbf{B}$, and $\mathbf{C}$ are identical in the physical system and in the model of the estimator [37, (Sect. 7.5.1)].

27.3.3 State Estimator Design — Noise-Corrupted Measurements

If we do not have an accurate model of the system $(\mathbf{A}, \mathbf{G}, \mathbf{C})$, the dynamics of the error is no longer governed by Equation (27.19). However, we can typically choose $\mathbf{L}$ so that the error is still at least stable and the error remains acceptable small, even with (small) modeling errors and disturbing inputs [37, (Sect. 7.5.1)].

Optimal Estimation

We wish to pick $\mathbf{L}$ so that the estimate of the state vector $\mathbf{x}$, given all the data up to and including time t, is optimal. $\mathbf{L}$ will be based on minimization of estimation errors. The time-varying optimal estimation solution is commonly known as the *Kalman filter*.

We will calculate the optimal estimation solution with a steady-state $\mathbf{L}$-matrix. This optimal state estimate $\widehat{\mathbf{x}}(t)$ minimizes the steady-state error covariance [41, (Sect. 4.3)]

$$\mathbf{P} = \lim_{t \longrightarrow \infty} E\left\{\left(\mathbf{x}(t) - \widehat{\mathbf{x}}(t)\right)\left(\mathbf{x}(t) - \widehat{\mathbf{x}}(t)\right)^T\right\}. \quad (27.21)$$

Implementation in MATLAB

The LQE[1] Kalman estimator design for continuous-time systems takes noise into account: Given the system (D not fixed to zero)

$$\begin{aligned}\dot{\mathbf{x}}(t) &= \mathbf{A}\mathbf{x}(t) + \mathbf{B}u(t) + \mathbf{K}'\mathbf{w}(t), & (27.22)\\ y(t) &= \mathbf{C}\mathbf{x}(t) + Du(t) + v(t) & (27.23)\end{aligned}$$

with unbiased process noise $w(t)$ and measurement noise $v(t)$ with covariances

$$\begin{aligned}E\{\mathbf{w}(t)\mathbf{w}(t')^T\} &= \mathbf{Q} \cdot \delta(t - t'), & (27.24)\\ E\{v(t)v(t')^T\} &= R \cdot \delta(t - t'), & (27.25)\\ E\{\mathbf{w}(t)v(t')^T\} &= \mathbf{N} \cdot \delta(t - t'), & (27.26)\end{aligned}$$

[1] LQE: A linear quadratic estimation problem, that is, an estimation problem in which the dynamic system is linear and the performance cost function is quadratic [41, (Sect. 4.1.2)].

the MATLAB command [**L**, **P**, **p**] = $LQE(\mathbf{A}, \mathbf{K}', \mathbf{C}, \mathbf{Q}, R, \mathbf{N})$ returns the observer gain matrix $\mathbf{L} = \begin{pmatrix} l_1 & l_2 & \cdots & l_n \end{pmatrix}^T$ such that the stationary Kalman filter

$$\dot{\widehat{\mathbf{x}}}(t) = \mathbf{A}\widehat{\mathbf{x}}(t) + \mathbf{B}u(t) + \mathbf{L}\Big(y(t) - \mathbf{C}\widehat{\mathbf{x}}(t) - Du(t)\Big) \tag{27.27}$$

produces an optimal state estimate $\widehat{\mathbf{x}}(t)$ of $\mathbf{x}(t)$ using the sensor measurements $u(t)$ and $y(t)$. Note that, if the input u is the most reliable signal, **L** will be small, whereas if the output y is the most reliable signal, **L** will be large. Also returned are the solution **P** of the associated Riccati equation

$$\mathbf{AP} + \mathbf{PA}^T - \left(\mathbf{PC}^T + \mathbf{K}'\mathbf{N}\right) R^{-1} \left(\mathbf{CP}^T + \mathbf{N}^T\mathbf{K}'^T\right) + \mathbf{K}'\mathbf{Q}\mathbf{K}'^T = 0 \tag{27.28}$$

and the estimator poles $\mathbf{p} = eig(\mathbf{A} - \mathbf{LC})$.

27.3.4 Estimator Design for the Grey-Box Model

Having constructed a state estimator $\widehat{\widetilde{\mathbf{x}}}(t)$, we may extract an estimator $\widehat{\widetilde{n}}(t)$ of the scaled concentration deviation $\widetilde{n}(t)$ as follows:

$$\begin{aligned} \dot{\widehat{\widetilde{\mathbf{x}}}}(t) &= \widetilde{\mathbf{F}}\widehat{\widetilde{\mathbf{x}}}(t) + \widetilde{\mathbf{G}}u(t) + \mathbf{L}\Big(y(t) - \widetilde{\mathbf{H}}\widehat{\widetilde{\mathbf{x}}}(t)\Big) \\ &= \Big(\widetilde{\mathbf{F}} - \mathbf{L}\widetilde{\mathbf{H}}\Big)\widehat{\widetilde{\mathbf{x}}}(t) + \begin{pmatrix} \widetilde{\mathbf{G}} & \mathbf{L} \end{pmatrix} \begin{pmatrix} u(t) \\ y(t) \end{pmatrix}, \qquad (27.29) \\ \widehat{\widetilde{n}}(t) &= \mathbf{H}_n\widehat{\widetilde{\mathbf{x}}}(t) = \begin{pmatrix} 0 & 1 \end{pmatrix}\widehat{\widetilde{\mathbf{x}}}(t). \qquad (27.30) \end{aligned}$$

This MISO model can be rewritten on state-space form:

$$\begin{aligned} \dot{\widehat{\widetilde{\mathbf{x}}}}(t) &= \Big(\widetilde{\mathbf{F}} - \mathbf{L}\widetilde{\mathbf{H}}\Big)\widehat{\widetilde{\mathbf{x}}}(t) + \begin{pmatrix} \widetilde{\mathbf{G}} & \mathbf{L} \end{pmatrix} \begin{pmatrix} u(t) \\ y(t) \end{pmatrix}, \qquad (27.31) \\ \widehat{\widetilde{n}}(t) &= \begin{pmatrix} 0 & 1 \end{pmatrix}\widehat{\widetilde{\mathbf{x}}}(t) + \begin{pmatrix} 0 & 0 \end{pmatrix} \begin{pmatrix} u(t) \\ y(t) \end{pmatrix}. \qquad (27.32) \end{aligned}$$

Note that the input to this state-space model is a two-dimensional vector consisting of the original input $u(t) = FPA_{pp}(t)$ to and output $y(t) = CBF(t)$ from the linear part of the grey-box model.

27.3.5 Implementation in MATLAB

First, the state-space model (23.33)–(23.34) on page 151 is extended with noise terms such that it appears on the form (27.22)–(27.23).

Secondly, the observer gain matrix **L** is found by means of the LQE-command with the matrices **A** and **C** being

$$\mathbf{A} = \widetilde{\mathbf{F}} = \begin{pmatrix} -(f+k) & 1 \\ -(f\cdot k + h\cdot l) & 0 \end{pmatrix}, \qquad \mathbf{C} = \widetilde{\mathbf{H}} = \begin{pmatrix} 1 & 0 \end{pmatrix}. \tag{27.33}$$

The values of the parameters $g\cdot h, f+k, f\cdot k + h\cdot l$ are listed in Table 25.2 on page 164. The parameters in the noise description have been specified as follows:

$$\mathbf{K}' = \begin{pmatrix} 1 & 0 \\ 0 & 1 \end{pmatrix}, \quad \mathbf{Q} = \begin{pmatrix} 1 & 0 \\ 0 & 1 \end{pmatrix}, \quad \mathbf{N} = \begin{pmatrix} 0 \\ 0 \end{pmatrix}. \tag{27.34}$$

That leaves the measurement noise covariance R as the design parameter. R is now a measure of how noisy the measurements of the output signal $y(t) = CBF(t)$ are compared to the measurements of the input signal $u(t) = FPA_{pp}(t)$.

Thirdly, when an appropriate **L**-matrix has been formed, an optimal estimate $\widehat{\widetilde{n}}(t)$ of the scaled concentration deviation $\widetilde{n}(t)$ can be calculated by simulating the noise-free Equations (27.31)–(27.32).

27.3.6 Time Series of $\widetilde{n}(t)$

Estimates of the time series of the scaled concentration deviation $\widehat{\widetilde{n}}(t)$ are depicted in Figure 27.8 for three different values of the measurement noise covariance R. It should be remembered that, according to Equations (23.2)–(23.4) with $f \equiv 0$, the rate of change of the concentration deviation is a result of two physiological processes: The release of nitric oxide from the neuron and the removal of nitric oxide by the blood flow.

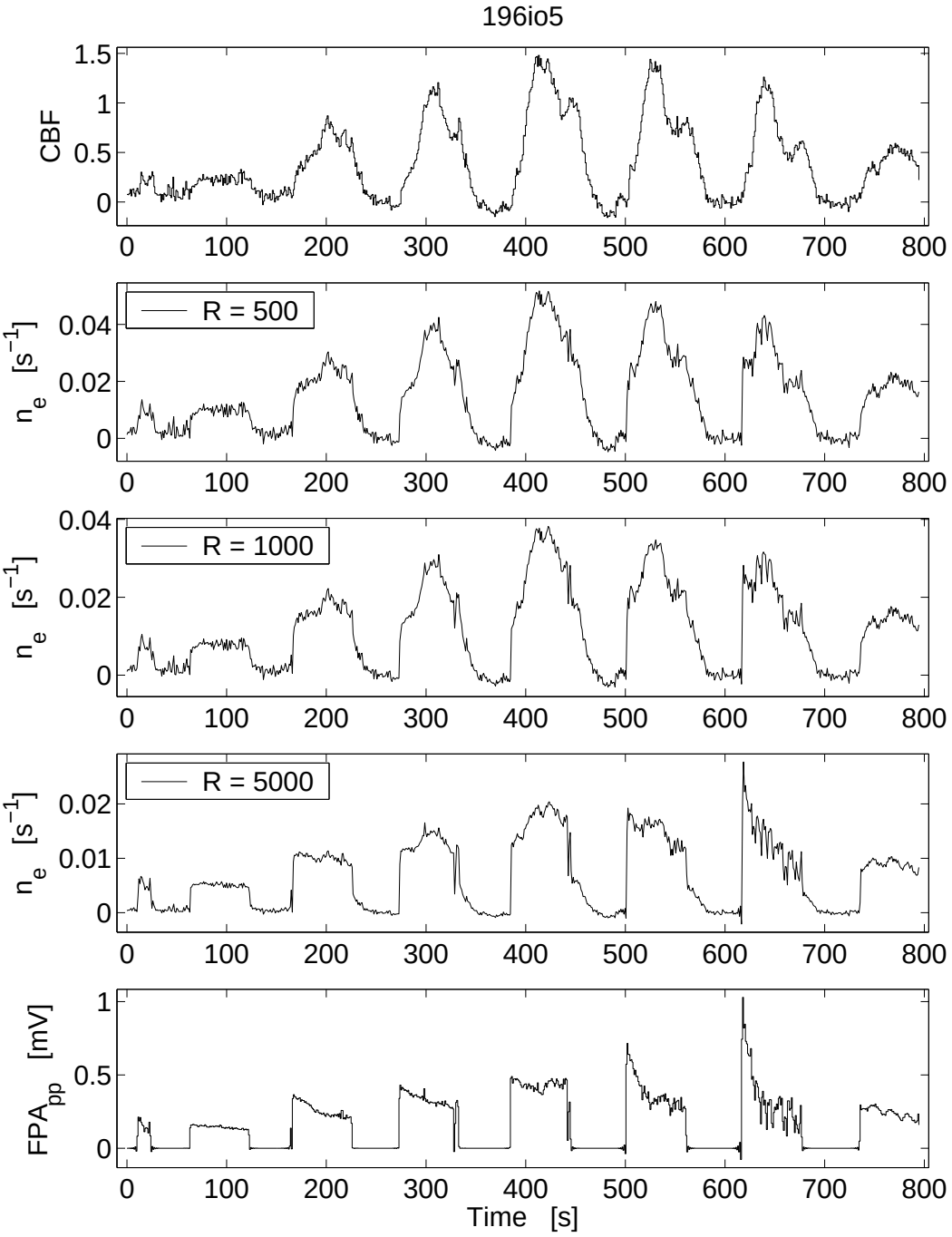

Figure 27.8: The grey-box model with the input threshold transform: Top panel: The output signal $y(t) = CBF(t)$. Second through fourth panel: The estimator $\widehat{\widehat{n}}(t)$ (in the figure denoted by n_e) of the scaled concentration deviation calculated from the input and output signals for three different values of the covariance of the measurement noise on $CBF(t)$: $R \in [500;\ 1000;\ 5000]$. Bottom panel: The input signal $u(t) = FPA_{pp}(t)$. For lower values of R the shape of $\widehat{\widehat{n}}(t)$ resembles $y(t)$, and for higher values of R the shape of $\widehat{\widehat{n}}(t)$ resembles $u(t)$.

27.3.7 Comparison to Measurements of $c(NO)$

We do not have access to *in vivo* measurements of the concentration of nitric oxide during inferior olive stimulation. Instead we will compare Figure 27.8 to *in vitro* measurements.

Shibuki *et al.* — cf. Refs. [85, (Fig. 2C)] and [86, (Fig. 1a)] — have performed *in vitro* measurements[2] of the NO concentration during climbing fiber activation. Their measurements expose a smooth and relatively fast increase in NO concentration during stimulation at 20 Hz for 5 s, and a smooth but much slower decrease towards the baseline concentration level after cessation of stimulation. We note that the NO trace estimated from the grey-box model with the smallest value of the design parameter R, $R = 500$, is closest to this behavior.

Another characteristic feature of both the estimated and the measured NO concentration signals is that the NO concentration never becomes lower than the baseline level in response to climbing fiber activation.

In vivo measurements of the extracellular potassium concentration during parallel fiber stimulation have been performed by Caesar *et al.* — cf. Ref. [19, (Fig. 3A)]. Those measurements expose quite different features: At onset of stimulation the potassium concentration rises very fast. After cessation of stimulation the concentration makes an undershoot, i.e., the potassium concentration becomes lower than the baseline level and then increases very slowly towards the baseline level.

[2] As there are no blood vessels, no hemoglobin can bind NO. This situation could be modeled by fixing the parameter l to zero: $l \equiv 0$.

Chapter 28

Discussion of Grey-Box Models

28.1 Overview of Grey-Box Models

The grey-box models, which have been developed in this part, consist of three interconnected subsystems as illustrated by Figure 28.1. Each of the models contains zero, one, or two parameters describing a

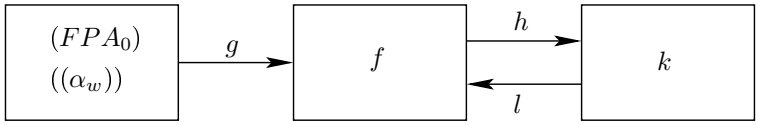

Figure 28.1: The grey-box model with the input weight transform: The diagram shows the five through seven parameters, which characterize the three subsystems (the neuronal subsystem, the extracellular space, and the vascular subsystem) of the neuro-vascular system and their interconnections.

nonlinear dynamic coupling and five parameters describing linear dynamic couplings.

The parameters in the grey-box models represent the following dynamic couplings:

- A coupling between the fast variation in the field potential signal and the slow time scale pertaining to changes in relative cerebellar blood flow. Three types of couplings — mathematically expressed as preprocessing procedures — have been tested:

  The Input Sampling Transform The coupling has been assumed to be linear and without memory.

  The Input Threshold Transform The coupling has been assumed to be nonlinear, without memory, and characterized by a single parameter: The threshold position (FPA_0).

  The Input Kink Transform The coupling has been described by a nonlinearity, without memory, containing two parameters: The kink position (FPA_0) and the kink slope (α_w).

  Chemical concentrations have been assumed to vary on an intermediate time scale. The transformation from the intermediate time scale to the slow time scale has not been specified in the grey-box models.

- A linear coupling (g) between the preprocessed field potential amplitude signal (pertaining to the neuronal subsystem) and the rate of change of the (possibly nonlinearly) preprocessed deviation of the NO concentration in the extracellular space from its baseline value.

- The internal dynamics (f) of the NO concentration in the extracellular space has been modeled as being linear on the slow time scale.

- The coupling (h) from the preprocessed concentration deviation in the extracellular space to the rate of change of the relative blood flow in the capillaries has been modeled as being linear.

- The coupling (l) from the relative blood flow in the capillaries to the rate of change of the NO concentration deviation in the extracellular space has been assumed to be linear.
- The internal dynamics (k) of the vascular subsystem has been assumed to be linear.

Some possible couplings have been excluded from the grey-box model structures:

- A static coupling between the NO concentration deviation and the relative blood flow level.
- A direct coupling between the neuronal subsystem and the vascular subsystem.

Due to the structure of the model only three through five parameters are identifiable: FPA_0 and α_w in the preprocessing procedures, and $g \cdot h$, $f + k$ and $f \cdot k + h \cdot l$ in the linear couplings.

28.2 Preconditions for the Grey-box Model

In the following the grey-box model with the input threshold transform will be considered. It has been constructed from a number of preconditions:

- **Only Three Subsystems are Necessary**
  The subsystems of the model are: The neuronal subsystem, the extracellular space, and the vascular subsystem.

  Fillenz *et al.* [35] have suggested that *"glial cells, specifically astrocytes, play a crucial role in the increase in cerebral blood flow during neuronal activation"*. As shown in Figure 28.2 introduction of this extra subsystem also introduces a number of extra variables, the most important one being the concentration of glucose. Thus inclusion of this extra subsystem also increases the complexity

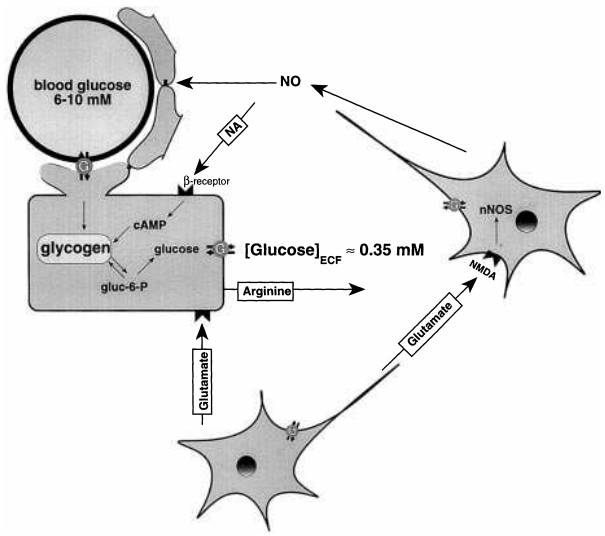

Figure 28.2: A schematic representation of the role of astrocytes in the activity-dependent increases in CBF. The picture is suggested in Ref. [35].

  of the model significantly. To the best of our knowledge, the picture has not been experimentally confirmed.

- **Only One Input is Necessary**
  It has been chosen not to consider the stimulation as the input even though all information about this signal is available. The reason is that it is exterior to cerebellum. Instead the field potential, which is measured interior to cerebellum, has been used as input.

  However, the stimulation maybe change other interior variables too, which effect the cerebellar blood flow. This means that maybe the input (vector) should be extended. Note that the analysis in Section 14.2.3 on page 91 excluded that the arterial blood pressure should be a dimension of the input vector.

- **The Amplitude Contains All Information on a FP Excitation**
  It is questionable whether the amplitude is a good representation of the information content of a field potential excitation: The signal analysis showed that at very low frequencies ($\sim 2\ Hz$) the field potential duration is smaller than at all other frequencies (cf. Section 14.1.3 on page 83). This indicates, that the shape of the evoked field potential excitations depends on their frequency. Thus the amplitude is very likely a much too simple representation of a FP excitation. Specifically, the amplitude may overestimate the information content at low frequencies.

  We have seen, that for some experiments the grey-box model with the input threshold transform considerably overestimates the blood flow at very low frequencies (cf. Figure 25.3 on page 162). The hypothesis that the amplitude overestimates the information content at low frequencies explains this fact. In other words: We suggest that the bad fit at low stimulation frequencies is not due to under-modeling, but rather a direct result of a too simple signal representation.

  The ionic and molecular concentrations in the extracellular space are of course related to the full field potential signal — not only to the amplitude of the time-localized events in the signal. Therefore the integral of the field potential signal over the duration of each event ($\int_0^{FPD} FP(t)dt$) would probably be a better representation of each event.

  Such a change of signal representation may furthermore have the advantage of making the model structure linearizable also at very low frequencies. We have already concluded, that the model structure is linearizable if the stimulation frequency is kept below $\sim 10\ Hz$, because in this frequency range almost all field potential amplitude are larger than the threshold (cf. Section 27.1.1 on page 176). We suggest that, if the resulting linear model structure is combined with the above-mentioned change of signal representation, a very good fit between measured and model output would be obtained in the whole frequency range $0 - 10\ Hz$.

- **No Scaling of FPA Signal**
  The field potential of a point current source changes with the distance from the point current source to the power of minus one [64, (Sect. 8.2.1)]. And the geometry vary from neuron to neuron. Furthermore, due to the small scales it is difficult to place the measuring electrode in exactly the same position in all experiments. Therefore one could expect that it would be necessary to scale the FPA measurements to some value. For instance the maximum value of FPA or an extrapolation of the FPA graph to the frequency $f = 0\ Hz$ could be tried. (The arithmetic mean value could not be used since it also depends on the choice of sequence of stimulation frequencies (besides the geometry).)

  However, since the coefficients of variance of FPA_0 have shown to be quite low, such considerations seems to be unnecessary.

- **Nonlinear Transformation from Fast to Slow Variables**
  In Section 24.3 on page 158 we argued that, since the analysis in Section 14.1.2 on page 82 showed that the size of the field potential amplitudes decreases as their frequency increases, it could be expected — from a mathematical point of view — that an increasing weight function imposed on the field potential amplitude signal could explain the frequency saturation of the cerebellar blood flow signal. This has now been confirmed.

- **Lumped Variables**
  In this study each subsystem has been characterized by only one variable.

  However, it should be remembered that the concentration of the chemical substance NO, $c(NO)$, is a lumped variable not only representing the extracellular space but also the capillaries coated with endothelium cells on the inner side, the blood-brain barrier and the glia cells. For instance, the blood flow removes NO from the endothelium cells on the inner side of the capillaries, not directly from the extracellular space.

  Similarly the blood vessel subsystem is a lumped concept. In the model it is only characterized by the blood flow level in the capillaries. However, the capillaries themselves are not affected by NO, since they have no smooth muscle structure. But NO affects the arterioles (upstream as compared to the capillaries) — cf. P: Section 5.2 on page 28. Thus in that sense the vascular subsystem has been described by a mixture of capillary and arteriolar properties.

Furthermore, since the LDF signal was measured at the capillaries it should not be influenced by volume changes as in the case of the BOLD signal.

- **One Mediator of Neuro-Vascular Coupling**
  Based upon the findings of Ref. [2] it has been assumed that NO is the dominant mediator across the extracellular space in case of climbing fiber activation. For the case of parallel fiber activation it would similarly be natural to assume that extracellular potassium ions, K^+, are responsible for the main part of the neuro-vascular coupling [19]. There could, however, be more chemical substances, X_i, mediating the coupling between evoked electrical activity and the change in relative cerebellar blood flow. In such case the internal state should be a vector containing all the (preprocessed) deviations of the concentrations from their equilibrium, or baseline, values:

$$\mathbf{n}(t) = \begin{pmatrix} \{c(NO)(t) - c_B(NO)\}_{pp} \\ \{c(X_2)(t) - c_B(X_2)\}_{pp} \\ \vdots \\ \{c(X_{n-1})(t) - c_B(X_{n-1})\}_{pp} \end{pmatrix}. \tag{28.1}$$

  Furthermore, a picture containing only a single or a few independent mediators of neuro-vascular coupling is probably much too simple. The mediators may interact mutually as well as with other elements of cerebellum. For instance measurements reported in Ref. [4] suggest that *"adenosine uses NO as a pathway to induce vasodilation"*. For the case of PF stimulation adenosine seems not to have function (cf. P: Section 6.5 on page 39). A suggestion to a more involved picture is discussed in Ref. [35]. Mathematical modeling of a complicated picture including interactions will require the introduction of more variables, and most likely more nonlinearities.

  Mathiesen *et al.* [67] have suggested that the action of different vasoactive compounds during the stimulation period might be responsible for the dip nonlinearity: *"For example, the first CBF peak might relate to the early non-exhausted phase of neuronal activity, which is delayed and reduced by nitric oxide synthase inhibitors. The second peak might relate to accumulation of vasoactive metabolites, e.g. adenosine (...), as the electrophysiological response adopts during continuous activation."*

- **Two-Dimensional State Vector**
  The state of a system determines which response (output) results from a certain stimulus (input).

  The state of the neuro-vascular system has been assumed to be characterized by two variables: The cerebellar blood flow level (the output) and the NO concentration (transformed to the blood flow time scale) in the extracellular space. From the model structure in Equations (23.10)–(23.11) it seems unlikely that the state should *not* contain the blood flow level CBF. If the state vector does *not* contain the blood flow level then the current blood flow level does not depend on previous values of the blood flow level but only depends statically on the NO concentration.

- **No Feedback**
  Fillenz *et al.* [35] mention that *"the role of cerebral blood supply is the delivery to the brain of metabolic substrates and the removal of waste products"*, and that *"as there are no energy reserves, a constant supply of oxygen and glucose, the main metabolic substrates, is required and any interruption of the blood supply rapidly produce profound and irreversible changes of brain function"*.

  Thus it is tempting to believe that feedbacks of oxygen and glucose from the vascular subsystem to the neuronal subsystem should be important components of the model.

  On the other hand Keener and Sneyd [47, (Sect. 15.6.1)] notes that *"in tissue for which the delivery of oxygen is of central importance (for example, the brain...) the local blood flow is regulated to be slightly higher than required, but no higher"*. This we may call a *buffer mechanism*.

  From these citations it is suggested that under physiological conditions oxygen and glucose do not have a regulatory effect on the neuronal subsystem and therefore need not be included as feedbacks in the model. However, if the model should cover pathophysiological or extreme conditions characterized by for example hypoxia, the feedbacks would have to be included. Consider, for example, hypoxia. The oxygen feedback should be positive since lack of oxygen supplies limit the neuronal activity.

  The question which remains to be answered is whether the anesthesia alters or knocks out the feedback mechanisms.

28.3 Interpretations of the Grey-Box Model

28.3.1 Frequency versus Amplitude

The ability of the grey-box model with the input threshold transform to reproduce parts of the dynamics in experimental data from Wistar rats is a result of strong smoothing of the neuronal signal. The weightening has a low-pass filtering effect since the analysis in Section 14.1.2 on page 82 showed that the low-frequency FPA's are the largest. Thus it is tempting to conclude that only the low-frequency FPA's contribute to the increase in CBF, and that only the low-frequency neuronal activity in cerebellum can be inferred from measurements of cerebellar blood flow. However, because the size of FPA's depends dynamically on the stimulation frequency, this is a wrong interpretation!

The right interpretation is the following: Only FPA's above a certain amplitude threshold contribute to increases in CBF. Another way to say this is: The CBF response is dynamically and linearly coupled to the neuronal activity above threshold, but un-coupled to the activity below threshold. Thus only field potential amplitudes above the threshold can be inferred from measurements of cerebellar blood flow — no matter their frequency. This also means that zero CBF response does *not* exclude neuronal activity *below* threshold.

Similar interpretations have been reached by Norup Nielsen *et al.* [76] for the somato-sensory cortex even though the mechanism behind that phenomenon is different. In that case the size of the FPA's is pretty constant for a given low stimulation frequency. But for larger frequencies the size of the FPA's makes a bifurcation-like transition into two interlacing levels (cf. Ref. [76, (Fig. 3)]).

28.3.2 Physiological Origin of the Threshold

The physiological origin of the threshold remains to be settled. We suggest that a depolarization of the nerve cell membrane stronger than a certain level is required in order to cause synthesis of the vasodilatory substance. The mechanism could be as follows — cf. P: Section 6.4 on page 38 and Ref. [14]: The depolarization of the nerve cell membrane forces voltage-dependent calcium channels to open, and thereby the intercellular calcium concentration increases. As a result NOS is activated, and NO is synthesized and released. Since NO diffuses through the extracellular space, it reaches the arterioles. The end result is vasodilation and flow increase.

Chapter 29

Conclusion on Grey-Box Models

Starting from a couple of simple ideas about the physiology of cerebellum in healthy rats, partially identifiable grey-box models of the relation between evoked neuronal activity in climbing fibers and changes in the blood flow level in nearby capillaries have been provided.

The grey-box models relate measurements of the event-sampled field potential amplitude signal (input) to measurements of the sampled relative cerebellar blood flow signal (output). Each of the models consists of a dynamic transformation of the input followed by a linear state-space model with coupled and constrained parameters.

Three input transforms have been tested:

- The input sampling transform (linear),
- The input threshold transform (nonlinear, one parameter), and
- The input kink transform (nonlinear, two parameters).

When the input transformation is chosen to be a threshold, thus containing only a single parameter (the threshold position), the performance of the model becomes better than that of the purely linear model. Furthermore, the sensitivity to the threshold position is significant, indicating it has physiological significance. However, smoothing out the threshold, so it becomes a kink, and thereby introducing an extra parameter (the kink slope) in the nonlinearity does not improve the performance of the model further. And the sensitivity to the kink slope is very low. Thus it cannot be interpreted in terms of physiology. The threshold nonlinearity satisfactorily took into account the feature of the data formerly characterized as frequency saturation. But the dips in the vascular signal are unaccounted for by the grey-box models.

The order of the linear state-space model is two, and the state vector consists of the relative cerebellar blood flow level and the preprocessed deviation of the concentration of nitric oxide in the extracellular space from its baseline value. The state-space part of the models is constrained in the sense that one of the parameters in the equivalent transfer function is fixed to the value zero. The five parameters are coupled in the sense that the equivalent transfer function only contains three parameters, which are nonlinear functions of the five parameters in the state-space part of the model. The estimates of the three identifiable parameters in the state-space model as well as the threshold position are consistent in the sense, that their coefficients of variance are much smaller than one. Furthermore, the model fit is almost equally sensitive to the three identifiable parameters in the linear part of the model.

The dynamics part of the grey-box models have been constructed from hypotheses concerning the mechanisms of neuro-vascular coupling. One of the hypotheses is, that the coupling is not direct, but is mediated via the extracellular space. The assumption that NO is a dominant mediator has made it possible to estimate a non-measured signal: The slow dynamics of the deviation of the concentration of NO in the extracellular space from its baseline value.

Part VI

Semi-Physical Models

The purpose of this part is to investigate whether too many constraints have been imposed on the linear state-space model part of the grey-box models developed in Part V.

The mean will be to combine the input transforms developed for the grey-box models in Part V with the high flexibility of the linear black-box state-space model structure investigated in Part IV. The resulting models are semi-physical SISO models. Inspired by these models a semi-physical MISO model is proposed. Thus this part considers

- Semi-Physical SISO Models
- A Semi-Physical MISO Model.

The goal is to obtain better model performance than has been reached by the grey-box models in Part V.

Chapter 30

Semi-Physical SISO Models

30.1 The Idea of Semi-Physical SISO Modeling

The grey-box models constructed in Part V are constrained as compared to general black-box models in the sense that one parameter in the equivalent transfer function have been fixed to a predefined value (zero, to be specific — cf. Section 23.4 on page 150). Furthermore the state vector showed up to be two-dimensional. The state of the system is thus described by two variables: The relative cerebellar blood flow level, and the preprocessed deviation of the NO concentration from its baseline value:

$$\mathbf{x}(t) = \begin{pmatrix} CBF(t) \\ n(t) \end{pmatrix} = \begin{pmatrix} CBF(t) \\ \{c(NO)(t) - c_B(NO)\}_{pp} \end{pmatrix}. \tag{30.1}$$

In this chapter it is investigated whether linear output-error black-box (i.e., unconstrained) state-space models combined with the preprocessing procedures developed for the grey-box models give better results than the grey-box models. The resulting models will thus be semi-physical models (cf. M: Section 11.1 on page 61). Furthermore it is investigated whether the linear model order actually should be equal to two, as in the grey-box models investigated in Part V, or maybe higher as in one of the linear black-box models presented in Part IV.

30.2 The SISO Model Structures

The semi-physical SISO output-error model structures are of the form

$$\begin{aligned} u(t) &= FPA_{pp}(t), && (30.2)\\ y(t) &= CBF(t), && (30.3)\\ \dot{\mathbf{x}}(t) &= \mathbf{F}\mathbf{x}(t) + \mathbf{G}u(t), && (30.4)\\ y(t) &= \mathbf{H}\mathbf{x}(t) + Ju(t) + e(t), && (30.5) \end{aligned}$$

where the state vector $\mathbf{x}$ is n-dimensional.

The 10 Hz sampled preprocessed field potential amplitude signal $FPA_{pp}(t)$ will be constructed from the event-sampled field potential amplitude signal $FPA(t_j)$ by means of an input transform. This chapter investigates the three input transforms which have been suggested in Part V:

- The input sampling transform,
- The input threshold transform, and
- The input kink transform.

30.3 Implementation of the SISO Models in MATLAB

The linear order n will be estimated following the procedure described in M: Section 11.3.2 on page 62.

30.4 A SISO Model with The Input Sampling Transform

30.4.1 The Input Sampling Transform

The FPA signal is preprocessed according to the linear input sampling transform:

$$u(t) = FPA_{pp}(t) = \sum_{t-\frac{\tau}{2}<t_j\leq t+\frac{\tau}{2}} FPA(t_j). \tag{30.6}$$

30.4.2 Model Results

Model Fit

The measures of model performance, that is the peak-to-peak value of the model error ΔCBF_{pp} and the noise-to-signal ratio NSR are listed in Table 30.1. The only difference between the semi-physical

Series	ΔCBF_{pp}	NSR [%]
196io4	0.99558	24.5
196io5	1.30134	35.6
197io1	0.88577	37.8
197io3	1.08141	53.0
Mean	1.06603	37.7

Table 30.1: The semi-physical model with the input sampling transform: The peak-to-peak value of the model error ΔCBF_{pp} and the noise-to-signal ratio NSR obtained for each of the four time series. Also their arithmetic mean values (*mean*) are listed. Note that the values are close to those obtained by the equivalent grey-box model — compare with Table 23.1 on page 153.

model with the input sampling transform and the equivalent black-box model, which was investigated in Chapter 18, is that the Kalman gain matrix $\mathbf{K}$ has been fixed to zero: $\mathbf{K} \equiv \mathbf{0}$. By comparing Table 30.1 with Table 18.3 on page 115 we reach the conclusion that the exclusion of the Kalman gain matrix from the model structure has not changed the model fit.

Comparisons of model output with the output measured by the LDF probe `Re140`, and the equivalent model error traces ΔCBF are shown in Figures 30.1. Despite the extra flexibility of the state-space part of the model — as compared to the equivalent grey-box model (Chapter 23) — the model is unable to account for the frequency saturation of and the dips in the measured output.

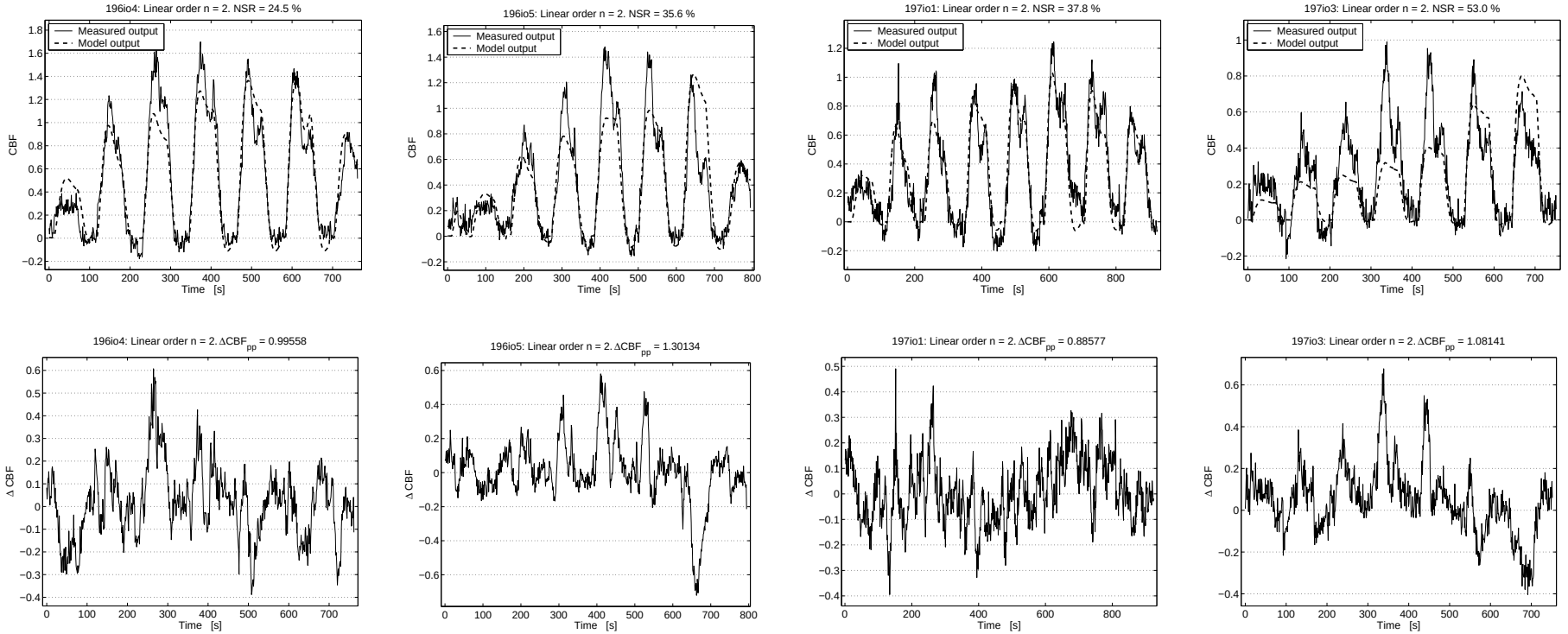

Figure 30.1: The semi-physical model with the input sampling transform: Top panels: Comparison of model output (dashed line) to measured output (full line). Note that the linear model is unable to reproduce two features of the measured output: The frequency saturation and the dips. Furthermore, these model output traces closely resemble those obtained by the equivalent grey-box model — see Figure 23.1 on page 154. Bottom panels: The model error traces ΔCBF. Note that these model error traces closely resemble those obtained by the equivalent grey-box model — compare with Figure 23.2 on page 155.

Estimates

The estimates of the linear order n are listed in Table 30.2. For all four experiments the linear order has

Series	n
196io4	2
196io5	2
197io1	2
197io3	2
Mean	2

Table 30.2: The semi-physical model with the input sampling transform: The estimated linear order n of the state-space model obtained from each of the four experiments. Also the arithmetic mean value (*mean*) is listed. Note that, for all four experiments, the estimate $n = 2$ corresponds to the linear order of the equivalent grey-box model — cf. Section 23.6 on page 152.

been estimated to $n = 2$.

30.5 A SISO Model with the Input Threshold Transform

30.5.1 The Input Threshold Transform

The FPA signal is preprocessed following the nonlinear input threshold transform:

$$u(t) = FPA_{pp}(t) = \sum_{t-\frac{\tau}{2}<t_j\leq t+\frac{\tau}{2}} \{FPA(t_j)\cdot w(FPA(t_j))\}\,, \tag{30.7}$$

$$w(FPA) = \theta\left(FPA - FPA_0\right). \tag{30.8}$$

30.5.2 Model Results

Model Fit

The measures describing the model fit are listed in Table 30.3. Compared to the results of the semi-

Series	ΔCBF_{pp}	NSR [%]
196io4	1.01336	23.9
196io5	0.76895	26.1
197io1	0.88624	37.8
197io3	0.89589	43.8
Mean	0.89111	32.9

Table 30.3: The semi-physical model with the input threshold transform: The peak-to-peak value of the model error ΔCBF_{pp} and the noise-to-signal ratio NSR for each of the four time series. Also their arithmetic mean values (*mean*) are listed. Note that the values are close to those obtained by the equivalent grey-box model — cf. Table 25.1 on page 161.

physical model with the input sampling transform (Table 30.1 on page 201), the input threshold transform has provided a significant improvement of the model performance. The model does not provide an improvement compared to the results of the grey-box model with the input threshold transform (cf. Table 25.1 on page 161) — despite the extra parameter in the numerator of the transfer function (cf. Section 23.4 on page 150).

A comparison of model output with the output measured by the LDF probe `Re140`, and the corresponding model error traces ΔCBF are given in Figures 30.2 and 30.3, respectively. As with the equivalent grey-box model, the semi-physical model with the input threshold transform reproduces the frequency saturation, but cannot explain the dips in the CBF signal.

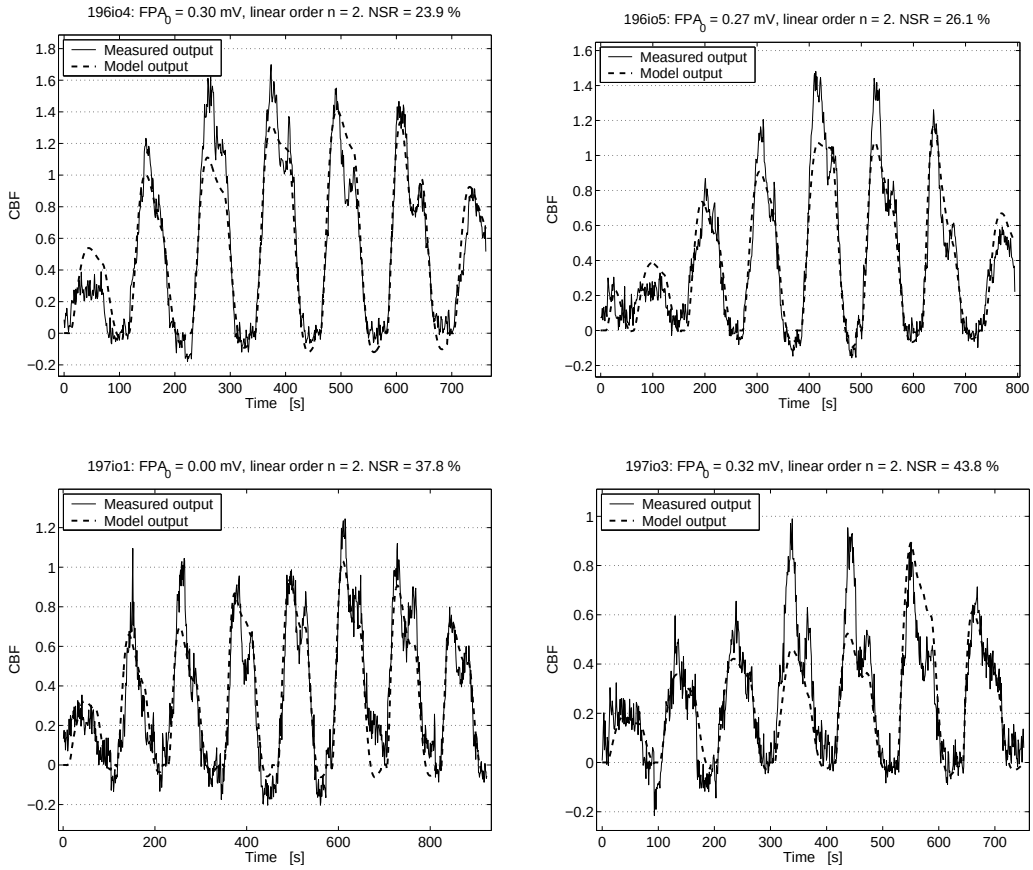

Figure 30.2: The semi-physical model with the input threshold transform: Comparison of model output (dashed line) with measured output (solid line) for each of the four inferior olive stimulation experiments. Note that a better fit has not been obtained by the semi-physical model as compared to the equivalent grey-box model. Accordingly, these model output traces closely resemble those obtained by the equivalent grey-box model, which are shown in Figure 25.3 on page 162. As the equivalent grey-box model, the semi-physical SISO model with the input threshold transform is able to reproduce the frequency saturation, but not the dips, in the measured output.

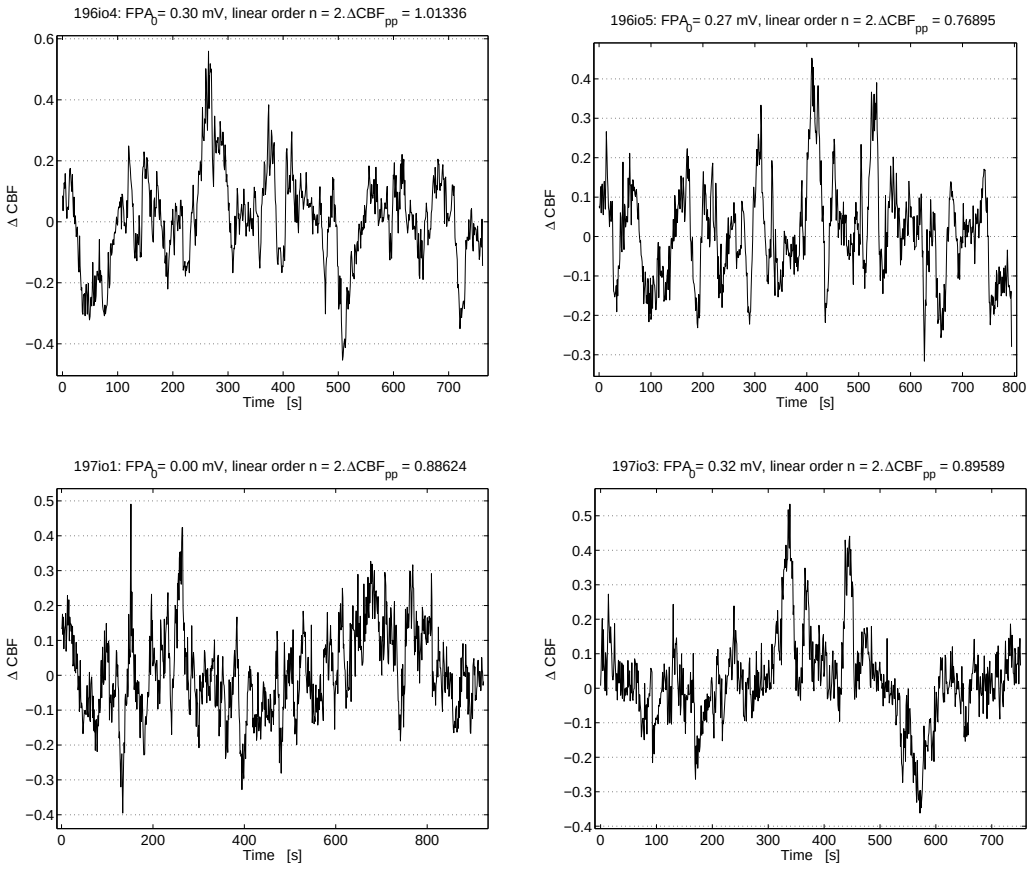

Figure 30.3: The semi-physical model with the input threshold transform: The model error traces ΔCBF obtained from each of the four time series. Note that these traces closely resemble those shown in Figure 25.4 on page 163 which stem from the equivalent grey-box model.

Cross Validation

The estimates of the threshold position FPA_0 and the linear state-space model order n are listed in Table 30.4. The estimated threshold positions are identical to those obtained by the equivalent grey-box model (cf. Table 25.2 on page 164). The estimates of the linear order of the semi-physical model is identical to the linear order of the equivalent grey-box model, which has been constructed with a 2nd order linearity.

Series	FPA_0 $[mV]$	n
196io4	0.30	2
196io5	0.27	2
197io1	0.00	2
197io3	0.32	2
Mean	0.22	2
Std	0.15	0
Cv	0.67	0

Table 30.4: The semi-physical model with the input threshold transform: The threshold position FPA_0 and linear order n estimated from each of the four time series. Also shown are their arithmetic mean values (*mean*), standard deviations (*std*), and coefficients of variance (*cv*). Note that the values of FPA_0 are almost identical to those obtained by the equivalent grey-box model — compare with Table 25.2 on page 164. Specifically, the linear order has un-ambiguously been estimated to $n = 2$, that is, the same as the value for the grey-box model.

Sensitivity to the Threshold Position FPA_0

The sensitivity to the threshold position FPA_0 is illustrated by Figure 30.4. The rather high sensitivity

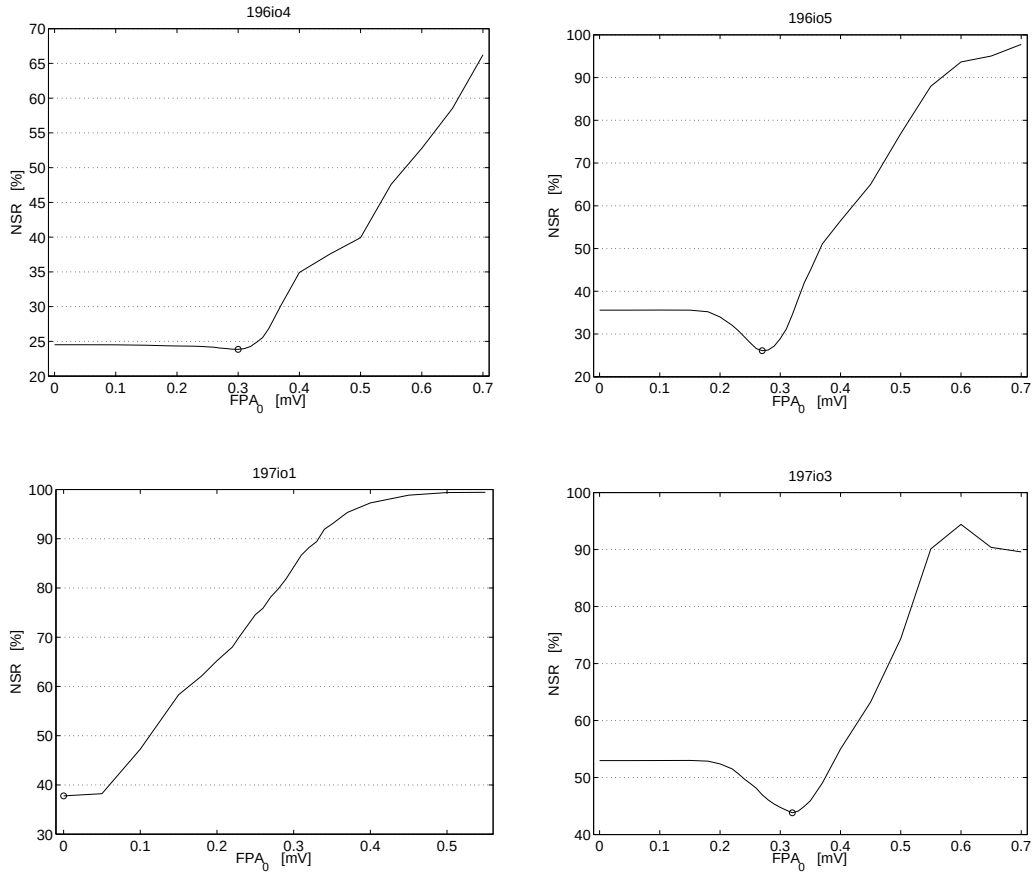

Figure 30.4: The semi-physical model with the input threshold transform: Variation in noise-to-signal ratio NSR with variation in the threshold position FPA_0 for each of the four inferior olive stimulation experiments. The minima of the noise-to-signal ratio are marked by a '$\circ$'. The data points at $FPA_0 = 0\ mV$ correspond to the linear model presented in Section 30.4. Note that these curves closely resemble those obtained by the equivalent grey-box model — compare with Figure 25.5 on page 165.

to FPA_0 indicates that FPA_0 has physical significance.

The variation in the estimated linear model order n with variation in the threshold position FPA_0 is shown in Figure 30.5.

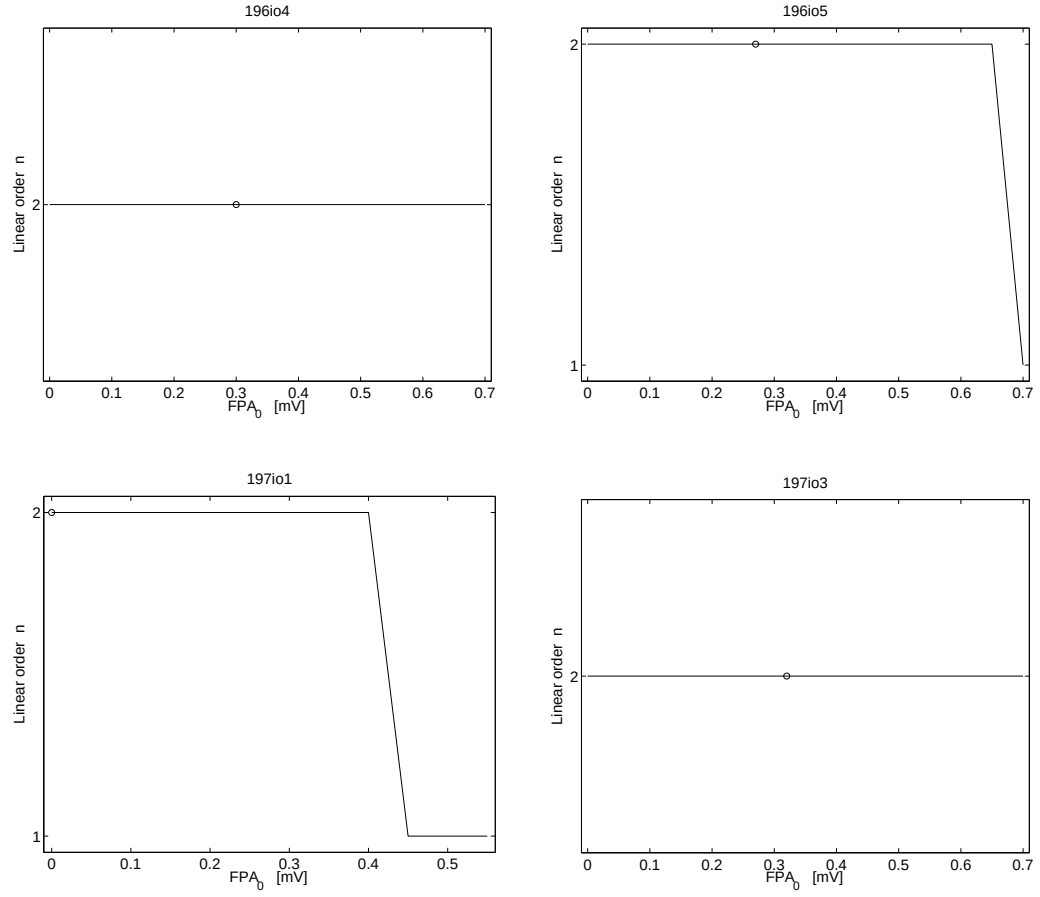

Figure 30.5: The semi-physical model with the input threshold transform: The variation in the estimated linear model order n with variation in the threshold position FPA_0 for each of the four inferior olive stimulation experiments. In each case, the point marked with a '$\circ$' corresponds to the minimum value of the noise-to-signal ratio, $\min_{FPA_0}(NSR)$. Note that for most values of the threshold position the linear order is estimated to be $n = 2$.

30.6 A SISO Model with the Input Kink Transform

30.6.1 The Input Kink Transform

Preprocessing of the FPA signal according to the input kink transform is nonlinear:

$$u(t) = FPA_{pp}(t) = \sum_{t-\frac{\tau}{2}<t_j\leq t+\frac{\tau}{2}} \{FPA(t_j)\cdot w(FPA(t_j))\}\,, \tag{30.9}$$

$$w(FPA) = \frac{1}{2}\cdot\{1+\tanh[2\cdot\alpha_w\cdot(FPA-FPA_0)]\}\,. \tag{30.10}$$

30.6.2 Model Results

Model Fit

The measures of model performance, that is, the peak-to-peak value of the model error ΔCBF_{pp} and the noise-to-signal ratio NSR, are listed in Table 30.5. These results should be compared to those obtained

Series	ΔCBF_{pp}	NSR [%]
196io4	0.91083	23.3
196io5	0.76404	26.1
197io1	0.88338	37.7
197io3	0.89667	43.8
Mean	0.86373	32.7

Table 30.5: The semi-physical model with the input kink transform: The peak-to-peak value of the model error ΔCBF_{pp} and the noise-to-signal ratio NSR for each of the four time series. Also their arithmetic mean values (*mean*) are shown. Note that the values of these performance measures are close to those in Table 26.1 on page 167 which stem from the equivalent grey-box model.

from the semi-physical model with the input threshold transform (cf. Table 30.3 on page 203) as well as to those obtained from the grey-box model with the input kink transform (cf. Table 26.1 on page 167). The performance of the present model is comparable to the semi-physical model with the input threshold transform — no improvement has been obtained. And lifting the constraints on the linear state-space part of the model only improves the performance slightly in comparison to the equivalent grey-box model.

A comparison of model output with measured output from the LDF probe `Re140` is made in Figure 30.6, and also the equivalent model error traces ΔCBF are shown. As expected, these traces closely resembles those obtained by the semi-physical model with the input threshold transform as well as the grey-box model with the input kink transform.

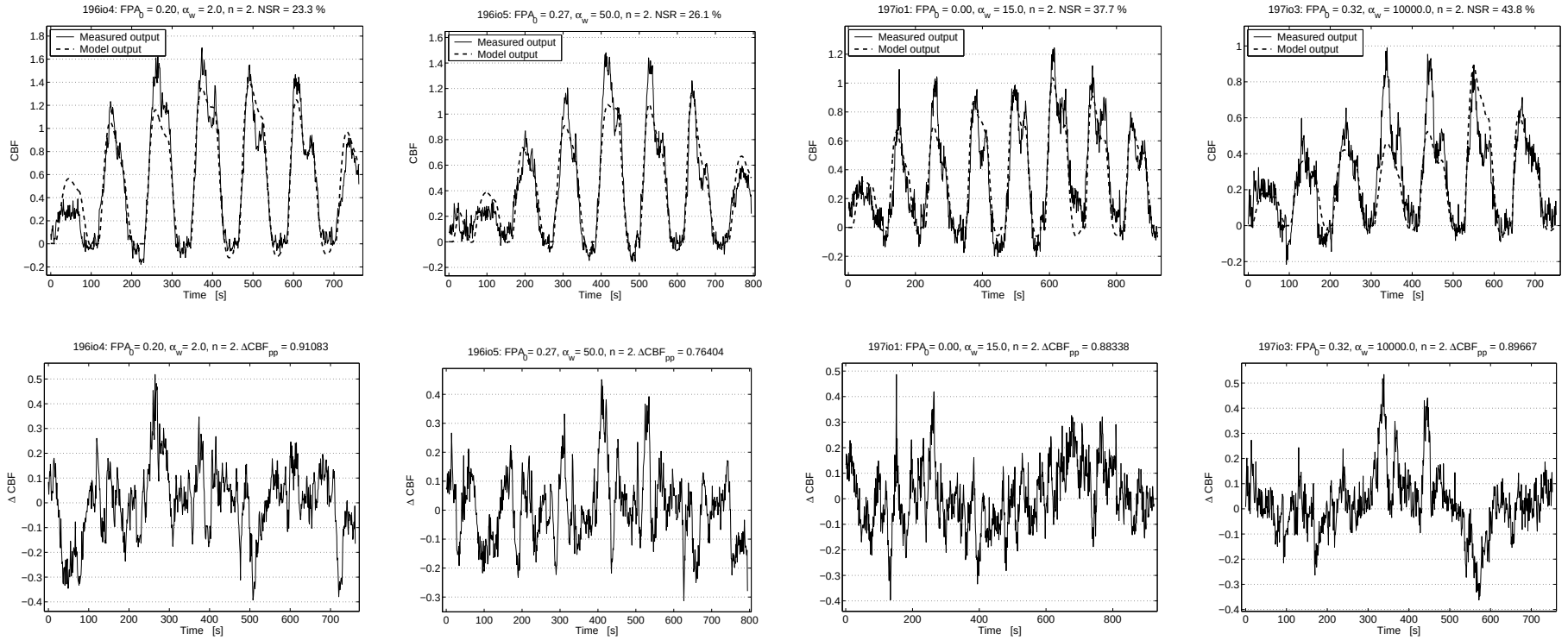

Figure 30.6: The semi-physical model with the input kink transform: Top panels: Comparison of model output (dashed line) with measured output (solid line). Note that — as for the equivalent grey-box model — these model output traces are very similar to those in Figure 30.2 on page 204 which result from the input threshold transform. Bottom panels: The model errors ΔCBF. These traces are similar to those obtained by the input threshold transform, which are shown in Figure 30.3 on page 205.

Cross Validation

The estimates of kink position FPA_0, kink slope α_w, and linear state-space model order n are compared in Table 30.6. As for the equivalent grey-box model, the coefficient of variance of the kink position is

Series	FPA_0 $[mV]$	α_w $[mV^{-1}]$	n
196io4	0.20	2.0	2
196io5	0.27	50.0	2
197io1	0.00	15.0	2
197io3	0.32	10000.0	2
Mean	0.20	2516.8	2
Std	0.14	4988.9	0
Cv	0.71	2.0	0

Table 30.6: The semi-physical model with the input kink transform: The estimated kink position FPA_0, kink slope α_w, and linear order n. Also their arithmetic mean values (*mean*), standard deviations (*std*), and coefficients of variance (*cv*) are shown. Note that — except for a single case — the values of FPA_0 and α_w are identical to those obtained by the equivalent grey-box model (Table 26.2 on page 171). In all four experiments, the linear order has been estimated to be $n = 2$. This value is the same as the linear order of the equivalent grey-box model.

low and the coefficient of variance of the kink slope is high. For all four experiments, the estimate of the linear order is $n = 2$.

Sensitivity to the Parameters FPA_0 and α_w

The sensitivity to the kink position FPA_0 and the kink slope α_w is illustrated by Figure 30.7. To

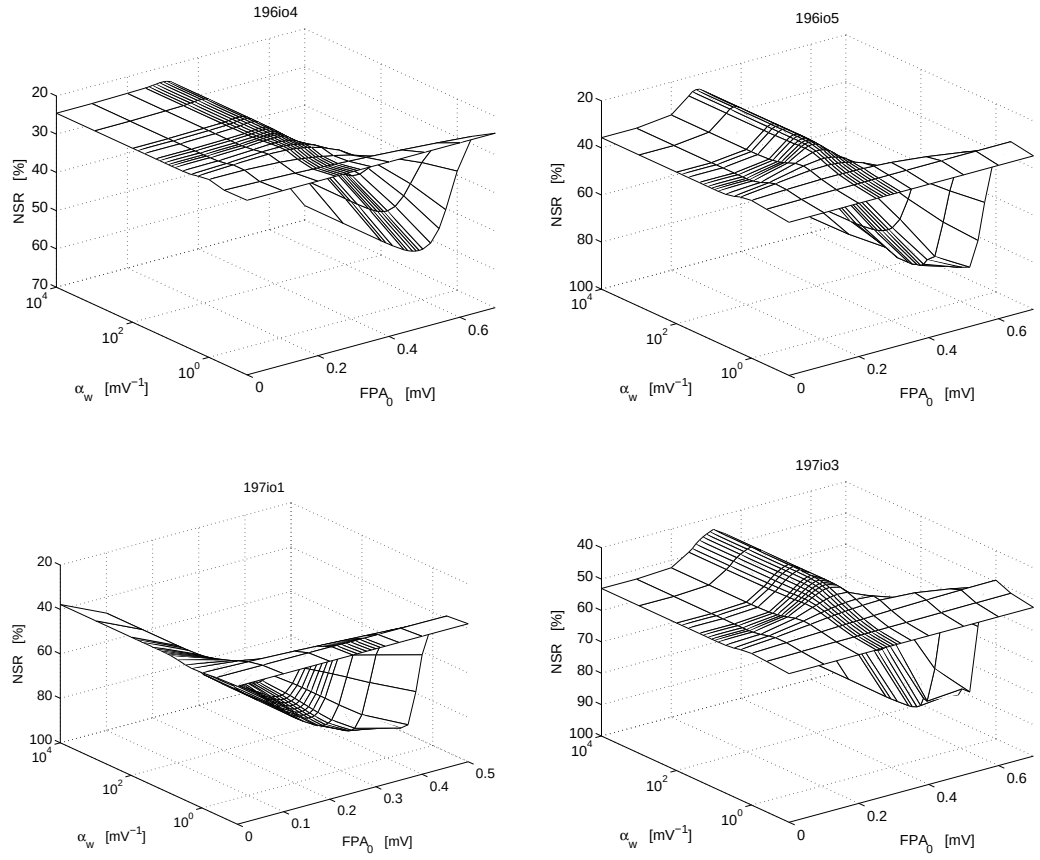

Figure 30.7: The semi-physical model with the input kink transform: Variation in noise-to-signal ratio NSR with variation in the kink position FPA_0 and the kink slope α_w. Note that the scales on the α_w-axes are logarithmic and that the NSR-axes are reversed. The points $(FPA_0,\ \alpha_w) = (0\ mV,\ \infty\ mV^{-1})$ correspond to the linear models investigated in Section 30.4. Note that these NSR surfaces resemble those of the equivalent grey-box model, which are shown in Figure 26.5 on page 172.

emphasize the variation with each of the parameters, plane sections through the NSR surfaces are shown in Figure 30.8. The rather high sensitivity to FPA_0 indicates that the kink position FPA_0 has physical significance. But the kink slope α_w cannot be interpreted in terms of physiology, because the model fit is bad at low values of α_w ($\alpha_w < 10\ mV^{-1}$), and good, but constant, at high values of α_w.

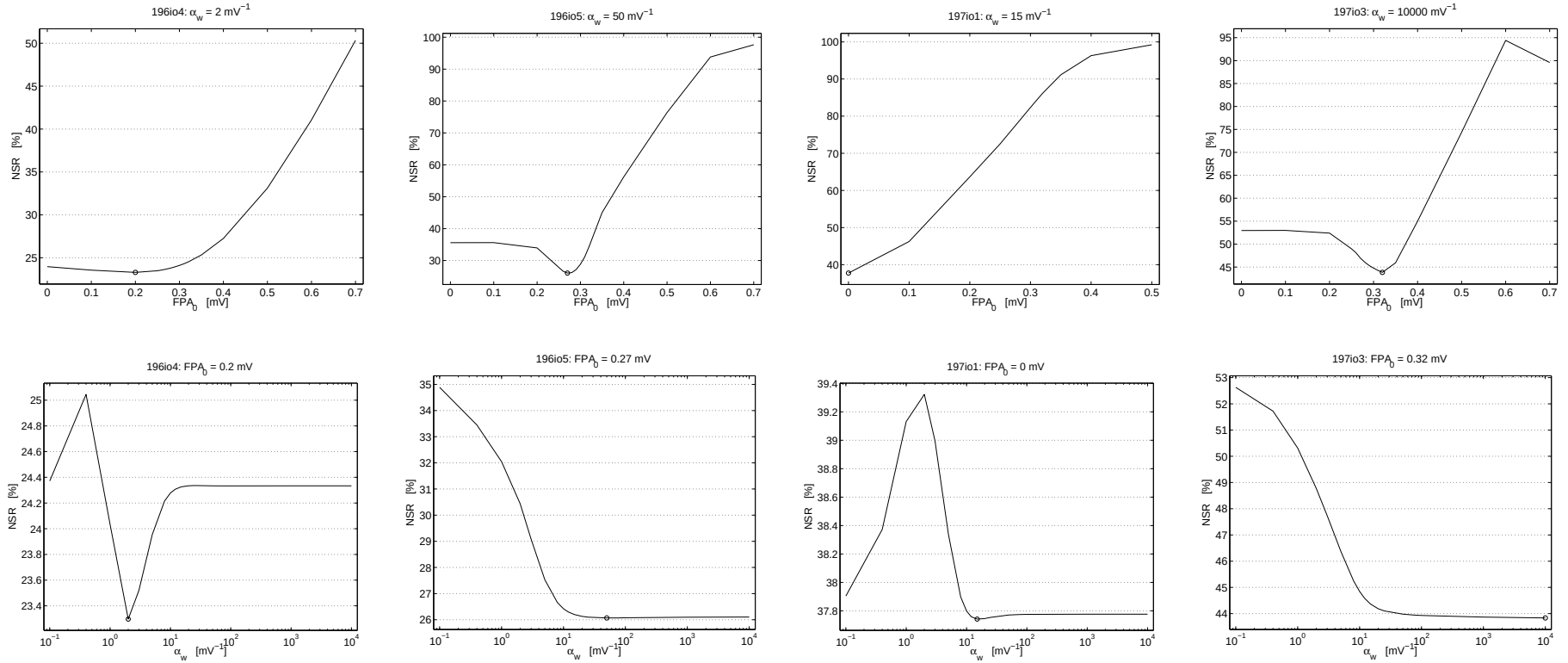

Figure 30.8: The semi-physical model with the input kink transform: Top panels: Variation in the noise-to-signal ratio NSR with variation in the kink position FPA_0. The value of the kink slope α_w has in each case been fixed to the value at the global minimum. Bottom panels: Variation in noise-to-signal ratio NSR with variation in the kink slope α_w. The value of the kink position FPA_0 has in each case been fixed to the value resulting in the global minimum. The global minimum is in each case marked by a 'o'. Note that these curves resemble those obtained by the equivalent grey-box model, which are shown in Figures 26.6 and 26.7 on pages 173–174. The noise-to-signal ratio is sensitive to the kink position FPA_0 and has a clear — typically non-zero — global minimum point. As long as the kink slope α_w is kept above 10 mV^{-1}, the noise-to-signal ratio is insensitive to the kink slope. For lower values of α_w, the noise-to-signal ratio typically increases.

The variation in the estimated linear model order n with variation in the parameters FPA_0 and α_w in the input kink transform is shown in Figure 30.9. Note that, for almost all values of the parameters

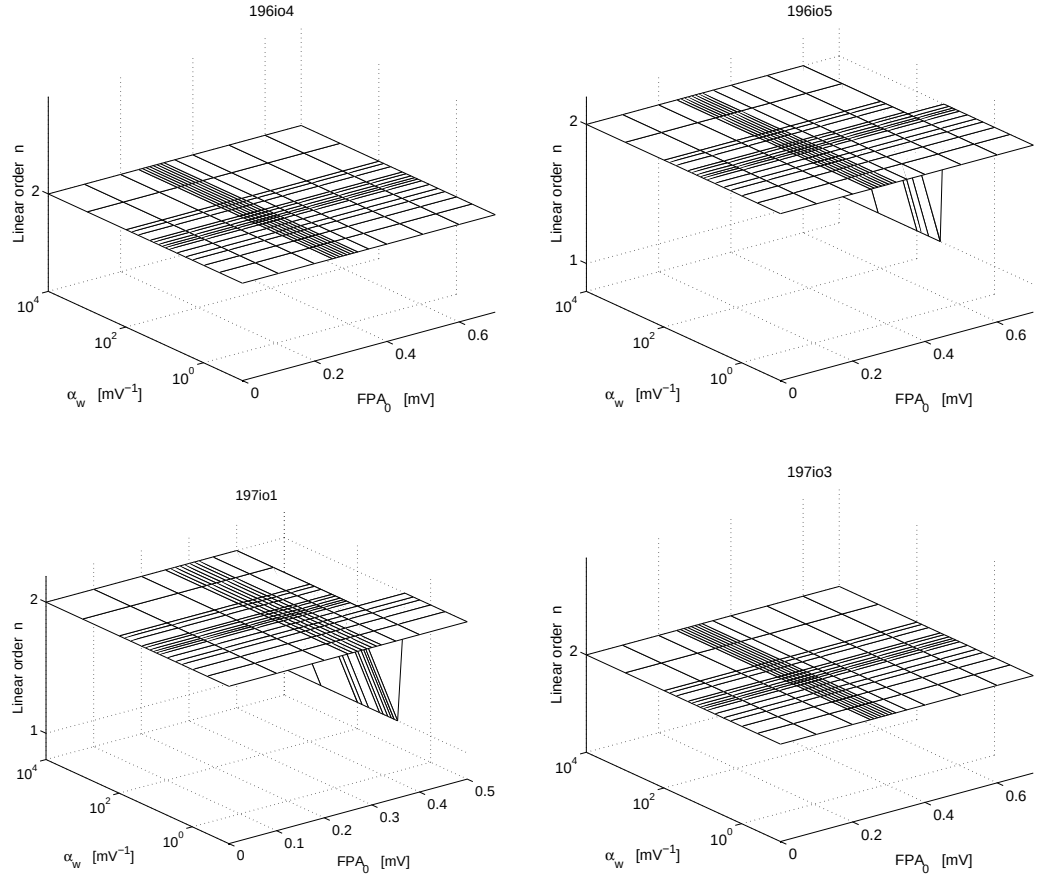

Figure 30.9: The semi-physical model with the input kink transform: The variation in the estimated linear order n with variation in the kink position FPA_0 and the kink slope α_w. Note that the estimate of the linear order is $n = 2$ independently of the values of FPA_0 and α_w.

in the input kink transform, the estimate of the linear order in $n = 2$.

30.7 Discussion of Semi-Physical SISO Models

Comparison to Earlier Models

The results of the SISO model with the input sampling transform (Section 30.4) are comparable to those obtained with the black-box model with the input sampling transform considered in Chapter 18 on page 108. The reason is that the only difference is that here we have excluded the process noise filter **K**.

As compared to the grey-box models investigated in Part V, the elimination of the constraints and couplings on the parameters in the linear state-space model as well as on the linear order of it only increases the model performance insignificantly. The reason is that the linear order of the SISO models is estimated to be two, i.e., identical to the linear order of the grey-box models, and a 2nd-order black-box state-space model structure only contain one identifiable parameter more than the state-space part of the grey-box model (cf. Section 23.4 on page 150).

The Linear order of the SISO Models

The linear order, i.e., the dimension of the internal state vector, has been estimated to be $n = 2$. We emphasize, that this result does not mean that the linear order of the neuro-vascular system has to be exactly equal to two. As described in M: Section 11.3.2 on page 62, the loss function V_N is a strictly decreasing function of the model order n. First, the value of V_N decreases, because the model includes more and more of the system's relevant properties. Later, the value of V_N continues to decrease, because the extra parameters are used to fit the variation in the measurements, which is due to the specific contribution from noise. This is illustrated by Figure 30.10. Because the cross-over from relevant model

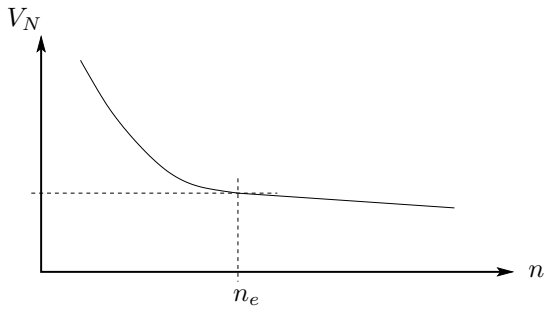

Figure 30.10: Illustration of the loss function V_N, which is a strictly decreasing function of the model order n. Also shown is a possible choice of the linear order n_e, which distinguishes between relevant model parameters and over-parameterization.

order to over-parameterization is not a sharp transition, MATLAB applies some kind of criterion to make the choice of linear order — cf. M: Section 11.3.2. As we will see in Section 31.1.1, we may apply other criteria.

30.8 Conclusion on Semi-Physical SISO Models

The semi-physical SISO models consist of an input transform (the input sampling transform, the input threshold transform, or the input kink transform, respectively) followed by a linear black-box output-error state-space model.

The high sensitivity to the threshold position FPA_0 indicates that it is a physiological parameter. Inclusion of the kink slope α_w in the model structure does not improve model performance further.

The linear order has been estimated to be two.

Chapter 31

A Semi-Physical MISO Model

31.1 Physiological and Mathematical Motivation

31.1.1 The Idea of Two Mediators

The grey-box models investigated in Part V are based on the assumption that nitric oxide, NO, is the dominant mediator (cf. Section 23.1.1 on page 148). Accordingly, they are expressed as an input transform followed by a linear state-space model with the state vector being

$$\mathbf{x}(t) = \begin{pmatrix} CBF(t) \\ \{c(NO)(t) - c_B(NO)\}_{pp} \end{pmatrix}, \tag{31.1}$$

which is 2-dimensional. However, as discussed in P: Section 6.3 on page 35 (and in Section 28.2 on page 193), there may be several — possibly interacting — mediators of neuro-vascular coupling. In this chapter we will assume, that there are *two* mediators: Nitric oxide, NO, and a second mediator, which we will denote by the symbol X. Accordingly, the state vector will be extended with the preprocessed concentration deviation of the chemical substance X:

$$\mathbf{x}(t) = \begin{pmatrix} CBF(t) \\ \{c(NO)(t) - c_B(NO)\}_{pp} \\ \{c(X)(t) - c_B(X)\}_{pp} \end{pmatrix}. \tag{31.2}$$

The resulting model is therefore of linear order three.

Furthermore, if there are two different chemical substances, which mediate neuro-vascular coupling, there is *a priori* no reason to believe that the thresholds, which have to be overcome in order that the neuronal activity causes release of the substances, are equal. Therefore in this chapter we will investigate the idea that there are two chemical substances characterized by each of their own threshold for release.

Since we are not in position of information on the interaction between the chemical substance X and the other elements (that is, the coupling between the concentration of X and the other variables), we will not specify the parameters in the state-space model.

31.1.2 Expected Performance Improvement

First, consider the special case of an experiment where only a single stimulation frequency is applied. In this case the dip in the vascular response can easily be reproduced by the MISO model with two thresholds: As shown in Figure 31.1, the first peak in CBF results from the FPA's, which are larger than both the thresholds FPA_1 and FPA_2. The dip occurs during a period, where the FPA's are smaller than both thresholds. The second, and slower, increase in CBF is caused by FPA's being larger than one threshold (FPA_2) but smaller than the other (FPA_1).

Second, since the overall level of FPA values decreases as the frequency is increased (cf. Section 14.1.2 on page 82) it is not straightforward to figure out, whether the existence of two mediators, characterized by each of their own threshold for release, can explain the dips at all frequencies.

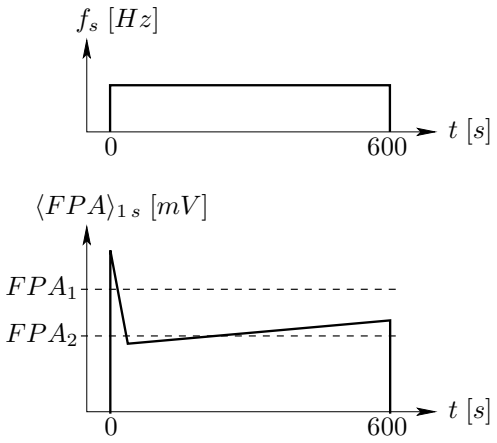

Figure 31.1: Sketch illustrating the dependence on time of the average field potential amplitude, $\langle FPA\rangle_{1\,s}$, during stimulation of the inferior olive with a single frequency f_s. (This feature has been investigated in Section 14.1.2 on page 82.) The threshold positions FPA_1 and FPA_2 are placed such that the existence of two mediators of neuro-vascular coupling can explain the dip in the vascular response to stimulation with a single frequency.

31.2 The Input Two-Thresholds Transform

We consider the following 2-dimensional input vector and 1-dimensional output:

$$\mathbf{u}(t) = \begin{pmatrix} u_1(t) \\ u_2(t) \end{pmatrix} = \begin{pmatrix} \sum_{t-\frac{\tau}{2}<t_j\le t+\frac{\tau}{2}} \{FPA(t_j)\cdot\theta\left(FPA(t_j)-FPA_1\right)\} \\ \sum_{t-\frac{\tau}{2}<t_j\le t+\frac{\tau}{2}} \{FPA(t_j)\cdot\theta\left(FPA(t_j)-FPA_2\right)\} \end{pmatrix} \tag{31.3}$$

$$y(t) = CBF(t). \tag{31.4}$$

We will term Equation (31.3) the *input two-thresholds transform*. It is specified by two parameters: The threshold positions FPA_1 and FPA_2. Correspondingly, we consider a linear MISO output-error state-space model of linear order $n = \dim \mathbf{x} = 3$:

$$\dot{\mathbf{x}}(t) = \mathbf{F}\mathbf{x}(t) + \mathbf{G}\mathbf{u}(t) = \mathbf{F}\mathbf{x}(t) + \mathbf{G}_1 u_1(t) + \mathbf{G}_2 u_2(t) \tag{31.5}$$

$$y(t) = \mathbf{H}\mathbf{x}(t) + \mathbf{J}\mathbf{u}(t) + e(t) = \mathbf{H}\mathbf{x}(t) + J_1 u_1(t) + J_2 u_2(t) + e(t). \tag{31.6}$$

31.3 Implementation of the MISO Model in MATLAB

The model structure is symmetric with respect to the parameters FPA_1 and FPA_2. Therefore only half of the parameter space, $FPA_1 \ge FPA_2$, will be searched through.

Two different implementations of the model structure in MATLAB will be applied:

- When estimating the parameters FPA_1 and FPA_2 in the nonlinear input two-thresholds transform as well as when investigating the sensitivity to these parameters, a free state-space parameterization will be applied — as with the previously investigated semi-physical SISO models.
- When estimating the parameters in the linear part of the model and when investigating the sensitivity to these parameters, the equivalent transfer function representation[1] (cf. M: Section 10.2.2)

$$Y(s) = G_{11}(s)U_1(s) + G_{12}(s)U_2(s) + E(s), \tag{31.9}$$

$$G_{11}(s) = \frac{b_{11}s^2 + b_{21}s + b_{31}}{s^3 + a_1 s^2 + a_2 s + a_3}, \tag{31.10}$$

$$G_{12}(s) = \frac{b_{12}s^2 + b_{22}s + b_{32}}{s^3 + a_1 s^2 + a_2 s + a_3} \tag{31.11}$$

will be applied. This representation contains 9 parameters:

$$\theta = \begin{pmatrix} a_1 & a_2 & a_3 & b_{11} & b_{21} & b_{31} & b_{12} & b_{22} & b_{32} \end{pmatrix}^T. \tag{31.12}$$

[1] A state-space representation on observer canonical form contains the same parameters as the transfer function representation [58, (Sect. 4.6)]. For a 3rd-order output-error state-space model the observer canonical form reads

$$\mathbf{F} = \begin{pmatrix} -a_1 & 1 & 0 \\ -a_2 & 0 & 1 \\ -a_3 & 0 & 0 \end{pmatrix}, \quad \mathbf{G} = \begin{pmatrix} \mathbf{G}_1 & \mathbf{G}_2 \end{pmatrix} = \begin{pmatrix} b_{11} & b_{12} \\ b_{21} & b_{22} \\ b_{31} & b_{32} \end{pmatrix}, \tag{31.7}$$

$$\mathbf{H} = \begin{pmatrix} 1 & 0 & 0 \end{pmatrix}, \quad \mathbf{J} = \begin{pmatrix} J_1 & J_2 \end{pmatrix} = \begin{pmatrix} 0 & 0 \end{pmatrix}. \tag{31.8}$$

31.4 Model Results

31.4.1 Model Fit

The values of the measures of model fit, which have been obtained by the MISO model, are listed in Table 31.1. Note, that the fit of the semi-physical MISO model to the experimental data is significantly

Series	ΔCBF_{pp}	NSR [%]
196io4	0.81972	21.7
196io5	0.65275	22.2
197io1	0.84832	33.3
197io3	0.72657	38.9
Mean	0.76184	29.0

Table 31.1: The semi-physical model with the input two-thresholds transform: The peak-to-peak value of the model error ΔCBF_{pp} and the noise-to-signal ratio NSR. Also their arithmetic mean values (*mean*) are shown. Note the significant improvement relatively to the SISO model with the input threshold transform — compare with Table 30.3 on page 203.

better than the fit of the SISO model with the input threshold transform — see Table 30.3 on page 203.

In Figure 31.2 the model output traces are compared to the measured outputs. The equivalent model error traces ΔCBF are shown in Figure 31.3. Both the performance measures and the plots emphasize the good fit of the semi-physical model with the input two-thresholds transform to the measurements. Inspection of the plots reveals that the improvement mainly is due to a better fit during the dips in the vascular response.

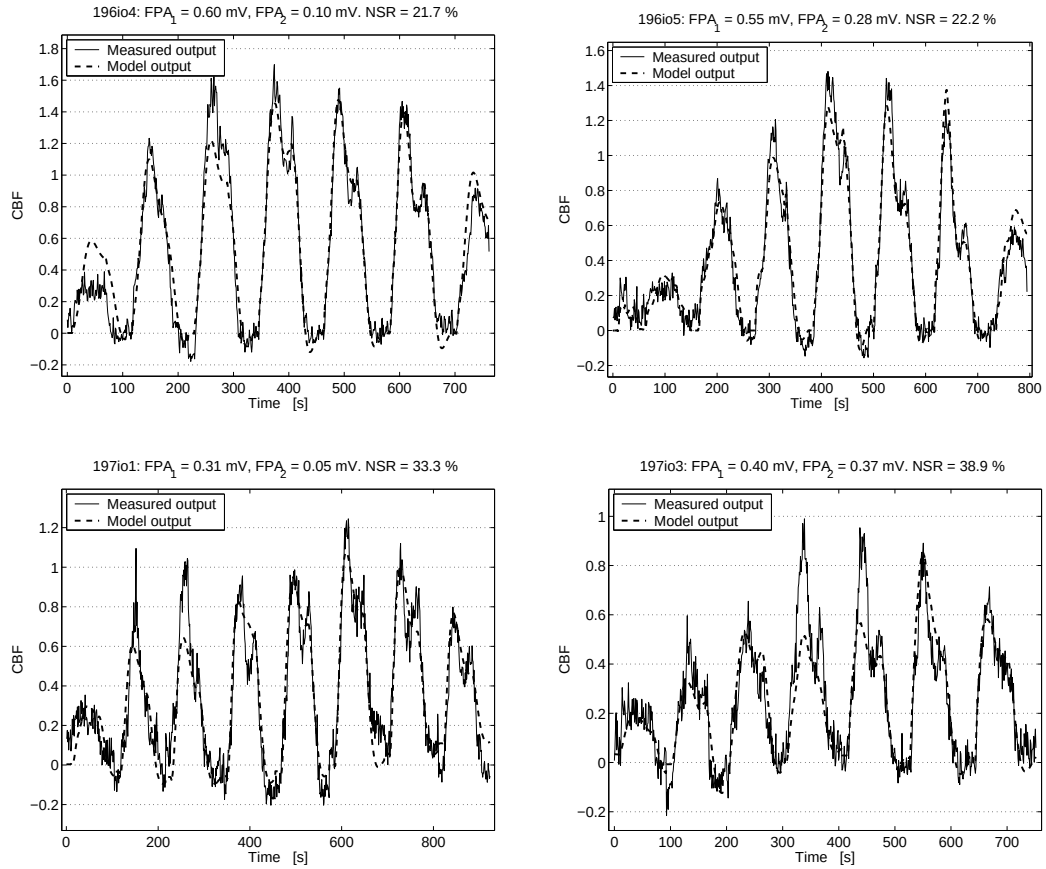

Figure 31.2: The semi-physical model with the input two-thresholds transform: Comparison of model output (dashed line) with measured output (solid line) for the four inferior olive stimulation experiments. Note that for each experiment the model fit has improved significantly — especially during the dips — compared to the model with only a single threshold (cf. Figure 30.2 on page 204). More specifically, for each experiment the fit has improved significantly for some frequencies whereas the fit during stimulation with other frequencies is unchanged.

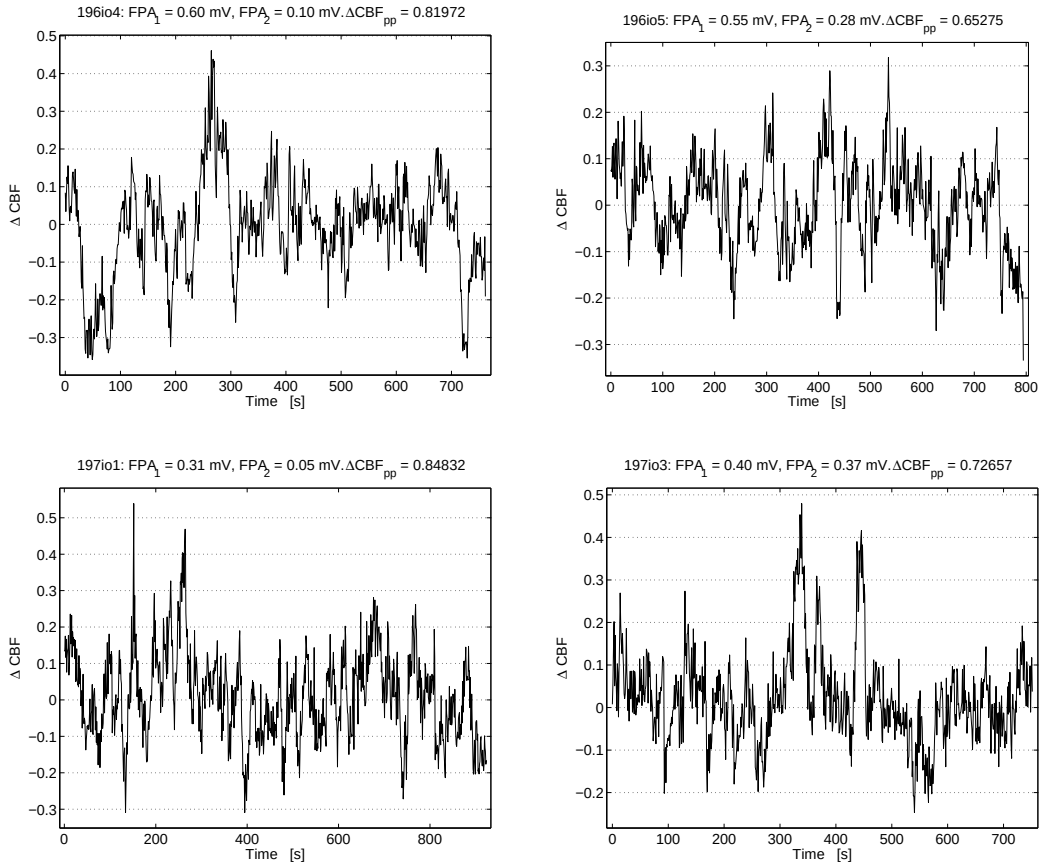

Figure 31.3: The semi-physical model with the input two-thresholds transform: The model error traces ΔCBF. Note that there is significantly less systematics in these error traces than in any of those obtained by the previously investigated model structures — see for instance Figure 30.3 on page 205. Beware of the error ranges on the y-axes.

31.4.2 Cross Validation

Parameters in the Input Two-Thresholds Transform

The estimates of the parameters FPA_1 and FPA_2 in the non-linear input two-thresholds transform are compared in Table 31.2. Note that the coefficients of variance of FPA_1 and FPA_2 are below one,

Series	FPA_1 $[mV]$	FPA_2 $[mV]$
196io4	0.60	0.10
196io5	0.55	0.28
197io1	0.31	0.05
197io3	0.40	0.37
Mean	0.46	0.20
Std	0.13	0.15
Cv	0.29	0.75

Table 31.2: The semi-physical model with the input two-thresholds transform: The estimates of the threshold positions FPA_1 and FPA_2 in the non-linear input two-thresholds transform. Also their arithmetic mean values (*mean*), standard deviations (*std*), and coefficients of variance (*cv*) are listed. Note that the coefficients of variance of both FPA_1 and FPA_2 are below one. Furthermore, the *cv* of FPA_1 is smaller than the *cv* of the threshold position FPA_0 ($cv(FPA_0) = 0.67$) in the SISO model, whereas the *cv* of FPA_2 is larger — cf. Table 30.4 on page 206.

indicating that both parameters have physiological significance.

Parameters in the Transfer Functions

The estimates of the parameters in the transfer functions are compared in Tables 31.3 and 31.4.

Series	a_1	a_2	a_3
196io4	0.29288	0.04205	0.00334
196io5	0.27317	0.04449	0.00406
197io1	0.13696	0.01270	−0.00000
197io3	0.11257	0.01301	0.00007
Mean	0.20389	0.02806	0.00187
Std	0.09226	0.01759	0.00214
Cv	0.45251	0.62677	1.14404

Table 31.3: The semi-physical model with the input two-thresholds transform: The estimates of the parameters in the denominator of the transfer functions. Also their arithmetic mean values (*mean*), standard deviations (*std*), and coefficients of variance (*cv*) are listed. Note that the estimates of the parameter a_3 are very close to zero, and that the *cv* of a_3 is larger than one.

Since the estimates of the denominator parameter a_3 are very close to zero and the *cv* of a_3 is larger than one, we conclude that the parameter a_3 ought to be excluded from the model structure. On the other hand, there seems to be consistency between the estimates of the other two denominator parameters a_1 and a_2.

In contrast to this, the estimates of the numerator parameters b_{ij} vary significantly from experiment to experiment. As outlined in Section 28.2 on page 193, this variation may be due to variation in the gain caused by variation in the position of the probe, which measure the field potential. Therefore, the variation in the estimates of the zeros and the gains is also of interest. We will return to these matters in Section 31.5.2 on page 234.

By comparing Tables 31.3 and 31.4 we observe that, for the two experiments performed on rat no. 197, the values of the parameters a_3, b_{31}, and b_{32} are close to zero. This means that both of the transfer

Series	b_{11}	b_{21}	b_{31}	b_{12}	b_{22}	b_{32}
196io4	0.03420	−0.01047	0.00139	0.06693	0.01019	0.00515
196io5	0.12454	0.00284	−0.00287	0.15891	−0.00559	0.01085
197io1	−0.06503	−0.00522	−0.00019	−0.04357	0.05120	0.00003
197io3	0.01237	−0.03572	−0.00082	0.03091	0.05124	0.00081
Mean	0.02652	−0.01214	−0.00062	0.05329	0.02676	0.00421
Std	0.07799	0.01664	0.00176	0.08411	0.02897	0.00497
Cv	2.94090	−1.37074	−2.83258	1.57823	1.08256	1.17975

Table 31.4: The semi-physical model with the input two-thresholds transform: The estimates of the parameters in the numerators of the transfer functions. Also their arithmetic mean values (*mean*), standard deviations (*std*), and coefficients of variance (*cv*) are listed. Note that the coefficients of variance of all the parameters b_{ij} are (numerically) larger than one. Furthermore, for rat no. 197 the values of the parameters b_{31} and b_{32} are an order of magnitude smaller than the other parameter values.

functions $G_{11}(s)$ and $G_{12}(s)$ are reduced to 2nd order. Contrary to this, for the two experiments performed on rat no 196, the linear order cannot be reduced from the value $n = 3$.

31.4.3 Parameter Sensitivity

Sensitivity to the Parameters FPA_1 and FPA_2

The NSR-surfaces obtained by the MISO model are depicted in Figure 31.4.

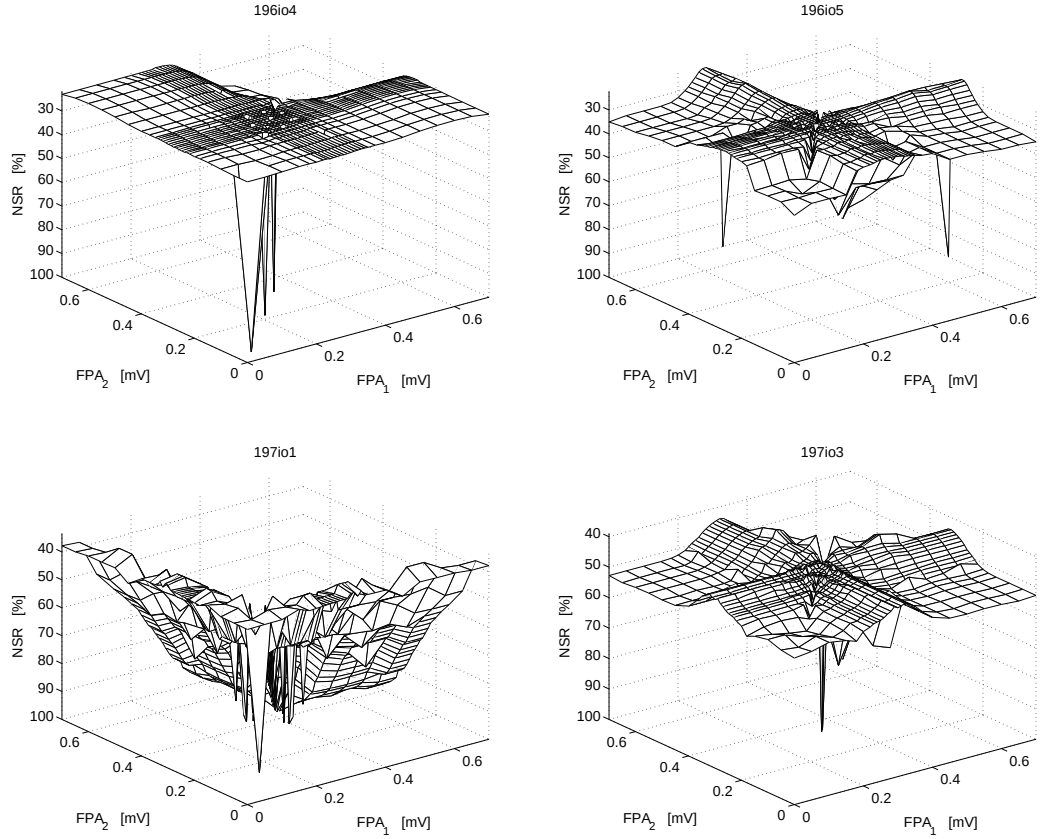

Figure 31.4: The semi-physical model with the input two-thresholds transform: Variation in obtained NSR value with variation in the threshold positions FPA_1 and FPA_2. Note that plane sections $FPA_1 = constant \geq \max(FPA) \approx 0.7\ mV$ correspond to the SISO model with the input threshold transform — cf. Section 30.5. Note also, that the NSR-axes are reversed.

In order to emphasize the dependence of the noise-to-signal ratio on each of the parameters FPA_1 and FPA_2, plane sections through the minimum points of the NSR-surfaces are shown in Figure 31.5. They show that in general the model performance is sensitive to both of the threshold positions FPA_1 and FPA_2. Therefore FPA_1 as well as FPA_2 can be interpreted in terms of physiology.

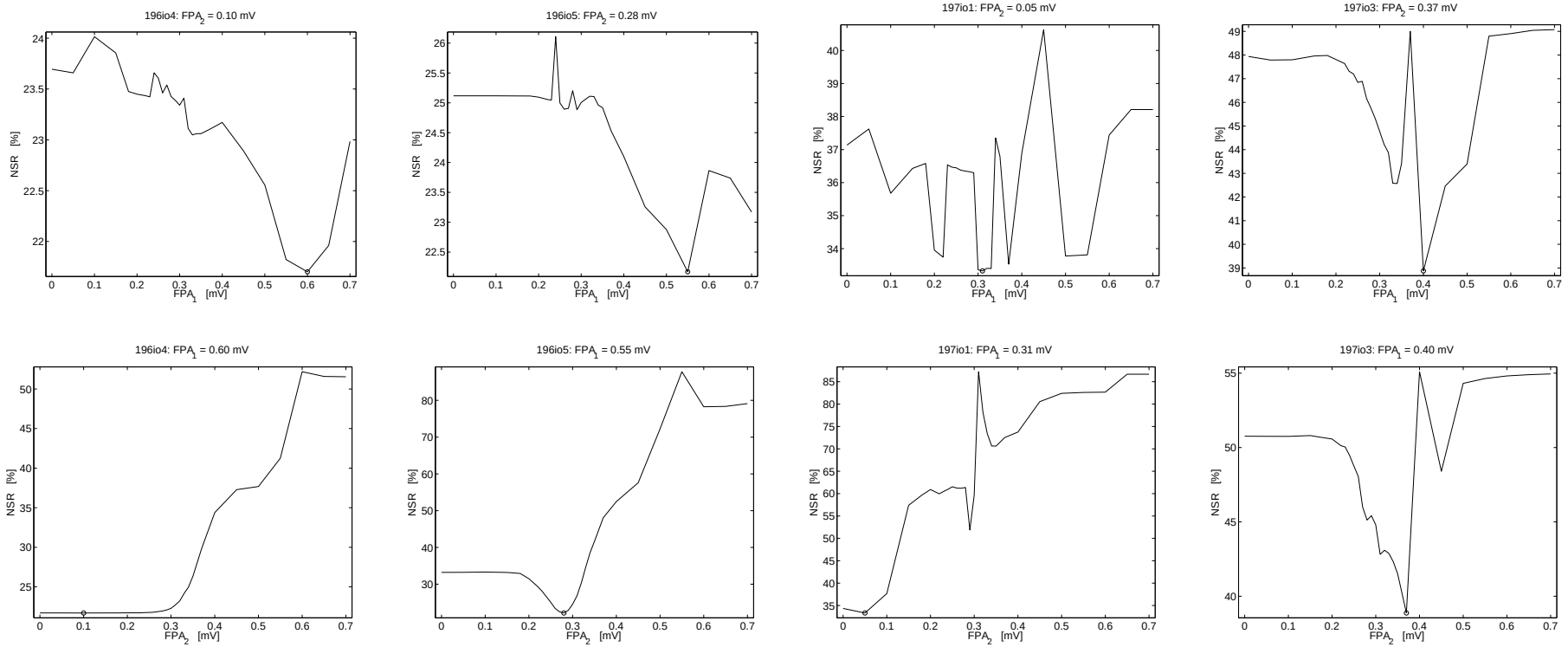

Figure 31.5: The semi-physical model with the input two-thresholds transform: Plane Sections through the global minimum of the NSR surfaces (which fulfills $FPA_1 \geq FPA_2$) show the variation in the noise-to-signal ratio NSR with variation in each of the two threshold positions FPA_1 (top panels) and FPA_2 (bottom panels). In each case, the global minimum point of NSR is marked by a '$\circ$'. Note that for two experiments (196io5 and 197io3) the model performance is strongly sensitive to both of the parameters FPA_1 and FPA_2. In the experiment 196io4 the performance is sensitive to the parameter FPA_1 but not to FPA_2. In the experiment 197io1 the performance is sensitive to FPA_2 whereas a clear conclusion on the sensitivity to FPA_1 cannot be made because there are a number of local minimum points with NSR values close to that of the global minimum point.

Sensitivity to Parameters in the Transfer Functions

First, we consider the sensitivity measures, which are related to the half axes of the sensitivity ellipsoid (cf. M: Section 12.5.4): Table 31.5 lists the minimum sensitivity $S_{\min}$ and the ratio R of maximum and minimum sensitivity in any direction. Note, that the values of $S_{\min}$ are very small, $S_{\min} < 0.01$.

Half axes	$S_{\min}$	R
196io5	0.0041	341
197io1	0.0088	181

Table 31.5: The semi-physical model with the input two-thresholds transform: Minimum sensitivity $S_{\min}$ and ratio of maximum and minimum sensitivities in any direction R. Note, that the values of $S_{\min}$ are rather small, and that the values of R are significantly larger than one. Furthermore, the values of $S_{\min}$ are smaller than the values obtained from the grey-box model with the input threshold transform, and the values of R are considerably larger than those obtained from the grey-box model (cf. Table 27.2 on page 184).

This indicates, that there are directions in the parameter space in which the sensitivity is very small. Furthermore, as R is much larger than one, there are large differences in the sensitivities in various directions in the parameter space.

Secondly, we consider the sensitivity to individual parameters (cf. M: Section 12.5.4): The minimum sensitivity $S_{i\,\min}$ to individual parameters θ_i is shown in Table 31.6.

$S_{i\,\min}$	a_1	a_2	a_3	b_{11}	b_{21}	b_{31}	b_{12}	b_{22}	b_{32}
196io5	0.0285	0.0262	0.0149	0.0202	0.0098	0.0159	0.0057	0.0178	0.0149
197io1	0.1713	0.2019	0.0147	0.0090	0.0098	0.0830	0.0632	0.1900	0.0198

Table 31.6: The semi-physical model with the input two-thresholds transform: The minimum sensitivity $S_{i\,\min}$ to the parameter θ_i. For most parameters θ_i, the values of $S_{i\,\min}$ vary considerably from experiment to experiment.

The values of the ratio R_i of the sensitivity to the parameter θ_i alone and the minimum sensitivity to the parameter are compared in Table 31.7. The fact, that the value of R_i for some parameters is much

R_i	a_1	a_2	a_3	b_{11}	b_{21}	b_{31}	b_{12}	b_{22}	b_{32}
196io5	10.4775	19.3987	65.1486	2.7607	3.5419	6.2238	8.8273	8.7052	70.3158
197io1	1.9874	5.2098	14.6932	1.2684	1.4350	7.9962	1.7523	5.8645	21.0500

Table 31.7: The semi-physical model with the input two-thresholds transform: The ratio R_i of the sensitivity to the parameter θ_i alone and the minimum sensitivity to the parameter.

larger than one, indicates correlation between parameters. On the other hand, R_i is close one for other parameters indicating that these parameters are uncorrelated (cf. M: Section 12.5.4 on page 72).

No values are reported for the experiments 196io4 and 197io3, because the algorithm calculating the sensitivity measures in both cases runs into unstable points in the parameter space (numerous initial values have been tested).

Parameter Accuracy

As explained in M: Section 12.6.2 measures of the parameter accuracy can be related to the sensitivity measures under various assumptions.

Under the assumption that the model deficiencies are only caused by noise, the spread $\sigma(\theta_{N,ri})$ of the estimate of the relative parameter θ_{ri} can be calculated. The results are listed in Table 31.8.

$\sigma(\theta_{N,ri})$ [%]	a_1	a_2	a_3	b_{11}	b_{21}	b_{31}	b_{12}	b_{22}	b_{32}
196io5	23.5882	25.6282	45.2104	33.3042	68.6732	42.1897	117.5179	37.7432	44.9482
197io1	4.1529	3.5224	48.4082	78.6458	72.7082	8.5647	11.2466	3.7423	35.9211

Table 31.8: The semi-physical model with the input two-thresholds transform: The relative spread $\sigma(\theta_{N,ri})$ of the estimate of θ_i calculated under the assumption that the model deficiencies are only caused by noise.

Similarly, under the assumption that the model deficiencies are solely caused by under-modeling, the equivalent relative error $\Delta\theta_{eq,ri}$ on the estimate of θ_i can be calculated. The results are listed in Table 31.9.

$\Delta\theta_{eq,ri} \cdot 10^{-3}$ [%]	a_1	a_2	a_3	b_{11}	b_{21}	b_{31}	b_{12}	b_{22}	b_{32}
196io5	1.0408	1.1308	1.9949	1.4695	3.0302	1.8616	5.1855	1.6654	1.9833
197io1	0.1993	0.1690	2.3226	3.7734	3.4885	0.4109	0.5396	0.1796	1.7235

Table 31.9: The semi-physical model with the input two-thresholds transform: The equivalent relative error on the estimate of θ_i, $\Delta\theta_{eq,ri}$, calculated under the assumption that the model deficiencies are solely caused by under-modeling.

No values are reported for the experiments 196io4 and 197io3, because the algorithm calculating the sensitivity measures in both cases runs into unstable points in the parameter space (numerous initial values have been tested).

31.5 Properties of the MISO Model

31.5.1 Time-Domain Model Properties

When do the Two Mediators Contribute to Coupling?

In Section 14.1.2 on page 82 we studied the time series of averaged field potential amplitudes $\langle FPA \rangle_{1\ s}(t)$. In Figure 31.6 this signal is compared to the threshold positions FPA_1 and FPA_2. Several conclusions

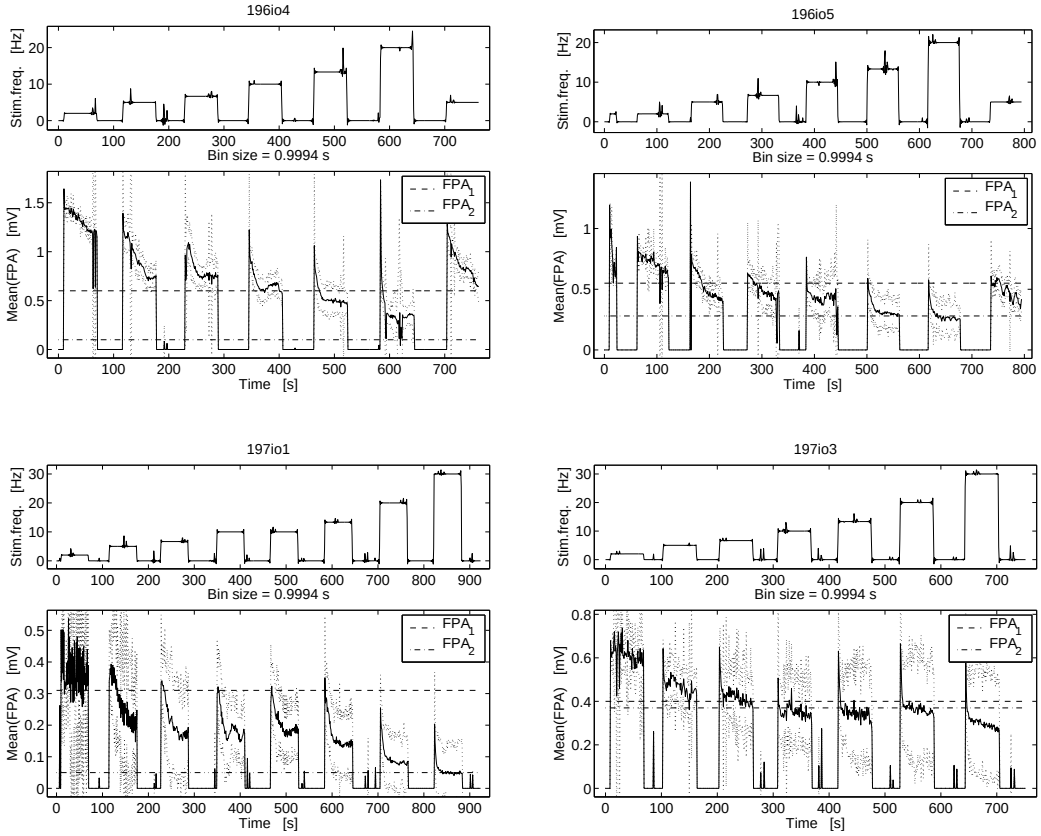

Figure 31.6: The semi-physical model with the input two-thresholds transform: Comparison of the estimated threshold positions FPA_1 and FPA_2 to the smoothed FPA signal ($mean(FPA)$). The dotted lines represent $mean(FPA) \pm 3 \cdot std(FPA)$.

arise from this comparison. Firstly, as the stimulation frequency is increased, the averaged FPA signal first exceeds both the threshold positions, then lies in the interval between the threshold positions, and at high frequencies falls below both the threshold positions. One consequence of this feature is that for experiments, where the stimulation frequency is kept low ($<\sim 10\ Hz$), the system appears to be linear. The reason is that, since most of the FPA's will be larger than both the threshold positions, both of the threshold transforms in the input two-thresholds transform reduce to the input sampling transform, which is a linear transformation. Secondly, due to the dynamic dependence of the FPA signal on the stimulation frequency, at most frequencies the averaged FPA signal usually exceeds both the threshold positions right after onset of stimulation. One consequence of this feature is that in experiments, where the stimulation duration is kept very short ($<\sim 5\ s$), the system can be approximated with a linear model.

The preprocessed field potential amplitude signal for the value of the parameter set (FPA_1, FPA_2) which results in the lowest noise-to-signal ratio as well as the cerebellar blood flow signal for the time series 196io5 are shown in Figure 31.7 — after resampling by a factor 10. Note, that the input signal $u_1(t) = FPA_{pp}(t)$ corresponding to the threshold position FPA_1 primarily excites the linear part of the system at low stimulation frequencies ($2-7\ Hz$) and is largest right after the onset of stimulation. In contrast to this, the input signal $u_2(t) = FPA_{pp}(t)$ corresponding to the threshold position FPA_2 excites the linear part of the system at all frequencies and as long as the system is stimulated. Furthermore, $u_2(t)$ is largest during intermediate and high stimulation frequencies.

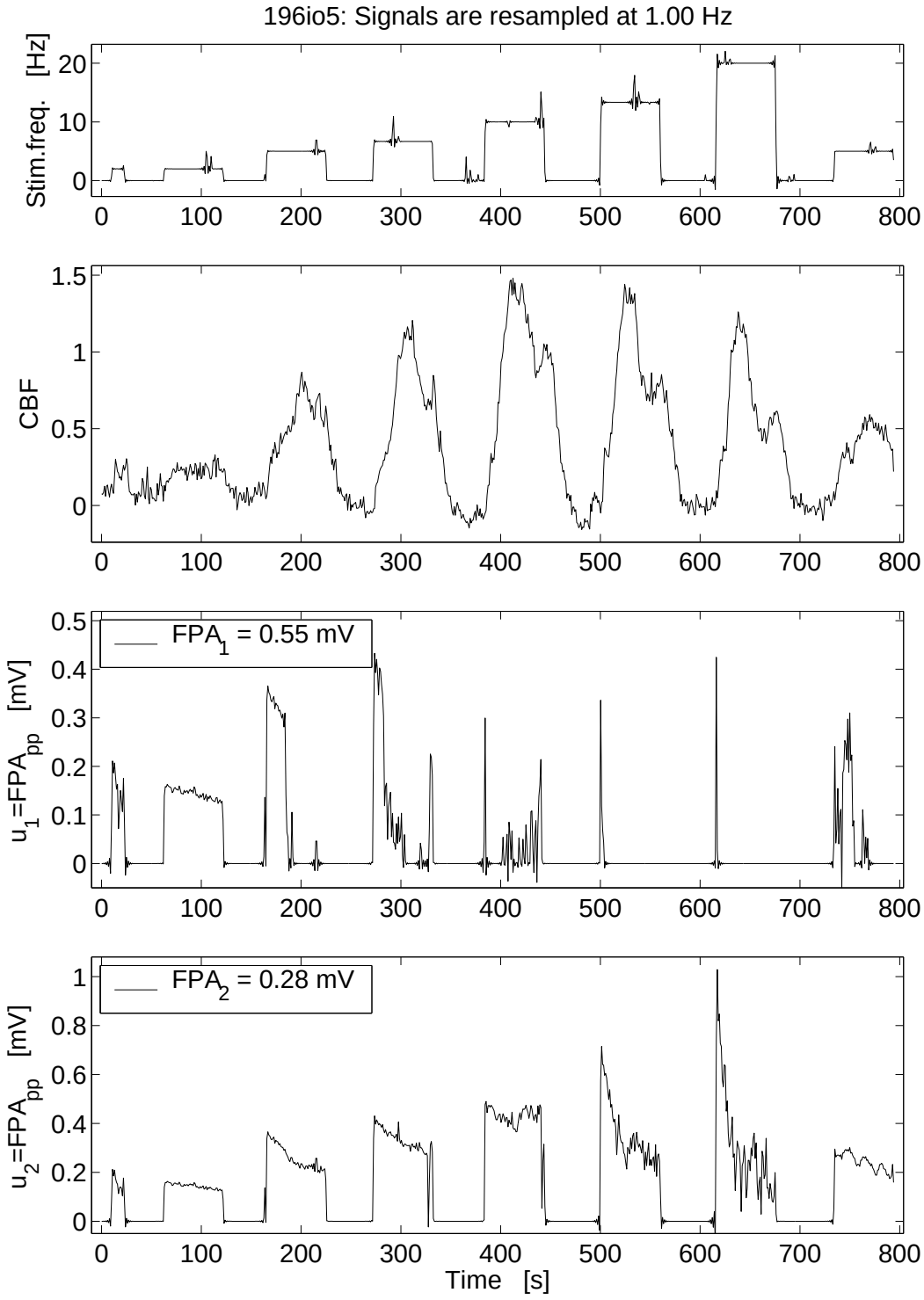

Figure 31.7: The semi-physical model with the input two-thresholds transform: The following signals are shown for the time series 196io5: Stimulation frequency (top panel), relative CBF signal (second panel), and the FPA signal preprocessed according to the input two-thresholds transform, u_1 (third panel) and u_2 (bottom panel), corresponding to the threshold positions FPA_1 and FPA_2, respectively. Note, that u_1 is largest at low frequencies and right after onset of stimulation, whereas u_2 excites the linear part of the system as long as the system is stimulated and has its largest values at intermediate and high frequencies.

Time Responses

In this section we investigate the time-domain properties of the linear part of the semi-physical MISO model, i.e., of the linear state-space model (31.5)–(31.6). That is, we investigate the response (output) of the model to certain pre-defined shapes of the preprocessed field potential amplitude signal $\mathbf{u}(t) = (u_1(t), u_2(t))^T$ — independently of whether we know how to stimulate the physiological system such that it produces this $\mathbf{u}$ signal. The resulting output signals are obtained by simulation of the linear state-space model.

Transient Responses We consider the transient behaviors of the state-space model, which result from driving the model by some simple inputs. The *impulse response*, that is, the output $y(t)$ from the model when the model is driven by an input $\mathbf{u}(t) = (u_1(t), u_2(t))^T$ with u_1 being an impulse at time zero, $u_1(t) = \delta(t)$, and u_2 is fixed to zero, $u_2 \equiv 0$, or vice versa, is depicted in Figure 31.8. We note that, for

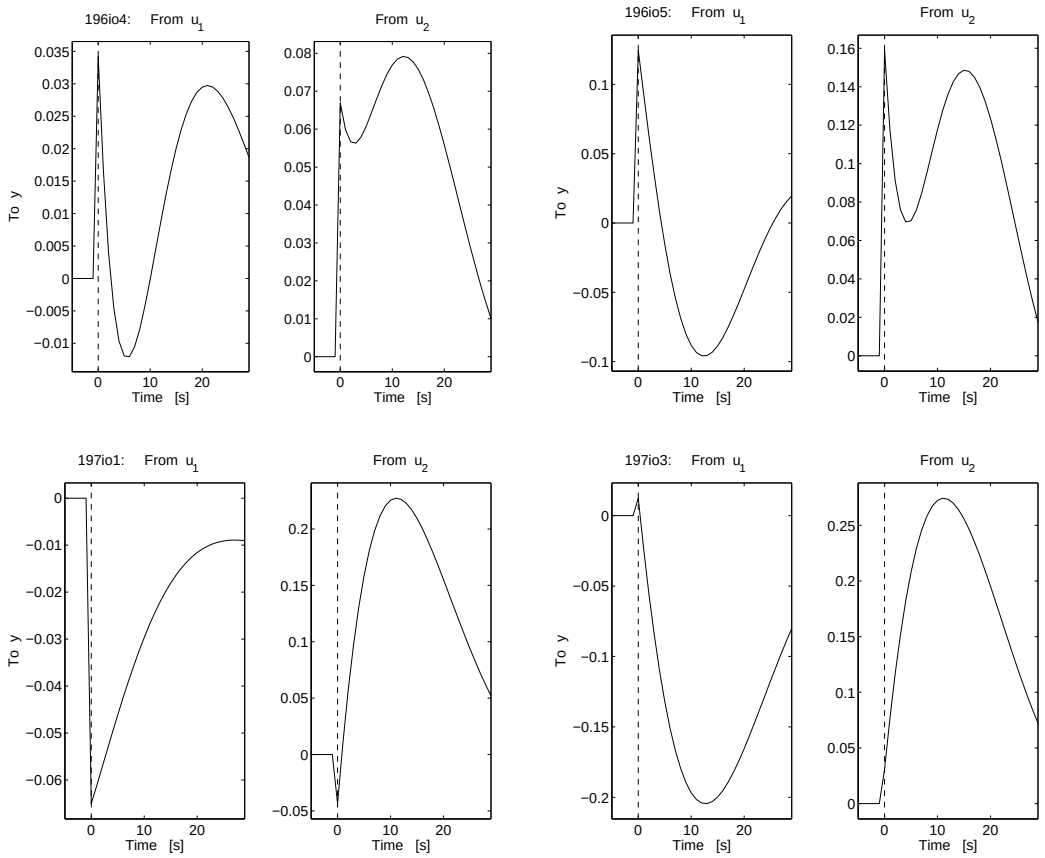

Figure 31.8: The semi-physical model with the input two-thresholds transform: The impulse response, that is, the output $y(t) = CBF(t)$ which results from exciting the linear part of the model by an input $\mathbf{u}(t) = (u_1(t), u_2(t))^T$, where either u_1 is an impulse at $t = 0$ and u_2 is zero (left panels), or oppositely (right panels). Note, that the state-space model in general produces an oscillating output.

a given rat, the impulse responses obtained from different experiments are alike, whereas there are some differences between the two rats. Furthermore, the model in general produces an oscillating output y when excited by an impulse. The *step response* in Figure 31.9 shows the output y, which results from exciting the state-space model with a step of amplitude one at time zero, $u_1(t) = \theta(t)$ and $u_2 \equiv 0$, or vice versa. Note that, whereas the responses to a step in u_2 are rather alike in shape (but not in gain), there are large differences — especially between the two rats — in the responses to a step in u_1.

Physiological Inputs First, we investigate the cases, where only one of the two mediators is available. This would correspond to cases, where the activity of the other mediator somehow has been inhibited

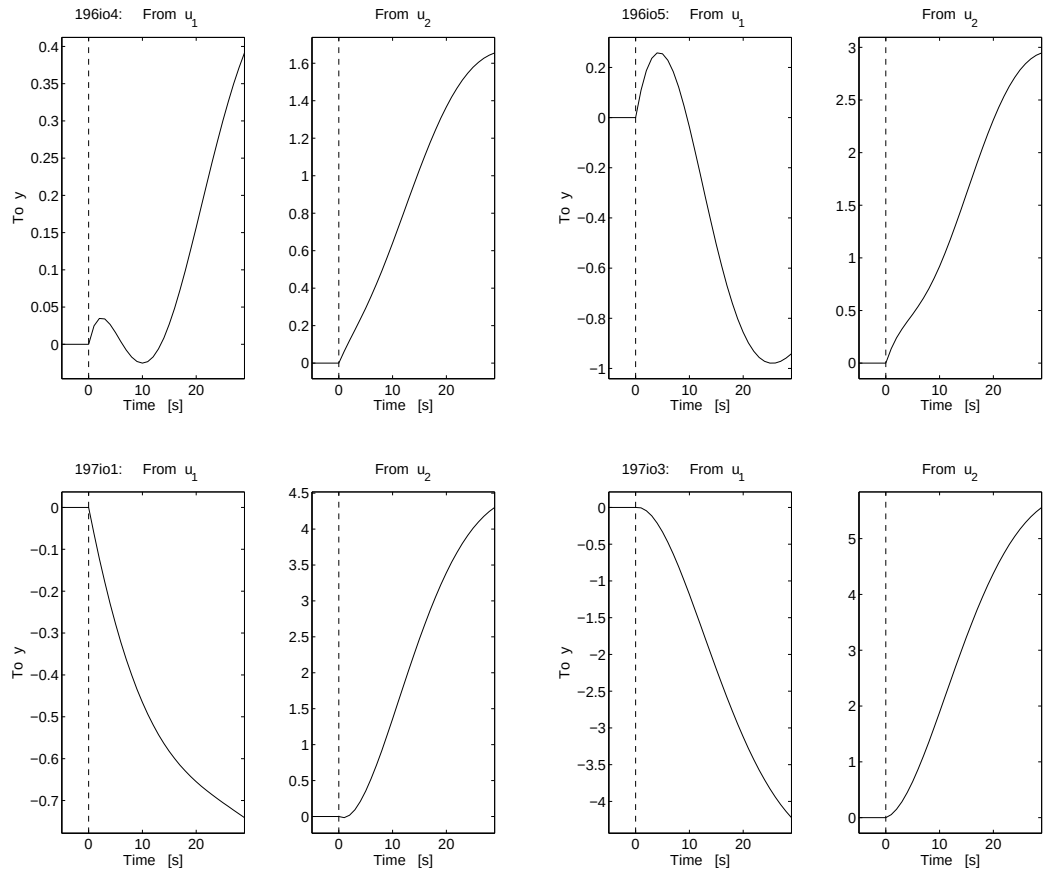

Figure 31.9: The semi-physical model with the input two-thresholds transform: The step response, that is, the output $y(t) = CBF(t)$ which results from exciting the linear part of the model by an input $\mathbf{u}(t) = (u_1(t), u_2(t))^T$ where either u_1 is a step at $t = 0$ and u_2 is zero (left panels), or oppositely (right panels). Note, that the response to u_1 differs between the two rats: For rat no. 196, y first increases, whereas for rat no. 197, y first decreases.

(for instance chemically). That is, either this mediator is not released as a result of neuronal activity, or its influence on the blood vessels is prevented. In any case, the equivalent transfer function ($G_{11}(s)$ or $G_{12}(s)$ in Equation (31.9)) would be fixed to zero. We do the investigation by simulating the MISO state-space model with the following inputs:

$$u_1(t) = FPA_{pp}(t) \quad \text{with} \quad FPA_1 \quad \wedge \quad u_2 \equiv 0, \qquad \text{and} \tag{31.13}$$

$$u_1 \equiv 0 \quad \wedge \quad u_2(t) = FPA_{pp}(t) \quad \text{with} \quad FPA_2. \tag{31.14}$$

The results are shown in Figure 31.10. Note the rather different results: For one experiment (196io4), both inputs cause vasodilation. For two experiments (196io5 and 197io3), the input u_1 results in vasoconstriction and the input u_2 causes vasodilation. For one experiment (197io1), the input u_1 does not cause flow changes and the input u_2 results in vasodilation. We may interpret these results in two ways:

- If the neuronal activity only causes *release* of the two mediators, then one of the mediators is vasodilatory, whereas the effect of the other is unclear (could be vasoconstrictory, without effect, or vasodilatory).
- Another possibility is that the neuronal activity causes release of one vasodilatory substance, but uptake (or at least clearance) of another, possibly vasoactive, substance.

In any case the results of the semi-physical MISO model indicates, that neuro-vascular coupling is mediated through two *pathways*.

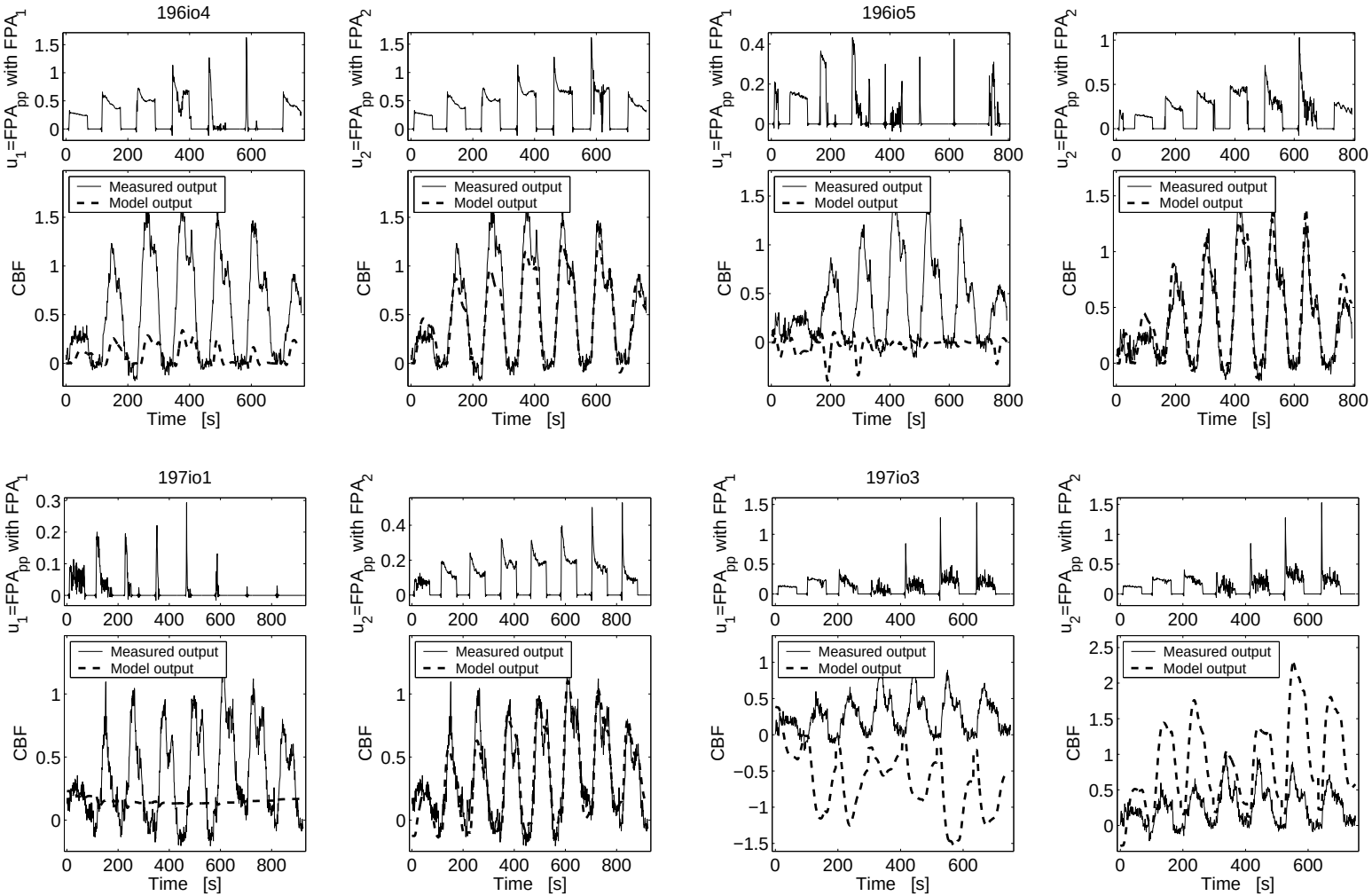

Figure 31.10: The semi-physical model with the input two-thresholds transform: Top panels: The inputs u_1 (left panel) and u_2 (right panel). Bottom panels: The outputs y (dashed lines) which occur, if only one of the two mediators contributes to neuro-vascular coupling, whereas the activity of the other chemical substance is inhibited. Also the measured output is shown (full line). Note, that whereas the input u_2 in all cases causes vasodilation, the effect of the input u_1 is ambiguous: It seems to be able to cause vasoconstriction (196io5 and 197io3), no effect (197io1), as well as vasodilation (196io4).

Secondly, we investigate whether the MISO model can account for the system dynamics also during the 600 s long stimulation sequence, that is, for the full time series. The answer to this question is sought by simulating the model using the full time series of the input $\mathbf{u}(t) = (u_1(t), u_2(t))^T$ and comparing the model output with the measured output. The comparison is made in Figure 31.11. We note, that the

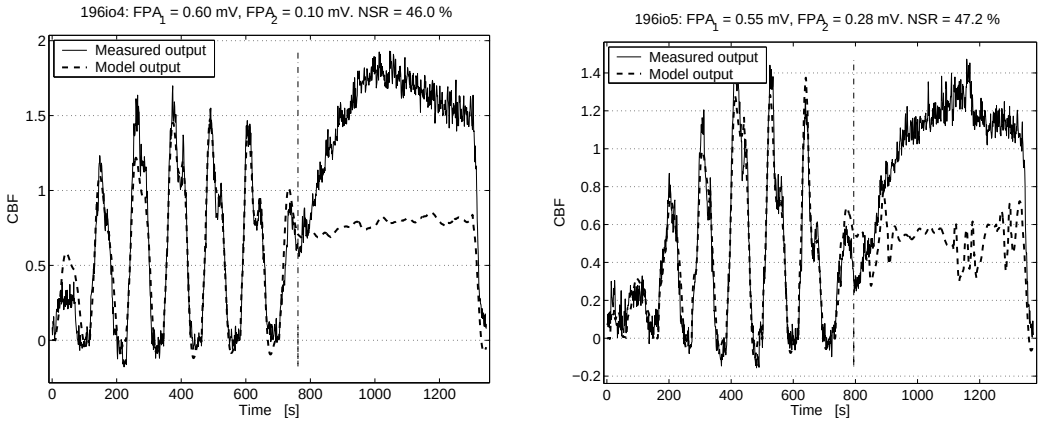

Figure 31.11: The semi-physical model with the input two-thresholds transform: Comparison of model output (dashed line) (obtained by simulation) to measured output (solid line). Samples earlier than the dash-dotted line (at $t \sim 750$ s) have been used for parameter estimation. Note that the MISO model cannot account for the overgrowth in the vascular response during prolonged stimulation.

MISO model cannot account for the behavior of the neuro-vascular system, when the stimulation lasts for much more than 60 s.

31.5.2 Frequency-Domain Model Properties

In this section we investigate the frequency-domain properties of the state-space part of the semi-physical MISO model.

Zeros, Poles, and Gains

As mentioned in Section 31.4.2 on page 221, we will cross validate the model rewritten in terms of zeros, poles, and gains. The model reads

$$Y(s) = G_{11}(s)U_1(s) + G_{12}(s)U_2(s) + E(s) \tag{31.15}$$

with the transfer functions being

$$G_{11}(s) = k_{11}\frac{(s-z_{11})(s-z_{21})}{(s-p_1)(s-p_2)(s-p_3)}, \tag{31.16}$$

$$G_{12}(s) = k_{12}\frac{(s-z_{12})(s-z_{22})}{(s-p_1)(s-p_2)(s-p_3)}. \tag{31.17}$$

The gains are denoted k_{11} and k_{12}, the zeros z_{11}, z_{21}, z_{12}, and z_{22}, and the poles p_1, p_2, and p_3. The poles — being common to the two transfer functions — are listed in Table 31.10. The estimates of the gain

Series	p_1	p_2	p_3
196io4	-0.16070	$-0.06609 - 0.12823i$	$-0.06609 + 0.12823i$
196io5	-0.15506	$-0.05905 - 0.15062i$	$-0.05905 + 0.15062i$
197io1	0.00031	$-0.06864 - 0.08963i$	$-0.06864 + 0.08963i$
197io3	-0.00528	$-0.05365 - 0.09782i$	$-0.05365 + 0.09782i$
Mean	-0.08018	$-0.06186 - 0.11658i$	$-0.06186 + 0.11658i$
Std(Re)+std(Im)i	0.08978	$0.00681 + 0.02812i$	$0.00681 + 0.02812i$
Cv(Re)+cv(Im)i	-1.11964	$-0.11010 - 0.24124i$	$-0.11010 + 0.24124i$

Table 31.10: The semi-physical model with the input two-thresholds transform: Estimates of the three poles p_1, p_2, and p_3. Note, that one pole is real and negative, corresponding to stable linear system dynamics, and two poles are complex and each other's complex conjugate, thus corresponding to oscillatory linear system dynamics. The coefficient of variance of the real pole p_1 is larger than one. The estimates of the two complex poles p_2 and p_3 are consistent in the sense that their coefficients of variance are much smaller than one.

and the zeros related to the input u_1 are listed in Table 31.11. The estimates of the gain and the zeros

Series	k_{11}	z_{11}	z_{21}
196io4	0.03420	$0.15298 - 0.13138i$	$0.15298 + 0.13138i$
196io5	0.12454	-0.16374	0.14091
197io1	-0.06503	$-0.04017 - 0.03611i$	$-0.04017 + 0.03611i$
197io3	0.01237	-0.02266	2.90969
Mean	0.02652	$-0.01840 - 0.04187i$	$0.79085 + 0.04187i$
Std(Re)+std(Im)i	0.07799	$0.13037 + 0.06205i$	$1.41532 + 0.06205i$
Cv(Re)+cv(Im)i	2.94090	$-7.08614 - 1.48193i$	$1.78961 + 1.48193i$

Table 31.11: The semi-physical model with the input two-thresholds transform: Estimates of the gain k_{11} and the two zeros z_{11} and z_{21} in the transfer function $G_{11}(s)$ from input u_1 to output y. Note, that the estimated gain and zeros vary considerably from one experiment to another. As expected (due to the lack of normalization of the FPA signal — cf. Section 28.2 on page 193) the coefficient of variance of the gain estimates is larger than one.

related to the input u_2 are listed in Table 31.12. The poles and zeros are illustrated by pole-zero plots in Figure 31.12.

Series	k_{12}	z_{12}	z_{22}
196io4	0.06693	$-0.07615 - 0.26659i$	$-0.07615 + 0.26659i$
196io5	0.15891	$0.01760 - 0.26066i$	$0.01760 + 0.26066i$
197io1	-0.04357	-0.00068	1.17589
197io3	0.03091	-1.64167	-0.01591
Mean	0.05329	$-0.42522 - 0.13181i$	$0.27536 + 0.13181i$
Std(Re)+std(Im)i	0.08411	$0.81198 + 0.15222i$	$0.60161 + 0.15222i$
Cv(Re)+cv(Im)i	1.57823	$-1.90953 - 1.15485i$	$2.18482 + 1.15485i$

Table 31.12: The semi-physical model with the input two-thresholds transform: Estimates of the gain k_{12} and the two zeros z_{12} and z_{22} in the transfer function $G_{12}(s)$ from input u_2 to output y. Note, that the estimated gain and zeros vary considerably from one experiment to another. As expected (due to the lack of normalization of the FPA signal) the coefficient of variance of the gain estimates is larger than one.

From the tables and the figure it is concluded, that the estimates of zeros vary considerably from one time series to another. The same is — as expected — true for the gains. Also the real pole (p_1) is not well-defined. Contrary to this, the estimates of the two mutually complex conjugate poles (p_2 and p_3) are consistent.

As in the case of the grey-box model, we now study the stable and the oscillatory linear system dynamics, respectively. The negative real pole corresponds to stable linear system dynamics with the following time constant τ:

$$\tau = \frac{1}{p_1} = \frac{1}{0.08018} \approx 12.47194\ s. \tag{31.18}$$

The two complex poles correspond to oscillatory linear system dynamics with the following undamped natural frequency ω_n and damping ratio ζ:

$$\omega_n = \sqrt{p_2 \cdot p_3} \approx 0.13198, \tag{31.19}$$

$$\zeta = -\frac{1}{2} \cdot \frac{(p_2 + p_3)}{\sqrt{p_2 \cdot p_3}} \approx 0.46872. \tag{31.20}$$

In units of Hertz the undamped natural frequency is

$$f_n = \frac{\omega_n}{2\pi} \approx 0.02100\ Hz \tag{31.21}$$

and corresponds to a period of

$$T_n = \frac{1}{f_n} \approx 47.60869\ s, \tag{31.22}$$

i.e., a very slow oscillation. Note that these values for the oscillatory dynamics of the MISO model are not very different from those obtained for the grey-box model (cf. Section 27.1.2 on page 181).

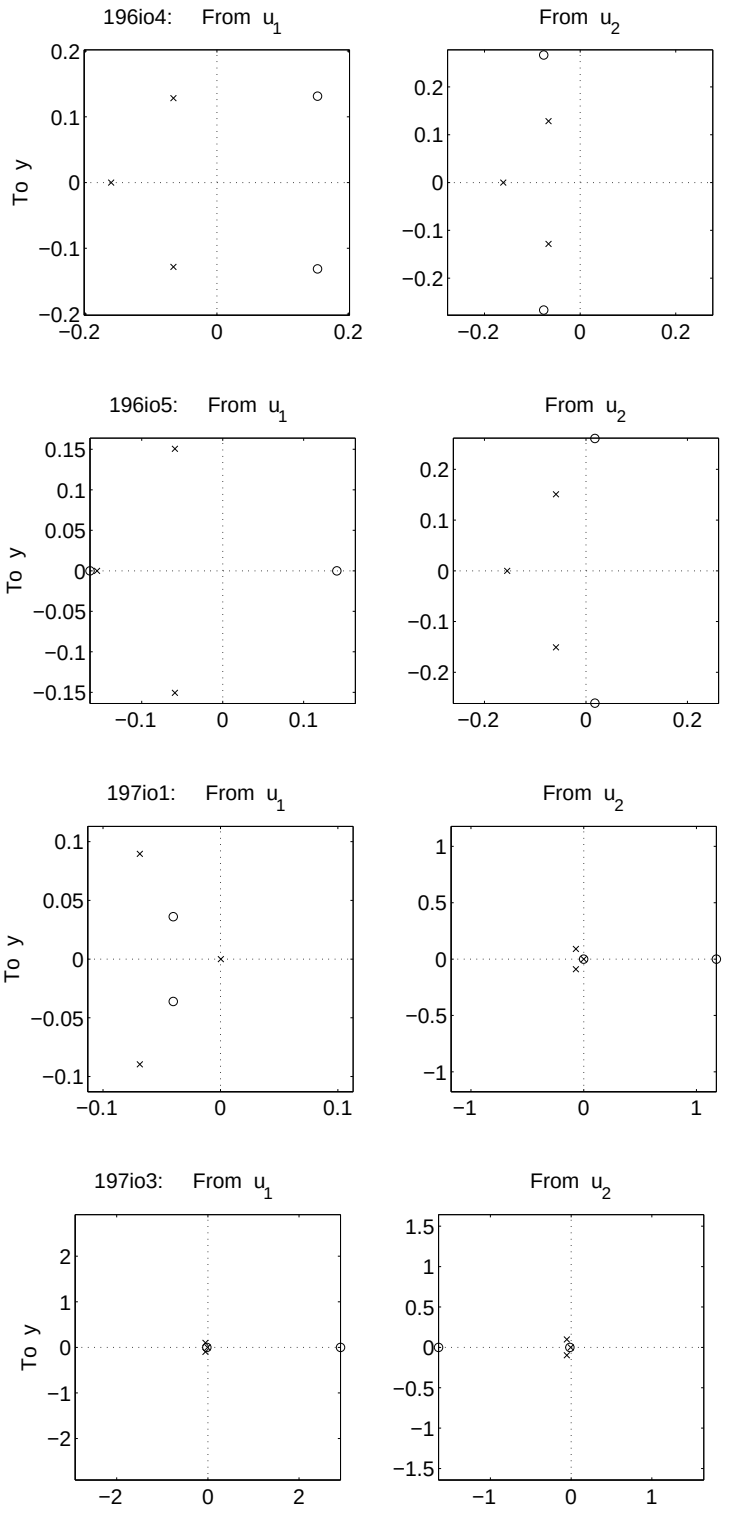

Figure 31.12: The semi-physical model with the input two-thresholds transform: Pole-zero map for each of the four time series. Poles are marked by x's, zeros by o's. Remember, that the transfer function from u_1 to y (left panels) has the same poles (x's) as the transfer function from u_2 to y (right panels). These maps emphasize, that the estimates of zeros vary considerably more than the estimates of poles. For the experiment 197io1 the pole $p_1 = 0.00031$ is positive (corresponding to unstable linear system dynamics) but very small — and furthermore very close to the zero $z_{12} = -0.00068$ of $G_{12}(s)$ (suggesting pole-zero cancellation).

Bode Plots

The Bode plots in Figure 31.13 show the magnitudes $|\,G_{11}(f)\,|$ and $|\,G_{12}(f)\,|$ (on logarithmic scales $M_{dB}(f) = 20 \cdot \log|G(f)|$) and the phases $\phi_{11}(f)$ and $\phi_{12}(f)$ of the transfer functions $G_{11}(f) = |G_{11}(f)| \cdot e^{i \cdot \phi_{11}(f)}$ and $G_{12}(f) = |G_{12}(f)| \cdot e^{i \cdot \phi_{12}(f)}$. Note that, due to the higher number of zeros and poles, there

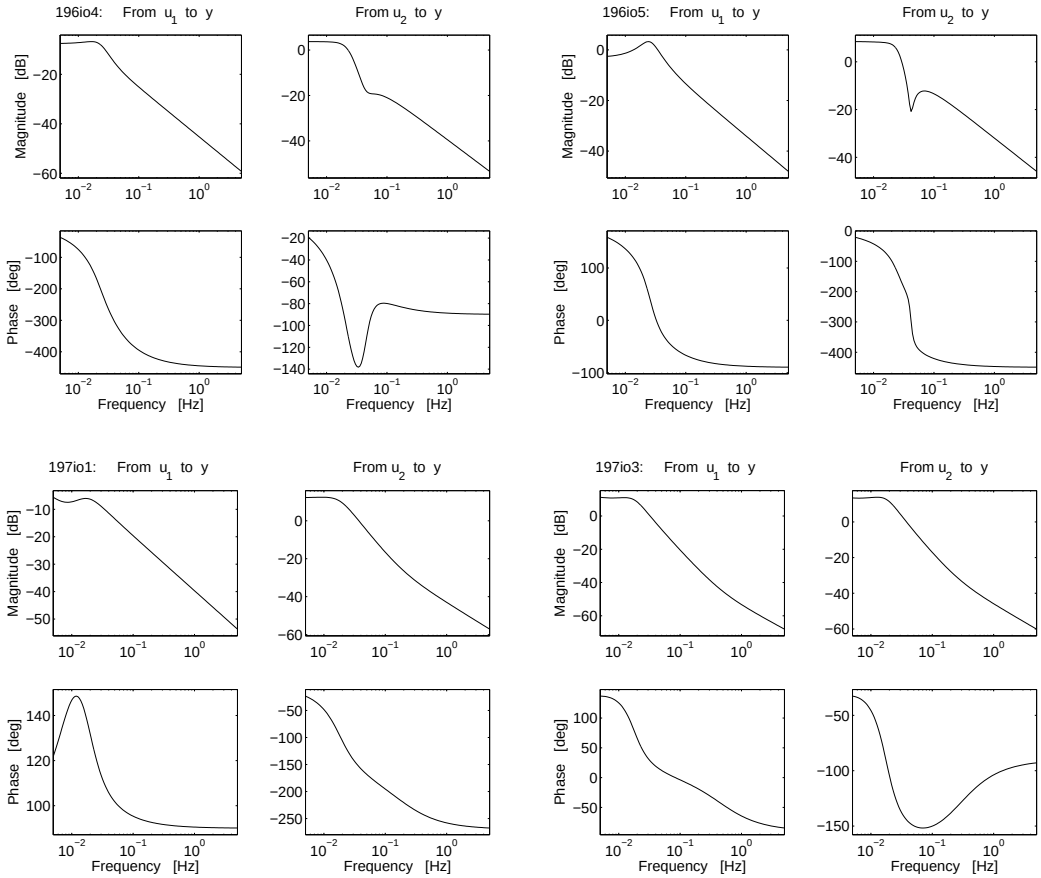

Figure 31.13: The semi-physical model with the input two-thresholds transform: Bode plots. Due to the higher number of zeros and poles, there are more features in the Bode plots of this model than in the Bode plots of the grey-box model with the input threshold transform — compare with Figure 27.6 on page 183.

are more features in the Bode plots of the semi-physical MISO model than in the Bode plots of the grey-box model with the input threshold transform — compare with Figure 27.6 on page 183. Note also, that these Bode plots differ considerably more from one experiment to another than those obtained from the grey-box model.

31.6 Discussion of the Input Two-Thresholds Transform

31.6.1 Mathematical Explanation of the Dips

In Section 31.1.2 we reached a suggestion to a mathematical model by studying the features of the input signal. We explained the dip in the vascular response from the idea that the first increase is mediated by two vasodilators and that the second increase is due to the release of only one of those vasodilators. This description corresponds to the situation illustrated by (a) in Figure 31.14.

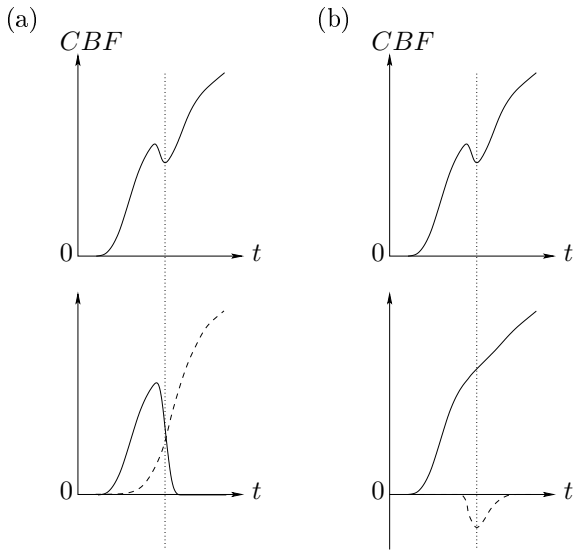

Figure 31.14: Examples of how the blood flow response (upper panels) to stimulation with a single frequency mathematically can be composed of two contributions (lower panels). In situation (a) two vasodilators contribute to the first increase whereas only one of them is responsible for the second increase. In situation (b) a vasodilator is responsible for the majority of the vascular response, whereas the dip is due to a vasoconstrictor.

The other extreme is to make suggestions to a mathematical model by looking only at the output signal. Another simple explanation then is that the majority of the vascular response is mediated by a vasodilator and that the dip is due to a vasoconstrictor, which is only released in a short time interval, as illustrated by (b) in Figure 31.14.

The simulations of the MISO model, which are shown in Figure 31.10 on page 232, support both pictures: The MISO model identified from the experiment 196io4 is closest to situation (a) and the MISO model identified from the experiment 196io5 is closest to situation (b).

31.6.2 When do the Two Mediators Contribute to Coupling?

It has been suggested — cf. Ref. [67] and P: Chapter 6 — that NO, which is a vasodilator (cf. P: Section 6.3.1 on page 35), is responsible for the first, fast CBF increase, and that the second, slower increase is mediated by adenosine, which also is a vasodilator (cf. P: Section 6.3.2 on page 36). The findings in Section 31.5.1 advocates for another picture: NO is a potent vasodilator and, at all stimulation frequencies, is released as long as the stimulation lasts. The second mediator, X, whose effect possibly is vasoconstrictory, is primarily released, when the field potential amplitudes are large, that is, upon stimulation with low frequencies and primarily right after the onset of stimulation — and therefore is responsible for the dips in the vascular signal. In the MISO model, the input signal $u_2(t)$ — corresponding to the very low threshold position FPA_2 — is an indicator of the neuronal signal which causes release into the extracellular space of nitric oxide, and $u_1(t)$ — with FPA_1 being high — is an indicator of the neuronal activity which causes release of the unknown mediator X.

31.6.3 Performance of the MISO Model

The model fit is better for the semi-physical MISO model than for any of the other models, which have been investigated in this thesis — especially during the dips. Also the cross validation of the parameters in the nonlinear input two-thresholds transform supports the picture from which the model originated. However, the cross validation of the parameters in the linear state-space part of the model reveals large variations among the experiments. Furthermore, the sensitivities to these parameters vary a lot. The question is, whether the discrepancies are due to variations in the experimental conditions or due to under-modeling (i.e., that the model structure does not cover the system dynamics) ? Since

nitric oxide (NO) and the other mediator (X) are probably *not* released into the extracellular space by the same physiological process, it is likely that the input two-thresholds transform does not represent the physiological processes well. The good fit may partly be due to the larger size of the MISO model structure.

The coefficient of variance of FPA_2 is much larger than the coefficient of variance of FPA_1. One reason is that the stimulation frequency is kept relatively low. As a result, there are few FPA events with values around FPA_2. Thus, one way to obtain better estimates of the threshold position FPA_2, that is, to diminish the coefficient of variance of FPA_2, could be to perform experiments, where stimulation is done with higher frequencies.

31.7 Conclusion on the Input Two-Thresholds Transform

The nonlinear input two-thresholds transform converts the event-sampled FPA signal into a two-dimensional signal, which forms the input signal to a third-order linear MISO output-error black-box state-space model. The CBF signal forms the one-dimensional output from the state-space model.

The MISO model performs well in the sense that it fits the experimental data well — it can reproduce both the frequency saturation and the dips in the CBF signal. The MISO model also gives consistent estimates of the two parameters in the input two-thresholds transform, and the sensitivity to these parameters is high. However, cross validation of the parameters in the linear state-space part of the model shows rather large variances, and the sensitivities to these parameters are very different and vary a lot from experiment to experiment.

Chapter 32

Discussion of Semi-Physical Models

32.1 Selection of Model Structure

The phenomena earlier characterized as frequency saturation of and dips in the CBF response to stimulation now have been explained from two features of the FPA signal: The decrease in overall FPA size with increasing frequency and the fact that the FPA's depend dynamically on the stimulation frequency. That is, the MISO model structure has been selected on basis of the features which were found through the signal analysis in Chapter 14.

32.2 The Origin of the Deficiencies of the MISO Model

Despite its rather large number of parameters (though only two parameters describe the nonlinearities) the MISO model is unable to account for the dynamics of the neuro-vascular system during prolonged stimulation. The semi-physical MISO model strongly underestimates the cerebellar blood flow during prolonged stimulation. We suggest, that the measured overgrowth is a result of one or more physiological processes, which have not been included in the model. Specifically, we hypothesize, that the overgrowth is a metabolic effect. During stimulation for relatively short times, neuro-vascular coupling is not affected by metabolism. However, on longer time scales metabolism may contribute to coupling.

Chapter 33

Conclusion on Semi-Physical Models

We have developed dynamic mathematical models of the coupling between the field potential amplitude signal (which is an indicator of neuronal activity) and the relative cerebellar blood flow signal, which exists during climbing fiber activation.

This part first considered semi-physical SISO models. Each of these consists of one of the dynamic input transforms, which have been developed for the grey-box models investigated in Part V:

- The input sampling transform (linear),
- The input threshold transform (nonlinear, one parameter), or
- The input kink transform (nonlinear, two parameters)

in combination with a linear black-box output-error state-space model structure. Their linear order has been estimated to be two. Each of the models therefore only contains one parameter more than the equivalent grey-box model. Accordingly, the properties of the semi-physical SISO models are very similar to the properties of the grey-box models.

Secondly, from the assumption that there are two mediators of neuro-vascular coupling, which are characterized by each of their own threshold for release, a semi-physical MISO model has been developed. It consists of a nonlinear transformation of the measured field potential amplitude signal into a two-dimensional input followed by a third-order linear black-box MISO output-error state-space model structure. The MISO model exposes high sensitivity to the two parameters in the input transformation, and the coefficients of variance of the two parameters are low. The importance of all of the parameters in the linear part of the model is more unclear. The structure of the MISO model has made it possible to conclude on the function of the two mediators:

- One mediator is characterized by a low threshold for release, operates as long as the climbing fiber is activated, and is clearly strongly vasodilatory.
- The other mediator is characterized by a high threshold for release, is therefore mainly released right after onset of stimulation, and is possibly weakly vasoconstrictory.

Part VII

Concluding Part

The purpose of this part is to put the obtained research results into a broader perspective and finally to summarize the conclusions.

The goal is to answer some of the questions which have been posed in *Chapter 1: Introduction.*

Thus this part includes:

- Discussion of Research Results
- Suggestions for Further Research
- Applications and Perspectives
- Conclusion on Research Results.

Chapter 34

Discussion of Research Results

34.1 Which Kind of Neuronal Activity is Coupled to Blood Flow?

Throughout this Ph.D. thesis it has been assumed that the field potential, not the spiking activity, represents the neuronal activity which is responsible for vascular responses.

Mathiesen *et al.* [66] have emphasized, that the issue of what type of nerve cell activity (synaptic excitation, spikes, or both) will trigger increased CBF, is of importance: *"Increases in regional CBF are commonly used to localize neuronal activity in humans and animals. The mechanisms that couple CBF and neuronal activity are still only incompletely understood, but the issue is of great interest since in an increasing number of studies in humans the vascular responses are used to map neuronal activity. It is implicit in most papers that regional increases of CBF ('brain activation') are associated with increases of net spike activity in the neurons of the active region, even though a reorganization of the activity without increases in net spike activity is more likely to occur in some neuronal networks, in humans as in other species. Only very few papers have addressed this issue directly by simultaneous recording of neuronal activity and CBF. Therefore, it is unclear what type of nerve cell activity (synaptic excitation, spikes, or both) will trigger increased CBF."*

The experiments performed by Mathiesen *et al.* [66] was the first study to demonstrate the strong relationship of CBF (measured by laser-Doppler flowmetry) to synchronized extracellular current flow. Their investigations have been extended and have lead to the conclusion that *"the afferent function, that is, pre- and post-synaptic activity (including synaptic processing in the efferent cell) determines all properties of the hemodynamic signals accompanying functional activation. Spiking activity in relay neurons and interneurons may contribute as well, but there is no evidence that spiking activity in the efferent cells — efferent function — plays any role"* [57]. Logothesis *et al.* [63] made similar investigations using BOLD fMRI to measure hemodynamic changes. They concluded that *"the BOLD contrast mechanism reflects the input and intracortical processing of a given area rather than its spiking output."*

This Ph.D. thesis has shown that the field potential signal can be mathematically related to the laser-Doppler flowmetry signal. This fact, however, does not exclude that other measurements of neuronal activity and cerebellar blood flow can by mathematically related (by other relations).

34.2 How many Mediators are there?

The linear order of the neuro-vascular system has been estimated to be $n = 2 - 3$. The question is whether this result corresponds to the existence of $1 - 2$ mediators or $1 - 2$ pools of similar mediators? The second situation would come about in case the parameters representing mediators in a pool were identical (the equations would then merge into a single equation). We will claim that this situation is unlikely. Let us say that one pool corresponded to a number of mediators. Then the matrix $\mathbf{F}$ would be large, and it would be unlikely that it would be mapped into a second-order transfer function $G(s)$. Therefore, we expect that the low estimate of the linear order reflects that the number of mediators is low.

34.3 The Origin of Model Deficiencies

34.3.1 Variation in Experimental Conditions

Part of the variation in the estimated parameter values may be attributed to the variation in the experimental conditions listed in Table A.1 on page 262.

34.3.2 Technical Limitations

Also drift in the LDF signal contributes to the variation in the parameter estimates. This is particularly evident for the time series 197io1, where, for instance, the baseline level CBF_B is not constant over time. As a result the estimate of the threshold position in the input threshold transform obtained from the experiment 197io1 deviates from the estimates obtained from the remainder three experiments.

34.3.3 The Influence of $50\ Hz$ Noise

We first note, that the FPA signal in general is a much more vulnerable signal than the LDF signal. At low frequencies there are much fewer FPA events than CBF samples, and at high frequencies the FPA's are so small that they easily drown in noise components.

In order to be able to conclude on the influence of the $50\ Hz$ network voltage on the model properties, we investigate how the input signal is changed by this noise signal:

We assume that the contribution to the field potential signal from the $50\ Hz$ noise is sinusoidal — compare with Figure A.5 on page 267. The field potential amplitude signal is therefore changed from its correct value FPA_c to the measured value FPA, i.e.,

$$FPA(t_j) = FPA_c(t_j) + \Delta(t_j), \tag{34.1}$$

$$\Delta(t_j) = A \cdot \cos(\omega \cdot t_j + \phi) \tag{34.2}$$

where the contribution from the network voltage has been denoted by Δ and $\omega = 2\pi \cdot f_{\text{noise}} = \pi \cdot 100\ rad/s$.

The Input Sampling Transform

The preprocessed field potential amplitude signal is changed to

$$FPA_{pp}(t) = \sum_{t-\frac{\tau}{2}<t_j\leq t+\frac{\tau}{2}} FPA(t_j) = FPA^c_{pp}(t) + \Delta FPA_{pp}(t), \tag{34.3}$$

$$FPA^c_{pp}(t) = \sum_{t-\frac{\tau}{2}<t_j\leq t+\frac{\tau}{2}} FPA_c(t_j), \tag{34.4}$$

$$\Delta FPA_{pp}(t) = \sum_{t-\frac{\tau}{2}<t_j\leq t+\frac{\tau}{2}} \Delta(t_j) = A \cdot \sum_{t-\frac{\tau}{2}<t_j\leq t+\frac{\tau}{2}} \cos(\omega \cdot t_j + \phi). \tag{34.5}$$

Only in case the event frequency $f_e(t_j) = \frac{1}{(t_j - t_{j-1})}$ equals a multiple of $50\ Hz$, $f_e = z \cdot f_{\text{noise}}, z \in \mathbb{Z}_+ = \mathbb{N}$, we get constructive interference. However, in the experiments the event frequency lies in the range $f_e \in [2\ Hz; 30\ Hz]$. Thus the contribution from the term ΔFPA_{pp} is in-significant. That is,

$$FPA_{pp}(t) = \sum_{t-\frac{\tau}{2}<t_j\leq t+\frac{\tau}{2}} FPA(t_j) \approx \sum_{t-\frac{\tau}{2}<t_j\leq t+\frac{\tau}{2}} FPA_c(t_j). \tag{34.6}$$

A similar conclusion can be reached for the input running summation transform. These results are due to the fact that the input sampling transform and the input running summation transform are linear transformations.

The Input Kink Transform

The Taylor expansion to first order around the kink position FPA_0 reads:

$$w(FPA) \approx w(FPA_0) + \frac{dw}{dFPA}_{|_{FPA_0}} \cdot (FPA - FPA_0) = \frac{1}{2} + \alpha_w \cdot (FPA - FPA_0)\,, \tag{34.7}$$

where the derivative is non-negative: $\alpha_w = \frac{dw}{dFPA}|_{FPA_0} \geq 0$ (cf. Section 24.2 on page 157 and Section 26.1 on page 166). Then the first-order approximation to the change in the preprocessed field potential amplitude resulting from the network voltage reads:

$$\begin{aligned}
\Delta FPA_{pp}(t) &= FPA_{pp}(t) - FPA^c_{pp}(t) && (34.8)\\
&= \sum_{t_j} \{FPA(t_j) \cdot w(FPA(t_j))\} - \sum_{t_j} \{FPA_c(t_j) \cdot w(FPA_c(t_j))\} && (34.9)\\
&\approx \sum_{t_j} \{[FPA_c + \Delta] \cdot [w(FPA_0) + \alpha_w \cdot (FPA_c + \Delta - FPA_0)]\} \\
&\quad - \sum_{t_j} \{FPA_c \cdot [w(FPA_0) + \alpha_w \cdot (FPA_c - FPA_0)]\} && (34.10)\\
&= \sum_{t_j} \{[FPA_c + \Delta] \cdot [w(FPA_0) + \alpha_w \cdot (FPA_c - FPA_0) + \alpha_w \cdot \Delta]\} \\
&\quad - \sum_{t_j} \{FPA_c \cdot [w(FPA_0) + \alpha_w \cdot (FPA_c - FPA_0)]\} && (34.11)\\
&= \sum_{t_j} \{FPA_c \cdot \alpha_w \cdot \Delta + \Delta \cdot [w(FPA_0) + \alpha_w \cdot (FPA_c - FPA_0) + \alpha_w \cdot \Delta]\} && (34.12)\\
&= \{w(FPA_0) - \alpha_w \cdot FPA_0\} \cdot \sum_{t_j} \Delta(t_j) + \alpha_w \cdot \sum_{t_j} \Delta(t_j)^2 && (34.13)\\
&= \{w(FPA_0) - \alpha_w \cdot FPA_0\} \cdot A \cdot \sum_{t_j} \sin(\omega \cdot t_j + \phi) \\
&\quad + \alpha_w \cdot A^2 \cdot \sum_{t_j} \sin^2(\omega \cdot t_j + \phi) && (34.14)\\
&\approx \alpha_w \cdot A^2 \cdot \sum_{t_j} \sin^2(\omega \cdot t_j + \phi)\,. && (34.15)
\end{aligned}$$

Since the value of this expression is strictly positive, this calculation shows that for periods during an experiment where the values of the FPA's are close to FPA_0 (so that the first-order Taylor expansion is a good approximation), the 50 Hz noise results in over-estimation of the preprocessed FPA signal, $FPA_{pp}(t)$. This is the situation in case of intermediate stimulation frequencies (around 10 Hz).

In case the stimulation frequency f_s is kept low, most of the FPA's are larger than the kink position, and the input kink transform reduces to the input sampling transform. Thus, in this case the preprocessed signal is not changed by the network voltage.

In case the stimulation frequency f_s is kept high, most of the FPA's are smaller than the kink position, and the input kink transformed signal becomes equal to zero — independently of the noise contribution.

34.3.4 The Model Structure is not Sufficiently Large

Throughout this Ph.D. thesis we have assumed that only three subsystems (the neuronal subsystem, the extracellular space, and the vascular subsystem) are necessary to create a good description of neuro-vascular coupling. And only a few coupling among them have been included in the models.

It could be that these assumptions are only appropriate when the stimulation duration is kept low, for instance below ~ 25 seconds. On longer time scales we may need to take into account features related to metabolism. Lauritzen [57] has hypothetized that *"The first CBF peak is delayed and reduced by nitric-oxide synthase inhibitors, whereas the second peak probably reflects accumulation of vaso-active metabolites (e.g., lactate or adenosine). Extracellular lactate increases rapidly in response to acute neuronal activation, and the time constants for the concentration changes of extracellular lactate and CBF are similar."* We suggest, that on time scales longer than 20 s metabolism contribute to coupling via lactate. Furthermore, the overgrowth during prolonged stimulation could be due to un-realized properties of the vessel wall. The model structure would have to be extended in order to incorporate these features.

Chapter 35

Suggestions for Further Research

Here we will consider some suggestions to research objectives and activities, which follows directly from the research results obtained in this Ph.D. thesis.

35.1 Basic Research: New Questions

We have found the answers to some of the questions posed in *Chapter 1: Introduction*. As expected from a basic research project, new questions have arisen:

- What is the second CBF increase (beyond the dip) due to? Is it due to the nonlinear properties of the smooth muscle cells? Or due to metabolic activity?
- How does metabolic activity influence the coupling? Can it be neglected when the neuronal activity lasts for short periods?
- Do vasoconstrictors mediate part of the coupling?

35.2 Experimental Work

35.2.1 Experimental Methods

Some suggestions to changes in the experimental procedures are:

Acquisition of FP Signal

It would be preferable to avoid on-line prefiltering of the electric signals before registration. Not only would it then be possible to experiment with various prefilters. Thereby also higher compatibility would be obtained, i.e., by doing the prefiltering off-line it would be possible to use data from many different experiments in a single theoretical or modeling study.

In case prefiltering cannot be avoid, it could be reconsidered. The FP prefilter could be changed to cover the frequency band $[10^{-3}\ Hz;\ 500\ Hz]$. This would allow more slow components but remove high-frequency noise — cf. Section 14.1.1 on page 80. Furthermore, the effect of the 50 Hz artifact could be diminished by means of a so-called notch filter. In that case the estimates of a field potential amplitude as well as its time of occurrence would become more well-defined. And the frequency of FPA events would move closer to the stimulation frequency.

In order to save memory, one could avoid saving the full field potential signal in a file. Only the intervals centered around the periods with activity needs to be saved. It would then be crucial to save so much of the signal that the FP prefiltering will not be distorted by edge effects.

Acquisition of CBF Signal

It should be investigated whether the two factors in the CBF signal, the concentration of moving blood cells and the mean velocity, are un-correlated. We suggest, that they may be un-correlated at low flow values. But at high concentrations of moving blood cells, the velocity distribution may be affected.

The decrease in maximum CBF response for high frequencies as well as the dips can be due to a decrease in the mean blood cell velocity and/or a decrease in the concentration of moving blood cells (cf. P: Section 7.4.4 on page 47). In order to investigate whether these nonlinearities are pertaining to a strong decrease in the mean velocity and/or in the concentration of red blood cells, these signals could be recorded instead of the CBF signal. Preliminary research along this line has been performed by Barfod *et al.* [9]. Their findings suggest that variations in flow velocity contribute relatively more to the variation in the CBF signal than variations in concentration of moving blood cells.

35.2.2 Experiment Design

We have exhausted the possibilities to extract information from the available data. Thus new experimental data are needed.

A general wish is to get data from more experiments. To compare a model with four experiments does not form a good basis for rejecting or accepting the model.

The duration of pauses could be diminished, and should not exceed 150 s significantly. Using longer pauses is a waste of experiment time — cf. Section B.4 on page 274. The need to establish well-defined baseline CBF values, however, is a limitation: A time series must always include several, quite long, intervals without stimulation (in order that transients die out) to be used for baseline definition, and for controlling that there is no drift in the baseline value.

In order to trigger more of the dynamics in the neuro-vascular system, new experiments could be designed. First of all, stimulation sequences with more frequencies (as compared to the only six frequencies in the data which has been used for this study) would offer the opportunity to get better parameter estimates. Specifically, stimulation sequences with frequencies around and above 30 Hz would offer the opportunity to get better estimates of the threshold positions FPA_1 and FPA_2 in the input threshold transform and in the input two-thresholds transform. Less variation in the values of the estimates of the threshold positions as well as higher sensitivity to these parameters could be obtained. It would also be possible to strengthen or reject the conclusion that the kink slope α_w shall be excluded from the model structure.

35.3 Modeling and Theoretical Work

35.3.1 Modeling Methods

The average FPA signal, $\langle FPA \rangle_{1\,s}$, could be modeled as a step response with the stimulation frequency as the step. The step response could then be described by a few shape parameters. This would give a signal representation on a slow time scale. Hubbard *et al.* [42, (Ch. 6)] used a similar approach. They defined the *shape index* as the (static) relation between the duration at half amplitude (FWHM) of unitary potentials and their time to peak.

The individual FP excitations could be modeled as an impulse response with the stimulation current as the impulse. This would give a representation of the field potential on a fast time scale.

The most important suggestion is to use wavelet analysis [46] to analyze the field potential signal. The wavelet representation is suited for describing both time-localized excitations (like the events in the field potential signal) and frequency-localized excitations (like the 50 Hz artifact originating from the network voltage). Wavelet analysis could then be a step in the process of constructing an event representation, which is better than the field potential amplitude signal.

The part of the time series, where the blood flow acquires its baseline value, could be cut out. In this way the loss function V_N would only represent the dynamic part of the system, and the loss function would become more sensitive to each parameter in the model.

The neuro-vascular system may be referred to as a *hybrid system* because it contains both discrete-time and continuous subsystems [23, (Sect. 1.4)].

35.3.2 A Model for the Case of Parallel Fiber Stimulation

The field potential excitations resulting from parallel fiber stimulation contain two time-localized components: The pre-synaptic potential (PSP) and the excitatory post-synaptic potential (EPSP). That is, the input have to be extended to a two-dimensional vector. Furthermore, the main mediator is K^+-ions,

which moves through both the extracellular space and the astrocytes. Therefore, a model of neuro-vascular coupling must contain four subsystems: The neuronal subsystem, the extracellular space, the astrocytes, and the vascular subsystem. We therefore conclude, that a model of neuro-vascular coupling in case of parallel fiber stimulation will be considerably more complex than a model describing the case of inferior olive stimulation.

In case the mathematical models reflect the neuronal organization of cerebellum it may be possible to distinguish between excitatory and inhibitory neuronal activity from measurements of cerebellar blood flow.

It would also be interesting to compare the two systems (involved during inferior olive stimulation and parallel fiber stimulation, respectively). Such a comparison could give insight into the effect of the inhibitory interneurons — cf. Figure 3.11 on page 25.

The parallel fiber stimulation experiments are interesting also for another reason: Since measurements of extracellular potassium have been made [19] it is possible to investigate subsystems of the neuro-vascular system. However, the CBF signal is more noisy.

Chapter 36

Applications and Perspectives

In this chapter we consider some applications of mathematical models of neuro-vascular coupling.

36.1 Scanning Tool

The Possibility of Imaging the Brain

We can monitor cerebellar blood flow non-invasively, but not nerve cell activity. A measurement of nerve cell activity is intrinsically invasive [100]. However, a long-time perspective is to be able to convert non-invasive measurements of blood flow signals into information about neuronal signals whose measurement would be invasive (and therefore un-suited for human studies and clinical practice).

Towards LDF as a Scanning Tool

Let us first recall, that we have claimed that LDF is a non-invasive technique for monitoring of CBF. However, even though the brain itself is not penetrated in the experiments, the skull and the two outermost meninges are removed. Even though the LDF method is destructive, we will use the models obtained with the LDF method to elaborate on, which steps are required in order to develop a scanning tool.

We have temporal resolution of both the field potential signal and the cerebellar blood flow signal. Spatial resolution in depth (perpendicularly to the brain surface) has been obtained by subtracting signals from different LDF probes [32], and 'horizontally' (parallel to the brain surface) by a scanning LDF technique [3].

The mathematical models presented in this Ph.D. thesis provide solutions to the forward problem of calculating the cerebellar blood flow from measurements of neuronal activity. What lacks is the inversion method needed to convert LDF-measurements of cerebellar blood flow into estimates of neuronal activity. The lesson, which can be learned from the mathematical models, is that the LDF-method suffers from a limitation: Only high neuronal activity (corresponding to field potential amplitudes larger than the threshold) can be retrieved. The color-coded images would contain dark areas where the neuronal activity cannot be retrieved from the CBF measurement. The only thing which would be known about the dark areas is that the neuronal activity is below threshold.

36.2 Diagnostic Tool

A mathematical model could constitute an important part of a diagnostic tool being able to distinguish between healthy subjects and certain pathological cases. This comes about in case the parameters in the mathematical model lies within certain ranges not too broad in case of healthy rats. It can then be expected that in pathological cases the parameters changes, either intrinsically, or because the model structure should be different due to other processes mediating the coupling.

The Grey-Box Model

In case of the grey-box model with the input threshold transform, certain conclusions may be made from the parameter estimates.

The values of the parameters $FPA_0, g \cdot h, f + k$ and $f \cdot k + h \cdot l$ which have been determined are the values for climbing fiber activation in healthy male Wistar rats, which are anesthetized and exposed to a muscle-relaxing drug.

In case of a disease pertaining to cerebellum the input-output relation can change. Assume that a disease do not cause new physiological processes to occur but rather that the values of the parameters FPA_0, f, g, h, k, and/or l change and thus deviate from their values in healthy rats. Then from estimation of $FPA_0, g \cdot\ h, f + k$, and $f \cdot k + h \cdot l$ it is possible to make plausible whether the disease is related to one of the following physiological defects:

- In case the estimated value $\widehat{FPA_0}$ deviates significantly from FPA_0 it is plausible that a change has occurred in the internal dynamics of the neuronal subsystem which determine the coupling between the fast and the slow time scale. That is, the physiological process by which the field potential is created may have been changed.
- In case the estimated value $\widehat{g \cdot h}$ deviates significantly from $g \cdot h$ it is plausible that either a change in the coupling between neuronal activity (FPA) and chemical activity ($c(NO)$) in the extracellular space (in which case $\widehat{g}$ will change) and/or a change in the coupling between chemical activity ($c(NO)$) in the extracellular space and the cerebellar blood flow (CBF) (in which case $\widehat{h}$ will change) has occurred. That is, either the process by which NO is released or how the smooth muscle cells respond to NO has been changed.
- In case the estimated value $\widehat{f} + \widehat{k}$ deviates significantly from $f + k$ it is plausible that a change has occurred either in the internal dynamics of the concentration of NO in the extracellular space or in the internal dynamics of the cerebellar blood flow. For instance, a property of the extracellular medium or the smooth muscle cells may have been changed.
- In case the estimated value $\widehat{f \cdot k} + \widehat{h \cdot l}$ deviates significantly from $f \cdot k + h \cdot l$ it is plausible that a change has occurred either in the internal dynamics of the concentration of NO in the extracellular space, in the internal dynamics of the cerebellar blood flow, or in the coupling between the extracellular space and the vascular subsystem.

These interpretations could be implemented as a MATLAB tool-box. Such a program would then act as a diagnostic tool, drawing conclusions about changes in neuro-vascular coupling in cerebellum only from input-output measurements.

A Transfer Function Model

Another way to use such a mathematical model for diagnostic purposes would be to realize that a disease most likely changes the physiological processes responsible for coupling.

A diagnostic tool could then be developed by estimating the parameter values from individuals suffering from specific, known diseases. An example is the work by Knudsen *et al.* [54]. They constructed a mathematical discriminator which could distinguish between normotensive and hypertensive rats.

Chapter 37

Conclusion on Research Results

The research object of this Ph.D. thesis is neuro-vascular coupling in cortex of cerebellum. Specifically, the blood flow response to activity in the so-called climbing fibers has been investigated.

The measurements, which have been studied, stem from experiments performed on anesthetized healthy male Wistar rats exposed to a muscle-relaxing drug. The extracellularly measured field potential is taken to be an indicator of neuronal activity, and the cerebellar blood flow has been measured by means of laser-Doppler flowmetry.

37.1 Conclusion w.r.t. Methodology

Previous research activities have focused on experimental investigations of neuro-vascular coupling. The experimentally reached conclusions have been summarized in qualitative models of the neuro-vascular system. This Ph.D. thesis represents a change of modeling approach: From qualitative modeling to quantitative modeling, i.e., mathematical modeling.

The main method has been system identification, which is a method for constructing a mathematical model of a dynamic system starting from measurements of input (field potential) and output (relative cerebellar blood flow) signals alone.

The thesis has emphasized the importance of analyzing the input and output signals thoroughly prior to system identification: All of the major changes to — and improvements of — the model structure have been based on information about the signal properties.

Compared to previously published papers on neuro-vascular coupling, this thesis represents a major change: Whereas previously reported models often use input and output signals, which are constructed from the original measurements by waveform averaging, in this thesis the models are identified directly from the original measurements.

The thesis has also exposed the strengths of as well as the limitations to system identification: In case the dynamics model is constructed from information on and/or hypothesis concerning the mechanisms responsible for the relation between input and output signals, it may be possible — through application of mathematical theory, such as Kalman filtering — to estimate signals, which have not been used for model construction. A mathematical model of a dynamic system consists of a model structure and a set of parameter values. Since the parameter values are estimated, their values are determined partly by the model structure and partly by the measurements. Therefore, the quality of a mathematical model found by system identification can be no better than the combined quality of the chosen model structure and the quality of the measurements, which are used for parameter estimation.

37.2 Conclusion w.r.t. Signal Properties

The characteristics of the input (the field potential) and output (the relative cerebellar blood flow) signals have been emphasized:

- The field potential signal varies on a fast time scale of a few milliseconds (10^{-3} s) whereas the relative cerebellar blood flow signal varies on a slow time scale on the order of up to ten seconds (10^{1} s).

- The information in the field potential signal lies mainly in the amplitude of the time-localized excitations (so-called events). The overall level of the sizes of field potential amplitudes decreases with increasing stimulation frequency. The field potential amplitude depends dynamically on the stimulation frequency: After onset of stimulation of the inferior olive with a constant frequency, the very first field potential amplitudes are very large. The amplitude of the following events decreases very fast towards a minimum size. During the remainder of the stimulation sequence the amplitude slowly increases.
- The relative cerebellar blood flow response to stimulation with constant frequency is characterized by a fast increase followed by a dip and afterwards an increase which slows down. Oscillations in the arterial blood pressure do not contaminate the relative cerebellar blood flow signal.

37.3 Conclusion w.r.t. Model Properties

The mathematical model design has taken four forms:

- **Non-Parametric Models:**
  The neuro-vascular system has been analyzed by means of a non-parametric model of the magnitude of the transfer function. It has been shown that most of the linear system dynamics pertains to frequencies below one Hertz.
- **Linear Black-Box Models:**
  General dynamic time-invariant linear black-box models have been studied. Each of these models had the form of a dynamic linear input transform followed by a linear black-box state-space model structure (containing a dynamics model and a noise model). Three features of the measured blood flow signal, which cannot be reproduced by these linear relations between the field potential amplitude signal and the relative cerebellar blood flow signal, have been emphasized: Frequency saturation and dips during short stimulation sequences (60 s), and overgrowth during prolonged stimulation (600 s).
- **Grey-Box Models:**
  These model structures have been constructed from the available physiological information in combination with some hypotheses. The system is divided into three subsystems: The neuronal subsystem, the extracellular space, and the vascular subsystem. It has been assumed that nitric oxide (NO) is a dominant mediator of coupling across the extracellular space. The model structures consist of a linear or nonlinear input transform followed by a second-order linear output-error state-space model with coupled and constrained parameters. The state vector contains the relative cerebellar blood flow and the preprocessed deviation of the concentration of nitric oxide in the extracellular space from its baseline level. The phenomenon of frequency saturation is explained by a threshold non-linearity. It describes mathematically the hypothesis that only field potential amplitudes larger than a certain threshold indicate neuronal activity which causes release of the vasodilatory chemical substance nitric oxide and thereby evoke blood flow increases. The cross validation shows high consistency of the parameter estimates, and the sensitivity to the parameters is relatively high. The strong physiological basis of the model structure has made it possible to extract information about the concentration of nitric oxide in the extracellular space, which is a non-measured signal, from the model.
- **Semi-Physical Models:**
  The first three semi-physical models, which have been investigated, preserves the features of the input transforms in the equivalent grey-box models, but removes the constraints on the dynamics part of the state-space model. The linear order has been estimated to be two. Furthermore, an extension to a MISO model has been provided. Due to the following properties, it has been named the *3-2-1 model*:
  - Linear order equal to 3.
  - 2 chemical substances couple neuronal activity to cerebellar blood flow increases.
  - The release of each of the mediators of neuro-vascular coupling requires a threshold field potential amplitude described by 1 parameter, the threshold position, to be overcome.

It has been hypothesized that one of the mediators across the extracellular space is nitric oxide (NO). No hypothesis concerning the other mediator has been posed. The MISO model provides a better fit, especially during the dips, and thus explains both the frequency saturation and the dips in the vascular response to neuronal activity. Cross validation shows high consistency of the parameters describing the nonlinearity (two thresholds), but large variability in the estimates of the parameters in the linear part of the model. The model fit is very sensitive to the values of the two parameters in the nonlinear part, but the sensitivity to the parameters in the linear part varies considerably from one experiment to another. According to the MISO model one of the mediators is clearly vasodilatory, but the effect of the other mediator is unclear (it is most likely vasodilatory, but it may be without effect or vasoconstrictory).

Throughout this Ph.D. thesis the model performance has been improved. The cost has been an increasing complexity of the model structure.

37.4 Conclusion w.r.t. System Properties

In *Chapter 1: Introduction* the question of which properties a mathematical model must posses in order to be able to reproduce the experimental data, was posed. Also some basic research questions concerning the physiological processes, which are responsible for neuro-vascular coupling, were posed. Some answers to these questions have now been given:

Mathematical Properties:

This Ph.D. thesis has verified that the field potential can be mathematically related to vascular responses. Furthermore, it has been shown that the quality of the experimental data is high enough for models of the neuro-vascular system to be reproduced from distinct experiments.

The relation between measurements at single points in space is time-invariant, dynamic, and nonlinear. The linear system dynamics pertains to frequencies below 1 Hz. Because the input (the field potential) consists of time-localized events of a duration in the millisecond range — which have been approximated by discrete events — while the output (the relative cerebellar blood flow) is a continuous signal varying on a time scale of less than ten seconds, the neuro-vascular system may be characterized as being discrete event driven and as being a hybrid system.

Physiological Properties:

This Ph.D. thesis has confirmed that the field potential (indicating post-synaptic neuronal activity) — as opposed to the spiking activity (that is, pre-synaptic activity) — is coupled to the local cerebellar blood flow.

The phenomenon of frequency saturation of the blood flow response to climbing fiber activation has been explained by a nonlinearity pertaining to the neuronal subsystem, not to the extracellular space or the vascular subsystem. The nonlinearity has the form of a threshold, that the field potential amplitude has to overcome in order that the associated neuronal activity causes release of the dominant mediator nitric oxide. This means that increases in blood flow reflect neuronal activity of large amplitude, independently of its frequency. It has been hypothesized, that the threshold originate from that fact that a depolarization of the nerve cell membrane stronger than a certain level is required to cause synthesis of nitric oxide. The mechanism could be as follows: The depolarization of the nerve cell membrane forces voltage-dependent calcium channels to open, and thereby the intercellular calcium concentration increases. As a result the enzyme NO-synthase (NOS) is activated, and NO is synthesized and released into the extracellular space. Since NO is a powerful vasodilator and distributes in the extracellular space, the end result is vasodilation and flow increase.

Neuro-vascular coupling during climbing fiber activation is mediated by a low number of chemical substances, probably one or two. Assuming there are exactly two mediators, which interact linearly with each other and with the blood vessels, it has been concluded that one of the mediators is clearly vasodilatory and the other is vasodilatory, vasoconstrictory, or has no effect on the blood vessels.

Part VIII

Bibliography and Appendices

In addition to

- The Bibliography

this part contains auxiliary information concerning

- The Raw Data
- Post-Treatment of Raw Data
- Frequency-Domain Considerations.

Bibliography

[1] Abbott, Laurence and Terrence J. Sejnowski, editors. *Neural Codes and Distributed Representations: Foundations of Neural Computation*. Massachusetts Institute of Technology, 1999.

[2] Akgören, Nuran, Peter Dalgaard, and Martin Lauritzen. Cerebral blood flow increases evoked by electrical stimulation of rat cerebellar cortex: relation to excitatory synaptic activity and nitric oxide synthesis. *Brain Research*, 710(1–2):204–214, 1996.

[3] Akgören, Nuran and Martin Lauritzen. Functional recruitment of red blood cells to rat brain microcirculation accompanying increased neuronal activity in cerebellar cortex. *NeuroReport*, 10:3257–3263, 1999.

[4] Akgören, Nuran, Claus Mathiesen, Inger Rubin, and Martin Lauritzen. Laminar analysis of activity-dependent increases of CBF in rat cerebellar cortex: dependence on synaptic strength. *Am. J. Physiol.*, 273(Heart Circ. Physiol. 42):H1166–H1176, 1997.

[5] Alstrøm, Preben, Victor M. Equiluz, Morten Colding-Jørgensen, Finn Gustafsson, and Niels-Henrik Holstein-Rathlou. Instability and "sausage-string" appearance in blood vessels during high blood pressure. *Physical Review Letters*, 82(9):1995–1998, March 1999.

[6] Ances, Beau M., Eric Zarahn, Joel H. Greenberg, and John A. Detre. Coupling af neural activation to blood flow in the somatosensory cortex of rats is time-intensity separable, but not linear. *Journal of Cerebral Blood Flow and Metabolism*, 20:921–930, 2000.

[7] Andresen, cand.mag. Aage and M.D. Kim Frost-Larsen, editors. *Lademanns Lægeleksikon*, volume 6 (K–lårkanalen), chapter Lillehjernen, pages 98–100. Lademann Forlagsaktieselskab, 1977–80.

[8] Andresen, cand.mag. Aage and cand.pharm. Anders Tuxen M.D., editors. *Lademanns Lægeleksikon*, volume 5 (H-juvenil), chapter Hjernen, pages 21–39. Lademann Forlagsaktieselskab, 1977–80.

[9] Barfod, C., N. Akgören, M. Fabricius, U. Dirnagl, and M. Lauritzen. Laser-Doppler measurements of concentration and velocity of moving blood cells in rat cerebral circulation. *Acta Physiol. Scand.*, 160(2):123–132, 1997.

[10] Beckman, Joseph S. and Willem H. Koppenol. Nitric oxide, superoxide, and peroxynitrite: The good, the bad, and the ugly. *Am. J. Physiol.*, 271(Cell Physiol. 40):C1424–C1437, 1996.

[11] Berg, Rune W. A quantitative experimental analysis of three brain areas involved in the sensory motor system of rat. Master's thesis, Niels Bohr Institute, University of Copenhagen and University of California at San Diego, 1999.

[12] Berne, Robert M. and Matthew N. Levy, editors. *Physiology*. Mosby-Year Book, third edition, 1993.

[13] Berne, Robert M., H. Richard Winn, and Rafael Rubio. The local regulation of cerebral blood flow. *Progress in Cardiovascular Diseases*, XXIV(3):243–260, November/December 1981.

[14] Bon, Christelle L. M. and John Garthwaite. Adenosine acting on A1 receptors protects NO-triggered rebound potentiation and LTD in rat hippocampal slices. *Journal of Neurophysiology*, 87:1781–1789, April 2002.

[15] Buonomano, Dean V. and Michael D. Mauk. Neural network model of the cerebellum: Temporal discrimination and the timing of motor responses. In Abbott and Sejnowski [1], chapter 17, pages 261–278.

[16] Buxton, Richard B. Coupling between CBF and $CMRO_2$ during neuronal activity. In Tomita *et al.* [93], pages 23–32.

[17] Buxton, Richard B. *Introduction to Functional Magnetic Resonance Imaging — Principles and Techniques.* Cambridge University Press, February 2002.

[18] Caesar, Kirsten. Potassium as mediator of functional cerebellar blood flow increases. Master's thesis, Department of Medical Physiology, Panum Institute, University of Copenhagen, 1998.

[19] Caesar, Kirsten, Nuran Akgören, Claus Mathiesen, and Martin Lauritzen. Modification of activity-dependent increases in cerebellar blood flow by extracellular potassium in anaesthetized rats. *Journal of Physiology*, 520(1):281–292, 1999.

[20] Cambridge Electronic Design Limited, Science Park, Milton Road, Cambridge, CB4 4FE, United Kingdom. SPIKE2 — *Training Course Manual*, January 1998.

[21] Cambridge Electronic Design Limited, Science Park, Milton Road, Cambridge, CB4 4FE, United Kingdom. SPIKE2 *for Windows*, fifth (version 3.00) edition, January 1998.

[22] Cambridge Electronic Design Limited, Science Park, Milton Road, Cambridge, CB4 4FE, United Kingdom. *The* SPIKE2 *Script Language*, version 3.00 edition, January 1998.

[23] Close, Charles M. and Dean K. Frederick. *Modeling and Analysis of Dynamic systems.* John Wiley & Sons, Inc., second edition, 1995.

[24] Crone, C., N. Bindslev, I. Engberg, L. Garby, H. Hultborn, and B. Saltin. Cellulær neurofysiologi. In Crone *et al.* [25], chapter 4, pages 63–71.

[25] Crone, C., N. Bindslev, I. Engberg, L. Garby, H. Hultborn, and B. Saltin. *Fysiologi.* FADL A/S, 1990.

[26] Crone, C., N. Bindslev, I. Engberg, L. Garby, H. Hultborn, and B. Saltin. Fysiologisk kontrolteori. In Crone *et al.* [25], chapter 23, pages 571–578.

[27] Dirnagl, U, K. Niwa, U. Lindauer, and A. Villringer. Coupling of cerebral blood flow to neuronal activation: Role of adenosine and nitric oxide. *Am. J. Physiol.*, 267(Heart Circ. Physiol. 36):H296–H301, July 1994.

[28] Dirnagl, Ulrich, Ute Lindauer, and Arno Villringer. Nitric oxide synthase blockade enhances vasomotion in the cerebral microcirculation of anestetized rats. *Microvascular Research*, 45:318–323, 1993.

[29] Doya, Kenji, Hidenori Kimura, and Mitsuo Kawato. Neural mechanisms of learning and control. *IEEE Control Systems Magazine*, 21(4):42–54, August 2001.

[30] Dyhrfjeld-Johnsen, Jonas. A large scale realistic network model of the rat cerebellar cortex: Scaling issues and transformation of mossy fiber input to purkinje cell output. Master's thesis, Niels Bohr Institute for Astronomy, Physics, and Geophysics, University of Copenhagen, Denmark, and Theoretical Neurobiology Unit, Born-Bunge Foundation, University of Antwerp - UIA, Belgium, December 1998.

[31] Euler, Thomas and Winfried Denk. Dendritic processing. *Current Opinion in Neurobiology*, 11:415–422, 2001.

[32] Fabricius, Martin, Nuran Akgören, Ulrich Dirnagl, and Martin Lauritzen. Laminar analysis of cerebral blood flow in cortex of rats by laser-Doppler flowmetry: A pilot study. *Journal of Cerebral Blood Flow and Metabolism*, 17(12):1326–1336, 1997.

[33] Fabricius, Martin and Martin Lauritzen. Examination of the role of nitric oxide for the hypercapnic rise of cerebral blood flow in rats. *Am. J. Physiol. Heart Circ. Physiol.*, 266(4):H1457–H1464, 1994.

[34] Fabricius, Martin and Martin Lauritzen. Laser-Doppler evaluation of rat brain microcirculation: Comparison with the [^{14}C]-iodoantipyrine method suggests discordance during cerebral blood flow increases. *Journal of Cerebral Blood Flow and Metabolism*, 16(1):156–161, 1996.

[35] Fillenz, M., J. P. Lowry, M. G. Boutelle, and A. E. Fray. The role of astrocytes and noradrenaline in neuronal glucose metabolism. *Acta Physiologica Scandinavica*, 167(4):275–284, 1999.

[36] Franklin, Gene F., J. David Powel, and Michael L. Workman. *Digital Control of Dynamic Systems.* World Student. Addison-Wesley Publishing Company, second edition, 1990.

[37] Franklin, Gene F., J. David Powell, and Abbas Emani-Naeini. *Feedback Control of Dynamic Systems.* World Student Series Control Engineering. Addison-Wesley Publishing Company, third edition, 1994.

[38] Ghosh, Bijoy K. and Jiping He. Dynamics and control problems in biology: Some new challenges. *IEEE Control systems Magazine*, 21(4):27, August 2001.

[39] Ghosh, Bijoy K. and Clyde F. Martin. Guest editorial: Special issue on systems and control problems in medicine. *IEEE Transactions on Automatic Control*, 43(6):763–764, June 1998.

[40] Gregers, R. and U. Windhorst, editors. *Comprehensive Human Physiology: From Cellular Mechanisms to Integration*, volume 2. Springer, 1996.

[41] Grewal, Mohinder S. and Angus P. Andrews. *Kalman filtering: Theory and Practice.* Printice-Hall Information and System Sciences Series. Printice-Hall, Inc., 1993.

[42] Hubbard, J. I., R. Llinás, and D. M. J. Quastel. *Electrophysiological Analysis of Synaptic Transmission.* Number 19 in Monographs of the Physiological Society. Edward Arnold Publishers Ltd., 1969.

[43] Iadecola, Costantino, Jun Li, Sherry Xu, and Guang Yang. Neural mechanisms of blood flow regulation during synaptic activity in cerebellar cortex. *Journal of Neurophysiology*, 75(2):940–950, 1996.

[44] Iadecola, Costantino, Kiyoshi Niwa, Yi Zhang, and Ken Kazama. Neurovascular coupling in health and disease: Lessons from transgenic mice. In Tomita *et al.* [93], pages 259–266.

[45] Jakobsson, A. and G. E. Nilsson. Prediction of sampling depth and photon pathlength in laser Doppler flowmetry. *Medical & Biological Engineering & Computing*, 31:301–307, 1993.

[46] Jensen, Arne and Anders la Cour-Harbo. *Ripples in Mathematics. The Discrete Wavelet Transform.* Springer Verlag, 2001.

[47] Keener, James P. and James Sneyd. *Mathematical Physiology.* Interdisciplinary Applied Mathematics. Springer, New York, 1998.

[48] Kincaid, David R. and E. Ward Cheney. *Numerical Analysis. Mathematics of Scientific Computing.* Brooks/Cole Publishing Company, 1991.

[49] Knudsen, Morten. *Estimation of Physical Parameters in Linear and Nonlinear Dynamic Systems.* PhD thesis, Department of Control Engineering, Institute of Electronic Systems, Aalborg University, Fredrik Bajers Vej 7, DK-9220 Aalborg Ø, Denmark, January 1993.

[50] Knudsen, Morten. *SENSTOOLS — A* MATLAB *toolkit for parameter estimation in linear and nonlinear systems using a sensitivity approach.* Department of Control Engineering, Aalborg University, September 1996. Vrs. 1.1.

[51] Knudsen, Morten. Experimental modelling of dynamic systems. Lecture Notes, Department of Control Engineering, Institute of Electronic Systems, Aalborg University, January 2003.

[52] Knudsen, Torben. Systemidentifikation. Lecture Notes, Department of Control Engineering, Institute of Electronic Systems, University of Aalborg, Denmark, January 1993.

[53] Knudsen, Torben. Mathematical models for the temporal relation between field potential and blood flow in rat cerebellum. Working paper, Center for Mathematical Modelling of Physiological Processes, Department of Control Engineering, Institute of Electronic Systems, Aalborg University, Denmark, May 23, 2000.

[54] Knudsen, Torben, Henrik Elmer, Morten Knudsen, Niels-Henrik Holstein-Rathlou, and Jakob Stoustrup. Dynamic modeling of renal blood flow in dahl hypertensive and normotensive rats. *IEEE Transactions on Biomedical Engineering*, 51(5):689–697, May 2004.

[55] Krauss, Thomas P., Loren Shure, and John N. Little. *Signal Processing Toolbox User's Guide*. The MathWorks Inc., 24 Prime Park Way, Natick, Mass. 01760-1500, February 1994.

[56] Lauritzen, M. and K. Caesar. Activity-induced changes in cerebellar blood flow. In Tomita *et al.* [93], pages 251–257.

[57] Lauritzen, Martin. Relationship of spikes, synaptic activity, and local changes of cerebral blood flow. *Journal of Cerebral Blood Flow and Metabolism*, 21(12):1367–1383, 2001.

[58] Ljung, Lennart. *System Identification, Theory for the User*. Prentice-Hall information and system sciences series. Prentice-Hall, second edition, 1999.

[59] Ljung, Lennart. *System Identification Toolbox User's Guide*. The MathWorks, Inc., May 1995.

[60] Ljung, Lennart. *System Identification Toolbox For Use with* MATLAB. The MathWorks, Inc., November 2000.

[61] Ljung, Lennart and Torkel Glad. *Modeling of Dynamic Systems*. Prentice-Hall information and system sciences series. Prentice Hall, 1994.

[62] Llinás, Rodolfo R. and Kerry D. Walton. Cerebellum. In Shepherd [84], chapter 7, pages 255–288.

[63] Logothesis, Nikos K., Jon Pauls, Mark Augath, Torsten Trinath, and Axel Oeltermann. Neurophysiological investigation of the basis of the fMRI signal. *Nature*, 412:150–157, 12 July 2001.

[64] Malmivuo, J. and R. Plonsey. *Bioelectromagnetism: Principles and applications of bioelectric and biomagnetic fields*. Oxford University Press, 1995.

[65] Martindale, John, John Mayhew, Jason Berwick, Myles Jones, Chris Martin, Dave Johnston, Peter Redgrave, and Ying Zheng. The hemodynamic impulse response to a single neural event. *Journal of Cerebral Blood Flow and Metabolism*, 23(5):546–555, 2003.

[66] Mathiesen, Claus, Kirsten Caesar, Nuran Akgören, and Martin Lauritzen. Modifications of activity-dependent increases of cerebral blood flow by excitatory synaptic activity and spikes in rat cerebellar cortex. *Journal of Physiology*, 512(2):555–566, 1998.

[67] Mathiesen, Claus, Kirsten Caesar, and Martin Lauritzen. Temporal coupling between neuronal activity and blood flow in rat cerebellar cortex as indicated by field potential analysis. *Journal of Physiology*, 523(1):235–246, 2000.

[68] The MathWorks, Inc., Cochituate Place, 24 Prime Park Way, Natick, MA 01760. MATLAB *Reference Guide*, August 1992.

[69] Mish, Frederick C., editor. *Webster's Ninth New Collegiate Dictionary*. Merriam-Webster Inc., 1987.

[70] Mørch, Carsten Dahl. Correlation between dorsal horn neurons and the spinal nociceptive withdrawal reflex. Master's thesis in biophysics, Niels Bohr Institute for Astronomy, Physics, and Geophysics, University of Copenhagen, Denmark, 2002.

[71] Nelson, Mark T. and John M. Quayle. Physiological roles and properties of potassium. *American Journal of Physiology*, 268(Cell Physiology 37):C799–C822, 1995.

[72] Nenadic, Zoran and Bijoy K. Ghosh. Signal processing and control problems in the brain. *IEEE Control Systems Magazine*, 21(4):28–41, August 2001.

[73] Nicholls, John G., A. Robert Martin, and Bruce G. Wallace. *From neuron to brain: A cellular and molecular approach to the function of the nervous system.* Sinauer Associates, Inc., third edition, 1992.

[74] Nicholson, Charles. Generation and analysis of extracellular field potentials. Course Notes, About 1980.

[75] Nicholson, Charles and Eva Syková. Extracellular space structure revealed by diffusion analysis. *Trends in Neurosciences*, 21(5):207–215, 1998.

[76] Nielsen, Alexander Norup and Martin Lauritzen. Coupling and uncoupling of activity-dependent increases of neuronal activity and blood flow in rat somatosensory cortex. *Journal of Physiology*, 533(3):773–785, 2001.

[77] Nielsson, G. E. Perimed's LDV flowmeter. In Shephard and Öberg [83], chapter 4, pages 57–72.

[78] Perimed AB, Box 564, S-175 26 Järfälle, Sweden. *PeriFlux 4001 Master/4002 Satellite v1.13 USER'S MANUAL*, March 6 1996.

[79] Read, S. J. and A. A. Parsons. Nitric oxide does not mediate cerebral blood flow changes during cortical spreading depresion in the anaesthetized rat. *Neuroscience Letters*, 250:115–118, 1998.

[80] Roy, C. S. and C. S. Sherrington. On the regulation of the blood supply to the brain. *J. Physiol. (London)*, 11:85–108, 1890.

[81] Sánchez-Sinencio, Edgar and Clifford Lau, editors. *Artificial Neural Networks: Paradigms, Applications, and Hardware Implementations.* IEEE Press, 1992.

[82] Schwarz, Hans Rudolf. *Numerical Analysis: A comprehensive Introduction.* John Wiley & Sons, Ltd., 1989.

[83] Shephard, A. P. and P. A. Öberg, editors. *Laser-Doppler Blood Flowmetry.* Kluwer Academic Publishers, Amsterdam, 1990.

[84] Shepherd, Gordon Murray, editor. *The synaptic organization of the brain.* Oxford University Press, New York, fourth edition, 1998.

[85] Shibuki, Katsuei and Shinji Kimura. Dynamic properties of nitric oxide release from parallel fibres in rat cerebellar slices. *Journal of Physiology*, 498(2):443–452, 1997.

[86] Shibuki, Katsuei and Daisuke Okada. Endogenous nitric oxide release required for long-term synaptic depression in the cerebellum. *Nature*, 349:326–328, January 1991.

[87] Simpson, David M., Ronney B. Panerai, David H. Evans, and A. Ross Naylor. A parametric approach to measuring cerebral blood flow autoregulation from spontaneous variations in blood pressure. *Annals of Biomedical Engineering*, 29:18–25, 2001.

[88] Simpson, Patrick K. Foundations of neural networks. In Sánchez-Sinencio and Lau [81], chapter 1.1, pages 3–24.

[89] Somjen, George G. Mechanisms of spreading depression and hypoxic spreading depression-like depolarization. *Physiological Reviews*, 81(3):1065–1096, July 2001.

[90] Sternheim, Morton M. and Joseph W. Kane. *General Physics*, chapter 18: Nerve Conduction, pages 455–470. John Wiley & Sons, second edition, 1991.

[91] Thomas, Clayton L., editor. *Taber's Cyclopedic Medical Dictionary.* F. A. Davis Company, 18th edition, 1997.

[92] Tian, Rong, Pia Vogel, Niels A. Lassen, Michael J. Mulvany, Frederik Andreasen, and Christian Aalkjær. Role of extracellular and intracellular acidosis for hypercapnia-induced inhibition of tension of isolated rat cerebral arteries. *Circulation Research*, 76:269–275, 1995.

[93] Tomita, M., I. Kanno, and E. Hamel, editors. *Brain Activation and CBF Control*, volume 1235 of *International Congress Series*. Elsevier Science B.V., 2002.

[94] Topsøe, Flemming. *Informationsteori*. Gyldendal, 1973.

[95] Ursino, M. and G. Fabbri. Role of the myogenic mechanism in the genesis of microvascular oscillations (vasomotion): Analysis with a mathematical model. *Microvasc. Res.*, 43:156–177, 1992.

[96] Ursino, M. and E. Magosso. The role of oxygen in cerebrovascular control: A mathematical analysis. In *2001 Proceedings of the 23rd Annual EMBS International Conference*, pages 247–250, Istanbul, Turkey, October 25–28 2001. IEEE.

[97] Ursino, Mauro. A mathematical model of overall cerebral blood flow regulation in the rat. *IEEE Transactions on Biomedical Engineering*, 38(8):795–807, August 1991.

[98] Ursino, Mauro, Patrizia Di Giammarco, and Enzo Belardinelli. A mathematical model of cerebral blood blow chemical regulation — Part I: Diffusion processes. *IEEE Transactions on Biomedical Engineering*, 36(2):183–191, February 1989.

[99] Ursino, Mauro, Patrizia Di Giammarco, and Enzo Belardinelli. A mathematical model of cerebral blood flow chemical regulation — Part II. Reactivity of cerebral vascular bed. *IEEE Transactions on Biomedical Engineering*, 36(2):192–201, February 1989.

[100] Villringer, Arno and Ulrich Dirnagl. Coupling of brain activity and cerebral blood flow: Basis of functional neuroimaging. *Cerebrovascular and Brain Metabolism Reviews*, 1995.

[101] Warberg, Jørgen. *Human Fysiologi – En Grundbog*. Polyteknisk Forlag, fourth edition, 1998.

[102] Westwick, David T. and Robert E. Kearney. Nonparametric identification of nonlinear biomedical systems, part I: Theory. *Critical Reviews in Biomedical Engineering*, 26(3):153–226, 1998.

[103] Young, Peter. Parameter estimation for continuous-time models — a survey. *Automatica*, 17(1):23–39, 1981.

[104] Zurada, Jacek M. *Introduction to Artificial Neural Systems*. West Publishing Company, 1992.

Appendix A

The Raw Data

A.1 Overview of Experimental Data

The models are tested on data from experiments performed on two male Wistar rats: No. 196 and no. 197. The experiments were performed by Claus Mathiesen in August 1997 and the experimental results were published in the paper [67].

A.1.1 Inferior Olive Stimulation Experiments

The conditions specific to each of the climbing fiber activation experiments are listed in Table A.1. An

Rat No.	Weight	Series	Electrode Depth	Stimulus Amplitude
196	320 g	196io4	400 μm	180 μA
		196io5	300 μm	100 μA
197	350 g	197io1	400 μm	200 μA
		197io3	400 μm	400 μA
FP Prefilter			0.1 $Hz - 3$ kHz	

Table A.1: The experimental conditions specific to each inferior olive time series. Below the field potential bandpass filter ('FP prefilter') common to all four time series is listed.

example of the registered data series in case of inferior olive stimulation is shown in Figure A.1.

A.1.2 Parallel Fiber Stimulation Experiments

The conditions specific to each of the parallel fiber activation experiments are listed in Table A.2. An

Rat No.	Weight	Series	Electrode Depth	Stimulus Amplitude
196	320 g	196pf1	Not registered	Not registered
		196pf2	Not registered	Not registered
		196pf3	Not registered	Not registered
197	350 g	197pf2	100 μm	2000 μA
FP Prefilter			0.1 $Hz - 3$ kHz	

Table A.2: The experimental conditions specific to each parallel fiber time series. Below the field potential bandpass filter ('FP prefilter') common to all four time series is listed.

example of the registered data series in case of parallel fiber stimulation is shown in Figure A.2.

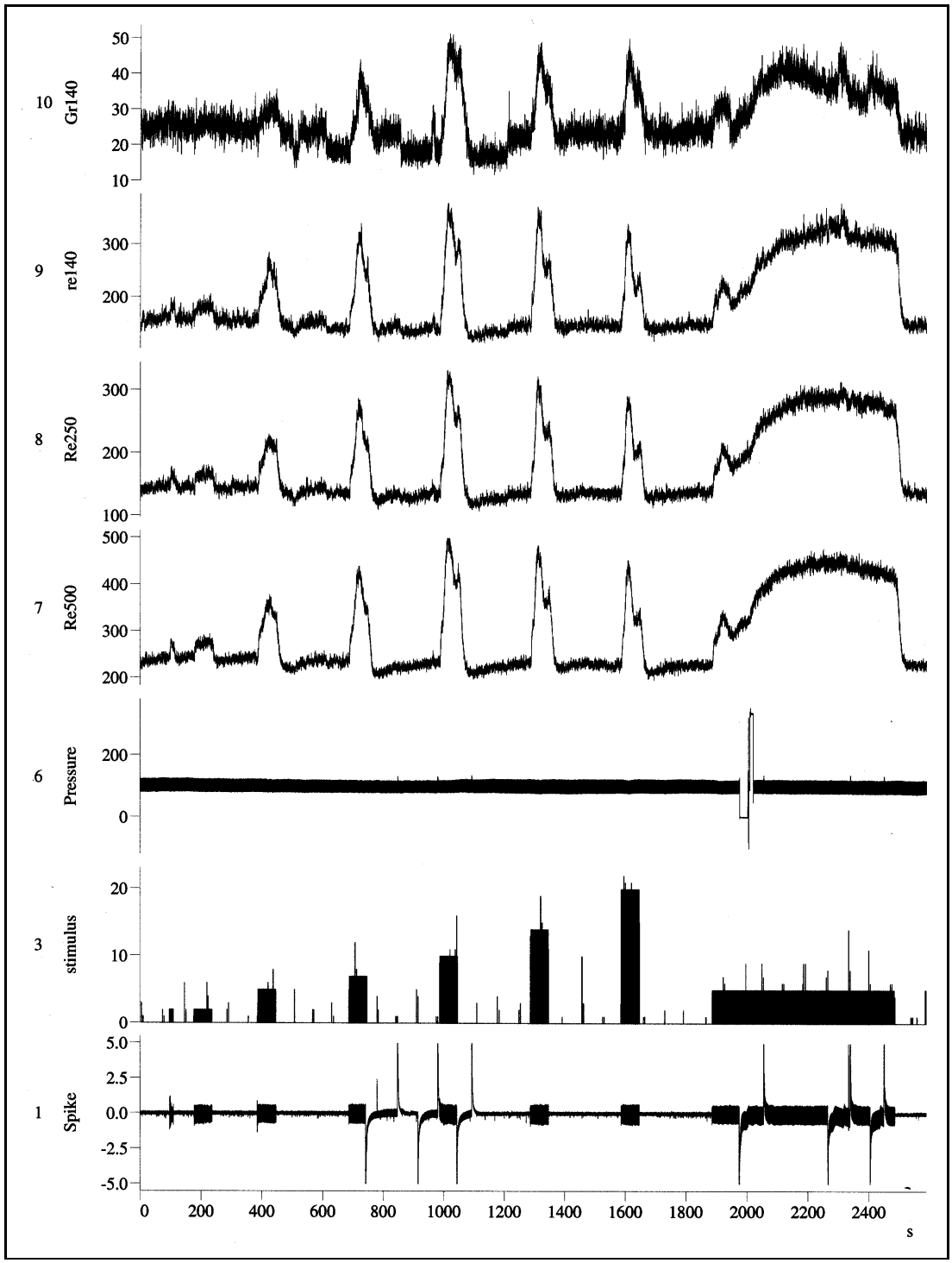

Figure A.1: An example of SPIKE2 data file for the case of inferior olive stimulation. The time series is labeled '196io5'. The units are: Field potential (`spike`): mV; stimulation frequency (`stimulus`): Hz; blood pressure (`pressure`): $mmHg$; cerebellar blood flow (`Re500`, `Re250`, `Re140`, and `Gr140`): PU. Note that some of the traces appear broad; this is due to fast and large variation in the signal — cf. Section A.3.

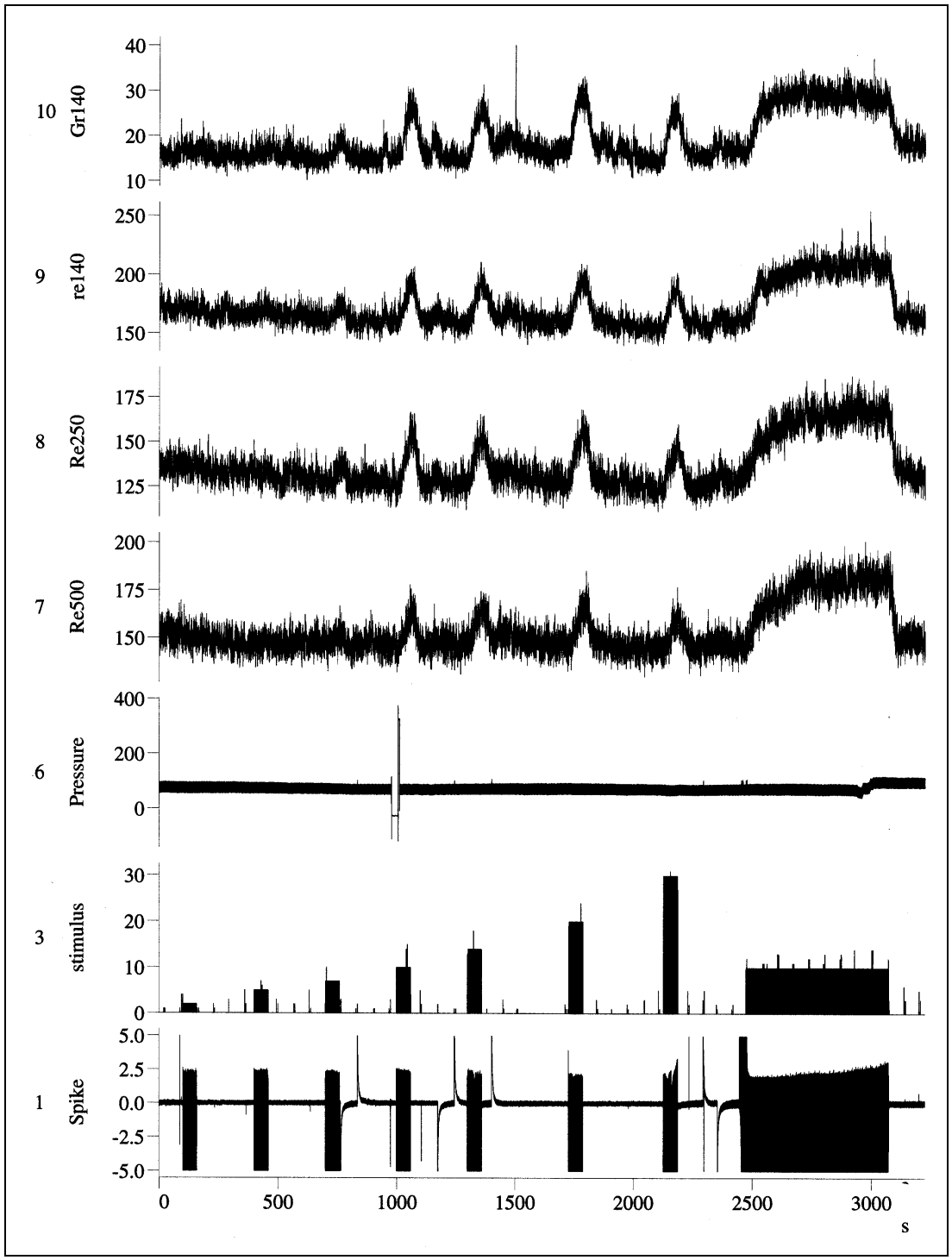

Figure A.2: An example of SPIKE2 data file for the case of parallel fiber stimulation. The time series is labeled '196pf2'. The units are: Field potential (`spike`): mV; stimulation frequency (`stimulus`): Hz; blood pressure (`pressure`): $mmHg$; cerebellar blood flow (`Re500`, `Re250`, `Re140`, and `Gr140`): PU. Note that some of the traces appear broad; this is due to fast and large variation in the signal — cf. Section A.3.

A.2 Description of the Data Files

This section describes how each data trace has been registered. The units of the variables are written in square brackets.

A.2.1 Stimulus (Channel no. 3)

Only the times $[s]$ of down-going pulses (events) have been registered. An example:

```
4.328956
4.338424
4.340600
9.295456
```

A.2.2 Field Potential (Channel no. 1)

This electrical signal $[mV]$ has been sampled at a constant frequency, here 6944.444444 Hz. The files contain the start time and the time interval between measurements, as well as a list of the measurements:

```
'START' 0.000024 0.000144
0.03906
0.02930
0.02441
0.01465
```

A.2.3 Arterial Blood Pressure (Channel no. 6)

The arterial blood pressure $[mmHg]$ has been sampled at a constant frequency of 100.064040 Hz. The registration consists of the starting time and the time interval between samples $[s]$ as well as the series of measurements:

```
'START' 0.000048 0.009936
84.84
92.77
109.25
115.97
```

A.2.4 Cerebellar Blood Flow (Channel no.'s 7–10)

The CBF signal has been sampled at a constant frequency, here 10.006404 Hz. First the start time $[s]$ as well as the time between the samples $[s]$ are registered. Afterwards follow the measurements of the CBF values $[PU]$:

```
'START' 0.000096 0.099936
2.678234
2.150177
0.740582
0.388544
```

A.3 Selected Extracts of Data Files

In order to give a better impression of the characteristics of each trace some selected extracts of the traces are shown.

A.3.1 Stimulus

A feature of the registered stimulation event times is illustrated by Figure A.3

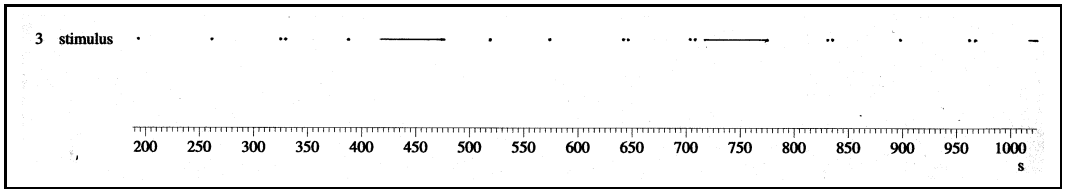

Figure A.3: An example of SPIKE2 data file for the case of parallel fiber stimulation. The trace is the stimulation event signal (no units) for the time series 197pf2. Note the noisy stimulation events occurring almost periodically with a frequency of one event per minute.

A.3.2 Field Potential

Various features of the field potential signal for the case of inferior olive stimulation are illustrated by Figures A.4, A.5, A.6, A.7, A.8, and A.9.

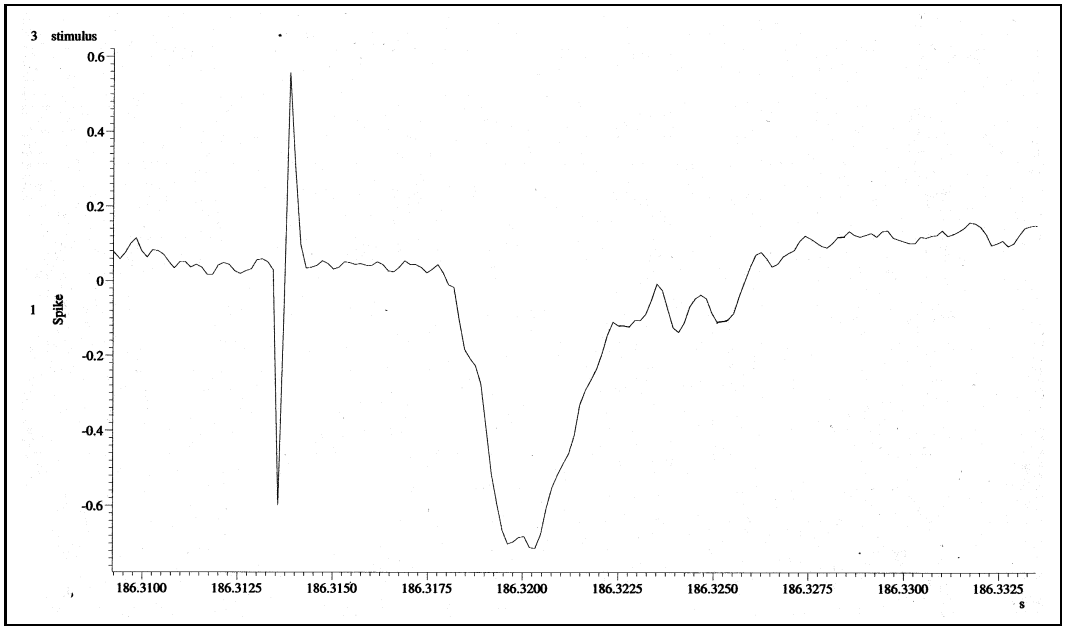

Figure A.4: An example of SPIKE2 data file for the case of inferior olive stimulation. The trace is the field potential (in units of mV) for the time series 196io5 obtained at a stimulation frequency of 2 Hz. Note the quite constant level (interrupted by the stimulus artifact) before the EPSP component.

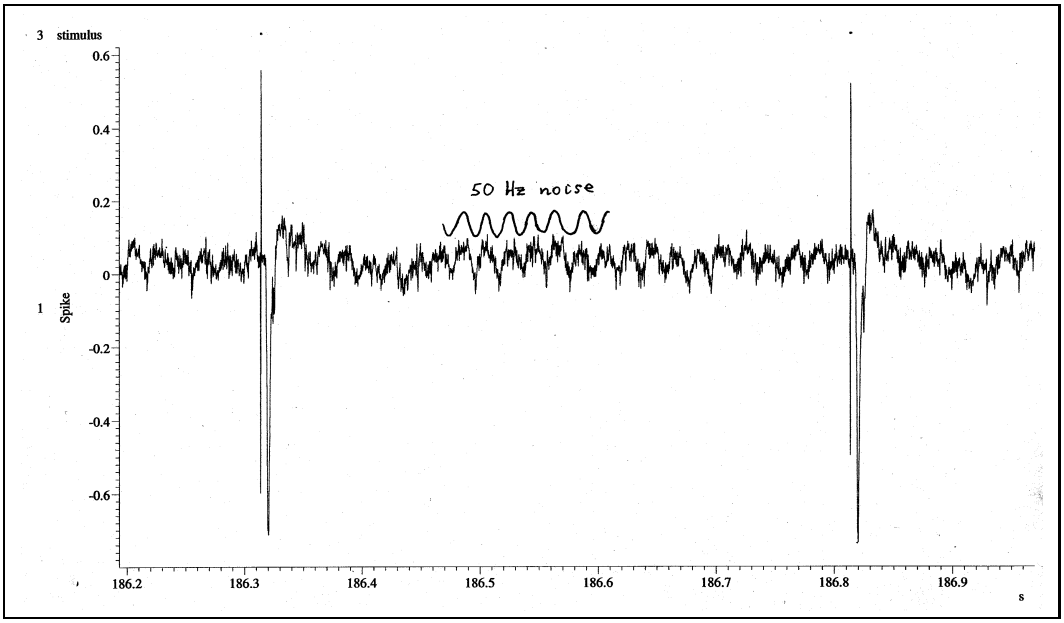

Figure A.5: Example of SPIKE2 data file for the case of inferior olive stimulation. The trace is the field potential (in units of mV) for the time series 196io5 obtained during stimulation with frequency 2 Hz. Note the quite large amplitude of the 50 Hz noise.

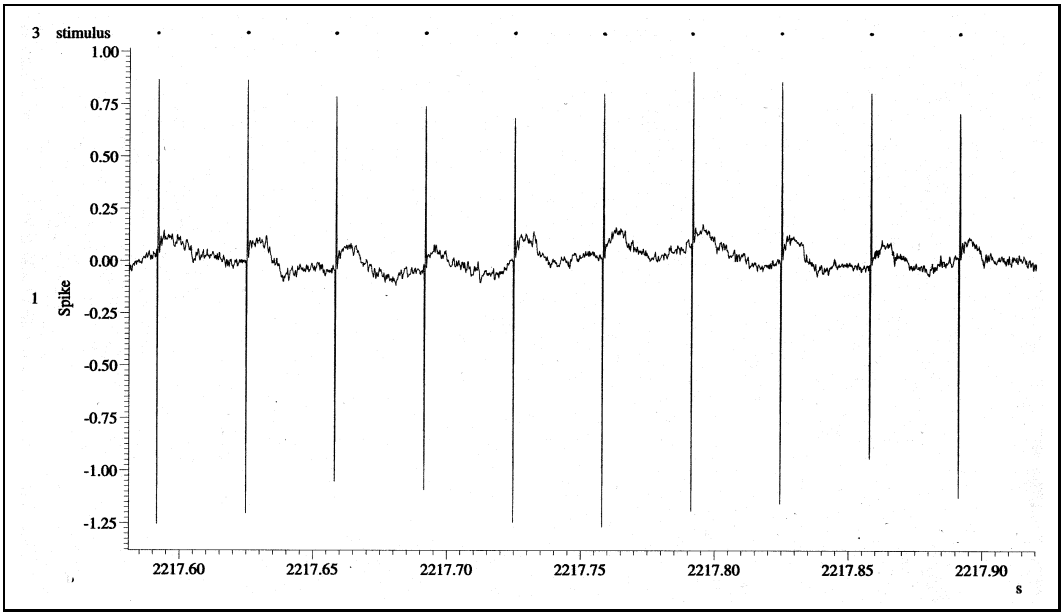

Figure A.6: An example of SPIKE2 data file for the case of inferior olive stimulation. The trace is the field potential (in units of mV) for the time series 197io1 obtained during stimulation with frequency 30 Hz. Note that it takes the field potential around 20 s to relax to the constant level right before the action potential.

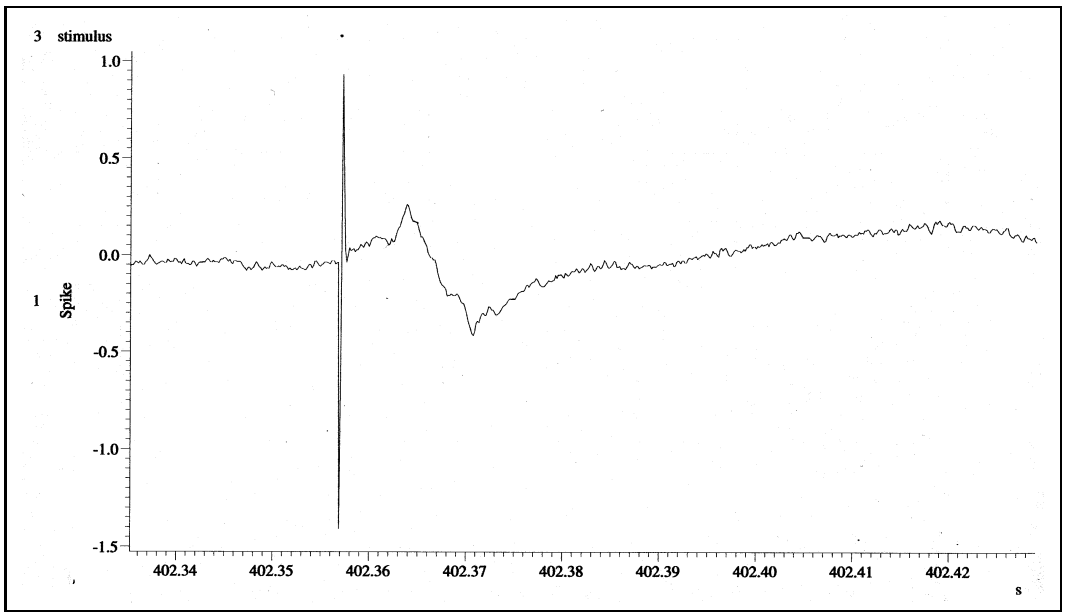

Figure A.7: An example of SPIKE2 data file for the case of inferior olive stimulation. The trace is the field potential (in units of mV) for the time series 197io1 obtained during stimulation with frequency 5 Hz. Note the shoulder before the EPSP component — which makes it impossible to use the plateau *after* the stimulus time as reference level.

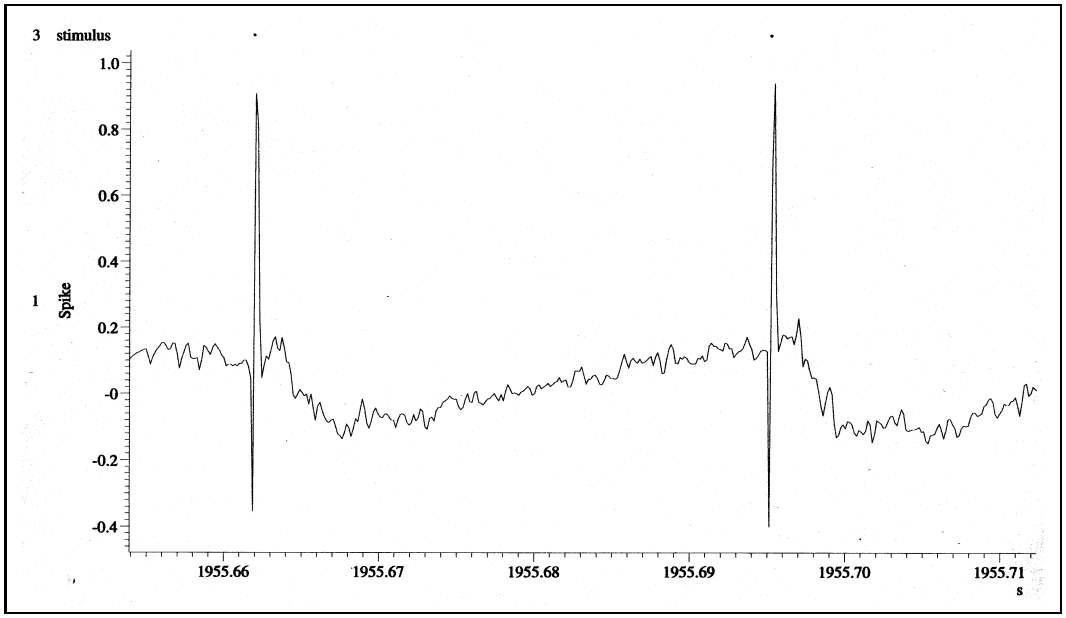

Figure A.8: An example of SPIKE2 data file for the case of inferior olive stimulation. The trace is the field potential (in units of mV) for the time series 197io3 obtained during stimulation with frequency 30 Hz. Note that the exact position of the minimum of the EPSP component is obscured by high-frequency noise.

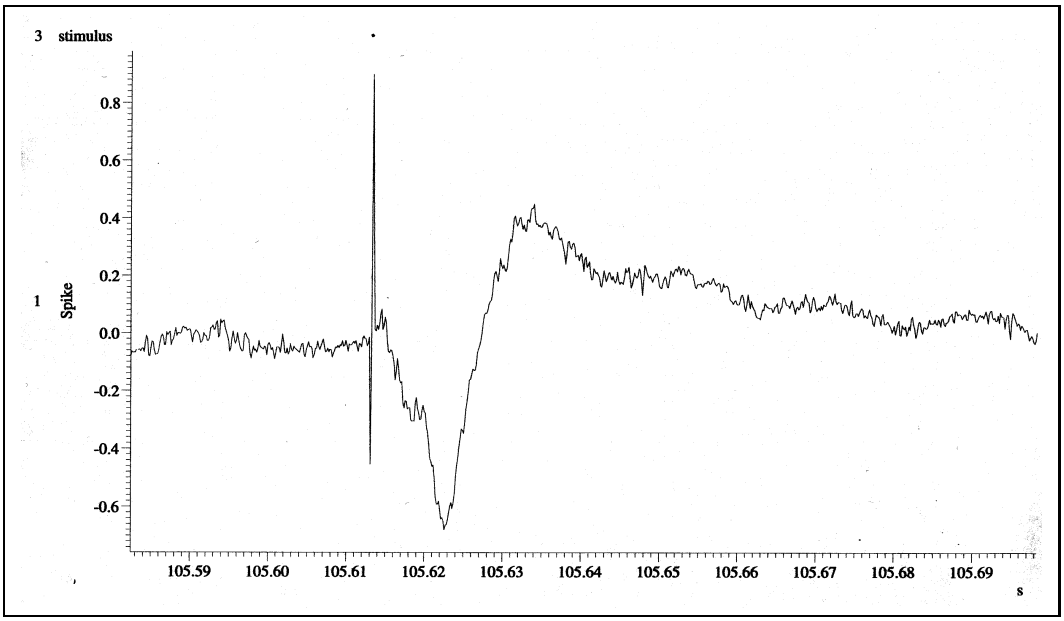

Figure A.9: An example of SPIKE2 data file for the case of inferior olive stimulation. The trace is the field potential (in units of mV) for the time series 197io3 obtained during stimulation with frequency 2 Hz. Note that the plateau between the stimulus time and the EPSP component is much too short to be used for calculation of the reference level. Therefore the plateau *before* the stimulus artifact is used.

A.3.3 Arterial Blood Pressure

See Figures A.10 and A.11.

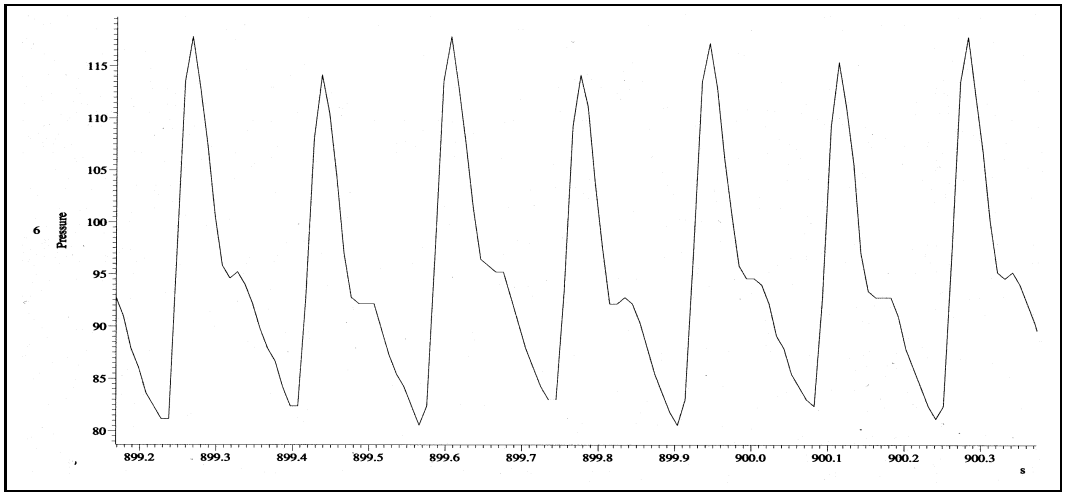

Figure A.10: An example of SPIKE2 data file for a case of inferior olive stimulation. The trace is the arterial blood pressure for the time series 196io5. Note the shift between two sets of extrema. This feature may be interpreted as a 3 Hz amplitude modulation of the 6 Hz arterial pulse.

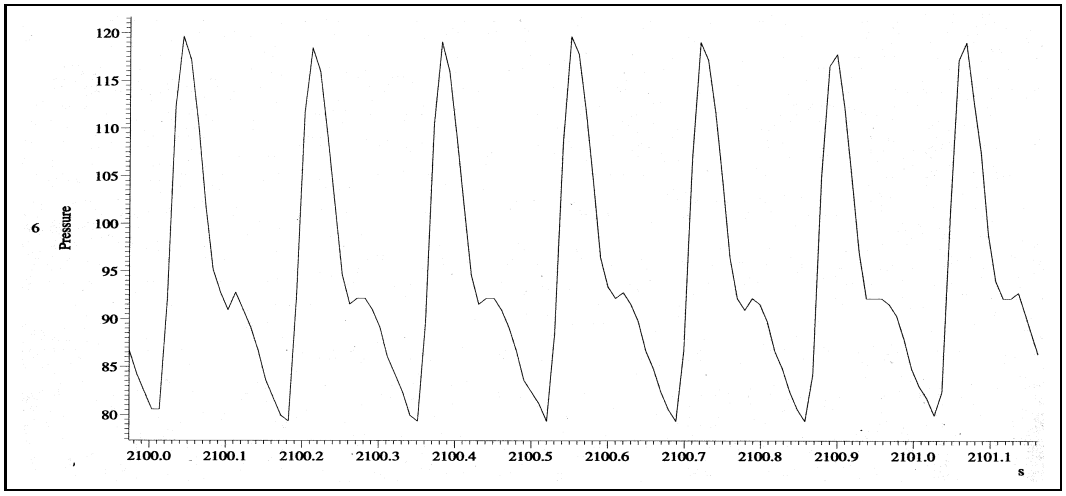

Figure A.11: An example of SPIKE2 data file for the case 197pf2 of parallel fiber stimulation. Note that there is only a single minimum level and a single maximum level. The pattern is repeated with a frequency of 6 Hz.

A.3.4 Cerebellar Blood Flow

See Figures A.12 and A.13.

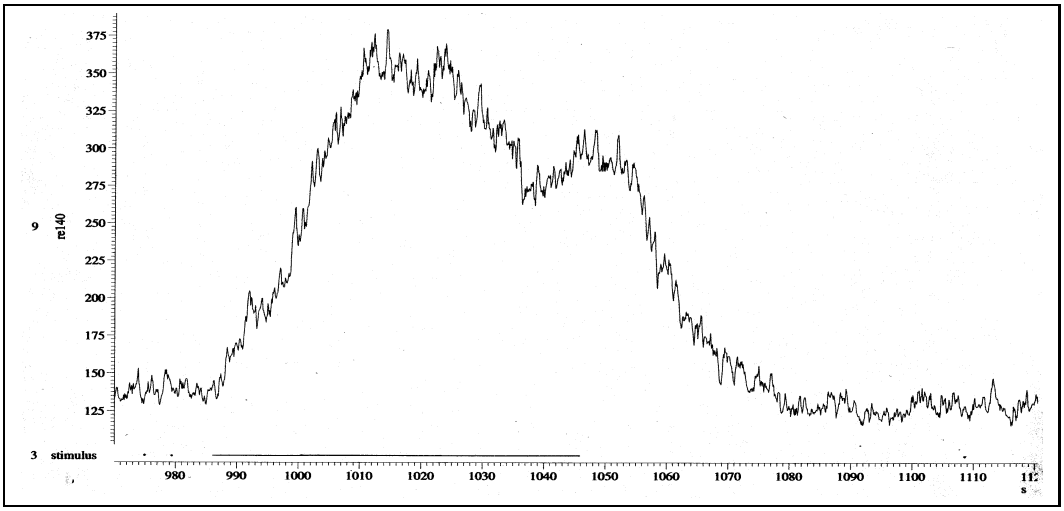

Figure A.12: An example of SPIKE2 data file for the inferior olive stimulation time series 196io5. Note that the output from the LDF probe `Re140` reaches a dip bottom around 48 s after on-set of stimulation with frequency 10 Hz. The stimulation sequence ends after 60 s.

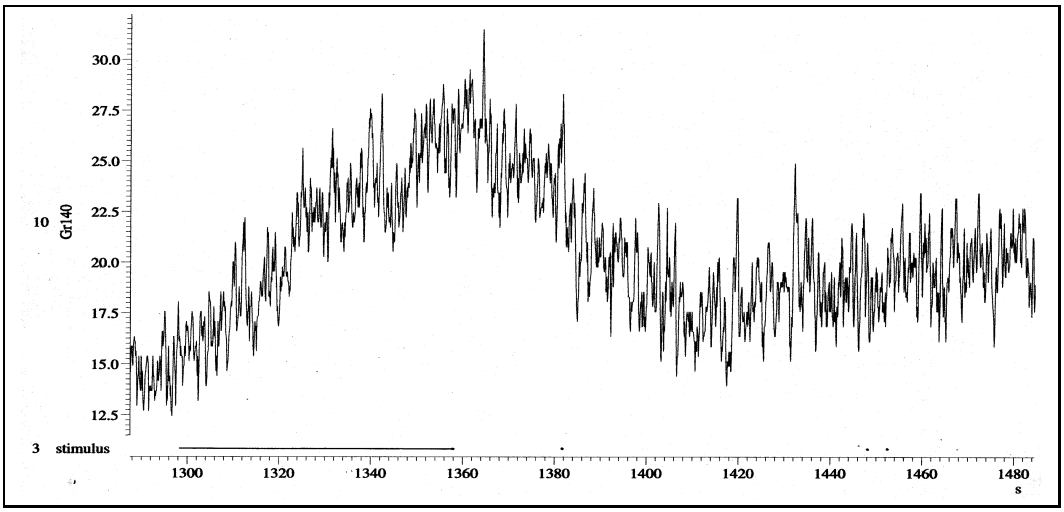

Figure A.13: An example of SPIKE2 data file for the parallel fiber stimulation time series 196pf2. Note that the output from the LDF probe `Gr140` increases almost linearly for the duration (60 s) of the stimulation with frequency 13 Hz.

Appendix B

Post-Treatment of Raw Data

Before the actual modeling task can take place post-treatment of some of the measurements has to be done. This appendix gives a description of the post-treatment procedures.

B.1 Stimulation Frequency

As the stimulus is event-sampled the distance between the data points varies. The stimulation frequency is obtained by counting the number of stimulation events in a time period of a certain length, the *bin length*, followed by a division by the bin length.

The bin length is chosen such that the stimulation frequency is determined at the same instants in time as the sampling instants of the CBF signal:

$$f_s(t_i) = \frac{\#\text{events} \in \left] t_i - \frac{\tau}{2}; t_i + \frac{\tau}{2} \right]}{\tau}. \tag{B.1}$$

t_i denotes the sampling instants and τ the sampling interval $\tau = t_i - t_{i-1} = 0.099936\ s$ of the CBF signal.

B.2 Field Potential Amplitude

The field potential amplitudes are extracted from the field potential signal (channel 1). Examples of the FP signal are shown in Figure 7.4 on page 46 as well as in Appendix A.3.2 on page 266. This off-line analysis is performed by a script [22] supplementing the SPIKE2 programme [21]. The script, which analyzes the field potential signal measured during inferior olive stimulation, operates as follows:

The script runs through the stimulus event channel and the field potential signal channel. Whenever a stimulus event is encountered two numbers are found — see Figure B.1:

- The local reference level, FP_{ref}, is calculated as the arithmetic mean value of the field potential in a predefined interval before the instant of the stimulus event.
- The local minimum value of the field potential in a predefined interval after the instant of the stimulus event.

Finally the field potential amplitude, FPA, of the excitatory post-synaptic potential (EPSP) is calculated as the difference between the local reference level and the local minimum value. The FPA event is assigned the time of occurrence of the local minimum. A similar procedure has been applied by Mathiesen *et al.* [66].

Thus the files contain lists of the times of occurrence $[s]$ as well as the field potential amplitudes $[mV]$, i.e., the sizes of the excitatory post-synaptic potentials EPSP. The distance between the instants varies. Since one stimulus event evokes one field potential event, the frequency of FPA events is on average equal to that of the stimulation.

Due to various kinds of noise in the registered field potential signal the calculated amplitude sometimes is assigned a negative or a very high value. Therefore values outside the range

$$0 \leq FPA \leq mean(FPA) + 5 \cdot std(FPA), \tag{B.2}$$

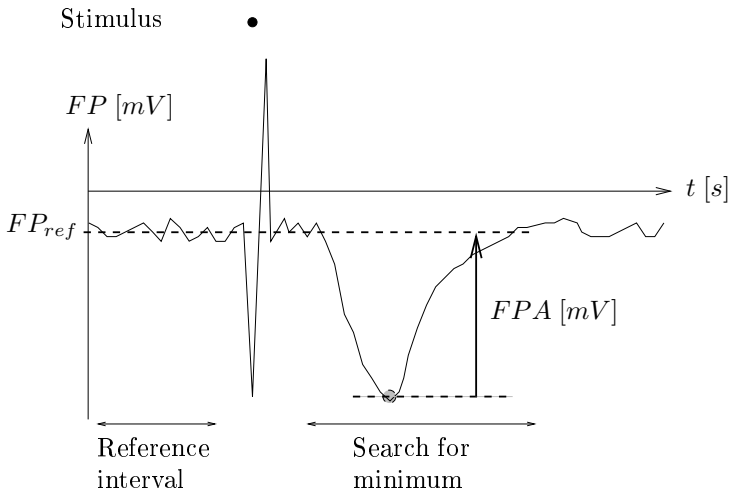

Figure B.1: Illustration of the calculation of the amplitude FPA of the excitatory post-synaptic potential in case of inferior olive stimulation.

where *mean* denotes the arithmetic mean value and *std* the standard deviation of all field potential amplitudes in the time series, are excluded from the analysis and modeling work.

B.3 Field Potential Duration

A measure of the duration of an EPSP event resulting from inferior olive stimulation, $FPD\ [s]$, is obtained from the following two observations — see Figure B.2:

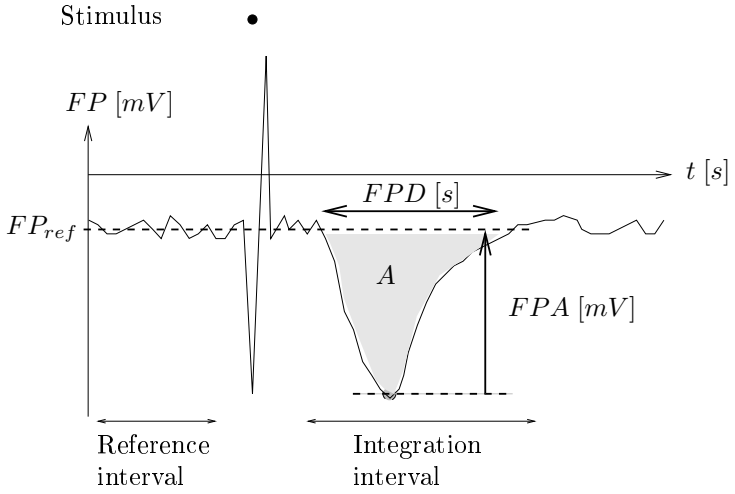

Figure B.2: Illustration of the calculation of the duration FPD of the excitatory post-synaptic potential (with amplitude FPA) in case of inferior olive stimulation.

- The area, A, between the field potential signal and the reference level is obtained by integrating the difference between the reference level FP_{ref} and the field potential FP over a predefined interval:

$$A = \int (FP_{ref} - FP(t))dt \qquad [mV \cdot s] \tag{B.3}$$

- As the shape of the area is close to being a triangle, the area and the field potential duration are approximately related by $A \approx \frac{1}{2} \cdot FPA \cdot FPD$.

Thus an estimate of the field potential duration is calculated as

$$FPD \approx \frac{2 \cdot A}{FPA} = \frac{2 \cdot \int (FP_{ref} - FP(t))dt}{FPA} \qquad [s] \tag{B.4}$$

Due to especially low-frequency noise components in the field potential (cf. Appendix A.3.2) the duration is not expected to be particularly well-defined.

B.4 Relative Cerebellar Blood Flow

As explained in P: Section 7.4.4 on page 47 the CBF values should be rescaled to the baseline value, CBF_B. Furthermore the baseline value is removed, since the system identification tool-box cannot operate on constant terms. Thus the *relative cerebellar blood flow* signal is defined as:

$$CBF(t) = \frac{CBF_{\text{measured}}(t) - CBF_B}{CBF_B}. \tag{B.5}$$

The calculation of the baseline value, CBF_B, is based on the idea that the CBF signal slowly approaches the baseline value when there is no stimulation and therefore no field potential amplitude. This idea is exploited to determine the baseline level by the following procedure — for illustration see Figure B.3:

(1) The time axis is divided into bins of the size of the sampling interval of the CBF signal, i.e., 0.099936 s, and the field potential amplitudes within each bin are summed. The resulting 10 Hz sampled signal $\sum FPA$ is shown in the second panel of Figure B.3.

(2) In order to provide a smooth signal which is zero when there is no stimulation except in a short period after cessation of stimulation and non-zero when the CBF signal increases above its baseline value the $\sum FPA$ signal is passed through the discrete linear filter $G(q) = \frac{0.01}{1-0.99 \cdot q^{-1}}$. The Bode plot of this filter is shown in Figure B.4. The resulting filtered signal

$$G(q) \sum FPA \tag{B.6}$$

is shown in the third panel of Figure B.3.

(3) The sampling instants at which the filtered signal $G(q) \sum FPA$ is below the threshold 0.01 mV are found. The CBF samples at these instants are shown in the fourth panel in Figure B.3. Note that the down-going parts of the original CBF trace (the top panel) have been excluded even though the original $\sum FPA$ signal is zero (second panel).

(4) The baseline value CBF_B is now calculated as the arithmetic mean value of the above-mentioned CBF samples. The resulting baseline level is also shown in the fourth panel in Figure B.3.

The resulting relative CBF signal as calculated from Equation (B.5) is shown in the bottom-most panel in Figure B.3.

The correct function of this normalization procedure requires that:

- In order that the CBF signal actually reaches the baseline level during periods without stimulation the quiet periods must be at least 150 s long.
- In order that the mean value becomes a good estimate of the baseline level there must not be drift in the CBF signal.

This normalization procedure is also applied to the CBF signals in the parallel fiber time series even though the FP signal and therefore also the FPA signal is corrupted.

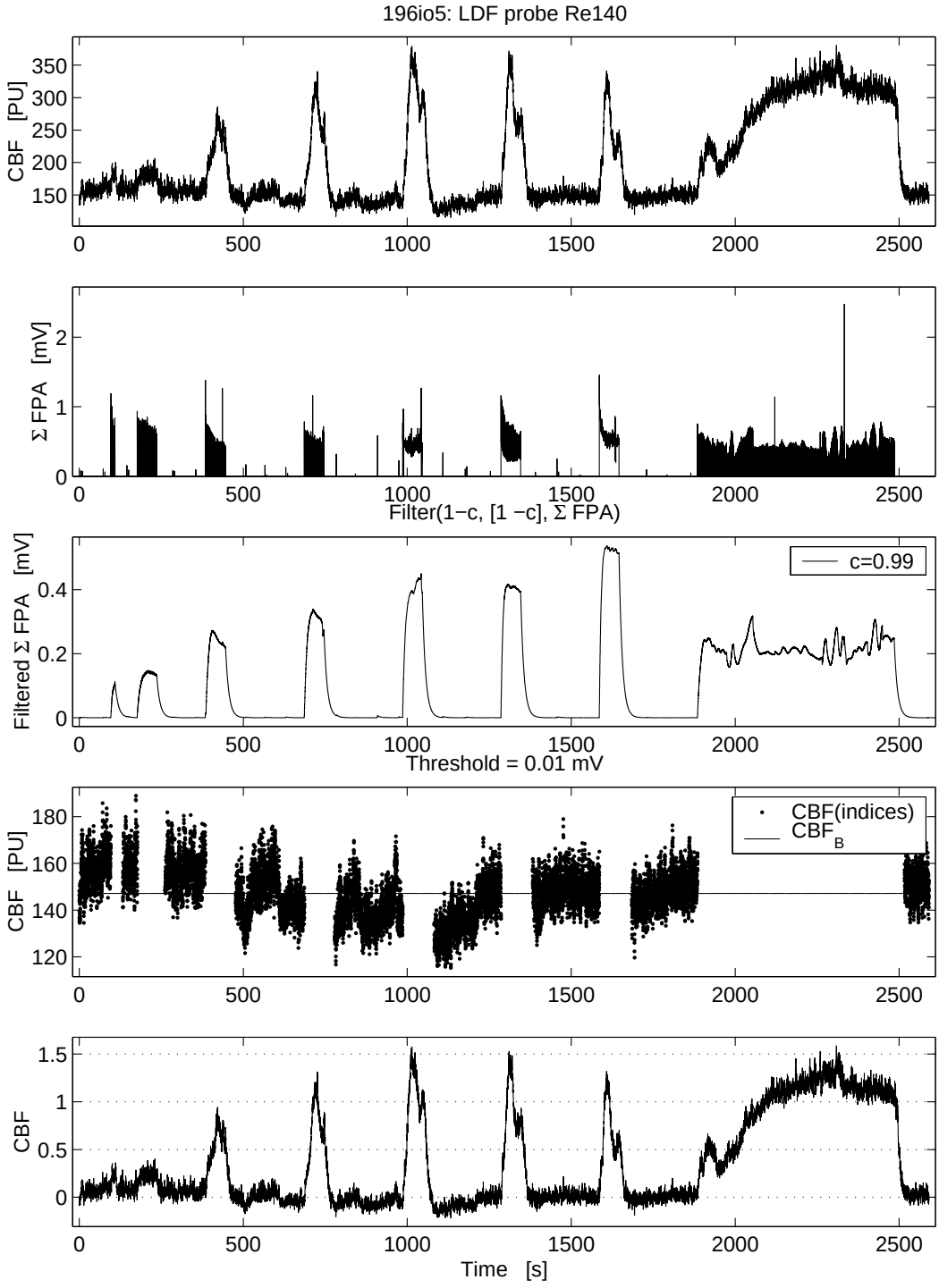

Figure B.3: Illustration of baseline calculation for the LDF probe `Re140` for the inferior olive time series 196io5. Top panel: Original CBF signal in perfusion units. Second panel: The 10 Hz sampled summed field potential amplitude signal. Third panel: The filtered summed field potential signal. Fourth panel: The CBF samples used for baseline calculation as well as the calculated baseline level. Bottom panel: The final relative CBF signal.

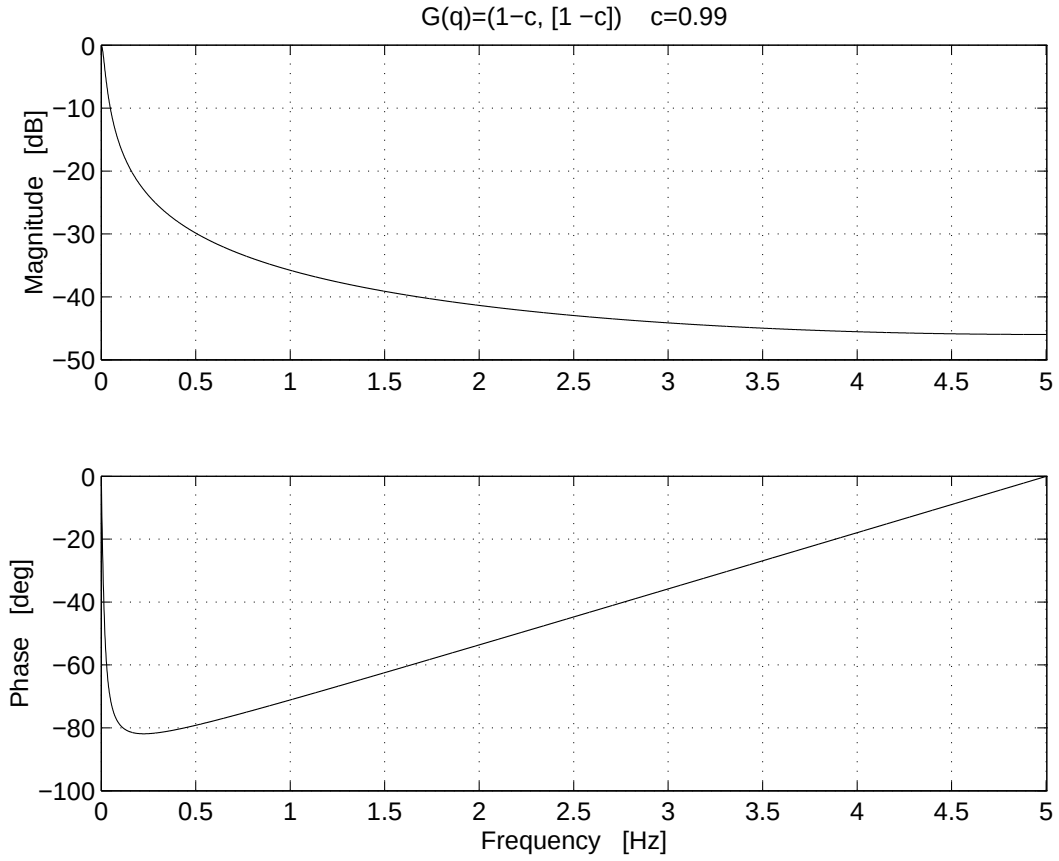

Figure B.4: Bode plot of the discrete linear low-pass filter $G(q) = \frac{0.01}{1-0.99 \cdot q^{-1}}$. Note that only very low frequency components pass un-attenuated through the filter.

B.5 Selection of Samples for Plots

Since this thesis only investigates the features of evoked activity, we have no interest in the dynamics responsible for the baseline level.

With the purpose of focusing figures on the evoked activity, this section describes how to extract and plot the relevant samples. The procedure, which is illustrated by Figure B.5, consists of four steps:

(0) The starting point, that is, the CBF signal resampled at 1 Hz is shown in the top panel of Figure B.5.

(1) The time axis is divided into bins of the size of the sampling interval of the CBF signal, i.e., 0.099936 s, and the field potential amplitudes within each bin are summed. The resulting 10 Hz sampled signal $\sum FPA$ is then resampled by a factor 10. This signal is shown in the second panel of Figure B.5.

(2) In order to provide a smooth signal which is zero when there is no stimulation and transients in the CBF signal have died out, and non-zero when the CBF signal is significantly larger than its baseline value, the $\sum FPA$ signal is passed through the discrete linear filter $G(q) = \frac{0.075}{1-0.925 \cdot q^{-10}}$. In order to avoid discarding the samples right after on-set of stimulation, the filter is shifted 10 samples, that is around 10 s, backwards in time. The resulting filtered signal

$$q^{-10} G(q) \sum FPA \tag{B.7}$$

is shown in the third panel of Figure B.5. Also the discriminating level, which has been defined as 1 % of the maximum value of the filtered signal, is shown.

(3) The sampling instants, at which the filtered signal $q^{-10} G(q) \sum FPA$ is above the discriminating level, are found. The CBF samples at these instants are shown in the fourth panel of Figure B.5.

(4) Now the parts of the time axis which have been selected are glued together in order to emphasize the interesting parts of the signals. The resulting plot of the CBF signal appears as shown in the bottom-most panel of Figure B.5.

This procedure apply the same strategy of using filtering of the input signal for picking out samples which in Appendix B.4 has been applied for definition of the baseline level.

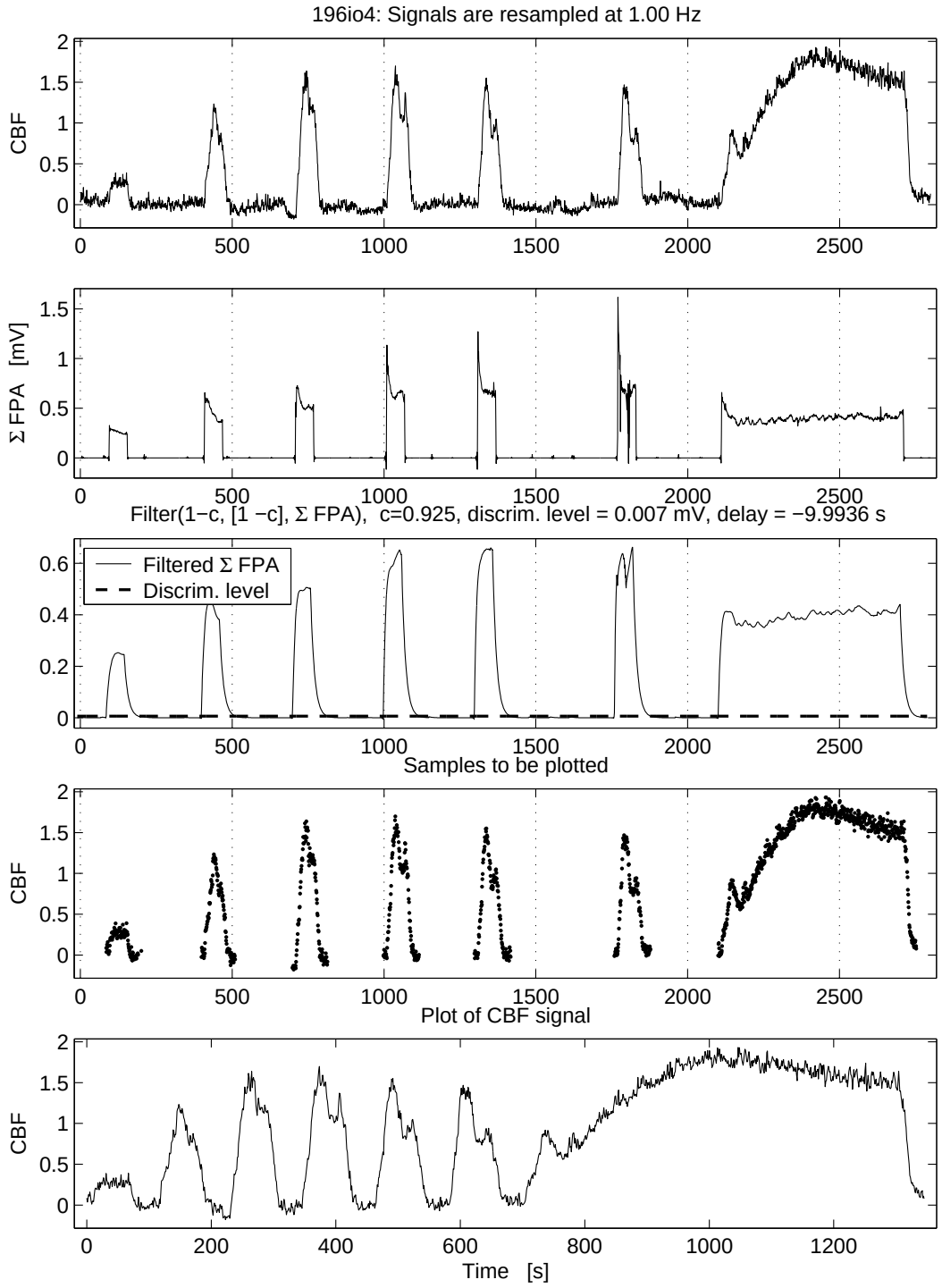

Figure B.5: Illustration of the procedure of selecting samples to be plotted. Top panel: Original CBF signal resampled at 1 Hz. Second panel: The summed field potential amplitude signal resampled at 1 Hz. Third panel: The (resampled and) filtered summed field potential amplitude signal and the discriminating level. Fourth panel: The CBF samples to be plotted. Bottom panel: The CBF trace which results from gluing together the interesting parts of the original signal.

Appendix C

Frequency Domain Considerations

These frequency domain considerations are only of relevance for linear functions and operators.

C.1 Considerations concerning Functions

C.1.1 Continuous-Time Functions

In the analysis of continuous systems, we use the *Laplace transform*, which is defined by [37, (Sect. 8.2.1)]

$$F(s) = \mathcal{L}\{f(t)\} = \int_0^\infty f(t)e^{-st}dt. \tag{C.1}$$

C.1.2 Discrete-Time Functions

The z-transform is a mathematical tool for the analysis of linear discrete systems. It plays the same role for discrete systems that the Laplace transform does for continuous systems.

Let k refer to the sampling instant $t = k \cdot \tau$, where τ is the sampling interval, and let $f(k\tau)$ be the sampled version of $f(t)$. The *z-transform* is defined by [37, (Sect. 8.2.1)]

$$F(z) = \mathcal{Z}\{f(k)\} = \sum_{k=0}^{\infty} f(k)z^{-k}. \tag{C.2}$$

C.1.3 Relationship Between Functions of s and z

Certain behaviors of a linear system result from different pole locations. The characteristics in the z-plane are related to those in the s-plane by the expression [37, (Sect. 8.2.3)]

$$z = e^{s\tau}. \tag{C.3}$$

C.2 Considerations concerning Operators

C.2.1 Continuous-Time Operators

Let p denote the time derivative operator $p = \frac{d}{dt}$. Then the transfer function $G(p)$ is a polynomial operator.

C.2.2 Discrete-Time Operators

Let q denote the forward shift operator $qx(k) = x(k+1)$. Then the transfer function $G(q) = \sum_{k=1}^{\infty} g(k)q^{-k}$ is a polynomial operator. $G(q)$ is also termed a filter.

C.3 Connections between Functions and Operators

C.3.1 Continuous-Time Descriptions

The complex function $G(s)$ is the Laplace transform of the operator $G(p)$.

C.3.2 Discrete-Time Descriptions

The function $G(z)$, which is defined on $\mathbb{C}$, is the z-transform of the filter $G(q)$. The properties of the filter $G(q)$ are quite analogous to those of the function $G(z)$ [58, (Sect. 3.2)].